IWAIS 2013 ADVANCING THE SCIENCE OF ICING

PROCEEDINGS

IWAIS

15TH INTERNATIONAL WORKSHOP ON ATMOSPHERIC ICING OF STRUCTURES

SEPTEMBER 8 - 11, 2013

ST. JOHNS, NEWFOUNDLAND & LABRADOR
CANADA

Organized by:

COMPUSULT

Proceedings of the 15th International Workshop on Atmospheric Icing of Structures (IWAIS 2013)

Keywords: Atmospheric Icing, Ice Storm, Icing, Ice Accretion, Ice Accumulation, Freezing Precipitation, Glaze Ice, Rime Ice, Wet Snow, Sea Spray, Anti-icing, De-icing, De-icer, Icing Forecasting, Icing Climate, Conductors, Insulators, Flashover, Transmission Lines, Wind Turbines, Wind Energy, Ice Adhesion, Superhydrophobic, Icephobic, Icing Measurement, Icing Modeling, Ice Loads, Ice Detection, Icing Monitoring

ISBN 978-0-9936284-0-5

IWAIS 2013 Overview

The 15th International Workshop on Atmospheric Icing of Structures (IWAIS 2013) was held in St. John’s, Newfoundland and Labrador, Canada from September 8 to 11, 2013. Compusult was very honoured to host and organize this event.

Atmospheric ice accumulation on structures is a serious and costly problem affecting a wide variety of human activities such as electric power transmission and distribution, transportation, wind energy, oil and gas production/exploration, telecommunications, Arctic and sub-Arctic operations, etc. The purpose of this workshop was to facilitate scientific and technical information exchanges among utilities and other industries operating in icing-prone environments, as well as meteorological services, technology companies, research centres, laboratories, and universities.

IWAIS 2013 included over 50 oral and poster presentations, thus providing a unique opportunity to present the latest research, development, and newly acquired knowledge in areas such as:

- Methods for protection against icing and reduction of risk and damage, such as anti-icing methods and hydrophobic coatings
- Theoretical studies and verification testing for in-cloud icing, wet snow accretion and freezing rain, and accumulation and shedding mechanisms
- Mapping and assessing climatic risks affecting various structures
- Techniques for icing forecasting and alerting systems
- Field observations and storm analyses for various types of atmospheric and spray icing
- Basic research and laboratory measurements associated with the physics and dynamics of ice accretion
- Analyses of the mechanical effects of ice accumulation on structures
- Effects of storms and icing on telecommunications, electrical distribution, and wind energy production systems
- Electrical properties of iced conductors and insulators, and flashover
- Catastrophic ice storms, analysis of meteorological situations and damage incurred, and the possibilities for forecasting such events

IWAIS 2013 attracted presenters and attendees from many different organizations and over 14 countries. This document contains the papers and posters submitted by workshop registrants on which the IWAIS 2013 presentations were based. They appear in the same order in which the workshop sessions and presentations took place.

On behalf of Compusult and the International Advisory Committee, I sincerely want to thank all those who participated in IWAIS 2013 and who contributed to these proceedings and the success of this workshop.

Paul Mitten, Vice-President, Compusult Limited

ABOUT COMPUSULT

Compusult Limited was the technical host and organizer of IWAIS 2013.

Compusult is a Canadian-owned and diversified Information Technology company in operation since 1985. We also specialize in physical environmental applications, including ice accretion studies, probabilistic ice and wind loading assessments on land-based and marine structures, ice accretion modelling and measurement, and many different types of data acquisition, monitoring, and management systems.

Compusult has previously completed ice accretion related projects and studies for clients such as Environment Canada, National Research Council Canada, Newfoundland and Labrador Hydro, Newfoundland Power, and Black & Veatch. We've also worked with leading ice accretion experts from the Technical Research Centre of Finland (VTT), University of Alberta (Canada), and other agencies and institutions.

Additionally, Compusult has extensive experience developing, implementing, and enhancing time-dependent and simple numerical models and alert systems for atmospheric icing and wind loading on structures, with respect to freezing precipitation (including icicle growth), wet snow, in-cloud (rime), and sea spray ice accretion.

For information on IWAIS 2013 and access to publicly available conference materials, please visit the workshop website at: **iwais.compusult.net**.

IWAIS 2013 apps will be freely available for most popular mobile devices at least until December 31, 2013 and possibly longer. Please visit your favourite app store and search for "**IWAIS**" to locate and download the app.

Session 1: Anti-icing and De-icing

Strategies and Status of Anti-icing and Disaster Reduction for Power Grid after the 2008' Ice Storm in China

JIANG Xing-liang[1], DONG Bing-bing[1], DONG Li-na[2], LU Jia-zheng[3], ZHANG Ji-wu[4]

1. State Key Laboratory of Power Transmission Equipment & System Security and New Technology & School of Electrical Engineering, Chongqing University, Chongqing 400030, P.R.China; *Email: xljiang@cqu.edu.cn

2. Urban Power Supply Bureau, Chongqing Electric Power Corporation, Yuzhong District, Chongqing 400067, P.R.China;

3. Power Transmission and Distribution Equipment Anti-icing and Reducing-disaster Technology Laboratory of State Grid, Hunan Electric Power Company Research Institute, Changsha 410007, P.R.China;

4. Huaihua Power Bureau Design Institute of Hunan Electric Power Company of State Grid, Huaihua 418000, P.R.China

Abstract — The ice storm of 2008 caused serious damage to power systems in Southern China, with more than 100 billion yuan ($ 16 billion) in direct economic losses. In order to prevent the large-scale ice disaster in grid, the Chinese government, the State Grid and China Southern Power Grid attach great importance to prevent the ice disaster in grid. The accident of the ice disaster has been reduced significantly by strengthening management, conducting scientific research, and applying new technologies and new methods. After five years of efforts, the ice map has been developed, and some de-icing methods have also been studied in China, such as coating, laser, robot, and AC/DC ice-melting. The experience of engineering applications and practices shows that the coating can not meet the requirements in a large area. Laser, robotic, and microwave technology are not yet mature and can not be used in engineering. AC ice-melting method consumes a large amount of reactive power. DC ice-melting is a good method with low power requirement, high efficiency, and convenience. Therefore, the fixed and mobile DC ice-melting devices are developed. The large fixed ice-melting device can meet the requirements in a range of 100 km radius, with a maximum capacity of 1200 MW. The small mobile ice-melting devices can only be used for local line, with a power of 100 kW to 500 kW and weight of 100~300 kg. So far, fixed DC ice-melting devices have been installed in more than 200 substations in State Grid and China Southern Power Grid in China. The DC ice-melting mobile devices have been applied in all the power companies with serious icing. Also, the ice-melting has been solved for the overhead ground and optic cable. These methods and technologies play an important role in Chinese grid in recent years and reduce the number of ice disaster accident effectively.

Keywords — ice disaster; power systems; anti-icing; de-icing; AC/DC ice-melting

1 INTRODUCTION

Prior to 2008, it has been often recorded the ice and snow disaster of power grid in China. The ice accretion has lead to extensive mechanical damages, such as sight of twisted towers or conductors weighed down to the ground, and serious flashover of insulators, etc. The catastrophic ice storm that occurred in the early 1980s in Guizhou, in the early 1990s in Hubei and Qinghai, in the winter of 2004-2005 in Hunan, Hubei and Chongqing, China, had affected the secure performance of the power system involving one or two Province Grid Corporation of China in one or two Province of China [1-2]. In January and February 2008, a severe ice and snow disaster occurred in Southern China, and caused serious damage to many power networks, including Hunan, Jiangxi, Zhejiang, Hubei, Guizhou, Anhui, Yunnan etc. involving 14 provinces, a total of more than 570 counties power networks and direct economic losses of more than 100 billion RMB (16 billion US dollars) [3-4]. The extremely ice disaster not only caught researchers' attention at home and abroad, but brought the Chinese top readers' attention. After the disaster, the Chinese government instructed “The researchers must make serious efforts to investigate anti/de-icing techniques in order to a trust of power grid”.

As global warming and environment worsening intensifies, the natural disaster events caused by the extreme climatic conditions such as ice disaster are more unpredictable. It is also difficult to be sure the occurrence of similar major ice disasters in the next few years, or even decades. Therefore, Chinese government gave high priority to take seriously anti/de-icing techniques of the power grid long-term since. It has accumulated rich engineering experiences on scientific studies, routine maintenance and emergency measurements. This report analyzed and summarized experiences and results of China power grid response to the sudden ice disaster after the 2008 ice storm disaster, and compared in detail the actual results of various measures taken in engineering applications.

2 ICING CHARACTERISTICS OF POWER GRID IN CHINA

Since the geographical and climatic features of China cover a vast territory, inevitably the ice accretion was occurred often in power transmission lines. The ice and snow storm of power grid were mainly occurred in Hunan, Hubei, Henan, Jiangxi, Anhui located in central China, and Yunan, Guizhou, Sichuan in southwest China, Hebei, Shanxi, Neimeng, Beijing, Tianjing in northern China, and Qinghai, Shaanxi in northwest China, and Liaoning in northeast China [5]. There are the following characteristics throughout ice accident of China power grid in the past few decades:

(1) The power grid blackouts caused by ice were mainly occurred in central China and southwest China mainly as the plenty of water and complex geographical and climatic features because of intersection of northern cold air and southern warm air, such as “South stationary peak” and “Kunming quasi-stationary peak”. Power line covered snow is easy to form because of the dry and cold climate in northern China. While the temperature of outside power Transmission Equipment was rarely nearly zero due to the warm climate in winter in southern regions, so it is rarely meet the meteorological conditions requirements of icing.

(2) The types of ice accretions are mainly affected by geographical and climatic conditions in China Power Grid. Glaze is commonly seen in Hunan, northern Guangdong, southern Jiangxi, Hubei, Henan and southern Anhui and other hilly areas. Rime is usually appeared in Yunnan-Guizhou Plateau, or more than 1 km, especially 2-3 km high altitude mountain regions. Snow or rime is mainly occurred in north China. Ice freezing fog is common in the early winter and late spring of southwest and Qinghai etc. high-altitude regions of China. While the crystalline rime is formed in windless night in cold winter due to radiation cooling in Yunnan, Guizhou, Sichuan regions.

(3) The grid icing is greatly influenced by altitude and “micro-topography, micro-climate”. In general, the higher the altitude is, the easier the icing occurs [5-6]. The mechanical and electrical faults of power transmission equipments are adversely occurred in winter from October to November to next March to April, especially in January. The results show that the ice accidents occurring in China have such characteristics as long duration, high frequency of occurrences, large coverage area and great loss to national economy, etc. For example, the average ice lasted for 40-60 days, even 80-90 days every year in alpine and cold regions in China.

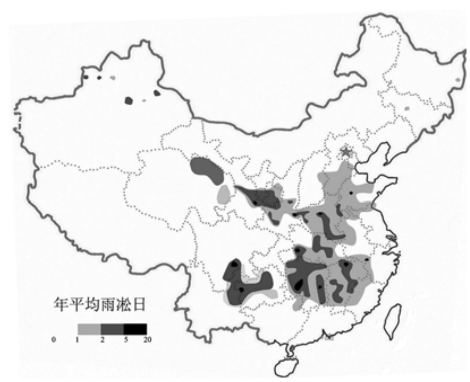

Fig. 1 Annual statistic of freezing rain days in China

In general, the higher the annual average temperature and humidity are, the more severe the icing occurs in the vast southern region of China. While the lower the annual temperature, humidity and precipitation are, the smaller or almost the icing probability is in the vast northern region of the Yellow River. It is also difficult to appear glaze mainly occurred in Southern regions even if the icing occurs in the local water-rich areas. The type of icing is mainly based on freezing fog ice i.e. rime or frost rime in north China. Therefore, flashover of insulators may occur in severe contamination areas, but it has not been identified as a significant risk factor that affects the mechanical properties of the transmission line. The annual average glaze or rime days in cold regions are closely related to icing accidents of transmission line. Glaze ice has been identified as a significant risk factor that affects the satisfactory reliability of outdoor insulators. Through the meteorological data statistics, the distribution of the annual average Glaze day of China is shown in Figure 1. From Figure 1, it can be observed that the glaze is distributed mainly in central and southwest of China, especially near the Yangtze River provinces. The glaze days are range for 20-30 in alpine regions, while the glaze ice is less than 5 days in alpine regions.

3 Coping strategies

3.1 Scientific research

After 2008 ice disaster, China power grid start the scientific and technological key tackling item in anti-icing and mitigating plans. Based on the results of anti-icing technology at home and abroad and ice characteristics of China power grid, the State Grid Corporation of China and China Southern Grid Corporation make research program on key technologies of anti-icing and mitigating. This plan mainly consists of power grid planning and construction, production maintenance, dispatching, power supply service and emergency disposal, and reflects the basic requirements "prevention first, comprehensive management, minimum loss, fastest recovery" for anti-icing and mitigating related to the ice disaster of power grid. The grid mitigation, early warning and monitoring ice storm, ice emergency and disaster recovery constitute scientific and technological support for anti-icing and mitigating and scientific development from the State Grid Corporation of China to building a strong and smart grid. The following eight breakthroughs for China Power Grid are as follows:

(1) Propose differentiated grid planning and construction standards, make further enhance the strategic transmission channel, backbone power lines at various voltage levels and withstand ice storm of power transmission and distribution equipment to the key user facility;

(2) Develop support systems of large power grid emergency communication system and emergency command, make further improve the emergency support and command capability;

(3) Research the law of hazard meteorological and icing mechanism of power transmission equipment, develop warning system of ice disaster weather and icing monitoring system transmission line, make further enhance the ice comprehensive management capabilities;

(4) Develop the high-capacity, high efficiency, auto-national electric ice-melting equipment and flexible and practical mechanical de-icing equipment, make further improve the de-icing efficiency of power transmission equipment;

(5) Put forward the technical measures for the fastest recovery and minimal damage for power grids and the power equipments in the case of extreme weather disasters, minimize the loss of the economy and society caused by natural disasters;

(6) Develop the new technology and materials of anti-icing or de-icing for electrical equipment;

(7) Research common technical problems and measures of anti-ice and mitigation for rural distribution network in high altitude and cold regions to provide technical support for the anti-ice and mitigation for rural distribution network;

(8) Make enhance the test ability construction respond to natural disasters, provide perfect research tool to in-depth study characteristics of electrical equipment resist in natural disasters.

3.1.1 Current research projects

The current research projects are mainly summarized as follows:

(1) "Study on meteorological formation rule and early warning system of power grid based on the large area and long duration icing conditions" researched systematically the icing characteristics, rules and mechanism of Hunan power grid, put forward the anti-ice, ice-melting technology, and achieved the engineering application.

(2) "Study on icing monitoring and early warning and emergency measures of transmission lines", "Research on icing warning system of power lines", "Study on prevention and mitigation disaster key technologies of transmission equipment in East China Power Grid" and

"Study on icing forecasting and monitoring warning system of ice conditions" developed the icing monitoring and early warning systems, proposed the icing emergency measures, improved the performance on power transmission equipment to withstand severe environmental conditions, realized device status monitoring by online monitoring combined meteorological environmental risk warning, improved efficiency of the power grid against catastrophic climate, make power transmission equipment in severe climates with higher reliability, more targeted operation and maintenance, closer to the equipment status of scheduling safety assessment. It provides a strong technical support for reduce losses of the freezing rain and snow disaster.

(3) "Research on 220 kV DC transmission line ice-melting technology", "Research on 220 kV AC transmission line ice-melting technology", "Research on 500 kV DC transmission line stationary ice-melting technical solutions and equipment development", "Research on 500 kV DC transmission line move financial ice-melting technical solutions and equipment development" and "AC-DC current characteristics of ice-melting" solved the theoretical research and development of research tools, equipment development, implementation of technical standards and the demonstration projects and other key technologies.

(4) "Artificial method of de-icing", "Research on icing or melting flashover performance of power transmission equipment" and "research on mechanical de-icing technology of transmission line" proposed the conditions, timing, methods and safety measures full requirements carried out artificial de-icing, developed manual de-icing procedures (trial), prepared standardized practices manual deicing, standardized firstly artificial deicing method in the domestic; proposed mechanical de-icing methods of transmission line used various voltage levels, split type conductors, research and drafting the manual de-icing precautions and guidelines, developed successfully a simple mechanical de-ice equipment, a single wire mechanical de-ice equipment, split wire mechanical de-ice equipment.

(5) "Study on anti-icing and de-icing design parameter optimization and universal design of transmission project in medium or heavy icing regions" combined with the actual situation of Hunan, Zhejiang and Sichuan power grid, has finished the completion of the transmission lines and foreign standards compared, statistical analysis of ice thickness under reproduce ice age, influence of altitude on ice thickness, meteorological parameter values under icing conditions, influence of micro-topography and micro-climate on uneven terrain tension, uneven tension value jumps off the ice, ice load combinations, A-type string mechanical testing, and isolating switch substation de-icing measures, anti-icing flashover of equipment external insulation, optimized anti-ice design parameters of the power transmission engineering, proposed universal design recommendations in of line tower heavy ice.

3.1.2 Progress and results

In terms of ice disaster prevention technology, the results are mainly the design standard of differentiation with grid, anti-icing and de-icing universal design in heavy ice regions, anti-icing standards technical and economic analysis of transmission line and study of anti-icing flashover type of insulators and anti-icing coatings. In terms of ice disaster disposal technologies, they have been developed micro-automatic weather stations, multi-cylinder measuring ice sensors, unmanned small grid monitoring, AC/DC ice-melting devices transmission lines used various voltage level. In terms of ice disaster recovery technology, they have been solved the grid de-icing operation mode, ice disaster recovery principles and control technology. The specific results are as follows:

(1) Study on operation monitoring and early warning and emergency measures of transmission line covered ice, study of geographic information system on ice disaster monitoring and integrated analysis system of transmission line: achieved automatically drawing ice maps, temperature maps, precipitation maps and corresponding forecast maps, improved mapping efficiency of distribution ice area and intuitive of ice display, reduced the labor intensity of the system running, helped staff at all levels to grasp the development trend of ice conditions, provided basis for decision making in order to ice protection and mitigation.

(2) Research on 220 kV transmission line DC ice-melting technology and 220 kV transmission line AC ice-melting technology, as well as of 500 kV

transmission line reconstruction DC ice-melting device development and 500 kV lines removable DC ice-melting technical solutions and device development: proposed firstly combination “fixed” with “mobile” DC ice-melting method of transmission line, developed 25 MW, 2 000 A removable DC ice-melting devices, 4.2 MW, 1 400 A fixed DC ice-melting device, the world's first 10 kV, 26 MVar AC series capacitor compensation ice-melting device; provided strong support for anti-ice disaster technology and equipment of the power grid, developed DC ice-melting functional specification guidelines.

(3) Development of artificial de-icing method and apparatus: standardized firstly manual de-icing method, developed trail procedures for artificial de-icing; and developed the de-icing tools of conductors, towers, insulators, automatic mechanical de-icing device of conductors, ice-melting apparatus with electric hot air, steam ice-melting device, de-icing equipment of substation to fill the gaps domestically.

(4) Technical specification guidelines on anti-icing disaster of power grid: proposed adjustment principle of power grid matching the implementation of ice-melting used short-circuit current and ice disaster recovery principle of power network, minimized the impact of power blackout on society and the grid itself.

(5) Study on super-hydrophobic coatings and umbrella structure optimization used for anti-icing flashover type of insulators, sheds configuration optimization of composite insulators used in icing regions.

(6) Research, development and application on emergency command centers and emergency platform State Grid Corporation of China: “Construction norms of the State Grid Corporation of emergency command center” and the relevant functional specification, effectively regulated and guided emergency management and emergency command center 30 provincial network system of State Grid Corporation of China, developed a software on emergency command information platform of power grid, and has been applied to the emergency command center of State Grid Corporation of China, Jiangxi and Ningxia Electric Power Company.

3.2 Strengthening design

After the ice disaster in 2008, the power grid has been adopted the fine design strategy in China. It has been improved the design standards roundly and revised the contents from strengthening the design according to the ice condition in the area where ice damage has been reported. Firstly, the 110-330 kV power grid fortification standard have been enhanced from once every 15 years to 30 years, from once every 30 years to 50 years for 500kv power grid, and the 750 kV power grid fortification standard is once every 30 years, and the building UHV projects fortification standards considerate to be once every 100 years by referring to the building structure design provisions of the state. Secondly, it can be increasing the design technical conditions in the medium icing area, insisting both the reliability and the economy, and improving the ability to resist ice in the widespread power grid reasonably. Thirdly, it is able to keep operation safely and stably for the important lines such as the UHV grid, the core network frame for different voltage level, the transmission lines of large-scale hydropower, coal and nuclear power, international and interregional network transmission line, some load power lines, etc. by indifferent planning and design under the severe natural disaster condition that have exceeded the general line fortification standard. Finally, it can be improving the construction standards for local line segment as it is particularly difficult to repair.

3.3 Strengthening operation and maintenance

In the daily operation of the transmission line, it can be conducting long-term observation, surveys and on-line monitoring for the icing situation of power grid by a series of measures such as constructing icing observation stations and observation sites, installing the icing on-line monitoring system, etc. At present, the China power grid has applied many kinds of icing monitoring technology such as based on the meteorological parameters and the tension change of the icing lines and the angle change of the insulators, video monitoring and so on, and has been achieved satisfactory results. But there are also some problems need to be solved. There are mainly the following respects:

(1) Artificial observation: It is able to know visually and clearly the line icing status. It can obtain the weather and ice conditions within a specific range in the icing observation stations, and it is beneficial to study on the icing model and mechanism. But it has the smaller

observation range of the line icing, higher labor intensity, higher investment, and the larger error between the test results and the actual icing.

(2) On-line monitoring

(a) Mechanics model method of icing monitoring: it can determine the line icing conditions by the changes of mechanical parameters obtained by monitoring device. According to the monitoring equipment, it can be divided into the icing monitoring model based on the traditional sensor, the icing model based on the optical fiber grating sensor and the icing model based on the traveling wave sensor. This method is widely used around the world, as the parameter setting is simple in the model and it is easy to calculate. But it also has a certain deviation to the actual icing situation, and further research needs to be done by the scholars.

(b) The image monitoring method: The image contains a large amount of information and it observes visually. But the camera lens surface will be iced and the image is vague and can't be recognized under the lines icing condition. As the resolution of image obtained by the camera is lower at present, the accuracy of the observation results will be badly affected. And the camera shooting range is limited, it is unable to monitor comprehensively when the span is large and is not ideal under the climatic conditions (such as fog). The weather is bad and has long duration for several days in the severe ice conditions, and the solar battery energy is limited. So it cannot start the monitoring equipment, such as camera. Therefore, the difference between the results of the existing image processing method and the actual icing is the larger.

(3) Small-sized automatic weather station: The monitoring parameters of this method as lacking of two parameters of water drops contain a certain differences. Moreover, the influence of the two parameters on the icing characteristics and icing quantity is the larger. Therefore, this method usually serves as the qualitative identification method for icing occurs or not.

3.4 Disposal measures

Operation and monitoring personnel take the following appropriate measures to deal with once they found that the ice thickness of power lines is larger than the design standards by on-line monitoring system.

3.4.1 Mechanics disposal measures

Currently, ice-melting with short-circuit current is one of the key technologies to prevent the Chinese power grid from ice storms. Both ac and dc can be used to melt ice on transmission lines. Compared with ac ice melting, dc ice melting is more advantageous for long high-voltage power lines with large cross-section conductors because reactive losses are eliminated. It has been developed, installed, and successfully used on a large scale in China to melt ice on long 500 kV lines

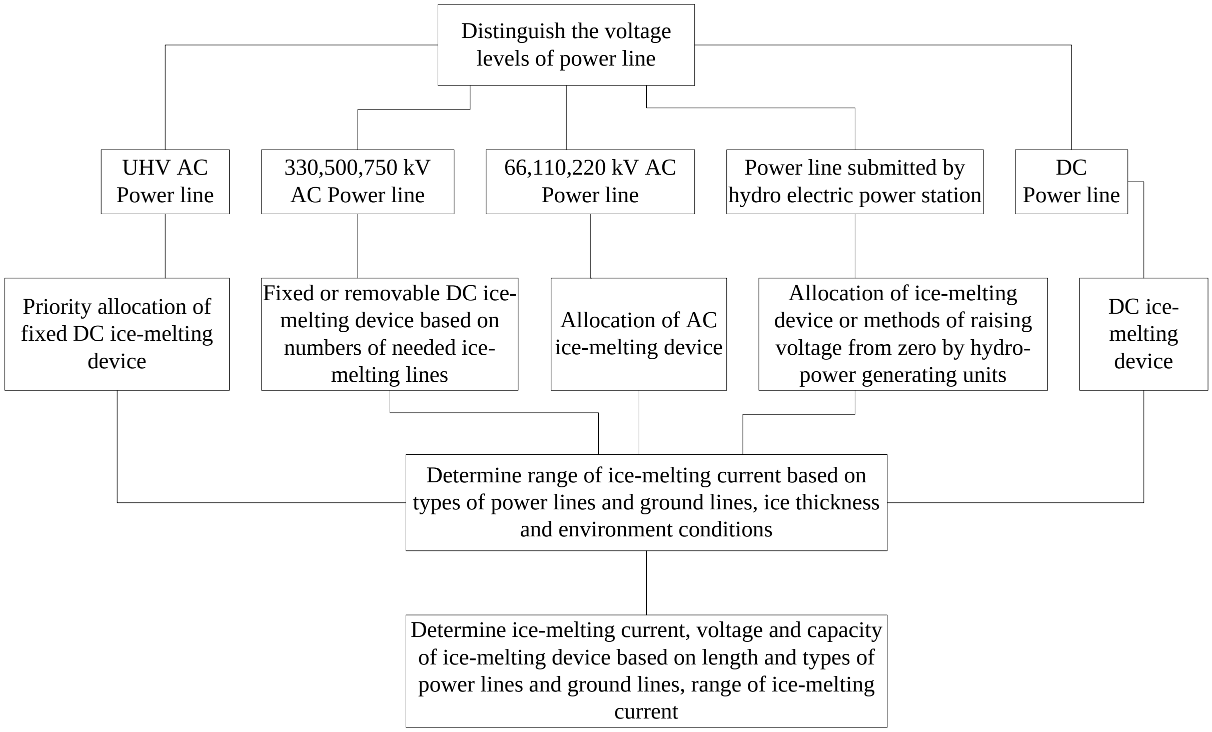

Fig. 2 Allocation flowchart of ice-melting device

with large, bundled phase conductors. In China, both the State Grid Corporation and the Southern Power Grid Company have taken dc ice melting as the main method to resist the ice accident on electrical network after the ice storm in 2008 [7], and they have put a lot of human, financial, and material resources to develop the methods and equipment of dc ice melting [8]. At the end of 2008, a set of ice-melting equipment, with a rated capacity of 120 MVA, and rated output current of 6 000 A, has been successfully developed in China. It can be applied to melt ice on the quad bundles lines with a cross-sectional area of 4*400 mm^2. In early 2011, the dc ice-melting equipment was applied to melt ice on the 110 kV, 220 kV, and 500 kV lines in the Hunan and Guizhou Power Grid, respectively. Allocation process of the Ice-melting device is shown in Figure 2.

3.4.2 Electrical disposal measures

(1) Anti-icing flashover type of composite insulators

After the 2008 ice disaster, many improved composite insulators have been designed and produced for anti-icing purpose by composite insulator manufacturers. The specimens consist of four types of composite insulators applied to 110 kV AC system (type A to D), another four types applied to 220 kV AC system (type E to H) and four more types applied to 500 kV AC system (type I, type J, type K and type L), see Figure 3. Type A, type E and type I are standard composite insulators and the others are insulators improved by insulator manufacturers for icing regions [9].

Fig. 3 Photos of ice-covered composite insulators.

The result indicates that, firstly, icing flashover performance of the improved composite insulators for icing regions is not always superior to that of the standard composite insulators when icing is light. Meanwhile, E_h (flashover voltage gradient of dry arcing distance) first increases and then decreases with the increase of CF (creepage factor, namely the ratio of creepage to dry arcing distance). Secondly, when icing is moderate, the icing flashover performance is influenced by such main factors as shed diameter, shed spacing and the configuration of sheds with different diameters. In this situation, E_h of the improved composite insulators is higher than that of the standard composite insulators, and ice-covered composite insulator with three or four different shed diameters has better flashover performance than that with two different shed diameters. Thirdly, when icing is heavy, compared with the moderate icing condition, the difference of E_h between the improved composite insulators and the standard composite insulators diminishes. Finally, when icing is moderate or heavy, there is no obvious regular relation between CF and E_h. The shed diameter, shed spacing and the configuration of shed with different diameters for composite insulators have remarkable effect on the AC/DC icing flashover performance.

(2) Optimization arrangement of insulator strings

The V-type, inverted v-type, insulator string and the insulator string composed by insulators with larger and smaller shed diameters alternatively can effectively increase the icing flashover voltage of insulator strings, so they are practicable approaches for the design and renovation of transmission lines in ice-covered regions.

(a) For various arrangements(see Figure 4), the icing flashover voltage of the horizontal string is the highest, the V-type string takes the second place, and the vertical string is the lowest. It is found that the flashover voltage of V-type insulator string is about 10%-20% larger than that of single insulator string under the same icing condition [10]. And the flashover voltage of double insulator string is 5%-6% for lower than that of single insulator string under the same icing condition [10-11].

(b) Using the type of iced insulators connected with alternately large and small diameter sheds (CALSDS, see figure 5) can improve icing flashover voltage. The research results show that: The icing flashover voltage of insulators arranged with the type of CALSDS with "3+1" and "4+1" is 14.6% and 12.0% higher than that of single insulator string arranged vertically, respectively.

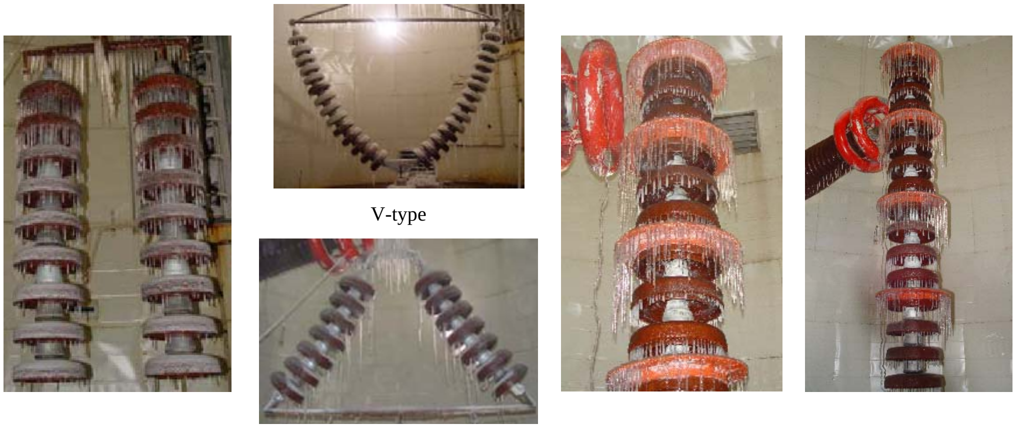

II-type Inverted V-type "2+1" "3+1"

Fig. 4 Arrangement types of insulator strings (DC XZP-210) [11]

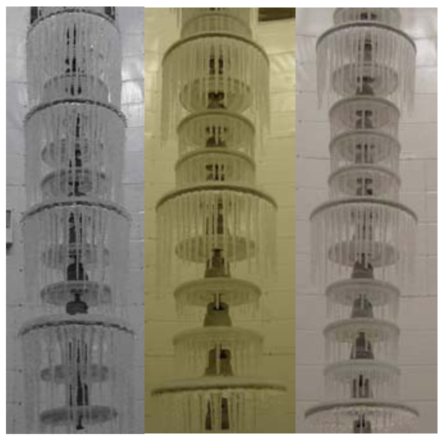

(a) "2+1" (b) "3+1" (c) "4+1"

Fig. 5 Icing results of insulator string with different connected types (FC–100/146) [10]

(c) It can increase the insulator string length to in heavy icing regions.

(d) The flashover voltage gradient of dry arcing distance is 70 kV / m (AC), 65 kV / m (DC) respectively.

(3) Applications of hydrophobic coating

Based on a large number of experimental investigations carried out on icing phenomena of insulators at Chongqing University over the last ten years, it is observed that PRTV coating material exerts no effect on increasing flashover voltage of iced insulators. Compared with the insulator string which is not coated with PRTV, the icing flashover voltage of the insulator string coated with PRTV decreases by about 10%-15%. Hence, the PRTV coating (permanent room temperature vulcanized anti-contamination flashover composite coating) cannot effectively prevent ice coating on insulator surface, thus it is not recommended to use PRTV coating to prevent icing flashover in icing regions.

4 Power grid icing events and their impact in nearly five years

From November 2009 to January 2010, a severe ice and snow event was occurred in Henan, Shanxi, Hunan, Jiangxi, Zhejiang, Liaoning, Hebei, Shandong in China, involving various voltage levels of power lines from 10 kV to 500 kV. The total number of tripping reached 231 times of 110-500 kV power transmission lines.

From January to February in 2011, the snow and freezing weather was suffered from Zhaotong City of Yunnan Province, the ground icing thickness is up to 10 cm, and the power line icing was more serious than the ice disaster in 2008. The icing constitutes a challenging problem for the safety and stability performance of the main power grid of Zhaotong power supply bureau.

From December 2011 to January 2012, the ice events were occurred in 57 transmission lines from 110 kV to 500 kV in Guizhou power grid, 29 power lines from 10 kV to 500 kV in Yunnan power grid, 4 lines for 110 kV in Guangxi power grid. The maximum icing thickness was 5, 24 and 8 mm, respectively.

From November 2012 to February 2013, the ice events were occurred in 113 lines for 35 kV and above in Hunan power grid. The ground snow thickness reached 30 cm in part of Anhui, and caused more than 149, 000 households to be without power. The sight of conductors weighed down to the ground by ice accretion and high wind speeds in Ningbo power grid has made a strong impression on the public and press. The ice events were occurred mainly in Zhaotong, Qujing, Guizhou Guiyang, Bijie, Liupanshui and Zunyi cities of Yunnan Province and Guilin, Hechi, Liuzhou, Hezhou cities of Guangxi Province and other regions in the China Southern Power Grid, the maximum icing thickness is up to 14 mm, without the appearance of line tripping, disconnection, inverted pole and so on.

In the past five years, the power grid in China is still suffered from the impact of ice disaster weather each year, and leading to different levels of grid power outage. The effect of the range of the snow and ice disaster, the caused economic loss was far lower than the ice disaster in 2008. The main reason is the freezing rain and snow weather lasted for a shorter time, and after the ice disaster in 2008, the China State Grid Corporation and China Southern Power Grid Company have greatly improved the icing prevention ability in the grid through line icing resistant reinforcement engineering, implementation of AC and DC ice-melting technology, construction of icing monitoring and warning system of "three measures". However, with the global climate warming and the deterioration of the environment, the natural disasters in this extreme environment like the ice disaster are unpredictable, and it is difficult to confirm no major disasters like the disaster in 2008 in the next few years, even decades. In addition, the Hunan Electric Power Research Institute, utilizing the extreme value I type distribution and Pearson III type distribution, calculated that the Hunan power grid iced particularly severely every average 12 years, and predicted that Hunan, Jiangxi, Guizhou areas entered a 15 to 20 years of frequent period of Glaze Icing since 2008. Therefore, the transmission line deicing and the study of the corresponding emergency response plan must be strengthened, and avoiding the major power outage and huge economic losses like the ice disaster in 2008.

5. DISCUSSION

5.1 Evaluation

After five years of research and practice, the China Power Grid has made many achievements in terms of anti-icing and mitigation, and achieved a breakthrough in power grid ice disasters prevention and disposal measures on ice events.

After the ice disaster in 2008, the China Power Grid has strengthened the deployment and the construction of automatic ice lookout and observation points in the provinces, and has done its best to against icing on duty and be ready for the defense during the icing period, increasing the transmission line patrol monitoring, real-time monitoring of transmission line icing situation, submitting transmission line icing conditions timely. Operation and monitoring personnel through the conductor icing on-line monitoring device system once find the icing exceeding the design standards, warning the low temperature freezing disaster for easily icing region timely, starting the icing contingency plans (detecting the state of the ice-melting device, reinforcement and reconstruction of transmission lines, etc.), and full force on the deicing and ensuring electrical. Using the ac/dc ice-melting devices developed with independent intellectual property rights to perform the short circuit deicing tests on the lines for different voltage levels, that had obtained remarkable result and guaranteed the safe and reliable of power supply. At present, it had equipped with 44 sets of DC ice-melting device only for the southern power grid, that can melt icing for 293 lines of above 110 kV directly, and for the additional 80 lines of 110 kV and above by the series connection. Connecting the device took about average 1 hour, it can be putted into the deicing test effectively, and achieved good results.

5.2 Analysis on existing problems

The icing problem on power grid is a very challenging subject, and it cannot be completely solved in the short term. Therefore, there is still a long way to go and many problems need to be solved in order to realize the requirements for the power grid without icing accidents. China will continue to carry out researches and summarize the application experiences. The existing problems for present mainly include the followings:

(1) Prediction on the icing disaster of power grid: the icing is a probability event with high random, extremely complicated factors, so it is difficult to predict accurately.

(2) The existing ice-melting method which has to be outage effects the power supply, when facing the large area icing accidents, the only one installed ice-melting device for each substation may not meet the requirements of deicing timely, so it is also important to research new technologies, such as intelligent deicing device.

(3) The forecast of the temperature, humidity and wind speed is inaccurate due to the monitoring device covered by ice based on meteorological parameters. The equivalent icing thickness prediction method based on the tension change of the icing lines and the angle change of the insulators has the larger error. It cannot solve the impact of fluctuating wind on the wire tension of different ice shapes. So the study on icing thickness prediction model is not perfect.

(4) As the icing flashover mechanism of insulators is not completely solved, the methods preventing icing flashover of insulator plays a role in a certain extent, but it is still unable to be solved for the micro-topography and micro-climate conditions.

(5) The icing of transmission lines in China has typical micro-topography and micro-climate characteristics, the accurate forecast and distribution of micro-topography and micro-climate icing are beneficial to solve the fundamental technical problem of power grid icing in china.

REFERENCES

[1] X. Wang, Icing overview of transmission lines [J]. *Water Power Technologies*, Vol. 34, pp. 14-26, 2008.

[2] X. Jiang, J. Ma, S. Wang, C. Sun and L. Shu, Transmission lines' ice accidents and analysis of the formative factors[J]. *Electrical Power*, Vol. 38, pp. 27-30, 2005.

[3] P. Zhang, Report on fighting the cold rain and snow freeze disaster and the post-disaster reconstruction [R]. 2008.

[4] Ministry of Civil Affairs Snow and ice disaster and relief work at recently[EB/OL].[2008-02-01].http://www.mca.gov.cn/article/special/xz/gzbs/200802/20080200011960.shtml.

[5] X. Jiang, L. Shu and C. Sun, *Insulation of Electric Power system under Pollution and Icing conditions*, Beijing, China Electric Power Press, 2009 (in Chinese).

[6] M. Farzaneh, *Atmospheric Icing of Power Networks*, New York, Springer, 2008.

[7] X. Shukai and Z. Jie, "Review of ice storm cases impacted seriously on power systems and de-icing technology," *Southern Power Syst. Technol.*, vol. 2, pp. 1–6, 2008.

[8] R. Hong, L. Licheng, L. Xiaolin, and F. Chuang, "Study of DC based DC-icing technology in China southern power grid," *Southern Power Syst. Technol.*, vol. 2, pp. 7–12, 2008.

[9] Q. Hu, L. Shu, X. Jiang, C. Sun, Z. Zhang and J. Hu, Effects of Shed Configuration on AC Flashover Performance of Ice-covered Composite Long-rod Insulators [J]. *IEEE Transactions on Dielectrics and Electrical Insulation*, Vol. 19, pp. 200-208, 2012.

[10] Z. Zhang, X. Jiang, C. Sun, J., H. Huang, Influence of Insulator String Positioning on AC Icing Flashover Performance[J]. *IEEE Transactions on Dielectrics and Electrical Insulation*, Vol. 19, pp. 1335-1343, 2012.

[11] X. Jiang, S. Zhao, J. Hu, Z. Zhang and L. Shu, Study of DC Flashover Performance of Ice-covered Insulators at High Altitude[J]. *IEEE Transactions on Dielectrics and Electrical Insulation*, Vol. 20, pp. 391-400, 2013.

Comparative Testing of Different Anti-Ice Coatings for Overhead Line Conductors with Special Focus on Ice Accretion, RIV and Visual Impact

Miroslav Radojcic
miroslav.radojcic@statnett.no

Igor Gutman

Lillemor Carlshem

Kjell Halsan
Statnett
Oslo, Norway

Andreas Dernfalk
STRI
Ludvika, Sweden

Lars Wallin
Svenska Kraftnät
Stockholm, Sweden

Abstract — A number of important tests for the first (screening type) evaluation of new types of super-hydrophobic coatings applicable for both conductors and insulators were identified and included: ice tests in laboratory and outdoors; audible noise test; ageing test; visual impact test. Based on the obtained results the authors believe that there are positive indications for the super-hydrophobic coating. Further work would be of interest, in order to explore nano-coating regarding ice formation and adhesion properties, and also to explore ageing performance of such coating in field conditions.

Keywords — conductor; super-hydrophobic coating; ice test; RIV test; salt fog test; visual impact

I. INTRODUCTION

A CIGRE Brochure 438 on ice and snow related issues published in 2010 [1] summarized knowledge on different anti-icing and de-icing methods. The countermeasures against ice were grouped as active methods (mechanical, thermal, vibration, etc.) and passive methods. Among passive methods, special coatings for conductors of overhead lines are of prime interest. At present the international work on anti-ice coatings is concentrated within CIGRE WG B2.44 and the new CIGRE Brochure is expected in the beginning of 2015. Scandinavian power companies experiencing ice and snow issues are very much involved in own research related to anti-ice coatings and this paper presents a summary of performed investigations which output is rather positive, however requires much more research to ensure commercial products with reasonable service life.

The prevention of ice accretion can be theoretically feasible by use of coatings with low adhesion against ice. Some experiments in Canada in 1977 demonstrated reduced adhesion to ice compared with fully hydrophilic surfaces. To test this possibility, a prototype of BLX conductor impregnated with 5% silicone was specially manufactured and tested at STRI about 10 years ago and the results showed that there was no evidence that "standard" hydrophobic materials lead to lower ice adhesion than hydrophilic materials. However, 10 years after, at the International Workshop on Atmospheric Icing of Structures (IWAIS) several research groups from different countries presented their positive results in developing, laboratory tests and even field tests of new super-hydrophobic materials using e.g. nanotechnology. According to the latest CIGRE definition, materials characterized by a contact angle of about 150° and more are considered as super-hydrophobic. This information has triggered investigation at STRI supported by Statnett and Svenska Kraftnät [2].

Differences in ice accretion performance was examined first through a laboratory comparative test where conductor samples of approximately 1 m length were mounted in a rotating rig and exposed to water spray. The set-up allows uniform exposure of all specimens to the spray from the single nozzle (type TEEJet8001) placed 0,5 m above and 1 m in front of the test rig. The nozzle was supplied by tap water at a rate of 27 l/h. Using this method the glaze type of ice was obtained and the main result was that the appearance of ice on super-hydrophobic coating was abnormal, i.e. ice grew from frozen droplets on the surfaces (normally it forms as a smooth cylinder), see **Figure 1**. It is interesting that these results are almost identical to the results obtained on another super-hydrophobic coating and the same type of ice in China, see also **Figure 1**.

Figure 1 Illustration of abnormal appearance of ice accretion on super-hydrophobic conductors: upper – the results from STRI test; bottom – adopted from Jiang Xingliang's presentation at the plenary session of IWAIS-2013.

Based on this positive physical indication a comprehensive test program was developed, which included a few important issues to be checked in comparison to traditional conductors:

- Ice accumulation
- Corona effects in the form of radio interference and audible noise
- Ageing
- Visual impact

Six different types of conductors/coatings were selected for this test matrix. All conductor samples were of ACSR Parrot-type (outer diameter of 38,25 mm). Tested conductors samples were in following condition:

1. "New conductor" – Non-used conductor taken from a drum
2. Conductor with normal hydrophobic RTV-coating
3. Conductor with super-hydrophobic coating
4. Blasted conductor – Conductor where the surface has been treated by blasting to make it less shiny
5. Painted conductor – New conductor painted with standard paint for metal
6. Acid treated conductor – Conductor which had been treated with acid in order to reduce visual impact

II. ICE ACCUMULATION

To develop and perform a relatively simple screening test in order to roughly evaluate the ability of different conductors to withstand ice accretion, the conductor samples were fixed in a rotating drum, as illustrated in **Figure 2.**

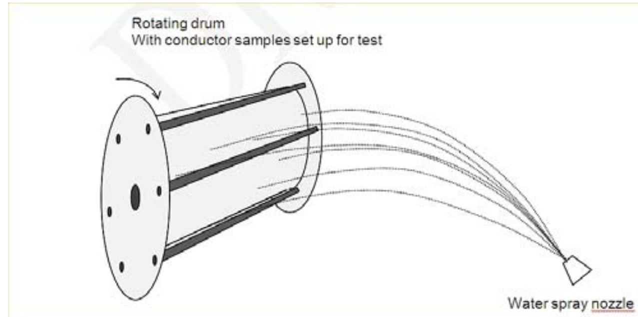

Figure 2 Illustration of principles for ice screening test.

This principle was realized first in the laboratory (for glazed type of ice) and later outdoors (primarily for the rime type of ice), see **Figure 3.**

The laboratory ice accretion tests were performed in STRI's climate chamber (45 m^3) where the temperature was kept between -7°C – -4°C. Before testing, the conductor samples had been pre-cooled to -7°C for a period of 24 h.

The outdoor tests were performed just outside the STRI office at about -10°C. Icing was produced, first with a high pressure washer, and secondly with a spray gun (spraying a mixture of air and water) in order to obtain more rime-like ice. The rig rotated with a speed of 6 RPM. The conductor length between fix points was 87 cm. The test rig was placed in the shadow to avoid direct sunshine.

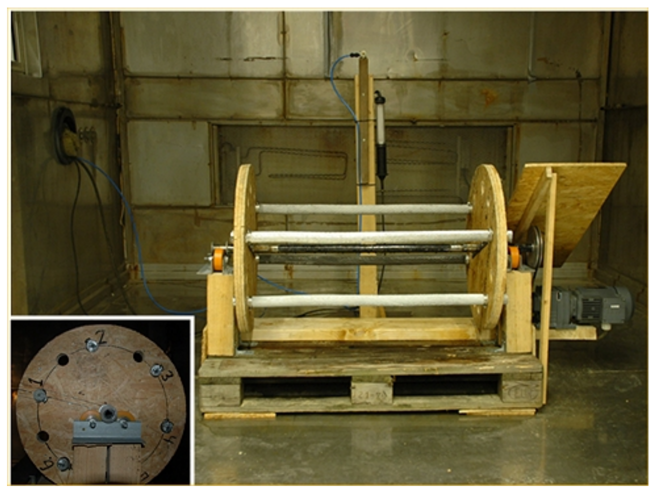

Figure 3 Ice test performed in laboratory (upper) and outdoors (bottom).

To evaluate ice adhesion forces a STRI-developed "tool" was used, see **Figure 4**. This simple tool seems to be interesting for CIGRE for further standardization as it can be used for field measurements. The intention of the tool is to standardize the impact (punch forces) on conductors covered with ice and perform measurements in outdoor conditions. In this case, a weight of 1,4 kg sliding on a rod was used. The rod was placed, resting by its own weight, on the conductor. The weight was let down on the conductor, first from half the length of the rod, 15 cm, then from the full length, 30 cm, this was called as “half punch” and “full punch”.

Figure 4 STRI-developed "tool" for comparison of ice adhesion.

The following results were obtained after LABORATORY investigations. The ice test representing glazed type of ice (transparent ice of high density) did not result in significant reduction of ice accretion on conductor with super-hydrophobic nano-coating. Similar amount of ice, in terms of weight, was accreted on all six conductors. The appearance of ice on both hydrophobic conductors (RTV and nano) did however differ from the smooth ice on the other specimens. The difference was mostly pronounced on the super-hydrophobic coating which still showed a “bumpy” surface after 3 h of ice accretion. The reason for this behavior could be strong polar properties of the molecules at the surface of the coating, resulting in orientation of water molecules affecting formation of ice also at some distance. Utilization of hydrophobic nano-particles would allow for very fast recovery of hydrophobicity, but probably not for penetration of hydrophobicity through pollution layers like low molecular weight (LMW) components in silicone rubber. Probably one of the most important observations made during this test was that isolated frozen drops on the super-hydrophobic coating could be very easily removed by just touching by hand, i.e. adhesion of ice was very low at this initial stage. On hydrophilic conductors, ice builds up simultaneously on large portions of the wetted surface, resulting in a strong adhesion. This difference could possibly be important for real applications where stresses from wind and mechanical movement of the conductor could play an important role for ice shedding.

The following was obtained after OUTDOOR test. It was confirmed that a thinner layer of rime type of ice than on the other three conductors was observed at the conductor with super-hydrophobic coating. As an example, it is seen in **Figure 5** that the RTV coated conductor is almost totally covered with ice, whereas the ice on the super-hydrophobic coated conductor has mainly adhered to the outer parts of the wires. No similar difference was seen in the previous laboratory tests in which glaze ice was created. One possible explanation of the difference in ice thickness may be that for the super-hydrophobic conductor the initial ice accretion has a different character.

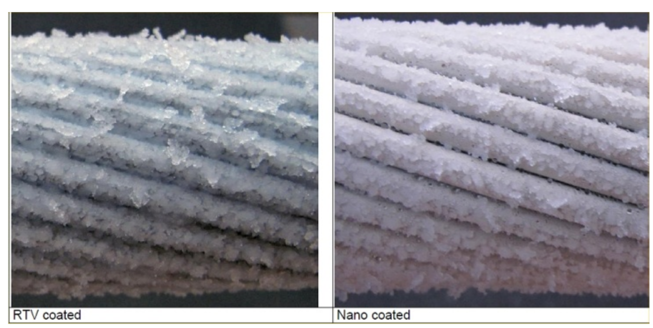

Figure 5 Ice accretion on RTV-coated and super-hydrophobic coated conductors.

III. CORONA EFFECTS AND AUDIBLE NOISE

Corona affects and especially Audible Noise (AN) are very important parameters for investigation of super-hydrophobic conductors. The common knowledge obtained up to now was that traditional hydrophobic conductors (i.e. new greased or RTV-coated) normally have higher AN levels than service-aged or intentionally sand-blasted conductors, see example in **Figure 6** adopted from [3].

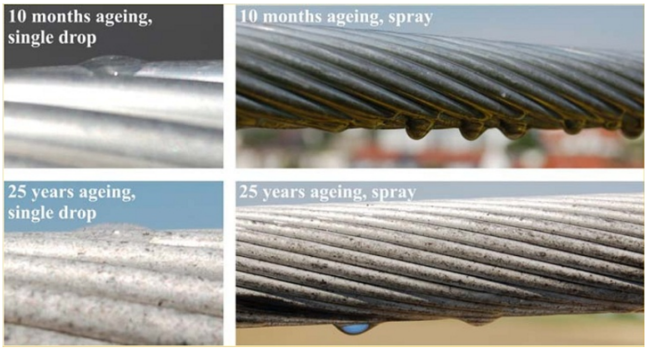

Figure 6 On-site test of wettability in the southern part of Germany (photo adopted from [3]).

More than that, proposals for the special hydrophilic paints to reduce the AN were issued and verified. Therefore, it was extremely important to make the first own verification of super-hydrophobic conductor. AN measurements were performed under dry and wet (rain) conditions for different conductors, i.e. new, sandblasted, painted, acid treated, RTV-coated and super-hydrophobic. The conductors were strained horizontally one by one 2 m above the floor in STRI's climate test hall, see **Figure 7.**

Noise was measured by a Norsonic Sound Analyser equipped with a microphone placed at a horizontal distance of 4 m from the conductor and 1 m above the floor. The equipment was configured to record spectrum from 10 Hz to 20 kHz for 1 min intervals. The rain was created by utilization of 10 nozzles mounted on a horizontal beam hung parallel to the conductor. The beam was placed at a horizontal distance of 2 m from the conductor and 5 m above the floor. The arrangement resulted in an average rain intensity of 3,5 mm/h at the conductor, i.e. a rain corresponding to a "light summer rain" (however, much higher than standard rain of IEC, 1-2 mm/min). Tests were performed in dry and rain conditions at representative maximum voltage gradients of 12, 14, 16, 18 and 20 kVrms/cm, this was achieved by adjusting the test voltage. The test procedure comprised twelve measurements: measurement of dry background noise (reference spectrum), application and stepwise increase of voltage with noise measurement at each voltage level, application of rain and measurement of noise at each voltage level, and finally, switch off and measurement of wet (rain) background noise level.

Considering the tests under rain, the performances of all types of conductors was surprisingly found to be rather similar (excluding the short acid treated conductor, because of its different length). This is shown in **Figure 8** where the influence of different background levels is taken out through subtraction. Excluding the short acid treated conductor, it is clear that the super-hydrophobic conductor performs something like the average conductor. The possible explanation is the appearance of water drops on an energized conductor shown in **Figure 9**. These photos were taken in conjunction with the AN measurements, and it is clear that water was present only on the top surface (for hydrophilic conductors the water drops are normally collected at the bottom surface of a conductor), see **Figure 10**. Further, the influence of the electric field can be seen as drops extend in radial direction (and explode) as the voltage is increased from level E1 to E2. Of course it is desirable to repeat similar tests at the test span in the field in natural wetting conditions; however the indication so far is that due to super-hydrophobic properties the discussed coating may behave similar to standard conductors, which is principally different to the comparison of normal hydrophobic/hydrophilic conductors mentioned above.

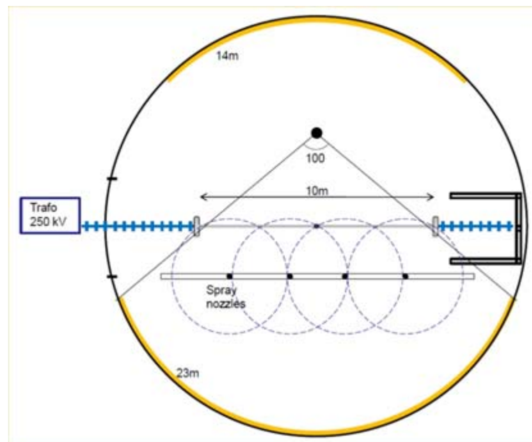

Figure 7 Test set-up for AN test.

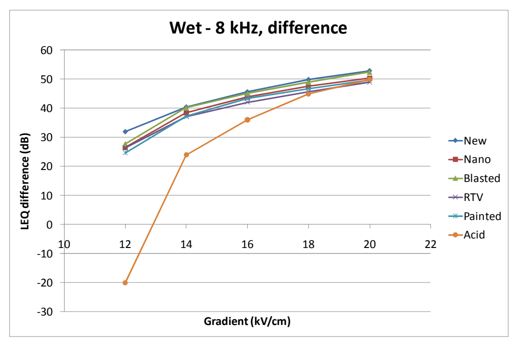

Figure 8 Test results for AN test. Acid treated conductor is much shorter and <u>should not be compared</u> with others.

Figure 9 Change of form of water drops under rain on the super-hydrophobic surface at different levels of voltage gradient.

Figure 10 Water drops at new conductor (classical performance).

IV. AGEING

The goal of this part of the project was to study the long-term performance of conductors with super-hydrophobic coating through 1000 h salt fog test (IEC 62217). This test is prescribed by IEC as “typical” tracking and erosion test for composite insulators. The test procedure prescribed by IEC was used as a basis for the test and complemented by visual and hydrophobicity inspections as follows. 1000 h tracking and erosion test with salt fog 8 kg/m^3 similar to the procedure described in IEC 62217. Visual inspections and Wettability Class (WC) measurements in accordance with IEC TS 62073 before the test, after 500 hours and after finishing the salt fog test. Super-hydrophobic conductor and RTV-coated conductor were tested. The test was carried out in a moisture-sealed corrosion-proof chamber, the volume of which was about 45 m³. Two conductors were mounted in the test chamber using composite line insulators hanging from the roof, see details in **Figure 11**. They were intentionally tested at elevated voltage to guarantee corona activity on the surface of conductors.

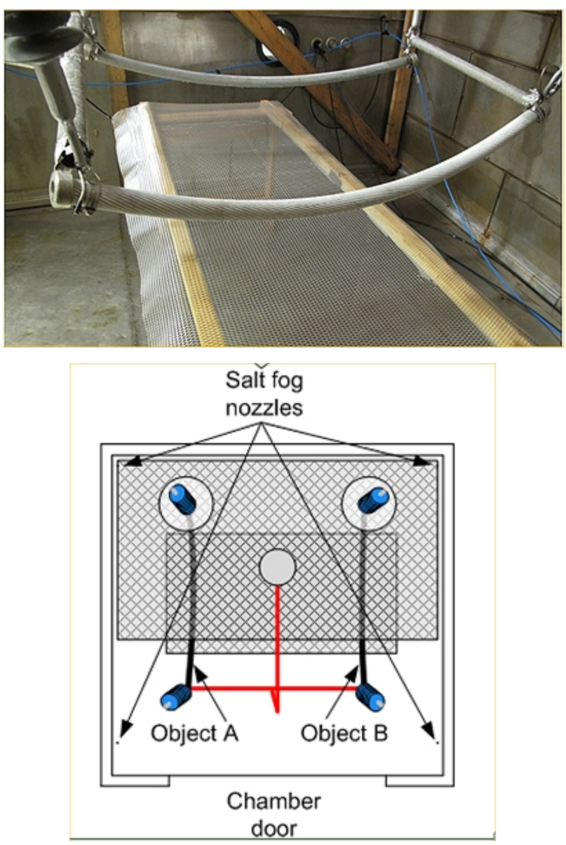

Figure 11 Set-up for 1000 hours salt fog tracking and erosion test.

From deterioration point of view both coatings passed the 1000 hours test without visible traces of deterioration, the coatings were still properly adhered at the conductors. Both super-hydrophobic and RTV-coating lost their hydrophobicity completely at the end of the test. However, super-hydrophobic coating lost hydrophobicity already within a few days, while RTV-coating lost it after about 500 hours of the test. After approximately 4 weeks after the end of the test, the hydrophobicity measurement was repeated and the result was that both coatings demonstrated a recovery in its hydrophobicity, see **Figure 12**. However, the RTV-coating had an almost complete recovery (WC 2-3) over the full length of the conductor; and the super-hydrophobic conductor had only recovered over the part of its length. Approximately 20% of the full length of the conductor had a WC of 2-3, the rest of it still had WC = 7 (i.e. was completely hydrophilic).

Figure 12 Super-hydrophobic coating after 4 weeks after the test.

V. VISUAL IMPACT

For many power companies in the world the visual impact became one of the important issues, because people would not like to see any transmission lines any more. The visual impact of conductors and insulators (and other components of the OHL) varies depending on appearance (i.e. colour, shininess and size), the background (e.g. sky, land, and forest), illumination and atmospheric visibility. Due to the large number of parameters, it was decided first to compare visibility through a simple direct comparative test where samples of coated conductors were mounted in a rig outdoors at STRI, see **Figure 13**. Differences in visibility of the conductor types were documented and compared through the photographs taken under different weather conditions and averaged ranking from 8 STRI employees; see **Figure 14**.

As a result, RTV-coated, new and blasted conductors were considered as least visible with similar total average rankings. In the evaluated photos, the dark conductors (painted and acid treated) are generally found to be most visible. Thus, super-hydrophobic conductor was somewhere in the middle in visibility (however, in intense illumination by the sun the almost white super-hydrophobic conductor was judged as most visible).

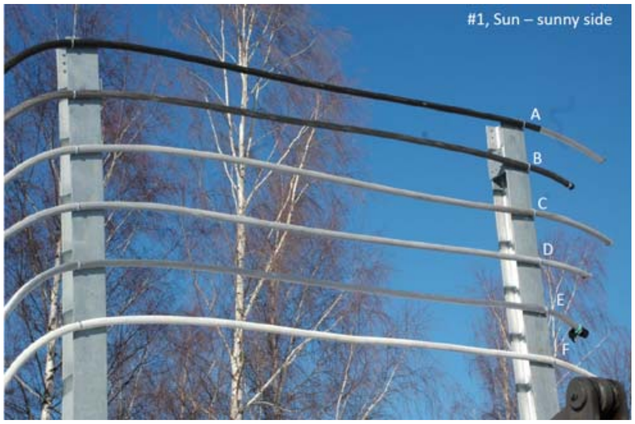

Figure 13 Example of photograph for ranking of visual impact of different conductors. A-painted; B-acid; C-blasted; D-RTV; E-new; F-super-hydrophobic (nano).

Sample	Ranking					
	Photo #1	Photo #2	Photo #3	Photo #4	Photo #5	Total Average
#6 Painted	5,8	4,4	6,0	5,9	5,9	5,6
#4 Acid	4,4	2,6	5,0	5,1	4,8	4,4
#5 Blasted	2,4	2,9	2,6	2,5	1,6	2,4
#2 RTV	2,6	***2,0***	2,1	3,0	***1,4***	***2,2***
#1 New	***1,0***	3,9	***2,0***	***1,6***	3,0	2,3
#3 Nano	4,9	5,3	3,3	2,9	4,4	4,1

Figure 14 Ranking of visibility of conductors. The best camouflaged conductor in each photo is indicated by ***bold italic*** font.

Later STRI got involved in a project aiming to quantify visibility of insulators with different coatings for a human observer looking at a typical transmission line and typical backgrounds (e.g. forest, sky). Low visibility was also preferred in this case so as to minimize the visual or environmental impact of transmission lines. The method has been tested for a number of images of an existing transmission line obtained by web-cameras. The results showed that it was possible to automatically quantify the visibility of insulators as a human observer, but in a more objective way [4].

VI. SUMMARY

A number of important tests for the first (screening type) evaluation of new types of super-hydrophobic coatings applicable for both conductors and insulators were identified and included: ice tests in laboratory and outdoors; audible noise test; ageing test; visual impact test.

<u>The ice test</u> performed indoor and simulated glazed ice revealed that the adhesion of isolated frozen water drops to the super-hydrophobic coating is low, but at high coverage ice adheres to the surface like onto any other conductor. The ice test performed outdoors and concentrated on rime ice type indicated less rime ice accretion on the nano-coated conductor. A possible explanation could be a difference noted in the initial ice formation on the conductor, which have the effect of delaying the formation of a continuous ice surface. The results also indicated reduced adhesion of rime ice on the RTV-coated conductor. A possible explanation could be that the RTV layer covers the conductor, and changes the surface geometry of the conductor into a smoother surface.

<u>Audible noise measurements</u> performed under dry and light rain conditions revealed that the super-hydrophobic conductor did not suffer from extraordinary high levels of noise. Except for at the highest stress under dry conditions, the levels were close to the average.

<u>The ageing tests</u> were performed as 1000 hours salt fog test with relatively high test voltage to create corona activity on the surface of the coating (two coatings were on trial). Both coatings lost their hydrophobicity and the nano-coating lost it much faster than RTV-coating. However, deterioration of neither nano-coating nor RTV-coating was observed after the test as well as no peeling from the conductor. Only minor flaws could be observed on both conductors.

<u>The visual impact evaluation</u> showed that the super-hydrophobic conductor was somewhere in the middle in visibility (however, in intense illumination by the sun the almost white super-hydrophobic conductor was judged as most visible).

Based on these positive indications the authors believe that further work would be of interest, in order to explore nano-coating regarding ice formation and adhesion properties, and also to explore ageing performance of such coating in field conditions.

VII. REFERENCES

[1] CIGRE WG B2.29: “Systems for prediction and monitoring of ice shedding, anti-icing and de-icing for power line conductors and ground wires”, Techical Brochure 438, December 2010

[2] I. Gutman, M. Radojcic, L. Carlshem: “Reducing Ice Accretion Using “Super-Hydrophobic” Coatings on Conductors & Insulators”, INMR, Issue 100, Quarter 2, Volume 21, N. 2, 2013, p.p. 70-75

[3] U. Straumann, H.J. Weber: “Potential reduction of audible noise from new and aged overhead transmission line conductors by increasing their hydrophilicity”, CIGRE Session 2010, Report B2-113

[4] I. Y.H. Gu, S. Berlijn, I. Gutman, M.H.J. Bollen: “Practical applications of automatic image analysis for overhead lines”, 22nd International Conference on Electricity Distribution CIRED-2013, 10-13 June 2013, Kista, Stockholm, Sweden, Paper 0560

Design of superhydrophobic/icephobic composite coatings

Reza Jafari and Masoud Farzaneh
NSERC / Hydro-Quebec / UQAC Industrial Chair on Atmospheric Icing of Power Network Equipment (CIGELE) and Canada Research Chair on Atmospheric Icing Engineering of Power Networks (INGIVRE) www.cigele.ca
Université du Québec à Chicoutimi, Chicoutimi, QC, Canada
/

Abstract — An easy and inexpensive method was used to elaborate superhydrophobic surfaces. A superhydrophobic surface was prepared by spray coating a mixture of calcium carbonate ($CaCO_3$) particles, stearic acid and polymer latex suspensions on an aluminum substrate. The Taguchi method was used to optimize the fabrication process parameters: the percentage of stearic acid, the $CaCO_3$ particles to copolymer weight ratio, and the spray distance from the substrate. It was found that the percentage of stearic acid plays the most significant role in affecting the coating's wettability. The optimal condition proposed by this method has been verified through additional experiments which showed an increase in static contact angle up to 158º. Study of its wettability at low temperature showed that the superhydrophobic surface becomes rather hydrophobic at supercooled temperatures. However, these results also showed a delayed freezing time of water droplets on its surface.

Keywords — component; Superhydrophobic surface, aluminium alloy, anti-icing coating, nanocomposite

I. INTRODUCTION

Ice accumulation can cause hazardous road conditions, reduce the efficiency of aircraft engines and helicopters and damage power transmission equipment [1-3]. An icephobic surface is one on which ice adhesion strength is lowered and/or freezing is delayed. The ice accreted can be removed from such surfaces by natural forces, such as gravity or wind. Conventionally, the development of icephobic surfaces is closely related to superhydrophobicity. Superhydrophobicity is a term attributed to the low adhesion of water droplets on a surface, leading to water contact angles higher than 150°. However, it has been proven that by modifying the surface chemical composition of a flat surface, and thus reducing the surface energy, the maximum contact angle achievable is 120°. Moreover, the addition of roughness to the surface can increase the contact angle of water without altering surface chemistry [4]. Several methods have been developed to create superhydrophobic surfaces [5-10]. However, most of these methods are limited as to time, fabrication cost and environmental concerns. The present study investigates a very simple one-step and low-cost superhydrophobic (contact angle ~158 º) coating prepared by incorporating $CaCO_3$ particles in a polymer latex matrix and applied by the spray coating method. The Taguchi method was used to optimize the fabrication process parameters, namely the percentage of stearic acid, the CaCO3 particles to copolymer weight ratio, and the spray distance from the substrate.

II. EXPERIMENTAL SECTION

Aluminum samples were cut from an Al-6061 plate to 50 mm × 30 mm pieces. These samples were then cleaned in an ultrasonic bath with acetone (5 min) and distilled water (5 min). A known amount of stearic acid was first dissolved in acetone. Then, the solution was mixed with a magnetic stirrer at 600 rpm for 20 min at 30 °C. An appropriate quantity of $CaCO_3$ particles (diameter ~5 µm, Alfa Aesar) was dissolved in double distilled water and then, the suspension was mixed with polymer latex (Acronal® NX4787X, copolymer of styrene and acrylate in water, BASF Corporation), with 10 min agitation at 600 rpm. Finally, the suspension of $CaCO_3$ and polymer latex was mixed with the stearic acid solution and agitated for 10 min at 600 rpm at 30 °C. The slurry was sprayed on aluminum substrates using a spray gun. Contact angle measurement was performed using a Kruss™ DSA100 goniometer equipped with a video camera at 25 °C. Static contact angle was measured by placing a water droplet with a volume of 4μL on the surface. The sample surface morphology was examined using a LEO field emission scanning electron microscope (FESEM).

III. RESULTS AND DISCUSSION

The following controlling parameters were considered to affect the coating water repellency properties: spraying distance and percentage of stearic acid, each one at three levels, and $CaCO_3$/polymer latex weight ratio at six levels [11]. Taguchi's factorial experiment approach was used to reduce the number of experiments. A Taguchi L18 orthogonal array consisting of 18 sets of experimental conditions was used to evaluate the effect of theses parameters on the wettability of coatings. The graphical representation of the S/N ratios is shown in Fig 1. In the Taguchi method, the term 'signal' (S) represents the desirable value (mean) for the output characteristic and the term 'noise' (N) represents the undesirable value for the output characteristic [12]. The factor levels with the largest S/N ratios are the optimum levels as they minimize the sensitivity over the range of noises. Therefore, the optimal conditions for the spray coating to obtain a superhydrophobic film according to their high S/N ratios correspond to a distance of 25 cm between the substrate and spray gun, a percentage of 2 % stearic acid and a weight percentage ratio of CaCO3/NX7487 at 20%. Also, the difference between the highest and lowest values of the S/N ratio is a decisive indicator with regard to the influence of a parameter. It can be observed that the percentage of stearic acid presents the most significant differences of S/N ratio at different levels and consequently plays the most important role as to overall water repellency performance. These results show that hydrophobicity is increased by increasing the stearic acid content of the coating. It was shown that stearic acid reacts with carbonate calcium particles and covers them with a monolayer of calcium stearate bicarbonate which creates a hydrophobic tail oriented toward the air [13, 14]. As the concentration of fatty acid is increased, the quantity of hydrophobic groups covering the particles increases, resulting in an increase in the water repellency properties of the obtained coating. The $CaCO_3$/NX7487 ratio also provides a quite large contribution to the hydrophobicity of the resulting coating. This increase in hydrophobicity with higher percentages of $CaCO_3$/NX4787 could be mainly attributed to the increase in surface roughness due to the increase in $CaCO_3$ particles and also to the low contact angle of the polymer itself as compared with calcium stearate bicarbonate. On the other hand, the distance between substrate and spray gun has a minor effect on the water repellency of the coating. However, at higher distances a decrease in water repellency was observed which can be explained by the decrease in surface micro/nano roughness as the distance from the substrate is increased.

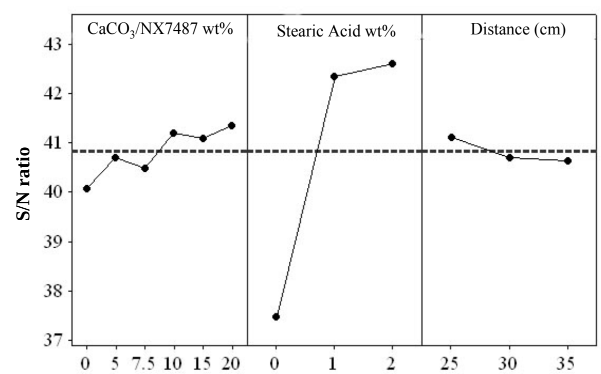

Figure 1. Effect of different factor levels on the average of S/N ratios

An additional experiment with the optimal conditions was carried out to confirm the influence of the optimal combination of the control factors and their levels on performance characteristics. The contact angle obtained at the optimal conditions resulted in greatly improved water repellency with the contact angle increasing to 158º.

The SEM images of Figs. 2a-2b, display a superhydrophobic coating deposited at the optimal conditions. They show the formation of a solid polymer foam-like structure where air can be trapped in the rough surface cavities. This surface morphology reduces the contact area between water and the surface, resulting in increased water repellency. The higher magnification image (Fig. 2b) shows the presence of micro/nanostructures on the superhydrophobic coating.

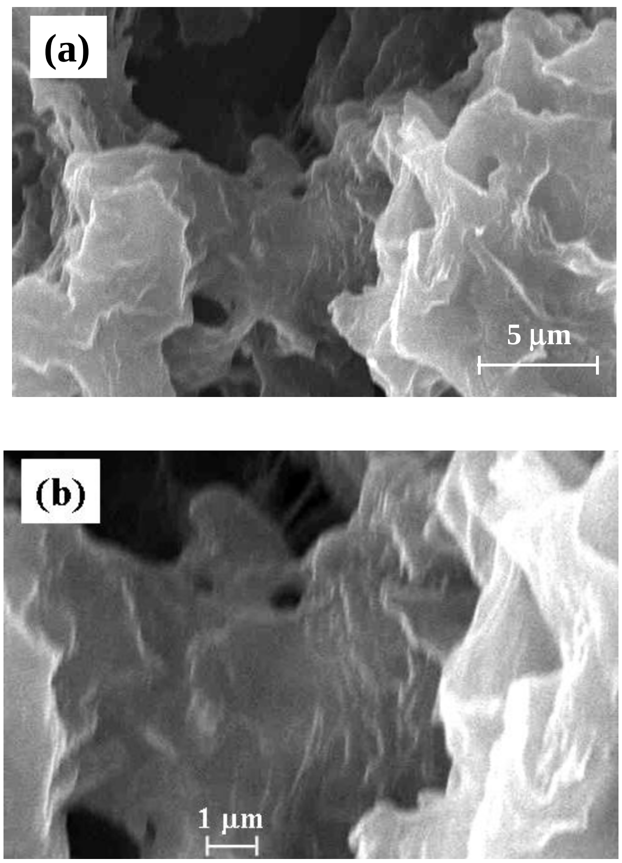

Figure 2. SEM image of the superhydrophobic film deposited at optimal conditions on an aluminium alloy surface (a) low magnification, and (b) higher magnification

The study of the wettability of superhydrophobic surfaces at supercooled temperature is of prime importance for the development of icephobic coatings [15, 16]. For this propose, the contact angle measurement of samples were carried out at low temperatures. For this purpose, the Kruss DSA 100 apparatus was fitted with a Peltier cooling element which allowed lowering the substrate temperature down to -30 ^{o}C.

The wettability of the fabricated surfaces was evaluated in a wide range of temperature. Fig. 3 shows the variation of static contact of composite coatings as a function of temperature. The results showed that the superhydrophobic surface became rather hydrophobic with the surface temperature descending from 25 °C to - 15 °C. In fact, when nanostructured surfaces are exposed to temperatures lower than zero, condensed water penetrates into the porosities of the coating and the water vapour condensation leads to a so-called Cassie-Wenzel regime transition resulting in lower contact angles [15].

Study of wettability at low temperature (-15 ºC) also showed delayed freezing time of water droplets on the superhydrophobic surface (Fig. 4). In other words, the water droplets on an aluminium surface froze more quickly (about 5-7 sec.) than those on the superhydrophobic surface (about 198 sec). It was also observed that the interface between water and ice kept moving from bottom to top during the transient heat conduction after which droplet crystallization occurred completely.

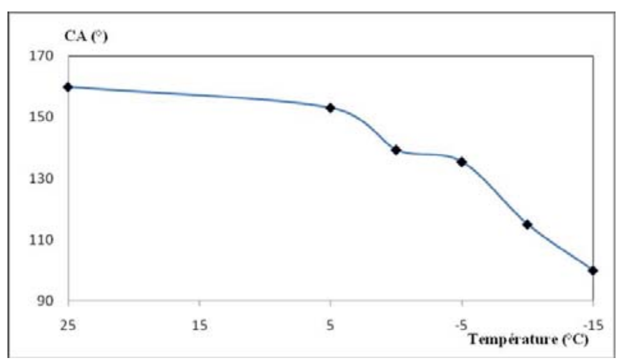

Figure 3. Evolution of static water contact angle of superhydrophobic polymer composite coating versus temperature

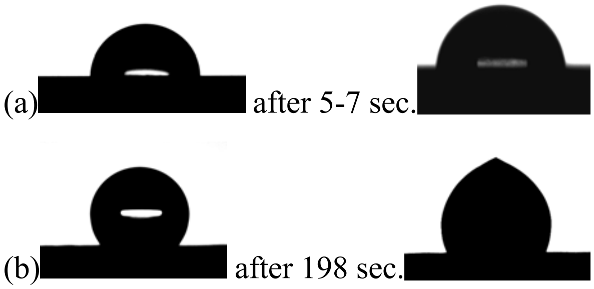

Figure 4. Image of water droplets (4 µL) on a) before and after freezing on a) aluminium surface and b) superhydrophobic coating -15 °C

IV. Conclusion

Spray coating which is a simple and low cost technique was proposed for elaborating superhydrophobic coatings. The Taguchi method was used to optimize the fabrication process parameters in order to obtain the maximum contact angle. The results showed that the percentage of stearic acid has the most significant influence on the water repellency of coating. The wettability results obtained by using the optimal conditions proposed by this method showed that the resulting superhydrophobic surface had a very high contact angle of about 158º. Study of wettability at low temperatures showed that the superhydrophobic surface became rather hydrophobic with descending surface temperature from 25 °C to -15 °C. These results also showed a delayed freezing time of water droplets on the superhydrophobic surface as compared to those on an aluminium surface.

Acknowledgment

This work was carried out within the framework of the NSERC/Hydro-Quebec/UQAC Industrial Chair on Atmospheric Icing of Power Network Equipment (CIGELE) and the Canada Research Chair on Engineering of Power Network Atmospheric Icing (INGIVRE) at Université du Québec à Chicoutimi. The authors would like to thank the CIGELE partners (Hydro-Québec, Hydro One, Réseau Transport d'Électricité (RTE) and Électricité de France (EDF), Rio Tinto Alcan, General Cable, K-Line Insulators, Tyco Electronics, Dual-ADE, and FUQAC) whose financial support made this research possible. The authors are grateful to Hélène Grégoire (NRC-ATC) for SEM analyses.

References

[1] Farzaneh M., ed., 2008, "Atmospheric Icing of Power", Springer, Berlin.

[2] Farzaneh M., 2000, "Ice Accretion on H.V. conductors and Insulators and Related Phenomena," Invited Paper, Philosophical Transactions, the Royal Society London, no. 358, pp. 1–35.

[3] Farzaneh M., and Kasaai M. R., "Analytical Evaluation of Existing Mechanisms of Ice Adhesion on Power Network Equipment," Proceedings of the 23rd International Conference on Offshore Mechanics and Arctic Engineering, American Society of Mechanical Engineers (ASME), New York, Vancouver, Canada, p. 51267.

[4] L. Feng, H. Zhang, P. Mao, Y. Wang.,Y. Ge, Appl. Surf. Sci. 257 (2011) 3959-3963

[5] X. Zhang, F. Shi, J. Niu, Y. Jiang, Z. Wang, J. Mater. Chem.18 (2008) 621-638

[6] G. Momen, M. Farzaneh, R. Jafari R, Appl. Surf. Sci. 257 (2011) 9489-9493

[7] R. Jafari, M. Farzaneh, Appl. Phys. A 102 (2011) 195-199

[8] X. Zhao, W. Li, Surf. Coat. Tech. 200 (2006) 3492-3495

[9] S. Ren, S. Yang, Y. Zhao, T. Yu, X. Xiao, Surf. Sci. 546 (2003) 64-74

[10] L. Foroughi mobarakeh, R. Jafari, M. Farzaneh, Adv. Mat. Res. 409 (2012) 783-787

[11] R. Jafari, M. Farzaneh, "Design Development a simple method to create the superhydrophobic composite coatings", Journal of Composite Materials, DOI: 10.1177/0021998312462429, 2012.

[12] M.S. Gök, Y. Küçük, O. Gencel, V. Koç, W. Brostow, Mech Adv Mater Struc, 18 (2011) 389–395

[13] M.A. Osman, W. Suter, Chem. Mater. 14 (2002) 4408-4415

[14] Z. Hu, X. Zen, J. Gong, Y. Deng, Colloids and Surfaces A., 351 (2009) 65-70

[15] L. Yin, Q. Xia, J. Xue, S. Yang, Q. Wang, Q. Chen, " In situ investigation of ice formation on surfaces with representative wettability", Appl. Surf. Sci. 256 (2010) pp. 6764-6769.

[16] R. Karmouch, G.G. Ross, "Experimental study on the Evolution of Contact Angles with Temperature Near the Freezing point", J. Phys. Chem. C 114 (2010) pp. 4063-4066.

Behavior of a Small Water Droplet on a Superhydrophobic Coating in a Cold Environment

H. Endo[*1], S. Kimura[*1], Y. Yamagishi[*1], I. Nakane[*1]
*1: Kanagawa Institute of Technology
1030 Shimo-Ogino, Atsugi, Kanagawa, Japan

Abstract — Icing causes various problems. To counter these problems, deicing methods are required. In recent times, a combination of an electrothermal heater and superhydrophobic paint has been suggested as an innovative deicing method. There are some deicing methods using only an electrothermal heater. However, such methods may cause secondary icing owing to water formed by melting ice. To counter this, a surface coated with superhydrophobic paint can quickly remove such water.

Therefore, this study examines the behavior of a water droplet on a superhydrophobic coated surface for the development of the above-described method. Two experiments are conducted in this study: in one, a droplet drips onto the inclined plate and falls naturally by gravity, and in the other, a droplet is fixed and the plate under the droplet is moved for a fixed point observation. The droplet is approximately 2 mm in diameter, and the ambient temperature is maintained at -15°C; the droplet is dripped onto the surface with several initial temperatures. These experiments showed that the distance by which a droplet moves varies with the droplet's initial temperature; specifically, the distance decreases with increasing of the initial temperature. This indicates that heating control is required to prevent an increase in the water temperature in the method employing a combination of an electrothermal heater and a superhydrophobic coating.

Ⅰ. Introduction

The one of the icing prevention methods of aircraft wings, wind turbine blades and metrological instruments is the electrothermal. This method is accomplished by electrically heating the body outer surface at some certain temperature in order to maintain the impinging water droplets in a liquid phase. Liquid water moves along the surface by the aerodynamic drag and/or the gravitational forces and then refreezes possibly on an unheated area when this process takes place in a relatively sluggish manner. Hence, liquid water has to be removed immediately after impingement.

On a superhydrophobically coated surface, contact angle of a water droplet become big. It makes the water small spherical droplets and the droplet can move like rolling motion and remove easily. This is the combination of heating and coating, Electrothermal Coating method (ETC method).

Designing of anti-icing device using ETC method needs knowledge of freezing behavior of small water droplets on the superhydrophobic coating.

There are some similar researches. Sturb et al. [1], Hindmarsh et al.[2], Kostinski and Cantrell [3], and Kawakami et al.[4] conducted the research for the characteristics of a droplet in a freezing process by various experimental and/or numerical approaches. However the droplet tested was at rest on a coated surface or on a suspended thermocouple. Therefore some problems accompanied by the rolling motion as considered in the present research were not dealt with.

This research was conducted to analyze droplet behavior in horizontal motion on a super-hydrophobically coated surface. In this research, tests on a coated flat plate were carried out in a sub-zero environment in order to determine the dynamic behavior of a minute droplet and measure the temperature of the droplet.

Ⅱ. Experimental approach

For the surface of an actual in-flight wing designed based on the electrothermal-coating concept under icing conditions, water droplets can be assumed to travel by aerodynamic force along the surface very rapidly. Observing these droplets can be difficult because of the small droplet size and high-speed motion. Thus, the present test used larger droplets that were 2 mm in diameter and instilled by a micro-syringe to substitute for the actual smaller droplets. The droplets were moved slowly in a sub-zero environment and observed with a thermograph and high-speed camera to record the images in order to analyze the behavior and temperature changes of a droplet traveling on a superhydrophobically coated surface. The droplets were moved in two different ways: the gravity fall method, where a droplet falls down freely on an inclined coated plate, and the forced roll method, where a droplet is fixed at the same position in space and then forced to rotate while in contact with the coated plate. These methods are described below.

A. Gravity fall method

The gravity fall method reduces the number of external factors with regard to movement of a droplet by as much as possible. In this method, a droplet is dropped on the edge of an inclined plate that is coated with superhydrophobic paint.

1. Apparatus and test procedure

Fig. 1 shows a device comprising a micro-syringe and heating unit for instillation of a single minute water droplet. An injection needle (0.4 mm outside diameter and 0.22 mm inside diameter) was used. This particularly thin needle produces droplets with a diameter of approximately 2 mm. The micro-syringe was set up on the test stand and positioned just a little above the inclined test plate. The heater unit was used to regulate the temperature of water inside the syringe in the sub-zero environment of the test chamber. The temperature of the syringe was measured and regulated at the prescribed value by the controller. During instillation, the temperature of the droplet coming out of the tip of the needle was monitored by a thermograph (FLIR SC655). If the droplet temperature was not at the prescribed value, all data for the test run was deleted from the record.

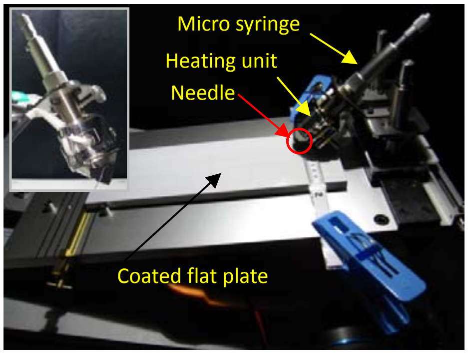

Fig. 1. Test stand for the gravity fall method

The test piece (flat plate on which a superhydrophobic paint was coated) was made of 7075 aluminum alloy and had dimensions of 300 mm × 100 mm × 10 mm. One flat surface was manually coated by HIREC450 with extreme caution in order to produce a constant and smooth surface condition. HIREC450 is a superhydrophobic paint produced by the Japanese manufacturer NTT-AT. The basic properties of HIREC450 are summarized in Table 1. The test stand upon which the test piece was placed was set up in the test chamber.
The measurement system is shown in Fig. 2. The droplet movement was monitored by a high-speed camera (Photoron FASTCAM-APX RS). A thermograph was installed beside the test stand. An LED-based lighting system was used in order to not warm the whole test system.

Table 1. Properties of HIREC

Property	Evaluation	Value
Repellency	Contact angle	> 150 deg
Coating strength	Bending	No crack
	Impact	No peeling
	Pencil stiffness	< 6B
Adhesion	Crosscut	10/100
Weathering	Water-resistance	not affected

The test conditions are shown in Table 2. The ambient temperature was constant at -15 °C for all test runs. The droplet temperatures were 5, 10, 15, and 30 °C. The speed of the droplet moving along the surface depended on the inclination of the plate. Lower inclinations were desired in order to observe the droplet motion as slow as possible. However, since the droplet did not start to move at all when the inclined angle was below 20°, the test was begun by setting the angle above this value.

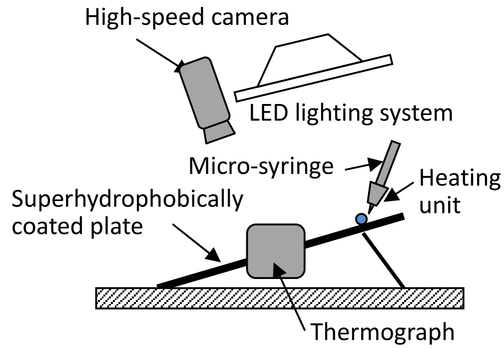

Fig. 2. Measurement system

Table 2. Test and observation conditions

Item	unit	Set value
Ambient temperature	deg. C	-15
Droplet temperature	deg. C	5,10,15,30
Inclination	deg.	20
H.S. Camera	fps	1000
Thermograph	fps	200

The test was carried out in accordance with the following procedure.
1. The micro-syringe was set in a prescribed spot on the test piece. The spots for instillation are indicated in Fig. 3.
2. The micro-syringe was warmed and maintained at the temperature set before the test.
3. The thermograph and high-speed camera were activated.
4. A water droplet was dropped onto the spot on the test piece surface.
5. Data from the thermograph were examined in order to confirm the correctness of the droplet temperature at the needle tip. If the temperature deviated from the target value, the collected data were deleted from the dataset.

2. Test results and discussion

First, the state of motion of a droplet (e.g., sliding and/or rotating) was analyzed by close examination of the images from the high-speed camera. Particles were thus mixed into the water for instillation; the properties of the particles are given in Table 3. Water was then dropped onto the surface of the inclined test piece. When the droplet started to move, the motion was recorded by the high-speed camera. In the analysis, a single particle inside the droplet was tracked. Successive tracking of the particle, as shown in Fig. 4, showed that the droplet rolled downward as if it were a rigid body.

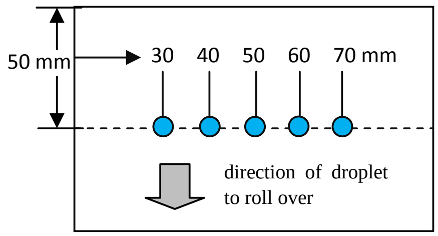

Fig. 3. Position of the instillation from the needle

Table 3. Property of the tracer particle

Material	Polyamid12 powder/white	
Density	1.0 – 1.2 g/cm^3	
Particle size	Median	145 microns
	Range	60 – 250 microns

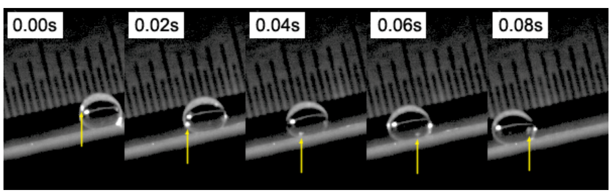

Fig. 4. Trajectory of the tracer particle

In the following stage, the drop test was begun. Based on several test runs, the droplet behavior just after instillation was divided into three categories, as shown in Fig. 5.

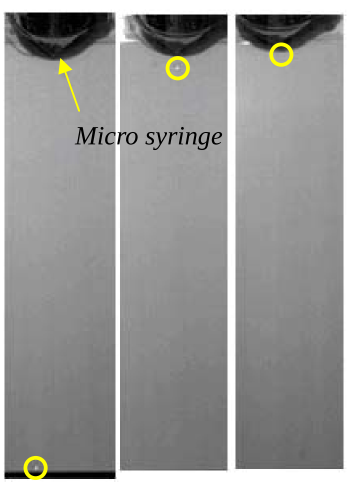

(*a*) (*b*) (*c*)

(*a*) *Rolling down toward the other end*
(including the case that the droplet halted on the way)
(*b*) *Halting immediately after instillation*
(*c*) *Standing still*

Fig. 5. Behavior of droplet after instillation

Case a: Immediately after instillation, the droplet started to roll down on the coated surface toward the other end. Some droplets stopped along the way for some reason.

Case b: The droplet fell, moved a short distance, and then stopped.

Case c: The droplet stood still without any movement after instillation.

Case a was when a droplet rolled down an inclined surface. Case a included two different types: a droplet left the test piece without any halt, and the droplet stopped somewhere along the way. Case b was when a droplet halted a small distance from the point of instillation, and case c indicated that a droplet did not move at all.

Fig. 6 shows the relation between the initial temperature of a droplet when it came out of the needle tip and the droplet behavior as categorized above. When the droplet temperature was 30 °C, every droplet stopped without any movement (i.e., case C). At 5 °C, 38% of the droplets belonged to case C.

The trend clearly showed that the rate of case C increased with the initial droplet temperature. The rate of case B revealed the same tendency as case C, although it was not as clear. The surface tension of a droplet is dependent on its temperature and decreases as the temperature increases. As a result, the spherical shape of a droplet on a superhydrophobic surface becomes a bit more flat as the temperature goes up; thus, the area of the interface between the droplet and coated surface may broaden, which may cause friction to suppress the droplet movement.

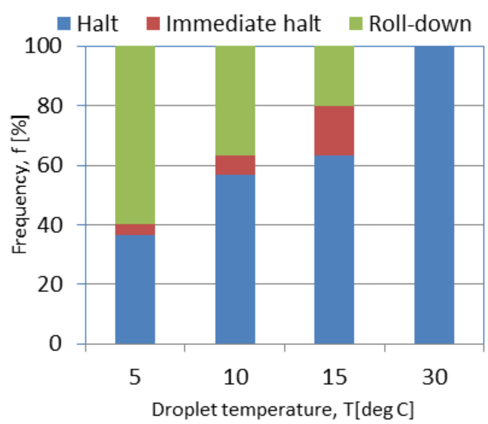

Fig. 6. Frequency of the droplet behavior after instillation on the coated surface

Fig. 7 indicates the relation between the surface condition of the test piece and the droplet behavior. The superhydrophobically coated surface intended for application to aircraft in the future is not a highly accurate industrial production. It is a surface created by hand when required by the occasion. Therefore, uneven and non-uniform surface conditions at the microscopic scale are unavoidable. This fig. shows the influences of coating unevenness on the droplet movement. The spots where the droplet was dropped are indicated by letters a–j. Fig. 7 shows the ratio of case C shown in Fig. 6 for different spots on the test pieces.

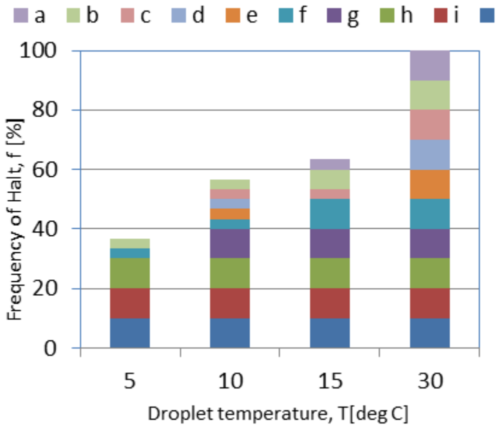

Fig. 7. Relation between the position of instillation and the halt of droplet

At a 5 °C water temperature, for which approximately 38 % of the droplets rolled down smoothly, the ratio of case C was higher at spots h–j, while all droplets at spots a and c–e successfully moved downward. This implies that the droplet movement strongly depends on the surface condition. Consider the droplet behavior if the superhydrophobic coating is applied to an actual aircraft wing with an electrothermal anti-icing device. Unlike the present test conditions, droplets would then be exposed to a high-speed airflow. They would be induced to start moving backward by the aerodynamic drag force acting on them even though their presence is within a boundary layer because of the small droplet size. The results of the present tests suggest that surface conditions that may hamper the smooth onset of movement have to be considered. In addition, consider case A, where the droplet rolls down after instillation. Fig. 8 shows the image of a single droplet's trajectory at regular intervals based on superimposing pictures taken by the high-speed camera. The droplet speed as calculated from the image is shown in Fig. 9.

A lower droplet temperature clearly tended to produce a higher droplet speed. The droplet was also found to travel at a constant acceleration regardless of the temperature. In the present test, the external forces acting on the droplet were the weight as the driving force and the resistance forces of the aerodynamic drag and force at the interface. The weight is always constant neglecting evaporation in a short period of time. The resistance force acting on a minute droplet in contact with the super-hydrophobic surface can be described as a function of the temperature under the assumption that the temperature difference exerts no significant influence on rotation of the droplet.

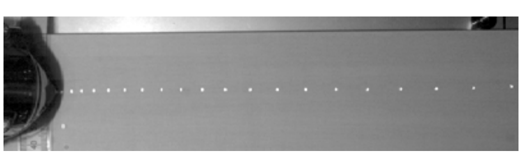

Fig. 8. Trajectory of the droplet

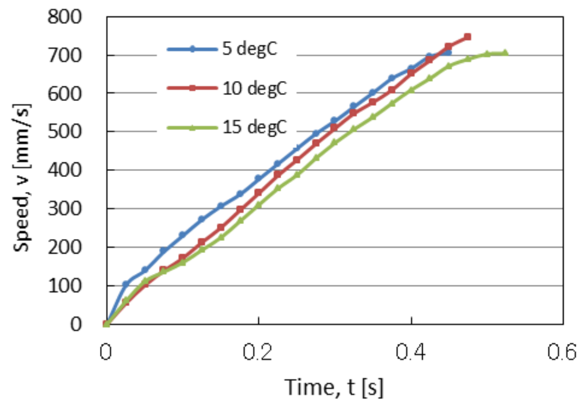

Fig. 9. Rolling-down speed of the droplet

B. Forced roll method

The gravity fall method presented above cannot be used to measure the temperature of the droplet during its movement. A new method, called the forced roll method, was used to do so. The basic concept for this method is "relative motion." The test apparatus, test procedure, and results are presented below.

1. Apparatus and test procedure

Fig. 10 shows a new device, where a droplet is fixed at the same position in space and the coated plate is moved horizontally in one direction at a constant speed. The device comprises a linear slide actuator and droplet positioner. The linear slide actuator is an actuator driven by a stepper motor to horizontally move the mounting block back and forth. The coated plate was fixed to the mounting block. The positioner of the water droplet was a 1.8 mm diameter ring made with a thin wire and a supporting rod.

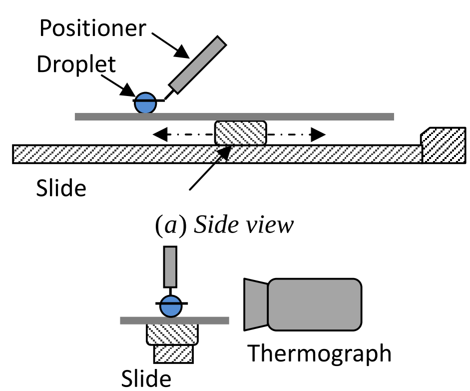

(*a*) *Side view*

(*b*) *Frontal view*

Fig. 10. Schematic view of the test stand for the forced roll method

A remarkable feature of the device is its capability for close-up observation of a droplet by a thermograph because the droplet can stay in the same position during the test run (shown in Fig. 10 (b)). The temperature of the droplet was detected by using the program installed in the thermograph. Since directly measuring the temperature distribution inside a 2-mm-diameter droplet by the contact method (e.g., by thermocouples) is quite difficult, the thermograph was not calibrated. Instead, the measurement accuracy of the thermograph was confirmed by another test using a black body model and thermocouples prior to the main test. In the present test, the only device measuring the temperature was the thermograph, and the measured object was a small water droplet. Therefore, the analytical process should take into consideration that the acquired temperature data may contain errors to a certain degree.

As in the gravity fall test, the motion of a droplet constrained by a small ring was examined by the same technique of using tracer particles and a high-speed camera. The results showed that water inside the droplet started to rotate in synchronicity with the droplet rotation soon after instillation and continued until the droplet reached the other end of the plate. The results validated the feasibility of the method as the droplet behaved similarly in the gravity fall test.

The same conditions as in the gravity fall test were selected for the temperature, droplet size, and water temperature. The speed of the droplet movement (i.e., speed of the sliding plate) was set to 10.0 mm/s. Test plates coated in the same manner were used. The one-way movement of the droplet was determined because the droplet revealed questionable behavior: for example, the retrieving edge of the droplet was dragged in the interface between the water and the coated surface when the plate reversed its motion. The test duration was almost 30 s because of the 30 cm length of the plate and the plate's speed of 10 mm/s. The test run was repeated 10 times for each set of test conditions.

2. Test results and discussion

The test results are presented in Table 5. The droplet did not freeze when the initial water temperatures were 5, 10 and 15 °C at ambient temperature of -15 °C. At an initial water temperature of 20 °C, the droplet with an initial temperature of 20 °C froze during motion in 2 out of 10 cases, and freezing occurred in 4 out of 10 cases when the droplets had an initial temperature of 30 °C. The distances for how far these droplets traveled until they froze are in the right column of Table 5. As shown in Table 5, there was no clear correlation between the distances, which suggests that no distinct reason can be found for what initiated freezing.

Table 5. Frequency of the droplet freeze in the test by the forced roll method

Droplet temperature [deg. C]	Freeze	Distance [mm]
5	-	-
10	-	-
15	-	-
20	2/10	75
		245
30	4/10	66
		150
		200
		275

Fig. 11 shows spots in the image of a droplet acquired from the thermograph when the temperature was measured continuously over the course of a test run. As shown in the fig., four spots were selected inside the droplet image, and one spot was in the peripheral area of the droplet. In the thermographic images, the droplet rotated in the clockwise direction. Hence, SP2 is a spot approaching the coated surface, and the temperature of the spot leaving the interface was measured at SP4.

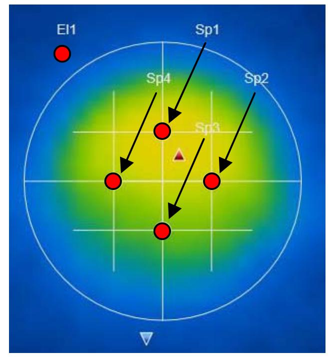

Fig. 11. Spots for the temperature measurement of the recorded images from the thermograph

The temperature change at the five spots is shown in Fig. 12; the initial droplet temperature was 5 °C. Overall, the temperature decreased gradually and approached -10 °C asymptotically (note that the value was not exact but can be tolerated for this discussion). Suppose that the discrepancy between the actual and measured temperatures is allowable; the results indicate that the droplet continued to rotate in a supercooled state for longer periods during the test run.

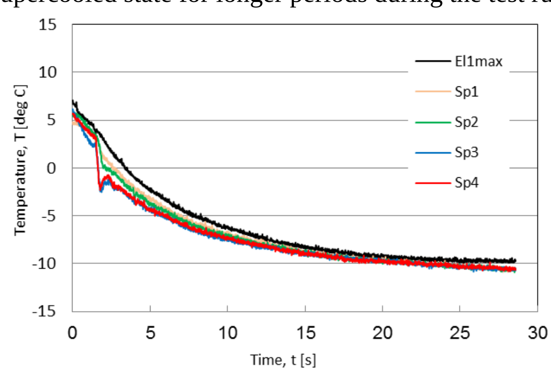

Fig. 12. Temperature change of 5 spots in the thermograph images of the droplet in the case of no freeze

The temperatures at SP3 and SP4 were lower than those at SP1 and SP2 from the onset of the test run up to 15 s. Since the area including SP3 was in contact with the interface and the area including SP4 was part of a droplet that had just left the interface, the droplet can be inferred to be cooled faster by thermal conduction through the interface than heat transfer through the outer surface of the droplet exposed to ambient air. After 15 s, the entire droplet became thermally uniform. When the average temperature inside the droplet was higher than the ambient temperature, the part cooled by contact with the coated surface may recover its temperature by contact with other parts of the water droplet with higher temperature and/or mixing with other water. Since the water droplet moved horizontally at 10 mm/s with rotational motion in this test, the motion was quite sluggish. Thus, the state of motion could be considered to be quasi-static. The test results suggest that a water droplet in quasi-static motion may continue its movement without freezing as long as it receives no stimulation to release the droplet itself from the supercooled state.

At an initial water temperature of 20 °C, the droplet temperature changed similarly to when the water temperature was 5 °C until approximately 26 s after the onset of the test, as shown in Fig. 13. The droplet temperature then suddenly jumped up due to the latent heat from freezing. As shown in the fig., the temperature was -4 °C (note that the temperature readings from the thermograph included some discrepancy). At the same time, the water droplet happened to stop its motion by freezing. Fig. 14 shows successive thermographic images of the droplet under the same conditions as the droplet in Fig. 13. In the test, the droplet was shot by a thermograph placed diagonally in front. This is why the test plate looks inclined. In these images, the test plate moved right to left, and the droplet rotated clockwise as seen from the front. The average temperature of the droplet decreased to the freezing point 4 s after the onset of the test run. The droplet continued to cool while maintaining the supercooled state. At 25.7 s, the droplet temperature was almost equal to that of the surrounding atmosphere, so the droplet was the same color as the air in the image.

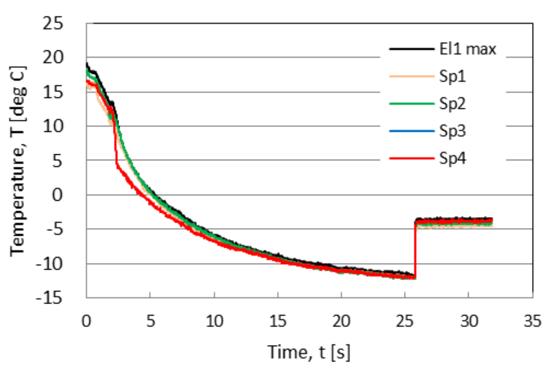

Fig. 13. Temperature change of the rolling droplet in the case of sudden occurrence after the release from the supercooled state

At 25.8 s, the lower left part of the droplet is released from supercooling (indicated by the circle in the fig.). The droplet froze completely 0.1 s later as recognized by the change in color in the thermographic image. The lower left part of the droplet, represented by SP4, is where water from the droplet was torn off from the coated surface against the adhesion force acting on the interface. If the release of a minute water droplet from supercooling depends on some external stimulus, the impact exerted by separation of the droplet from the coated surface can be considered to be the cause of the supercooling release. However, the supercooling release did not always occur in the droplet under the same test conditions. Consequently, the freezing of a droplet moving on a coated surface could be very stochastic.

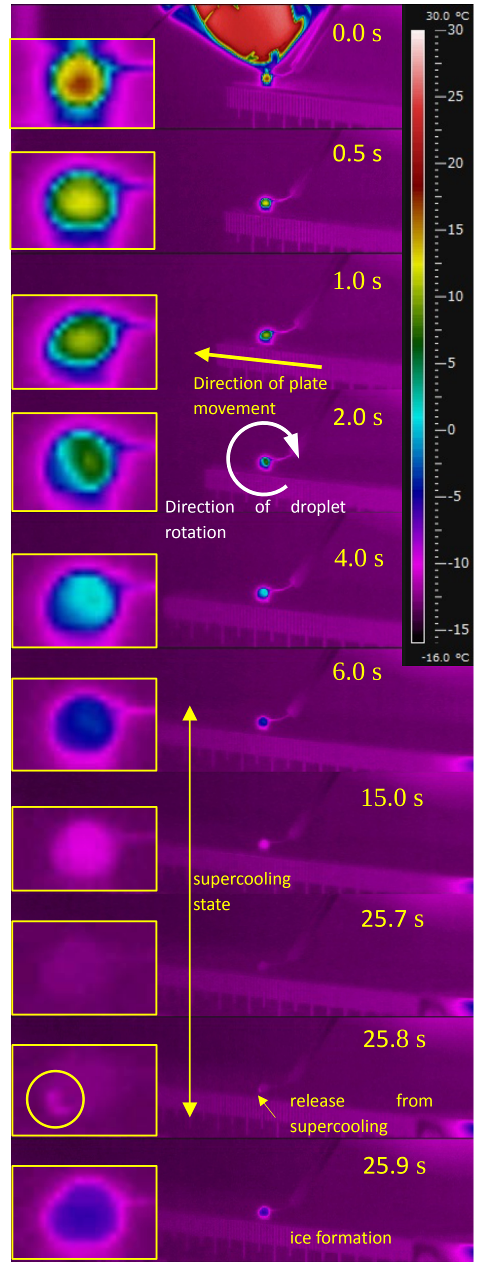

Fig. 14.Thermographic images of the rolling minute water droplet

Ⅲ. Conclusions

The freezing process of a minute water droplet in quasi-static motion on a superhydrophobically coated surface in a sub-zero environment was studied experimentally using two approaches and numerical calculations. The findings derived from the results are as follows:

- On a surface coated by a superhydrophobic paint, a droplet rolls with a rigid motion. When the droplet's motion is quasi-static, it continues the motion even in a supercooling state.

- Freezing of a droplet in a supercooling state is so highly stochastic that estimation using a theoretical or physical model is not easy.
- The onset of motion by an external force and the stopping of a droplet in motion are strongly dependent on the conditions of the surface in contact with the droplet. Therefore, estimating the droplet's behavior as to how to start its motion and/or where it stops is not easy.
- The behavior of a droplet on a superhydrophobic surface depends on the droplet temperature. A lower temperature that is as close to the freezing point as possible allows the droplet to move more smoothly. Thus, application of such coatings to icing prevention on heated wings may require a thermal capacity and heating scheme that do not greatly increase the droplet temperature.

Ⅳ. Acknowledgments

Authors are thankful to Dr. H. Sakaue and Dr. K. Morita of Japan Aerospace Exploration Agency and A. Aoki for their assistance of this research. The Center of Solar Energy research and Development of Kanagawa Institute of Technology and Ministry of Economy, Trade and Industry are acknowledged for financial support.

Ⅴ. References

1. Strub, M., O. Jabbour, F. Strub and J.P. Bedecarrats: Experimental study and modeling of the crystallization of a water droplet, International Journal of refrigeration, 26, 2003, pp.59-68
2. Hindmarsh, J.P., A.B.Russel and X.D. Chen: Experimental and numerical analysis of the temperature transition of a suspended freezing water droplet, International Journal of Heat and Mass transfer, 46, 2003, pp.1199-1213
3. Kostinsky, Alexander and Will Cantrell: Entropic Aspects of Supercooled Droplet Freezing, Journal of the Atmospheric Science, 65, 2007, pp.2961-2971
4. Tsuyoshi Kawakami, Masahiko Yamada, Shoichiro Fukusako and Hiroaki Kawai: Solidification Characteristics of a Droplet on a Horizontal Cooled Wall, Heat Transfer-Japanese Research, 26-7, 1997, pp.469-483

Effect of plasma deposition time on ice repellency of plasma polymerized HMDSO film

L. Foroughi Mobarakeh *, R. Jafari, M. Farzaneh

NSERC / Hydro-Quebec / UQAC Industrial Chair on Atmospheric Icing of Power Network Equipment (CIGELE) and Canada Research Chair on Atmospheric Icing Engineering of Power Networks (INGIVRE), www.cigele.ca
Université du Québec à Chicoutimi, Chicoutimi, QC, Canada
* Email: Ladan.Foroughi-mobarakeh@uqac.ca

Abstract — Plasma polymerization is a suitable technique for thin film deposition with widespread applications in domains as biomedical, biofouling, anti-corrosion and anti-icing. In this study, low pressure plasma polymerization of Hexamethyldisiloxane (PP-HMDSO) was carried out to impart a superhydrophobic coating with icephobic properties on anodized aluminium surfaces. Before low surface energy coating, an aluminium surface was anodized to make it rough. The superhydrophobic and icephobic properties of the developed coating were studied by considering the effects of deposition time (t = 15 to 25 min) of the plasma polymerization process. The results showed that increasing the treatment time leads to an increase of the contact angle from 158º to 164º while the sliding angle decreases from 8º to 3º. It was also observed that the ice adhesion strength of coatings decreased to 100 kPa for t = 15 min and to 83 kPa for t = 25 min compared to ice adhesion strength of an untreated aluminium surface (350 kPa). The durability of the PP-HMDSO coatings showed that after 15 consecutive icing/de-icing cycles the shear stress for t = 15 min increased to 250 kPa whereas it was 130 kPa for t = 25 min. The surfaces can keep their icephobic properties after 15 consecutive icing/de-icing cycles.

Keywords — Superhydrophobicity, plasma polymerization, Hexamethyldisiloxane, Icephobicity, Contact angle.

I. INTRODUCTION

In many cold regions of the world, ice accumulation on aircrafts and aerospace components, transporting vehicles, electrical fittings and connectors creates a lot of problems. For example, in January 1998, it caused massive damage to the electrical infrastructure all over the area touched by North American ice storm, leading to widespread long-term power outages [1–4]. Hence, developing techniques to reduce ice accumulation on structures is getting special attention. One solution to this problem is producing a weak ice adhesion material coating called icephobic coating [5]. Many researches are underway to develop a superhydrophobic and hydrophobic coating with icephobic properties [6–9].

In general, the superhydrophobicity of a surface is the result of a combination of low surface free energy and surface roughness [10]. It was shown that to obtain a superhydrophobic coating with icephobic properties, the surface should have a low adhesion to ice, and the ice has to be also easily removed from the surface.

Plasma technology is one of the appropriate methods used to create superhydrophobic surfaces. Plasma technology takes advantage of highly reactive plasma species to modify the functionality of various substrates. It is one of the most common surface treatment technologies widely being used for surface activation, cleaning, adhesion improvement, anti-corrosion coatings and biomedical coatings. Plasma polymerization process serves to deposit the coating by using plasma activation. It is used in the development of thin films of materials, but it may also be used to increase surface roughness. This plasma polymerization method is typically an environmentally friendly, short and low-energy consumption process which can be used to deposit a thin polymer film by using a low quantity of reagents, making it economically and industrially attractive [11].

A wide variety of plasma processing parameters such as input power, monomer flow rate, distance between substrate and monomer inlet as well as deposition time and pressure can directly affect the chemical and physical characteristics of the plasma thin film.

The durability and reliability of the coatings are important factors in the lifetime of a coating under extreme environmental conditions. Many experimental studies created the superhydrophobic coating by different methods, but a few researches examine the durability of these coatings under simulated environmental conditions. One of them is exposed after several icing/de-icing cycles as a serious factor in cold regions.

The present study proposes the elaboration of water and ice-repellent coatings by following two steps: first, anodization of aluminium (Al_2O_3), which is generally used to improve the corrosion properties of aluminium, in order to create micro/nano-structured roughness; and second, low pressure plasma polymerization of HMDSO coating to deposit low surface energy material. The wettability of coating was evaluated by contact angle measurements. The icephobic properties of the plasma polymerized thin film were investigated under atmospheric conditions in a wind tunnel at sub-zero temperature for two different deposition times.

II. EXPERIMENTAL APPARATUS

The aluminum alloy 6061 coupons (5cm × 3cm × 0.15 cm) obtained from Rio Tinto Alcan (Mg 1.0, Si 0.6, Cu 0.28, Cr 0.05, Zn 0.1, Fe 0.25 and Mn 0.15, all in wt %) was used as a substrate [12]. Anodization is a common electrochemical technology that is used to create an artificial porous oxide layer [13]. The aluminum to be anodized is immersed in phosphoric acid (10%wt, certified grade from LabMat Company) as an electrolyte at a temperature of 18ºC, voltage 50V for duration 90 minutes [14]. Hexamethyldisiloxane (HMDSO, whose chemical formula (CH3)3-Si-O-Si-(CH3)3) was used as an organosilicon precursor with 98% purity from Aldrich. The RF plasma polymerization process was carried out in an inductively coupled radio frequency (13.56 MHz) system (HICP-600SB PECVD; Plasmionique Inc). Further details regarding the reactor setup and the process are given elsewhere [15,16]. In this study, plasma polymerization parameters were input power 60W, distances between substrate and monomer inlet 17cm, monomer liquid flow rate 20 g/hr, pressure 8Pa and deposition time 15minute and 25 minute.

The hydrophobic characteristics of the surface were measured with static contact angle analysis using a Kruss DSA 100 goniometer (double distilled water drop volume ~ 4μL). The values of the contact angles are the average of 5 values measured over an extended area of each sample. The surface chemical structure was also examined by X-ray photoelectron spectroscopy (XPS) with a VG ESCALAB 3 Mk II surface analytical instrument. The thickness was measured by RC2 ellipsometry from J.A. Woollam Co. The icephobic properties of developed surfaces were studied by the ice accumulation in the icing wind tunnel and the ice detachment in a centrifugal instrument. The atmospheric ice (glaze) was accumulated by spraying super-cooled micro-droplets of water on the substrates at air pressure 100 kPa, water pressure 325 kPa, air velocity 10 m/s, air temperature -10 ºC and droplet size 67μm which were placed in the wind tunnel and mounted on the end of a supporting beam. After the ice accumulation, an ice adhesion strength test of the samples was done at temperature of -10 ºC by a centrifuge instrument in order to compare the treated and untreated aluminum samples. Surfaces are covered with the ices which are placed on the beams in a centrifugal instrument. The ice adhesion strength is assumed to be equal F = mrω2, where m is the ice mass (kg), r is the beam radius (m), ω is the rotation speed (rad.s-1). The shear stress was then calculated as, τ = F/A, where A is the iced surface area, and F is ice adhesion strength. To reduce the bias caused by potential experimental errors, the adhesion reduction factors (ARF) were calculated. ARF is defined as the ratio between ice shear stresses on untreated aluminium and ice shear stress on aluminium after immersion and plasma polymerization, ($ARF = \tau_{Al\ without\ coating}/\tau_{Al\ with\ coating}$).

III. RESULTS AND DISCUSSION

The SEM image of the anodized aluminum surface at 50 V and 90 minutes is depicted in Figure 1. It exhibits the presence of a pore structure with a diameter of about 80-160 nm as an “hexagonal bird’s nest” structure separated by thinner pore walls.

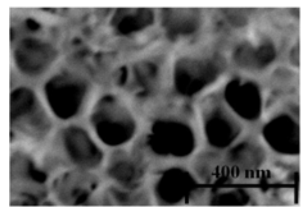

Figure 1: SEM image of anodized aluminum surface.

An ellipsometry instrument was used to measure the thickness of the coating following the increase of the deposition time. The results show that by increasing the deposition time from 15 to 25 minutes, the thickness of the coating increased from 12 nm to 18 nm and the refractive index decreased from 1.57 to 1.42.

The XPS analysis was carried out to study the effect of increment of the deposition time on the chemical composition of the PP-HMDSO coating. Figure 2 depicts high resolution peaks of C1s and Si2p. The bonding energy of the C1s peak is around 285 eV, and 103 eV for the Si2p peak [17]. It can be seen that by increasing deposition time, the percentage of carbon to silicon ratio (C/Si) increases from 1.5 for 15 minutes to 2.15 for 25 minutes. These results show that the methyl group as a functional hydrophobic group is increased on the coating. Additionally, the percentage of Al2P (at 75 eV) and O1S (at 533 eV) on the coating is decreased (from 11% to 4% and from 52% to 34%) by increasing the deposition time (from 15 to 25 minutes). These results indicate that the surface is more covered after the PP-HMDSO coating is deposited while deposition time is increased.

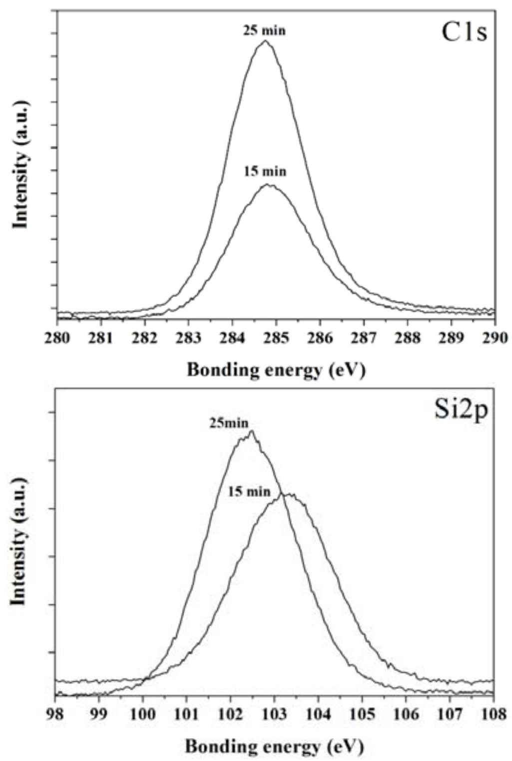

Figure 2: XPS high resolution of C_{1s} and Si_{2p} spectrums of PP-HMDSO coating on an anodized aluminum at 15 and 25 minute deposition times.

The results of the contact angle (CA), the contact angle hysteresis (CAH) and the sliding angle (SA) of different surfaces for different deposition times are given in Table 1. It is shown that by increasing the deposition time from 15 to 25 minutes, the contact angle experiences a slight increase from 158° to 161°, and the sliding angle has a low decrease from 8º to 3º.

Table 1: Variation of contact angle, contact angle hysteresis and sliding of PP-HMDSO coating at different deposition times on anodized aluminum surfaces.

PP-HMDSO coating at	CA (º)	CAH (º)	SA (º)
15 minute	158 ± 3	13 ± 2	8 ± 0.5
25 minute	164 ± 2	11± 1.2	3 ± 0.4

The ice adhesion strength of PP-HMDSO coated surfaces at different deposition time periods is compared in Table 2. The results show that by increasing of deposition time from 15 to 25 minutes, the ice adhesion strength is decreased slightly from 100 kPa to 83 kPa.

Table 2: Comparison of ice adhesion strength of untreated and PP-HMDSO coated aluminum substrates at different deposition time.

Name	Ice adhesion strength (kPa)	ARF
Untreated aluminum	350 ± 25	1
PP-HMDSO coating for 15 minute deposition	100 ± 9	3.5
PP-HMDSO coating for 25 minute deposition	83 ± 5	4.2

In order to evaluate the longevity of the surfaces and to assess their potential outdoor applications, their durability was studied following several icing/de-icing cycles. Ice adhesion strength and contact angle of PP-HMDSO coating at two deposition time were measured after each successive icing/de-icing cycle.

The variation of ice adhesion strength of for two surfaces during fifteen icing/de-icing cycles is shown in Figure 3a-b. The ice adhesion stress for 15 minutes deposition, as shown in Figure 3a, remains approximately constant at 100 ± 9 kPa (ARF = 3.5) for the first seven icing/de-icing cycles, after which it increased to 250 ± 25 kPa (ARF = 1.4). Then shear stress increased and after fifteen icing/de-icing cycles, it reached 250 kPa; however, the surface retained its icephobic properties (ARF = 1.4). In Figure 3b, the ice adhesion stress of 25 minute deposition had a minor increment after fifteen icing/de-icing cycles. Ice adhesion strength started from 83 ± 5 and reached 130 ± 30 kPa. Also, it was noticed that the surface can keep its icephobic characteristic (ARF = 2.7).

These results show that the ice adhesion amount of 25 minutes PP-HMDSO coating (130 kPa) is almost half of the ice adhesion amount of 15 minutes of that (250 kPa) after fifteen icing/de-icing cycles. Therefore, by comparing the results of the shear stress value of 25 minutes deposition time after fifteen icing/de-icing cycles (ARF = 2.7) with the results obtained for 15 minutes deposition time (ARF = 1.4), a significant improvement of stability against several icing/de-icing cycles can be observed. However, two surfaces can keep their icephobic properties after 15 consecutive icing/de-icing cycles.

a)

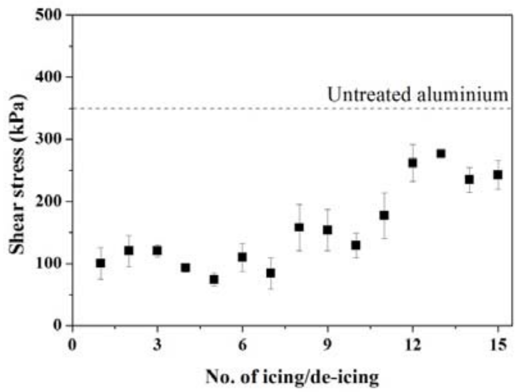

b)

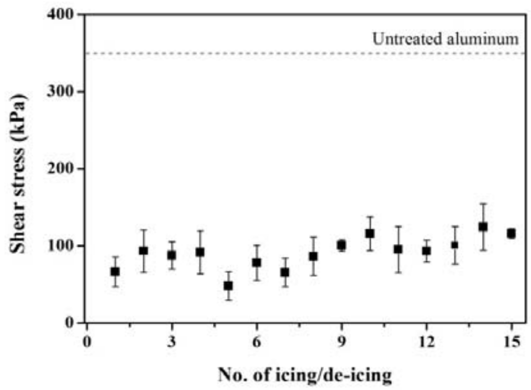

Figure 3: Variation of shear stress versus fifteen icing/de-icing cycles for PP-HMDSO coating on anodized aluminum surface at for a) 15 minute and b) 25 minute depostion.

The evaluation of contact angle as a factor of icing/de-icing cycles is shown in Figures 4a-b. It can be observed that the contact angle for 15 minute deposition decreases from 158 ± 2 º to 145 ± 4º after fifteen icing/de-icing cycles (see Figure 4a). Even though the contact angle is still high, water droplets are unable to move freely on the surface as the sliding angle value of the surface has increased from 8 º to 25 º after the fifteen icing/de-icing cycles. These results show that a transition has occurred from Cassie-Baxter to Wenzel wetting regime after the fifteen icing/de-icing cycles. Figure 4b shows that the contact angle slightly decreased from 164 ± 2º to 156 ± 2º after fifteen icing/de-icing cycles. The water droplet can roll off easily on the surface as the sliding angle has remained constant, around 3º, after fifteen icing/de-icing cycles. It can also be assumed that the Cassie-Baxter wetting regime is still dominant after fifteen icing/de-icing cycles on the surface.

Therefore, the increment of deposition time of PP-HMDSO coating on anodized aluminum surface lead to enhance the contact angle value of t = 15 minute (156°) compared to contact angle value of the t = 25 minute (145°) after fifteen icing/de-icing cycles. The reduction in the icephobic properties of the superhydrophobic surfaces may be due to a change in surface roughness during the icing/de-icing cycles and/or the decrease of the surface energy of the materials.

a)

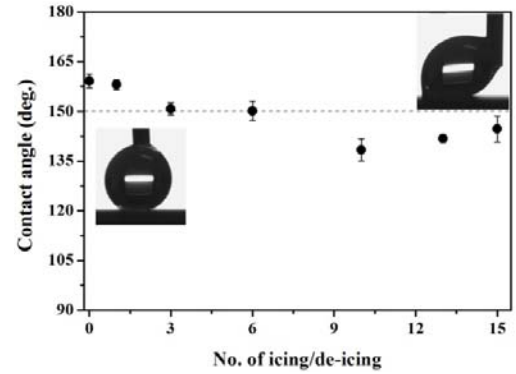

b)

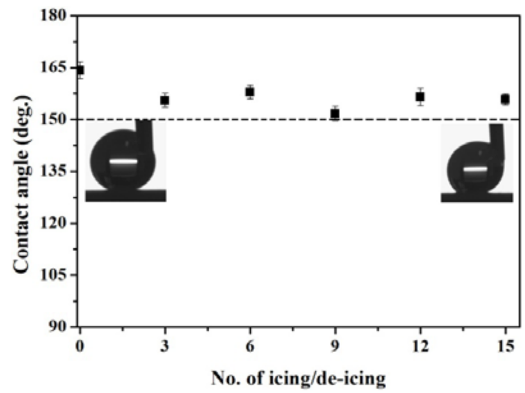

Figure 4: Variation of contact angle and images of contact angle hysteresis versus icing/de-icing cycles for PP-HMDSO coating on a anodized aluminum surfaces at a) 15 minute and b) 25 minute deposition.

III. CONCLUSION

A superhydrophobic surface was obtained on an aluminium substrate by using two industrial processes in succession, first by anodized aluminum to obtain a micro/nano-structured surface and then by PP-HMDSO to create a low surface energy coating on the aluminium oxide. By increasing deposition time, the thickness of the coatings was increased as well. The XPS analysis showed an increase in the hydrophobic functional group on the surface. Under atmospheric icing conditions, the icephobic properties of PP-HMDSO coating for t = 25 minutes was improved to an ARF is 4.2 times more than untreated aluminum surface related to t = 15 minute with ARF equal 3.5. Also the durability of coating by increasing deposition time was improved.

ACKNOWLEDGMENT

This work was carried out within the framework of the NSERC/Hydro-Quebec/UQAC Industrial Chair on Atmospheric Icing of Power Network Equipment (CIGELE) and the Canada Research Chair on Engineering of Power Network Atmospheric Icing (INGIVRE) at Université du Québec à Chicoutimi. The authors would like to thank the CIGELE partners (Hydro-Québec, Hydro One, Réseau Transport d'Électricité (RTE), Alcan Cable, K-Line Insulators, Dual-ADE, and FUQAC) whose financial support made this research possible. The authors are grateful to CURAL (Centre universitaire de recherche sur l'aluminium) for SEM analysis and to Suzie Poulin and Richard Vernhes (University École Polytechnique) for XPS analysis and Ellipsometry measurement.

REFERENCES

[1] Farzaneh M., ed., 2008, "Atmospheric Icing of Power", Springer, Berlin.

[2] Farzaneh M., 2000, "Ice Accretion on H.V. conductors and Insulators and Related Phenomena," Invited Paper, Philosophical Transactions, the Royal Society London, no. 358, pp. 1–35.

[3] Farzaneh M., and Kasaai M. R., "Analytical Evaluation of Existing Mechanisms of Ice Adhesion on Power Network Equipment," Proceedings of the 23rd International Conference on Offshore Mechanics and Arctic Engineering, American Society of Mechanical Engineers (ASME), New York, Vancouver, Canada, p. 51267.

[4] Farzaneh M., and Kasaai M. R., "A Critical Evaluation of the Existing Methods to Determine Ice Adhesion Strength," Proceedings of the 23rd International Conference on Offshore Mechanics and Arctic Engineering, American Society of Mechanical Engineers (ASME), New York, Vancouver, Canada, p. 51264.

[5] Farzaneh M., Volat C., and Leblond, 2008, "Anti-icing and De-icing Techniques for Overhead Lines," Atmospheric Icing of Power Networks, M. Farzaneh, ed., Elsevier, pp. 229–268.

[6] Menini R., Ghalmi Z., and Farzaneh M., 2011, "Highly resistant icephobic coatings on aluminum alloys," Cold Regions Science and Technology, **65**(1), pp. 65–69.

[7] Jafari R., Menini R., and Farzaneh M., 2010, "Superhydrophobic and Icephobic Surfaces Prepared by RF-sputtered polytetrafluoroethylene coatings," Applied Surface Science, **257**(5), pp. 1540–1543.

[8] Farhadi S., Farzaneh M., and Kulinich S. A., 2010, "Nanostructured Superhydrophobic Surfaces with Anti-Ice Properties," (387), pp. 4–6.

[9] Arianpour F., Farzaneh M., and Kulinich S. A., 2010, "Nanopowder-Doped Silicone Rubber Coatings for Anti-Ice Applications," Scanning Electron Microscopy, (497), pp. 4–6.

[10] Ma M., and Hill R. M., 2006, "Superhydrophobic surfaces," Current Opinion in Colloid & Interface Science, **11**(4), pp. 193–202.

[11] Inagaki N., 1996, "Plasma Surface Modification and Plasma Polymerization", Technomic Publishing Company, Inc.

[12] "http://asm.matweb.com."

[13] Hennesthal C., 2003, Application Report NanoWizard.

[14] Momen G., Farzaneh M., and Jafari R., 2011, "Wettability behaviour of RTV silicone rubber coated on nanostructured aluminium surface," Applied Surface Science, **257**(15), pp. 6489–6493.

[15] Foroughi Mobarakeh L., Jafari R., and Farzaneh M., 2011, "Superhydrophobic Surface Elaboration Using Plasma Polymerization of Hexamethyldisiloxane (HMDSO)," Advanced Materials Research, **409**, pp. 783–787.

[16] Jafari R., Foroughi Mobarakeh L., and Farzaneh M., 2011, "Water-repellency enhancement of nanostructured plasma-polymerized HMDSO coatings," Nanoscience and Nanotechnology Letters, **4**(3), pp. 369–374.

[17] Barreto M. C., Borris J., Thomas M., Hänsel R., Stoll M., and Klages C.-P., 2012, "Reduction of Plasticizer Leaching from PVC by Barrier Coatings Deposited Using DBD Processes at Atmospheric Pressure," Plasma Processes and Polymers, **9**(11-12), pp. 1208–1214.

Numerical study of the freezing process of minute water droplet on superhydrophobic surface

Mitsugu Hasegawa, Shigeo Kimura and Youichi Yamagishi

Kanagawa Institute of Technology, 1030 Shimoogino, Atsugi, Kanagawa, Japan

Abstract — A new anti-icing / de-icing method using the combination of heating and superhydrophobic surface has been developed to prevent ice accretion on structures in cold climate. Liquid water effectively can be removed from the surface in this method. The motion of a droplet of molten water can affect the cooling behavior while the droplet is moving on cooled surface. The numerical analysis of two-dimensional heat transfer for hypothetical liquid cylinder was performed to consider how rolling motion affects the cooling behavior of the droplet. The numerical model calculates temperature distribution on the cross section of the cylinder rolling on the surface. The experiments were also carried out to measure the surface temperature of a water droplet rolling on cooled plate. The droplet was deposited on cooled plate and then forcedly rolled. The model results showed the motion of rotation cause the effect of heat advection to the cooling behavior. The location near three-phase point at one side then can become the coldest any time during temperature transition in the case of motion of rotation. The qualitative comparison of experimental and numerical results showed that the motion of the real moving droplet also affects the cooling behavior.

I. Introduction

THE METHOD to avoid the adverse effects of ice accretion on structures has been proposed and studied. Traditional approach to anti-icing / de-icing method is thermal ice protection. We have been engaged in the research on advanced ice protection system, which combined electrical thermal heater with superhydrophobic-coated surface [1]. This method can be more efficient than the conventional thermal ice protection system, because no excess energy can be needed to anti-icing / de-icing.

The scenario is, briefly, to melt ice and then remove it from structures by potential energy. The airflow or gravity forces, which are potential energy, can carry away the molten water on the coated surface of structures. Great sliding performance of a water droplet on a superhydrophobic surface enhances the movement of a droplet of molten water. The power demands to melt ice or to evaporate them can be avoided. Melting and separation of ice are performed with constantly heating by electrical heater. However, a droplet of molten water can freeze again somewhere unheated and accrete there while a droplet of molten water is released from the surface. A droplet of molten water is cooled during the time. Therefore, appropriate design of heater power and application area of heating is necessary and to know how long a droplet can move in the view of thermal physics.

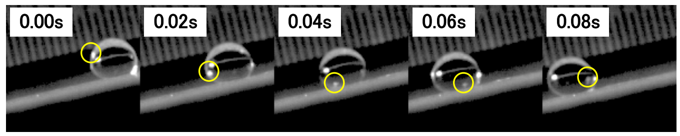

Figure 1. Trajectory of the tracer particle, Volume : 10 microL, Velocity : 62.5mm/s, Ambient temperature : 20 ºC, Tracer : Polyamid12 powder (Density : 1.0 - 1.2 g/cm^3, Particle size : Median : 145 microns, Range : 60 - 250 microns, Daicel evonik)

The motion of a water droplet can affect the cooling behavior of it. Several experimental analyses on the motion of sliding droplet on inclined coated surface have been studied. Reportedly, a water droplet on superhydrophobic surfaces typically slides down [2,3], and the sliding water droplet on hydrophobic surfaces has both rolling and slipping motion [4]. The motion of a water droplet seems to be affected by droplet volume, inclined angle or other initial situation. In our preliminary experiment, mostly rolling motion was observed on superhydrophobic surface as shown Figure 1. Although several experimental and numerical studies on freezing behavior of a water droplet deposited on cooled plate have been reported [5,6], there seems to be little study on a water droplet moving on cooled plate. The analysis of cooling and freezing behavior of a moving droplet, which the motion of a droplet is taken into account, should be studied.

The aim of this study is to show how rolling motion affects the cooling behavior of a water droplet in motion. In this paper, numerical modeling on hypothetical cylinder, which is made of liquid water, was performed instead of a water droplet rolling on cooled surface. We solved the transient temperature distribution within the cylinder and examined the effect of rolling. The experiments were also carried out to measure the surface temperature of a water droplet rolling on cooled plate. The droplet was deposited on cooled plate and then forcedly rolled. The temperature distribution of both numerical and experimental was compared and discussed the expected form of cooling in rolling and the location where temperature is the lowest.

II. Numerical Model

Numerical model on hypothetical cylinder, which is made out of liquid water, was developed instead of a water droplet rolling on cooled surface. Although three-dimensional effects of a deposited droplet which is approximately spherical need to be considered for accuracy, each of them is the same cross-section in circle at the location where we are interested in. This simplified way is used to reduce complication of numerical treatment and to identify the effect of rolling qualitatively. The two-dimensional cylindrical coordinate system adopted for the calculation is shown in Figure 2. Symbols used for the model are also shown in Table 1.

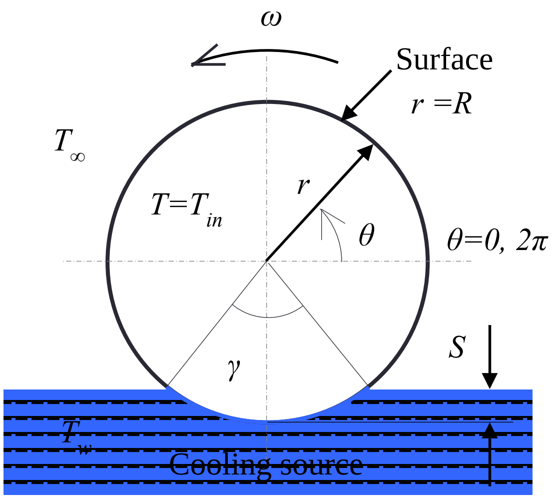

Figure 2. Physical model and the coordinate system

For the model, the following assumptions and conditions were given to simplify analysis.

(1) The lengthy of the cylinder is sufficiently longer than its diameter.
(2) The shape of the cylinder is a completely circle cross-section and have the constant contact surface acting as cooled source.
(3) Heat transfer between surrounding and the cylinder is considered only through the contact surface and the surface of the cylinder is given isothermal condition.
(4) Internal flow of water in the cylinder is neglected and the cylinder can role as rigid-body.
(5) Phase change is ignored.
(6) The thermo physical property of the cylinder is the same constant value as water and do not change with temperature.

For initial conditions, temperature of the cylinder is uniform temperature of T_{in} ºC and the motion is in a state of rest at $t = 0$. Cooling process of the cylinder is described by heat transfer coefficient h at contact surface with a temperature of T_w ºC constantly. The rolling motion of the cylinder is at constant angular velocity ω.

TABLE I
NOMENCLATURE

Symbol	Quantity
Bi	Biot number
h	heat transfer coefficient (W m^{-2} K^{-1})
r	radial coordinate (m)
R	radius of cylinder (m)
T	temperature (ºC)
T_{in}	initial temperature (ºC)
T_w	cooled wall temperature (ºC)
t_ρ	time (s)
α	thermal diffusivity (m^2 s^{-1})
θ	coordinate angle (rad)
λ	themal conductivity (W m^{-1} K^{-1})
ω	angular velocity (rad/s)
Subscripts	
*	non dimensional number

The transient temperature distribution within the cylinder then was solved as a heat conduction problem for solid cylinder. Due to symmetry of the temperature field, a two-dimensional cylindrical polar coordinate system was adopted for the calculation. The temperature distribution is described by following equation:

$$\frac{\partial T}{\partial t} = \alpha\left(\frac{\partial^2 T}{\partial r^2} + \frac{1}{r}\frac{\partial T}{\partial r} + \frac{1}{r^2}\frac{\partial^2 T}{\partial \theta^2}\right) \tag{1}$$

The boundary conditions are given by:

$$t = 0 \quad ; \quad T = T_{in} \tag{2}$$

$$r = R\,,\ 0 \le \theta \le \frac{3\pi - \gamma}{2} \quad ; \quad \frac{\partial T}{\partial r} = 0 \tag{3}$$

$$r = R\,,\ \frac{3\pi + \gamma}{2} \le \theta \le 2\pi \quad ; \quad \frac{\partial T}{\partial r} = 0 \tag{4}$$

$$r = R\,,\ \frac{3\pi - \gamma}{2} < \theta < \frac{3\pi + \gamma}{2} \quad ; \quad -\lambda\frac{\partial T}{\partial r} = h(T - T_w) \tag{5}$$

$$\theta = 0 \quad ; \quad T(r,0) = T(r,2\pi) \tag{6}$$

where γ is geometric relationship shown in Figure 2 as follows

$$\gamma = 2\arccos\left(1 - \frac{S}{R}\right) \tag{7}$$

Once dimensionless variables are introduced, such as Coordinates

$$r^* = \frac{r}{R} \tag{8}$$

Temperature

$$T^* = \frac{T - T_w}{T_{in} - T_w} \tag{9}$$

time

$$t^* = \frac{\alpha t}{R^2} \tag{10}$$

and Biot number

$$Bi = \frac{hR}{\lambda} \tag{11}$$

The problem Eq. (1) – Eq. (5) can be written in the dimensionless form as follows:

$$\frac{\partial T^*}{\partial t^*}=\frac{\partial^2 T^*}{\partial r^{*2}}+\frac{1}{r^*}\frac{\partial T^*}{\partial r^*}+\frac{1}{r^{*2}}\frac{\partial^2 T^*}{\partial \theta^2} \tag{12}$$

$$t^*=0 \quad ; \quad T^*=1 \tag{13}$$

$$r^*=1,\ 0\le\theta\le\frac{3\pi-\gamma}{2} \quad ; \quad \frac{\partial T^*}{\partial r^*}=0 \tag{14}$$

$$r^*=1,\ 0\le\theta\le\frac{3\pi-\gamma}{2} \quad ; \quad \frac{\partial T^*}{\partial r^*}=0 \tag{15}$$

$$r^*=1,\ \frac{3\pi+\gamma}{2}\le\theta\le 2\pi \quad ; \quad \frac{\partial T^*}{\partial r^*}=0 \tag{16}$$

$$r^*=1,\ \frac{3\pi-\gamma}{2}<\theta<\frac{3\pi+\gamma}{2} \quad ; \quad \frac{\partial T^*}{\partial r^*}=-Bi\cdot T^* \tag{17}$$

To solve the problem formulated above numerically, we employed finite difference method. Uniform spacing was given for the computation grid. Rotation of the cylinder was expressed by the way that relocate the value on each grid point to subsequent grid point based on the angular velocity and time steps in calculation. Thermal physical properties used for the numerical calculation are shown in Table 2.

TABLE II
THERMAL PHYSICAL PROPERTIES OF CYLINDER

Parameter	Unit	Value
Bi	-	2.7 (R=0.001m)
h	W m^{-2} K^{-1}	1500 (determined by preliminary experiment)
α	m^2 s^{-1}	1.333×10^{-7} (water at 273.16K)
λ	W m^{-1} K^{-1}	0.5619 (water at 273.16K)

III. EXPERIMENT

The experiments were carried out to measure the surface temperature of a water droplet rolling on superhydrophobic coated plate. To measure the temperature of the droplet rolling on the plate is practically most difficult so we developed alternative method to roll a droplet forcedly. Figure 3 shows a experiment device for the method. Describes simply, a water droplet was deposited on the plate. The initial temperature of water droplet was 20 ºC and the plate and ambient air were -15 ºC. Positioner, which is ring-shaped holder, was holding the droplet and fixed on the spot, only the plate then was moved horizontally. The droplet was drove with the friction between the droplet and the plate by the motion of the plate. The surface temperature of the droplet was measured with Infrared camera during the test duration of 30 s.

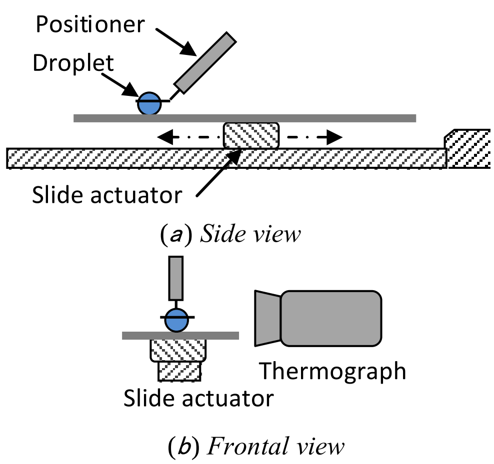

Figure 3. Schematic view of experiment device

A water droplet with an initial temperature of 20 ºC was deposited within the positioner on the plate. The micro syringe with injection needle G27 (TERUMO Corp., Japan), which is 0.22 mm in inside diameter, was used to drop the droplet. The droplet was about 2 mm in diameter on the plate. The heater covering the micro syringe entirely was used to control initial temperature of a water droplet. The dimensions of the plate were H 10 mm x W 50 mm x L 300 mm and the material was Aluminum (A7075). A superhydrophobic coating was applied by spraying a paint HIREC450 (NTT A.T. Corp., Japan) on the plate. The plate previously was sufficiently stored in the experimental room to be the same temperature as the ambient air.

The positioner was used to remain the droplet on the plate on the spot. The ring of positioner is metal wire with a diameter of 1.8 mm and the thin metal wire was 0.15 mm in diameter. The plate was movable horizontally, but the positioner was fixed.

The cooled plate moved at a speed of 10mm/s under the positioner's fixed-position, so that the rolling motion of the droplet was forcedly caused with the friction between the droplet and the plate on contact surface. The electric actuator (IAI Inc., RCA2-SA4C, Japan) was used to move the plate in horizontal direction and the plate was mounted on the unit. Since the actuator was able to operate at a constant speed, stable motion of the plate was achieved.

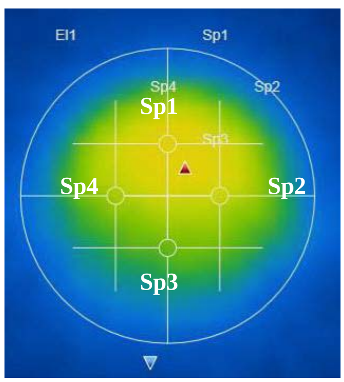

Figure 4. Spots for the temperature measurement of the recorded images from the infrared camera

The surface temperature of the droplet was measured with infrared camera A655SC (FLIR Inc., USA). The edge of a droplet, which is sphere, can change the indicated temperature due to the effect of directional emissivity. For appropriate data analyze, we specified the spot as shown in Figure 4 to extract data for temperature history. We conducted the experiment in temperature-controlled room at a temperature of -15 ºC and there was no airflow.

IV. Results and Discussion

A. Numerical Results

The distribution of isotherms of hypothetical water cylinder at time t=0.2 s, t=2.0 s, t=5.0 s and t=15.0 s are presented in Figure 5. The temperature history is also presented in Figure 6. The cylinder radius was 0.001 m. The initial temperature of the cylinder T_{in} was 20 ºC and temperature of cooled surface T_w was -15 ºC. The direction of rotation was counter clockwise and angular velocity was 10 rad/s.

Typically 2 types of direction of temperature gradient, which are toward center from outer of the cylinder and along the direction of rotation, are shown in Figure 5, (b), (c), (d). The effect of thermal diffusion was demonstrated by the temperature gradient toward center from outer. The cylinder was treated as heat conduction problem like solid in the modeling since internal flow was neglected. Cooling source was given only from contact surface as shown in Figure 5, (a). Primary temperature difference can exists between the hottest area, which is around center, and coldest area, which is around surface. Hence, the effect of thermal diffusion of cylinder toward center along radius direction was shown.

The effect of heat advection was demonstrated by the temperature gradient gradually along the direction of rotation. The elements of the cylinder move as the cylinder rotated. The motion of the cylinder can act as the bulk motion because the cylinder was treated as solid-body. This indicates advection which is the transportation of an element by bulk flow or bulk motion. Therefore, the advection effect along the direction of rotation was added and temperature gradient along the direction of rotation was shown. As cooling proceeded, temperature distribution led to be less gradient and to be uniform as shown in Figure. 5, (d).

These imply that the motion of a water droplet affects the cooling behavior of it. The advection depends on the state of bulk flow induced from motion of a moving droplet. Internal circulation of a moving droplet can depend on the motion whether slipping or rolling or other which induces the complex internal circulation. In addition, the effect of buoyancy dependent on temperature difference, especially effect of density inversion at 4ºC of water, need to be considered. To examine how the buoyancy affect to cooling behavior of moving droplet is also needed.

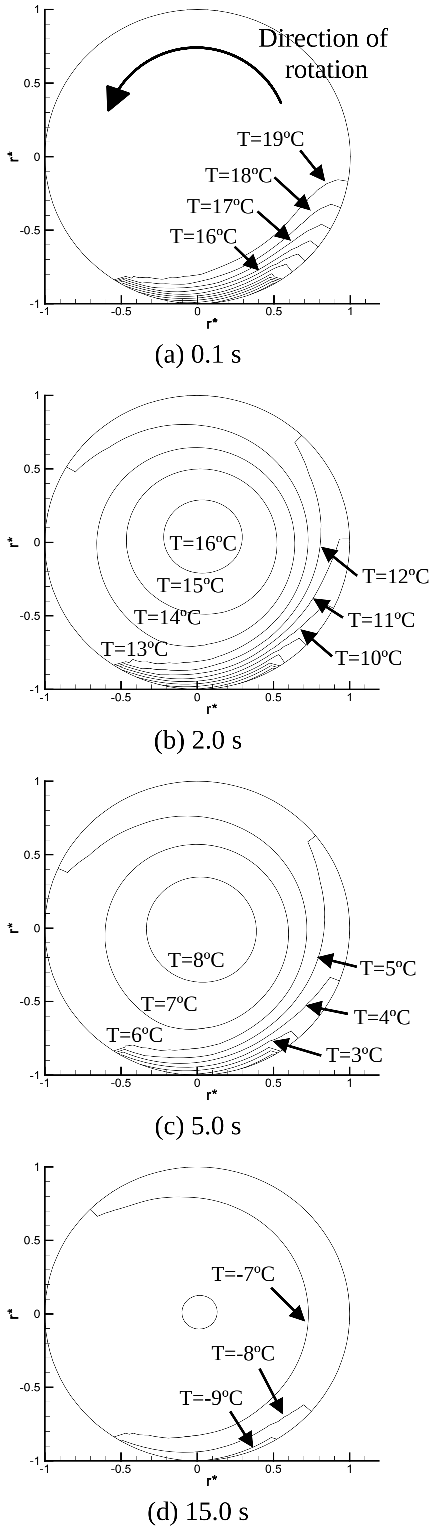

Figure 5. The distribution of isotherms of hypothetical cylinder

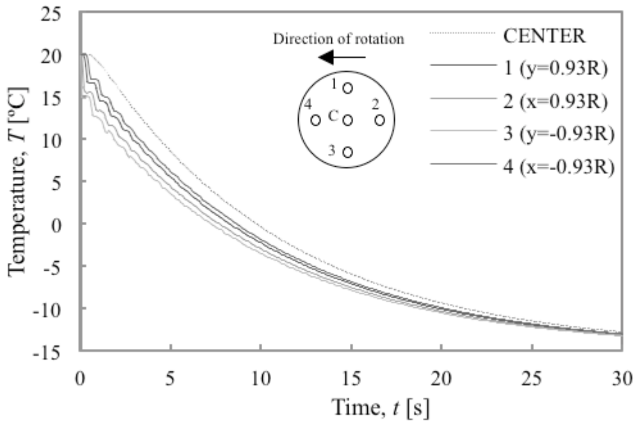

Figure 6. Temperature history of hypothetical cylinder

The most intense temperature gradient is shown at the location near contact surface and the coldest region is shown at the location near three-phase point at backward side. The contact surface is the only cooling sources to the cylinder. As we mentioned above, for the effect of advection to cooling, temperature near the surface can become lower clockwise. Therefore, the location near three-phase point at backward side can become the coldest at any time during temperature transition. This indicates that freezing can starts at the location when it reaches to freezing point.

B. Experiment Results

Infrared camera images of the water droplet forcedly rolling on the superhydrophobic-coated plate are presented in Figure 7. Temperature history for the surface of the water droplet (specified 4 points in Figure 4) is also presented in Figure 8. The initial temperature of the hypothetical cylinder was 20 ºC and temperature of ambient air and cooled surface were -15 ºC. The speed of plate was 10 mm/s and the direction was indicated in the Figure 7.

Temperature gradient along the direction of rotation are observed as shown at time t=2.0 s, t=4.0 s and t=6.0 s in Figure 7. The coldest region is also shown at the location near three-phase point at backward side. The results appear to be qualitatively analogous to the numerical results as shown in Figure 5. The rolling motion of the droplet appear to have been forcedly caused with the friction between the droplet and the plate while the plate horizontally moved under the positioner's fixed-position. Cooling source was given primarily from contact surface and airflow around the droplet was none in the experiment. Thus, the droplet was considered to be the motion of mostly rotation and the surface temperature distribution affected by the motion occurred due to comparison with numerical results.

After time at t=6.0 s, the state of supercooling of the water droplet was shown. Then more times elapsed, supercooling release suddenly was taken place and finally ice was formed as shown at time t=25.9 s in Figure 7. The sudden rise in temperature was also observed due to release of latent heat to freeze as shown in Figure 8. The edge of a droplet, which is

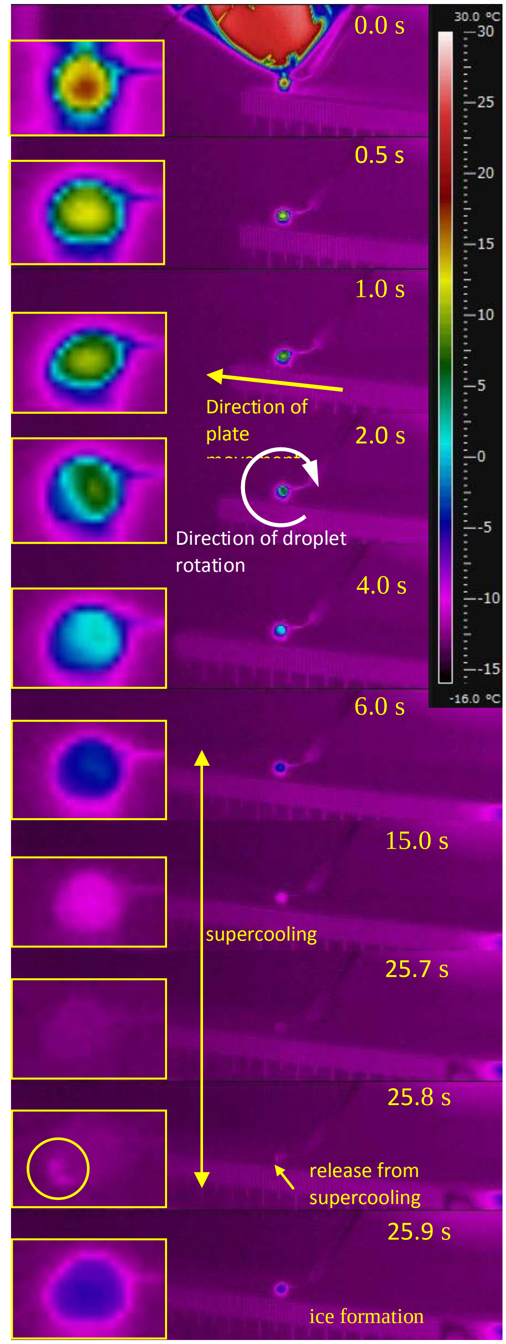

Figure 7. Infrared camera images of the rolling water droplet

sphere, will change the indicated temperature due to the effect of directional emissivity. The limitation of environmental calibration or extents of measurement error need to be considered. Though the droplet is considered to be the mostly rolling motion because of qualitative comparison of experimental results, numerical results, and physical process of occurrence of flow by moving plate. The motion of droplet practically affects the cooling behavior but the freezing behavior can be uncertain due to supercooling.

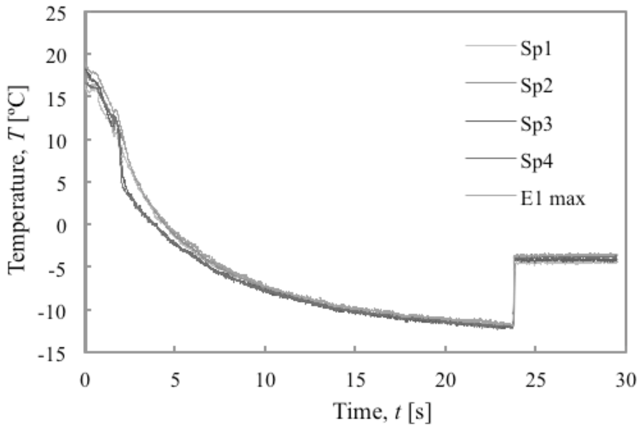

Figure 8. Temperature profile of water droplet

V. Conclusion

The numerical model showed that the motion of rotation affect the cooling behavior due to the effect of heat advection. Temperature can change toward center from outer and can change along the direction of rotation. The intensity of advection effect can depend on the angular velocity because the advection is caused by the motion of rotation. The location near three-phase point at one side can become the coldest any time during temperature transition in the case of motion of rotation. Hence freezing can starts at the location when it reaches to freezing point although the actual situation is really complex due to supercooling of water. The qualitative comparison of experimental and numerical results showed that the motion of a real moving droplet affect the cooling behavior, but the freezing behavior might be uncertain due to supercooling.

References

[1] Shigeo Kimura, Atsuhiko Sakabe, Masakazu Shimanuki and Yoichi Yamagishi, “A new surface coating of prevention of icing on airfoil”, SAE2007-01-3315, SAE Aircraft & Engine Icing International Conference and Exhibition, 2007, Seville, Spain

[2] Munetoshi Sakai, Jeong-Hwan Song, Naoya Yoshida, Shunsuke Suzuke, Yoshikazu Kameshima and Akira Nakajima, “Direct Observation of Internal Fluidity in a Water Droplet during Sliding on Hydrophobic Surfaces”, Langmuir 2006, 22, pp. 4906-4909

[3] Masashi Miwa, Akira Nakajima, Akira Fujishima, Kazuhito Hashimoto and Toshiya Watanabe, “Effects of the Surface Roughness on Sliding Water Droplets on Superhydrophobic Surfaces”, Langmuir 2000, 16, pp.5754-5760

[4] Munetoshi Sakai, Ayako Hashimoto, Naoya Yoshida, Shunsuke Suzuki, Yoshikazu Kameshima, and Akira Nakajima, “Image analysis system for evaluating sliding behavior of a liquid droplet on a hydrophobic surface”, Rev. Sci. Instrum., 78, 045103, 2007

[5] Kawakami Tsuyoshi, Masahiko Yamada, Shoichiro Fukusako and Hiroaki Kawai, ”Solidification Characteristics of a Droplet on a Horizontal Cooled Wall”, Heat Transfer-Japanse Research, 26-7, 1997, pp. 469-483

[6] Koji Fumoto, Masahiro Ikegawa and Hideaki Yamagishi, “Study on Freezing of a Single Droplet”, Trans. of the JSRAE, vol. 20, no. 2, 2003 pp. 127-134

Effect of immersion time on the hydrophobic and icephobic properties of self-assembled silane coatings on Al substrates

F. Arianpour*, M. Farzaneh, R. Jafari,
NSERC / Hydro-Quebec / UQAC Industrial Chair on Atmospheric Icing of Power Network Equipment (CIGELE) and Canada Research Chair on Atmospheric Icing Engineering of Power Networks (INGIVRE)
www.cigele.ca
Université du Québec à Chicoutimi, Canada
*Email: faranak.arianpour@uqac.ca

Abstract — The effect of immersion time on hydrophobic and icephobic properties of self-assembled monolayers (*SAM*s) thin films of OD (octadecyltrichlorosilane) on flat aluminum alloy (AA6061) substrate was investigated. By rising the immersion time from 15 minutes to 12 hours, the hydrophobic properties of the coating were improved. More precisely, in their corresponding baths, hydrophobic properties improved as contact angle (CA) increased from about 108° to 160° while contact angle hysteresis (CAH) decreased as much as 7°, corresponding to superhydrophobic characteristics (switching wetting regime from Wenzel to Cassie-Baxter regime). Icing tests showed delayed ice formation and lower adhesion strength on samples with large and small wetting hysteresis.

Keywords — Self-assembled monolayers (*SAM*s); Wetting behavior; Hydrophobic property; Superhydrophobic; Wenzel regime; Cassie-Baxter mode; Ice adhesion strength

I. Introduction

In cold climate regions, ice and wet-snow accumulation on overhead power transmission lines are sometime the source of damage and malfunctions which may lead to mechanical line failures, insulator flashovers, etc. [1-4]. Reducing or preventing ice accumulation on exposed surfaces can be accomplished by developing icephobic coatings [5-8]. The wetting behavior of a surface can be determined by the contact angle (CA) which is the angle between the surface and a water liquid drop [9]. Development of self-assembled monolayer (*SAM*) coatings with -CH_3 or -CF_3 groups oriented outward from the ice surface is one of the most successful approaches to chemically modify hydrophilic surfaces [10]. The *SAMs* through processes involving adsorption, hydrolysis, and polymerization can lead to spontaneously assembled low energy surfaces of many solids and oxides (Al_2O_3, SiO_2, etc.) [11-14]. The aim of this work is to study of the effect of immersion time on the hydrophobic and icephobic properties of *SAM*s coatings of trichloro(octadecyl)silane ($C_{18}H_{37}Cl_3Si$, OD) on polished aluminum alloy 6061 (AA6061).

II. Experimental procedure

Aluminium alloy 6061 composed of Al 97.9 wt.%, Mg 1.0 wt.%, Si 0.60 wt.%, Cu 0.28 wt.%, Cr 0.20 wt.% from industrial rolled sheets was cut into 5.1 × 3.2 cm samples used as substrates. This alloy is used widely in power transmission and distribution line conductors. The organic molecules providing low surface energy, Trichloro(octadecyl)silane ($C_{18}H_{37}Cl_3Si$), was purchased from Sigma-Aldrich® and used as received. The as-received AA6061 samples were ultrasonically cleaned in acetone and distilled water each for 5 minutes. Subsequently, the cleaned samples were first mechanically polished via 320-800-1200 and 4000-grit sand papers, then with successively finer SiC abrasive papers lubricated with water, and finally were mirror-polished with aqueous 1.0 µm alumina slurry. The polished substrate were then cleaned and degreased ultrasonically in organic solvents of methanol (99.8%), acetone (99.5%) and finally de-ionized water. The cleaned and polished Al plates were then blow-dried in a N_2 gas flow followed by a 1-hour post-treatment in oven at 70 ^{o}C. Later, they were placed in *SAM*s baths of octadecyltrichlorosilane (OD) in toluene (1 mM) via dip coating technique. The substrates were then removed from their corresponding solutions after 15 minutes, 2, 6, and 12 hours. They were rinsed with toluene and blow dried under nitrogen gas. Finally, they were post-treated in an oven for 2 hours drying at 70 ^{o}C.

The dried samples were stored in clean Petri dishes at ambient conditions and characterization was conducted immediately after. The coated samples were characterized by measuring their hydrophobic and icephobic properties. The wetting characteristics reported in this study were obtained following the standard sessile drop method on a fully automated contact angle goniometer (DSA100 from Krüss) with controllable volume (4 µl) of water droplets. These measurements were performed with the Young–Laplace method. For each samples, at least five different spots were randomly selected and measured. The CA reported for each sample is the average value of about 10 measurements. Surface topographies were studied via scanning electron microscopy (SEM, Hitachi S-4700 Field-Emission SEM with accelerating voltages from 500 V to 25 kV) to take surface images of coated samples and therefore reveal their surface characteristics. The ice-repellent performance of bare as well as prepared coatings was evaluated using a home-made centrifugal apparatus which was placed in a climate room at subzero temperature (-10^{o}C). The detail of ice preparation procedure has been described previously [15].

III. RESULTS AND DISCUSSION

Figure 1 illustrates the immersion time effect on wetting behavior of sample surfaces coated with OD (1 mM). By increasing the immersion time from 15 min to 12 hours, the contact angles of coated samples increased. In fact, a remarkable enhancement of the contact angle value was observed after a 12-hour immersion time, with a value of ~160^{o}, corresponding to superhydrophobic characteristics. The reason is that increased immersion time probably induces better ordered SAM fabrication on aluminium oxide layers as compared to shorter periods of immersion time [16, 17]. Therefore, the immersion time parameter plays very important role on the self-assembly process [18, 20].

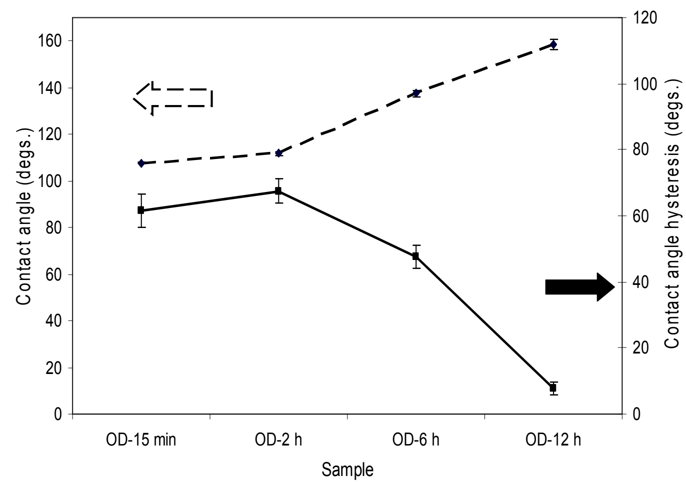

Fig. 1. Contact angle and contact angle hysteresis of coated samples with OD (1mM) for different immersion time.

As shown in Fig.1, the CAH values decrease with increasing immersion time. A significant decrease in CAH values were also observed in case of 12-hour immersion time (~7^{o}) while the CAH values were ~ 40-70^{o} for the samples with 15-min, 2- and 6-h immersion time. The high values of CA and low values of CAH in the case of coatings with 12-hour immersion time qualify them as superhydrophobic surfaces. Meanwhile, superhydrophic coatings with very low wetting hysteresis (CAH) are considered as ice-repellent coated samples [21]. As previously mentioned, the hydrophobic properties of samples coated with OD (1 mM) were enhanced by increasing the immersion time from 15 min to 12h.

In order to study the effect of immersion time on the ice-repellent properties of the coatings, ice adhesion tests were carried out on the coatings with different immersion times. Figure 2 shows that by increasing the immersion time from 15 min to 12h, ice adhesion strength of coated samples were decreased. Also, it shows that the result for 12-h immersion time demonstrates a greater reduction in ice adhesion strength as compared to all the other samples.

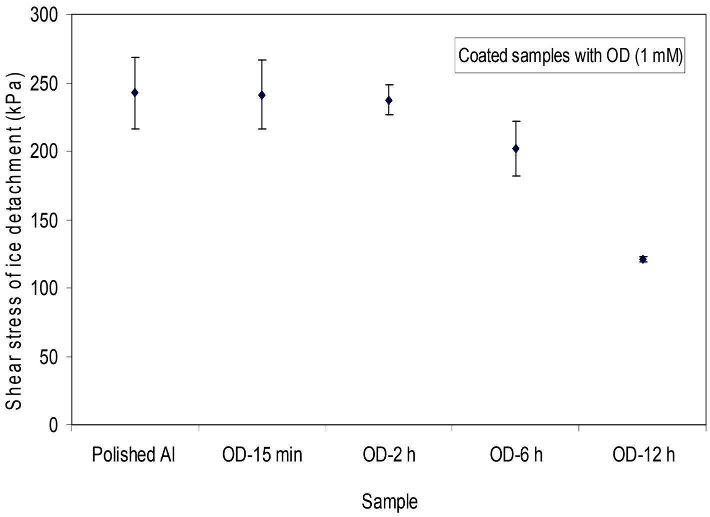

Fig. 2. Shear stress of ice detachment vs. icing/de-icing cycle number of prepared Samples from OD (1 mM) for different immersion times.

This great difference in ice adhesion strength between the 12-h sample and the others is due to its very low CAH value. As well, the ice adhesion reduction factor (*ARF*) of prepared sample for the 12-h immersion time showed ice adhesion strength at least twice lower than those obtained on polished bare Al sample. This reduced ice adhesion can be attributed to better ordered *SAM* creation on the aluminum oxide layer as well as to lesser erosion of the aluminum substrate during the process as compared to shorter immersion times.

Figure 3 presents the shear stress of ice detachment values of the 12-h coated sample as a function of icing/de-icing cycles to assess the durability of the coated sample. For the coating in question, one sample was subjected to 9 consecutive icing/de-icing cycles. It is obvious from Figure 3 that the ice-releasing performance of the coated sample slightly degraded after 9 icing/de-icing cycles which can be explained partially by the damage to the coating caused by icing/de-icing experiment and the ice removal step.

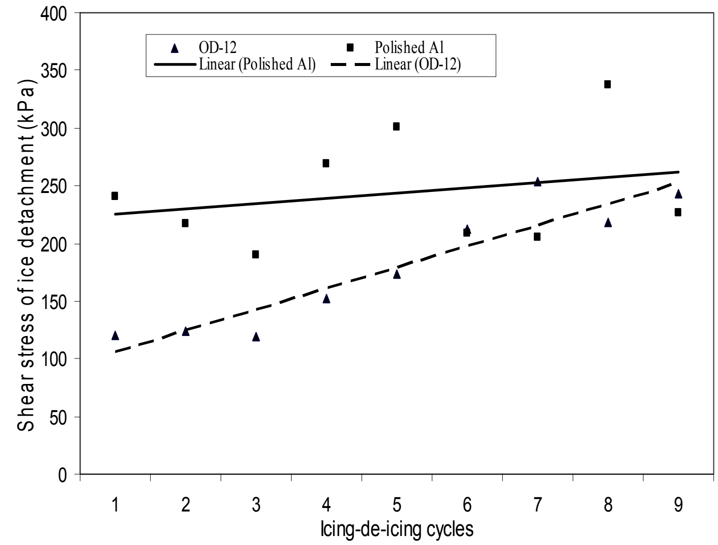

Fig. 3. Shear stress of ice detachment vs. icing/de-icing cycles number of prepared sample, OD (1mM) for the 12-h immersion time.

Figure 4 shows scanning electron microscopy (SEM) images of Al sample coated with OD (1 mM) for 12 hours immersion time with 2000X and 11000X magnifications. The SEM images of the coated surface demonstrate a rough structure at micrometer scale on a polished aluminium surface. This micro scale roughness was obtained following immersion of aluminium samples in a chemical solution bath and which corresponds to the hydrolysis step of *SAMs* process, where chloride ions are released to form hydrochloric acid (HCl). More precisely, the HCl contains Cl- ions causing erosion of aluminium surface sample which is increased with the immersion time. This reaction can express by following equation [21]:

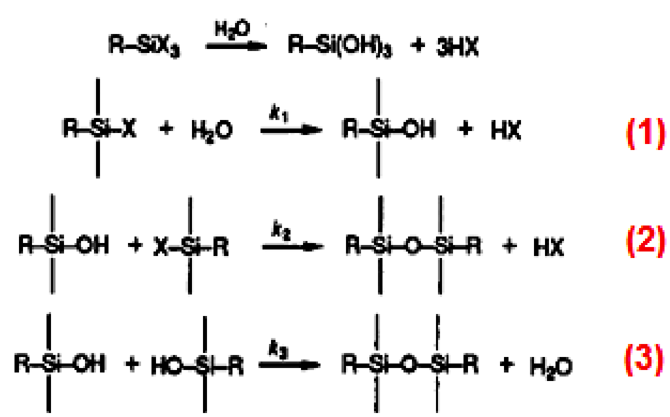

This rough structure on the polished Al surface composed of low surface energy material (e.g. OD) leads to switching its wetting regime from Wenzel to Cassie-Baxter [13] and is the mainly responsible for turning the hydrophobic surface to a superhydrophobic one. The effect of surface roughness on wetting properties can also be observed at macro/nano scale level as the CA values shift to values as high as ~160^{o}.

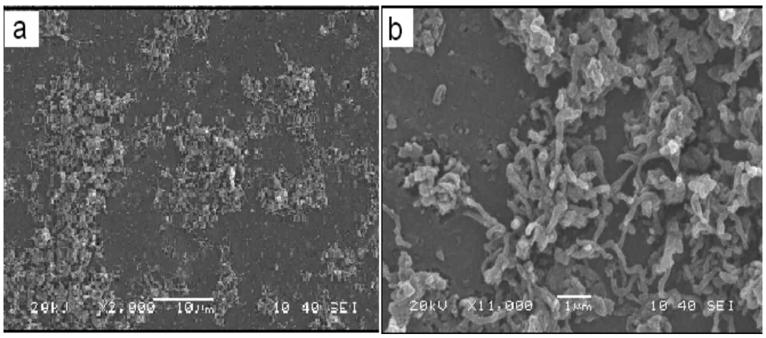

Fig. 4. Scanning electron microscopy (SEM) images of sample coated with ODS (12 hours). Magnification is (a) 2000X and (b) 11000X.

IV. Conclusions

In this work, the possible effect of octadecyltrichlorosilane (OD) immersion time on the formation, wetting behavior and icephobic performance of prepared *SAM*s coatings on flat aluminum alloy (AA6061) surfaces were studied and evaluated. For this purpose, self-assembled monolayer of alkylsilane compound with immersion times of 15 min, 2, 6 and 12 hours were permitted to assemble on polished aluminum substrates by dip-coating. It was demonstrated that the hydrophobic and icephobic properties of all coated samples were improved after increasing the immersion time from 15 minutes to 12 hours. The reason for that is most likely due to the fact that the *SAM*s creation process on aluminum oxide layer is better ordered for a long immersion time compared to shorter periods of immersion as revealed by wetting experiment results. The SEM images of a superhydrophobic sample coated with OD (12-h immersion) demonstrated micro/nano scale roughness which was obtained following aluminum sample immersion in their corresponding chemical baths resulting in the erosion of the aluminum substrate during the *SAM*s process. This rough structure on a polished aluminum surface composed of low surface energy material (e.g. OD) leads to changing its wetting regime from Wenzel to Cassie-Baxter regime and is mainly responsible for altering their surface wetting properties from hydrophobic surfaces to superhydrophobic ones.

V. Acknowledgements

This research work has been conducted within the framework of the NSERC/Hydro-Quebec/UQAC Industrial Chair on Atmospheric Icing of Power Network Equipment (CIGELE) and the Canada Research Chair on Atmospheric Icing Engineering of Power Networks (INGIVRE) at Université du Québec à Chicoutimi. The authors would like to thank the CIGELE partners (Hydro-Québec, Hydro One, Réseau Transport d'Électricité (RTE), Rio Tinto Alcan, General Cable, K-Line Insulators, Dual-ADE, and FUQAC) whose financial support made this research possible.

VI. References

[1] M. Farzaneh, "Atmospheric Icing of Power Networks" Springer, Berlin, 381 pp, 2008.

[2] M. Farzaneh, "guide for test methods and procedures to evaluate the electrical performance of insulators in freezing conditions", IEEE standard 1783 –. IEEE Press, New York, 2009.

[3] M. Farzaneh, W. A. Chisholm (2009). Insulators for icing and polluted environments, IEEE Press series on Power Engineering, IEEE/John Wiley, New York, 680 p.

[4] M. Farzaneh. Melo. O. T., (1994), Flashover performance of insulators in the presence of short icicles, Int. J. Offshore Polar Eng, 4, 112.

[5] C. Laforte, J. L. Laforte, J. C. Carrier, "How a solid coating can reduce the adhesion of ice on a structure", Proceedings of the International Workshop

on Atmospheric Icing of Structures (IWAIS), pp. 1-5, 2002.

[6] R. Jafari, R. Menini, M. Farzaneh, "Superhydrophobic and icephobic surfaces prepared by RF-sputtered polytetrafluoroethylene coatings Appl. Surf. Sci. Vol. 257, pp. 1540–1543, 2010.

[7] V. F. Petrenko and S. Peng, "Reduction of ice adhesion to metal by using selfassembling monolayers (SAMs)", J. Phys. Vol. 81, pp 387, 2003.

[8] J. L. Laforte, M. A. Allaire and J. Laflamme, "State-of-the-art on power line de-icing", Atm. Res. Vol. 46, pp. 143 1998.

[9] V. K. Croutch and R. A. Hartley, "Adhesion of ice to coatings and the performance of ice release coatings", J. Coat. Technol., Vol. 64, pp. 41, 1992.

[10] S. A. Kulinich and M. Farzaneh, "Hydrophobic properties of surfaces coated with fluoroalkylsiloxane and alkylsiloxane monolayers '', Surf. Sci., Vol. 573, pp. 379, 2004.

[11] R. Menini and M. Farzaneh, "Advanced icephobic coatings", J. Adhe. Sci. Tech. Vol. 25, pp. 971, 2011.

[12] D. Quéré, "Non-sticking drops", Rep. Prog. Phys. Vol. 68, pp. 2495, 2005.

[13] S. Farhadi, M. Farzaneh, S.A. Kulinich, "Anti-icing performance of superhydrophobic surfaces", Surf. Sci., Vol. 257, pp. 6264, 2011.

[14] V. Subramanian, and W. J. van Ooij, "Silane based metal pretreatments as alternatives to choromating" Surface Eng., Vol. 15, pp. 168, 1999.

[15] F. Arianpour, M. Farzaneh, S. A. kulinich, "Hydrophobic and ice-retarding properties of doped silicon rubber coatings", Appl. Surf. Sci., vol. 265, pp.546-552, 2013.

[16] A. Franquet, J. De Laet, T. Schram, et al., "Determination of the thickness of thin silane films on aluminium surfaces by means of spectroscopic ellipsometry", Thin Solid Films, Vol. 384, pp. 37, 2001.

[17] M. J. Pellerite, T. D. Dunbar, L. D. Boardman et al., "Effects of Fluorination on Self-Assembled Monolayer Formation from Alkanephosphonic Acids on Aluminum: Kinetics and Structure", J. Phys. Chem., Vol. 107, pp. 11726, 2003.

[18] W. Limbut, P. Kanatharana, B. Mattiasson et al., "A comparative study of capacitive immunosensors based on self-assembled monolayers formed from thiourea, thioctic acid, and 3-mercaptopropionic acid" , J. Biosens. Bioelectron., Vol. 22, pp. 233, 2006.

[19] V. Lakshminarayanan, and U. K. Sur, "Hydrophobicity-induced drying transition in alkanethiol self-assembled monolayer–water interface", J. Phys., Vol. 61, pp. 36, 2003.

[20] S. A. Kulinich and M. Farzaneh, "How Wetting Hysteresis Influences Ice Adhesion Strength on Superhydrophobic Surfaces", Langmuir, Vol. 25, pp. 8854, 2009.

[21] C. R. Kessel and S. Granick, "Formation and Characterization of a Highly Ordered and Well- Anchored Alkylsilane Monolayer on Mica by Self –Assembly", Langmuir., Vol. 7, pp. 532-538, 1991.

Corrosion Resistance, Ice-Releasing Performance and Stability of Nanostructured AA2024-T3 Superhydrophobic Surfaces

S. Farhadi[1], M. Farzaneh[1], and S. Simard[2]

[1]NSERC / Hydro-Quebec / UQAC Industrial Chair on Atmospheric Icing of Power Network Equipment (CIGELE) and Canada Research Chair on Atmospheric Icing Engineering of Power Networks (INGIVRE) www.cigele.ca, Université du Québec à Chicoutimi, Chicoutimi, QC, Canada

[2] Aluminium Technology Centre, Industrial Materials Institute, National Research Council Canada (CNRC) (www.cta-atc.cnrc-nrc.gc.ca) 501, boul. de l'Université Est, Chicoutimi, QC, Canada, G7H 8C3

Email: shahram.farhadi@uqac.ca

Abstract — Ice and wet-snow adhesion and its accumulation on exposed structures and equipment is well known to cause serious problems in cold climate regions such as Canada, the U.S, China, Russia etc. To counter this problem, various anti-icing and de-icing techniques have been introduced and developed over years. Among these, superhydrophobic coatings have been recently proposed as a passive technique to reduce or prevent ice build-ups on outdoor structures. In this study, hydrophobic and ice-repellent properties as well as anti-corrosive performance of hierarchical micro-/nano-rough superhydrophobic coatings prepared on Al alloy 2024-T3 substrates were studied. The samples were prepared by etching the Al substrate in HCl followed by further hydrophobization of the rough nanostructured surface with octadecyltrimethoxysilane $C_{18}H_{37}Si(OCH_3)_3$, known as wet-chemistry technique. The stability of the prepared coated samples was evaluated over time and in different conditions, in terms of their ice-repellent behaviour and anti-corrosive performance. Artificially created glaze ice was deposited on the nanostructured coated surfaces by spraying supercooled water micro-droplets with an average size of ~65 µm in a wind tunnel at subzero temperature (-10 ^{o}C) and a wind speed of 11 m/s to simulate most severe natural atmospheric icing. Ice adhesion strength was evaluated by spinning the samples in a centrifuge machine at constantly increasing speed until the accumulated ice detached from the samples. The samples were tested over repeated icing/de-icing cycles in order to assess the durability of their ice-repellent properties. The results showed that both water-repellent and ice-repellent properties of the surfaces degraded over time and after successive icing/de-icing cycles. Potentiodynamic polarization tests and salt spray exposure studies revealed that the corrosion resistance of the modified substrates improved compared to the unmodified ones. While extensive corrosion appeared on unmodified flat Al samples after only 8 cycles of salt spray exposure, early stage corrosion was observed for rough modified samples only after 18 cycles of exposure.

Keywords — Self-assembling; Low surface energy coating; Nanostructured AA2024-T3; Sperhydrophobicity; Ice adhesion strength; Potentiodynamic polarization; Salt-Spray test and durability; Wetting hysteresis

I. I. Introduction

Ice and/or wet-snow formation and accumulation hinders the operation and impairs the efficiency of infrastructural components, mechanisms and machines, including aircraft, ships, offshore oil platforms, dams, electrical power plants, power transmission lines and telecoms equipment etc. Atmospheric icing occurs when surfaces of exposed structures come into contact with supercooled water droplets or snow particles [1]. Prevention or retardation of icing process requires reducing adhesive strength of ice onto the surface. In recent years, much effort has been made to attain a more detailed understanding of the physicochemical phenomena governing icing processes and to develop more efficient systems for prevention or mitigating ice accumulation. For that reason, various de-icing and anti-icing techniques have been developed. For instance, a number of coatings have been elaborated to reduce ice adhesion resulting in lower ice or snow accumulation [2]-[9]. The ideal solution would be applying a durable, easy to process, and inexpensive material which would reduce adhesion to such an extent that ice would fall off under the pull of gravity, e.g. alkyl-terminated coatings such as alkylsilane and fluoroalkylsilane-based layers [3, 10, 11]. Meanwhile, reasonable correlation between hydrophobicity of a surface and its ice repellecy was reported earlier [2, 6, 8, 10]. Superhydrophobic surfaces defined as having a static water contact angle of (CA)>150^{o} and low value of CA hysteresis (CAH) have attracted considerable interest in this area. It is well known that the key factors underlying superhydrophobicity are the chemical composition of the surface along with its micro-/nano-hierarchical texture [3], [12]-[14]. Arianpour *et al.,* 2012, reported delayed water freezing on rough superhydrophobic surfaces. Superhydrophobicity can also improve anti-corrosive performance of coated metallic substrates such as Al, as it can prevent or diminish penetration of water molecules and other aggressive moieties to the metallic surface underneath [15, 16]. Numerous method and techniques have been already reported to create superhydrophobic surfaces on metallic and non-metallic substrates [6, 8, 9], [16]-[18]. However, no systematic study of their superhydrophobicity and ice-repellency over time as well as their anti-corrosive properties has yet been reported. As a matter of fact, in most methods used to evaluate ice-solid adhesion [19]-[21], water is artificially frozen on top of the samples tested under unrealistic icing conditions. Therefore, testing adhesion of glaze ice prepared by spraying supercooled water droplets is expected to give more reliable and most-simulated-natural atmospheric icing results [5, 6, 8, 18]. It was clearly shown that CAH along with static CA governs the ice-solid adhesion strength [5, 6, 8].

In this study, superhydrophobic aluminium alloy 2024 (AA2024) surfaces were fabricated via a simple and easy-to-use method. More precisely, organic coatings terminated with alkyl groups were prepared as potential ice and snow-repellent layers on AA2024-T3 samples by means of etching in diluted HCl (~9 wt%) for different time periods followed by further surface modification (hydrophobization of rough nanostructured surfaces with octadecyltrimethoxysilane). The prepared samples with etching time of three or four minutes in HCl presented enhanced superhydrophobicity with CA>156° and CAH≤5.5°, demonstrating excellent superhydrophobic properties, i.e. water droplets rolling off the surface easily. These nanostructured surfaces were then characterized and tested, and both coating stability (in water, base and acid) as well as ice-repellent performance over time were carefully studied. Furthermore, potentiodynamic polarization tests and salt spray exposure were done to study and evaluate corrosion resistance of the prepared samples.

II. Experimental procedure

A. Sample Preparation

The substrates tested in this study were made of AA2024-T3 with the following composition: Al 90.7-94.7wt.%, Si 0.5wt.%, Fe 0.5wt.%, Cu 3.8–4.9wt.%, Mn 0.3-0.9wt.%, Zn 0.25wt.%, Mg 1.2–1.8wt.%, other impurity 0.15wt.% [22]. This Al alloy, with Cu as the primary alloying element, is typically between 3.8-4.9 % (wt. %) [23], and is used extensively in applications requiring high strength to weight ratio and good fatigue resistance as well. The as-received Al substrates, 2-mm thick, were ultrasonically cleaned and degreased in water and organic solvents (acetone and absolute ethanol), each for 5 min. The unpolished cleaned samples were then etched in ~9 wt % HCl at room temperature for different time periods. This was followed by ultrasonically rinsing 2-3 times in deionized water to remove any unstable or loose particles on the surface resulting from the etching process. The etched samples were dried in a N_2 flow and were kept in oven at 80°C atmospheric temperature for 3 hrs. Finally, the Al surfaces were modified with isopropyl solution of octadecyltrimethoxysilane $C_{18}H_{37}Si(OCH_3)_3$ abbreviated here as TMSOD from SIGMA-ALDRICH® for 1 min to 2h. The solvent isopropanol used in the cleaning and sell-assembling process was ACS grade purchased from EMD® with water content ≤0.2%. It should be noted that different concentrations of the silane solution were tested. However, no significant difference was found within a few mM range. Upon coating and prior to tests, the modified samples were removed from the solution, rinsed with copious amounts of isopropanol and blown-dried with N_2. Subsequently, they were heated at 80 °C for 2 h to remove any volatile components or residual solvents. The dried samples were stored in clean Petri dishes at ambient conditions and the characterization procedures were conducted immediately following the sample preparation. Figure 1 schematically shows the sample preparation process.

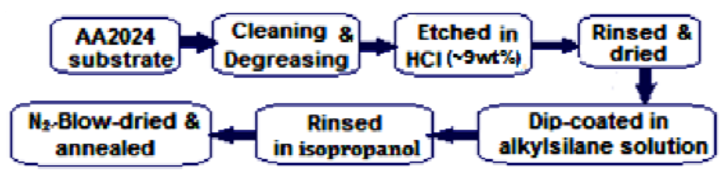

Fig. 1. Applied procedure to prepare superhydrophobic AA2024 samples.

While smaller samples (2cm×2cm) were used to test the stability of the coatings in different media, larger ones (3.2cm×5.2cm) were used to evaluate their ice-repellent performance and corrosion measurements.

B. Sample Analyses

The sample stability over time in water, basic and acidic media was characterized by means of CA measurements on samples immersed in nano-pure water, tap water as well as basic (pH: 10.1) and acid (pH:4) buffer solutions after different periods of time (at ~18-20 °C). The wetting characteristics, reported in Fig.2, were obtained following the standard sessile drop method on a CA goniometer (DSA100 from Krüss) with controllable volume (4 µl) of water droplets. These measurements were performed with the Young–Laplace method [4, 6, 18]. For each samples, at least five different spots were randomly selected and measured. The CA reported for each sample is the average value of about 12 measurements. Surface topographies were studied via scanning electron microscopy (SEM, Hitachi FEGSEM-SU 70) in high-vacuum mode and atomic force microscopy (AFM, Escope from Veeco). X-ray photoelectron spectroscopy (XPS) was performed with a Quantum-2000 instrument from PHI with Pass Energy of 100 eV, measurement step of 1.0 eV and time/step of 100 ms and X-Ray source of achromatic Al Kα. (1486.6 eV). Emitted photoelectrons were detected by a multichannel detector at a take-off angle of 90◦ relative to the surface. During analysis, the base pressure was less than 10-9 mbar. The ice adhesion test was conducted by creating glaze-type-ice of up to ~1 cm thick and ~4-5 gr weight over the ~3.2×3.0 cm^2 surface area and prepared by spraying supercooled micro-droplets of water (average size of ~65 μm) in a wind tunnel at subzero temperature (-10 ^oC), wind speed of 11 m/s, water pressure of 325 kPa, and water feed rate of 6.3 g/m^3 to simulate freezing rain. With these conditions, the required time to accumulate 1-cm thick glaze ice on sample surface in the wind tunnel was about 8-10 min. Prior to icing, all samples were placed in cold room for approximately 5 min to cool down. The iced samples were then spun in the centrifuge at constantly increasing speed. The shear stress was calculated taking into account the mass and area of the ice detached and by precisely detecting the rotational speed of the sample at the moment of ice failure (adhesive). The procedures of ice preparation and ice adhesion evaluation have been described in greater detail elsewhere [5, 6]. Potentiodynamic polarization was used to examine the overall corrosion behaviour of the bare and coated Al samples. The working cell was a standard three-electrode cell. The area of the working electrode (bare Al or coated sample in question) was 1 cm^2. A platinized platinum net and saturated calomel electrode (SCE) were used as counter and reference electrode, respectively. Prior to test, 30 min of immersion with O_2 bubbling into cell was allowed to ensure steady-state conditions. The measurements were done at constant room temperature of 20 ^oC. The setup used to control the experiments was a potentiostat/galvanostat system composed of a Solartron analytical 1252A frequency response analyzer (FRA) coupled to a Solartron SI 1287A electrochemical interface and were controlled by the software Corrware®. Measurements were performed in 3.5 wt.% NaCl solutions at room temperature. Potentiodynamic polarization curves were established and the corrosion potential (E_{corr}) and corrosion current density (i_{corr}) were determined using the Tafel extrapolation method. The polarization scan was started from 250 mV below the open circuit potential (OCP) in the cathodic region, through the corrosion potential, and 250 mV above the open circuit potential in the anodic region and with a constant scan rate of 1 mV/s. The bare as well as coated Al panels with dimension 3.2×5.2cm^2 (two panels for each) were placed into the salt-spray chamber (Ascott) with the unmodified surface protected by a scotch tape and the modified surfaces exposed alternatively to salt mist, dry and wet conditions in accordance with International Organization for Standardization ISO14993-Corrosion of metals and alloys: accelerated testing involving cyclic exposure to salt mist, "dry" and "wet" conditions [24]. Test specimens were placed in an enclosed chamber and exposed to a changing climate. The number of cycle repeated to vary test duration. After removal from the chamber, the panels were rinsed gently with nano-pure water and dried thoroughly by N_2 flow and stored at room temperature under ambient conditions. Stereomicroscope images were obtained from a Leica Model MZ16 microscope equipped with a camera (Leica Microsystems, Banuockburn, IL, USA) and XYZ motorized stage (Clemex Technologies Inc., Longueil, Canada).

III. RESULTS AND DISCUSSION

A. CA and CAH of samples

Aluminium alloy is a hydrophilic material with native oxidized layer demonstrating water contact angle and surface energy of ~41.5±3^O and 58.56±1.64 (mN/m), respectively. The Al substrates were etched in diluted HCl from 1 to 5 minutes followed by immersion in TMSOD. By immersing Al samples in HCl, Al samples react with HCl and $AlCl_3$ is produced while releasing $H_2\uparrow$. The deposition baths used in this study were diluted TMSOD 1% (V/V %) in isopropanol-water. Prior to use, the baths were vigorously stirred for 3 h to allow adequate dissolution and hydrolysis according to the following reaction:

$$R\text{-}Si(OMe)_3 + 3\,H_2O \rightarrow R\text{-}Si(OH)_3 + 3\,MeOH$$

The freshly formed thin layer of metal oxide on the Al surface after exposure to air reacted with precursor molecules to form a covalently bound coating material on the surface. The obtained results, listed in Fig, 2, were calculated according to the Young–Laplace method considered as the most theoretically accurate method [18]. The bare Al sample etched for 4 minutes showed water CA and surface energy of ~21.2±5^O and 68.30±1.16 (mN/m), respectively (Fig.2). However, after modifying the etched Al surfaces with TMSOD, the as-prepared surfaces demonstrated superhydrophobicity with water CA>150°, as shown in Fig. 3. While the measured CA on the Al sample coated with TMSOD is about 111±2^{O} (and surface energy of 16.28 (±1.14) (mN/m)), it is evident that samples etched for 3 and 4 minutes show improved superhydrophobicity with CA>156° and CAH<6°. However, the sample etched for 5 min shows hydrophobic properties as its CA and CAH values are ~143.4^{o}±2 and ~12.1°, respectively.

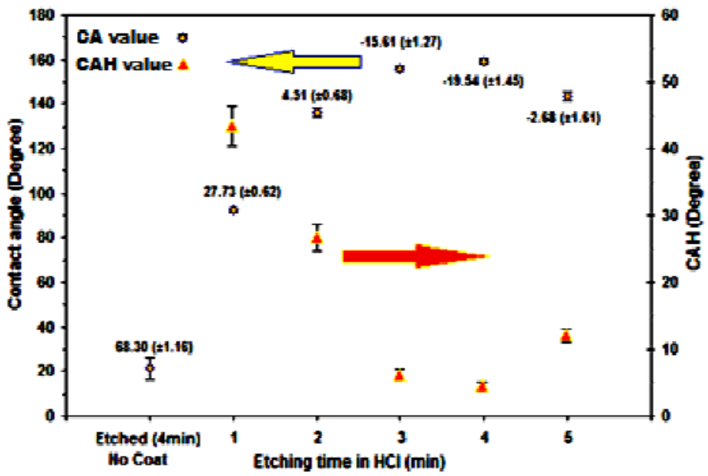

Fig. 2. CA, CAH and free surface energy (ε, mN/m) values of Al surfaces prepared with different etching times in HCl and coated with TMSOD (15min).

The 4-min etched Al samples were immersed for 1, 15, 30, 60 and 120 min in the bath. However, the best results were obtained after 15 and 30 min of immersion. Less than 5 min was not enough time to create a uniform self-assembled layer on Al and more than 30 min was long enough to increase and accelerate the rate of the dissolution process of the deposited *SAM* layer on Al (competition between deposition and dissolution reactions). These values of CA and CAH imply that water droplets rest on top of rough asperities of solid-air composite surfaces (Cassie-Baxter wetting regime). In this regime, CA can be expressed as follows:

$$\cos\theta^{*} = f\,(1+\cos\theta) - 1 \qquad (1)$$

where θ* and θ are the CA of rough and flat surfaces with the same surface chemistry, respectively, and *f* is the area fraction of solid surface that contacts water [12, 13, 25]. The Cassie-Baxter model assumes that a water droplet is suspended on rough asperities and allows air trapping between asperities on a surface underneath the droplet. This air trapping is a key factor for superhydrophobic behaviour, so that the *f* values of superhydrophobic surfaces are small [12, 13, 25].

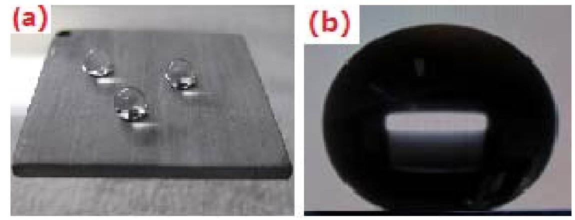

Fig. 3. (a) Water droplets on as-prepared superhydrophobic Al surface, (b) water droplet profile on Al surface with CA>150°.

The XPS signals of C, O and Si, displayed in Fig.4 for prepared superhydrophobic Al surfaces show that the surfaces well covered with a low surface energy coating of TMSOD layer. Water droplets easily roll off from coated surface even when the surface is not tilt much (sliding angle of <5^{o}).

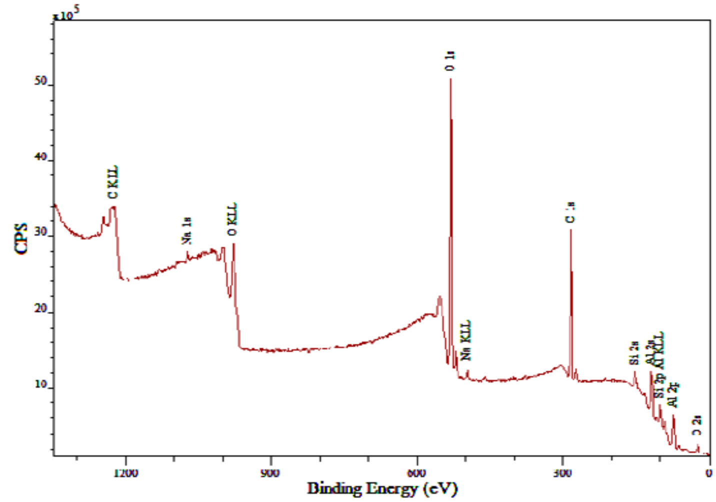

Fig. 4. XPS spectrum of TMSOD *SAM* coating on a 4-min etched superhydrophobic AA2024 surface.

Based on CA values and applying the Cassie-Baxter equation, therefore, solid fraction (%) area of 43.78, 13.48, 10.36 and 31.41 were obtained for samples etched for 2, 3, 4 and 5 min, respectively. With regards to obtained CA values and calculated *f*, thus, it can be concluded that a large amount of air is trapped beneath the water droplets, thus preventing water droplet penetration into the surface resulting in enhanced superhydrophobicity [5]. By decreasing the contact area between water droplets and the surface, the three-phase contact line at the solid/liquid interface consequently decreases. To account for variation in sample surface roughness, their surface parameters were measured by means of AFM, i.e. root-mean-square roughness (R_{rms}), Skewness (S_{sk}) and Kurtosis (S_{ku}) as shown in Table 1. While the first parameter represents the standard deviation of surface profile from its mean value, the second parameter (S_{sk}) measures the asymmetry of the profile about its mean plane (being positive for surfaces with peaks and negative for surfaces with valleys), and last parameter (S_{ku}) is a measure of “spikiness” of the surface [8].

Table 1. Root-mean-square roughness, skewness, and kurtosis values of etched samples in HCl at different times.

Sample \ Surface parameters	Root-mean-square roughness (R_{rms})	Skewness (S_{sk})	Kurtosis (S_{ku})
1-Min etched AA2024	117 ± 18	0.2 ± 0.4	3.1 ± 02
2-Min etched AA2024	317 ± 40	1.7 ± 0.3	5.4 ± 02
3-Min etched AA2024	395 ± 30	2.6 ± 0.3	10.2 ± 03
4-Min etched AA2024	425 ± 35	3.1 ± 0.2	14.5 ± 02
5-Min etched AA2024	412 ± 38	1.9 ± 0.3	7.3 ± 03

It is obvious that hydrophobic surfaces with higher roughness, with a dominance of peaks and more “spiky” peaks, should demonstrate improved water repellency and therefore lower CAH values. However, at this moment it is not well obvious which roughness parameter is most crucial and correlates best with the wetting hysteresis and surface hydrophobicity [8]. A systematic comparison of dependency presented in Fig. 2 with those presented in Table.1 with the mentioned parameters permits to conclude that improved CA and CAH in the case of sample etched for 4 min is due to higher values of S_{ku} and S_{sk}. Scanning electron micrographs (SEM) of Al sample etched for 1 and 4 minutes at different magnifications are shown in Figure 5 showing rough samples at micro/nano-scale.

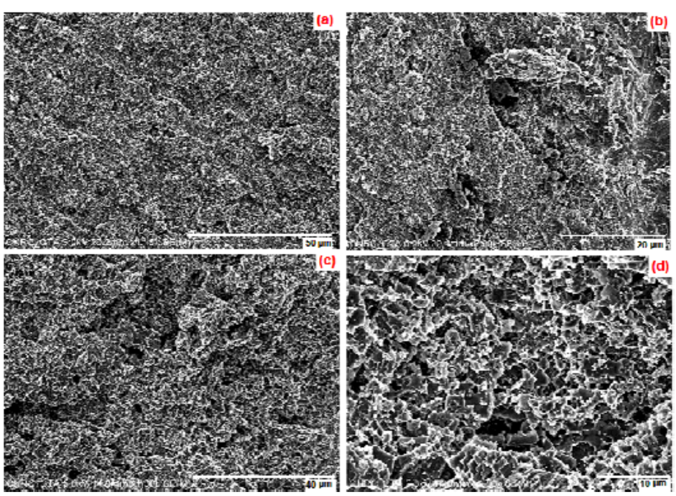

Fig. 5. (a and b) Low and high magnification SEM images of 2-min-etched hydrophobic AA2024 sample, (c and d) 4-min-etched superhydrophobic Al sample.

While the value of R_{rms} measured automatically by AFM was <460 nm, the R_{rms} values measured for as-received and mirror-polished samples were ~109 and ~25 nm, respectively. Since air was expected to be entrapped into such structures during wetting, the Cassie-Baxter wetting mode was expected for these samples with high surface roughness [3]. The water-solid contact area on these samples was expected to be small, which is consistent with the small CAH values (<6°) and high CA values (≥156°), characteristic of superhydrophobic surfaces. Also, the high CA and low CAH values observed let us assume good surface coverage with TMSOD molecules.

B. *Coating durability in aggressive media*

Figure 6 presents CA values as a function of immersion time in nano-pure and tap water, basic and acidic solutions for 4-min-etched coated Al samples. This sample demonstrates initial values of CA>156°, indicating well-coated nano-structured superhydrophobic surfaces. However, the coatings in question were found to lose completely their superhydrophobic properties after ~720 to ~1000-h of immersion in basic and nano-pure media, respectively, associated with a decrease in their CA values. This tendency to lose surface hydrophobicity is most likely due to a Si-O-Al bond rupture between TMSOD molecules and Al surface due to bond hydrolysis. Indeed, after subjecting the Al surfaces to an aggressive environment, the TMSOD layer undergoes degradation [26]. Consequently, alkylsilane molecules were removed from the surface, resulting in a decrease of surface hydrophobicity.

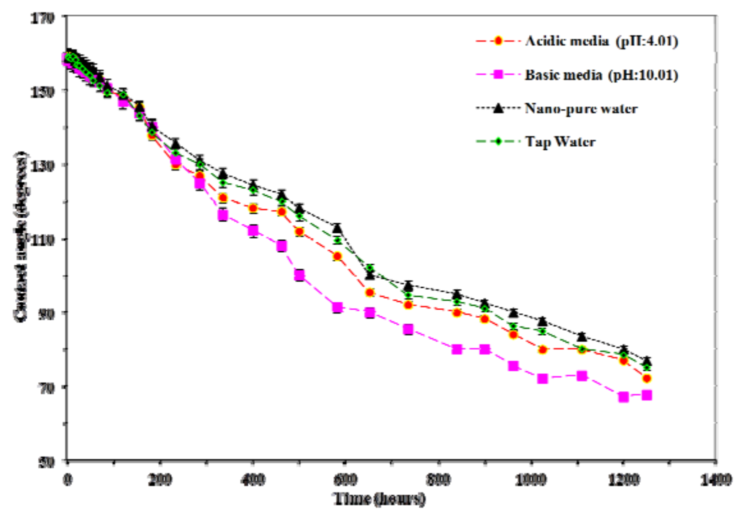

Fig. 6. Contact angle *vs.* immersion time in various media for rough Al samples coated with TMSOD layer.

C. *Ice-repellent performance*

As natural icing occur under dynamic conditions than those previously reported [10, 21], this implies that the dynamic hydrophobicity of surfaces may play an important role. This is believed to be even more important for nanostructured surfaces. The glaze ice used to evaluate sample ice repellency was prepared in a wind tunnel by spraying water micro-droplets with an average size of ~65 µm at subzero temperature (-10°C) that is under conditions very close to outdoor ice accretion [5]-[8]. The procedure to evaluate ice adhesion strength was previously reported in detail elsewhere [5, 18]. Each sample studied was subjected to 12 successive icing/de-icing cycles and thus, ice adhesion strength was analyzed as a function of the number of successive icing/de-icing cycles (Fig.7). Due to high mobility of water (low CAH), the accretion of ice from freezing rain is delayed on these surfaces [6, 8]. While uncoated as-received Al samples showed initial values of shear stress of ice detachment of ~370±30 kPa, the samples coated with TMSOD layer showed reduced values of ~62 kPa which is ~6 times lower than those on as-received Al standard and is in agreement with previous works on low-CAH surfaces [5, 6, 27]. It is consistent with the above mentioned Cassie-Baxter wetting regime.

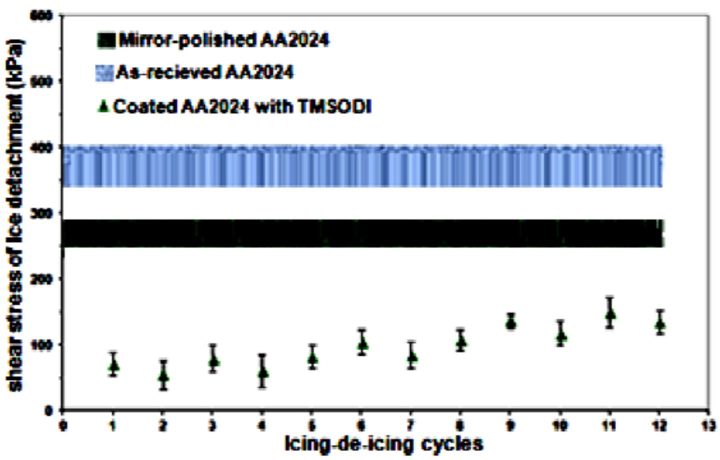

Fig.7. Shear stress of ice detachment *vs.* icing/de-icing cycles for coated Al with TMSOD. The blue and green bares stand for bare as-received and mirror-polished Al samples, respectively.

This reduction is attributed to the presence of micro-/nano-hierarchical surface structures and low surface energy layers. However, the ice releasing performance was gradually altered after several icing/de-icing cycles. In other word, superhydrophobic samples demonstrated increase of ice adhesion strength if compared to the as-prepared surfaces. The observed increase in ice adhesion strength values is believed to be associated with both a decay of the TMSOD layer on the samples and a larger ice-solid contact area on these surfaces after 12 icing/de-icing cycles [5]. The wetting properties of this sample after several icing/de-icing cycles were studied to better understanding of observed results by measuring CA and CAH values (Fig.8).

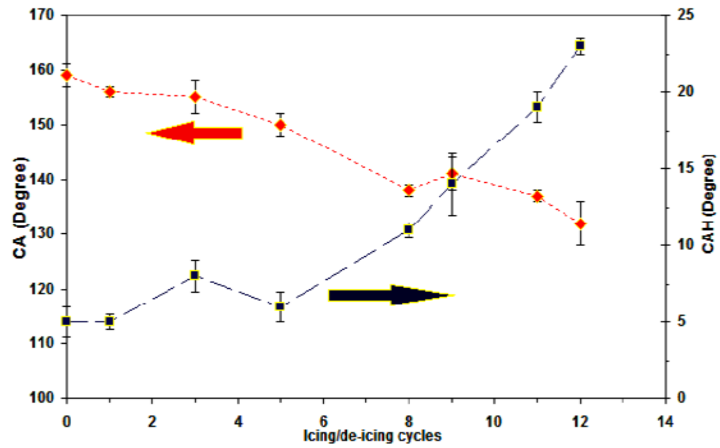

Fig. 8. CA and CAH values *vs.* icing/de-icing cycles for Al surfaces coated with TMSOD.

Water repellency of the coated sample gradually deteriorated over time as CA decreased and CAH increased. By increasing the number of icing/de-icing cycles, the sample should demonstrates lower values of CA, and eventually loose its superhydrophobicity. It is reasonable to assume that deteriorating water repellency and increased ice adhesion strength after icing/de-icing cycles can be related to gradual damage of rough structures of the sample surface. In other words, as the surface roughness decreases, partial switch of wetting regime from a pure Cassie (low CAH and high CA values) to a mixed Wenzel-Cassie regime is expected on such surfaces, with a gradual increase of ice adhesion strength [5, 6].

D. Corrosion resistance of superhydrophobic coatings

AA2024 is an Al alloy with Cu as the main alloying element, typically between 3.8-4.9% (wt. %) [23], which is used extensively in applications requiring high strength to weight ratio and good fatigue resistance as well. Due to these properties, it is widely used in aircraft structures, especially wing and fuselage structures under tension. However, due to poor corrosion resistance (high Cu content), it is frequently clad with other Al alloy or Al-Zn to protect it, although this reduces the fatigue strength. Therefore, evaluating the anti-corrosive performance of coated AA2024 would be of interest. The potentiodynamic polarization curves of (a) rough bare AA2024 and (b) a super-hydrophobic coating on Al alloy in 3.5 wt.% NaCl solution using the Tafel extrapolation method are presented in Fig. 9. The corrosion potential (E_{corr}) and the corrosion current density (i_{corr}) derived from the potentiodynamic polarization curves are summarized in Table 2.

Table 2. Potentiodynamic results of Al alloy with and without coating in 3.5 wt.% NaCl solution.

Sample	Ecorr (V)	icorr (Amps/cm²)
Bare Al sample	-0.65 ± 0.05	2.7835 E−5
Coated Al sample	-0.52 ± 0.04	1.1845 E−7

As clearly seen in Fig. 9, the corrosion potential positively increases from -0.65±0.05V for the bare Al alloy sample to -0.52±0.04V for the sample with superhydrophobic coating. The shift in E_{corr} in the positive direction could be attributed to improvement resulting from protective performance of the superhydrophobic coating formed on Al alloy. The corrosion current density, i_{corr}, of the superhydrophobic coating (1.1845E−7 Amps/cm^2) decreased about 2 orders of magnitude as compared to that of the bare surface (2.7835E−5 Amps/cm^2). These results indicate that the superhydrophobic coating on Al alloy has improved its corrosion resistance. The Al_2O_3 layer is permeable to electrolytes and moisture and is prone to undergo dissolution in a humid environment, leading to an accelerated corrosion. In contrast, the film formed from TMSOD is impermeable to corrosion accelerants and insulating. In other words, comparison of these data suggests that the barrier property of the TMSOD-modified Al samples was improved compared to the unmodified ones.

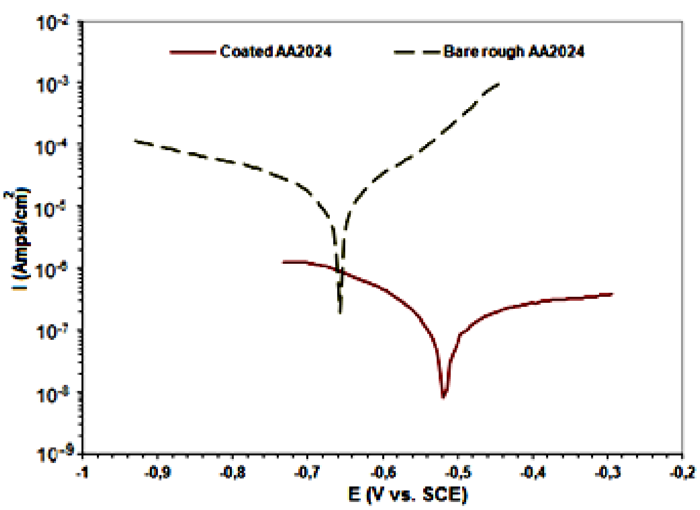

Fig. 9. Polarization curves of AA2024 with and without coating.

However, it worth to note that although TMSOD-modified samples exhibited large CA, potentiodynamic polarization test did not show significant improvement in either E_{corr} or I_{corr} compared to the unmodified samples. This is possibly due to presence of defects in the trimethoxysilane films. Indeed, hydrolysis and condensation reactions in trimethoxysilane are slow, which means it is possible that under current experimental conditions, the hydrolysis and condensation reaction of such molecules is incomplete, resulting in a film with defective areas.

E. Salt spray exposure

The corrosion property of the modified and unmodified samples was further studied by Salt Spray Exposure testing. More precisely, the Al panels (two panels for each) were placed into the salt-spray chamber (Ascott) with the unmodified surface protected by a scotch tape and the modified surfaces exposed alternatively to salt mist, dry and wet conditions in accordance with International Organization for Standardization ISO14993-Corrosion of metals and alloys: accelerated testing involving cyclic exposure to salt mist, *"dry"* and *"wet"* conditions [24]. This test is also referred to as a "*Cyclic Corrosion Test*", often abbreviated to "*CCT*". Test specimens were placed in an enclosed chamber and exposed to a changing climate that comprises of the following three partly repeating cycle: **1)** 2 h exposure to a continuous indirect spray of neutral salt water solution (pH: 6.5-7.2), which is poured on the specimens at a rate of 1 to 2ml/80cm²/hour, at chamber temperature of 35°C. **2)** It is followed by 4-h air drying in a climate of >30 %RH at 60 °C. **3)** This is followed by 2-h exposure to a condensing water climate (wetting) of 95 to 100 %RH at 50 °C. Indeed, salt spray testing provides a controlled accelerated corrosive environment to evaluate the relative corrosion resistance of the coating. It should be noted that all previous studies on alkylsilane-based monolayer thin films on Al alloy surfaces were related to alkysilane compounds on flat samples and no work has been reported on corrosion protection of rough AA2024 substrates in accordance with ISO14993 standard so far. The unmodified flat Al samples exhibited extensive corrosion after only 8 cycles of salt spray exposure with appearance of numerous small black dots (pits) at micrometer scale, as shown in Fig. 10. The size and density of the black dots increased as the salt spray cycle number increased which is due to further expansion of localized corrosion. However, the superhydrophobic samples modified by TMSOD exhibited obvious corrosion or corrosion products after 18 cycles of exposure (Fig.10). This implies on improvement in corrosion resistance of the modified samples compared to the unmodified ones. These observations revealed by salt-spray test correlate well to what was obtained earlier with the Potentiodyanamic test. Because of improved barrier property of Al surface modified by TMSOD, the corrosion resistance of these samples, thus, improved compared to the bare samples.

However, as it was explained earlier, it is believed that the TMSOD film contains defective areas. Through these defective areas, corrosion accelerants such as electrolytes and moisture can easily penetrate through the film to the metallic substrate. However, the reasonable barrier property of *SAM* can prevent electrolytes or water molecules penetration to the metal surface to introduce further expansion of corrosion to the surrounding areas.

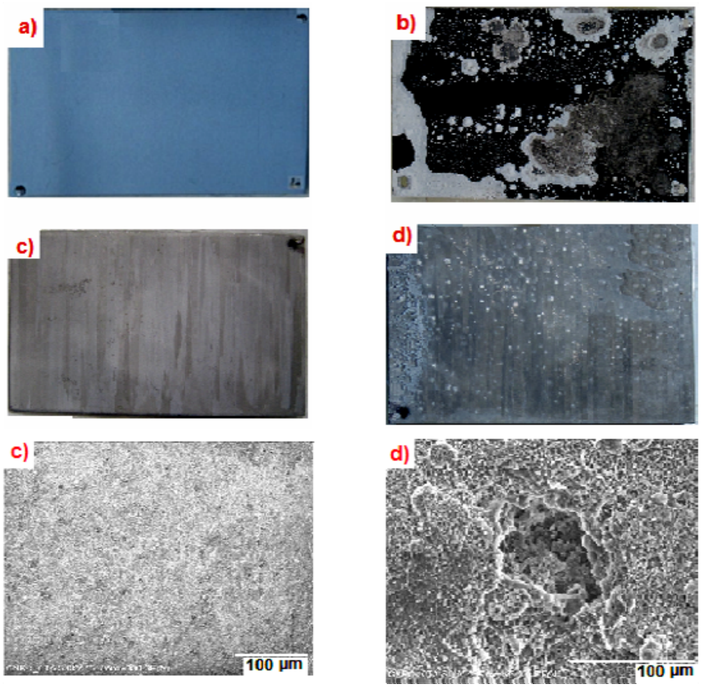

Fig. 10. Optical images of unmodified and modified AA2024 before and after 18 cycles of salt spray test: a, b) flat bare; c, d) 4-min-etched TMSOD-treated sample; e, f) low and high magnification SEM images of d.

IV. Conclusions

In this study, alkyl-terminated nanostructured superhydrophobic AA2024 surfaces were made by depositing a layer of TMSOD on HCl-etched substrates. They showed good superhydrophobic and improved anti-corrosive properties. Their stability in different media was tested by means of CA measurements, showing a gradual loss of superhydrophobicity after ~720- to ~1000-h of immersion in basic and nano-pure media. This was associated with decrease in CA values and increase in CAH. The ice repellent performance of the treated samples was evaluated following 12 successive icing/de-icing cycles and the results were compared to those on uncoated Al as reference. The ice adhesion strength results demonstrated a gradual deterioration of the anti-ice performance of the robust surfaces prepared by etching Al alloy substrates. Electrochemical measurement results showed that the corrosion potential of superhydrophobic coatings increased, and that their corrosion current density decreased by 2 orders of magnitude as compared to that of uncoated ones. These results point out that superhydrophobic coatings on AA2024 have reasonable enhanced corrosion resistance.

V. Acknowledgements

This research work has been conducted within the framework of the NSERC/Hydro-Quebec/UQAC Industrial Chair on Atmospheric Icing of Power Network Equipment (CIGELE) and the Canada Research Chair on Atmospheric Icing Engineering of Power Networks (INGIVRE) at Université du Québec à Chicoutimi. The authors would like to thank the CIGELE partners (Hydro-Québec, Hydro One, Réseau Transport d'Électricité (RTE), Rio Tinto Alcan, General Cable, K-Line Insulators, Dual-ADE, and FUQAC) whose financial support made this research possible. The authors also wish to thank Mrs. Gregoire (NRC, Canada) for her help with SEM analysis.

VI. References

[1] M. Farzaneh, 'Atmospheric Icing of Power Networks', Ed., Springer, Berlin, pp. 320, August 2008.
[2] H. Saito, K. Takai, G. Yamauchi, ' Water- and ice-repellent coatings'. Surface Coatings International, vol. 80, pp. 168–171, 1997.
[3] S. A. Kulinich, M. Farzaneh, ' Hydrophobic properties of surfaces coated with fluoroalkylsiloxane and alkylsiloxane monolayers', Surface Science vol. 573, pp. 379–390, 2004.
[4] S. A. Kulinich, M. Farzaneh, 'On wetting behavior of fluorocarbon coatings with various chemical and roughness characteristics'. Vacuum 79, pp. 255–264, 2005.
[5] S. A. Kulinich, M. Farzaneh, 'How wetting hysteresis influences ice adhesion strength on superhydrophobic surfaces', Langmuir, vol. 25, pp. 8854–8856, 2009.
[6] S. Farhadi, M. Farzaneh, S. A. Kulinich, 'Anti-Icing Performance of Superhydrophobic Surfaces', Applied Surface Science, vol. 257, pp. 6264–6269, 2011.
[7] Z. Ghalmi, R. Menini, M. Farzaneh, 'Effect of different aluminium surface treatments on ice adhesion strength', Advanced Materials Research, vol. 409, pp. 788-792, 2012.
[8] F. Arianpour, M. Farzaneh, S. Kulinich, 'Hydrophobic and ice-retarding properties of doped silicone rubber coatings', Applied Surface Science, vol. 265, pp. 546-552, 2013.
[9] R. Jafari, M. Farzaneh, 'A simple method to create superhydrophobic aluminum surfaces', Materials Science Forum, vol. 706-709, pp. 2874-2879, 2012.
[10] V. F. Petrenko and S. Peng, "Reduction of ice adhesion to metal by using self-assembling monolayers (SAMs)", Can. J. Phys, vol. 8, pp. 387-393, 2003.
[11] M. Farzaneh, ' Systems for prediction and monitoring of ice shedding, anti-icing and de-icing for overhead lines' CIGRÉ WG B2.29, CIGRE Publications, Technical Brochure #438, pp. 100, 2010.
[12] D. Quéré, ' Non-sticking drops', Reports on Progress in Physics, vol. 68, pp. 2495–2532, 2005.
[13] C. R. Crick, I. P. Parkin, 'Preparation and Characterisation of Super-Hydrophobic Surfaces', Chemistry A European Journal, vol. 16, pp. 3568–3588, 2010.

[14] X. YaoQ. W. Chen, L. Xu, Q. K. Li, Y. L. Song, X. F. Gao, D. Quéré, L. Jiang, 'Bioinspired ribbed nanoneedles with robust superhydrophobicity', Advanced Functional Materials, vol. 20, pp. 656– 662, 2010.

[15] Z. Guo, F. Zhou, J. Hao, W. Liu, ' Stable Biomimetic super-hydrophobic engineering materials', Journal of the American Chemical Society, vol. 127, pp.15670–15671, 2005.

[16] Y. Shaojun, S. O. Pehkonenb, L. Bin, Y. P. Ting, K.G. Neoh, E. T. Kang, 'Superhydrophobic fluoropolymer-modified copper surface via surface graft polymerisation for corrosion protection', Corrosion Science, vol. 53, pp. 2738–2747, 2011.

[17] L. Mingjie, Z. Yongmei Z. Jin, J. Lei, 'Bioinspired Super-antiwetting Interfaces with Special Liquid−Solid Adhesion', Acc. Chem. Res., vol. 43, pp. 368–377, 2010.

[18] R. Menini and M. Farzaneh, "Elaboration of Al_2O_3/PTFE icephobic coatings for protecting aluminium surfaces", ***Surf. Coat. Technol.,*** vol. 203, pp. 1941-1946, 2009.

[19] E. H. Andrews, H. A. Majid, N. A. Lockington, 'Adhesion of ice to a flexible substrate', Journal Materials Science, vol. 19, pp. 73-81, 19984.

[20] V. K. Croutch and R. A. Hartley, "Adhesion of ice to coatings and the performance of ice release coatings", ***J. Coat. Technol*.,** vol. 64, pp. 41-52, 1992.

[21] B. Somlo and V. Gupta, ''A hydrophobic self-assembled monolayer with improved adhesion to aluminium for de-icing application'', ***Mech. Mater.***, vol. 33, pp. 471-480, 2001.

[22] http://www.matweb.com/search/DataSheet.aspx?MatGUID=57483b4d782940faaf12964a1821fb61.

[23] L. E. M. Palomino, Z. Pászti, I. V. Aoki, H. G. De. Melo De, 'Comparative investigation of the adhesion of Ce conversion layers and silane layers to a AA 2024-T3 substrate through mechanical and electrochemical tests', Materials Research, vol. 10, pp. 399-406, 2007.

[24] http://www.iso.org/iso/home/store/catalogue_tc/catalogue_detail.htm?csnumber=24372.

[25] T. Furuta, M. Sakai, T. Isobe, A. Nakajima, 'Evaporation Behavior of Microliter- and Sub-nanoliter-Scale Water Droplets on Two Different Fluoroalkylsilane Coatings', Langmuir, vol. 25, pp. 11998, 2009.

[26] A. Frignani, F. Zucchi, G. Trabanelli, V. Grassi, 'Protective Action towards Aluminium Corrosion by Silanes with a Long Aliphatic Chain', Corrosion Science, vol. 48, pp. 2258–2273, 2006.

[27] S. Farhadi, M. Farzaneh, S. Simard, 'Nanostructured ultra superhydrophobic Al surfaces: stability and icephobic properties', International Journal of Theoretical and Applied Nanotechnology, vol. 1, pp. 38-44, 2013.

.

Delayed freezing time on ZnO based nanocomposite superhydrophobic surface

G. Momen and M. Farzaneh
NSERC / Hydro-Quebec / UQAC Industrial Chair on Atmospheric Icing of Power Network Equipment (CIGELE) and Canada Research Chair on Atmospheric Icing Engineering of Power Networks (INGIVRE), www.cigele.ca
Université du Québec à Chicoutimi, Chicoutimi, QC, Canada
* Email: gmomen@uqac.ca

Abstract — Superhydrophobic silicone rubber nanocomposite coatings based on the addition of ZnO nanoparticles have been developed and their wettability behaviour was analysed in the temperature range from 20 to −15 °C. At 20 °C, high static contact angle > 155º and low contact angle hysteresis of about 5º was obtained for the as-prepared superhydrophobic surfaces from which water drops easily roll off. Such surfaces at supercooled temperature showed important delayed freezing time of water droplets onto the silicone rubber hydrophobic surface and aluminum bar. Drop crystallization on superhydrophobic surfaces was observed after 4-5 min, which is significantly longer than on an aluminium surface (~40s) or on an RTV-coated surface (~100 s). Lower wettability was observed when the surface temperature went down from 20 to -15 °C. Indeed, when nanocomposites surfaces were exposed to temperatures lower than 0 °C, condensed water penetrated into the porosities of the coating and water vapour condensation lead to a transition to the Cassie-Wenzel regime resulting in lower contact angles. The surface energy of aluminum bar, and the hydrophobic and superhydrophobic surfaces was investigated by estimating the free energy of the total surface using the Owens–Wendt equation.

The free energy of the total surface for the superhydrophobic nanocomposites showed an important reduction as compared to aluminum.

Keywords — Superhydrophobicity, Surface energy, Nanocomposite , Freezing time , Contact angle

I. INTRODUCTION

Ice accumulation can cause hazardous road conditions, reduce the efficiency of aircraft engines and helicopters and damage the power transmission equipment. The development of superhydrophobic coatings that limit and ultimately prevent ice accretion on their surfaces has been the subject of considerable attention lately. To address this question, the freezing behavior of water droplets has been studied, as it is of prime importance in the development of icephobic and superhydrophobic coatings.

Some works are underway to develop a superhydrophobic and hydrophobic coating with icephobic properties [1-2].

In general, the superhydrophobicity of a surface is the result of a combination of low surface free energy and surface roughness [3]. A common two-step process has been generally utilized by many researchers to create superhydrophobic surfaces: i) roughness creation, and ii) low surface energy material coating. Wet chemical reaction [4], electrochemical deposition [5], self-assembly [6], layer-by-layer methods [7], plasma treatments [8], chemical vapor deposition [9], sol–gel methods [10], polymerization reaction [11], templates [12], electrospray [13] and sandblasting [14] have been the most popular methods to create superhydrophobic surfaces in the last five years.

In the present study, the transformation of hydrophilic aluminium surfaces into superhydrophobic surfaces was obtained via the incorporation of appropriate quantity of ZnO nanoparticle into a low surface energy material deposited by spin coating process.

II. EXPERIMENTAL APPARATUS

6061 Aluminium alloy plates (2.54 cm×2.54 cm×0.15 cm) from Rio Tinto Alcan (Mg 1.0, Si 0.6, Cu 0.28, Cr 0.05, Zn 0.1, Fe 0.25 and Mn 0.15 ,all in wt %) were grinded by sand paper .

The RTV Silicone Rubber HVIC 1547 (containing 40-70 wt% alumina hydrate) was obtained from Dow Corning and the ZnO nanoparticles from

Sigma Aldrich Company. This type of silicone rubber was selected because it is used in industry.
The solution of silicone rubber was deposited on the substrates using a sol-gel spin coating device (WS-400B-6NPP spin-coater from Laurel). The spinning speed was set at 500 rpm (5 s) and 3000 rpm (20 s) for the first and second stages, respectively. The heat treatment of the coatings was done at 85 °C in air, and was left overnight to remove the residual solvents.
The morphological characterization was carried out using a LEO field emission scanning electron microscope (FESEM). Water contact angle measurements were conducted using distilled water and a Krüss DSA 100 contact angle measuring instrument (water drop volume ~ 4 µL). This apparatus was fitted with a Peltier cooling element which allows lowering the substrate temperature down to -30 ^{o}C.

III. RESULTS AND DISCUSSION

Scanning electron microscopy of surface coated by RTV silicone rubber and silicone rubber /ZnO nanocomposite surface was shown in Figure 1.
Figure 1a exhibited a uniform coating of SR with dispersed microparticles of alumina hydrate (1-2 µm) already existed in silicone rubber compositions. It is evident from Fig. 1b that incorporation of appropriate quantity of ZnO nanoparticles resulted in the formation of a rough surface with features revealing island-like micro/nano structures comparable to that of lotus leave leafs.
The resulting micro/nanoscale hierarchical structure is very important in the determination of superhydrophobic properties of the surface, owing to its nanoporous structure, as observed on lotus leaves.

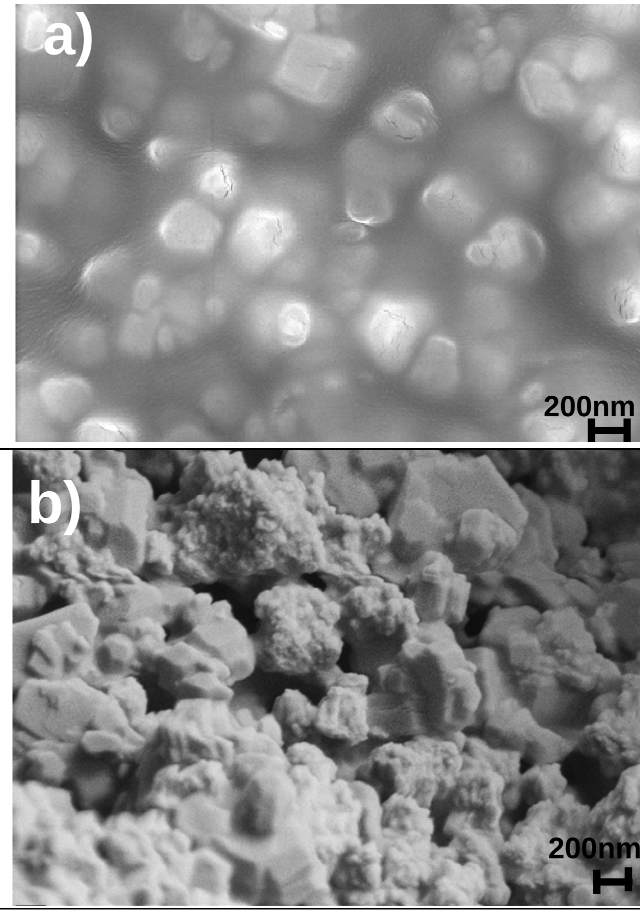

Figure1: FESEM micrographs of a) Silicone rubber coated on aluminum, b) Silicone rubber /ZnO solution coated on aluminium

The sessile drop method, which measures the contact angle (CA) of a water droplet on a surface, was used to characterize the wetting properties of the resulting micro/nanostructures.
The samples were placed on a test stage and 4 µl deionised water droplets were introduced onto the surface through a microsyringe. At least five different measurements were performed on different areas of each sample at room temperature. For a grinding aluminum surface a water contact angle of 75 ±2 º was observed.
The results showed that the static contact angle (θs) increased by appropriate incorporation of ZnO nanoparticles from 115° ±2 for RTV SR to 160 ° ±4 for superhydrophobic coating .
The hysteresis contact angle is also an important criterion to characterize superhydrophobic and icephobic surfaces [15]. As nanoparticle was incorporated into silicone rubber solution, we notice

a decrease in hysteresis from 26° to 5°. The water drop easily slide off the superhydrophobic surface while it's spread on the aluminum surface.
To investigate the change of surface-free energy upon as-prepared superhydrophobic surface, water and ethylene glycol (EG) were used as probe liquids.
Surface energy parameters of the probe liquids and contact angles measurement are listed in Table 1. The symbols γ_l, γ^d_l and γ^P_l represent the total, the dispersive and the polar component of the probe liquid surface free energy, respectively.

Table.1 Surface energy parameters of the probe liquids used in experiment and contact angles measured experimentally.

Probe liquid	γ^d_l (mN/m)	γ^P_l (mN/m)	γ_l (mN/m)	Contact angle (°)	
				Hydrophobic surface	Super-hydrophobic surface
Water	19	52	72	120±4	160±4
Ethylene glycol	29	19	48	108.4±2	152.9±2

The subscripts *s* and *l* represent solid and liquid, respectively.
The components of the total surface free energy for hydrophobic and superhydrophobic surface were determined from the Owens and Wendt equation . The equation is a linear equation as shown in Figure 3, Y = mX + b, in which the slope *m* and intercept *b* are given by the square root of polar and dispersive components of the solid surface free energy such as :

$$Y = \frac{\gamma_l(1+\cos\theta)}{2\sqrt{\gamma_l^d}} = \sqrt{\gamma_s^P}X + \sqrt{\gamma_s^d} \qquad (1)$$

Where

$$X = \left(\gamma_l^P\right)^{1/2} \Big/ \left(\gamma_l^d\right)^{1/2}$$

The X values are given by X = 0.809 for EG, and 1.61 for water. According to Eq. (1), the surface-free energy components of three surfaces were calculated from contact angle measurements. We determine the polar and dispersive components of the total surface-free energy from the slope and the intercept of the linear fit.

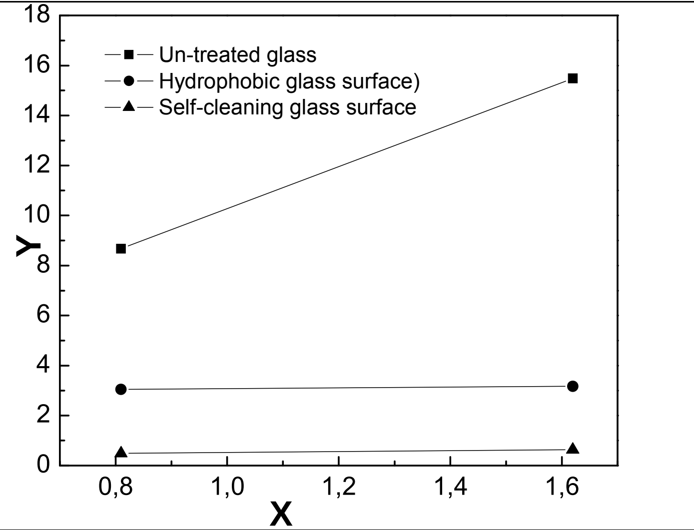

Figure 3: Owens-Wendt plots for three surfaces: hand-polished aluminum, SR Hydrophobic and superhydrophobic surface.

The total surface free energy ($\gamma_s^d+\gamma_s^P$) for hand-polished aluminum was determined to be 74.26 mN/m (γ_s^d = 3.45, γ_s^P =70.81). Silicone rubber coated on aluminum substrate resulted in significant reduction of the total surface energy of 8.65 mN/m (γ_s^d = 8.63, γ_s^P =0.02). The total surface energy for superhydrophobic surface was drastically much less that of hydrophobic silicone rubber coated surface and its value attained 0.15 mN/m (γ_s^d = 0.12, γ_s^P =0.03).

The study of the water contact angle at supercool temperature is of prime importance for the development of icephobic superhydrophobic coatings. For this propose, CA measurement of samples were carried out at temperature as low as -10 °C. The Kruss DSA 100 apparatus was fitted with a Peltier cooling element which allowed lowering the substrate temperature down to -30 °C. At 0 °C, the freezing time of 4-µl water droplets on the superhydrophobic surfaces was longer than 15 minutes. Figure 4 shows the image of water droplets frozen on (a) RTV a silicone rubber coated aluminium surface, and (b) the as-prepared superhydrophobic aluminium surface, at -10 °C.

Droplet crystallization on such surfaces was observed after 300 s, which is significantly longer than on a aluminium surface (~40 s) or on an RTV-coated aluminium surface (~100 s). Indeed, entrapped air in the cavities of superhydrophobic surfaces can act as a thermal barrier between the solid and the liquid delaying the freezing time on these surfaces [16].

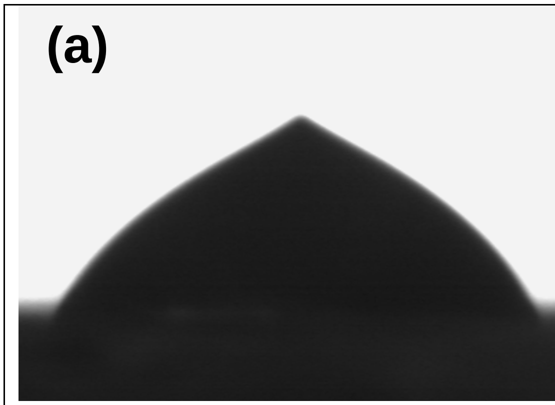

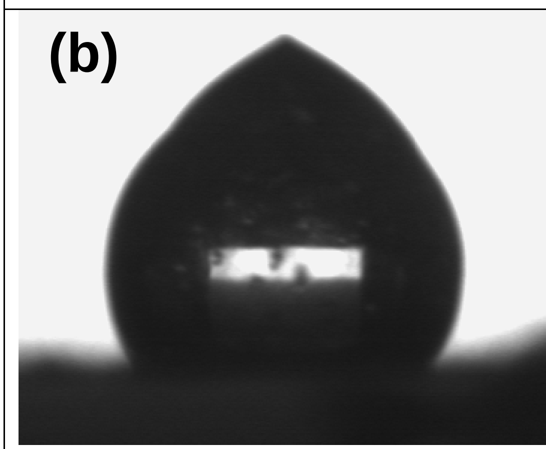

Figure 4: Image of water droplets (4 µl) frozen on (a): a RTV-coated aluminium surface, and the (b) as- prepared superhydrophobic surface.

III. CONCLUSION

The static and dynamic contact angle measurement showed that superhydrophobic surface was provided by ZnO nanoparticles incorporation. A water drop easily rolls off the as-prepared surface. The SEM observation revealed that the hierarchical structure in micro and nano scale was created on this surface. The wettability properties of hand-polished aluminum, hydrophobic and superhydrophobic surface were investigated by estimating total surface free energies from the Owens–Wendt equation. The total surface free energy for superhydrophobic surface reduced by two orders of magnitudes compared with that of aluminum surface.

Freezing time of surface-deposited droplets was significantly longer on the elaborated superhydrophobic surfaces than those obtained by RTV coating on hand-polished Al surfaces.

ACKNOWLEDGMENT

This work was carried out within the framework of the NSERC/Hydro-Quebec/UQAC Industrial Chair on Atmospheric Icing of Power Network Equipment (CIGELE) and the Canada Research Chair on Engineering of Power Network Atmospheric Icing (INGIVRE) at Université du Québec à Chicoutimi. The authors would like to thank the CIGELE partners (Hydro-Québec, Hydro One, Réseau Transport d'Électricité (RTE), Alcan Cable, K-Line Insulators, Dual-ADE, and FUQAC) whose financial support made this research possible.

REFERENCES

[1] Menini R., Ghalmi Z., and Farzaneh M., 2011, Cold Regions Science and Technology, **65(1), 65.**

[2] Jafari R, Menini R, Farzaneh M, Appl Surf Sci 257 (2010) 1540.

[3] G. Momen & M. Farzaneh, Applied Surface Science Volume 258, Issue 15(2012) 5723.

[4] S. Wang, L. Feng, L. Jiang, Adv Mater 18 (2006) 767.

[5] Jafari R, L. Foroughi L, Farzaneh M, Nanoscience and Nanotechnology Letters, 4, (2012).pp. 369-374.

[6] Zhang LB, Chen H, Sun JQ, Shen JC. Chem Mater 19 (2007) 948.

[7] Zhu Y, Hu D, M.X. Wang, Jiang L, Wei Y. Adv Mater 19 (2007) 2092.

[8] Jafari R, Farzaneh M. Journal of Applied physics A 102, Issue 1 (2011), 195.

[9] Yan XB, Tay BK, Yang Y, Po YK. J Phys Chem C. 111 (2007) 17254.

[10] Y. Li, Duan GT, Cai WP. J Colloid Interface Sci. 314 (2007) 615.
[11] Garcia N, Benito E, Guzman J, Tiemblo P. J Am Chem Soc. 129 (2007) 5052
[12] Li Y, Li CC, Cho SO, Duan GT, Cai WP. Langmuir 2007; 239802.
[13] Burkarter E, Saul CK, Thomazi F, Cruz NC, Roman LS, Schreiner WH. Surf Coat Technol. 202 (2007)194.
[14] Guo ZG, Liang J, Fang J, Guo BG, Liu WM. Adv Eng Mater. 9 (2007) 316.
[15] S.A. Kulinich & M. Farzaneh, Langmuir, 25, no.16 (2009) 8854.
[16] G. Momen, M. Farzaneh, R. Jafari, Applied Surface Science, 257 15(2011) 9489.

Development of Silicon-based Superhydrophobic/icephobic Surfaces Using an Atmospheric Pressure Plasma Jet

Siavash Asadollahi[#1], Reza Jafari[#2], Masoud Farzaneh[#3]

[#] NSERC / Hydro-Quebec / UQAC Industrial Chair on Atmospheric Icing of Power Network Equipment (CIGELE) and Canada Research Chair on Atmospheric Icing Engineering of Power Networks (INGIVRE)
Université du Québec à Chicoutimi, Chicoutimi, QC, Canada

[1] siavash.asadollahi1@uqac.ca
[2] reza.jafari@uqac.ca
[3] masoud.farzaneh@uqac.ca

Abstract — During the past few decades, superhydrophobic coatings have gained a lot of interest due to their several applications, most notably self-cleaning icephobic surfaces. On the other hand, plasma based surface treatment techniques have proven to be an economical, quick and environmental method for development of various organic and inorganic coatings. In this study the plasma process parameters are optimized in an atmospheric pressure plasma jet system with an organosilicon based monomer (HMDSO) to deposit superhydrophobic coatings on aluminum substrates with contact angles as high as 160°. A wind tunnel which operates in sub-zero temperatures is then used to simulate the severe winter conditions that such coatings are usually exposed to. Ice adhesion strength is measured by a centrifugal method. Furthermore, contact angle goniometry and FT-IR confirm the presence of low surface energy chemical functions on the coating and a micro roughened structure which leads to a high contact angle and low contact angle hysteresis. The results show that an atmospheric pressure plasma jet technique may be an industrial, economic and environmental-friendly method to prevent or reduce the ice accumulation on aluminum substrates.

I. Introduction

Introduction

Atmospheric icing during a freezing rain is a common phenomenon in several cold climates regions, notably south-eastern Canada, north-eastern United States, Northern China, Scandinavia and Russia. Freezing rain occurs when rain drops pass through a thin layer of cold air near the ground, thus becoming super-cooled water droplets. These super-cooled droplets will freeze upon impact, forming a thick clear layer of dense ice on outdoor structures. Usually, the power transmission pylons or conductors are not designed to withhold such loads, and therefore they can break or collapse leading to long periods of power shortage for millions of people. In one case of an ice storm in 1998 in Canada, the overall damage to power transmission networks in two provinces (Québec and Ontario) was estimated to be more than 1 billion dollars.

In order to address the atmospheric icing issue, several studies have taken different approaches to remove, reduce or prevent the ice accumulation on outdoor structures. Most of these approaches can be categorized into two main lines: (1) de-icing methods and (2) anti-icing methods [1]. De-icing methods usually attempt to remove the ice after the accumulation. The removal process can be done mechanically, thermally or using Joules-Effect. Although such approaches can prove useful and efficient in some cases, they are usually costly and time-consuming. Moreover, most of such approaches require direct human intervention, which makes it more difficult to deal with the icing occurrences in time.

Another approach would be to somehow reduce the ice adhesion strength on the structures or prevent the ice accumulation altogether. Such approaches, which are called the anti-icing methods, are relatively more recent and still under development [2]. In this case, a coating is applied on the surfaces which can mobilize the water droplets, delay the freezing or reduce the ice adhesion strength. Such surfaces are generally called icephobic surfaces.

During the past few decades, a correlation has been found between icephobicity and superhydrophobicity. A superhydrophobic surface is a surface on which the water contact angle is higher than 150° [3]. It has been shown that two main factors contribute to the wetting behavior of a surface: (1) surface chemistry (the presence of low surface energy chemical functions) and (2) surface roughness (the presence of a micro/nano structured features) [3]. With a combination of these two factors, a surface can be fabricated on which the water droplets may rest on a part-air/part-solid interface (Figure 1). Furthermore, a superhydrophobic surface may exhibit rolling behavior, where water droplets will roll-off easily from a surface due to the low adhesion forces in the water/solid interface [3].

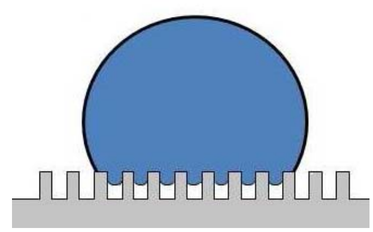

Fig. 1. A water droplet on a superhydrophobic surface.

The exact nature of the correlation between superhydrophobicity and icephobicity was unknown until recently, when a certain interest in the field gave raise toseveral explanations. Currently this correlation is known to be due to one or more of the following reasons:

1) The heat insulation between the surface and the water droplets due to the micro/nano structured surface, which hinders the heat conduction and delays the freezing point [4–6].
2) Lower contact area between water and the surface due to the mixed interface, which leads to less potential ice nucleation area [7].
3) Higher droplet mobility due to the rolling phenomena which may lead to the removal of droplets before freezing [8–11].

Several methods have been developed to fabricate artificial superhydrophobic surfaces. Among these methods, sol-gel reactions [12], electrochemical depositions [13], layer-by-layer depositions [14], spin-coatings [15] and plasma-based techniques [3] have been used more than others.

In the past few years, plasma-based surface treatment techniques have gained a lot of interest. Several studies have investigated the vast possibilities and advantages offered by different plasma related approaches, such as plasma polymerization, plasma etching or plasma sputtering. Plasma polymerization is referred to the deposition of polymer films through dissociation and excitation of a monomer gas in plasma and subsequent deposition and polymerization of the excited species on the surface of a substrate [16]. Generally, plasma polymerization is categorized according to the pressure in which the process is carried out: (1) low pressure plasma polymerization (the pressure is lower than atmospheric pressure, usually in the range of a few millitorrs) [17–19] and (2) atmospheric pressure plasma polymerization. Atmospheric pressure plasma polymerization offers several advantages compared to low pressure plasma polymerization, such as lower energy consumption, shorter processing times, lack of need for vacuum equipment and considerably higher growth rates [20–22].

In this study, an atmospheric pressure plasma jet (APPJ) is used to generate an organosilicon-based coating on the surface of aluminum substrates. Hexamethyldisiloxane (HMDSO) is used as the polymerization monomer with two different plasma gases: compressed air or nitrogen. Water contact angle was measured on the surface of the samples and the surface chemical composition was studied using FT-IR. The results show that a silicon-oxide based structure may be formed on the surface which can be responsible for superhydrophobic/icephobic characteristics in plasma polymerized samples.

II. Experimental Procedure

A. Plasma Polymerization

Aluminum samples were cut from an Al-6061 plate to 50mm×30mm pieces. These samples were then cleaned in an ultrasonic bath with acetone (15 minutes) and distilled water (15 minutes). Plasma polymerization was performed using a PlasmaTreat™ OpenAir® AS400 (PlasmaTreat GmbH) atmospheric pressure plasma jet (Figure 2). HMDSO (≥98%) was provided by Sigma Aldrich and was used as received. In this study, monomer flow rate was set to 70 gr/h, jet speed was kept constant at 1 m/s, carrier gas flow rate (nitrogen) at 150 lit/h and ionization gas (compressed air or nitrogen) flow rate at 2400 lit/h. Plasma generation voltage was set to 215V and the generation current was 10.2A.

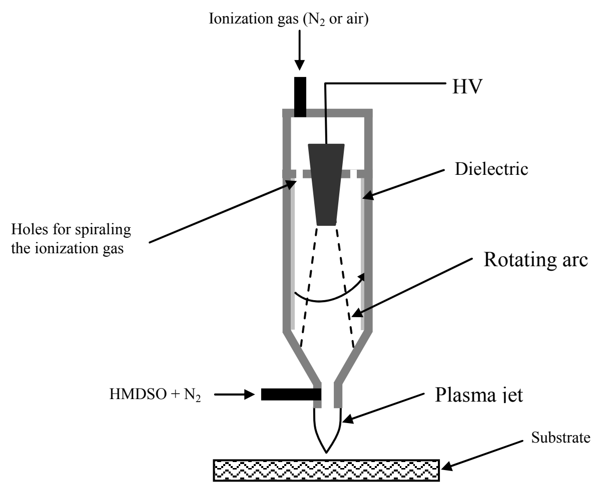

Fig. 2. Schematic figure of the atmospheric pressure plasma jet.

B. Scanning Electron Microscopy

To analyze the micro/nano structured silicon oxide deposited in high flow rates, the samples were studied using a INCAx-sight scanning electron microscope (Oxford Instruments).

C. Contact Angle Measurements

Contact angle measurement was performed using a Kruss™ DSA100 goniometer equipped with a video camera at 25 °C. Static contact angle was measured by placing a water droplet with a volume of 4μL on the surface. The contact angle was then determined by Young-Laplace approximation. Young-Laplace method approximates the whole shape of the droplet (and not only the 3 phase interface points), thus the effect of gravity on droplet shape and contact angle will be also taken into account. In order to ensure accuracy and reproducibility, two identical samples for each plasma gas were fabricated and the data presented in this paper are acquired from 6-20 points on each sample.

D. Fourier Transform Infrared Spectroscopy

Fourier transform infrared spectroscopy (FT-IR) was used to analyze the chemical functions deposited by plasma polymerization. The results presented in this paper are acquired from a Perkin-Elmer (Waltham) SpectrumOne FT-IR equipment. The reflected beam was collected for 24 scans at a resolution of 4 cm^{-1}.

E. Atmospheric Icing and Ice Adhesion Measurement

In order to simulate the outdoor conditions, a wind tunnel was utilized to accumulate atmospheric ice on the surface. The wind speed was set to 10 m/s and the temperature in which the icing was performed was set to -10 °C. By adjusting the water pressure and the air pressure, it was ensured that the LWC (liquid water content) and MVD (median volume diameter) remain close to the actual values in a severe ice storm. After the icing was done in the wind tunnel, the samples were transferred to another cold room with a centrifugal instrument to measure the ice adhesion strength. The samples were installed at the end of a beam and were rotated in a controlled frequency. The force applied to the ice at the point of breaking was measured using the following equation:

$$F=mr\omega^2$$

where m is the mass of the accumulated ice, r is the beam radius and ω is the rotation frequency at the breaking point. Therefore the adhesion strength could be determined by dividing the breaking force (F) to the icing area (A):

$$\tau=F/A$$

III. Results and Discussion

As mentioned before, the wetting behaviour of a surface is affected by two main aspects: (1) the presence of low surface energy materials and (2) the surface micro and/or nano structured roughness [3], [23]. In this study, at first the presence of a micro nano structured coating is confirmed by SEM. Then the chemical composition of the surface is studied using Fourier transform infrared spectroscopy. Water contact angle was also measured using a goniometer equipped with a video camera. Finally, ice adhesion strength was measured to evaluate the surface performance under severe weather conditions.

In the first step, surface morphology was studied using scanning electron microscopy (Figure 3). It is clear that a hierarchical micro/nano structured surface is formed via plasma polymerization. As it will be confirmed later via FT-IR spectroscopy, this structure is mainly composed of SiO_x. However, the structure is noticeably finer in the sample polymerized by nitrogen plasma. Few other studies have also reported the generation of smaller SiO_x particles with the introduction of argon or nitrogen to the plasma gas [24].

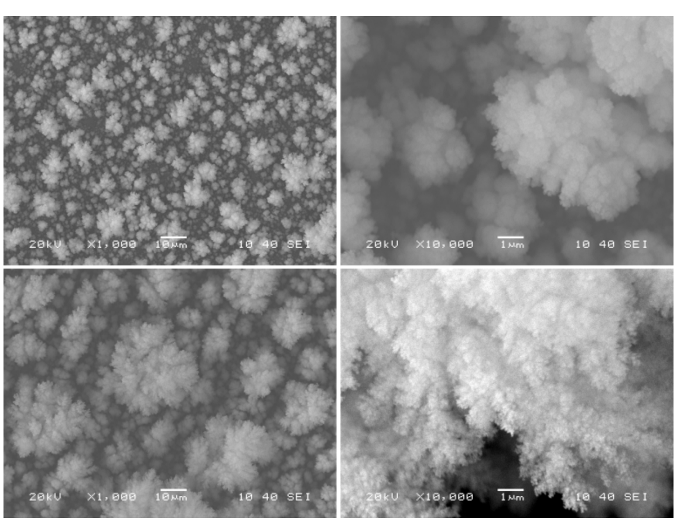

Fig. 3. SEM images with different magnifications of two samples polymerized using the nitrogen plasma (top) and the air plasma (bottom).

Fourier transform infrared spectroscopy was used to evaluate the surface chemistry. FT-IR spectra for the two samples studied can be seen in Figure 4. The wide peak at 1000-1150 cm^{-1} is usually attributed to Si-O-Si bond [25], which is present in both samples at different ionization gases. However, comparing this peak in different spectra for air plasma and nitrogen plasma, it can be deducted that nitrogen plasma will decrease the amount of oxidized silicon. This can be explained by the fact that nitrogen gas may act as a protective layer against oxidation of the plasma species. Furthermore, $Si\text{-}CH_3$ peak at 1275 cm^{-1}, along with two other peaks related to Si-C bonds in $Si\text{-}(CH_3)_x$ groups at 800 cm^{-1} and 850 cm^{-1} are significantly stronger in nitrogen plasma [25]. Furthermore, the peaks at 915 cm^{-1} and 1410 cm^{-1} are attributed to C-H bonds and are clearly stronger in nitrogen plasma [26]. Finally, a peak at 2960 cm^{-1} which is generally related to $R\text{-}CH_3$ groups is visible in nitrogen plasma. Thus it can be concluded that compared to the air plasma, nitrogen plasma leads to a more prominent deposition of organic chemical functions. It is notable that the peak at 670 cm^{-1} is related to carbon dioxide degenerate bend [27], which is present on all samples and is noticeably stronger in air plasma.

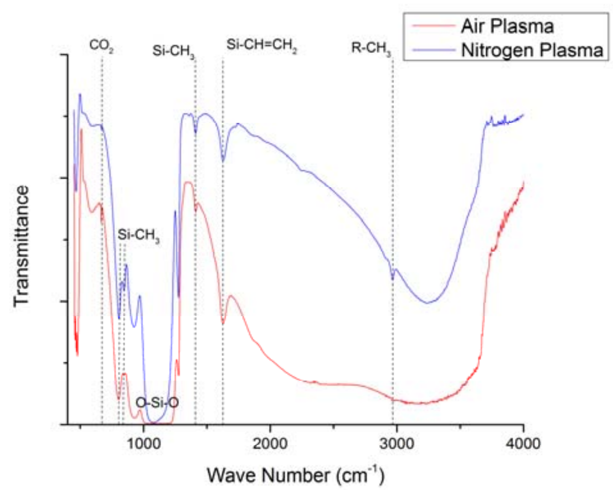

Fig. 4. FT-IR spectra for nitrogen plasma polymerization and air plasma polymerization at monomer flow rate of 70 gr/h.

According to the results from FT-IR spectroscopy, it can be concluded that in order to achieve hydrophobicity, nitrogen plasma is preferable. This is due to the presence of oxygen in the air plasma, which can enhance the oxidation process and increase the deposition of active and hydrophilic oxide groups on the surface. On the other hand, It has been shown repeatedly that nitrogen plasma can generate a more organic and thus hydrophobic coating [13], [28], [29].

Water contact angle was measured on two different samples in order to evaluate the wetting behaviour of the fabricated coatings. After performing several tests, water contact angle on nitrogen and air plasma polymerized surfaces were determined to be 162.7°±5.2° and 155.4°±3.1°, respectively.

The results show that although both surfaces are showing contact angles higher than 150° and thus are superhydrophobic, nitrogen plasma leads to a higher contact angle. This can be due to the fact that the deposition of oxide functions via plasma is weaker in nitrogen plasma.

The ice adhesion strength was measured on the two samples in a simulated icing condition. Ice adhesion strength for nitrogen and air plasma polymerized surfaces were determined to be 156 kPa and 299 kPa respectively. These results show that although both surfaces are superhydrophobic, nitrogen plasma polymerized surface acts significantly better in icing conditions. Contact angle measurements before and after (not shown here) the icing/de-icing cycle show that the samples retain their hydrophobic characteristics even after being exposed to an aggressive environment in the wind tunnel. Further investigation on the coating stability against several icing/de-icing cycles seems necessary to comprehensively evaluate the potentials of this method.

IV. Conclusion

A superhydrophobic/icephobic micro/nano-structured hierarchical coating was formed on aluminum substrates in a fast and one-step process using an atmospheric pressure plasma jet. HMDSO was used as the monomer gas and two different gases were studied as the ionization medium. Nitrogen proved to act as a protective layer to prevent the surface from extensive oxidation during the plasma polymerization process. Further studies on this structure proved its chemical composition to be closest to silicon dioxide. Atmospheric icing was simulated for these samples in a wind tunnel operating in sub-zero temperatures. Then the ice adhesion strength was measured using a centrifugal instrument. The results show that the all of the surfaces retain their hydrophobic characteristics after ice accumulation and de-icing, but nitrogen plasma leads to significantly lower ice adhesion strength. Further studies seem to be necessary to evaluate the stability of these surfaces against several natural factors, such as UV exposure or Icing/de-icing cycles.

Acknowledgment

This work was carried out within the framework of the NSERC/Hydro-Quebec/UQAC Industrial Chair on Atmospheric Icing of Power Network Equipment (CIGELE) and the Canada Research Chair on Engineering of Power Network Atmospheric Icing (INGIVRE) at the Université du Québec à Chicoutimi. The authors would like to thank the CIGELE partners (Hydro-Quebec, Hydro One, Réseau Transport d'Électricité (RTE), Rio Tinto Alcan, General Cable, K-Line Insulators, Dual-ADE, and FUQAC) whose financial support made this research possible. The authors are also grateful to Zhan Zhang of the Centre universitaire de recherche sur l'aluminium (CURAL, Chicoutimi, Canada) for SEM characterizations and Mathilde Bottois of Polytech Nantes (Nantes, France) for the icing tests.

References

[1] M. Farzaneh and C. Volat, “Atmospheric Icing of Power Networks,” Berlin: Springer, 2008, pp. 229–268.

[2] R. Menini and M. Farzaneh, “Advanced Icephobic Coatings,” *J. Adhes. Sci. Technol.*, vol. 25, no. 9, pp. 971–992, Mar. 2011.

[3] R. Jafari, S. Asadollahi, and M. Farzaneh, “Applications of Plasma Technology in Development of Superhydrophobic Surfaces,” *Plasma Chem. Plasma Process.*, vol. 33, no. 1, pp. 177–200, 2013.

[4] P. Guo, Y. Zheng, M. Wen, C. Song, Y. Lin, and L. Jiang, “Icephobic / Anti-Icing Properties of Micro / Nanostructured Surfaces,” *Adv. Mater.*, vol. 24, no. 19, pp. 2642–2648, 2012.

[5] A. Alizadeh, M. Yamada, R. Li, W. Shang, S. Otta, S. Zhong, L. Ge, A. Dhinojwala, K. R. Conway, V. Bahadur, a J. Vinciquerra, B. Stephens, and M. L. Blohm, “Dynamics of ice nucleation on water repellent surfaces.,” *Langmuir*, vol. 28, no. 6, pp. 3180–6, Mar. 2012.

[6] Y. Zhang, X. Yu, H. Wu, and J. Wu, “Facile fabrication of superhydrophobic nanostructures on aluminum foils with controlled-condensation and delayed-icing effects,” *Appl. Surf. Sci.*, vol. 258, no. 20, pp. 8253–8257, Aug. 2012.

[7] P. Tourkine, M. Le Merrer, and D. Quéré, “Delayed freezing on water repellent materials.,” *Langmuir*, vol. 25, no. 13, pp. 7214–6, Jul. 2009.

[8] V. Bahadur, L. Mishchenko, B. Hatton, J. A. Taylor, J. Aizenberg, and T. Krupenkin, “Predictive model for ice formation on superhydrophobic surfaces.,” *Langmuir*, vol. 27, no. 23, pp. 14143–50, Dec. 2011.

[9] C. Antonini, M. Innocenti, T. Horn, M. Marengo, and A. Amirfazli, “Understanding the effect of superhydrophobic coatings on energy reduction in anti-icing systems,” *Cold Regions Sci. Tech.*, vol. 67, no. 1–2, pp. 58–67, Jun. 2011.

[10] L. Mishchenko, B. Hatton, V. Bahadur, J. A. Taylor, T. Krupenkin, and J. Aizenberg, “Design of Ice-free Nanostructured Impacting Water Droplets,” *ACS Nano*, vol. 4, no. 12, pp. 7699–7707, 2010.

[11] D. Arnaldo del Cerro, G. R. B. E. Römer, and a. J. Huis in’t Veld, “Erosion resistant anti-ice surfaces generated by ultra short laser pulses,” *Physics Procedia*, vol. 5, pp. 231–235, Jan. 2010.

[12] H. F. Hoefnagels, D. Wu, G. de With, and W. Ming, “Biomimetic superhydrophobic and highly oleophobic cotton textiles.,” *Langmuir*, vol. 23, no. 26, pp. 13158–63, Dec. 2007.

[13] N. D. Boscher, P. Choquet, D. Duday, and S. Verdier, “Chemical compositions of organosilicon thin films deposited on aluminium foil by atmospheric pressure dielectric barrier discharge and their electrochemical behaviour,” *Surf. Coat. Technol.*, vol. 205, no. 7, pp. 2438–2448, Dec. 2010.

[14] M. E. Buck, S. C. Schwartz, and D. M. Lynn, “Superhydrophobic Thin Films Fabricated by Reactive Layer-by-Layer Assembly of Azlactone-Functionalized Polymers.,” *Chem. Mater.*, vol. 22, no. 23, pp. 6319–6327, Sep. 2010.

[15] X. Zhang, H. Kono, Z. Liu, S. Nishimoto, D. a. Tryk, T. Murakami, H. Sakai, M. Abe, and A. Fujishima, “A transparent and photo-patternable superhydrophobic film,” *Chem. Commun.*, vol. 2007, no. 46, p. 4949, 2007.

[16] A. Grill, *Cold Plasma in Materials Fabrication: From Fundamentals to Applications*. New York: IEEE Press, 1994.

[17] R. Jafari and M. Farzaneh, "Fabrication of superhydrophobic nanostructured surface on aluminum alloy," *Appl. Phys. A: Mater. Sci. Process.*, vol. 102, no. 1, pp. 195–199, Nov. 2010.

[18] L. Foroughi Mobarakeh, R. Jafari, and M. Farzaneh, "Superhydrophobic Surface Elaboration Using Plasma Polymerization of Hexamethyldisiloxane (HMDSO)," *Advanced Materials Research*, vol. 409, pp. 783–787, Nov. 2011.

[19] R. Jafari, R. Menini, and M. Farzaneh, "Superhydrophobic and icephobic surfaces prepared by RF-sputtered polytetrafluoroethylene coatings," *Appl. Surf. Sci.*, vol. 257, no. 5, pp. 1540–1543, Dec. 2010.

[20] J. Pulpytel, V. Kumar, P. Peng, V. Micheli, N. Laidani, and F. Arefi-Khonsari, "Deposition of Organosilicon Coatings by a Non-Equilibrium Atmospheric Pressure Plasma Jet: Design, Analysis and Macroscopic Scaling Law of the Process," *Plasma Processes Polym.*, vol. 8, no. 7, pp. 664–675, Jul. 2011.

[21] U. Lommatzsch and J. Ihde, "Plasma Polymerization of HMDSO with an Atmospheric Pressure Plasma Jet for Corrosion Protection of Aluminum and Low-Adhesion Surfaces," *Plasma Processes Polym.*, vol. 6, no. 10, pp. 642–648, Oct. 2009.

[22] L. Ward, W. Schofield, J. Badyal, A. Goodwin, and P. Merlin, "Atmospheric Pressure Glow Discharge Deposition of Polysiloxane and SiO x Films," *Langmuir*, vol. 19, no. 6, pp. 2110–2114, 2003.

[23] H. Ogihara, T. Katayama, and T. Saji, "One-step electrophoretic deposition for the preparation of superhydrophobic silica particle/trimethylsiloxysilicate composite coatings.," *J. Colloid Interface Sci.*, vol. 362, no. 2, pp. 560–6, Oct. 2011.

[24] M. Ricci, J.-L. Dorier, C. Hollenstein, and P. Fayet, "Influence of Argon and Nitrogen Admixture in HMDSO/O2 Plasmas onto Powder Formation," *Plasma Processes Polym.*, vol. 8, p. n/a–n/a, Dec. 2010.

[25] P. J. Launer, "Infrared analysis of organosilicon compounds: Spectra-structure correclation," 1987.

[26] J. Coates and R. A. M. Ed, "Interpretation of Infrared Spectra , A Practical Approach," in *Encyclopedia of Analytical Chemistry*, 2000, pp. 10815–10837.

[27] T. Tso and E. K. C. Lee, "Role of hydrogen bonding studied by the FTIR spectroscopy of the matrix-isolated molecular complexes, dimer of H2O, H2O.CO2 and H2O2.nCO in solic O2 at 12-17K," *J. Phys. Chem.*, vol. 89, pp. 1612–1618, 1985.

[28] R. Maurau, N. D. Boscher, J. Guillot, and P. Choquet, "Nitrogen Introduction in pp-HMDSO Thin Films Deposited by Atmospheric Pressure Dielectric Barrier Discharge: An XPS Study," *Plasma Processes Polym.*, vol. 9, no. 3, pp. 316–323, Mar. 2012.

[29] R. a. Siliprandi, S. Zanini, E. Grimoldi, F. S. Fumagalli, R. Barni, and C. Riccardi, "Atmospheric Pressure Plasma Discharge for Polysiloxane Thin Films Deposition and Comparison with Low Pressure Process," *Plasma Chem. Plasma Process.*, vol. 31, no. 2, pp. 353–372, Jan. 2011.

Session 2: Icing in Wind Energy

Design and Implementation of a Wind and Icing Monitoring System for 80m Wind Turbines in Northern Labrador

Michael Abbott
AMEC, Environment & Infrastructure
St. John's, NL, Canada

William Henson
AMEC, Environment & Infrastructure
Ottawa, ON, Canada

Eric Gionet
AMEC, Environment & Infrastructure
Halifax, NS, Canada

David Bryan
AMEC, Environment & Infrastructure
St. John's, NL, Canada

Abstract **—** The coastal region of Labrador is populated with many isolated communities that face challenges in providing electrical power generation. Vale NL Ltd. is investigating the use of wind turbines to provide electrical power for its mining facility at Voisey's Bay. Vale has commissioned AMEC to perform a wind resource assessment and evaluation of icing potential at a candidate site near Voisey's Bay.

The candidate site is located in a harsh, marine environment, in close proximity to the Labrador Sea, that experiences extreme cold temperatures, high winds and significant icing events. Compounding the challenge is the remote nature of the candidate site; it can only be accessed by helicopter, making inspection and maintenance visits difficult and infrequent.

Because of these challenges, AMEC undertook a system design that recognized the harshness of the environment and the potential for failures. The monitoring tower was commissioned in December 2012 and the data recording and analysis program will proceed for at least 12 months. A suite of monitoring sensors was deployed at the site to provide real-time data recording of the critical meteorological parameters (primarily wind speed, wind direction, temperature, etc.) and icing accumulation. The system design incorporated several levels of redundancy at the sensor level, data storage level and power levels to mitigate the impacts of an individual failure. An overview will be presented of the system design to suit the project requirements and challenges, as well as a preliminary, qualitative assessment of the performance of the monitoring system.

I. Introduction

The objective of this paper is to discuss the design and implementation of a wind and ice monitoring station at Voisey's Bay, Newfoundland and Labrador to assess the potential for a wind farm installation.

Voisey's Bay is the site of a nickel mine, operated by Vale NL Ltd. The mining operation and the encampment are remote and therefore are powered with fossil fuel generators. The northern location of Voisey's Bay (56º N latitude) limits access to the site during the winter months. Consequently the cost of fuel shipment and storage is quite high and has associated risks. Installation of a wind farm to provide an alternate source of electricity generation would reduce the risk and reduce the cost of power for the site.

The remote northern location of Voisey's Bay makes the wind resource assessment difficult both in terms of the extreme environment and access. All of the equipment to be used in the installation of the monitoring system, had to be shipped by boat. The northern location of Voisey's Bay produces extreme cold during the winter months, with temperatures frequently going below -20º C. Because it is located near the Labrador Sea, it also experiences numerous icing events throughout the winter. Previous tower installations in the region have experienced catastrophic failure due to icing accumulation [2].

An additional challenge is the further remote situation of the monitoring site. The monitoring site is located (latitude: 56.399575, longitude: -62.050756 – see Figure 1) on a plateau approximately 315m elevation above Voisey's Bay and 1.5 kilometres from the nearest road.

The exposed character of the monitoring site also provided challenges during the installation. The installation of the monitoring station was conducted during October-November 2012. This period of the year was characterized by short working days, high winds and cold weather. During the installation, work was halted on numerous days due to the prohibitive weather conditions.

The remainder of this paper describes the design, installation and data gathering that was conducted as part of this project. The paper is organized as follows. The system design is described in Section 2. In Section 3 a preliminary analysis of the data is presented and finally summarized in Section 4.

Figure 1: Location of Met Tower [source Google Maps]

II. System Design

A. Requirements

The goal of a wind resource assessment is to determine whether the candidate site is suitable as a reliable source of wind power. There are several key criteria to assess the site's suitability:

- Does the site have a characteristic wind that is sufficient in strength to produce the required power?
- Is the wind reliable and consistent so that it produces electricity when desired?
- Is the wind steady or does it feature gusts and turbulence?
- Does the site experience phenomena such as frequent icing or over-speed that would make the electricity production unreliable or unpredictable?

To address these questions, it is required to determine the meteorological characteristics of the site for an extended period (at least 12 months). It is necessary to monitor and capture the wind speed at the site using calibrated anemometers. In addition to wind speed, the wind direction, temperature, atmospheric pressure and relative humidity are useful to fully characterize the meteorological conditions of the site. Because of Voisey's Bay northern location and proximity to the ocean, icing is a concern and so it is also required to measure the amount of icing that accumulates at the site.

Due to the remote nature of the site, it is necessary for the monitoring system to operate as reliably as possible, without manual intervention or on-site maintenance. Therefore, a degree of redundancy is desirable to reduce the potential for data loss. There should be minimal opportunity for single-point failures within the monitoring system. A reliable source of electrical power is required. The system should incorporate features that make it resist the accumulation of ice or have the capability to shed accumulated ice. The components should be resistant to potential damage of falling ice.

B. Tower Design

The meteorological tower (met-tower) was designed and installed by WesTower Communications. The structure is a guyed tower with horizontal booms for attaching the monitoring sensors (see Figure 2). There is a "goalpost" structure at the top of the tower allowing the uppermost sensors to be mounted at 80m above ground level. The tower was designed to meet the CSA S-37 standards to ensure that it would withstand the potential ice accumulation that was anticipated for the site.

The met-tower was delivered in sections to Voisey's Bay via ship. The sections were airlifted to the met-tower site via helicopter, where the sections were assembled and the tower was erected using a "jin-pole".

C. Monitoring Sensor Design

The most critical data required to perform a wind resource assessment is time-series information of the wind speed at the site. Due to the limited access to the site, it was decided to use multiple wind speed anemometers to ensure that there was sufficient redundancy in data capture. Sensors sometimes fail without warning, they may experience a temporary loss of data measurement (eg. due to icing), or their measurement accuracy may "drift" over time. Utilizing multiple sensors reduces the impact of these issues.

The system design features anemometers mounted at 80m, 60m, 40m and 20m. Installing anemometers at multiple heights, in addition to providing redundancy, also provides a good measurement of the vertical wind profile which is useful in analyzing the wind resource at the site.

Two (2) anemometers were mounted at each of the vertical levels, providing a total of eight (8) wind speed anemometers. Six out of the eight anemometers were heated to reduce the likelihood of data loss due to icing. Two of the anemometers were unheated which, in addition to providing wind speed data, also provides a secondary indication of icing incidents; when the unheated sensors stop reporting data, it can be inferred that there is an icing event.

The anemometers are mounted on horizontal booms that protrude from the tower by approximately 10m. The anemometers are mounted sufficient distance (in accordance with the IEC 61400-12-1 standard [1]) to minimize any upstream effects from the tower. The sensors are also mounted 0.5m above the boom to minimize effects from the boom itself.

Two sensors, mounted at 60m and 40m, are sonic wind anemometers which also record the wind direction at the site. Two vertical wind speed sensors are mounted on the tower at 60m and 40m to identify the vertical component of the wind speed.

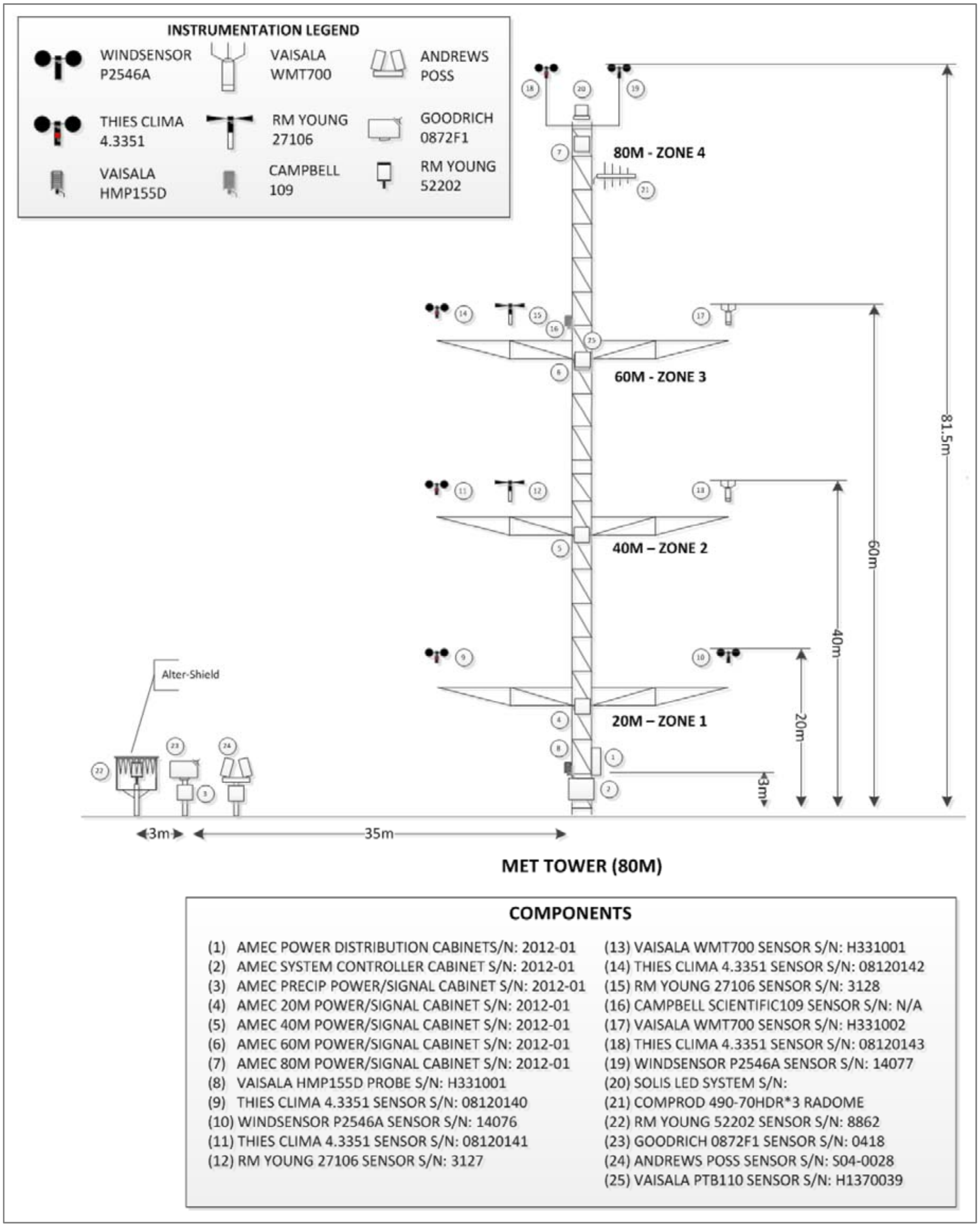

Figure 2: Schematic of Met Tower and Monitoring System

Temperature sensors are mounted on the tower at 60m and at 3m; this not only provides redundancy of data collection but also an indication of the temperature lapse rate. There is a barometric pressure sensor mounted at 60m. A relative humidity sensor is mounted at 3m.

Located approximately 35m upwind (relative to the prevailing wind direction) of the tower are several instruments for characterizing the precipitation. There is an ice accumulation rate sensor. This sensor has an exposed cylindrical surface upon which ice will accumulate. When a specific mass threshold of ice has accumulated, a heating unit is activated which will melt the ice, allowing more ice to accumulate.

There is also a tipping-bucket rain gauge which measures the precipitation rate. The rain gauge contains a heating unit to melt any snow accumulation to provide an accurate measurement of the liquid precipitation.

A vertically-pointing, bi-static X-band Doppler radar was installed at the site to provide additional precipitation measurements. This system measures the Doppler velocity of the volume of air above the sensors, analyzing the measured velocity spectrum and estimating the phase (or different phase types) of the precipitation.

D. Data Collection System

Data from all of the sensors is collected in one of two data logging controllers. The specific data loggers selected are models rated for extreme temperature operation. The recorded data is stored in non-volatile battery backed Static Random-Access Memory (SRAM) to minimize any loss of data in case there is a power failure or loss of communications. Two controllers are used because the many sensors yield a significant amount of data, and should a failure occur, the potential for data loss is reduced.

The data from the sensors is received at a frequency of 60 Hz. The data is processed by the controller into 10-minute average data which is stored by the controller; the 60 Hz data is not retained. This increases the amount of data that can be stored locally and reduces the amount of data that has to be transmitted, without an appreciable loss of data fidelity. For most parameters, the following data characteristics are stored every 10 minutes:

- Mean value
- Standard deviation
- 10-minute maximum value
- 10-minute minimum value

For parameters related to liquid precipitation observations, the total accumulation over a 1-hour and 24-hour periods is recorded. For icing observation, the accumulation at the time of observation trigger is recorded.

Once per day, the data is transferred from the data loggers to a server located at the Voisey's Bay site. The data is transferred via a wireless antenna mounted on the tower to a corresponding receiver at the Vale facility located 2 km away. The data is stored on the Vale server and a copy of the data is uploaded daily to the AMEC secured FTP site.

E. Power System

The data monitoring system is reliant on a robust power supply to operate all of the sensors, and in particular, to meet the power needs of several components that consume a non-trivial amount of power. The major power consuming components include:

- Wind sensor heaters 400W
- Ice detection sensor 350W
- X-band Doppler radar 230W

While the system can retain data if there is a temporary power outage, the remote nature of the site means that unplanned maintenance visits to the site would be difficult and only performed in a critical situation. Two planned maintenance visits per year (in Spring and Fall) are the most likely opportunity to address any problems or failures.

Two options were considered for the site power supply. The first option was a self-contained power system featuring a combination of diesel generator, solar panels and batteries. Because of the relative close proximity of the site to nearby infrastructure, the second option was an AC power line connected to the site infrastructure. The AC power line was selected as the preferred option because it presented a more reliable power supply with minimal support required. This avoided the need for refueling excursions and allowed access to a greater power budget.

The power distribution for the instruments at the site was designed to provide reliability and avoid single point failures. One risk is the hazard of falling ice that can potentially damage power and/or communication cables. Such an incident can cause a critical failure to the entire system. The monitoring sensors at each height above ground level (e.g. 20m, 40m, 60m, 80m) were supplied with power via a dedicated power distribution box. Therefore, if a cable were damaged, only the sensors at one height would be affected. Armour-shielded cable was used to protect the power and communications cables to minimize the possibility of damage due to harsh elements, falling ice or other hazards.

III. Summary of Data Collection Program

The data monitoring system at Voisey's Bay became operational in December 2012. The monitoring system has been collecting data since that time and will continue until at least 12 months of data have been acquired (12 months is deemed to be the minimum amount of data required to perform a wind resource assessment).

Throughout this period, the data monitoring system has collected data reliably. Figure 3 illustrates the time series plots of the wind speed from the eight horizontal wind speed sensors. The chart indicates that the sensors provided good agreement among the data measurements. The plots for different heights also reveal the expected increase in wind speed with height above ground.

During the initial period of the program, a problem with a server caused several brief periods of data loss. There were several periods when icing events caused some of the sensors to report inaccurate data or no data.

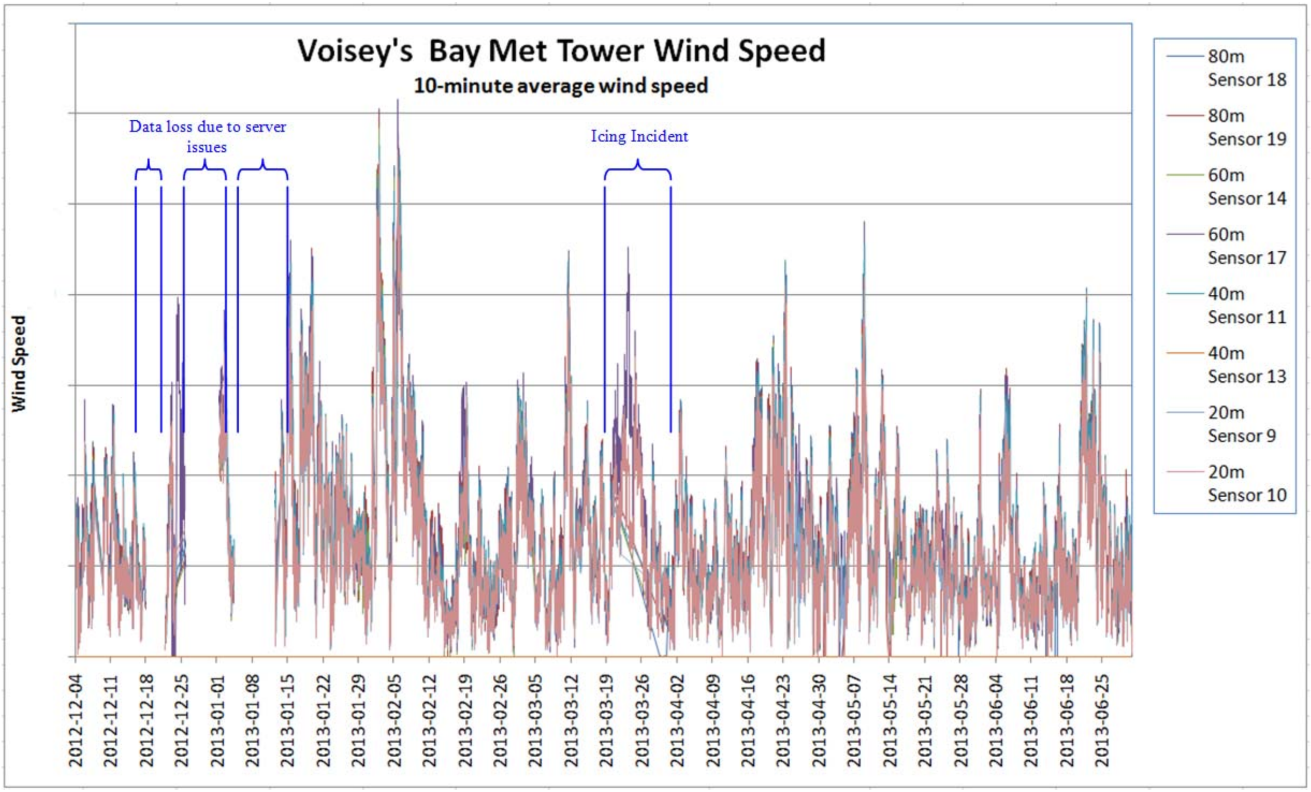

Figure 3: Wind Speed Anemometer Observed Data

The loss of anemometer data during these periods is insignificant to the overall data program. These incidents give a good indication of the frequency and severity of the icing that would be expected to affect future wind turbines that may be installed at the site. The data recorded by the icing observation sensor indicated icing events (see Figure 4) that are corroborated by the wind speed anemometer behaviour.

Some of the sensors did not perform as desired. Analysis of the data yielded by the X-band Doppler radar indicated that the system suffered from "noise" issues. This issue could not be resolved remotely and so the data acquired by the system is not useful. During a maintenance trip in July 2013, the radar system was disengaged.

During April 2013, one of the sonic wind sensors (40m) stopped recording data. This device records both wind speed and wind direction data. However, the loss of the data from this device is not critical because there is a second anemometer at the 40m level which records the wind speed. There is another sonic anemometer at the 60m level which records the wind direction.

One of the vertical wind speed sensors (40m) also stopped recording data during January 2013. There is a second vertical wind speed sensor (60m) which has continued to provide wind speed observations.

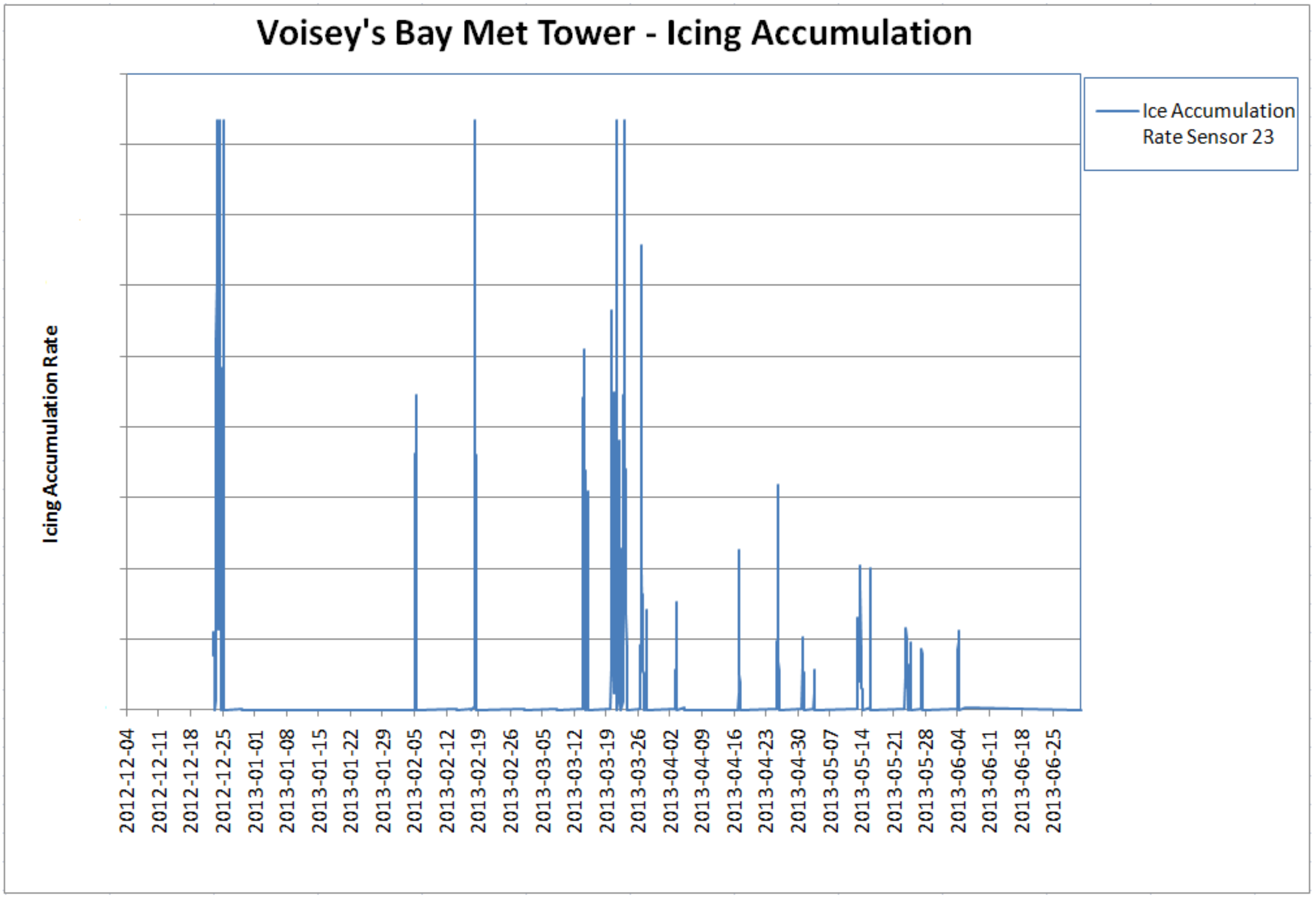

Figure 4: Icing Events During Monitoring Program

IV. SUMMARY

The monitoring system at the Voisey's Bay met tower was designed to be robust and with high redundancy to address the harsh environmental conditions that were anticipated to occur at the site. It was expected that there would be some periods of data loss due to the conditions, and even some equipment failures. The design of the system was intended to accommodate such failures and still provide a reliable data record that would allow completion of the wind resource assessment analysis.

The site did present several extreme meteorological conditions during the first six months of observations. The site experienced a range of temperatures from -36ºC to +22ºC. As illustrated in Figure 4, there were several notable icing events, some for a sustained period of time.

At some point during the data monitoring program, each of the wind speed anemometers failed to record data at least once (not all at the same time). This included the heated sensors. As expected, some of the sensors ceased to provide useful data, however the deployment of redundant sensors has mitigated the impact of these losses.

ACKNOWLEDGMENT

The authors would like to thank Vale NL Ltd. for making the wind monitoring project observation data available for this paper.

REFERENCES

[1] IEC 61400-12-1 International Standard, Wind turbines – Part 12-1: Power performance measurements of electricity producing wind turbines, Edition 1.0, 2005

[2] Canadian Radio-television and Telecommunications Commission, April 15, 2010, Telecom Decision CRTC 2010-216, Available: http://www.crtc.gc.ca/eng/archive/2010/2010-216.htm

Assessment of Wind Energy Production Penalties Due to Cold Climate in Canada

Antoine Lacroix, Melinda Tan and Paul Dockrill
CanmetENERGY
Natural Resources Canada
Ottawa, Canada
alacroix@nrcan.gc.ca; mtan@nrcan.gc.ca; pdockril@nrcan.gc.ca

Abstract — Canada's total installed wind energy capacity has grown by more than 900 percent over the last decade, resulting in an installed capacity of 6,500 MW as of January 2013. With this significant growth in wind power development, operational impacts due to Canada's cold climate are becoming evident.

A study was undertaken to evaluate the impact of cold climate conditions on wind energy production. Actual production data from 24 wind farms located across Canada were compared with reference data generated using wind data from Environment Canada's weather stations, a measure-correlate-predict algorithm (MCP), and wind energy production simulation software. The study also looked at the predicted losses in the projects' preliminary feasibility studies. The initial results indicate that cold climate losses in the order of $100 million occur annually. The presentation will break down cold climate losses into national and regional production loss percentages.

Wind farm sites located in regions where colder temperatures occur over greater parts of the year represent a significant wind energy production potential for Canada. As fewer temperate sites become available, large wind energy projects in colder climates will increasingly be developed. Better understanding of the losses associated with cold climate operation, coupled with research into areas such as icing characterization, icing maps, along with ice detection and protection, will improve the performance of existing wind farms and most certainly enhance the productivity of future wind farms.

Keywords — *wind energy; turbine; icing; losses; cold climates; rime*

I. INTRODUCTION

The pace of new wind power development has stepped up dramatically in Canada. In the eight years between 2003 and 2011, Canada's total installed wind energy capacity grew by more than 900 percent, from 322 MW to 5,260 MW. With this remarkable growth in installed capacity, operational impacts due to cold climate phenomena are beginning to be seen. Wind farm sites located in regions where colder temperatures occur through greater parts of the year represent a vast wind energy production potential, and as fewer temperate sites become available, large wind energy projects in cold climates will increasingly be developed.

The objective of this study is to offer an assessment of cold climate issues and how they impact on the electricity production of commercial wind farms in Canada. Thanks to the programs managed by the Renewable and Electrical Energy Division of NRCan, wind farm production data have been obtained and compared to reference outputs generated by wind energy simulation using actual meteorological information.

The results of this effort yielded production loss factors for each wind farm under review. This information is used to develop regional loss factors that will be applied to existing and future wind farms in Canada. Therefore, it will be possible to roughly estimate the production losses associated with cold climate issues for existing and future wind farms..

II. COLD CLIMATE ISSUES

In Canada, cold climate issues could be divided in two categories: the impact caused by cold air temperatures and the impact caused by atmospheric icing. Turbine manufacturers are now offering packages to allow operation at temperatures as low as -30°C, thereby addressing most of the impacts caused by cold air temperatures. It is therefore expected that the vast majority of the impacts related to cold climate are of an icing nature. However, if wind turbines are not producing due to cold air related issues, this will be included in this study. Icing occurs when surfaces are struck by freezing precipitation (glaze) or by the supercooled water droplets found in clouds (rime). Because freezing conditions can be expected at one time or another throughout the country, essentially all of Canada's wind turbines can be affected by icing. The accumulation of ice on wind turbine blades results in a power output reduction, an increase in the rotor loads, and may require stopping the turbine for safety reasons and not to exceed the operational limits of the wind turbine.

A. Effect of Icing on Wind Turbines

Haapanen [1] performed ice accretion simulations on two wind turbines: one stall-regulated and one pitch-regulated. Modern utility-scale turbines are now all pitch-regulated. For these, he found that when ice is present on the blades, an increase in wind speed is required before reaching nominal power. This can be explained because pitching to reduce power is delayed until the wind has reached a higher velocity than when no ice is present on the blade [1]. The presence of ice on the blades increases their weight and fatigue load, thereby resulting in performance losses and eventual shutdown. Furthermore, ice fragments can detach and represent a safety concern for people and properties around the turbines.

III. Methodology

A. *Wind Energy Prediction Model and Wind Farm Production Data*

In order to forecast the wind energy production during icing periods, a model was developed around Windographer, a commercially available wind data analysis program. The model was used to generate reference wind power production data to which actual production could be compared.

The actual production data were obtained from the Renewable and Electrical Energy Division (REED) at NRCan. REED, through its production incentive programs, has wind farm production data since the Wind Power Production Incentive (WPPI) program began in 2002. The WPPI program was followed by another incentive program, ecoENERGY for Renewable Power (ecoERP) that began in 2007. For this study, at all but two locations, the ecoERP data were used because they were available on a monthly basis. The 'gross' production data were used to ensure that all the energy produced by the turbines were evaluated.

The underlying principle of this approach is that actual production data will suffer from cold climate effects while the data generated from the model will not because the learning period is based on summer months that include only the normal operating losses. Therefore, during cold climate months, any additional losses will be interpreted as cold climate related and processed as such. One caveat however, is that this approach does not take into account the unscheduled maintenance during winter months.

B. *Wind Data for Model*

The model uses hourly meteorological data from the weather stations operated by Environment Canada. In addition to wind speed, atmospheric pressure and air temperature are also used. When calculating power, Windographer computes the value of the air density and adjusts the energy production accordingly as the power in the wind is directly proportional to density.

Prior to their use by Windographer, the data downloaded from the Environment Canada website are processed and formatted in the appropriate units. An effort is made to obtain data from the station located closest to the wind farm under evaluation but this is not always possible as some stations do not record the wind speed. In that case, the nearest station with a complete set of parameters is used. It is possible that selecting further located stations impact on the data correlation.

C. *Wind Energy Prediction*

Estimations of the wind energy production are obtained from Windographer. This software features a function to estimate the production of a wind turbine based on the wind resource contained in the input file. The power curves of practically all the utility-scale turbines are built-into Windographer and results are provided in terms of monthly energy output for a single turbine. A loss factor of 5% is included to account for array losses. As part of the forecasting process, these data are then copied on an Excel spreadsheet and multiplied by number of turbines in the wind farm. This gives the unadjusted wind energy prediction for a given wind farm.

1) *Improving the Prediction Model*

However, because the Environment Canada weather stations are not located precisely at the wind farms and also because the height of the mast at these stations is usually set at 10 meters, the model output does not match the actual production of the wind farms.

In order to address this discrepancy, a measure-correlate-predict algorithm (MCP) is used to predict the wind farm energy output. This is the last stage in determining the reference production level. Because the statistical relationship is quite linear between the predicted and actual energy outputs, the linear-regression method outlined in Rogers [2] is applied (see figure 1). The linearity can be observed by examining a full dataset at a location where little or no icing is expected. For instance, for the wind farm in Figure 1, the Pearson's coefficients for the full dataset and learning period are 0.9675 and 0.9796 respectively.

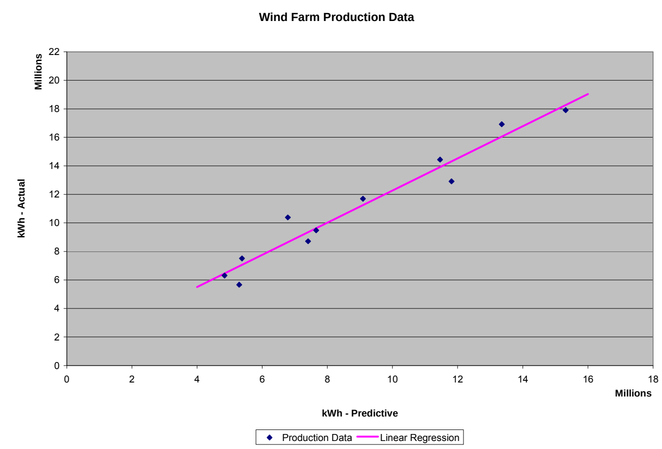

Fig. 1. Linearity between the actual and predicted data. Each marker represents one month during which cold climate issues are not expected. For this example, the Pearson r factor is 0.9741.

The degree of correlation is estimated by the Pearson product-moment correlation coefficient (typically denoted by r). The Pearson coefficient is a measure of the correlation between two variables X and Y, giving a value between +1 and −1 inclusive, respectively indicating perfect positive and negative correlation in the XY pair. In the case of this study, it is a measure of the correlation between the actual production data and the potential or expected production as approximated by the Windographer analysis. The learning periods used in the MCP algorithm are the months free of icing and a high correlation factor will ensure a higher accuracy. The learning can be defined as the (x;y) pairs that were used to calculate the parameters of the linear regression equation. The MCP routine is performed in Excel thanks to a built-in function that provides for the linear regression model, the slope and the y-intercept of the equation. The Pearson's r coefficient can also be calculated in Excel.

D. Estimating Wind Energy Losses

Once the parameters defining the linear regression (slope and intercept) are determined, it is possible to complete the reference production level. This last stage takes the output from uncorrelated output (the purple line) and performs a statistical adjustment that will maximize the correlation between the actual and predicted production data, the blue and yellow lines respectively. Since the actual production data incorporates losses inherent in the wind farm, so should the predicted data (that is derived from the actual data).

Production losses are calculated by subtracting the actual production value (blue line) from the theoretical potential production (yellow line). This calculation is made between the months of November and April inclusively. If a negative result is obtained, it is assigned a value of zero.

In Figure 2, one can observe that for the months of December 2009 and January 2010, the actual production of the wind farm has been significantly less than its potential (reference). On the other hand, for March and April 2010, the wind farm output more or less corresponds to the availability of the wind resource.

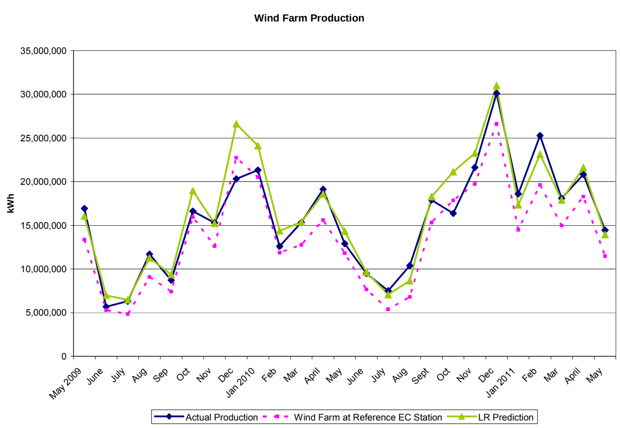

Fig. 2. Typical wind farm production outputs showing actual (blue), uncorrelated model output (purple) and correlated data (reference) (yellow).

In order to calculate the annual losses, a reference year has been determined and it is based on the twelve-month period between May 2010 and April 2011 inclusively. Losses encountered outside the November to April interval, are not included in the calculation. The reference year spans two calendar years in order to include the wind farms that were recently commissioned.

The process described above has been performed for all of the 28 wind farms under review for this study. Because monthly production data were available, all the wind farms across Canada under the ecoERP program were selected. Several farms were then screened out due to a too short period of operation offering insufficient months for the analysis and the prediction model. Wind farms were also left out because they were too small, having only one or two turbines. In order to review wind farms in all regions and provinces, it became necessary to add wind farms that are part of the WPPI program. As a result, wind farms from all provinces were examined. This required additional work as monthly production data are not available electronically. They had to be manually extracted from paper records. The results are presented in the next section.

IV. Results and Discussion

The production losses due to atmospheric icing for the wind farms that were examined are presented in Table 1. A total of 24 wind farms were selected for this study. The wind farms have been grouped into five regions, for the purposes of protecting the privacy of individual wind farms.

A. Overview of Results

The results in Table 1 show that cold climate issues impact wind energy production in Canada. Based on the findings of the study, the NB-NS region is one of the most severely affected. The region's average annual production loss percentage is 15.7%, and the average winter loss factor, recorded between November and April is 26.5%. The province of British Columbia is not discussed in the study results. However, British Columbia is included in the region of "Western Canada" for calculations of Canada's total production, from both current and future wind farms.

Note that in some cases the relatively small size of a wind farm, where losses from a single turbine, related to cold climate or not, can distort the sampling.

TABLE I. Wind Production Losses

Region	Capacity (MW)	Production Losses	
		Ref. Year	Ref. Winter
AB + MB	254	3.2%	5.7%
ON	688	3.5%	5.7%
QC	445	7.4%	12.4%
NB + NS	285	15.7%	26.5%
PEI + NL	96	3.4%	5.8%

Fig. 3. Regional production losses of the wind farms that were surveyed

In the PEI-NL region, annual losses average 3.4%. It has been observed and documented that the sort of icing occurring in these two provinces consists mainly of glaze ice. This claim is supported by a map spanning thirty years of observations, between 1950 and 1980, titled 'Mean Number of Days With Freezing Precipitation' [3] that was produced by Environment Canada. This map shows between 10 and 20 days of freezing precipitation every year for the regions of Prince Edward Island, Nova Scotia and Newfoundland.

The average annual production loss observed for the Québec wind farms is 7.4%. In some cases, the proximity of wind farms to the Environment Canada stations, the similar landscape and the availability of reliable airport data add to the confidence in the results in this region. For wind farms located at lower elevations, close to sea level, the probability of in-cloud (rime) icing is reduced. This suggests the presence of glaze ice from precipitation or rime icing caused by evaporation from the St. Lawrence River.

In Ontario the wind farms surveyed show an average annual loss of 3.5%. For the period of time that wind turbines have been in operation around the Great Lakes, atmospheric icing has not been an issue and these numbers seem to confirm it.

The results for Ontario are somewhat in contradiction with the literature, at least for the Great Lakes region. In 1973, Tattelman and Gringorten [4] reviewed data obtained from several meteorological publications spanning over a period of 50 years from 1919 to 1969. Their major contribution was to add probability estimates to groups of progressive ice thickness for all the ice storms covered by their study. They divided the United States into eight regions of similar glaze characteristics and also according to latitude, land area, geography and climatology. In their study, the two regions neighbouring the Great Lakes exhibit probabilities of experiencing an ice storm of any thickness during one year of 0.98 and 0.99. This information is consistent with the Environment Canada freezing precipitation map cited previously, where for Southern Ontario, between 10 and 20 days of freezing precipitation can be expected in one year. However, this is not what was observed in the course of this study, and to some extent would indicate that the question of cold climate and icing losses should be revisited when operational data over a longer time period is available.

For the wind farms located in the AB-MB region, average annual cold climate related loss is 3.2%.

The results for Quebec and NB-NS regions are consistent with the literature. Bailey [5] has observed that during the icing season in the US Northeast, between the months of November and April, elevations above 700 meters can expect riming conditions at least 10% of the time. It is likely that this could also be said for locations with similar elevation in Nova Scotia.

B. *2011 Production Losses for Existing Wind Farms in Canada*

An analysis of wind energy losses due to icing was performed for all the wind farms operating in Canada by the end of 2011. The results are presented in Table 2. Based on the loss factors calculated for the wind farms reviewed in this study, regional loss factors were developed and applied to the 5,260 MW of wind capacity currently in operation. An average capacity factor of 31% (based on the total installed capacity and the annual electricity production) was applied across all wind farms.

Table 2 shows that for the country in 2011, the model-based cold climate related losses amount to approximately 1,010,000 MWh. An online search was performed to determine the average tariff rates paid by utilities to wind farm operators within each province, for wind generated electricity.

TABLE II. VALUE OF WIND PRODUCTION LOSSES

Region	**Estimated Annual Production w/ Cold Climate Loss (MWh)**	**Annual Cold Climate Production Loss (MWh)**	**Annual Cold Climate Loss ($)**	**Annual Cold Climate Loss (tons CO_2 eq)**
Western Canada	4,282,718	168,910	11,668,706	82,070
ON	5,348,401	321,282	43,373,070	41,767
QC	2,494,958	198,272	17,249,658	397
NB-NS	1,567,607	296,858	25,727,144	181,076
PE-NL	590,806	24,304	1,861,999	140

Fig. 4. Estimation of the annual production losses due to cold climate issues for all the wind farms operating in Canada by the end of 2011 (Note: Western Canada includes BC, AB, SK, MB)

The provincial tariffs were then applied to the production losses in order to determine the financial impact of cold climate on wind farm economics. The total impact of cold climate losses amounts to a value of almost $100 million. Likewise, a search was performed to determine the GHG intensity of electricity generated within each province (see Table 2). The provincial intensities were then applied to production losses in order to determine the penalty of decreased wind energy production in cold climate on GHG emissions. The total impact corresponds to a penalty of 305,450 tons of CO2 equivalent.

C. *Estimating Losses Due to Cold Climate During Planning Phase of Wind Farms*

A comparison of estimated annual production loss due to cold climate for selected wind farms surveyed in this study was performed. The results indicate that cold climate impacts on wind energy production have been consistently underestimated. Wind farms with the highest and lowest estimated production loss were identified for comparison. The estimated annual production loss derived in this study was compared with that found in the technical report for each wind farm. The reports were submitted to REED as part of the application process for ecoERP funding, and were typically authored by engineering consultants subcontracted by the wind farm developers.

A review of the technical reports provided some indication of the consideration given to cold climate impacts on wind farm performance. In one case, the consultant performed an analysis of potential icing and low temperature losses. Wind data collected at an Environment Canada meteorological station co-located with the wind farm indicated a large number of icing incidences during cold climate months (October to May). However, the consultant noted that operational data for the turbines operating in cold climate conditions was not available. Therefore, there was considerable uncertainty regarding the expected losses due to icing.

In another example, the consultant applied only wake losses when calculating net energy yield. No consideration was given to cold climate operation. In general, most of the technical reports under estimated production losses due to cold climate, when compared to corresponding predictions in this study. Cold climate was seen as having an impact primarily on aerodynamic performance (due to icing on blades), and in some cases on availability (due to cold temperature shutdown).

This review and comparison of estimated annual production losses due to cold climate suggests that cold climate losses are not adequately quantified prior to wind farm development. Cold climate impacts are generally not considered significant, and in some cases did not even warrant consideration. Wind farm developers therefore do not perceive cold climate as having an impact on wind energy production due to a general lack of knowledge across the wind industry in Canada. While this is true in some areas of Canada, wind farms in other regions of Canada do indeed experience production losses in cold climate.

V. Conclusion

This study has examined the impact of cold climates on the production level of 24 wind farms in Canada. A wind energy forecast model, including an MCP algorithm, was developed to establish a reference potential wind energy production. This reference was then compared to the actual wind production in order to determine the cold climate production losses for 24 wind farms.

The study shows that cold climate issues impact wind energy production in Canada. Annual average regional losses vary between 3.2% and 15.7%, while the average regional winter losses vary between 5.7% and 26.5%. The highest annual and winter losses occur in the NB-NS region. Based on 2011 data, the cumulative weighted average loss for all the wind farms in Canada is estimated at 6.6%.

Based on the findings of this study, it is estimated that the production losses for 2011 due to cold climate issues for the wind farms currently installed in Canada is 1,010,000 MWh. At the current wholesale price for new electricity generation, this represents a value of almost $100 million. In terms of GHG emissions, this corresponds to a missed opportunity to offset 305,450 tons of CO2 equivalent.

A review of the project proposals submitted to REED for ecoERP funding has shown that limited considerations were given to cold climate impacts on wind farm performance. In preparation of this study, eight wind energy projects feasibility studies were reviewed. These feasibility studies were performed by recognized engineering firms responsible for wind resource assessment. It was found that these feasibility studies underestimated or simply omitted to calculate the production losses due to icing and cold climate. It could be said that cold climate issues were generally not perceived as having a significant impact on wind energy production.

Acknowledgment

The wind energy group at CanmetENERGY Ottawa wishes to thank the Office of Energy Research and Development for supporting this work. Thanks are also addressed to the Renewable Energy and Electrical Division, specifically to Jimmy Royer and Jack Jensen for providing us with the actual wind farm production data without which this study could not have been undertaken, and for their comments and observations.

References

[1] E. Haapanen, "Influence of ice accretion on wind turbine performance," Proceedings of Boreas III Conference, 1996, pp. 268-278.

[2] A. Rogers, J.W. Roger and J. Manwell, "Comparison of the performance of four measure-correlate-predict algorithms," Proceedings of the 2005 American Wind Energy Conference.

[3] "Map: number days freezing rain annual," Environment Canada, 1980.

[4] P. Tattelman and I.I. Gringorten, "Estimated glaze ice and wind loads at the earth's surface for the contiguous United States," Air Force Cambridge Research Laboratories Report AFCRL-TR-73-0646, 1973.

[5] B.H. Bailey, "The potential for icing of wind turbines in the Northeastern U.S.," Windpower 1990, pp. 286-291.

Recommended Practices for Wind Energy in Cold Climates: Resource Assessment and Site Classification

Niels-Erik Clausen (DTU Wind Energy, Denmark), Matthew Wadham-Gagnon (TechnoCentre Éolien, Canada), Tomas Wallenius (VTT, Finland), René Cattin (Meteotest, Switzerland), Göran Ronsten (WindREN, Sweden), Rebecka Klintström (Vattenfall, Sweden), Michael Durstewitz (Fraunhofer IWES, Germany), Ian Baring-Gould (NREL, United States of America), Øyvind Byrkjedal (Kjeller Vindteknik, Norway), Andreas Krenn (Energiewerkstatt, Austria), Zhang Qiying (Guodian United Power Technology, China)

Abstract — Deployment of wind energy in cold climate (CC) areas is growing rapidly. The main issues of wind energy in CC arise from icing of wind turbine rotor blades which reduces energy yield, mechanical life time of turbines and increases safety risks due to ice throw. Another aspect of CC is low temperatures, which also can reduce a turbine's mechanical lifetime. Wind resources in CC areas are typically good and large-scale exploitation of cold climate sites has started, but despite of new technical solutions for wind turbines for CC the question "how does CC affect wind resources and resource assessment" still remains largely unanswered.

Cold Climates is defined by IEA RD&D Wind's Task 19 – Wind Energy in Cold Climates, research collaboration under the (IEA Task 19), as regions where significant icing events or periods with temperatures below the operational limits of standard wind turbines occur. These factors along with large amounts of snow may impact project implementation, economics and safety. IEA Task 19 has produced the report "Recommended practices for wind energy projects in cold climates" in which special requirements for CC wind energy projects are proposed in order to reduce uncertainties and lower the risks of a project.

The severity of the CC issues at the site under interest is to be determined in the resource assessment phase. In the "Recommended practices for wind energy projects in cold climates" report IEA Wind's Task 19 introduced for the first time a site classification, which allows planners to classify a project site according to the site-specific icing frequency. Based on this site ice classification, the order of magnitude of production losses due to icing can be estimated and classified already in the planning phase. This is the first step towards a standardisation of wind energy sites with regard to icing and forms the basis for a future wind turbine classification related to icing. The Recommended Practices report also describes how to properly plan for and install measurement equipment for resource assessment in CC, how to interpret the measurement results, and mitigate the risk associated with measrements in icing conditions and low temperatures.

Two sites were studied to provide examples of site classification: One in Québec, Canada and one in Switzerland.

These examples highlight the importance of using multiple ice assessment methods as well as the value of having long term data in order to reduce uncertainties related to icing during the project development stage of a CC site.

I. Nomenclature

ASL	Altitude above sea level
AGL	Altitude above ground level
CC	Cold Climate
IC	Icing Climate
IEA	International Energy Agency =
IEA Task 19	IEA RD&D Wind Task 19 – WE in CC
LTC	Low Temperature Climate
R&D	Research and Development
RD&D	Research, Development and Demonstration
RaR	Rivière-au-Renard wind farm, Québec, Canada
StB	St-Brais Wind Farm, Switzerland
TCE	TechnoCentre Éolien, Québec, Canada
WE	Wind Energy
WT	Wind Turbine

II. Introduction

Global wind energy capacity has exceeded 285 GW in 2012, 25% of which is installed in CC [1]. And an additional 45-50GW is expected to be installed in CC by 2017 [1].

IEA Task 19's definition of "cold climate" (CC) refers to regions where significant icing events or periods with temperatures below the operational limits of standard wind turbines occur, which may impact project implementation, economics and safety. The two challenges; icing and low temperature, can occur at the same site but normally never simultaneously as icing in low temperatures is quite rare.

The environmental conditions at CC sites can be challenging. Rime ice, snow, and super cooled rain are typical and frequent weather phenomena that can significantly affect turbine operation and lifetime.

The performance of an iced-up wind turbine will normally degrade rapidly as the ice accumulates. If the icing continues without a method to prevent the ice accretion or remove it, the turbine will either stop because of excess vibrations due to aerodynamic and/or mass imbalances or due to very low power production compared to wind speed. Another cause of turbine shutdown can be control errors due to iced up measurement equipment. Figure 1 **Error! Reference source not found.**shows iced up measurement devices on the top of a WT nacelle.

The turbine designer should also consider the influence of fatigue loads caused by icing. The cause of the fatigue loads is the combined aerodynamic penalty of ice on blades and imbalance caused by an uneven mass distribution [13].

Damage to the blade surface may occur if ice falls from the nacelle or blades and hits the modern, thin blade shells. Such damage can be quite expensive to repair and is rarely visible from the ground. The damaged blade surface may become soft, allowing water to penetrate the shell. If the water is allowed to freeze it will lead to consequential damages, which by definition are not covered by any insurance.

Figure 1: Instruments on top of cooling system of nacelle; wind vane heating is insufficient and the boom is collecting ice and causing errors in measurements. The condenser air inlet is partly blocked by ice accumulation. © Kent Larsson.

IEA Task 19[1] has gathered information about wind turbine operation in icy and low-temperature environments. Although experience has been gained, improvements in CC wind technologies are needed to further reduce the higher economic risk associated with deployment in these regions. Under this international collaboration, various R&D projects are under way, including the development of methodologies to provide a more reliable estimate of production to lower investor risk, development and testing of new anti- and de-icing technology solutions, measurement of turbine performance in CCs, and improving market information for CC technology. This paper provides an outlook of CC wind energy development and introduces the on-going CC R&D trends.

III. Background

The International Energy Agency (IEA) Implementing Agreement for Co-operation in the Research, Development, and Deployment of Wind Energy Systems IEA Wind RD&D, [2], is an agreement between 20 countries and the European Commission to follow international development on wind energy deployment and to stimulate cooperative research, demonstration and development (RD&D) of wind technology. The cooperation takes places in form of Annexes to the main agreement, called tasks.

IEA Task 19, “Wind Energy in Cold Climates”, was started in 2002. Two goals of IEA Task 19 are to collate information on available adapted wind energy technology and to formulate recommended practices for project developers. Once up to date these will enable improvements of the overall economy of wind energy projects and lower the risks associated with CC projects. Reducing risk will reduce the cost of wind electricity produced in CC’s. More information about IEA Task 19 and access to reports developed can be found at [9]. Other important goals of IEA Task 19 are to initiate research projects and to enable international collaboration between member countries.

IV. Definitions

An area where periods with temperatures below the operational limits of standard wind turbines occur is defined as Low Temperature Climate (LTC). An area exposed to significant icing events is defined as Icing Climate (IC). Although theoretically possible, active icing rarely occurs at temperatures below minus 20°C. In some areas wind turbines (WT) are only exposed to either icing or low temperature events. In some regions both low temperatures and icing events may take place. Therefore, CC embraces both LTC and IC. These definitions are further illustrated in Figure 2

[1] IEA Task 19, also known as the IEA Wind RD&D Task 19 – Wind Energy in Cold Climates, functions within a framework created by the International Energy Agency (IEA). Views, findings and publications of IEA Task 19 do not necessarily represent the views or policies of the IEA Secretariat or of all its individual member countries.

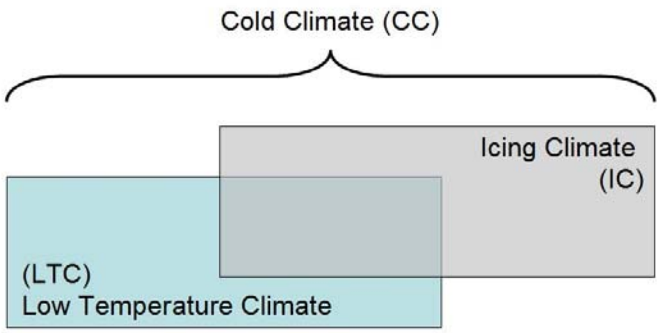

Figure 2: Definition of cold climate, low temperature climate and icing climate

Atmospheric icing is defined as the accretion of ice or wet snow on structures exposed to the atmosphere. In general, two different types of atmospheric icing that impact wind turbine development can be distinguished: in-cloud icing (rime ice or glaze ice) and precipitation icing (freezing rain, drizzle, and wet snow).

An icing event can be described with the following expressions [4], applicable to all structures and instruments exposed to atmospheric icing:

- **Meteorological icing:** Period during which the meteorological conditions for ice accretion are favourable (active ice formation)
- **Instrumental icing:** Period during which a structure and/or an instrument, a component or a wind turbine is disturbed by ice. Instrumental icing in the IEA Ice Classification is defined as the time during which a standard unheated cup anemometer is disturbed by ice.
- **Incubation time:** Delay between the start of meteorological and the start of instrumental icing (dependant on the shape, size, radius, surface and the temperature of the structure)
- **Recovery time:** Delay between the end of meteorological and the end of instrumental icing (period during which the ice remains but is not actively formed)

Figure 3 illustrates how a wind measurement is affected by icing according to the definitions described above.

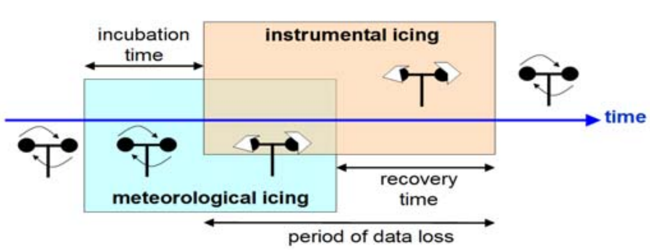

Figure 3: Definition of meteorological and instrumental icing.

V. Site Classification

Since the wind resource outside the operational icing limit of a wind turbine design cannot be harvested, consequently, the local icing distribution, including icing event length and severity, must be measured along with the wind speed and temperature during the site investigation so that a suitable turbine can be selected or an understanding of power losses obtained.

A site classification with respect to icing conditions for wind energy sites, IEA ice classification, was established by the IEA Task 19 expert group, see Table 1. The IEA ice classification gives a first indication on the severity of icing and its consequences at a given site. A good way to determine the site classification can be to evaluate actual energy production at a nearby wind farm or, if such data isn't available, use site measurements of meteorological icing and/or instrumental icing (ideally both) during the site assessment phase of a project. Icing is typically measured with web cameras, ice sensors and/or heated/unheated anemometers. . Alternatively, icing can be modelled numerically with meso-scale weather prediction models. If an icing map is available, one can obtain some good starting figures there. It is also possible to correlate airport (if there is a nearby airport) data to determine ice classification. Airport data may not be as accurate as site measurement due to the type of data available, as well as distance and altitude relative to the site, but often has the advantage of providing several years' worth of information.

Table 1: IEA ice classification

IEA Ice Class	Meteorological Icing	Instrumental Icing	Production Loss
	% of year	% of year	% of annual production
5	>10	>20	>20
4	5-10	10-30	10-25
3	3-5	6-15	3-12
2	0.5-3	1-9	0.5-5
1	0-0.5	<1.5	0-0.5

When using the IEA Ice Classification, there is a chance that a site can end up in two or three different IEA Ice Classes depending on whether meteorological icing, instrumental icing and/or production loss is used as input. Variations may also occur depending on the used instrumentation and the chosen measurement period. In such case it is recommended to use the highest class.

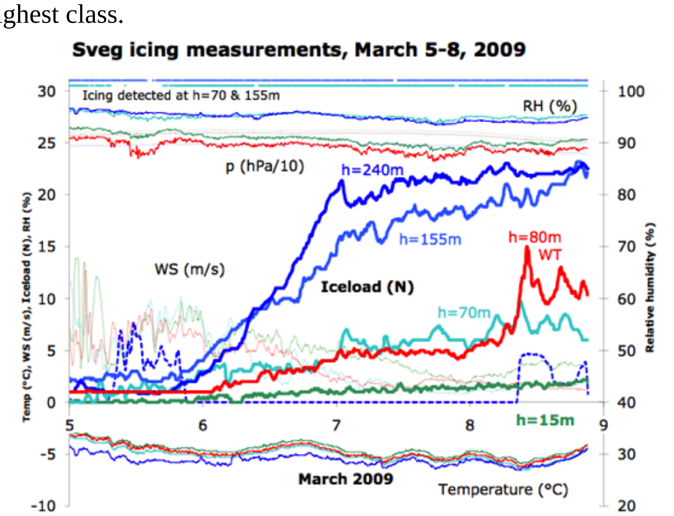

Figure 4: Icing measurement from different heights at Sveg, Sweden

Icing measurements from different heights were performed in Sveg, Sweden[], as shown in Figure 4. Measurements show significant increase in icing with increasing height. Higher ice mass and icing rate are critical issues when the turbines and meteorological masts are reaching higher altitudes. Most national meteorological services regularly predict icing at low altitudes for the aviation industry. The relevance of such ice prognosis for wind energy is still unknown, as no regular icing measurements are carried out, but those still can provide a rough guide to the level of icing that might be expected at a specific site.

A. Site Classification Example (Canada) Based on Measurement Data

The Rivière-au-Renard wind farm (RaR), located in Quebec, Canada consists of two REpower MM92 CCV 2.05MW wind turbines (see Table 2). The TechnoCentre Éolien (TCE), who owns and operates the wind farm, also has a 126m met mast on site. A picture of RaR is provided in Figure 5.

Table 2: Description of example CC wind turbines in Canada

Location	Rivière-au-Renard, Qc, Canada
Elevation	340m asl
Turbine Type	Repower MM92 CCV 2.05MW
Hub Height	80m agl
Blade Heating	no[2]

Figure 5: Picture of RaR taken from the hub camera on WEC2 showing one of WEC2's blades, WEC1 and the 126m met mast

[2] One of RaR's wind turbines was equipped with a prototype blade heating system. This turbine was not considered for the analysis presented in this paper

The IEA ice classification for RaR, presented in Table 3, was established based on two winters of measurement data from the site. Meteorological icing was determined based on cloud base height and temperature and/or using an optic ice sensor whereas instrumental icing was measured using heated and unheated anemometers [8]. Production losses were determined based on a calculated power curve and heated anemometer wind speed.

Table 3 shows a significant variation in icing duration, enough for the site to change IEA ice classes, from one winter to the next.

Meteorological icing over the last 35 years for RaR was determined based on cloud base height (CBH) and temperature (T) from a local airport as described in Table 4.

Table 3: IEA ice classification of RaR wind farm based on 2 winters of measurement data

Winter	Meteorological Icing	Instrumental Icing	Production Loss	IEA Ice Class
2011-2012	2.2%	4.0%	1.5%	2
2012-2013	4.7%	10.3%	5.0%	3
Average	**3.5%**	**7.2%**	**3.2%**	**3**

Table 4: Description of airport data used to determine meteorological icing near RaR

Location	Gaspé Airport, Qc, Canada
Years	1979 to 2013
Elevation	33m asl
Distance from RaR	23 km
CBH threshold	400m
T threshold	2.5 °C
Availability threshold	95%

A CBH threshold of 400m and temperature (T) threshold of 2.5°C was used to determine duration of meteorological icing for each year. It is noted that there was low data availability (<95%) for 9 out of 10 years between 1995 and 2004, these years were removed from the analysis. The yearly variation in IEA ice classification is shown in Figure 6.

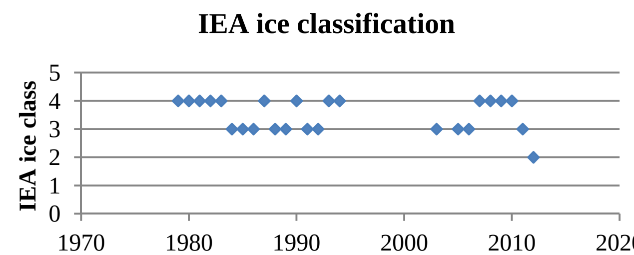

Figure 6: IEA ice class per year for RaR based on local airport cloud base height and temperature.

With the remaining 25 years of good airport data between 1979 and 2013, it was estimated that meteorological icing occurred 5.2% of the time, which represents an IEA ice class of 3. While this is consistent with the 2 year analysis of data from RaR, a closer comparison of airport data and wind farm data for winters 2011-2012 and 2012-2013 shows significant variation in meteorological icing, as seen in Table 5.

Table 5: Comparison of Gaspé airport data and RaR data

Winter	Gaspé Airport		RaR	
	Meteorological Icing	IEA Ice Class	Meteorological Icing	IEA Ice Class
2011-2012	2.2%	2	4.1%	3
2012-2013	4.7%	3	2.1%	2
Average	**3.5%**	**3**	**3.1%**	**3**

The CBH and T method is not the most accurate way of measuring meteorological icing, this becomes even less accurate when the data comes from an airport 23 km away. The airport data nonetheless seems to provide a valid statistical comparison.

Another factor that is difficult to consider is climate change and how it may affect the trend in IEA ice class over the next 25 years.

B. Site Classification Example (Switzerland) Based on Site Observations and Measurement Data

The St-Brais wind farm (StB), located in Switzerland, is used as a second example for ice classification. StB has two Enercon E-82 2MW turbines (see Table 6). A picture of StB is provided in Figure 7. The StB wind turbines are equipped with a blade heating system used for de-icing.

Meteorological and instrumental icing were observed by manual classification of camera images of a web camera mounted at the nacelle of the wind turbine pointing at the structures on the nacelle. Production losses were calculated based on the analysis of operational data and effective production.

Table 7 provides meteorological and instrumental icing as well as production losses and corresponding IEA ice classification for three winters from 2010 to 2012.

Again, it is seen that there is a significant variation in duration of icing from one year to the next.

It is also noted that the active de-icing system used in StB seems to keep production losses in the lower limit or even below the expected values provided in Table 1 for the respective IEA ice classes.

Table 6: Description of example CC wind turbines in Switzerland

Location	St-Brais, Switzerland
Elevation	1060m asl
Turbine Type	Enercon E-82 2MW
Hub Height	78m agl
Blade Heating	yes

Figure 7: Picture of StB, Switzerland taken from a web camera on the nacelle of one of the turbines

Table 7: IEA ice classification of StB wind farm with blade heating based on 3 winters of icing measurements obtained with a web cam

Winter	Meteorological Icing	Instrumental Icing	Production Loss	IEA Ice Class[3]
2010	3.1%	11.7%	2.5%	3
2011	1.8%	5.8%	0.5%	2
2012	3.0%	9.7%	2.1%	3
Average	**2.6%**	**9.1%**	**1.7%**	**3***

*IEA ice class 2 according to meteorological icing assessment and barely 3 according to instrumental icing.

VI. Recommendations for Project Development in Cold Climates

A large number of factors must be addressed as part of any wind energy development project; however, some additional considerations become important in CC's. The key considerations in addition to IEA site classification are described in this chapter. More detailed recommendations and guidelines are given in Task 19 expert group study on "Recommended Practices for Wind Energy Projects in Cold Climates", [3].

A. Accessibility

Icing and snow drifts can make standard vehicle access to the site difficult, expensive or impossible. Access roads are likely to face seasonal restrictions because of ice, snow drifts, and even avalanches during the winter and possibly swampy conditions or flooding during spring and summer. The logistics of turbine installation must be planned according to seasonal and climatic limitations, and special care may be required to avoid damage to equipment and nature during transportation. Access roads shall be designed to enable maintenance and repair to be carried out also when the frost in the ground recently has broken up.

Severe weather conditions can also be an obstacle for site service visits. Consequently, it may pay off to make an extra

3 As the annual production loss was measured from turbines with an ice prevention system (blade heating), the IEA Ice Class was determined based on Meteorological and Instrumental icing

effort when designing the measurement campaign by expanding the number and type of sensors, communications and logger memory to ensure that all relevant data can be captured.

B. Wind measurements

The specification of measurement equipment and procedures must take the harsh climate into account. Not only the wind turbines need to be specified based on the expected conditions at the site, but initially all meteorological towers, masts and site assessment equipment must be rated for the expected climate. Staff trained in the implementation and service of wind monitoring equipment must be employed to insure a safe and effective measurement program. Figure 8 paints the picture of the harsh environment for meteorological masts and instruments in severe icing climates.

Figure 8: Iced meteorological mast. © VTT Technical research centre of Finland.

Wind resource measurement in CC can be challenging as many factors can reduce the quality and availability of the input data, specifically wind speed measurements. Anemometers might stop or slow down, wind vanes might stop, icing of booms, towers, or lightning rods might affect the measurements and/or damage instruments. As a rule, heated sensors, heated booms and lightning rods are recommended at sites with frequent icing, however at sites with heavy icing even the use of heated sensors is not a guarantee of high availability data capture Because many heated sensors are not as precise as first class […] cup anemometers, conventional precision cup anemometers should also be used to obtain as accurate as possible data during non-icing conditions.

Operation of WT's is impacted by low temperatures. WT components can often be adapted to low temperatures but the lowest operational temperature limit for the turbine is usually governed by the qualities of steel and welding. The wind resource below the operational temperature limit of WT cannot be harvested while cold, high density air can also increase the power production of a wind turbine in CC's. Consequently, the local temperature distribution must also be measured to obtain an accurate energy production estimate and enable a turbine to be selected with the correct low temperature modifications.

Once the data has been collected, efforts have to be undertaken to assess the accuracy of the data and then determine this impact on power performance of the turbine and on annual energy production estimate. Keeping these additional considerations in mind during the implementation of site assessment will help to ensure that the assessment runs smoothly and that the risks associated with estimating the performance of the resulting wind development projects are kept to a minimum.

C. Power supply to measurement system

Monitoring systems implemented in low temperatures and icing conditions need additional power for the use of heated sensors and other equipment, which may greatly expand installation requirements and cost. At remote locations with no electrical infrastructure, remote area power systems incorporating generators requiring fuel and/or small renewable power generators will be needed. Figure 9 depicts a remote monitoring site in northern Norway. The power supply, only identified by the exhaust pipe of the generator, must be uncovered as part of regular maintenance.

Figure 9: Remote monitoring site in northern Norway where the power supply must be uncovered as part of the serving process. © Lars Tallhaug - Kjeller Vindteknikk, Norway.

D. Environmental concerns

All of the standard environmental assessment and permitting issues will have to be assessed as part of a project development in a cold climate site; however the additional assessment of general public and private safety must also be addressed. Ice fall from towers or ice throw from the wind turbine blades are real dangers that must be addressed and suitable safety measures chosen as part of the project development to ensure that public and maintenance staff safety is not put in jeopardy. Ice might also cause surfaces to be unserviceable which would prevent access for example to the nacelle roof. An example of ice throw distribution is shown in Figure 10. **Error! Reference source not found.**Directions where ice pieces are thrown are typically dependant on wind direction, wind speed and the size of the ice piece. This wind direction dependency could be utilized when planning ice throw mitigation strategies.

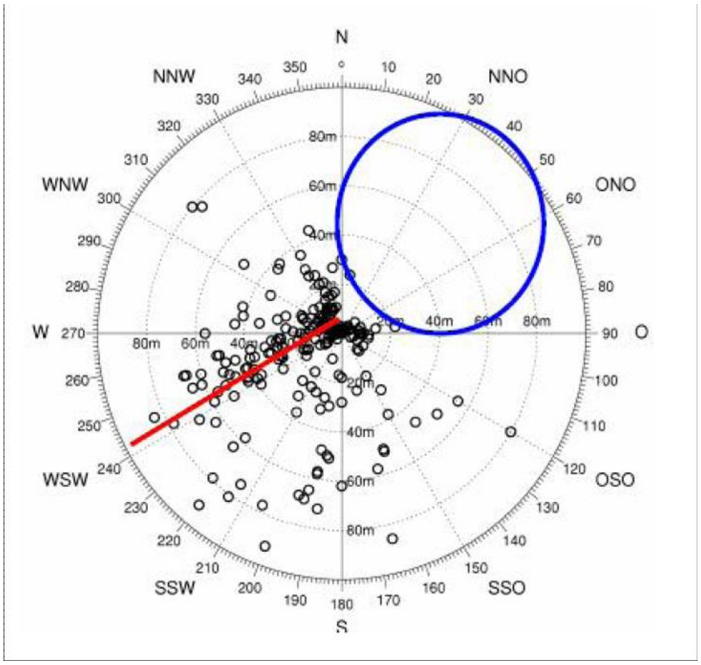

Figure 10: Example of ice throw distribution

VII. R&D Trends

A. Mapping of ice and icing

Mapping of ice and icing is one of the key areas where cold climate wind energy related research is done currently. Mapping is carried out by using weather prediction models and validating the model results with field measurements. Icing maps are essential to wind farm developers to obtain an indication of the severity of the icing conditions at possible wind farm sites. As with all such maps, the severity and intensity of actual icing may vary greatly within short distance and over time .An icing map should therefore be used as indicative only.

For example Finland has published the Finnish Icing Atlas in the beginning of 2012, [6]. The Finnish Icing Atlas gives estimations of icing durations and production losses. For example, Figure 11 shows a map of active icing hours per year. The basis of the icing calculations is the atmospheric weather model (AROME) data that is fed to the separate icing model according to standard of atmospheric icing on structures, [7]. Norway has published icing maps, calculated by applying the WRF weather model. Switzerland also has an updated icing map […]. In addition studies of modelling icing with validation using field measurements have been executed, [5]. Models and results should always be validated with field measurements.

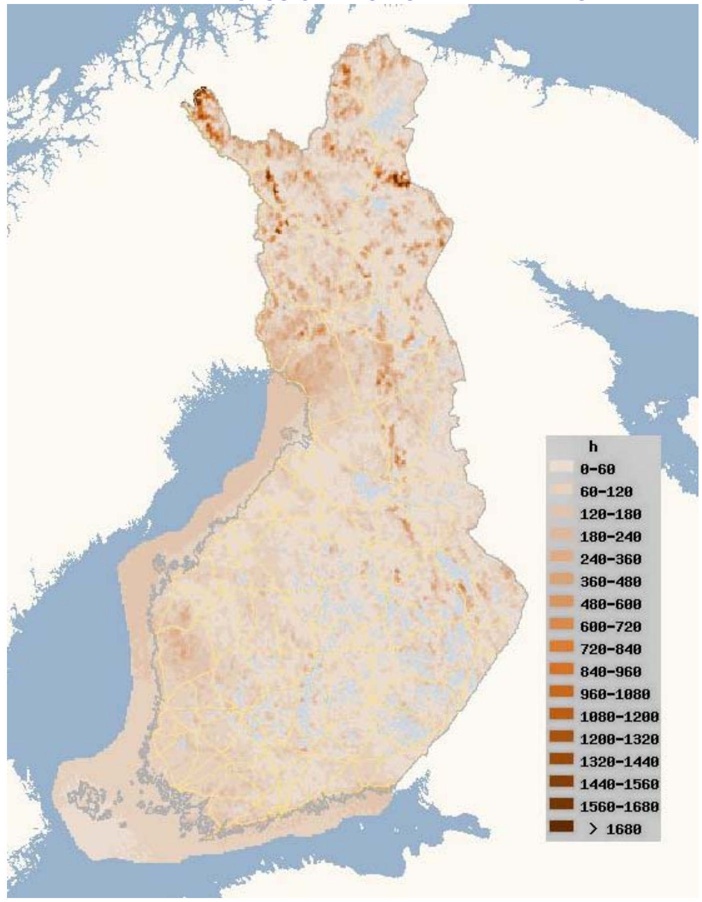

Figure 11: The modelled number of active icing hours in a year. Icing hour defined as hour when icing intensity is greater than or equal to 10 g of ice for a standard cylinder[4].

B. Field measurements

Reliable wind measurements are challenging to perform with low uncertainty in cold and icing conditions. Heated anemometers and wind vanes are available, but those instruments are not yet as precise as instruments targeted to non-icing conditions. The reliability of ice detectors still needs to be enhanced and standardisation of ice detection should be developed. Icing measurements including ice mass and icing rate are done in many countries, especially in Sweden.

A rapidly growing trend in wind measurements is to use remote sensing, especially LIDAR. This is valid also in CC conditions. In Sweden, Finland, Denmark and Canada there is on-going research on how SODAR and LIDAR can operate in CC conditions.

C. Production losses

Production loss estimation due to icing plays an important role during the project planning phase when a decision about needed counter measures against icing is made. A general method for an annual energy production estimate for site with CC sites has not yet been developed. Field measurements have shown the effect of ice on wind turbine energy production [8]. The icing duration and intensity can be predicted with weather

[4] ISO-12494:2001 requires the use of a rotating, forced or freely, 500 mm long 30 mm diameter cylinder.

prediction models, but the complicated nature and interaction of icing and aerodynamics have hindered the implementation of this phenomenon to AEP estimations. In a R&D project in Finland [10], advanced simulation programs were used to model the ice accretion on wind turbine blades, computational fluid dynamics were used to predict the aerodynamic effects of ice, and multi-body simulations were conducted to evaluate the power performance of WT with iced blades. The results of this study were used as part of Finnish Icing Atlas, part of Finnish Wind Atlas, [6].

Laboratory of Energy Conversion (ETH Zürich, Switzerland) has used both field observations and computer simulations to find out typical ice accretion on wind turbine blades, [11]. Here, experimental tests were carried out with scale model in water towing tank to find out how ice affect to aerodynamics and thus power production of a wind turbine.

Results from field measurements in Switzerland showed production losses of 10% of annual energy production without any anti- or de-icing, [5]. With de-icing, consuming heating energy approximately 0,5% of AEP, by circulating warm air inside the rotor blades, the production losses were reduced to 3%. It has to be highlighted that icing is site specific and anti- or de-icing systems can operate differently, thus these figures cannot be generalized to every case, but instead used as an example.

Thermoelectric heating solutions integrated or retro-fitted to the blade are also available at different stages of development and/or commercial deployment, [1].

VIII. Conclusions

CC sites offer vast wind energy potential, but on the other hand adverse weather conditions require extra effort in wind energy projects compared to projects in standard sites. However, this wind energy potential is exploitable with adequate counter measures; careful site assessment, including icing measurements, adapted technology for wind turbines, and mitigation of risk of ice throw. It is underlined that the CC issues have to be taken into account in the very beginning of the project in order to minimize extra costs and to keep the project economical.

Acknowledgements

The IEA Task 19 participants acknowledge the funding agencies and companies from their respective countries that allow them to participate in the IEA workgroup on wind energy in cold climates.

References

[1] BTM World Market Update 2012, Special Chapter: Cold Climate Turbines, Navigant Research, Copenhagen, Denmark, March 2013

[2] The International Energy Agency (IEA): Implementing Agreement for Co-operation in the Research, Development, and Deployment of Wind Energy Systems - www.ieawind.org.

[3] Ian Baring-Gould, René Cattin, Michael Durstewitz, Mira Hulkkonen, Andreas Krenn, Timo Laakso, Antoine Lacroix, Esa Peltola, Göran Ronsten, Lars Tallhaug, Tomas Wallenius, Expert Group Study on Recommended Practices for Wind Energy Projects in Cold Climates. IEA Wind Recommended practices no. 13. 2012. Available at: http://arcticwind.vtt.fi/

[4] Heimo A., Cattin R., Calpini B., Recommendations for Meteorological measurements under Icing Conditions. International workshop on Atmospheric Icing of Structures, IWAIS 2009, Andermatt.

[5] Dierer, S., Oechslin, R., and Cattin R., Wind turbines in icing conditions: performance and prediction. Adv. Sci. Res., 6, 245–250, 2011. doi:10.5194/asr-6-245-2011

[6] The Finnish Icing Atlas, http://www.tuuliatlas.fi/en

[7] ISO 12494:2001 Atmospheric icing of structures

[8] Bolduc, D., Wadham-Gagnon, M., Boucher, B., Jolin, N., Camion, A., Petersen, J., Friedrich, H., Field Measurement of Wind Turbine Icing, IWAIS 2013, St-Johns, Newfoundland

[9] http://arcticwind.vtt.fi

[10] Turkia, V., Huttunen, S., and Wallenius, T., Method for Estimating Wind Turbine Production Losses Due to Icing. VTT Technology, 2013. (In press).

[11] Barber, S., Wang, Y., Jafari, S., Chokani, N., Abhari, R.S., The Impact of Ice Formation on Wind Turbine Performance and Aerodynamics. Proceedings of European Wind Energy Conference (EWEC) 2010.

[12] www.icewind.dk

[13] Wadham-Gagnon, M., Lehtomäki, V., Bolduc, D., Boucher, B., Jolin, N., Rissanen, S., Karlsson, T., Bechoefer, E., Sandel, K., Ice Induced Vibration on Wind Turbines, IWAIS 2013, St-Johns, Newfoundland

The Research Review of Wind Turbine Blade's Icing and Anti-icing/De-icing

Qin Hu, Lichun Shu, Xingliang Jiang, Zhijin Zhang, Jianlin Hu, Jian Liang, Pancheng Yin
State Key Laboratory of Power Transmission Equipment & System Security and New Technology, College of Electrical Engineering, Chongqing University, Chongqing 400044, China

Abstract — In recent years, the wind power installed capacity of China has ranked first in the world, and is showing a trend of rapid development. Wind turbine blade's icing has serious harms. It will affect the safety of equipment and operation, and reduce power generation. However, because the wind power industry started very late in China, the research about wind turbine blade's icing and anti-icing/de-icing has not attracted people's attention and there is few related research in China. In this paper, the physical model of wind turbine blade's icing as well as the simulation method, the anti-icing/de-icing thermodynamic model of blades, and some technical methods about wind blade's anti-icing/de-icing are reviewed. It's regarded that most of the present wind turbine blade's icing model are established on basis of aircraft icing model. As wind turbine blade is very different from aircraft in working environment and working mode, it is necessary to establish the wind turbine blade's icing model with considering the actual operation of wind turbine blades, and to verify the icing model of wind turbine blades in natural icing stations. In addition, some studies about choice of heating power of wind turbine blade's anti-icing/de-icing has been conducted by some institutions and manufacturers, but much of them are based on empirical formula rather than physical models. This paper puts forward that it is necessary to carry out researches on some fundamental problems such as wind turbine blade's icing mechanism, icing model, anti-icing/de-icing model and methods as soon as possible, and only by this way can we take preventive measures to protect the healthy development of China's wind power industry.

Keywords — wind turbine blade, icing, anti-icing, de-icing, review

1 INTRODUCTION

AS one of the most competitive new energy, wind power plays an important role not only in energy security and energy supply, but also in the economic growth, environment prevention and greenhouse gas emissions reduction. Some developed countries such as the United States, Germany, France, Denmark and Finland have paid close attention to the development of wind power, and have actively implemented relevant policies and regulations to promote the development of the world's wind power industry. Until mid-2012, the global wind power installed capacity had reached 254GW, and more than 100 countries were involved in wind power development, 17 of which had a cumulative installed capacity of more than million kilowatts [1].

In recent years, due to the progression of wind power technology, the enlargement of market scale, the reduction of construction cost and the national policy support, China's wind power industry shows a rapid development tendency. According to the report of China Association of Resource Comprehensive Utilization, by the end of 2010, Chinese wind power added 16 million kilowatts of power-generating capacity throughout the year. Cumulative installed capacity reached 41.827 million kilowatts, which surpassed the United States for the first time and ranked first around the world. *China Wind Power Development Report 2010* predicted that Chinese wind power cumulative capacity would reach 230 million kilowatts by 2020 which is equivalent to 13 Three Gorges Power Plants and the total generating capacity can reach 464.9 billion KWH which is equivalent to 200 coal-fired power plants [2].

The blade is one of the key components of wind turbine, whose performance will directly affect the stability of operation. Ice accreted on blade will affect blade's external shape and then change its aerodynamic performance. As a result, the iced blades will do great harms as follows [3-6]:

(1) Wind turbine blade's icing will increase the load of wind turbine blades and main shaft and affect the life of

the related parts.

(2) Icing will change the blade airfoil, affect aerodynamic characteristics of wind turbine and reduce output power of wind turbine.

(3) The adhesive force between ice and blade goes down when the ambient temperature rises. The ice may be thrown away due to wind speed and rotating centrifugal force during the operation of wind turbine, which will cause a great security risk to the assembly and operating staff.

European and American countries have a longer history of wind power development. They have carried out some research on wind turbine blade's icing and anti-icing/de-icing issues. However, because wind power industry starts very late in China, the research of wind turbine blade's icing and anti-icing/de-icing have not attracted people's attention yet, and relevant study is almost in the blank .

2 THE RESEARCH STATUS OF WIND TURBINE BLADE'S ICING MODEL AND NUMERICAL CALCULATIONS

Till now, there are only a few studies on wind turbine blade's icing model at home and abroad, which usually refer to the research results of wire and aerofoil's icing.

2.1 WIRE

Many scholars have conducted deep research on physical process of wire icing. They argue that the process mainly includes droplets capture and droplets freezing.

Langmuir and Blodgeet [7] successfully calculated the movement of droplets around the cylinder, put forward the concept of collision rate and described the process of water droplets colliding wire. Messinger [8] and List [9, 10] introduced heat balance equation in icing process and obtained the freeze coefficient, which describes the freezing situations in icing process. Now collision coefficient and freeze coefficient have become general parameters for all models to describe icing process.

The development of Computational Fluid Dynamics (CFD) has greatly promoted the research of collide characteristics of water droplets. The method calculates the flow field, obtains the movement of droplets based on force analysis of droplets in the flow field and gains the collide coefficient. With further development of computer technology, researchers introduce more complex turbulence models to make it closer to real situation. Currently, the most widely used turbulence model is standard *k-e* model [11] proposed by Launder and Spalding .

In recent years, China's power grid ice accidents have occurred frequently, some domestic research institutes have conducted many researches in the field of wire icing, among which Chongqing University is in a leading position.

2.2 AIRCRAFT

Compared with wire icing, aircraft icing process is more similar to wind turbine blade's icing. Many researches on aircraft icing model and numerical calculations were carried out at home and abroad.

In the late 1950s, Gray et al. studied the NACA65A004 airfoil icing conditions [12], and analyzed the impact of icing on the wing. In 1958, Gray put forward the empirical formula for calculating resistance after freezing [12]. Due to computer limitations, the research developed slowly in the next period of time. In the late 1970s, NASA Lewis Research Center did a series of experiments to study new airfoil ice data. In addition, the development of computer also provided a powerful tool for numerical simulation of freezing process. Since the 1980s, based on the research of Bragg, Lozowski, Oleskiw, Frost, Cansdale, Gent, etc., some research institutions such as NASA (United States), DRA (UK), ONERA (France) and BC (Canada) developed two-dimensional and three-dimensional icing models and made prediction for aircraft components icing [13-18].

So far, the main software in the field of aircraft icing are LEWICE (United States), ONERA (France), DRA (UK), FENSAP-ICE (Canada) and the latest CIRA (Italian). All the software plays significant roles in the design of anti-icing/de-icing system of aircraft.

2.3 WIND TURBINE BLADES

Based on the research of wire and aircraft icing model, some foreign researchers carried out a few of researches on wind turbine blade's icing model and simulation.

In 2001, Lasse Makkonen et al. proposed a model of wind turbine blade's icing based on the TURBICE model of aircraft wing icing [19], simulated and calculated wind turbine blade's icing weight and icing shape under different angles of attack. The model also takes into account the heating element built into wind turbine blade. However, because wind turbine blade's icing data on the scene were quite limited, the model was not efficiently verified.

In 2010, research scholar Ping Fu and Masoud

Farzaneh, who come from University of Quebec (Canada), studied the establishing and solving of rime icing model of horizontal axis wind turbine blade [20].The solving process of this model is divided into two steps: First, calculating the two-phase flow that consists of air and water droplets. The two-phase flow is calculated by Fluent software which uses Euler calculation method. Second, calculating the newly formed ice thickness and shape, internal smoothing algorithm is used in the calculation process. By means of simulation, the three-dimensional shape of ice and the ice load of wind turbine blade can be obtained. The main input parameters of the model include: wind speed, mean volume diameter (MVD) of droplets, liquid water content (LWC) and air temperature.

In 2010, Matthew C. Homola et al. studied the relationship between wind turbine blade's size and rime icing based on TURBICE [21]. Lots of simulation works were carried out in this research on four different sizes (450kW, 600kW, 1MW and 2MW) of wind generators. The results showed that, either from the ice mass per unit area, or from the relative ice thickness, the larger size of wind turbine blade is, the slighter icing is.

In 2010, Muhammad S.Virk et al. studied the relationships between the angle of attack of wind turbine blade and icing [22]. This research used three-dimensional fluid dynamics method to simulate the changes of the angle of attack after the vicinity of the wind turbine blade's tip is frozen. The research was carried on NACA 64618 wind turbine blades and the angle of attack was chosen as five values from -5°to 7.5°. Based on the calculation of flow field and super-cooled water droplets collision coefficient, icing speed and shapes were simulated under rime and glaze icing conditions. The results showed that, either from the ice mass per unit area or from the relative ice thickness, the smaller the angle of attack is, the slighter icing is.

In China, so far only a small number of researchers have launched a small amount of research in this area.

3 WIND TURBINE BLADE ANTI-ICING AND DE-ICING RESEARCH STATUS

Researches on blade anti-icing and de-icing are relatively more in foreign countries than in China. However the domestic researchers pay more attention on low temperature problems concerning lubricating oil, grease, electrical components and metals than on blade anti-icing and de-icing [23]. The main methods of wind turbine blade anti-icing and de-icing are as follows.

3.1 LiQUID ANTI-ICING

The liquid anti-icing solution adopts anti-icing liquids such as ethylene glycol, isopropyl alcohol, ethanol, etc. and mixes them with the water from plane surface or wind turbine blades. Due to the freezing point of the mixture greatly reduced, the water can hardly freeze on the surface [3]. In cold weather, the plane needs to be sprayed anti-icing liquid outside it before flight. The disadvantage of liquid anti-icing is as follows: 1) Effective time is short and this is only a short-term anti-icing method; 2) large dosage; 3) the de-icing effect is poor in a severe icing condition

3.2 MECHANICAL DE-ICING

The mechanical de-icing solution is to use mechanical method to break the ice. Then air blow, centrifugal force or vibration is used to remove the ice. Currently, the widely used method on wind power turbine is to break ice artificially. This belongs to one of the mechanical de-icing method [3].

3.3 THERMAL ANTI-ICING

Thermal anti-icing is to use various thermal energy to heat objects, whose surface temperature finally will exceed 0℃. Then the purpose of anti-icing or de-icing will be achieved.

3.3.1 ELECTRO-THERMAL ANTI-ICING

Electro-thermal deicing is the most widely used and effective method. When a wind turbine blade is produced, electro-thermal anti-icing system which consists of heating element, converters, overheating protection device and power is installed. This technology transforms electrical energy into heat, so that the blade will not be frozen. Ice sensors installed on blade will accept ice signals. Then the power supply of the system will automatically be connected or disconnected. Overheating protection device is used to prevent skin of the blade being overheated and deformed. The heating mode includes continuous heating and intermittent heating [24]. Some research institutions and manufacturers have studied the choice of electric heating power. In 1994, Tammelin pointed out that the estimated heating power to keep the total blade area ice-free was about 1.2 kW/m [25]. In 1998, Marjaniemi argued that, in order to prevent blade from icing, electric heating power should be about 0.5 kW/m, i.e. 5% of the wind turbine rated power [26]. In 2003, Pinard pointed out the heating power on a small 150 kW turbine should be about 3.4 kW per blade [27]. In

2005, Laakso used 15 kW heating power per blade for a 600 kW wind turbine, corresponding to 14% of annual production [28]. In 2007, Mayer pointed out that 82 kW per blade or 14% of power output would be needed for a 1.8 MW turbine when the wind speed is 8 m/s [29]. In 1996, Peltola thought the minimum time of heating after the icing event is usually about 15-30 minutes [30]. In 1998, Marjaniemi and Peltola put forward that the heating power is almost linear to the temperature difference between the air and the blade surface [26]. In 2007, Mayer put forward that more energy is needed to de-ice the tip's leading edge than the hub's (3.5 to 3.9 times more), and more energy is also needed to de-ice the tip's trailing edge than the hub's (2.6 to 2.9 times more) and to de-ice the lower surface rather than the upper (1.3 to 1.5 times more) [29].

3.3.2 WARM AIR ANTI-ICING

Warm air anti-icing solution uses warm air ventilation pipes which are installed in the blade as heating components. The warm air will circulate in the pipe. This technique is also used in airfoil anti-icing. This solution is simple in operation and maintenance. The operation is reliable, but the heat utilization efficiency is low [31].

3.3.3 MICROWAVE DE-ICING

Microwave de-icing is to lead microwave energy to blade surface, using microwave energy to heat the ice to greatly reduce the binding force between ice and blade surface, then using centrifugal force and aerodynamic force to remove ice [31].

3.4 ELECTRICAL PULSE DE-ICING

Electrical pulse de-icing solution uses high-energy electrical pulses on the skin of wind turbine blades. The pulses will make the skin quickly vibrate while within the scope of elastic deformation, so as to break the ice on the skin. Electrical pulse de-icing system generally consists of the power supply, electrical pulse source, power storage, pulse generator and control devices, etc. [31, 32]

3.5 COATING ANTI-ICING

Coating anti-icing solution uses physical or chemical effect of special coatings, which makes the ice melt or reduces the cohesive force between ice and the blade surface, to remove the ice from the surface. The main advantages of anti-icing coating are: (1) It has an anti-icing effect. (2) It has a variety of protection function (sealed waterproof, anti-corrosion, electrical insulation, ice prevention). (3) The implementation of the method is simple, safe, environment friendly. The main problems of the existing anti-icing coatings are [31]: Because anti-icing coatings must have two characteristics of low surface energy and strong hydrophobic, thus seriously affect the other performance of the coating, especially the adhesive. In addition, weather resistance and anti-aging performance of anti-icing coatings also need to be improved.

3.6 PNEUMATIC DE-ICING

This technology is also called "expansion pipe de-icing technology". This is a mechanical de-icing technology using expansion effect of the expansion pipes installed on the leading edge surface of a blade. The expansion effect will break the outer surface ice and make the ice fall off. The technology system consists of air pump, control valve, pressure relief valves, pipelines and expansion pipe, etc. [33].

3.7 ULTRASONIC DE-ICING

The principle of ultrasonic deicing is that: When ultrasonic is transmitting on ice blades, besides the Lamb wave, there is a list of time harmonic vibration, which is called horizontal shear wave (i.e., SH wave). Both Lamb wave and SH wave are guided wave. When the two kinds of wave transmission in anisotropic medium, there is speed difference between the ice coating and substrate interface, thus produces shear stress at the interfaces [34-35].

3.8 BLOW AIR ANTI-ICING

In 2004, Battisti developed a new kind of anti-icing system. This system uses air layer to protect blade surface. Air (if needed can be heated into warm air) is blown out from the blade through several exhaust port near the blade leading edge and trailing edge, forming air layer on the blade surface. The air layer will make most water which impacts blades excurse, and prevent water drops which impact the blade from freezing [24].

4 PROBLEMS AND SUGGESTIONS

Through the research review of wind turbine blade's icing and anti-icing/de-icing at home and abroad, the following problems could be found in the current study:

(1) At present, icing model and numerical simulation method are mainly used for wire icing and aircraft icing, while little is applied in studies of wind turbine blade's icing. It's regarded that most of the present wind turbine blade's icing model are established on basis of aircraft icing model. As wind turbine blade is very different from aircraft in operating conditions, working environment

and working mode, it is necessary to establish the wind turbine blade's icing model with considering the actual operation of wind turbine blades, and to verify the icing model of wind turbine blades in natural icing stations or wind farms.

(2) Basically, the current research of wind turbine blade's icing focus on the simulation calculation of physical model. The field tests of wind turbine blade's icing and the verifiable experiment of blade's icing model are both rare.

(3) Although there were many methods of blade's anti-icing/de-icing, the method which can obtain good effect and has been widely used is electro-thermal anti-icing. However, so far there is no research on the physical models of electro-thermal anti-icing. In addition, some studies about choice of heating power of wind turbine blade's anti-icing/de-icing has been conducted by some institutions and manufacturers, but most of them are based on empirical formulas rather than physical models.

(4) Because different anti-icing/de-icing power is required in different environmental conditions, using a single kind of electrical heating power may cause a waste of energy or failure of anti-icing/de-icing. However, there is no study about choice of electrical heating power in different environmental conditions. Furthermore, because different places on wind turbine blade have different icing conditions and different aerodynamic characteristics, different heat power should be selected for different places on the blade. However, at present there is no study on the arrangement of electrical heating source.

Based on the above issues, this paper put forward that the following research should be carried out in the future:

(1) The relationship between wind turbine blade's icing and environmental parameters should be researched in climate chambers, natural icing test stations or wind farms. Model of ice growing and forecasting should be established by the theory of hydromechanics, aerodynamics and thermodynamics.

(2) Heat balance model on the blade surface should be built to determine the required heating power and the arrangement of heating source under different environmental conditions.

(3) Model of wind turbine blade's icing and method of anti-icing/de-icing should be tested and verified in climate chambers，natural icing test stations or wind farms.

5 CONCLUSION

Based on the research review of wind turbine blade's icing and anti-icing/de-icing at home and abroad, some problems in the present research are raised and research suggestions are proposed. Because extreme climate and ice disasters take place frequently in China in recent years, it's pointed out that, under the background of the burst of growth in the wind power market, it is necessary to carry out systematic study on some fundamental problems about wind turbine blade's icing, anti-icing/de-icing as soon as possible, and only by this way can we take preventive measures to protect the healthy development of China's wind power industry.

ACKNOWLEDGMENT

This work was supported by the Fundamental Research Funds for the Central Universities (No. CDJZR12150015), Research Fund for the Doctoral Program of Higher Education of China (No. 201201911100092) and National Basic Research Program of China (973 Program) (No. 2009CB724502).

REFERENCE

[1] World Wind Energy Association, "2012 Half Year Report", WWEA Publication, 2012.

[2] J. li, P. Shi, H Gao, China's Wind Power Development Report 2010, Hainan Press, Haikou, China, 2010 (in Chinese).

[3] J. Wang, "Research on Wind Turbine Blade's Anti-icing Technology", Mechanical and Electrical Information, Vol. 291, No. 9, pp. 91, 2011 (in Chinese).

[4] J. Wu, "Icing Effect on Wind Farm Operation", Wind Power, Vol. 2, pp. 42-45, 1999 (in Chinese).

[5] Seifert, H. Seifert, "Technical Requirements for Rotor Blades Operating in Cold Climate", Proceedings of the 2003 BOREASVI, Finland, pp. 50-55, 2003.

[6] Clement Hochartm, Guy Fortin, Jean Perron, etal., "Wind Turbine Performance under Icing Conditions", Wind Energy, Vol. 11, No. 4, pp. 319-333, 2008.

[7] Langmuir I, Blodgett K., "A Mathematical Investigation of Water Droplet Trajectories", Army Air Force Technical Report No. 5418, 1946.

[8] Messinger B. L., "Equilibrium Temperature of an Unheated Icing Surface as a Function of Airspeed", Journal of the Aeronautical Sciences, Vol. 20, pp. 195-200, 1953.

[9] List R., "General Heat and Mass Exchange of Spherical

Hailstones", Journal of Atmospheric Sciences, Vol. 20, No. 3, pp. 189-197, 1963.

[10] List R., "Ice Accretions on Structures, Journal of Glaciology", Vol. 19, No. 8, pp. 451-465, 1977.

[11] B.E. Launder, D.B. Spalding, "The Numerical Computation of Turbulent Flows", Computer Methods in Applied Mechanics and Engineering, Vol.3, No. 2, pp. 269-289, 1974.

[12] I Paraschivoiu, F Saeed. *Aircraft Icing* ,New York: John Wiley & Sons, INC. 2005.

[13] Ruff G A, Berkowitz B M., "User's Manual for the NASA Lewis Ice Accretion Prediction Code (LEWICE)",NASA CR-185129, May 1990.

[14] Cebeci T, Chen H H, Alemdaroglu N, "Fortified LEWICE with Viscous Effects",AIAA Journal of Aircraft, Vol. 28, No. 9, pp. 564-571, 1991.

[15] Potapczuk M G, "LEWICE/E: An Euler Based Ice Accretion Code", AIAA Paper 92-0037, 1993.

[16] Potapczuk M G, Al-Khalil K M, Velazquez M T. "Ice Accretion and Performance Degradation Calculations with LEWICE/NS", AIAA Paper 93-0173, 1993.

[17] Hedde T, Guffond D, "Improvement of the ONERA 3D Icing Code, Comparison with 3D Experimental Shapes", AIAA Paper 93-0169.

[18] Gent R W. TRAJICE2, "A Combined Water Droplet Trajectory and Ice Accretion Prediction Program for Aerofoil. DRA Technical Report TR90054", Nov. 1990.

[19] Makkonen L, Laakso T, Marjaniemi M, etal. "Modeling and Prevention of Ice Accretion on Wind Turbine Wind Engineering", Vol.25, No.1, pp.3-21,2001.

[20] P Fu, M Farzaneh, "A CFD Approach for Modeling the Rime-Ice Accretion Process on a Horizontal-axis Wind Turbine". Journal of Wind Engineering and Industrial, Vol.98, No.4-5,pp.181-188,2010 .

[21] MC Homola, T Wallenius, L Makkonen, "The Relationship between Chord Length and Rime Icing on Wind Turbines", Wind Energy, Vol. 13, pp. 627-632, 2010.

[22] Muhammad S.Virk1, Matthew C. Homola, Per J, "Nicklasson. Relation between Angle of Attack and Atmospheric Ice Accretion on Large Wind Turbine's Blade", Wind Engineering, Vol. 34, No. 6, pp. 607-614, 2010.

[23] L. Zhang, L. Ren, "Analysis of Hydroelectric Power by the Influence of Severe Weather Conditions on the Wind Turbines", Vol. 33, No. 10, pp.67-69, 2007(in Chinese).

[24] Lorenzo Battisti, "Anti-icing System for Wind Turbines", United States Patent.No.US 7637715B2, 2009.

[25] Tammelin, B., Säntti, K., "Effect of Rime Accretion on Wind Energy Production in the Top Areas of Fells ", BOREAS II. FMI, Pyhätunturi, Finland, pp. 265–275, 1994.

[26] Marjaniemi, M., Peltola, E., "Blade Heating Element Design and Practical Experiences", BOREAS IV. FMI, Hetta, Finland, pp. 197–209, 1998.

[27] Pinard, J.-P., Maissan, J.F., "Experience from Use of Heated Wind Sensors and Rime Ice Detectors over the Past 12 Years ", BOREAS VI. FMI, Pyhätunturi, Finland, p. 7, 2003.

[28] Laakso, T., Peltola, E., "Review on Blade Heating Technology and Future Prospects", BOREAS VII. FMI, Saariselkä, Finland, p.12, 2005.

[29] Mayer, C., "Système Électrothermique de Dégivrage pour une Pale d'Éolienne", Master Thesis, UQAR, Rimouski, Canada, p.193, 2007.

[30] Peltola, E., Marjaniemi, M., Kaas, J., Aarnio, E., "Pyhätunturi Operational Experiences", BOREAS III. FMI, Saariselkä, Finland, pp. 131-144, 1996.

[31] Olivier Parent, Adrian Ilinca, "Anti-icing and De-icing Techniques for Wind Turbines: Critical Review ", Cold Regions Science and Technology, Num.65, pp. 8-96, 2011.

[32] Antoine Lacroix. Wind Energy: Cold Weather Issues [R]. University of Massachusetts at Amherst, Renewable Energy Research Laboratory, June 2000.

[33] Anders Björck, "Icing of Wind Turbines", Elforsk report, Stockholm, 2003.

[34] Venna S, Lin Y, Botura G. Piezoelectric Transducer Actuated Leading Edge De-icing with Simultaneous Shear and Impulse Forces[J]. Journal of Aircraft, 2007, 44(2): 509-515.

[35] Clement Hochart, Guy Fortin, Jean Perron, etal. Wind Turbine Performance under Icing Conditions [J]. Wind Energy, 2008, 11(4): 319-333.

Ice Accretion on Wind Turbine Blades

Adriána Hudecz[#1], Holger Koss [*2], Martin O. L. Hansen [#†3]

[#]Department of Wind Energy, Technical University of Denmark
[1] ahud@dtu.dk
[3] molh@dtu.dk

[*]Department of Civil Engineering, Technical University of Denmark
[2] hko@byg.dtu.dk

[†]Centre for Ships and Ocean Structures, Department of Marine Technology, Norwegian University of Science and Technology

***Abstract* —** In this paper, both experimental and numerical simulations of the effects of ice accretion on a NACA 64-618 airfoil section with 7° angle of attack are presented. The wind tunnel tests were conducted in a closed-circuit climatic wind tunnel at Force Technology in Denmark. The changes of aerodynamic forces were monitored as ice was building up on the airfoil for glaze, rime and mixed ice. In the first part of the numerical analysis, the resulted ice profiles of the wind tunnel tests were compared to profiles estimated by using the 2D ice accretion code TURBICE. In the second part, Ansys Fluent was used to estimate the aerodynamic coefficients of the iced profiles. It was found that both reduction of lift coefficient and increase of drag coefficient is a nearly linear process. Mixed ice formation causes the largest flow disturbance and thus the most lift degradation. Whereas, the suction side of the rime iced ice profile follows the streamlines quite well, disturbing the flow the least. The TURBICE analysis agrees fairly with the profiles produced during the wind tunnel testing.

I. Introduction

In cold climate areas with temperatures below 0°C and humid environment for larger periods of the year icing represents an significant threat to the performance and durability of wind turbines (Tammelin et al. [1], Tallhaug et al. [2] and Baring-Gould et al. [3]). In this paper, both experimental and numerical simulations of the effects of ice accretion on a NACA 64-618 airfoil section are presented. The experiments were performed in a closed-circuit climatic wind tunnel at FORCE Technology in Denmark. Aerodynamic forces were monitored throughout the icing process for 7° angle of attack at different temperatures, which were used to ensure adequate environment for the typical ice types, rime, glaze and mixed ice, which threaten the operation of wind turbine.

There were already a number of wind tunnel tests conducted on iced airfoils in the past. Seifert and Richert [4] and Jasinski et al. [5] used artificial ice deposits during their experiments. In case of Seifert and Richert's tests [4], the molds were made of actual ice fragments from a wind turbine, whereas Jasinski et al. [5] simulated the ice profiles with Nasa's ice accretion code, LEWICE. Hochart et al. [6] performed two-phase experiments. In the first phase, the ice deposit was grown and then in the second phase, efficiency tests were performed. The main difference from these tests and the ones presented in this paper is the fact that the aerodynamic forces were monitored as ice was accumulating. At the end of the tests, the ice profiles were documented by contour tracing for further, numerical analysis.

In the recent years, especially due to the increased computer power, it became possible to determine the performance of iced wind turbine much faster and more accurately with computational fluid dynamics (CFD) and panel method based models. Homola et al. [7] have used a two-steps method, combining TURBICE and Ansys Fluent to investigate the effect of ice similarly on a NACA 64-618 profile. TURBICE is comprehensive numerical ice accretion software from VTT, Technical Research Centre of Finland, which uses panel method to calculate the potential flow. It was verified by icing wind tunnel testing of both aircraft and wind turbine airfoils. The accuracy of the solution is dependent on the number of the panels and their distribution around the section (Makkonen et al., [8]). Homola et al. [7] found that the lift coefficient was reduced in all cases and the smallest change was observed in case of rime ice. During the CFD simulations, it was found that the horn type glaze ice shape causes the largest separation, which leads to a significantly reduced lift and higher drag coefficient.

Etemaddar et al. [9] has also used the same profile in their numerical analysis. In their study, they combined Nasa's LEWICE code with Ansys Fluent and pointed out that the ice load increases with liquid water content (LWC), median volumetric diameter (MVD) and relative wind speed.

The numerical simulations presented in this paper were carried out in two parts. First, the collected ice profiles were compared to profiles generated in TURBICE. In the second part, numerical analyses were done on the iced profiles from the wind tunnel tests in Ansys Fluent.

The aim of the wind tunnel tests was to investigate the changes of aerodynamics as ice built up on the airfoil for glaze, rime and mixed ice tests. The relative changes of lift and drag coefficients along with the shape of the ice deposits could be compared to results of the numerical analysis.

II. Abbreviations and Nomenclature

AOA, α – angle of attack
C_L – lift coefficient

C_D – drag coefficient
D – drag force
G_{ice} – gravity force of ice deposit
L – lift force
LWC – liquid water content
MVD – median volumetric diameter
SP – separation point
U – mean wind speed

III. Methods

In this section, both experimental and numerical set-up of the analyses is detailed.

A. *Wind Tunnel Tests – Experimental Setup*

The tests were performed in the Collaborative Climatic Wind Tunnel (CWT) at FORCE Technology. The wind tunnel was developed and built as a collaboration project between Technical University of Denmark and FORCE Technology. The main specifications are listed in TABLE I.

TABLE I Basic specifications of the wind tunnel (based on Georgakis et al. [10])

Temperature	-5 to 40 °C
Minimum liquid water content (LWC)	0.2 g/m^3
Test section cross-sectional area	2.0x2.0 m
Test section length	5 m
Maximum wind speed velocity	31 m/s
Turbulence intensity	0.6 to 20 %

NACA 64-618 airfoil section (900 mm chord length and 1350 mm width) provided by LM Wind Power was used during the experiments. A pair of AMTI MC5 force and torque transducers was used to measure the loading simultaneously around 6 degrees of freedom. Based on the measured forces (F_x and F_y), which are visualized in Fig. 1, and the known angle of attack (α) and wind speed (U), the lift (L) and drag (D) forces along with the weight of ice (G_{ice}) can be calculated.

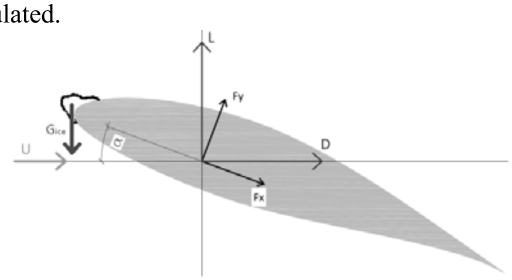

Fig. 1. Forces acting on the iced airfoil. F_y and F_x are directly measured by the force transducers and based on these and the known angle of attack and wind speed (U), the lift (L) and drag (D) forces along with the weight of ice (G_{ice}) can be calculated.

The tests were performed by first setting the target wind speed and temperature in the test section. A constant angle of attack, 7° was used in these experiments. As soon as the target temperature was reached, the water spray, and thus in-cloud environment, was set. For glaze and mixed ice tests, 15 m/s wind speed was applied during ice build-up while for the rime ice test due to the limitation of the wind tunnel's cooling unit, it was necessary to reduce the wind speed to 10 m/s in order to ensure cold enough temperature. The ice accretion process was running for 60 minutes and every five minutes the forces were measured. Based on the force measurements, not only the aerodynamic forces but also the gravity force of the accumulated ice was calculated. In order to study the pure effect of the altered airfoil profile, this force was subtracted from the lift measurements. At the end of the tests, the ice profiles were documented by contour tracing and were used in the numerical simulation part.

The flow in a wind tunnel is different from that, which occurs in the free-air due to the presence of the tunnel walls, therefore the measurements were corrected by following ESDU 76028, *Lift-interference and blockage corrections for two-dimensional subsonic flow in ventilated and closed wind-tunnels methodology* [11].

The specifications of the presented tests are summarized in TABLE II. The temperatures listed here are the mean values of the established temperature during the tests. The MVD and LWC values are target values based on the specification of the manufacturer of the spray nozzles (Schick [12]).

TABLE II The specification of the presented tests.

	Glaze ice test	Mixed ice test	Rime ice test
AOA (°)	7	7	7
T (°C)	-3	-5	-8
MVD (µm)	25	25	20
LWC (g/m^3)	0.7	0.7	0.7
U_{accr} (m/s)	15	15	10
U_{test} (m/s)	15	15	15

B. *Numerical Simulation Setup – TURBICE.*

TURBICE simulations were performed at VTT, Technical Research Centre of Finland in order to compare the results of the wind tunnel tests to a numerical ice accretion model. For the air temperature only a constant value can be defined in the simulation program. Hence, mixed ice simulation could not be modeled. There are a number of other input parameters, such as MVD, LWC, meteorological wind speed, rotating speed of the wind turbine, pitch angle, air temperature, air pressure and accretion time. These parameters were set to ensure similar conditions as it was in the wind tunnel.

Since the MVD and LWC were only target values in the wind tunnel tests, several scenarios were analyzed in TURBICE and only the best fits are presented here. The input parameters of the different tests are listed in TABLE III.

TABLE III Input Parameters for the presented Turbice Tests

Parameters	Glaze test 1.	Glaze test 2.	Rime test 1.	Rime test 2.
AOA (°)	7	7	7	7
MVD (µm)	25	30	25	25
LWC (g/m^3)	0.65	0.65	0.4	0.6
Temp (°C)	-3	-3	-8	-8
Time (min)	60	90	60	90

C. *Numerical Simulation Setup – Ansys Fluent.*

CFD simulations are used to analyze numerically the impacts of ice accretion on the flow behavior and on the aerodynamic characteristics of the airfoil. As it was mentioned before, the ice profiles were collected at the end of the wind tunnel tests and were further analyzed by Ansys Fluent. Since the ice profiles were collected from specific locations, 2D models were done. The construction and meshing of each model was done using Ansys Workbench. The control volume around the blade was rectangular with edges positioned at 50 chords length away in vertical direction and 20 chords length from the horizontal direction (cross flow). It was necessary to set the horizontal boundaries further away to avoid any effect caused by these boundaries on the flow around the airfoil.

An inflation layer was added to the mesh in order to produce a structured, fine mesh in the vicinity of the airfoil to achieve a better representation of the flow near the airfoil surface. The first layer height is dependent on the surface roughness, since the roughness height may not exceed it. However, it was found that Ansys Fluent cannot properly handle surface roughness; therefore it was not included in the analysis. In TABLE IV, the setup of the inflation layer is listed. The height of the first layer was set small enough to ensure the validity of the log law.

TABLE IV SETUP OF INFLATION IN ANSYS MODEL

	Clean profile	Glaze ice test	Mixed ice test	Rime ice test
First layer height (m)	1e-5	1e-5	1e-5	1e-5
Nr. of layers of inflation layer	40	40	40	35
Growth rate	1.2	1.2	1.2	1.2

In Fig. 2, an example of the mesh around the leading edge is shown. An appropriate size was chosen for the quadrilaterals so they can follow the complex curve of the ice deposit.

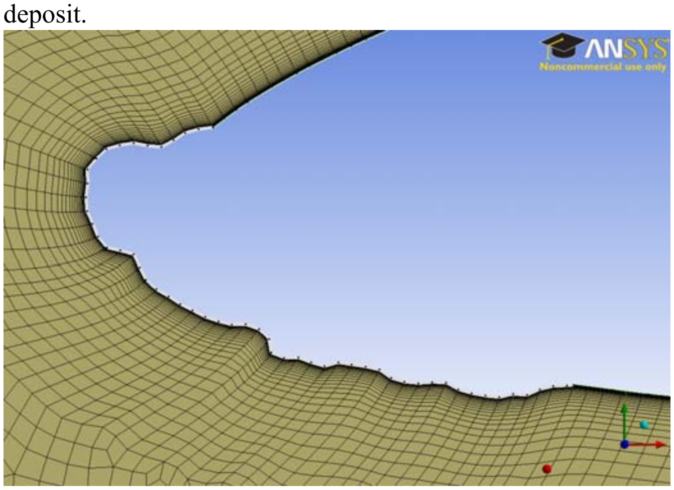

Fig. 2 Mesh around the iced leading edge in case of glaze iced airfoil. The height of the first layer is 1e-5 m and there are 40 layers in the inflation layer.

During the simulation Spalart-Allmaras and k-Ω SST turbulence models were used. It was found in previous studies (e.g. Mortensen [13]) that the solution using Spalart-Allmaras model converges faster and easier than with the k-Ω SST turbulence model. Therefore the first 500 iterations were done by using Spalart-Allmaras model providing an initial guess for the k- Ω SST turbulence model and achieving more stable convergence. However, Chung and Addy [14] pointed out that Spalart-Allmaras model is the best performing model when simulating ice accretions; therefore that model was used for the iced profiles.

IV. RESULTS

The above discussed simulations' results are presented in this section. It should be kept in mind that these values are only valid for the set-up used in these particular tests.

A. *Wind tunnel tests*

The forces caused by the wind acting on the iced airfoil along with the gravity force of ice were measured throughout the accretion process. Based on these force measurements, it was possible to calculate the lift and drag coefficient of the continuously altered airfoil. The reduction of the lift coefficient as a function of accretion time for the three different ice types is shown in Fig. 3. As it is seen, first order polynomials could be fitted to the points, thus the degradation process is almost linear. Even though the accretion time was only 60 minutes, significant changes were monitored. The lift coefficient decreased the least, 22 % in case of rime ice tests and most significant for mixed ice tests, 34 %. For the glaze ice test, the degradation was 25 %.

The degradation is already visible after 5 minutes into the accretion. This sudden drop seems to be more severe than the one happened between 5 and 10 min. The slope of the drop in the first 5 minutes is much steeper than of the polynomials fitted to the points.

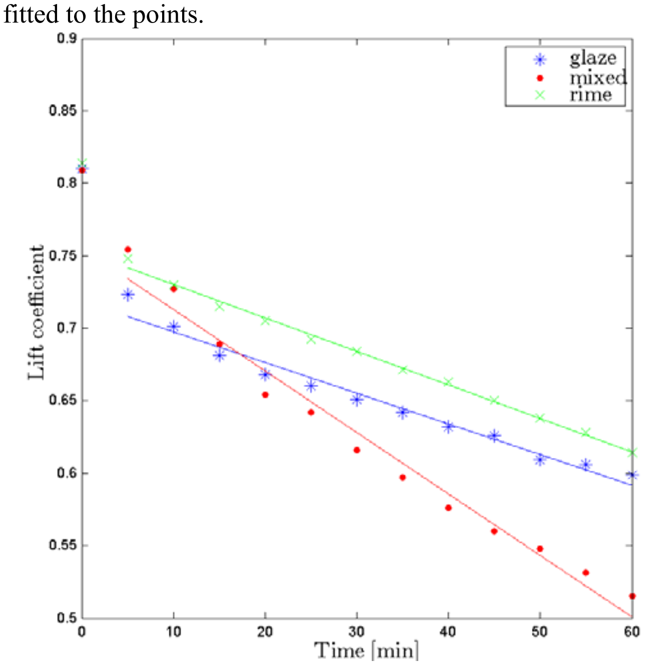

Fig. 3 Alteration of lift coefficient as a function of ice accretion time for 7° AOA in case of glaze (*), mixed (.) and rime ice (x). The environmental conditions were the following: LWC~0.7 g/m^3, MVD~25 for glaze and mixed ice and MVD~20 for rime ice and Re~1e6.

An increase of drag force and hence an increase of drag coefficient was experienced during the tests. This tendency is illustrated in Fig. 4. Similarly to the initial lift coefficient degradation, rapid increase of drag coefficient can be observed in the first five minutes. However, contrary to the lift curves, the process does not seem to slow down, i.e. the slope of the initial increase does not differ significantly from the slope of the fitted polynomials. It is clearly visible in Fig. 4 that the smallest increase of the drag coefficient occurs under rime ice conditions.

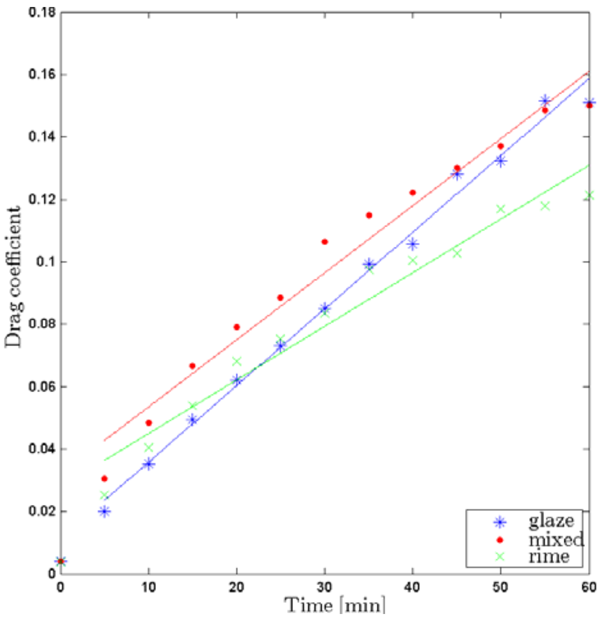

Fig. 4 Alteration of drag coefficient as a function of ice accretion time for 7° AOA in case of glaze (*), mixed (.) and rime ice (x). The environmental conditions were the following: LWC~0.7 g/m^3, MVD~25 µm for glaze and mixed ice and MVD~20 for rime ice and Re~1e6.

In Fig. 5, the collected ice profiles are shown. It can be seen, that the smallest ice deposit was building up in case of the rime ice test while the largest one in case of the mixed ice test. The rime ice accreted only on the leading edge of the airfoil, whereas the other two types accumulated also on the pressure side of the airfoil. The stagnation point is quite clear in all three cases (marked with orange circles in Fig. 5).

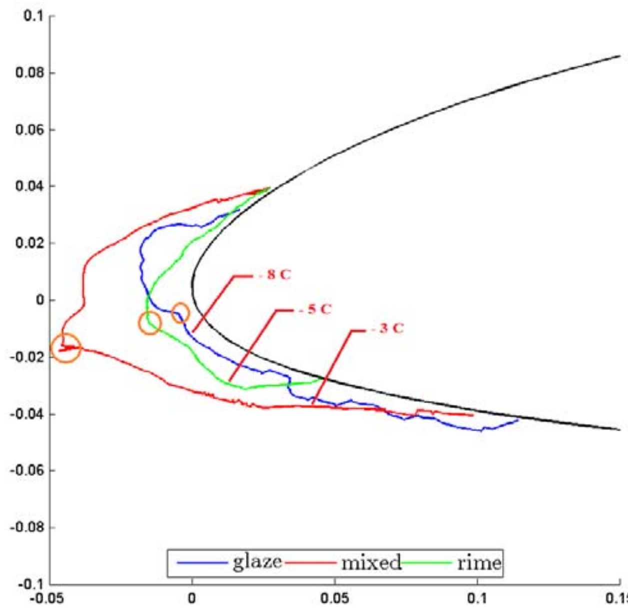

Fig. 5 Collected ice profiles from the wind tunnel tests for α=7° after 60 minutes of accretion. The environmental conditions were the following: U~15 m/s, LWC~0.7 g/m^3, MVD~25 for glaze and mixed ice and U~10m/s, MVD~20 for rime ice. The orange circles illustrates the stagnation points.

B. Numerical Simulation – TURBICE

As it was mentioned above, it was only possible to simulate conditions resulting in glaze and rime ice accretion on the airfoil. The results are plotted against the shapes collected from the climatic wind tunnel tests. Fig. 6 shows the results from the glaze simulations. The red curve represents the profile collected from the wind tunnel for LWC~0.7 g/m^3, MVD~25 µm, the blue line illustrates the result from TURBICE with LWC~0.65 g/m^3, MVD~25 µm during 60 minutes of accretion time, whereas the TURBICE results of LWC~0.65 g/m^3, MVD~30 µm and 90 minutes of accretion time are plotted in green.

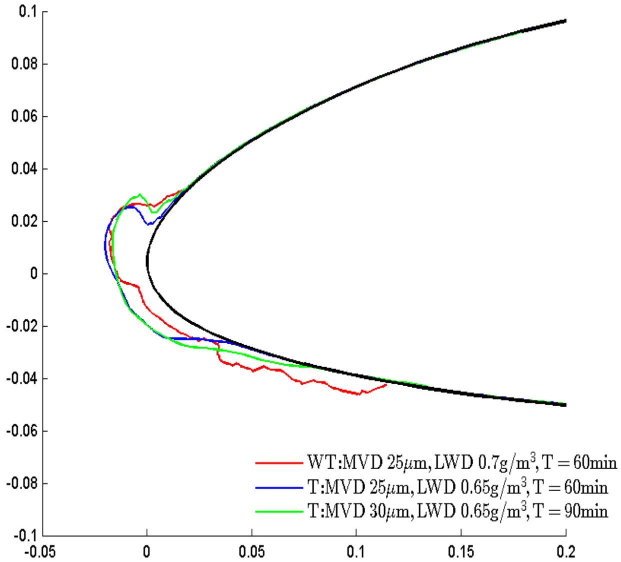

Fig. 6 Ice profiles from both the wind tunnel (WT) test and TURBICE (T) simulations for glaze ice. The red curve represents the profile collected from the wind tunnel for LWC~0.7 g/m^3, MVD~25 µm, the blue line illustrates the result of LWC~0.65 g/m^3, MVD~25 µm during 60 minutes of accretion time, whereas the results of LWC~0.65 g/m^3, MVD~30 µm and 90 minutes of accretion time plotted in green.

In Fig. 7, the results of the rime ice test are shown. The red curve represents the profile collected from the wind tunnel for LWC~0.7 g/m^3, MVD~20 µm, the blue line illustrates the result from TURBICE of LWC~0.4 g/m^3, MVD~25 µm during 60 minutes of accretion time, whereas the results of LWC~0.6 g/m^3, MVD~25 µm and 90 minutes of accretion time from TURBICE are plotted in green.

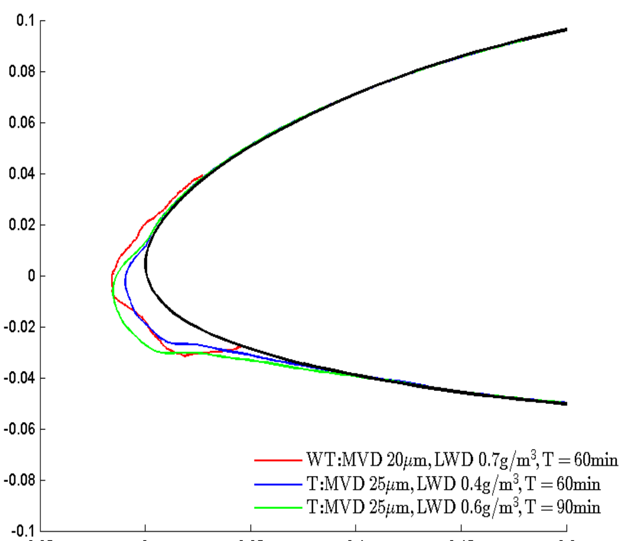

Fig. 7 Ice profiles from both the wind tunnel (WT) test and TURBICE (T) simulations for rime ice. The red curve represents the profile collected from the wind tunnel for LWC~0.7 g/m^3, MVD~20 µm, the blue line illustrates the result of LWC~0.4 g/m^3, MVD~25 µm during 60 minutes of accretion time, whereas the results of LWC~0.6 g/m^3, MVD~25 µm and 90 minutes of accretion time plotted in green.

C. Numerical Simulation – Ansys Fluent

The results of the numerical simulation with Ansys Fluent are summarized in TABLE V. The relative change refers to the reduction of lift coefficient of iced airfoil related to the lift coefficient of the clean profile. As it can be read from the table, mixed ice accretion caused the most significant reduction of lift coefficient whereas the least was found for rime ice.

TABLE V RESULTS OF NUMERICAL SIMULATIONS BY ANSYS FLUENT

Test	C_L	Relative change [%]
Clean profile	1.01	-
Glaze iced profile	0.784	22
Mixed iced profile	0.762	25
Rime iced profile	0.831	18

In Fig. 8, the velocity vectors colored by the velocity magnitude around the leading edge of the clean airfoil are shown. The color-range represents the flow speed around the airfoil ranging from 0 to 22m/s (blue to red). It can be seen that the incoming velocity decreases to 0 m/s at the stagnation point (represented by blue arrows) and speeds up at the suction side. The flow around the airfoil is rather smooth and well attached.

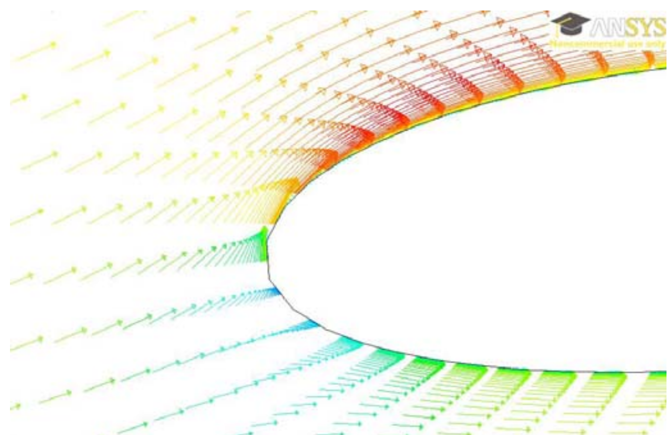

Fig. 8 Velocity vectors colored by the velocity magnitude (m/s) around the clean airfoil for inlet velocity 14 m/s and α=7°. The color-range from 0 to 22 m/s.

In Fig. 9, Fig. 10 and Fig. 11 the velocity vectors colored by the velocity magnitude around the leading edge of the iced airfoil is shown for glaze, mixed and rime ice, respectively. It can be seen that the ice deposit in each case disturbs the flow quite significantly. SP1 and SP2 illustrated the flow separation points at the suction and pressure side, respectively.

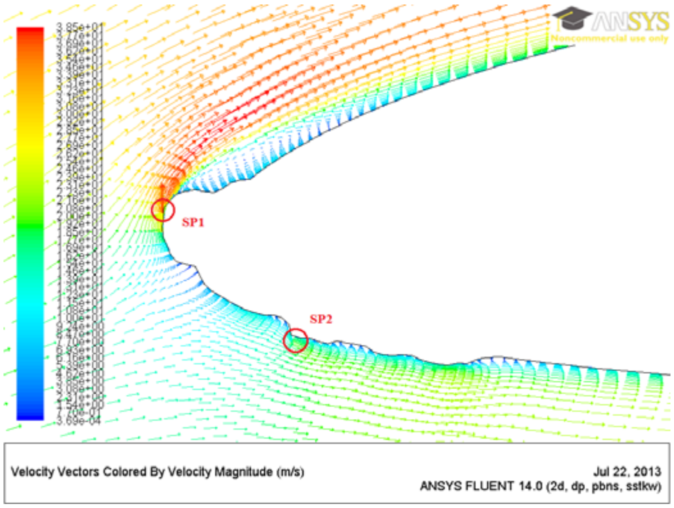

Fig. 9 Velocity vectors colored by the velocity magnitude (m/s) around the glaze iced airfoil for inlet velocity 14 m/s and α=7°. The color-range from 0 to 22 m/s. SP1 and SP2 illustrated the flow separation points at the suction and pressure side, respectively.

A large separation bubble is formed behind the leading edge separation point 1 (SL1) on the suction side of the airfoil, see Fig. 9.

In case of mixed ice deposit, a peak (SP1) was formed around the stagnation point, which reduces the flow speed at the suction side (see Fig. 10). A "nose" shaped ice formation can be also seen around the stagnation point, which was not seen in case of the other two types of ice simulations.

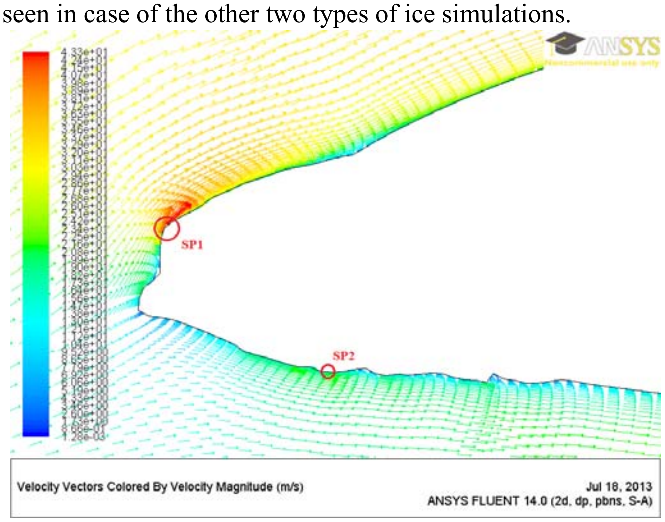

Fig. 10 Velocity vectors colored by the velocity magnitude (m/s) around the mixed iced airfoil for inlet velocity 14 m/s. The color-range from 0 to 22 m/s. SP1 and SP2 illustrated the flow separation points at the suction and pressure side, respectively.

At the suction side in Fig. 11, the accreted rime ice caused small disturbance on the flow pattern, compared to the clean airfoil. However, multiple local separation points can be found on the suction side (marked with red circles), which are causing lower slightly lower velocity zones compared to the clean profile.

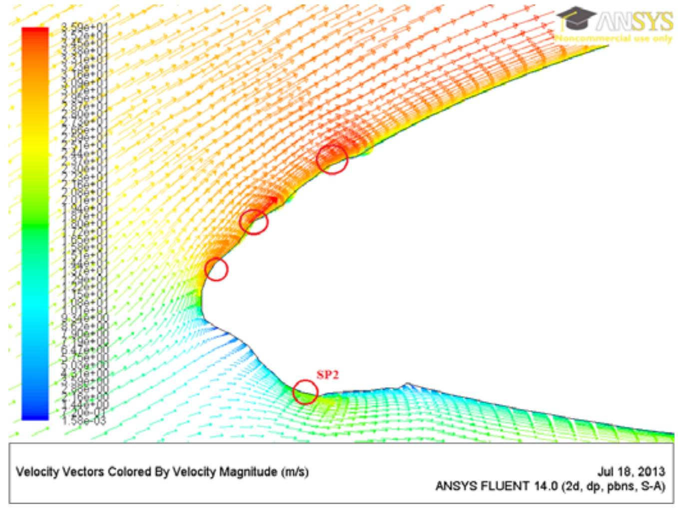

Fig. 11 Velocity vectors colored by the velocity magnitude (m/s) around the rime iced airfoil for inlet velocity 14 m/s and α=7°. The color-range from 0 to 22 m/s. SP2 illustrated the flow separation points at the pressure side, whereas there are multiple separation points marked by red circles at the suction side.

At the pressure side, small recirculation zones can be spotted behind the ice peaks (SL2) for each ice tests.

V. Discussion

A. *Wind Tunnel Tests*

The results of the wind tunnel tests shows that the lift coefficient decreased whereas the drag coefficient increased for all three ice types (see Fig. 3 and Fig. 4). The same conclusion was drawn in the studies mentioned in the *Introduction*. However, Jasinski et al. [5] showed that in some cases of rime ice accretion, the lift coefficient increased. This behavior was not experienced during the tests presented in this paper.

It can be observed from Fig. 3 that the initial degradation in the first 5 minutes is highly significant in each test, and hence if the reduction would follow this trend, the lift degradation would be much more severe. The immediate reduction of lift coefficient was caused by the changed surface roughness, as it was also shown by e.g. Lynch and Khodadoust [15].

It can be also noticed in Fig. 3, that the difference between the immediate reduction of lift coefficient for the different ice types is not significant, which indicates that the initial degradation is independent of the ice formation type for the same angle of attack.

It was also found that the least lift decrease and drag increase were caused by rime ice accretion. It is because in case of rime ice, the water droplets freeze on impact at the leading edge and this deposit acts as an extended leading edge causing less flow disturbance. For glaze and mixed ice, some of the droplets did not freeze on the surface but ran off along the airfoil and freeze aft, which resulted in larger iced surface area (see Fig. 5), and thus more disturbed flow field. The mixed ice profile had the highest negative influence on the flow and therefore it caused the highest lift degradation.

B. Numerical Simulation – TURBICE

Fig. 6 and Fig. 7 shows the results of TURBICE analyses for both rime and glaze ice together with the wind tunnel results for comparison. The TURBICE profiles and the profiles from the wind tunnel tests were not identical; however, they were in good agreement considering the circumstance that LWC and MVD are not known in the wind tunnel experiment. This leads to that these parameters could not be set accurately for the TURBICE simulation. Since it was not possible to measure LWC and MVD accurately in the wind tunnel, it was not possible to set the correct values in TURBICE. This could be a reason for the differences.

Some of the TURBICE tests used 90 minutes accretion time, which is longer than the duration of the wind tunnel tests. However, this should not be a major issue, because it was seen that the ice build-up is a nearly linear process. Therefore it can be assumed that the shape of an ice profile accreted in 60 minutes is similar to the one presented here.

C. Numerical Simulation – Ansys Fluent.

The trend of the reduction of lift coefficients agrees quite well with the wind tunnel test results. However, the relative degradation was found to be lower than it was for the experiments. The reason could be that with the contour tracing method, the small changes of surface roughness could not be documented therefore they were not implemented in the numerical analysis.

It was seen that the glaze and mixed ice formations caused the most flow disturbance. The sharp edges at the suction side seen in both Fig. 9 and Fig. 10 led to a speed up, which caused a large separation bubble especially in case of glaze ice. In case of rime iced profile, the flow followed a similar pattern as it was observed for the clean airfoil and comparing Fig. 11 and Fig. 8, the magnitude of the velocity did not differ significantly from the clean profile. For all three cases, there were some vortex formations noticed behind the ice peaks at the pressure side causing recirculation zones, which lead to some flow disturbance and retardation. However, it seems that they do not have a large influence on the change of the overall leading edge aerodynamics.

VI. CONCLUSION

Both experimental and numerical analyses have been performed to study the effect of glaze, rime and mixed ice accretion on the aerodynamics of an iced NACA 64-618 profile for 7^{o} angle of attack. The experiments were carried out in a climatic wind tunnel, and for the numerical analyses, TURBICE ice accretion model and Ansys Fluent were used to verify the findings from the wind tunnel tests.

During the wind tunnel tests, the aerodynamic forces were monitored as ice was building up on the surface. Similarly to other studies and also to the numerical investigation, lift coefficient was found to decrease and drag coefficient increased as ice accreted. These processes were found to be nearly linear.

Mixed ice formation caused the most severe lift coefficient reduction, whereas the least was found for rime ice. The largest ice deposit accreted on the profile in case of mixed ice and thus the largest disturbance was seen here. The flow around the rime iced ice profile followed a pattern similar to the streamlines around the clean profile, hence causing low disturbance.

The ice accretion model TURBICE was used to estimate ice profiles for similar conditions as it was set in the wind tunnel. These profiles agree, considering the limitations of known experimental boundary conditions, fairly with the profiles produced during the wind tunnel testing.

It can be concluded that significant lift reduction and thus power production loss can be achieved even in the first hour of ice accretion.

ACKNOWLEDGMENT

Force Technology, LM Wind Power and Cowifonden are acknowledged for allowing us to use their unique facility to conduct the tests, for lending the NACA 64-618 profile and for the financial support, respectively. The authors would also like to acknowledge VTT, Technical Research Centre of Finland, for the support they provided for using TURBICE ice accretion model.

REFERENCES

[1] B. Tammelin, M. Cavaliere, H. Holttinen, C. Morgan, H. Seifert, and K. Santti, Wind energy production in cold climate (WECO). Technical report, Finnish Meteorological Institute, 1998.

[2] L. Tallhaug, G. Ronsten, R. Horbaty, R. Cattin, T. Laakso, M. Durstewitz, A. Lacroix, E. Peltola, and T. Wallnius, "Wind energy projects in cold climate. Technical report, Executive Committee of the International Energy Agency Programme for Research and Development on Wind Energy Conversion Systems, 2009.

[3] I. Baring-Gould, R. Cattin, M. Durstewitz, M. Hulkkonen, A. Krenn, T. Laakso, A. Lacroix, E. Peltola, G. Ronsten, L. Tallhaug, and T. Wallenius. 13. Wind Energy Projects in Cold Climates. Technical report, 2011.

[4] H. Seifert and F. Richert. Aerodynamics of iced airfoils and their influence on loads and power production. European Wind Energy Conference, 1997.

[5] W. J. Jasinski, S. C. Noe, M. S. Selig, and M. B. Bragg. Wind turbine performance under icing conditions. Journal of Solar Energy Engineering, ASME, 120(1):60-65, 1997.

[6] C. Hochart, G. Fortin, and J. Perron. Wind turbine performance under icing conditions. Wind Energy, 11:319333, 2008.

[7] M. C. Homola, M. S. Virk, T. Wallenius, P. J. Nicklasson, and P. a. Sundsbø. Effect of atmospheric temperature and droplet size variation on ice accretion of wind turbine blades. Journal of Wind Engineering and Industrial Aerodynamics, 98(12):724–729, 2010.

[8] L. Makkonen, T. Laakso, M. Marjaniemi, and K. J. Finstad. Modelling and prevention of ice accretion on wind turbines. Wind Energy, 25(1):3–21, 2001.

[9] M. Etemaddar, M. O. L. Hansen and T. Moan. Wind turbine aerodynamic response under atmospheric icing conditions. Wind Energy, DOI: 10.1002/we.1573, 2012.

[10] C. Georgakis, H. Koss, and F. Ricciardelli. Design specifications for a novel climatic wind tunnel for the testing of structural cables. International Symposium on Cable Dynamics (ISCD) - 8, 2009, Paris, France.

[11] ESDU 76028, Lift-Interference and Blockage Corrections for Two-Dimensional Subsonic Flow in Ventilated and Closed Wind Tunnel, ESDU 1976.

[12] R. J. Schick. Spray technology reference guide: Understanding drop size, bulletin 459c. Technical report, Spraying Systems Co.
[13] K. Mortensen, CFD Simulation of an airfoil with leading edge ice accretion, Department of Mechanical Engineering, Technical University of Denmark, 2008
[14] J.J. Chung and H.E. Addy, Jr. A Numerical Evaluation of Icing effects on a Natural Laminar Flow Airfoil. NASA TM-2000-209775, January 2000.
[15] F. T. Lynch and A. Khodadoust. Effects of ice accretions on aircraft aerodynamics. Progress in Aerospace Sciences, 37(8):669-767, 2001.

Field Measurement of Wind Turbine Icing

Dominic Bolduc[1], Matthew Wadham-Gagnon[1], Bruno Boucher[1], Nicolas Jolin[1], Amélie Camion[2], Jens Petersen[3], Hannes Friedrich[3]
[1]TechnoCentre Éolien, Canada, [2]Repower Systems Inc, Canada, [3]Repower Systems SE, Germany
[1]Corresponding author address: 70 rue Bolduc, Gaspé, QC, G4X 1G2, Canada, dbolduc@eolien.qc.ca

Abstract **—** In 2011, the TechnoCentre Éolien (TCE) and Repower initiated an ice measurement campaign conducted at TCE's Site Nordique Expérimental Éolien CORUS (SNEEC) in Rivière-au-Renard, Qc, Canada. The outcome of this ongoing campaign has and will continue to serve the following objectives:

1) study ice loads on wind turbine blades;
2) improve ice detection methods based on computer vision;
3) have a better understanding of ice throw;
4) correlate icing to weather forecasts;
5) assess ice protection systems like passive anti icing and de-icing;
6) create a database with visual observations and meteorological data.

But one of the most significant outcomes to date of the measurement campaign resulted from a dimensional analysis of the different observations (ice on blades, ice on nacelle weather mast and ice throw) which has led to a classification of ice profiles for different icing events with a distinction between rime and glaze.

With this methodology and results presented in this paper, the severity of ice on nacelle weather mast during an icing event can be correlated to productions losses. Furthermore, the distribution of icing severities over the course of a year combined with correlations to production losses could eventually lead to improved resource assessment and site classification.

I. Nomenclature

C= Chord of turbine blade
CBH/T= Cloud Base Height and temperature method
D/A= Double Anemometry ice detection method
D= Width of the ice profile ice
γ= Density of ice (kg/m^3)
IC = Ice Class
ICRi= Ice Class for rime with severity increasing with i
ICGi=Ice Class for glaze with severity increasing with i
L= Length of ice profile in windward direction (mm)
m= Ice load (kg/m)
SNEEC= Site Nordique Expérimental en Éolien Corus
t= Tickness of accreted ice perp. to windward direction (mm)
TCE= Techno-Centre Éolien
W= Width of object where accretion occurs (mm)
WEC= Wind Energy Converter
WS= Wind speed

II. Introduction

Low temperature and icing climate are not standard regions in which modern wind turbine are normally installed. However, the wind resource availability in these climates has one of the largest potential for the industry. That's why producers and manufacturer have started to develops new projects in these regions at an increased rate for the past few years [1]. However, many of them are facing a lot of problems in operating wind farm in these harsh conditions (power loss, shutdown, breakage). One of the reasons is that no standard methodologies are yet available for icing resource assessment and ice detection. That's why a series of expert are now developing state-of-the art methods and hardware to face these challenges [2]-[4].

Techno-Centre Éolien (TCE) in partnership with RePower is taking place in these studies and has conducted an ice measurement campaign during the 2011-2012 winter and 2012-2013 winter. The project has many objectives such as ice loading on turbines, safety issues due to ice throw, weather forecast of icing and ice protection system. This paper focus on 2 other goals of the project which are resource assessment and ice detection based on visual acquisition. The icing campaign took place at TCE's Site Nordique Expérimental en Éolien Corus (SNEEC).

The infrastructure at the SNEEC consists of two REpower MM92 CCV turbines of 2.05MW, installed in 2009 and a 126m met mast, installed in February 2011. The ice measurement campaign involved collecting and analysing visual observations during icing events, meteorological data from the wind turbines and met mast as well as ice throw. Pictures of ice on blades, on the nacelle weather masts, of ice throw and of ice on the 126m met mast were taken with cameras from the ground as well as from remote cameras installed on the nacelles of the turbines. Ice throw was documented relative to weight, dimensions, density as well as distance and position from turbine. Meteorological data assessment included heated and unheated anemometers, an optic ice sensor, temperatures, relative humidity, solar radiation and cloud height. Correlations between meteorological icing, instrumental icing, production losses and visual observations have been established.

Classification of nacelle's weather mast, blades and ice throw was based on ISO12494 standard [5] in order to find a visual icing indicator that could lead to an icing detector based on computer vision system. The classification method was compared to other detection method usually used in the wind turbine industry. The methodology was also used to characterize the site with respect to icing time and severity and to produce a correlation with the power curve of the turbine.

III. Methodology

The ice profiles are a geometrical assessment of the severity of the icing event for which the data (pictures and geometrical measurements) are available. Quantitative evaluation was used when possible in reference to the ISO12494 standard [5]. This standard is based on the assumption of a linear density of ice accretion (ice load in kg/m) with an elliptical cross-section for rime and a constant thickness accumulation for glaze.

The Ice Classes (ICs) associated with these accretions follow a logarithmic rule for rime with respect to ice load (*m*), see equation (1), and are proportional to ice thickness (*t*) for glaze, see equation (2).

$$ICR = 1.739 \cdot ln(m) + 2.195 \quad (1)$$

$$ICG = {}^{t}/_{10} \text{ where } t \text{ is in mm} \quad (2)$$

A. Weather mast ice profiles

One of the first visual indications of ice accretion can be found on the weather mast of a nacelle. To evaluate the ice profiles on this structure, images from a web camera were captured every 5 minutes and analysed manually at intervals of 1 to 3 hours depending on accretion rate and picture quality.

For rime ice, the severities of the weather mast icing events were evaluated using the ISO12494 standard [5] by estimating the ice thickness on the same cylindrical tubes (assuming a type A elliptical ice accretion, as shown in Fig. 1). This estimation was done by comparing the width of the tube with ice to the width of the tube without ice (48,5mm reference). The ice load and ice classes were then calculated for each photo using equations (3) to (5) as well as equation (1) assuming a rime ice density γ of 600kg/m^3.

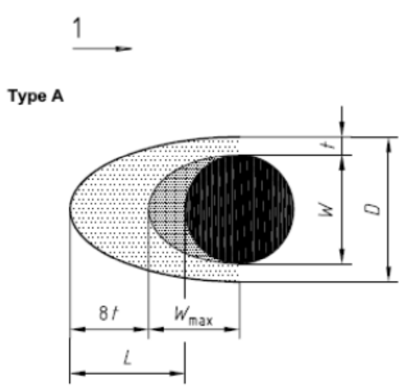

Fig. 1: Rime ice accretion profile on cylinder [5]

For $L \leq \frac{W}{2}$

$$L = \frac{m \cdot 4 \times 10^6}{\pi \gamma W}[mm] \quad (3)$$

For $L > \frac{W}{2}$

$$L = \frac{W}{2} + 8 \cdot t\,[mm] \quad (4)$$

$$t = \frac{1}{32}\left\{-10W + \left(68W^2 + \frac{m}{\gamma} \times 8.149 \times 10^7\right)^{1/2}\right\}[mm] \quad (5)$$

Therefore, for a tube of 48.5mm the transition from the two set of equation occur when the ice load is about 0.55kg/m. The following methodology was used in the calculation:

- *m* is calculated with the first set of equation using L=D/2 for ice accretion that doesn't cover the entire tube (D<W). Where D equal the width of the apparent ice accretion on the tube (white trace smaller than W)
- *m*=0.55kg/m for ice accretion that covers the tube but with no apparent change in width (D=W and L=W/2)
- *m* is calculated with the second set of equation for ice accretion wider than the tube (D>W)

Fig. 2 provides images of the nacelle weather mast showing examples (a) where the tube has no ice, (b) where the ice width is not as wide as the tube width, (c) where the ice width is approximately equal to the tube width, and (d) where the ice width exceeds the tube width.

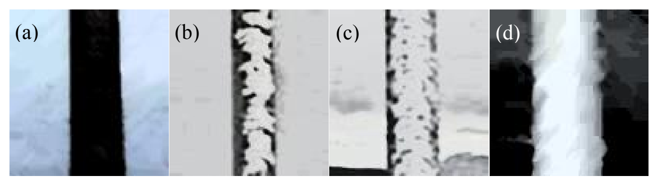

Fig. 2: Ice accretion on the nacelle weather mast (a) with no ice, (b) D<W, (c) D=W and (d) D>W

For glaze icing events, the estimation of thickness is a lot more difficult due to the transparency of this type of ice and the resolution of the images. Therefore, horizontal tubes of the mast which accumulate glaze more easily were used instead to measure the ice thickness. Ice class was then calculated with equation (2).

B. Blade ice profiles

Blade ice profiles were measured with pictures taken from the ground during TCE visits for almost all icing events confirmed by weather mast icing pictures.

In order to establish the severity of blade icing quantitatively, a methodology was developed based on the ISO12494 standard [5] and the following assumptions:

- volumetric density of rime ice is assumed to be 600kg/m^3
- accretion is assumed to be similar to a cylindrical object (type A of the ISO12494) and W is assumed to be 10% of blade chord

- the reference used to measure L is the line created by the abrasive tape located on the leading edge (see Fig. 4). The offset of this line from the leading edge is assumed to be 4 inch (101,6mm).

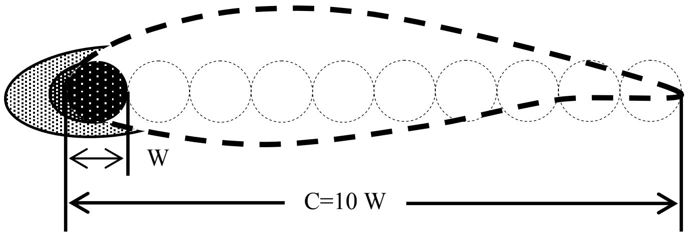

Fig. 3: Blade ice accretion assumption used

It should be noted that this method is very dependent on the choice and the number of pictures used to estimate L for an event. For several icing events, it was impossible to use this estimate because of poor visibility or bad orientation of the picture that could not lead to a good evaluation of L based on the reference line. As ice accretion on blades change along blade span, a particular attention was taken to associate an ice load (*m*) at specifics position on the blade for each picture. However, it was difficult to make precise positioning as there are no reference marks along that direction.

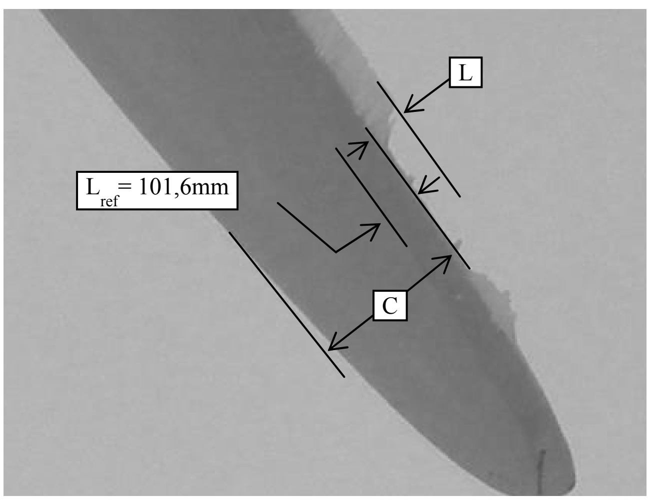

Fig. 4: Blade icing profiles measurements

C. Ice throw profiles

Ice throw assessments were performed on a regular basis during icing events. The availability of the data was mostly dependent on safety hazards and integrity of the collected sample. The data collected for risk assessment was the distance and orientation from the turbine and the weight of the ice throws. For severity analysis, quality of the collected data (weight, dimensions) associated with the corresponding pictures were the main factors that lead to accurate estimation of ice accretion.

In order to compare the icing severities of the ice throw data with the blade icing and the weather mast severities a method based on ISO12494 standard [5] was also used. This way, the results can be compared with less subjectivities and scaling error. For this purpose, two ways of calculating the linear density (kg/m) and ICRs were used for rime ice.

The first, and simplest, is based on the weight and length of the ice throw measured in the direction of the blade span. By dividing the weight by the length, we can have a very good estimate of the average ice load (*m*) without requiring the volumetric density (kg/m^3) which is normally unknown.

The second, which is very time consuming, is based on fitting geometrical cross-section of the collected ice throw with the elliptical cross-section proposed by ISO12494 [5]. To achieve this, equations (3) to (5) were used along with the following assumptions:

- The ICRs are only evaluated for pictures where the leading edge can be measured and approximated by a circular arch of constant radius with:

$$W = \frac{W'}{4h} + h \tag{6}$$

- The volumetric density is 600kg/m^3 for rime ice cases and 900kg/m^3 for glaze.

An example of cross-section fitting for an ice throw sample is provided in Fig. 5. It should be noted that the second method introduces some uncertainties related to the perspective of the images used to fit the cross-section. Approximation needed to be made regarding the measurements and the relative proportion of other dimensions.

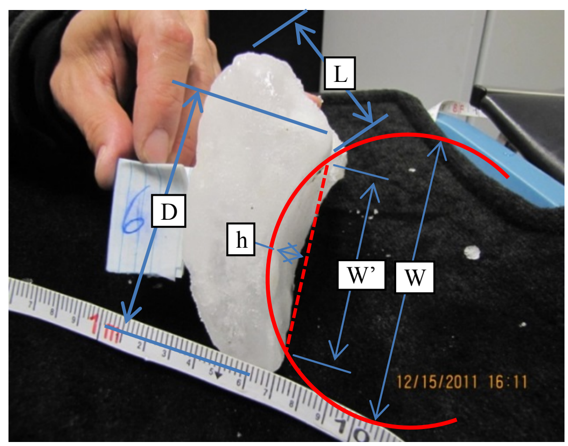

Fig. 5: Ice throw cross-section fitting

D. Comparison with other ice detection methods

In order to validate the icing events durations and intensities, the icing profiles measured during this campaign were compared to other icing detection methods.

Double anemometry (D/A): Difference in wind speed between heated and unheated anemometer is a basic detection method to measure the duration of instrumental icing. Different pairs of anemometers were used on TCE weather mast MMV2 at different altitude and on both test turbine (MM92) nacelles.

The threshold for ice detection was set to 20% difference between both anemometer reading for windspeed above 5m/s and temperature below 3ºC.

Cloud Base Height and temperature (CBH/T): One method to detect meteorological icing is to detect the presence of cloud at low temperature. For this purpose the use of a WeatherInc8339 ceilometer and temperature sensor at 80m on MMV2 was used. The threshold to detect in-cloud icing was the presence of cloud below 80m for temperature below 3ºC.

Optic icing detector (Holo): Direct ice detection instruments were tested during the 2011-2012 icing campaign. A Holo-Optics T41 was installed on one of the turbines and a T44 was installed on TCE met mast at 76m. The duration and intensity of meteorological icing events were monitored and compared to other ice detection methods.

Power Loss: It is assumed that power losses are associated to icing when temperatures are below 3ºC. Then we can predict the presence of ice when the actual power of the turbine is below a certain threshold if compared to the calculated power for a given wind speed. This method was use with a threshold of 80% of calculated power and wind speed above 5m/s.

E. Power Curves vs Ice Profiles

One of the objectives to classify the severity of icing on a wind turbine is to correlate to the power production for different intensities of ice. The progression of the severity of icing on a timescale compared to the active power of the tubine at the same time can be used to build icing severity specific power curves. For this purpose, the ice profiles on the nacelle weather mast were used as they were recorded at more regular and frequent time intervals. In order to have representative data for these power curves, a methodology inspired by IEC61400-12 [6] standard was used with dataset from winter 2011-2012 and 2012-2013:

- 10 minute averages were used for wind speed and active power;
- Wind speed were separated in bins of 0.5m/s;
- Ice Classes on weather mast were binned by type of ice and intensity steps of 1 starting at IC=0.5. ICs lower than 0.5 were considered as not iced;
- Combined data of both wind turbines are used for analysis. Average values are calculated by a weighted average based on the valid number of points for each turbine;
- A minimum of 8 points per bins were needed (combined data of both turbine);
- Only data points where the turbines were in main operation for the whole 10 minutes were used

Each power curve was fitted using a sigmoid function, see equation (7) with a maximum at the rated power of 2.05MW. The sum of square of residuals was minimized for each fit and the coefficient of determination (R^2) was calculated.

$$P(WS)\frac{P_{rated}}{1+e^{(a\cdot WS+b)}} \tag{7}$$

In the sigmoid equation, we can see the scale coefficient (a) controls the slope of the curve whereas the bias coefficient (b) translates the curve from right to left. Fig. 6 shows the effect of both of these coefficients.

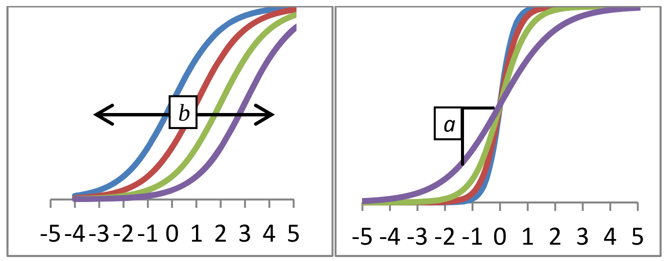

Fig. 6: Sigmoïd function coefficient effects

IV. Results

This section presents an example of ice profile classification during the winter 2011-2012 measurement campaign as well as a summary of the season.

A. Icing event example (April 2012)

Fig. 7 presents the results of the ice profile classification methodology for a selected rime icing event that occurred in April 2012. It shows the ice classes progression on the nacelle weather mast, punctual assessment of the severity on the blade and on collected ice throws. An interesting aspect of this event is that it shows 2 phases of accretion (meteorological icing). One from the beginning up to the end of the 22nd and a short one starting around 9:00 on the 23rd up to 19:00.

It can be seen that weather mast monitoring could detect ice accretion faster than any other detection method if an automatic visual detection algorithm was implement. However, the power recovery at an ICs of 4 suggest that the ice shed from the blade before the met mast of the nacelle. This observation was confirmed for almost all the icing event during the winter. The recovery of the unheated anemometer also happens generally before the ice disappears on the met mast. This is probably caused by different rigidity, geometry and colors of each element that will melt and break the ice at different times.

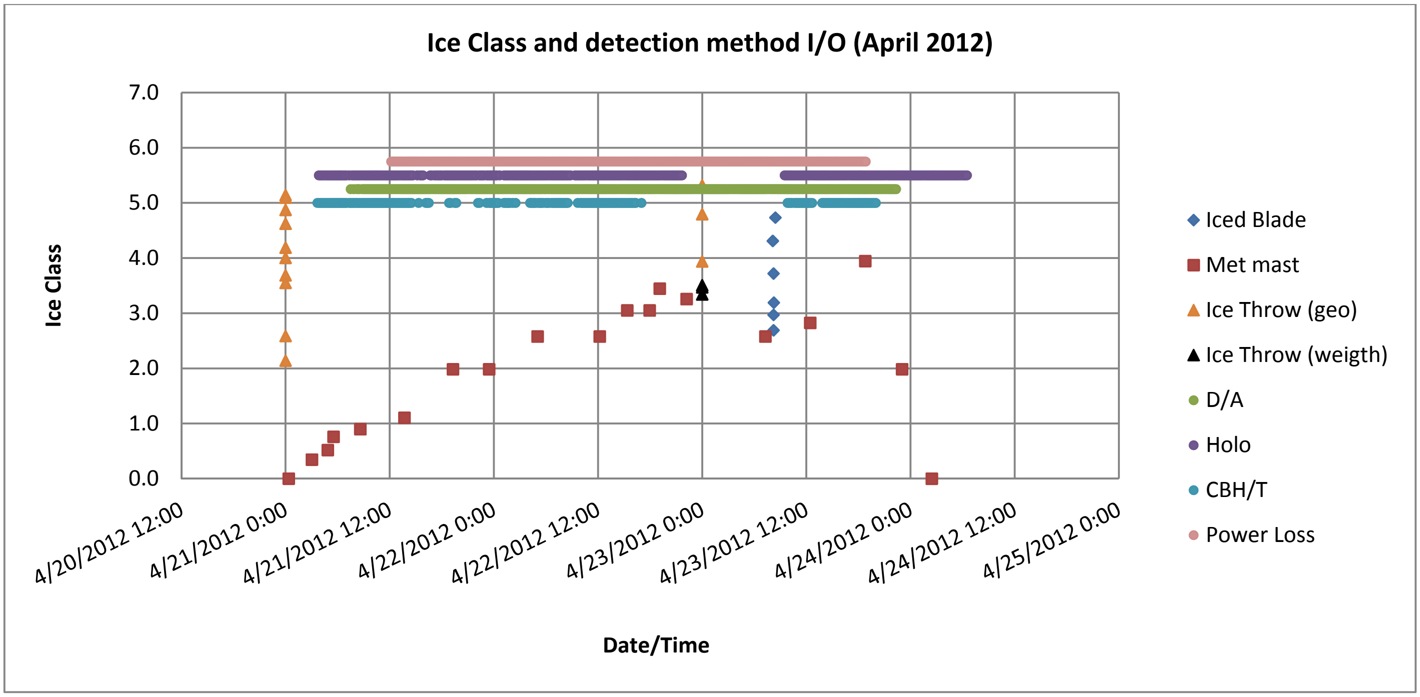

Fig. 7: Ice profile classification and detection method for April 21st to 24th

Meteorological icing was also analyzed with the Holo-Optic sensor and CBH/T method. We can see that met mast monitoring can also detect ice accretion when we look at the slopes between data points. Each method seems to perform equally with respect to the start and end of meteorological icing. However, the Holo-Optic seems to be very sensitive to heavy ice accretion as the sensor will saturate because of insufficient heating. Such a situation was observed at the end of this event with ice that couldn't melt off of the sensor for almost 8 hours. This problem also occured during other icing events.

Ice classification on the blade was also processed during a visit on the site. The spread of ICs for the blade is mainly caused by different measures along the blade span that will lead to heavier load on the blade tips compared to the root. This observation complies with theoretical ice accretion model that associate icing rate to relative wind speed that increases at blade tip. However the icing rate depends also on collection area that decreases at the tip. These combined factors lead to a relatively constant ice load on the last third of the blade tips but could not be confirmed by observation because of too much uncertainty in locating the ICs measurements along the blade span.

Ice throws were also analyzed during 2 visits during this icing event. The results on Fig. 7 shows a very wide spread of ICs for ice throws measured by cross-section fitting (geo). Those differences are caused by the scaling and perspective error introduced in the process. These variations were also observed for other icing events. On the other hand, ICs classification based on weight and length of ice throws showed a narrower distribution but fewer points because the weight was not recorded on a regular basis. But the most important reason why ice profile classification of ice throw is not reliable for analysis is because of the difficulty to attribute an ice throw to an icing event. Some ice throws are covered by snow during a storm and can reappear 2 weeks later after a strong wind and 2 other icing events.

B. *Results summary*

This section presents the summary of winter 2011-2013 icing data. It shows the icing duration and accretion for different methods of detection and classification for winter 2011-2012, the ICs distribution and the power curves generated with the methodology described earlier for winter 2011-2013.

1) *Icing duration*

Table 1 presents the overall duration of icing for winter 2011-2012 based on the different ice detection methods used. Icing duration for iced blades and ice throw is not available as those measurements were made punctually. Shaded cells show partial or no data for instruments that were commissioned during the winter.

Table 1: Icing time summary for winter 2011-2012

	DEC	JAN	FEB	MAR	APR	TOTAL
WM icing	108:50	308:10	154:40	37:50	158:10	**767:40**
D/A -MMV2 -34m			2:20	0:30	78:50	**81:40**
D/A -MMV2 -57m			1:20	0:00	67:20	**68:40**
D/A -MMV2 -80m			24:10	0:40	118:20	**143:10**
D/A -MMV2 -126m			68:50	4:30	145:10	**218:30**
D/A – WEC1	44:00	111:20	54:00	17:40	126:10	**353:10**
D/A – WEC2	37:40	149:30	90:30	19:30	136:10	**433:20**
Power loss - WEC1	95:30	76:50	8:40	0:00	73:50	**254:50**
Power loss - WEC2	104:20	80:40	9:50	0:00	68:00	**262:50**
WM accretion	54:50	127:50	35:00	25:20	61:50	**304:50**
CBH/T			31:40	17:50	83:00	**132:30**

Holo		51:30	23:20	16:40	98:00	**189:30**

The results show that nacelle weather mast icing duration is a much longer than instrumental icing or power loss. This is caused by the fact that weather mast icing is generally detected earlier but mostly because ice stays longer on the mast compared to the anemometer and the blades. This difference will probably have an impact on the power curves based on weather mast ICs.

Another aspect that stands out of the results is the effect of altitude on instrumental icing. The different pairs of anemometer on MMV2 met mast clearly show an important increase in icing time after 57m and even more between 80 and 126m.

Accretion time of the nacelle weather mast (positive slope) is also compared with CBH/T method and the Holo-Optic sensor. The results show similarities in accretion time for March and April but cannot be compared for other month because of data availability. The differences in duration for the last 2 months are caused by the Holo-Optic saturation in April and a glaze event that makes difficult to measure ICGs and slopes on the weather mast. CBH/T method also presents holes in the data because of data treatment of the ceilometer that doesn’t make the difference between clear sky and cloud to the ground. In both cases the instruments indicate 0m of cloud height and data are rejected in quality control.

2) Ice Classes distribution for 2011-2012 and 2012-2013 winter

Fig.8 presents the ICs level distribution for winter 2011-2012 and 2012-2013. The results are presented with the same bins used for power curves calculation. ICs below 0.5 are shown to give an insight about the total time of icing even if this level of icing was not considered in the power curves analysis. The total of 767 and 964 hours of icing on the nacelle weather mast represents 8.76% and 11% of the year for respective winters.

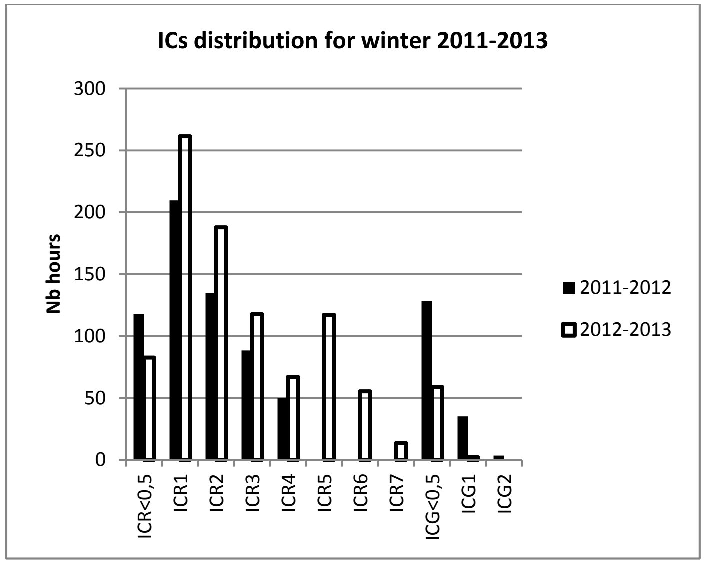

Fig.8: ICs distribution for winter 2011-2012

3) Power curves with ice for 2011-2012 and 2012-2013 winter

The power curves calculated based on ice profile classification of the nacelle weather mast are presented in Fig.9. The graphic shows the average power output from both turbines that satisfy the criteria described in the methodology for each bin (WS, ICs). The curve fitted sigmoid functions are also presented for each ICs with the R^2 all above 95%.

The data clearly show a shift of the power curves with respect to wind speed for increasing ICs. The slopes of the central portion also have a tendency to decrease for some ICs. The power loss compared to non-iced curves can go up to 80% for ICR6 for a total annual loss of 1.5%AEP for 2011-212 and 5%AEP for 2012-2013 [2], [8]. However, some discrepancies exist for ICR3 that should normally give more power loss than ICR2 and less than ICR4 for the entire range. This difference is likely caused by the wide spread of power output of the dataset for ICR3 attributed to the ice shed from the blade when icing severity gets high enough. Observations show that starting from this level of icing severities, the weather mast ICs no longer correlate to the blade ICs for the end of the event and different portions of the blade can have strong variation of ICs. For some data points the turbine has already come back to normal production while the weather mast is still at severities above 3. This has the effect to shift the average power to the left. For ICR6, the curve doesn’t seem to have this kind of problem but this is mainly caused by the fact that there are not enough data points in the central portion of the power curves.

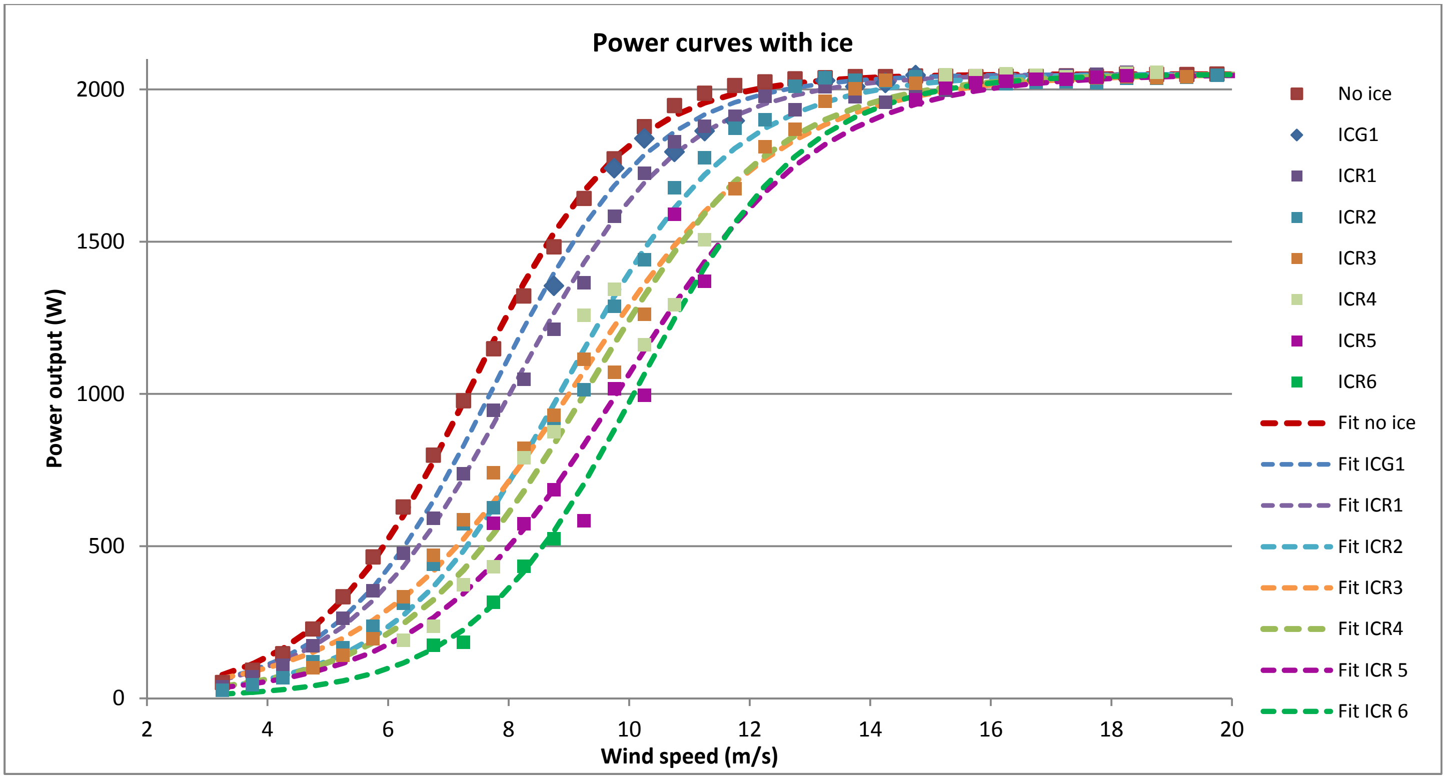

Fig.9: Power curves of MM92 based on nacelle weather mast ICs

V. Conclusions

The key parameters used in ISO12494 standard like the width (W) or the length (L) of ice profiles on structure are an interesting and simple way to characterize the ice load (m) and severity (IC) of ice accretion. These parameters could be implemented in image analysis algorithms in order to detect ice accretion automatically on different part of wind turbine. This study used different sources of images acquired during an ice measurement campaign at TCE's test site in partnership with Repower.

The first source of images was taken at 5 minutes intervals on the nacelle of a turbine and was analyzed manually to classify the icing severity on a weather mast tube. The methodology gave fairly good results and could be easily implemented automatically in a computer vision algorithm. Some concerns regarding camera resolution and illumination at night could be upgraded to improve the quality of output data. However, the observation and comparison with other ice detection methods demonstrates that monitoring of this part of the turbine do not reflect the ice accretion on the rotor that affect the performance of the turbine. Ice shed from the blades normally occurs before ice shed from the weather mast so that correlation to power curves using classification on this structure underestimates power loss at higher severities.

The second source of images was the pictures of the iced blade taken from the ground during TCE's team visits on test site. The measurements from this source could not be as accurate as for the mast because the reference dimension was not visible enough. The use of high visibility labeled reference markers like checkerboard could improve the accuracy of these measurements. However, the frequency of the pictures taken from the ground could not lead to automatic ice detection. In order have real-time monitoring of the blade, a camera installed on the hub or the nacelle could give valuable information on ice accretion severities on the blades. This setup is technically more challenging because of rotor's movement.

The last source of images came from the collected ice throw on test site. This process is time consuming and correlation with turbines performance is almost impossible. However, the information gathered from these samples give valuable data for validation of ice density.

The empirically determined power curves associated to different levels of icing severity provide valuable insight on the behavior of a wind turbine in icing conditions. The performance degradation due to icing is clearly a function of icing severity for wind speeds up to ~16 m/s. At wind speeds greater than 16m/s, the power seems to return to its nominal expected output. This may be explained partly by the active pitch control system that is torque driven and therefore will wait for the rotor to reach required torque before pitching to maintain nominal power output. Another explanation would be that ice sheds more easily on the highly flexible blades (tip displacement of up to 5m) at higher wind speeds allowing aerodynamics of the blade to return to normal.

The Weibull-like distribution in Fig.8 suggests that as total hours of icing (regardless of severity) increase in a year, the more likely the number of hours with higher icing severity will increase. As the SNEEC is considered a level 2 or 3 according

IEA site icing classification [2], [8], one would expect a site of IEA classification 4 or 5 to experience higher severity (higher ice load) icing events.

While more data is required to improve their accuracy, these power curves provide a basis for performance degradation due to icing and may eventually be used to validate and improve site assessment, ice accretion simulations tools, weather forecasting models and ice protection system performance as well as lead to a better understanding of ice induced fatigue loads.

References

[1] BTM World Market Update 2013, Special Chapter: Cold Climate Turbines, Navigant Research, Copenhagen, Denmark

[2] Ian Baring-Gould, *et al.*, Expert Group Study on Recommended Practices for Wind Energy Projects in Cold Climates. IEA Wind Recommended practices no. 13. 2012. Available at: http://arcticwind.vtt.fi/

[3] Wadham-Gagnon, M., *et al.*, "Ice profile classification, based on ISO 12949", presented at WinterWind Conf., Ostersund, Sweden, 2013

[4] M.C. Homola, J. Nicklasson, A. Sundsbø, "Ice sensors for wind turbines", Cold Regions Science and Technology, vol. 46, pp.125–131, Jun., 2006

[5] Atmospheric Icing of structures, ISO 12494, 2001

[6] Wind turbines – Power performance measuements of electricity producing wind turbines, IEC 61400-12-1, 2005

[7] M.C. Homola, *et al.*, "Modelling of ice induced power losses and comparison with observations", presented at Winterwind Conf., Umea, Sweden, 2011

[8] Clausen N.-E., et. al., Recommended Practices for Wind Energy in Cold Climates: Resource Assessment and Site Classification. IWAIS 2013, St-Johns, Newfoundland.

Ice Induced Vibration on Wind Turbines

Matthew Wadham-Gagnon[1], Ville Lehtomäki[2], Dominic Bolduc[1], Nicolas Jolin[1], Bruno Boucher[1],
Simo Rissanen[2], Timo Karlsson[2], E. Bechoefer[3], Klaus Sandel[4]
[1]TechnoCentre Éolien, Canada, [2]VTT Technical Research Centre of Finland, Finland,
[3]NRG Systems, USA, [4]Repower Systems SE, Germany
[1]Corresponding author address: 70 rue Bolduc, Gaspé, QC, G4X 1G2, Canada, mgagnon@eolien.qc.ca
[2]Corresponding author address: Tekniikantie 4 A, Espoo, P.O. Box 1000, FI-02044 VTT, Finland, ville.lehtomaki@vtt.fi

Abstract — Technological advancements are making cold climate sites, which generally have excellent wind resources, more and more attractive for wind farm deployment. Most turbine manufacturers have designed turbines capable of operating in low temperatures. Much effort has and still is being put in to reducing uncertainties associated with and developing technologies to reduce the production losses caused by ice accretion on blades. However there is still very limited understanding of the longer term effects of dynamic loads caused by ice on the design life of a wind turbine.

In order to investigate these dynamic effects, two measurement campaigns were conducted on two different sites; one in Canada and one in Finland. Load measurements were collected between 2007-2010 on a 2MW turbine in Southern Finland and between 2011-2013 load and acceleration measurements on two 2MW turbines in Eastern Canada.

The results of the case study in Finland indicate that ice accretion affects the dynamics of the turbine. An imbalance in strain measured between two different blades during icing events suggests aerodynamic imbalance due to ice on blades simultaneously increasing tower base fatigue loads.

The study in Canada revealed that ice accretion on the rotor blades can induce higher tower oscillations and increase tower base fatigue loads.

Finally, the two cases support each other well. It can be concluded that icing can cause imbalances to the rotor that results in additional oscillations which should be considered during fatigue life design of wind turbines.

I. Nomenclature

agl = Above ground level
asl = Above sea level
CAM = Ice load (kg/m) measured on turbine 3 (Canada's WEC2) nacelle weather mast using a remote camera.
CAN = Canada
CBH = Cloud Base Height
CBH1 = Cloud Base Height from meteorological station 1 near T1 (Finland)
CBH2 = Cloud Base Height from meteorological station 2 near T1 (Finland)
CBHM2 = Cloud Base Height from Met mast (MMV2) in Canada
F&A = Normalised peak amplitude of first natural frequency from FFT analysis of tower accelerations in the x-direction tower top reference coordinate system (fore-and-aft sway).
FFT = Fast Fourrier Transform
FFT1 = Amplitude of first natural frequency of FFT
FIN = Finland
h = hour
IE = Icing event
LTIC = Low Temperature and Icing Climate
MET = Two meteorological stations near T1 (<60km)
min = minute
MM1 = Meteorological Mast in Finland
MM2 = Meteorological Mast in Canada (MMV2)
Mxf3 = Normalised tower base Moment in x-direction with respect to tower base coordinate system, turbine 3 (Canada's WEC2)
Myb11 = Normalised blade Moment in y-direction with respect to blade coordinate system, turbine 1 (Finland), blade 1
Myb12 = Normalised blade Moment in y-direction with respect to blade coordinate system, turbine 1 (Finland), blade 2
Myb3 = Normalised blade Moment in y-direction with respect to blade coordinate system, turbine 3 (Canada's WEC2)
Myf1 = Normalised tower base Moment in y-direction with respect to tower base coordinate system, turbine 1 (Finland)
Myf3 = Normalised tower base Moment in y-direction with respect to tower base coordinate system, turbine 3 (Canada's WEC2)
NY1 = Nacelle Yaw position on turbine 1 (Finland)
NY2 = Nacelle Yaw position on turbine 2 (Canada's WEC1)
NY3 = Nacelle Yaw position on turbine 3 (Canada's WEC2)
OS1= Operating State on turbine 1
OS2= Operating State on turbine 2
OS3= Operating State on turbine 3
P1 = Output power on turbine 1 (Finland)
P2 = Output power on turbine 2 (Canada's WEC1)
P3 = Output power on turbine 3 (Canada's WEC2)
RaR = Rivière-au-Renard wind farm, Quebec, Canada
rpm = Revolutions per minute

S2S = Normalised peak amplitude of first natural frequency from FFT analysis of tower accelerations in the y-direction tower top reference coordinate system (side-to-side sway).
SNEEC = Site Nordique Expérimental en Éolien CORUS
T1 = Wind Turbine 1 – Finland
T2 = Wind Turbine 1 – Canada (WEC1)
T3 = Wind Turbine 2 – Canada (WEC2)
TCE = TechnoCentre Éolien
TI = Turbulence intensity
TM1 = Temperature from met mast 1 (Finland)
TM2 = Temperature from met mast 2 (Canada)
TSA = Time Synchronous Average
W1 = Winter 2011-2012 from November-April
W2 = Winter 2012-2013 from November-April
WEC = Wind Energy Converter
WS11 = Wind Speed on turbine 1 (Finland), heated
WS21 = Wind Speed on turbine 2 (Canada), heated
WS22 = Wind Speed on turbine 2 (Canada), non-heated
WS31 = Wind Speed on turbine 3 (Canada), heated
WS32 = Wind Speed on turbine 3 (Canada), non-heated
WSM11 = Wind Speed on Met mast 1 (Finland), heated
WSM12 = Wind Speed on Met mast 1 (Finland), non-heated
WSM21 = Wind Speed on Met mast 2 (Canada), heated
WSM22 = Wind Speed on Met mast 2 (Canada), non-heated

II. Introduction

Wind energy has had a significant boost in the 21st century regarding technology development, world-wide investment and wind turbine installation figures. As easily accessible, good wind resource sites rapidly decrease, potential wind resources are seeked outside IEC standard [2] wind energy climates at an increasing rate to fulfill international sustainable energy goals.

Wind energy in low temperature and icing climate (LTIC) can be considered as one of the largest, non-standard climates, in wind energy today. As of the beginning of 2013, 69 GW (24% of global wind energy capacity) were installed in LTIC. Another 50GW are expected to be installed in LTIC by 2017 (20% of global forecast) indicating significant forecasted growth for wind energy in LTIC [3]. However, ice accretion on wind turbine blades in LTIC can lead to production losses, requires risk management associated with ice throw and may decrease turbine lifetime. Blade ice accretion is typically a result of exposure to supercooled liquid water (in-cloud or meteorological icing) or freezing rain. A typical modern 3 MW turbine with a tower height of 100 m and rotor diameter of 120m will have a tip height of 160 m above ground level (agl). Such a turbine will have a substantially higher risk of being exposed to low-level cloud base height (CBH) in sub-zero temperatures than older turbines with tip heights below 100 m. Therefor in-cloud icing induced problems for wind turbines are likely to increase in the future if no preventive measures, such as blade ice prevention systems, are used.

Currently, large scale and detailed research of ice induced problems on wind turbines is scarce and more recent research efforts have focused on ice accretions aerodynamics [9,10,11], load analysis from small, stall controlled wind turbines [12] and simple aerodynamic penalty formulation for new icing design load cases [13,14]. The duration and severity of ice induced problems to modern MW-scale turbines is relatively unknown and the focus of this paper is to give more insight to this untouched research area.

III. Datasets

In this study, three different datasets were used from two sites; one dataset from Southern Finland (FIN) and two datasets from Eastern Canada (CAN). All data from turbines and met masts are presented in mean 10 minute time intervals unless stated otherwise. For both sites, component loads were measured with strain gages from blade root (Mxb,Myb), and tower base (Mxf,Myf) according Figure 1 coordinate system description. Turbine oscillations were measured with accelerometers located in T2 nacelle. All signals used in FIN and CAN cases are summarized in Table 1.

A. Case FIN site description

In Case FIN, a megawatt (MW) scale turbine (T1) is located in a small wind farm near the coastline of Southern Finland. T1 has a hub height 100 m above sea level (asl) and the blade tip height of 130 m asl. The following measurements were recorded from T1 between December 2007 and January 2010 and used in the analysis presented herein:

- Power output (P1)
- Wind speed from heated cup anemometer (WS11)
- Nacelle yaw angle (NY1)
- Turbine operating state (OS1)
- Blade#1,2 flapwise bending moment (Myb11,12)
- Tower base fore-aft bending moment (Myf1)

Nacelle yaw angle was used in combination with tower base strain gages to calculate tower base loads following the rotating nacelle according to tower base coordinate system in Figure 1. The strain gage measurements from T1 were conducted according to relevant IEC standard to obtain component mechanical loads for blade root (Myb) and tower base bending moments (Myf) [7]. Site temperature (TM1) and wind (WS11,12) measurements were recorded at hub height from site met mast (MM1) 300 m from T1. In addition, two nearby meteorological stations measuring cloud base height asl (CBH1,2) were used as meteorological icing indicators.

B. Case CAN site description

In case CAN, data from two identical MW-scale turbines (T2,T3) as well as from a 126m met mast (MM2) were analysed.

The turbines and the met mast are located at TCE's Site Nordique Expérimental en Éolien CORUS (SNEEC), also known as the Rivière-au-Renard (RaR) windfarm in eastern Canada. The analysis presented herein are based on the following measurements from T2 and T3. T2 measurement campaign was taken between December 2011 and April 2013 and for T3 between December 2011 and May 2012 :

- T2 and T3 wind speed from heated/unheated anemometers (WS21,22, WS31,32)
- T2 and T3 nacelle yaw angle (NY2, NY3)
- T2 side-to-side and fore-and-aft nacelle oscillations (S2S and F&A: Yk- and Xk- directions respectively according to tower top coordinate system shown in Figure 1)
- T2 and T3 operating states (OS2,3)
- T3's nacelle weather mast ice load (CAM pictures)
- T3's blade flapwise and edgewise bending moments (Myb3,Mxb3)
- T3's tower base fore-and-aft and side-to-side bending moments (Myf3, Mxf3)

Site met mast (MM2) has wind speed measurements with a pair of heated/unheated cup anemometers (WSM21,22) as well as cloud base height (CBHM2, available from 2012.2.22) and temperature measurements (TM2) that were used as icing event indicators.

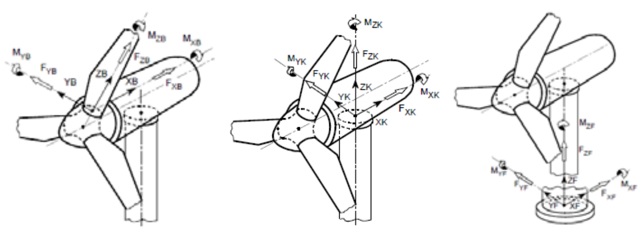

Figure 1: Turbine component coordinate systems, left: blade coordinate, middle: tower top coordinate, right: tower base coordinate system [16]

Table 1: List of signals analysed in FIN and CAN cases

FIN			CAN		
T1	**MM1**	**MET**	**T2**	**T3**	**MM2**
P1 [kW]	TM1 [C]	CBH1 [m]	P2 [kW]	P3 [kW]	WSM21 [m/s]
WS11 [m/s]	WSM11 [m/s]	CBH2 [m]	WS21 [m/s]	WS31 [m/s]	WSM22 [m/s]
NY1 [deg]	WSM12 [m/s]		WS22 [m/s]	WS32 [m/s]	CBHM2 [m]
Myb11 [kNm]			WD2 [°abs]	NY3 [deg]	TM2 [°C]
Myb12 [kNm]			S2S [-]	Myb3 [kNm]	
Myf1 [kNm]			F&A [-]	Mxb3 [kNm]	
OS1 [-]			Holo [-]	Myf3 [kNm]	
			OS2 [-]	Mxf3 [kNm]	
				CAM [-]	
				OS3 [-]	

IV. Methodology

A. *Case FIN*

For ice detection indication, three separate methods were used as on-off criteria and summarized in Table 2. As method #0, a pair of heated/unheated cup anemometers (Table 1 : WSM11,12) in met mast MM1 were used to indicate instrumental icing duration. In order to minimize the amount of false alarms for method #0, 0.5 h of continuous underperformance for unheated anemometer WSM12 was selected. In addition to method #0 (instrumental icing indicator), method #1 presents two nearby (<60 km from site) meteorological stations with CBH measurements (CBH1,2) in combination with site met mast temperature (TM1) measurements. CBH1,2 and TM1 measurements were used in analyses as active meteorological icing (in-cloud icing) indicators according to method presented by Bernstein, Makkonen, Järvinen [15]. As a final icing indicator method #2, T1 output power loss versus reference, calculated output power curve was used as a third icing indicator. The three different icing indicator methods and respective on-off criteria thresholds are summarized in Table 2. Icing indicator methods #1 or #2 were grouped as one icing warning signal called « Ice Warning » and icing indicator method #0 « InstrIce » was treated separately.

Table 2: List of ice detection methods for case FIN

#	**Icing indicator criteria**	**Name**
0	**IF** WSM12 < 80% of WSM11 for > 0.5h	**InstrIce**
1	CBH1,2 < 150 m **AND** TmpM1 < 0 C **OR**	**Ice Warning**
2	TM1 < 0 C **AND** P1 < 85% ref for > 1h	

Figure 2 summarizes all icing indicators for time period December 2007 to January 2010. Figure 2 results are presented as on-off criteria. If Table 2 icing indicator criteria is fulfilled, it is plotted in Figure 2. Summed alarm hours are presented in top right corner. A high icing risk occurs when all indicator are positive.

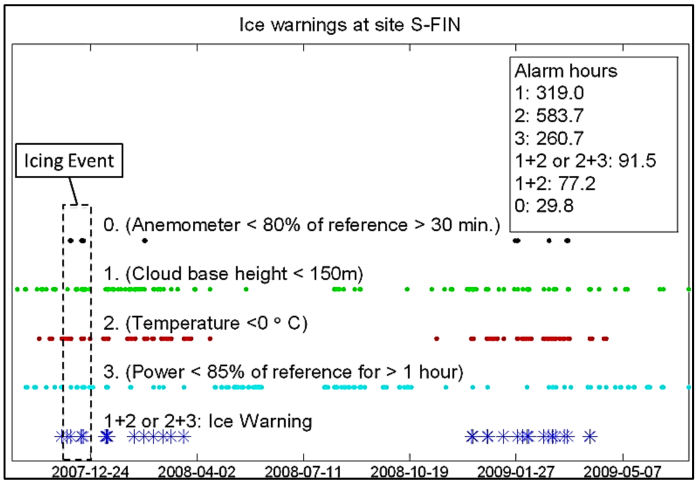

Figure 2: Case FIN icing indicators and durations

Before evaluating icing event effects more closely on output power and loads for turbine T1, a reference, non-iced dataset called baseline values is needed. Baseline values are then compared to icing event values in order to detect and evaluate non-normal turbine behaviour. Baseline values for turbine outout power (P1), blade (Myb1) and tower (Myf1) loads were calculated as a function of turbine wind speed (WS11, 1m/s bin), turbulence intensity (2% bin), nacelle yaw angle (NY1, taking into account wake effects from neighbouring turbines), turbine state (OS1, power production states only) and temperature (TM1) > 0 C according to relevant IEC standard [7]. As a result, a 3-dimensional capture matrix of baseline values is created describing normal operational values. For component load analysis, two calculation methods for each 10 min timeseries were used:

- short-term damage equivalent load (DEL) methodology via signal Rainflow counting and
- 10 min mean values.

To insure that capture matrix results were statistically significancant, all capture matrix bins had at least 20x10 min datapoints and interpolation was used to increase accuracy for results between bins.

When all Table 2 icing risk indicators where positive (meaning high risk of meteorological icing), potential icing event case values were compared to baseline values using Equation 1.

$$Relative = \frac{Iced_{f(WS11,TI,NY1,TM1)}}{Baseline_{f(WS11,TI,NY1,TM1)}} \quad (1)$$

Relative values then indicate, if icing event values were above or below normal, non-iced baseline values (for a long term average, a relative value of 1.0 indicates normal operational values for the selected signal). Due to variance in measured data, minimum and maximum thresholds for normal, non-iced operational values were needed in order to detect abnormal behaviour of the turbine. It was determined that if 80% of baseline data (cutting out top 10 % or 90th percentile and minimum 10 % or 10th percentile of all baseline values, respectively) is continuously within its limits, the data represents normal, non-iced operational values. This 80% limit represents a simple analysis method as it does not take into account varying wind speed, turbulence intensity and nacelle angle effects thus increasing the uncertainty of the method. However for this paper, the 80 % limit is used as a threshold to detect abnormal behaviour during icing events.

B. Case CAN

Icing events in RaR were determined using two different ice detection methods. The first method, as in case FIN, was based on instrumental icing which consisted in using a pair of heated/unheated anemometers (Table 1 : WS21,22) located on T2's nacelle weather mast. The methodology described in Table 3 was applied to determine when the unheated anemometer was disturbed by ice. The second method consisted in processing 10 min interval pictures of T3's nacelle weather mast (Table 1 : CAM). These pictures were also used to assess the progression of ice load during events [7], [17]. Typically rime ice load is measured as kg/m. However, for glaze icing events presented here, a new ice load calculation method was used in order to have a more representative quantification of icing severity and ease the comparison to pictures of iced blades. Event's glaze loads are calculated using equation 2 [18].

$$Glaze\ Ice\ Load\ (kg/m^2) = \gamma * t \quad (2)$$

$\gamma = ice\ density\ (900\ kg/m^3)$
$t = ice\ thickness\ on\ met\ mast\ (m)$

Table 3 : List of ice detection methods for case CAN

#	**Icing indicator criteria**
0	**IF** WS22 < 80% of Wnd21 for WS21 > 5 m/s
1	**IF** CAM's met mast pictures show ice

Icing events detected using both detection methods for winter 2011-2012 (W1) and winter 2012-2013 (W2) are shown in Figure 3.

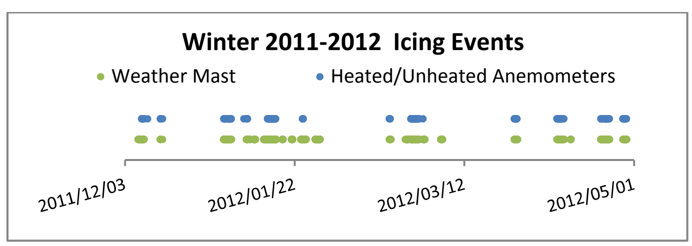

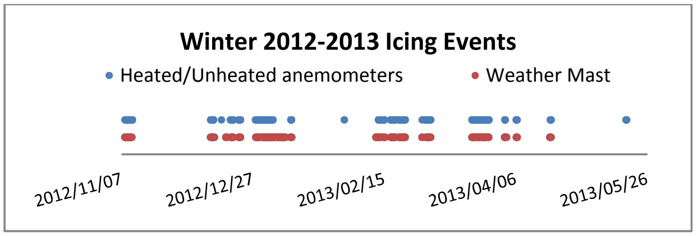

Figure 3: Case CAN W1 and W2 Icing Events

1) *Tower Oscillations:* The processed signals used to analyse tower oscillations on T2 were taken from Turbine PhD, a health monitoring system developped by NRG Systems. They represent the amplitudes of the first natural frequency of the tower determined by a Fast Fourrier Transform (FFT) conducted on a reconstructed sway cycle with approximately 45 seconds of accelerations (or as a minimum requirement, three rotor revolutions) using Time Synchronous Averaging (TSA) [19]. This amplitude is hereafter referred to as FFT1. FFT1 for tower sway is, in principle, calculated every 10 minutes. As the original purpose of PhD Turbine was mainly focused on health monitoring of the gearbox, data is not recorded on a regular basis and time between 2 records can vary from 9 minutes up to 2 days. This is particularly true for W1 where only 13 % of the data intervals were below 11 minutes. For this winter the average time interval between data was 23 minutes.

Due mainly to this limitation but also to other circumstances (such as grid failure, turbine maintenance, etc) that may affect data availability, tower oscillation data is available for 42 % of the winters.

Baseline (non-iced) values for T2 oscillations were calculated as a function of wind speed (WS21, with 2 m/s bin), turbulence intensity (2 % bin), nacelle position (NY2, excluding wake effect from T3), T2 operating state (running in main operation) and instrumental icing (excluding hours of iced unheated anemometer). Similar to case FIN, a baseline capture matrix of normal operational values was created.

In order to have statistically significant reference values, bins with less than 12 data points were rejected and no extrapolations were made for wind speed and turbulence intensity over 20 m/s and 20 % respectively (due to lack of data). An additional 3 % of the data were rejected due to this quality control.

Following the same methodology as in the FIN case, relative values were calculated using Equation 1 and a normal behaviour limit was established such that 80% of the baseline values are within this threshold. For relative values over the threshold, the tower oscillations are considered non-normal. Relative values for tower sway in the fore-and-aft direction as well as the side-to-side direction are referred to herein as F&A and S2S respectively.

2) *Strain Gage Measurements:* Similarly as for case FIN, baseline, non-iced values for blade (Myb3, Mxb3) and tower (Myf3, Mxf3) loads were calculated as a function of turbine wind speed (WS31, 1m/s bin), turbulence intensity (4% bin), nacelle yaw angle (NY3, taking into account wake effects from T2), turbine operating state (power production only), excluding low wind speeds (< 5 m/s) and excluding icing events determined in Table 3. As a result, a 3-dimensional capture matrix of baseline values was created describing normal operational values of short-term damage equivalent loads (DEL) and 10 min mean values.

To insure that capture matrix results were statistically significancant, all capture matrix bins had at least 6x10 min of datapoints and interpolation was used to increase accuracy for results between bins.

As a result of above filters used, the duration of available Mxf3 and Myf3 fatigue load data reduces. For example when looking from Table 5 at W1-IE3 that had an instrumental icing duration of 51 h for T3, wind speed, power production and minimum number of datapoint filters reduced the usable fatigue data to 85 %. As a summary for winter 2011-2012, 254 h of usable T2 fatigue load data (representing 58 % of total instrumental icing duration of 439 h) is used in the analysis as a result of the above data filters used.

When method #0 from Table 3 indicated icing, the load values were compared to baseline values using Equation 1. Normal behaviour limit was established such that 80% of the reference values are within this threshold.

As an example, Figure 4 presents 12h of normal, baseline T3 operation defined by the 80 % baseline variance thresholds of output power and tower base fatigue loads. Figure 4 a) shows the wind speed and turbulence intensity and Figure 4 b) the nacelle yaw angle with wake sector marked in red. Figure 4 c) shows that the output power is within normal variance because all the datapoints are with baseline threshold values of 1.09 and 0.82 for maximum-minumum thresholds respectively. Tower base fatigue loads (Figure 4 d-e) have some individual points above upper baseline threshold value of 1.2 but are not continuously above threshold values for long periods of time. A 1 h moving average (seen as black dots) for output power and tower base fatigue loads were used in Figure 4 c-e) to smoothen out variations in measured 10 min signals.

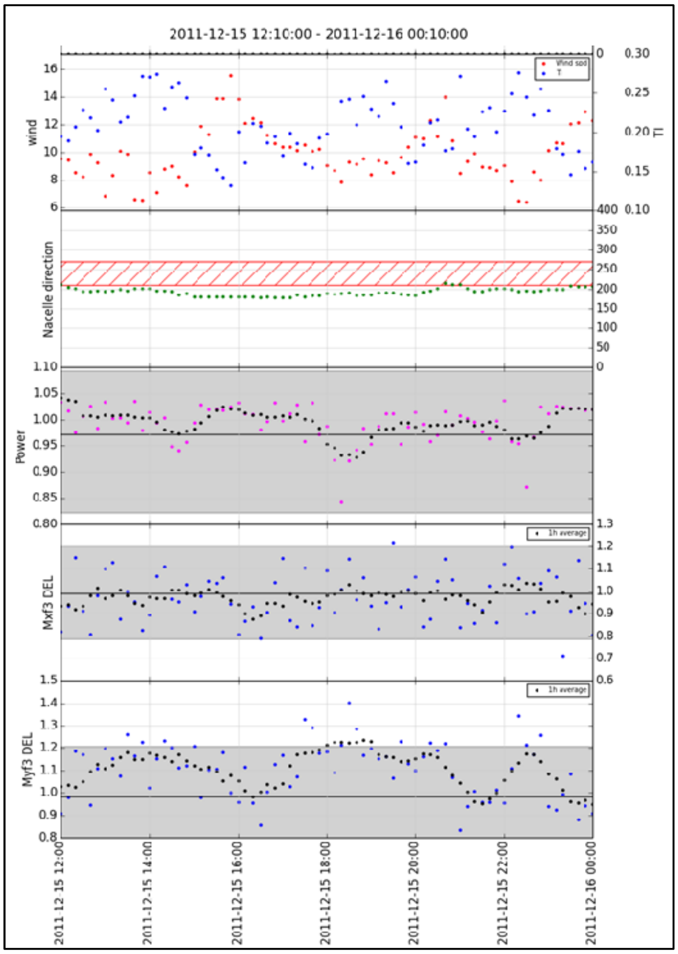

Figure 4: Example of T3 non-iced, baseline operational values, from top-down:
a) WS21: 10min mean and TI
b) Nacelle yaw angle (NY3) with wake sector in red
c) Relative power (P3) with 80 % baseline threhold in grey and 1h moving average
d) Relative tower base S2S fatigue load (Mxf3) with 80 % baseline threshold and 1h moving average
e) Relative tower base F&A fatigue load (Myf3) with 80 % baseline threshold and 1h moving average

V. Results

A. Example 1: Case FIN icing event

In Figure 2, one potential icing event is identified with dashed lines where all icing indicators show increasing icing risk. Figure 5 zooms closer to the icing event identified in Figure 2.

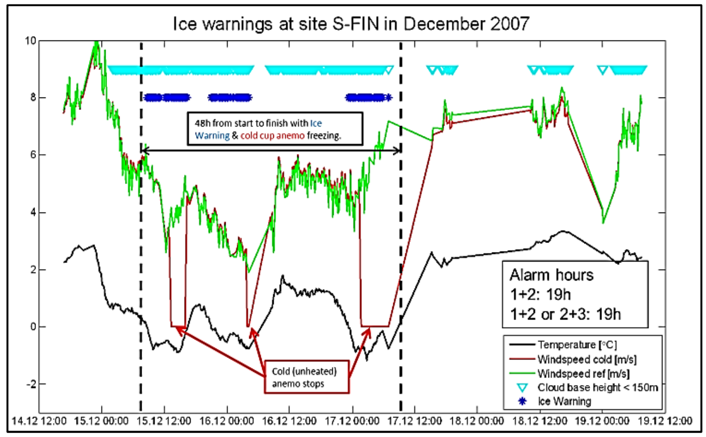

Figure 5: Case FIN icing event: meteorological and instrumental icing

During the FIN icing event, below turbine tip height clouds CBH1,2 (cayan triangle) were observed from two nearby meteorological stations respectively. The icing event consisted of three shorter active icing periods mainly due to flucuating temperature around 0 C. From start to finish, low level clouds were observed in total for about 48 h. During these low level clouds, 19 h of meteorological icing clearly affected the unheated cup anemometer which stopped three times for a total of 12 hours.

Figure 6 presents the effects of the FIN icing event on the turbine output power, blade and tower fatigue loads. On top, Figure 6 a) shows the Ice Warning, mean wind speed and temperature The icing event also influenced the behaviour of the wind turbine. In Figure 6 b) and c), mean relative power and effects to blade Myb11,12 relative loads are seen during Ice Warning indicating that icing has decreased the aerodynamic efficiency of the blades. In Figure 6 d), the blade#2 mean Myb12 loads are compared to blade#1 Myb11 simultaneous load behaviour that clearly deviates from normal operational behaviour which is defined by the "grey tube" representing 80 % of baseline values. During Ice Warning, there is on average a 4 % mean flapwise bending moment deviation between Myb11 and Myb12 resulting to aerodynamic imbalance of the rotor. This imbalance is simultaneously visible as increased tower base Myf1 fatigue loads. Due to high variation on relative tower fatigue Myf1 values, a moving 3 h average was used to better capture the tower base fatigue loading trend which is elevated above threshold values between 2007.12.15 and 2007.12.17 in Figure 6 e). After Ice Warning ends and the wind re-energizes on 2007.12.19, T1 output power, blade and tower loads return to normal, baseline values within the "grey tube".

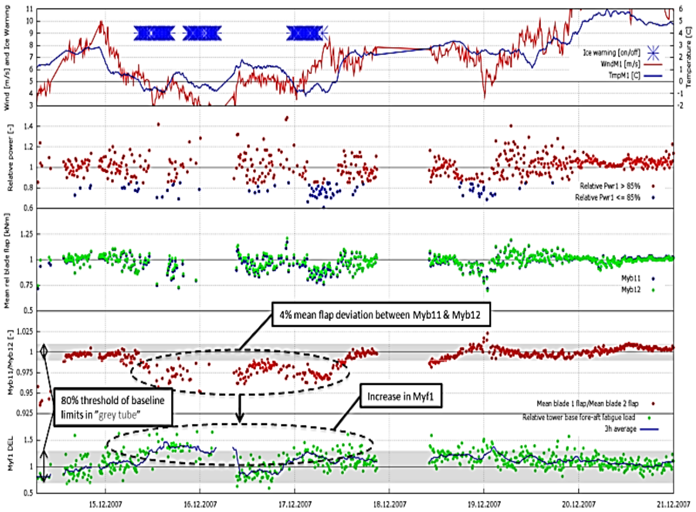

Figure 6: Case FIN icing event effects on T1, from top-down:
a) wind speed, temperature and Ice Warning
b) relative output power
c) blade#1,2 relative flapwise bending moment
d) mean blade#1/blade#2 flapwise bending moment with 80% baseline threshold
e) relative tower base fatigue loads with 80% baseline threshold

Figure 7 presents the relative mean (left) and fatigue load (right) effects for turbine blade and tower, Myb11,12 and Myf1 respectively, as a function of wind speed. During the FIN icing event, both blades Myb11,12 and tower Myf1 mean loads decrease versus baseline loads. The reduced aerodynamic efficiency of the iced blades lower the static rotor thrust force on the tower and this in return lowers the relative tower mean base load Myf1.

The relative fatigue loads for Myb11,12 and Myf1 during the icing event are presented in Figure 7 (right) as a function of wind speed. Blade Myb11,12 relative fatigue loads are all below baseline values indicating that individual iced blades fatigue loads do not increase. However, an increase in tower base relative Myf1 fatigue loads is more clearly seen. In total, 14 h of above threshold Myf1 fatigue loads are recorded during the icing event.

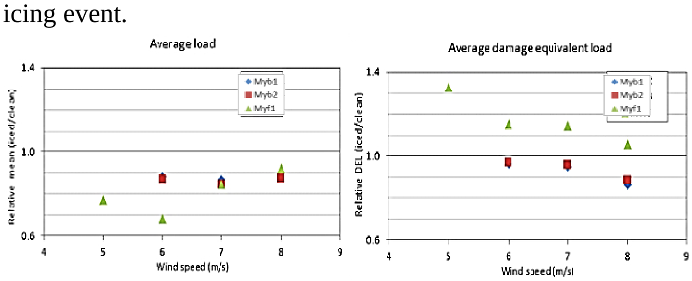

Figure 7: Icing event effects on turbine relative mean (left) and fatigue (right) loads for blades and tower base

B. Example 2: TCE January 2012 glaze event

Between 2012.01.13 and 2012.01.16 a significant freezing rain event (W1-IE05) occurred covering the RaR windfarm in glaze. During this event T2's unheated anemometer was disturbed by ice for 59 hours. Image analysis of T3 weather mast indicated a maximum glaze ice load of 5.5 kg/m^2 (equation 2) on the 2012.01.14. Pictures taken from the ground confirmed the presence of glaze on the blades on 2012.01.16, around 15:00 Eastern time (see Figure 8).

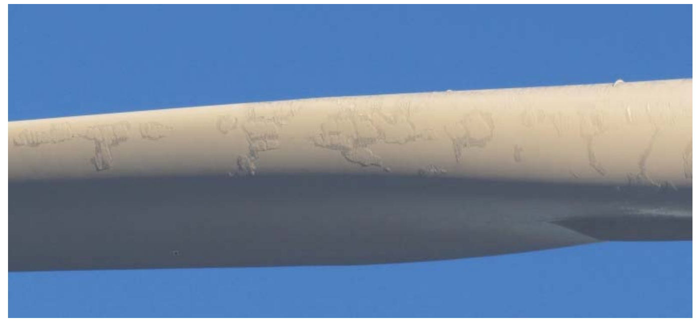

Figure 8: Glaze still present on T2 blades on 2012.01.16 around 15:00.

Figure 9 presents results of multiple ice detection methods, turbine output power as well as the tower base fatigue loads. Available signals were analysed with similar methods as for case FIN. Low winds (WS31 > 5 m/s), non power production states (P3 < 0 kW) and statistically uncertain environmental conditions [N < 6 for winds f(WS31, TI, NY3] were rejected from the analysis in order to decrease data scatter and focus on relevant and statistically significant conditions for fatigue load analysis (removed datapoints visible as grey crosses in Figure 9 b-f). In Figure 9 a), the meteorological and instrumental icing event progress was defined from 7 available ice detection signals all as on-off criteria except glaze ice load (CAM). Icing event effects on the turbine were measured by output power loss (Table 2, method #2) showing that power losses were observed only at the beginning of W1-IE05 between 2012.01.12 06:00 and 2012.01.13 22:00. Meteorological icing was detected by using a dedicated ice sensor (Holo) showing similar icing event start time as for turbine power losses.

Instrumental icing was detected from both turbines T2 and T3 and from onsite met mast MM2. The two turbines and met mast used instrumental ice detection with heated/unheated cup anemometer pairs with Table 3 method #0. The selected T3 instrumental icing start-stop times are made clearly visible in all Figure 9 a-e with the diagonal light blue bar. A webcam (CAM) was used on T3 to detect ice load.

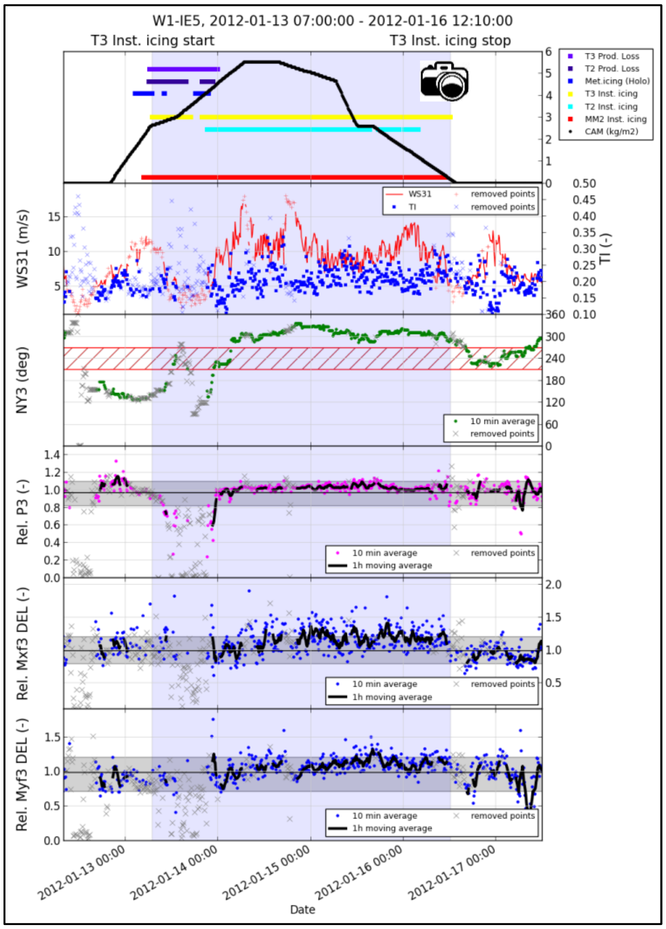

Figure 9: Case CAN icing event W1-IE05 effects on T3, from top-down:
a) Ice detection: T2 and T3 power loss, atmospheric icing with Holo, instrumental icing with T2 and T3 heated/unheated anemometers, MM2; heated/unheated anemeoters , ice load (CAM) at 80 m agl and camera silhouette indicating time of Figure 8 photo
b) WS31: 10min mean and TI with removed datapoints in grey crosses
c) Nacelle yaw angle (NY3) with wake sector in red
d) Relative power (P3) with 80 % baseline threshold in grey
e) Relative tower base S2S fatigue load (Mxf3) with 80 % baseline threshold and 1h moving average
f) Relative tower base F&A fatigue load (Myf3) with 80 % baseline threshold and 1h moving average

Figure 9 b) presents the W1-IE05 10min mean wind speed and turbulence intensity. Figure 9 c) presents the nacelle yaw angle (NY3) during the icing event showing that most of the time T3 is not in a wake sector. Figure 9 d) shows the relative output power which has dramatically dropped below baseline values during the start of W1-IE05 but this is more likely caused by very low winds (<5 m/s), wake sector effects (seen as high turbulence values of >25 %) and the nacelle yaw changes on 2012-01-13 (see Figure 9 b-c) than by reduced efficiency of iced blades. Figure 9 e-f) shows the relative tower base S2S (Mxf3) and F&A (Myf3) fatigue loads during W1-IE05. Tower base fatigue loads seem to decrease during turbine power loss periods but, again, very low winds, wake sector effects and the nacelle yaw changes are the most probable causes for these results. The wind re-energizes during instrumental icing period between 2012.01.13 06:10 and 2012.01.16 12:10 for a total of 77h (light blue diagonal bar in all Figure 9 a-f)). As seen in Figure 9 e) during this time period, the 1 h average Mxf3 fatigue load exceeds occasionally the upper threshold limit ("grey tube") for baseline values but still high variation in Mxf3 values is clearly visible. In total, 44 % of Mxf3 and 23 % of Myf3 fatigue load values during W1-IE05 are above baseline threshold values, respectively. Tower base fatigue loads return to normal operational values simutaneously as instrumental icing ends but this may also be a result of T3 being influenced by T2 wake.

T2 tower oscillation data for the same glaze event (W1-IE05) is provided in Figure 10. On 2012.01.14, during maximum measured glaze ice load, T2 tower oscillations exceeded the set threshold significantly for a few hours then continued to exceed threshold values for the remainder of the duration of the instrumental icing event. Non-normal ice induced oscillations occurred for 50 % of the data available for this event (estimated 29.5 h).

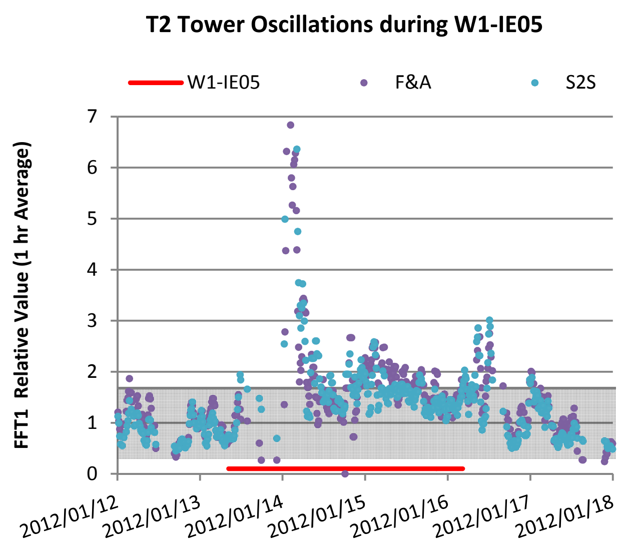

Figure 10 : T2 tower oscillations (F&A and S2S) and instrumental icing (red line) during a glaze event.

C. CAN summary of winters 2011-2012 & 2012-2013

Table 5 summarizes all relevant icing events at CAN site during winters 2011-2012 and 2012-2013 for T2 and T3. In total, 12 icing events were recorded during winter 2011-2012 and 14 icing events during winter 2012-2013. Icing event start-stop times were selected based on the deviations of relevant turbine heated/unheated cup anemometers (instrumental icing). In total, instrumental icing durations from both winters varied significantly between one another, from 5h to 193h. Measured, average wind speed during most icing events of winter 2011-2012 were above 6 m/s indicating good power production and relevant fatigue load wind conditions for turbines T2,3.

During non-iced operation, non-normal S2S and F&A oscillations were defined to occur 10% of the time. The table shows that during certain events (highlighted in yellow), tower oscillations exceeded the 10% threshold suggesting that icing caused the amount of non-normal tower oscillations to increase. The duration of ice induced tower oscillations is estimated for each event. Note that for certain events there were not enough tower oscillation data available; these events were not considered for analysis.

In total, 6 out of 9 icing events (W1-IE03,05,06,08,09,11) with usable data, T2 and T3 show similar behaviour in terms of above baseline threshold values for tower oscillations and tower base fatigue loads. Measured maximum ice loads during these events vary from 0.5 to 3.7 kg/m for rime and 3.2 to 5.5 kg/m^2 for glaze ice.

The glaze event of January 2012 (W1-IE05) induced more oscillations on T2 than all other icing events of that winter, combined. Similarly, 44 % of Mxf3 fatigue loads were above threshold values (see Table 5) contributing to roughly 44 % of winter 2011-2012 T3 above baseline threshold fatigue loads.

Table 4 summarises individual icing events (listed in Table 5) as total increase in tower oscillations for T2 and tower base fatigue loads for T3 per winter and for the two winters combined. A total duration of ice induced tower oscillations and fatigue loads is estimated as well.

Table 4 : Above threshold tower oscillations and fatigue loads on T2 and T3

Winter	Duration of Instr. Icing from T2 with usable FFT data[1]	Duration of Instr. Icing from T3 with usable DEL data[1]	**Duration of ice induced vibrations above baseline threshold from usable data**			
			T2 oscillations		**T3 fatigue**	
			S2S	F&A	Mxf3	Myf3
2011-2012	207h	254 h	25% (47h)	15% (30h)	24% (61h)	10% (25h)
2012-2013	355h	N/A	35% (122h)	14% (51h)	N/A	N/A
Total	**562 h**	**254 h**	**30% (169h)**	**14% (81h)**	**24% (61h)**	**10% (25h)**

S2S tower oscillations on T2 were above threshold during icing events 25% for winter 2011-2012 and 35% of the time for winter 2012-2013. F&A tower oscillations on T2 were not as significantly affected by icing as S2S oscillations with 15% and 14% for winters 2011-2012 and 2012-2013 respectively. For the two winters combined, S2S and F&A oscillations above threshold during icing events 30% and 14% of the time respectively. These values are above the non-iced baseline variance of 10%.

For T3 during winter 2011-2012, 24% of the icing event time was above the baseline threshold for Mxf3. Results for Myf3, (10 %, Table 4) suggest that icing events on average did not cause excess fatigue loads compared to baseline load variance of 10 %.

During winter 2011-2012 and 2012-2013, ice seems to have induced more S2S above threshold oscillations than F&A for T2. T3 had increased occurance of Mxf3 values above threshold during icing events whereas Myf3 did not seem to be significantly affected during winter 2011-2012.

Some additional uncertainty is added to the results as the 80 % threshold simply uses all baseline data points as input and does not take individual wind speed, turbulence intensity and nacelle angle bin variance effects into account.

There is significant variance in non-normal oscillations from one event to another but the effect of ice on tower oscillations is not clearly linked to ice load, or ice type.

The duration of above threshold tower oscillations was greater in winter 2012-2013 than in winter 2011-2012. This seems to be proportional with duration of instrumental icing.

VI. Conclusions

For Case FIN, using meteorological station cloud base height data proved to be useful as an in-cloud icing indicator to increase ice detection reliability in flat terrain areas. The icing event in Case FIN resulted to an aerodynamic imbalance of the rotor which increased the tower base fore-aft fatigue loads.

For Case CAN, in summary, similar behaviour for T2 and T3 can be seen during the icing events supporting the conclusion that ice induced vibrations are increasing the tower oscillations and fatigue loads. The data from case CAN also suggests that side-to-side oscillations and loads are more affected by ice than in the fore-and-aft direction.

The percent of icing event time of increased oscillations and tower base fatigue load could be determined by comparing normal, above threshold variance values to similar above baseline threshold values during icing events. By correlating increase of ice induced oscillations with expected annual instrumental icing, one could use this as a basis for new design load cases based on IEA icing site classification [4], [20].

In order to evaluate the long-term effects of ice induced vibrations on turbine lifetime; a more thorough analysis of lifetime fatigue loads effects and correlations between tower oscillations and fatigue loads is required as well more as data from additional winters and different IEA icing site classification levels. Also investigations on choosing different start-stop times (e.g. meteorological icing) for icing event analysis will follow because especially the time above baseline threshold values for tower base fatigue loads were sensitive to the final results. The research presented here will continue under an international research project “IcedBlades” until 2015.

Acknowledgements

The authors would especially like to thank colleagues from VTT and TechnoCentre in supporting the work presented here.

[1] Actual number of hours of instrumental icing is greater, these numbers represent hours of instrumental icing where usable tower oscillation and fatigue load data was available.

References

[1] Lehtomäki, V. et al., IcedBlades - Modelling of ice accretion on rotor blades in a coupled wind turbine tool, WinterWind 2012 conference, Skellefteå, Sweden

[2] IEC 61400-1:2005 ed3, Wind Turbines – Part 1: Design requirements, International Electrotechnical Commission, 3, rue de Varembé, PO Box 131, CH-1211 Geneva 20, Switzerland

[3] BTM World Market Update 2013, Special Chapter: Cold Climate Turbines, Navigant Research, Copenhagen, Denmark

[4] IEA Wind TASK 19, Expert Group Study on Recommended Practices: 13. Wind Energy Project in Cold Climates, 1. Edition 2011, Approved by the Executive Committee of IEA Wind May 22, 2012.

[5] Baring-Gould, I. US Wind Market Overview, WinterWind 2011 conference

[6] Laakso, T. et al., IEA WIND TASK 19 WIND ENERGY IN COLD CLIMATES: Cold Climate Challenges, EWEA 2011 side event, Brussels, Belgium

[7] Wadham-Gagnon, M., et. al., Ice profile classification, based on ISO 12949, WinterWind 2013, Ostersund, Sweden.

[8] IEC 61400-13:2001 ed1,Wind turbine generator systems – Part 13: Measurement of mechanical loads, International Electrotechnical Commission, 3, rue de Varembé, PO Box 131, CH-1211 Geneva 20, Switzerland

[9] NASA/TP—2000-210031:Ice Accretions and Icing Effects for Modern Airfoils,

[10] Wind Turbine Performance under Icing Conditions, Quebec 2008

[11] Effect of High-Fidelity Ice-Accretion Simulations on Full-Scale Airfoil Performance, 2010

[12] Antikainen, P. et al., Wind turbine ice loads and vibration control, ISSN 1457-3350, VTT Energy Reports 3/2001

[13] Tammelin, B. at al., Wind energy production in cold climate (WECO), EU/JOULE3 JOR3-CT95-0014, 1998

[14] Tammelin, B. et al., Wind Turbines in Icing Environment: Improvement of Tools for Siting, Certification and Operation - NEW ICETOOLS, ISBN 951- 0782-6079, 2005

[15] Bernstein, B., Makkonen, L., Järvinen, E., European Icing Frequency Derived From Surface Observations, IWAIS XIII Andermatt, 2009

[16] Guideline for the certification of Wind Turbines, Germanischer Lloyd Industrial Services Gmbh – Renewables certification, 2010

[17] Bolduc, D., et. al., Field Measurement of Wind Turbine Icing, IWAIS 2013, St-Johns, Newfoundland.

[18] Atmospheric Icing of structures, ISO 12494, 2001

[19] Bechhoefer, E., Wadham-Gagnon, M., Boucher, B., Initial Condition Monitoring Experience on a Wind Turbine, Proceeding of the Annual Conference of the Prognostics and Health Management Society 2012, pp.63-70.

[20] Wadham-Gagnon, M., et al., et. al., Recommended Practices for Wind Energy in Cold Climates: Resource Assessment and Site Classification. IWAIS 2013, St-Johns, Newfoundland.

Table 5: Summary of icing events in RaR and ice induced vibrations on T2 as well as fatigue loads for T3 during W1 and W2 (yellow shading indicating above baseline values)

Icing Events	Icing Events Start date	Icing Events Duration (Hours)		Mean wind speed during IE (m/s)	Max Ice Load (kg/m)	Type	T2: % of Event Duration with usable FFT1 data[1]	T3: % of Event Duration with usable DEL data[2]	T2: % of event with above threshold oscillations		T3 Fatigue loads (DEL) above threshold	
		T2	T3						S2S	F&A	Mxf3	Myf3
W1-IE01	2011-12-07	41	40	10.8	1.2	rime	23%	N/A			N/A	N/A
W1-IE02	2011-12-13	17	16	4.3	0.9	rime	6%	N/A			N/A	N/A
W1-IE03	2012-01-01	52	51	8.2	1.4	rime	58%	85 %	26 %	4 %	18 %	5 %
W1-IE04	2012-01-07	25	28	5.6	3.7	rime	17%	41 %			16 %	0 %
W1-IE05	2012-01-13	57	77	9.9	5.5 *	glaze	68%	79 %	50 %	49 %	44 %	23 %
W1-IE06	2012-01-24	5	5	8.8	3.5*	glaze	68%	47 %	42 %	26 %	7 %	21 %
W1-IE07	2012-02-18	6	7	8.6	1.1	rime	52%	100 %	5 %	5 %	30 %	0 %
W1-IE08	2012-02-25	85	59	11.9	2.3	rime	48%	41 %	15 %	11 %	14 %	12 %
W1-IE09	2012-03-26	18	17	15.6	0.5	rime	68%	66 %	12 %	11 %	20 %	0 %
W1-IE10	2012-04-08	48	48	11.2	1.6	rime	46%	43 %	8 %	4 %	14 %	15 %
W1-IE11	2012-04-21	59	63	8.8	2.7	rime	48%	79 %	24 %	0 %	23 %	1 %
W1-IE12	2012-04-27	24	28	13.2	3.2*	glaze	56%	81 %	18 %	16 %	8 %	9 %
W2-IE01	2012-11-08	67	64	14.5	N/A	rime	78 %	N/A	52 %	21 %	N/A	N/A
W2-IE02	2012-12-10	27	36	9.9	N/A	rime	59 %	N/A	19 %	9 %	N/A	N/A
W2-IE03	2012-12-17	124	125	9.6	15,0	rime	23 %	N/A			N/A	N/A
W2-IE04	2012-12-27	160	193	13.4	6,4	soft rime	64 %	N/A	8 %	14 %	N/A	N/A
W2-IE05	2013-01-10	6	9	12.2	0,9	rime	100 %	N/A	3 %	20 %	N/A	N/A
W2-IE06	2013-02-12	57	68	11.5	1,2	rime	26 %	N/A			N/A	N/A
W2-IE07	2013-02-17	134	145	14.5	2,0	rime	61 %	N/A	52 %	19 %	N/A	N/A
W2-IE08	2013-03-01	51	53	11.0	2,3*	glaze	28 %	N/A			N/A	N/A
W2-IE09	2013-03-03	82	84	12.7	6,1	mixed	15 %	N/A			N/A	N/A
W2-IE10	2013-03-20	155	154	11.5	4,0	rime	50 %	N/A	42 %	5 %	N/A	N/A
W2-IE11	2013-04-01	7	9	11.3	0,3	rime	33%	N/A			N/A	N/A
W2-IE12	2013-04-06	7	8	13.6	0,4	rime	97%	N/A	39 %	5 %	N/A	N/A
W2-IE13	2013-04-19	8	7	12.0	0,8	mixed	53%	N/A	42 %	42 %	N/A	N/A
W2-IE14	2013-05-17	23	29	8.7	N/A	mixed	8%	N/A			N/A	N/A
		* Glaze ice load in kg/m^2 (Equation 2)										
		[1]: filters used: WS21 > 5m/s, T2 running in main operation										
		[2]: filters used: WS31 > 5m/s, P3 > 0 kW										

Forecasting Production Losses by Applying the Makkonen Icing Model to Wind Turbine Blades

Neil Davis* †‡, Andrea Hahmann*, Niels-Erik Clausen*, Mark Žagar‡, and Pierre Pinson§
*DTU Wind Energy, Danish Technical University
Roskilde, Denmark
†neda@dtu.dk
‡Vestas Wind Systems A/S
Aarhus Denmark
‡DTU Electro, Danish Technical University
Lyngby, Denmark

***Abstract*—In the work presented here, the iceBlade model is used to simulate ice growth on both an ISO standard cylinder and on a cylinder representing the blade airfoil, using inputs from an atmospheric model. The airfoil like approach has shown to better correlate with the periods of reduced production, which are believed to be due to icing. These results when coupled to a statistical model show improvements in production loss estimation compared to the standard Makkonen model approach, however the use of only results from the meteorological model are shown to perform similarly to models using the icing forecasts. The ability to accurately model wind turbine production losses due to icing can greatly improve the siting and power forecasting of wind energy projects in cold climates. Unlike wind speed, measuring icing directly is a challenging task, and current measurement techniques do not correlate well with periods of decreased production. Therefore, numerical modeling is required to gain a better understanding of the impact blade icing has on wind power production. The aviation industry has developed many advanced models for ice growth on airfoils, but these tend to be computationally expensive. For siting and power forecasting cheaper models such as iceBlade are required to ensure reasonable simulation times.**

***Keywords* — icing, Weather Forecasting and Research, wind energy**

I. Introduction

Wind energy is a growing part of electricity generation throughout the world. A substantial amount of this growth is taking place in areas defined as Cold Climate (CC), including regions prone to icing. BTM World Market Update 2012 included a chapter on Cold Climate Turbines [1], which estimated that 24% of current installed turbine capacity is located in CC. It was also estimated that 4% of turbines are located in heavy icing regions. Heavy icing is defined as regions where icing is expected to have a major impact on annual energy production. This capacity is expected to grow from 11.5 GW to 19.5 GW by 2017. IEA Task 19 – Wind Energy in Cold Climates has created a five tier classification for icing [2]. This classification scheme has 3 independent criteria relating to 1) meteorological icing, periods of when ice is under active accretion, 2) instrumental icing, periods when ice is impacting the observational equipment, and 3) energy production loss.

Due to the increasing capacity in icing regions, and the identification of energy production loss as a key criteria in determining the classification of icing sites, it is important to develop model based estimates of production loss for siting turbines in regions with icing potential. These models can also aid in providing the most accurate power forecast for the energy markets. Prior studies have investigated production loss by modeling ice accumulation on a standard cylinder and then determining a statistical relationship between the cylinder ice mass and the production loss. Ice growth is modeled using the Makkonen model [3], and most schemes include algorithms for melting, and sublimation [4], [5], [6]. This study expands on that technique by modifying the cylinder size and several of the input parameters to better represent a turbine blade, leading to the development of the iceBlade model. A previous study [7] has shown that the iceBlade model better represents periods of production loss, compared with the standard cylinder approach for a wind farm in Northern Sweden. This study expands on those findings by presenting a production loss model based on the results from the iceBlade model.

II. Observations

This study focuses on production and meteorological data from a wind farm in central Sweden. The wind farm consists of 48 Vestas V90 turbines. The dataset contains 10 minute average values for the month of January 2011 and includes nacelle measured wind speed and temperature and power production.

The data was quality assured using two counters provided with the dataset. The first counter provided the number of seconds out of 600 where the wind was within the operational range of the turbine. The second provided the number of seconds the turbine was running in normal operation. If either of these values deviated from the optimal value by more than 10s, those time-steps were flagged and dropped from the analysis. After the data cleansing, two turbines were dropped which contained less than 50% of the possible time-steps for the month, and three other turbines were dropped as they were slightly different models than the others, and would have complicated the analysis. This left 43 turbines in the study. These 43 turbines were then averaged to the farm level by taking the mean of all turbines at each time-step. Finally only the top of the hour time-steps were kept to match the hourly output of the meteorological model data.

III. Models

A. Icing Model

The icing model used in this study, iceBlade, uses the Makkonen [3] model to calculate ice accretion, and models the sublimation and total shedding ablation processes. Partial shedding is not included, and due to the implementation of the total shedding scheme, melting is not significant enough to be included. In iceBlade, the turbine blade is represented as a cylinder for all equations except the heat and mass transfer coefficients. The heat and mass transfer coefficients are calculated on an airfoil, as defined in [8]. While the turbine blade is represented as a cylinder several changes from the standard cylinder approach have been made to better represent the turbine blade. The diameter of the cylinder was changed from the standard 0.03 m to 0.144 m, which approximates the leading edge radius the blade used in the NREL 5 MW reference turbine, at 70% of the blade length. Additionally the ambient wind speed was converted to a blade relative wind speed at 85% of the blade length, using a generic RPM curve. This increased the wind speed at the icing contact point, and generally lead to an increased mass flux during ice accretion. Finally, a constant diameter was used for the cylinder, as the blade does not rotate around its acis as a rotating cyilinder would. Therfore the ice would not build cylindrically, but rather grow outward from the leading edge of the airfoil. Because the model uses a constant diameter cylinder, iceBlade uses the same time-step as the model output, in this case one hour.

The ablation model included both sublimation and total shedding. The total shedding algorithm was based on a threshold value of 0.5°C for 1 hour at which point all ice would be removed from the turbine blade. This approach was tuned to this specific site, and a more advanced shedding algorithm is currently under development. Ice sublimation is modeled using a modified version of the explicit solution from [9]. The modification was to account for the change in shape, from spherical to the airfoil profile in both the convective heat and mass transfer terms.

The inputs to the icing model were supplied by the atmospheric model for a grid cell representing the wind farm as described in the next section. A more detailed description of the icing model can be found in [7].

B. Atmospheric Model

To provide inputs to the icing model, the Weather Research & Forecasting model (WRF) version 3.3 [10] was used to simulate the atmospheric conditions for this region. The model was configured with 2 nested domains approximately centered on the wind farm, with resolutions of 30 km and 10 km. The atmospheric input and boundary data was provided by the the Global Forecast System's Final Analysis Product (FNL), and the sea surface temperatures were from the NOAA Optimum Interpolation Sea Surface Temperature (OISST) version 2. The FNL data was also used for grid based four dimensional data assimilation nudging on the outer nest. 63 vertical levels were used, with 26 levels in the lowest 1000 m. The model simulation was carried out by running three 10-day periods, with 24 hours of spin-up for each.

The physics options were the defaults of the RRTM longwave radiation scheme, Dudhia shortwave radiation scheme, the Noah Land Surface Model, and the Kain-Fritsch cumulus parameterization scheme, with the PBL being set to the MYJ scheme [11], and the microphysical scheme being the WSM5 scheme [12]. In [7], 9 WRF sensitivities were compared in their ability to estimate periods of icing. The tests included combinations of 3 PBL schemes and 3 microphysical schemes, of which the combination used here, MYJ /WSM5, was found to perform among the best.

For input to iceBlade, the key parameters of temperature, liquid water content, wind speed, pressure and humidity were output by the model directly. A separate liquid water content was output for both cloud water and cloud rain. The parameter of median volumetric diameter (MVD) is not output by the WSM5 scheme. For this parameter the algorithm presented in [13] was applied to a lumped LWC of cloud water and ice to calculate the MVD to be used in iceBlade using an N_c value of 250 cm^{-3}. As with the icing model, more details on the meteorological model setup and how the inputs were formulated for the icing model can be found in [7].

C. Production Loss Model

The production loss model is a statistically-based model which uses the outputs from the WRF and iceBlade models, fit to the wind farm average power deviation from the idealized power output. The first step in the process was fitting a LOESS regression, with a span of 0.3 $m\,s^{-1}$, to the observed power curve using only those values where the average wind farm temperature was above 0°C (Fig. 1). The regression line is used as the non-icing forecast and is an approximation of the wind farm power curve. Next, the deviation from the non-icing forecast, production loss, was calculated for each point in Fig. 1, and it is this value which was fit to the statistical model.

Five different statistical models were created and compared against the non-icing forecast and a legacy threshold model. In the threshold model, park production was estimated to be 0 MW during periods when the forecast temperature was below 0°C and the total cloud mixing ratio was greater than 0.05 g kg^{-1}. At all other times, the power value was estimated to be the non-icing forecast.

Of the five statistical models, the first model (Wrf) only uses parameters output from the WRF atmospheric model. This approach provides a baseline for how well the production loss can be estimated without the use of an icing model. The last four models use a mixture of the icing model output and WRF output. Mak and iB do not use any of the cloud variables from WRF and use the icing results from the standard cylinder icing

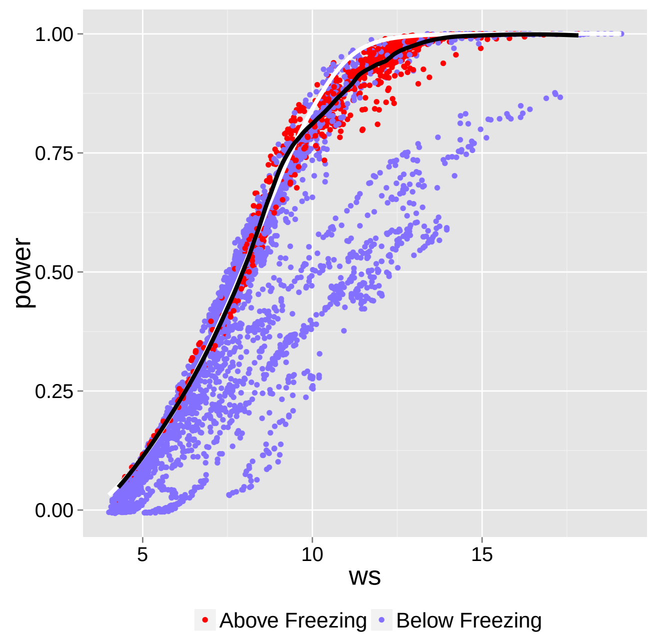

Figure 1. Wind park power curve with non-iced power forecast (black line) represented as a LOESS fit of the data. The white curve shows the idealized power curve. The blue data points are points where the temperature is below 0°C, while the red points are above 0°C.

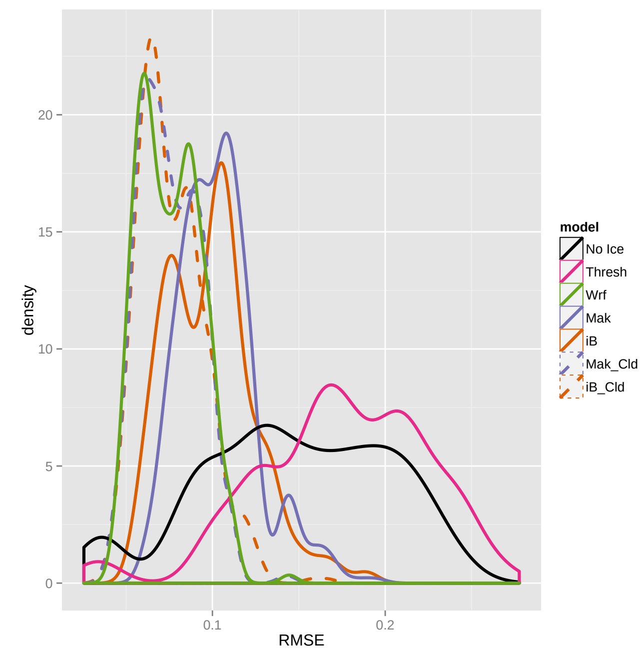

Figure 2. Density plots of the RMSE from each of the 495 model fits, at each of the wind farms. The different models are the non-ice power curve model (red), the threshold based model (green), the enhanced model (blue) and the ice only model(purple). The x-axis represents root mean squared error of the normalized power.

model, and iceBlade model respectively. Mak_Cld and iB_Cld include the WRF cloud parameters which improve the model fit.

The first guess model parameters were selected based on their correlation to the power loss. This was done using a cross correlation matrix allowing for the identification of parameters which were correlated with each other as well. In cases where two parameters were highly correlated both with the production loss and each other, only the parameter with the higher correlation to the production loss was kept. Ordinary least squares models were then fit to the entire dataset using all of the first guess parameters. In an iterative fashion, the parameter with the highest p-value was removed. The two models were then compared by examining the change mean bias, mean error, and adjusted R^2. Parameters were removed until the model performance significantly degraded upon parameter removal. Table I lists the final parameters used for each of the models. Due to the fits being obtained using the entire dataset there is a possibility of over-fitting, but given the limited amount of data, this risk was deemed reasonable. Future studies are planned to work with longer time periods to avoid this issue.

To evaluate the models, a k-fold cross validation technique was applied using a Monte Carlo approach. The Monte Carlo approach allowed the dataset to be extended to provide multiple model estimates. Under this approach, the hourly data was cut into 12 pieces. Those pieces were than combined into 495 different sets of 8 training pieces, and 4 test pieces. The results from each of these combinations were evaluated using root mean squared error (RMSE) and mean bias. Distribution plots were created to capture the variation in the model fits with the different training and model datasets, providing an estimate of model performance under a range of conditions.

IV. Results and Discussion

Fig. 1, shows that there is a large amount of spread for temperatures below 0°C, compared to temperatures above zero. This difference was larger for the individual turbines, likely due to the averaging of the temperature field. Since the average value was used it is reasonable to assume that for average temperature near 0°C, some turbines would be both above and below this critical value, leading to the possibility that some turbines may be ice free while others are iced. The degraded power near the knee of the power curve can be seen by comparing the idealized power curve (white), with the LOESS fit to the park averaged data (black). The idealized power curve provides power estimates significantly larger than the LOESS fit for wind speeds between 9 and 12.5 $\mathrm{m\,s^{-1}}$. With a larger dataset the park average power curve should more closely follow that of an individual turbine, as the temperature threshold could be set a few degrees away from 0°C, allowing more certainty that all turbines would be ice free. Additionally, a threshold which utilized the wind farm minimum temperature, rather than the average, may also lead to a better agreement between the wind farm power curve and the idealized power curve.

The model evaluation shown in Fig. 2 and Fig. 3 illustrates

Table I
PARAMETERS USED IN EACH OF THE MODEL FITS.

Model	WRF	Mak	iB	Mak_Cld	iB_Cld
Parameters	Estimated Power Temperature Cloud Ice	Estimated Power Temperature Sublimation	Estimated Power Temperature Sublimation Accumulated Ice Mass	Estimated Power Temperature Sublimation Cloud Ice	Estimated Power Temperature Sublimation Accumulated Ice Mass Cloud Ice Instantaneous Ice Mass

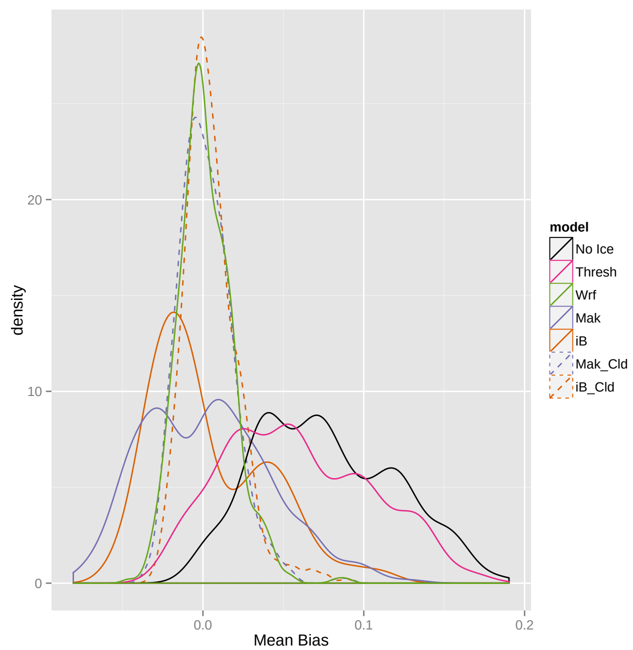

Figure 3. Same as Fig. 2, but analyzing the model mean bias.

the challenge in identifying the appropriate model. These plots show the density functions of the RMSE and mean bias for each of the 495 model fits. In both of these plots a perfect model would have a single peak at 0. Therefore a better model is identified by a distribution closer to zero with less spread.

The No Ice model (black line) is the baseline for these results, and represents the best possible non-iced model for this dataset. As the No Ice model was a LOESS fit of the nacelle wind speed and the observed power, there is no atmospheric model error in its result. The No Ice model has very little density near 0 in either of the RMSE or the bias plots, and has a very wide spread of errors, with a large plateau between 0.1 and 0.2 RMSE. The bias curves for the No Ice model are similar in shape to the RMSE curves, with a slight shift toward 0. The No Ice model is strongly biased to the positive, which is to be expected given the bulk of the points in Fig. 1 lie below the black curve.

The threshold model is found to have significantly larger RMSE than the No Ice model, but shifts the bias toward zero. This result was expected due to the design of the threshold model. Since the threshold model forecasts 0 MW of power during periods of active icing, it produces very large error during times when the farm is producing any power and the threshold is met, greatly increasing the RMSE. However, by reducing the total power estimate for the forecast period, the threshold model decreased the positive bias of the No Ice model leading to better model performance. In previous implementations, the threshold method was found to produce a symmetric bias for annual time-series. One possible explanation for the bias still remaining predominately on the positive side of 0 in this study, is the choice of hydrometeors selected for the threshold model. In [7], the WSM5 model was found to produce a large amount of cloud ice, which they proposed lead to the decreased the amount of cloud water in the WSM5 scheme. Based on the model fitting performed in this study, cloud ice was found to have the largest correlation with the power loss. The decision to exclude cloud ice from the threshold method was made to provide a better comparison with the iceBlade model, which does not have the capability of utilizing cloud ice at this time.

The WRF model outperforms all models except the iceBlade model with cloud ice. As this model only includes the cloud ice parameter, for identifying atmospheric moisture and therefore icing, it illustrates the importance of the cloud ice term for estimating icing, when using the WSM5 microphysical scheme. All five of the statistical models show a double peaked distribution in RMSE. This suggests that there was not always enough data in the training dataset to accurately forecast the test dataset. The iceBlade based models, iB and iB_Cld, show slight improvement in both RMSE and bias when compared with the standard cylinder approach, particularly when the cloud ice is not included in the statistical model fitting. This suggests that the iceBlade model is adding more value than just using the standard cylinder approach. However given how well the WRF model is performing, no icing models were required to obtain the same level of performance in this study, as the slight improvements offered by the iB_Cld model are likely not worth the effort of running the icing model.

V. CONCLUSIONS

In this study, it was shown that a statistically based model using inputs from both the iceBlade and WRF models, can more accurately estimate the power production of a wind farm which experiences icing, than the threshold based model. It has also been shown that a statistically based model using only the raw outputs from the WRF atmospheric model, can produce similar results to any model using iceBlade inputs, and better results than a statistically based model using only outputs from the icing model.

These results are due in part to the choice of microphysical scheme. As the icing models only include the liquid phases of the microphysical model, they do not include the hydrometeor which is most highly correlated with production loss from the atmospheric model, cloud ice. As shown in [7], this term is only dominant in the WSM5 scheme, and therefore had another scheme been used the results may have been dramatically different. This result suggests that there is a need to examine how best to incorporate the frozen hydrometeors from the WSM5 scheme into the iceBlade model to better represent turbine icing.

This study has several limitations, not the least of which is that it was only for 1 month, where significant icing induced losses occurred. Therefore more testing of the model framework needs to be completed before this approach can be successfully applied to wind farm siting analysis. Work is currently underway to enhance the model utilizing results from the TURBICE 2D icing model for airfoils, incorporating a more advanced shedding scheme, and adding frozen hydrometeors to the icing estimate.

REFERENCES

[1] Navigant Research, "Special Chapter: Cold Climate Turbines", in *BTM World Market Update*, chapter 7. Navigant Research, Copenhagen, Denmark, 2013.

[2] Göran Ronsten, Tomas Wallenius, Mira Hulkkonen, Ian Baring-Gould, René Cattin, Michael Durstewitz, Andreas Krenn, Timo Laakso, Antoine Lacroix, Lars Tallhaug, Øyvind Byrkjedal, and Esa Peltola, "State-of-the-Art of Wind Energy in Cold Climates", Tech. Rep., IEA Wind Task 19, 2012.

[3] Lasse Makkonen, "Models for the growth of rime, glaze, icicles and wet snow on structures", *Philosophical Transactions of the Royal Society A: Mathematical, Physical and Engineering Sciences*, vol. 358, no. 1776, pp. 2913–2939, November 2000.

[4] Roger Oechslin, *Wind Power Forecasting Considering Icing*, Msc., University of Innsbruck, Austria, 2011.

[5] Øyvind Byrkjedal, "Mapping of icing in Sweden – On the influence from icing on wind energy production", in *Winterwind*, Skellefteå, Sweden, 2012.

[6] Magnus Baltscheffky, "Modelling of production losses due to icing for individual turbines in a wind farm – development of techniques for forecasting and site assessment", in *Winterwind*, Östersund, Sweden, 2013.

[7] Neil Davis, Andrea N Hahmann, Niels-Erik Clausen, and Mark Žagar, "Forecast of Icing Events at a Wind Farm in Sweden", *Journal of Applied Meteorology and Climatology*, vol. Submitted, no. Submitted.

[8] S.a. Sherif, N. Pasumarthi, and C.S. Bartlett, "A semi-empirical model for heat transfer and ice accretion on aircraft wings in supercooled clouds", *Cold Regions Science and Technology*, vol. 26, no. 3, pp. 165–179, December 1997.

[9] R. C. Srivastava and J. L. Coen, "New Explicit Equations for the Accurate Calculation of the Growth and Evaporation of Hydrometeors by the Diffusion of Water Vapor", *Journal of the Atmospheric Sciences*, vol. 49, no. 17, pp. 1643–1651, September 1992.

[10] William C. Skamarock, Joseph B. Klemp, Jimy Dudhia, David O. Gill, Dale M. Barker, Michael G. Duda, Xiang-Yu Huang, Wei Wang, and Jordan G. Powers, "A Description of the Advanced Research WRF Version 3", 2008.

[11] Zaviša I. Janjić, "The Step-Mountain Eta Coordinate Model: Further Developments of the Convection, Viscous Sublayer, and Turbulence Closure Schemes", *Monthly Weather Review*, vol. 122, no. 5, pp. 927–945, May 1994.

[12] Song-You Hong, Jimy Dudhia, and Shu-Hua Chen, "A Revised Approach to Ice Microphysical Processes for the Bulk Parameterization of Clouds and Precipitation", *Monthly Weather Review*, vol. 132, no. 1, pp. 103–120, January 2004.

[13] Bjørn Egil Kringlebotn Nygaard, Jón Egill Kristjánsson, and Lasse Makkonen, "Prediction of In-Cloud Icing Conditions at Ground Level Using the WRF Model", *Journal of Applied Meteorology and Climatology*, vol. 50, no. 12, pp. 2445–2459, December 2011.

Session 3: Icing Measurement and Modeling

Wet-snow accumulation

A study of two severe events in complex terrain in Iceland

Árni Jón Elíasson
Landsnet
Reykjavik, Iceland
arnije@landsnet.is

Hálfdán Ágústsson
Reiknistofa í veðurfræði
Reykjavik, Iceland
halfdana@belgingur.is

Guðmundur M. Hannesson
EFLA Consulting Engineers
Reykjavik, Iceland
gudmundur.m.hannesson@efla.is

Abstract — On 10 September 2012 and 30 December 2012, two severe northeasterly wet-snow storms caused extreme ice load on many transmission and distribution lines in North Iceland. The wet-snow accretion was combined with strong winds, resulting in broken wooden poles and H-frame towers. The September event was exceptional because of extreme snowfall so early in the autumn. The snowfall was associated with average wind speeds in excess of 20 m/s, causing widespread accumulation of wet snow within a certain altitude interval in North Iceland. In the latter event, heavy snowfall and gale-force winds, as well as extreme wet-snow loading, were more localized, occurring mostly in the lee of the complex orography of Northwest Iceland. The wet snow data are based on: 1) detailed in-situ inspection of accumulated wet snow on conductors of transmission and distribution lines in the affected areas. 2) accurate measurements of accumulation with load cells installed in suspension towers of operating overhead transmission lines and special test span in the areas where the most extreme accumulation occurred. The collected load data are unique in the sense that they describe in detail both the exact timing and magnitude of the wet snow accumulation. Meteorological observations of wind, temperature and precipitation are moreover available from synoptic and automatic weather stations in the areas. The atmospheric flow during the events is analyzed, based on weather observations and simulations at high resolution with an atmospheric model. The simulated data are subsequently used as input for a cylindrical wet-snow accretion model. The measured and simulated wet-snow loading are analyzed and put in relation with the weather during the event, highlighting several key aspects of the flow and icing process that needs further attention.

I. Introduction

Wet-snow accumulation on overhead structures is of particular interest to both the scientific and engineering communities as such accumulation causes external mechanical load on the structures [1], and is needed for their safe operation and design. In this context, the accretion on overhead power lines has received special attention due to the vulnerability of the system to the accretion and the societal impacts of faults and blackouts. This vulnerability was in particular evident in the wet snow storm of 2005 in Germany, where 82 transmission towers collapsed and 250 000 people were without electricity for days [2]. Severe events have been documented in other high latitude and/or high altitude regions of the world, e.g., in Europe [1] and [3], Japan [4], and Iceland as documented in [5], [6] and [7], as well as reported here for two severe events occurring in the latter half of 2012 in North Iceland.

Wet-snow accretion on overhead conductors is particularly effective due to the strong adhesive forces within the compact snow sleeve which forms on the conductor as it rotates or the accreted mass slides around it [4]. The accretion process itself is critically sensitive to small variations in the wind speed and direction, surface characteristics of the conductor, atmospheric water mass loading as well as the liquid water content of the falling snow, which, among other things, depends on the (wet bulb) temperature in the lowest layers of the atmosphere. Wet-snow loading has traditionally been parameterized based on observational data (e.g., [1], [8] and [9]). Such methods suffer from the lack of accurate estimates of atmospheric parameters that are not routinely observed, but it has been shown that better results can be gained based on output from state-of-the-art mesoscale atmospheric models (e.g., [10]). Accurate and physically sound parameterizations of the wet-snow loading are needed to aid in forecasting wet-snow events and estimating climatological and regional design loads with regard to a given return period. These loads must by necessity be based on output from atmospheric models instead of observational data and are critically dependent on correct representation of the atmospheric flow in complex terrain as well as accurate wet-snow accretion parameterization. Systematic and extensive observations during wet-snow events are however necessary for verifying the accretion methods, as was done in [10], based on simulated and observed climatology of wet-snow events in Southeast Iceland.

This paper presents an analysis of weather and wet-snow accumulation during two severe wet-snow storms occurring in northern Iceland in 2012. Both storms caused extreme wet-snow loading on transmission and distribution lines in the affected regions. The wet-snow accretion was combined with strong winds, resulting in many broken wooden poles in the distribution system and 132 kV H-frame transmission towers, as well as, e.g., significant damage to property and loss of livestock. Unique and detailed data of accumulated wet snow on conductors during the events as well as extensive weather observations, are used to investigate the wet snow accumulation and highlighting, in particular, the differences in the spatial extent of accretion as well as several key aspects requiring special attention.

II. The atmospheric situation

The two events of 10 September and 29 December 2012 share some similarities with each other, as well as with other significant wet-snow events in northern Iceland. Both events occur in relation to a northward moving and deepening extratropical low off the east coast of Iceland, as seen in the atmospheric analysis (Fig. 1) from the European Centre for Medium-range Weather Forecasts (ECMWF). The strong pressure gradients gave rise to the very strong northerly and northwesterly flow over Northeast Iceland in the September event, and the northeasterly flow over Northwest Iceland in the December event, as observed above the Keflavík upper-air station in Southwest Iceland (not shown), as well as at many automatic weather stations (example given in Fig. 2).

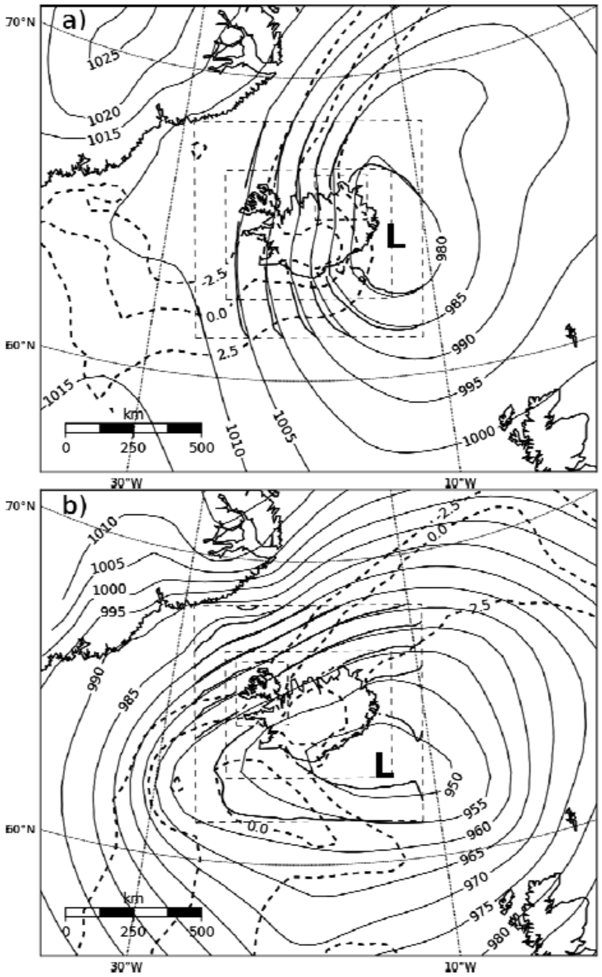

Fig. 1. Mean sea level pressure and 2-meter temperature at 12 UTC on 10 September 2012 (a) and at 6 UTC December 2012 (b) according to the analysis of ECMWF. Also shown is the pressure simulated at 9 km horizontal resolution (thick solid lines), as well as the 9, 3 and 1 km domain bounds (dashed lines) and location of extratropical low (L).

10-minute mean winds at 10 meters exceeded 20 m/s at many locations in North Iceland during the period of most active wet-snow accretion on 10 September, and were as great as 25 m/s at several stations, which can also be considered to be the large-scale wind aloft in the boundary layer and away from complex orography. Weaker winds were observed at several more sheltered locations in Northeast Iceland as well as away from the most affected region, while at the same time there was a severe northerly windstorm in Southeast Iceland. The winds were slowly turning anticlockwise from the northeast as the low approached and winds increased. The large-scale wind direction was close to north at the start of the wet-snow event and close to northwesterly at its end and immediately after the event.

The December event in Northwest Iceland occurred in far more complex orography than the event in September. This is reflected by the strongest winds, being associated with downslope windstorms in the lee of mountains; these winds (10-minute) were as great as 40 m/s and exceeded 30 m/s at many locations, with far stronger gusts (3-second). Mountain top winds were on average close to 30 m/s and not as gusty, while far weaker winds were in general observed close to the upstream side of the mountains. The wind direction varied somewhat between the stations as can be expected in complex orography, but the large-scale wind direction was close to being northeasterly during the event, but gradually turned more towards north. It should be noted that wind observations may in general be expected to be severely affected by wet-snow accretion slowing, or even stopping, the anemometers, but to a lesser extent during wet-snow accretion than in-cloud icing.

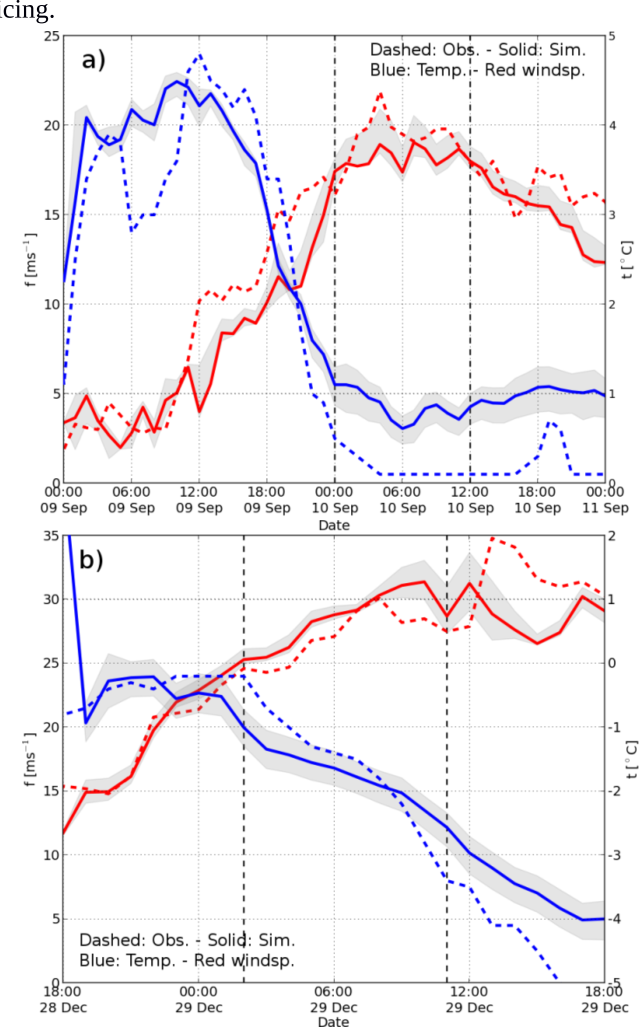

Fig. 2. Observed (dashed) and simulated (solid) 10-meter mean wind speed (red), as well as 2-meter temperature (blue) at Þeistareykir in Northeast Iceland (a) and at Þröskuldar in Northwest Iceland (b). Also shown with dashed vertical lines is the approximate timing of active wet-snow accretion.

A backward trajectory analysis reveals the southern origin of the relatively warm and moist air mass immediately to the east of Iceland, while to the north of Iceland the air was cold and of arctic origin (not shown). This contributed to the deepening of the lows and the extreme amounts of precipitation that fell during the events. The September event was in fact associated with unprecedented snowfall for the time of year and widespread wet-snow accretion in a certain altitude interval, while in the latter event, the most extreme accretion was confined to locations on the immediate leeside of the complex orography in Northwest Iceland. The unprecedented snowfall in September further disrupted traffic, and caused the loss of thousands of sheep still grazing in the highlands when the storm hit, which were consequently buried under thick layer of snow. Fences for livestock fell or were greatly damaged throughout the region, and in the relatively small and few forested areas, there was great damage to tree growth in an elevation interval associated with the wettest and heaviest snow. Precipitation observations during the events were very unreliable due to undercatch of snow during such strong winds. During the December event synoptic observations of the snowfall were nevertheless 40-50 mm (water-equivalent) in 12-15 hours in the accelerated flow in the lee of the mountains and were generally far smaller in weaker winds on the upstream side. Precipitation was more intense and widespread during the September event, with up to 40 mm of rain in 24 hours observed at sea level. In the most affected region the observed precipitation was approximately 50-130 mm (water-equivalent) in 24 hours of what was described as very wet and heavy snow.

In the presence of enough precipitation, but away from complex orography, the largescale (wet bulb) temperature field (Fig. 1) is decisive for the possibility of wet-snow accretion. The temperature must be in the approximate range of 0 to 1.5°C in some elevation intervals in the region, as was the case in large areas in North Iceland in September 2012. Temperatures dropped sharply from 4-8°C in approximately 8 hours preceding the event and were in general below approximately 0.5°C when the most intense precipitation and wet-snow accretion started. Temperature observations from automatic weather stations are unreliable at most of the wet snow locations, as shortly after the onset of wet-snow accretion the strong winds drove the intense precipitation into the thermometer shelter, after which the sensors showed 0°C while covered in melting snow for at least 24 hours before temperatures dropped sharply again. In complex orography, as in Northwest Iceland, the response of the atmospheric flow to the orography is an additional factor which can cause localized enhancement of wet-snow accretion in spite of, for example, the larger scale temperature and/or precipitation fields not being optimal for accretion on a larger scale. Observations from the December event reveal this with lowland temperatures slowly decreasing from 2-3°C at the start of the event and being at or below 0°C at its end. In this temperature range, widespread wet-snow accretion could be expected, but in fact only occurred in the lee of the mountains where the precipitation was concentrated.

In addition to the example data presented in Fig. 2, data from a large number of automatic and synoptic weather stations spread throughout Iceland have been used in analyzing the two events and validating atmospheric simulations of the events. The data from all the stations is stored and checked for systematic errors at the Icelandic Meteorological Office.

III. NUMERICAL SIMULATIONS OF THE ATMOSPHERIC FLOW

Both events are simulated with the non-hydrostatic mesoscale Advanced Research WRF-model (ARW-V3.4.1, [11]). The model is initialized and forced at its boundaries with the ECMWF analysis. The simulations are done at a resolution of 9, 3 and 1 km with, respectively, 95x90, 205x157 and 190x175 grid points in the 2-way nested domains (locations in Fig. 1) The model top is at 50 hPa and the simulations use 50 layers in the vertical, with higher resolution in the lower parts of the troposphere compared to further aloft. The model is run for the whole accretion period as indicated by the wet snow observations, with a delay of approximately 12 hours before starting the nested domains at 3 and 1 km, which allows for at least 24 hours of total spin-up time before the time of interest.

Two most relevant parameterizations employed are those for boundary layer processes and atmosphere moisture physics. The boundary-layer parameterization uses the Mellor-Yamada-Janjic scheme (ETA, [12]), which is centered on the prognostic equation for the turbulence kinetic energy and is frequently used for both operational and research simulations. The structure and magnitude of the atmospheric water content is particularly dependent on the parameterization of atmospheric water and precipitation physics. This is done with the Thompson scheme [13], which predicts mass mixing ratios of cloud water, cloud ice, graupel (QGRAUP), snow (QSNOW) and rain (QRAIN), as well as number concentrations of ice and rain. The graupel, snow and rain phases are relevant for studies of wet snow and have been converted to mass content. The Thompson scheme has previously been reported to give good results in studies of atmospheric icing as in [14].

Considerable work was dedicated to optimizing and improving the simulations based on several different sensitivity tests. The main points that needed addressing, in addition to careful considerations regarding the simulation setup described above, include:

- Improved land-use classification for the whole of Iceland, based on the Corine-dataset from 2007 and a one-to-one projection to the prescribed land use characteristics of the original 30" dataset from the United States Geological Survey.
- An additional correction to the land-use classification, based on the best representation of the outlines of the Icelandic glaciers. A significant error in this is present in the USGS-dataset, as well as in all the global atmospheric datasets available for Iceland, including those from the ECMWF.
- Correction of errors related to skin temperatures and land-sea mask in the ECMWF-analysis in some coastal regions of Iceland. The error is presumably related to post-processing and interpolation of skin temperatures in the ECMWF-data.
- A better representation of skin temperatures of inland water bodies which have previously often been initialized with skin temperatures of the closest ocean-grid point, which can be very wrong for inland bodies in complex orography.

These modifications lead to improvements in, but are not limited to: 1) A more correct representation of surface roughness and hence better reproduced surface winds. 2) A better representation of moisture fluxes from the surface and hence better reproduced surface temperature and energy budget. 3) More accurate surface temperatures and significant modifications to low-level atmospheric stability. The modifications affect the surface and low-level flow throughout Iceland.

In addition, after careful verification of the general validity of the simulation of each event, simulated data at relevant locations were post-processed by comparison with available observations. This was done in order to correct (mostly small) errors in the simulated datasets and make them more accurate and suitable for input into the wet-snow accretion models. In light of the previously mentioned sensitivity of wet-snow accretion to small variations in atmospheric water content and temperature, a single atmospheric simulation cannot be expected to correctly capture all the relevant atmospheric variables with sufficient accuracy. Even in the presence of perfect input data, inaccurate model parameterizations and surface characteristics are only a few of the important sources of model errors.

Overall, the large-scale fields are well represented by the atmospheric simulations, as is for example seen for the surface pressure field, where errors are on average well below 1 hPa (Fig. 1). The errors are greatest in the lee of mountains, as can be expected since the relatively coarse resolution of the ECMWF-data is not sufficient to correctly represent the large-scale orography. Simulated surface winds and temperatures have been validated for the relevant regions in northern Iceland, using observations from a large set of automatic weather stations. The biggest errors, both in temperature and wind, are found in locations of complex orography, for example, in the December event in several locations in the lee of large mountains. Errors are generally smaller for the simulated September events, presumably a result of better representation of the topography by the model. Surface winds at 10 m are in general very well captured away from complex orography with mean errors of less than 2 m/s, and peak winds are well represented (Fig. 3). Errors are somewhat greater at locations downstream from high and complex orography: however, the observations are well represented if the high spatial variability in the simulated winds is taken into account (e.g., Fig. 2). Observed temperatures are slightly overestimated (less than 1°C) at several stations but generally accurately captured at others. This error appears to be related to errors in the forcing data or the vertical heat flux from the surface, and is greatest over the ocean or near water bodies.

The flow aloft is revealed to be strongly affected by the complex orography. Gravity wave activity is particularly strong in the December event, as revealed by the isentropes (isentropes can considered to be equivalent to streamlines) in a section across the Snæfellsnes Peninsula in West Iceland (Fig. 4). A dramatic gravity wave resembling a hydraulic jump is set up above the peninsula when the flow impinges on the mountain barrier. Large amounts of super-cooled cloud and/or rain water form when the low level upstream flow is lifted over the mountains, and are subsequently carried down the lee slopes of the mountains in the fast plunging flow below the wave. Due to the strong descending flow, there is very small simulated evaporation and scavenging by snowflakes, allowing significant amounts of this dynamically created atmospheric water to reach the lowlands in the lee. This appears to introduce a new method to enhance the amount of atmospheric water and its liquid water fraction in the lee of mountains. Previously, it was only the melting of the larger scale snowfall below the 0°C isotherm which was considered to introduce the necessary liquid water content of the snow, as is presumably the case in general during the September event, and as can be deduced from the section in Fig. 4. The gravity wave mechanism of enhancing the atmospheric water flux on the leeside needs more investigation and observations to be verified; however, it is supported by observations of leeside precipitation maxima during orographic precipitation events.

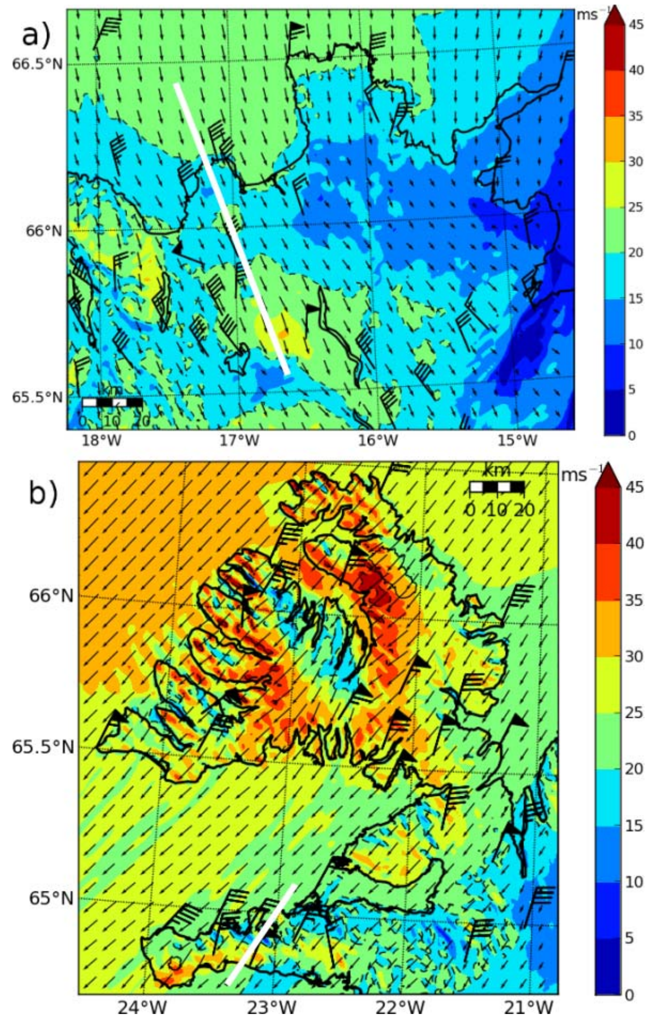

Fig. 3. Simulated 10-meter mean wind speed [m/s] and wind vectors at a horizontal resolution of 1 km, as well as observed winds at automatic weather stations (5 m/s each half barb, 25 m/s each flag) at 0600 UTC on 10 September in North Iceland (a) and on 29 December in Northwest Iceland (b). Contours of 20 and 40 m/s are indicated by dashed lines, coastline and location of sections in bold.

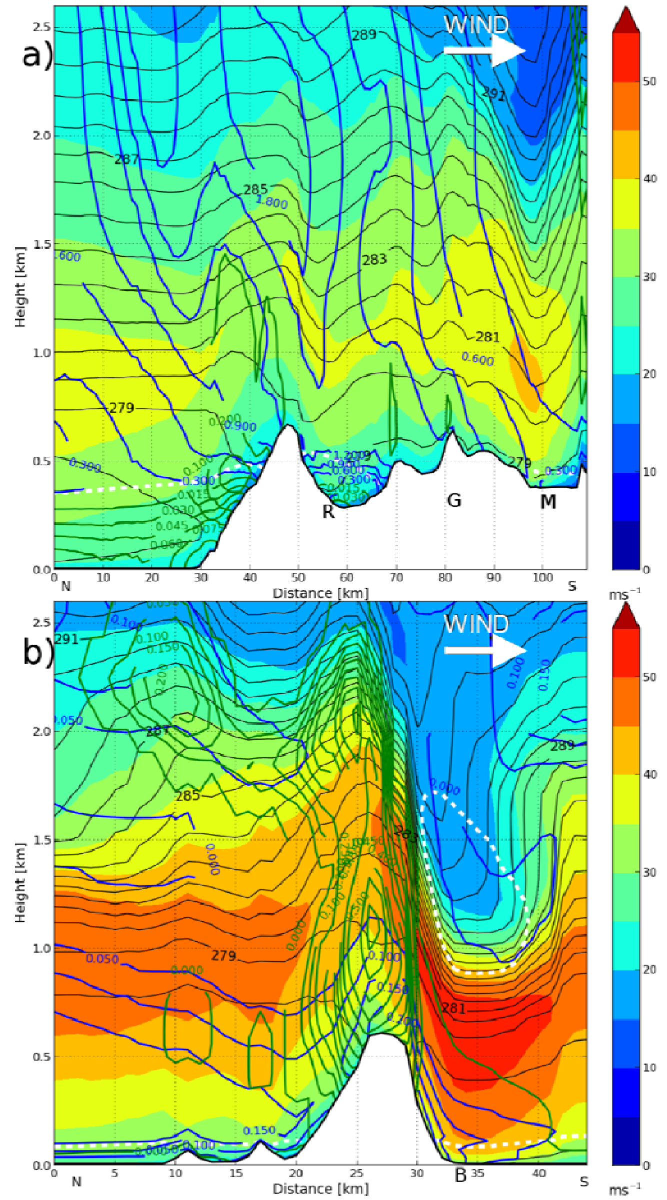

Fig. 4. Wind speed contours [m/s] in color, isentropes [K] (thin, black) as well as isolines of atmospheric water [kg/m3] (blue=snow, green=rain and cloud) content in sections at 0600 UTC on 10 September 2012 (a) and on 29 December 2012 (b). White dashed lines are the 0°C isotherm. Wind is from the left and follows the isentropes. Locations of sections are shown in Fig. 3. Approximate projections of locations of wet snow sites on to the section are indicted in bold: Reykjaheiði (R), Gæsafjöll (G), Mývatn (M) and Bláfeldarhraun (B).

IV. Wet Snow Accumulation

Observations of the wet snow accumulation during the two events reveal large spatial differences in the extent of the affected regions during the events. The event of 10 September was associated with widespread wet-snow accretion on overhead conductors in a certain elevation interval in North Iceland (cf. Fig. 5). However, during the December event, the greatest accumulation was observed at locations in the lee, and close to mountains of significant height and in very complex topography (cf. Fig. 9). Furthermore, there were indications of small-scale topography enhancing the accretion process, e.g., through drifting snow associated with locally accelerated surface flow, or when it was lifted by small scale topographic features in the immediate vicinity of the power lines.

The Event of 10 September 2012

The wet-snow event in September 2012 was most severe in the eastern part of North Iceland (Fig. 5). Active wet-snow accretion started at approximately 0100 UTC during the night of 10 September, as is seen from operational observations with a suspended load cell in a 132 kV KS1 transmission line on Reykjaheiði, approximately 20 km south of the coast. The line at this site is approximately perpendicular to the prevailing northerly and northwesterly winds, at an elevation of approximately 275 m above sea level, and a relatively short distance downstream from an approximately 700 m high mountain ridge. The topography at the site is flat up to 2 km from the measuring tower. Based on observations and simulated data, mean winds are expected to have peaked at the site early in the night at 27 m/s, with gusts exceeding 40 m/s. At approximately 1145 UTC the total measured load was 2600 kg with 150 m weight span, and the towers on both sides of the tower with suspended load cell broke. The load measurements indicate that wet-snow accretion continued until at least 1445 UTC and possibly longer, but the actual load cannot be calculated after the failure (Fig. 7). At the time of the failure the equivalent ice load is estimated to be 14.5 kg/m, which, with a mean density of 750 kg/m3, is characteristic for similar events in Iceland, gives an equivalent mean diameter of 16.2 cm. A total of 23 wooden H-frame towers broke or fell at this site during the event, with the damage in general limited to the upper parts of the towers, i.e., cross-arms and X-braces (sample photos in Fig. 6b). Slightly farther the south and west in the same region, eight similar towers broke in a 132 kV transmission line. Most of the wet snow fell off the conductors in the afternoon of 11 September.

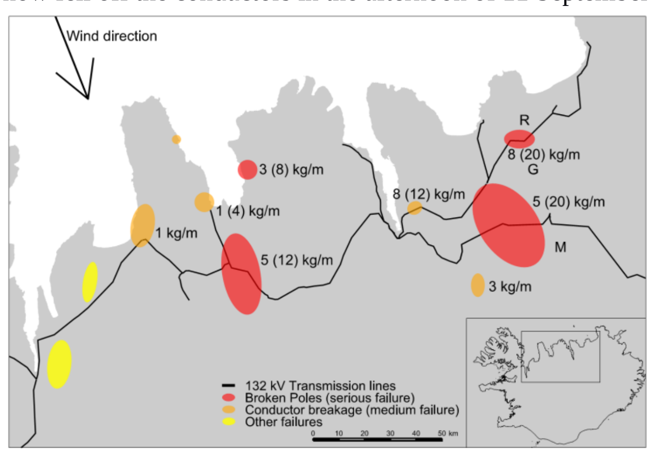

Fig. 5. Overview of measured/estimated wet-snow loading as well as main regions of failures during the event on 10 September 2012 in North Iceland. Values shows median (max) loading. Also shown are approximate locations of the measuring sites on Reykjaheiði (R), Gæsafjöll (G) as well as that of Lake Mývatn (M).

Fig. 6. Photos from the wet-snow event on 10 September in North Iceland. a) Loaded conductors and leaning poles of the distribution system north of Lake Mývatn. b) Accumulated wet snow and broken transmission towers in 132 kV KS1 at Reykjaheiði. c) Wet snow sample on a faulted transmission line conductor on Reykjaheiði, measuring 21 cm mid-span which is however not an average value for the area.

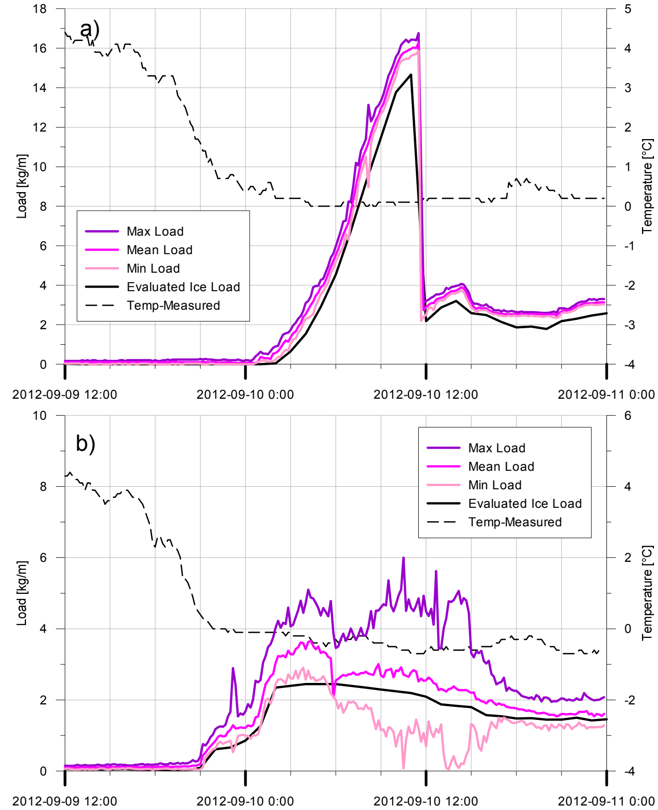

Fig. 7. Measured and evaluated ice load a) in 132 kV KS1 and b) in test span in Gæsafjöll.

The 11 kV distribution system was severely damaged in several areas farther inland, and after the event most of the overhead conductors in the affected areas were replaced with 11 kV underground cables. The most serious failure occurred at Lake Mývatn (300 m a.s.l., sample photo in Fig. 6a), where approximately 100 distribution poles fell or broke, causing widespread blackout lasting for four days. The measured snow sleeve was up to 13-14 cm in diameter at some locations, but was on average close to 10 cm on conductors oriented perpendicularly to the prevailing winds.

Fig. 8. Suspension tower in 132 kV KS1 with measuring equipment in left phase at Reykjaheiði site.

THE EVENT OF 29 DECEMBER 2012

A severe northeasterly windstorm occurred in Iceland during the night of 29 December 2012. The storm was associated with significant wet-snow loading on many distribution and transmission lines in Northwest Iceland. All the major icing occurred in the lee of mountains of significant height, i.e., on the southern and western side of the complex orography of the region (Fig. 9). Temperatures were on average coldest in the northern part of the region where the least accumulation occurred, but temperatures were slightly higher towards the south where the greatest accumulation and the most failures occurred.

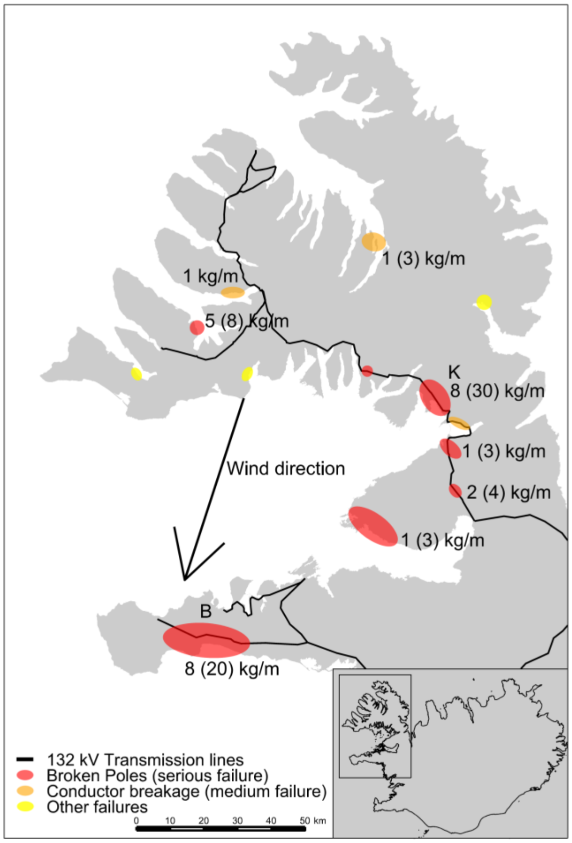

Fig. 9. Overview of measured/estimated wet-snow loading as well as main regions of failures during the 29 December event in Northwest Iceland. Values shows median (max) loading. Also shown is the approximate location of Kambur (K) and Bláfeldarhraun (B).

The accumulation started around 0300 UTC and continued for approximately nine hours, as is seen from operational measurements from a load cell (Fig. 10) suspended in a 132 kV MJ1 transmission line at Kambur, in the lee of very complex topography (Fig. 11 and Fig. 12). The maximum load measured was 3220 kg with 124 m weight span, but at that time the conductor was so loaded that it lay on the snow layer below. The largest diameter was measured to be up to 40 cm, with an equivalent mean diameter of 22-25 cm. The most intense loading occurred on a very short interval between three transmission towers and was presumably strongly affected by the upstream topography enhancing the atmospheric water flux through drifting snow caused by channeling or lifting of the surface flow to the elevation of the conductors. This may be deduced from Fig. 12, which shows the topography on a section through the site at Kambur, along the main wind direction. The density of the accreted wet snow was found to be 700-740 kg/m^3, based on four samples. Measurements of the orientation of snow keels on the poles indicate that the prevailing wind during the accretion period was slightly east of north.

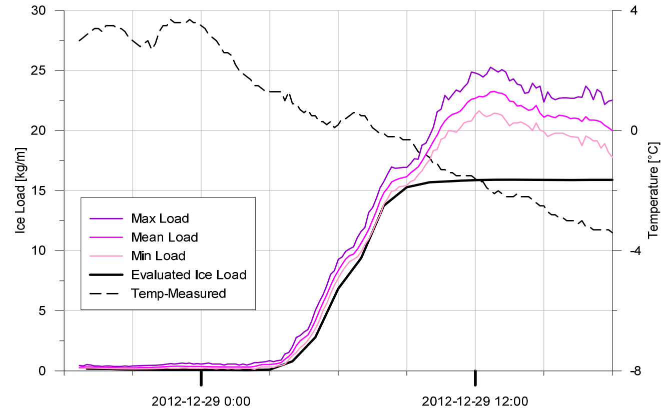

Fig. 10. Measured and evaluated ice-load at Kambur in 132 kV MJ1.

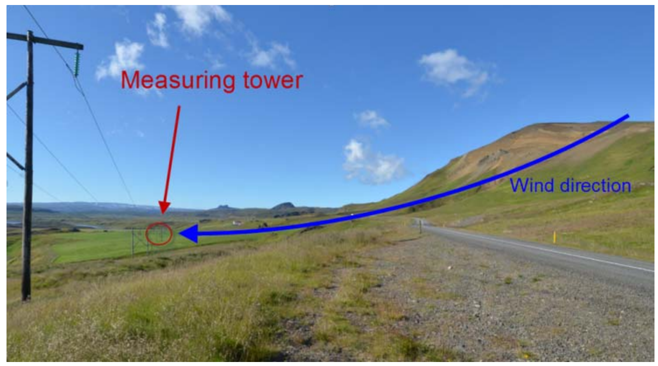

Fig. 11. Suspension tower at Kambur in 132 kV MJ1 with measuring equipment.

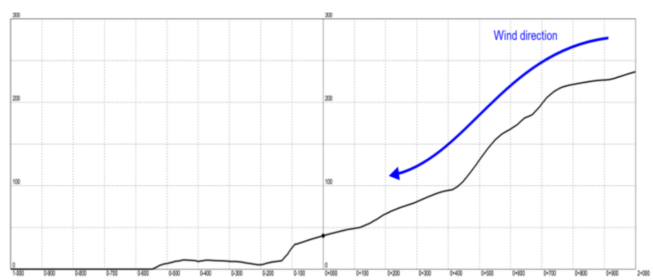

Fig. 12. Topography on a section through the site at Kambur, along the main wind direction.

At the same time severe accretion occurred at many locations in the region, but most significantly on a 66 kV OL1 transmission line at Bláfeldarhraun on the southern (downstream) side of the Snæfellsnes Peninsula (Fig. 9). The line was out of operation for seven and half days. The diameter of accreted wet snow was estimated to be 8-18 cm, with serious failures, including 42 broken H-frame wooden towers, 55 cross-arms, and torn conductors (sample photos are given in Fig. 13).

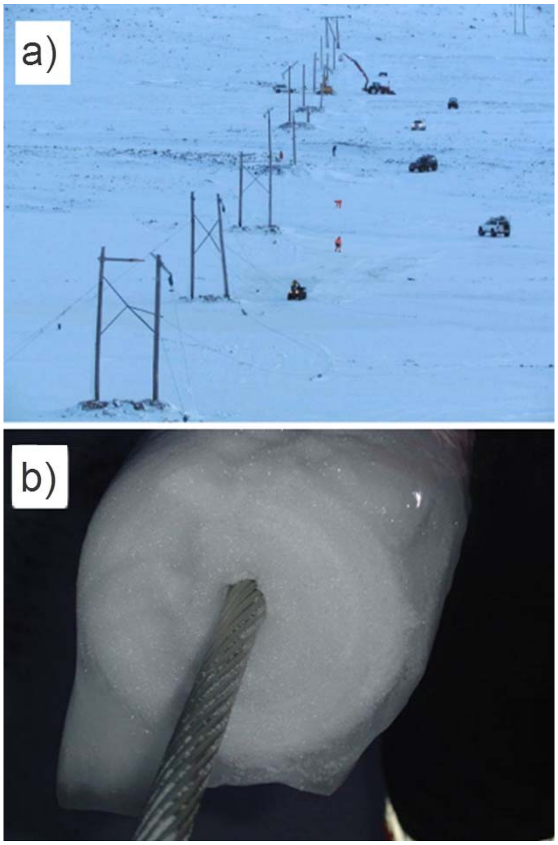

Fig. 13. Photos from the wet-snow event of 29 December in Northwest Iceland. a) Reparation work on faulted 66 kV OL1 at Bláfeldarhraun. b) Wet snow sample east of Bláfeldarhraun, measuring 14 cm in diameter.

V. Simulated Wet-Snow Accumulation

The direct model output data from the atmospheric simulations are used as input data for the wet-snow accretion model presented in [10] and subsequently used to prepare maps of the spatial structure of the simulated accumulation (Fig. 14). The direct model output was furthermore post-processed in an attempt to correct for errors present in the data at several locations where wet snow load measurements are available from test spans. The post-processed data was then used as input to the same icing model to prepare time-series of simulated accumulation to be compared with the observed loading at the measurement sites (Fig. 15). It should be noted that the simulated loads are here done on a vertical, rotating, cylinder and are thus independent of the wind direction and greater than simulated loads taking wind direction into account, as in [15]. The overall spatial structure of the simulated wet-snow accumulation compares well with locations of reported failures and other damage observed during the events. Large accumulated wet-snow masses are simulated at the location of a measuring site at 132 kV KS1 and around Lake Mývatn, where the greatest damage occurred to the overhead distribution and transmission system in September 2012 (Fig. 5). Icing is on average underestimated during the December 2012 event, but the pattern of largest wet snow sleeve diameters is correctly located in the lee of the mountains, in areas where the greatest damage was observed in on the overhead system at Bláfeldarhraun and near the measuring site at Kambur (Fig. 9). Gravity wave activity above the Snæfellsnes Peninsula may have affected the accumulation in Bláfeldarhraun, as previously mentioned. A comparison of the measured and simulated wet-snow loading at the measuring site at Reykjaheiði and test span in Gæsafjöll in the September event, and at Kambur in the December event, shows that extreme wet-snow accumulation is underestimated at Reykjaheiði and Kambur, while the less severe accumulation at the test span in Gæsafjöll is well reproduced. A comparison with the spatial structure of the simulated accretion at Reykjaheiði reveals that only a small shift in the extent of the extreme icing region is needed to reproduce the measured accumulation at the site. This appears not to be the case at Kambur in Northwest Iceland, but there are indeed indications that local small-scale topography may have locally increased the atmospheric water flux, possibly due to drifting snow or channeling of the flow. Such phenomena may be partly reproduced at far higher resolutions, but not at the current resolution of the atmospheric model. A more detailed discussion of the icing models themselves and their performance is given in [15], for both the current cases and several other severe events.

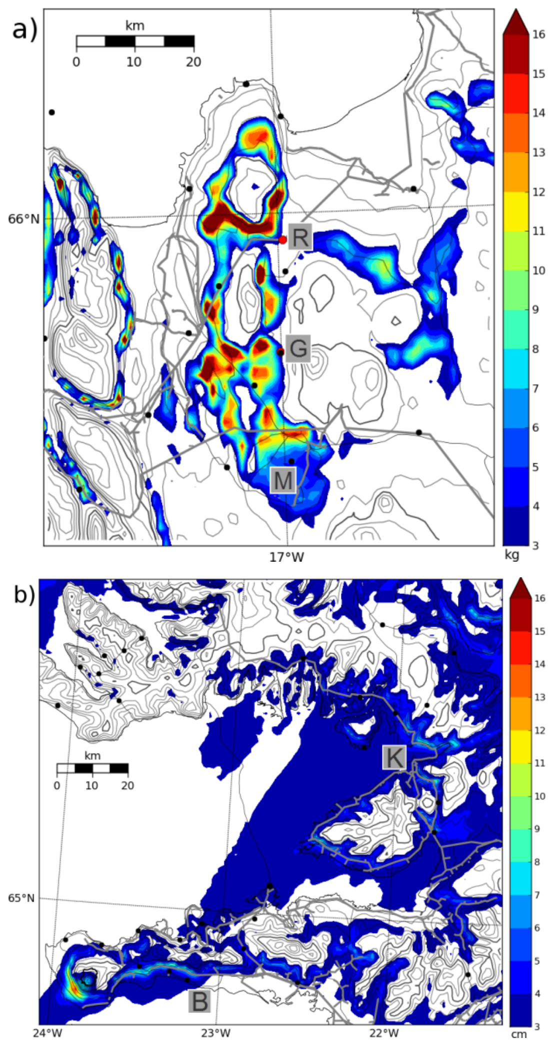

Fig. 14. Simulated wet snow mass [kg/m] in North Iceland (a) and accreted wet snow diameter [cm] in Northwest Iceland (b). Also shown are locations in Reykjaheiði (R), Gæsafjöll (G), Mývatn (M), Kambur (K) and Bláfeldarhraun (B).

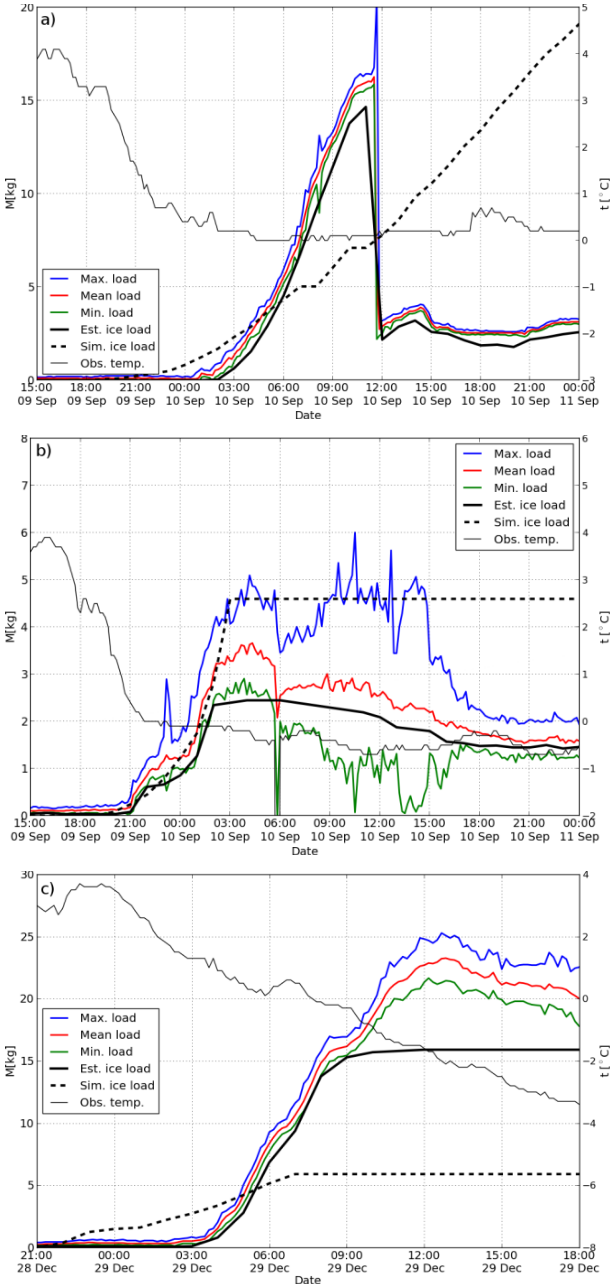

Fig. 15. Measured loading, estimated and simulated ice load, as well as temperature at Reykjaheiði (a) and in Gæsafjöll (b) in Northeast Iceland and Kambur in Northwest Iceland (c).

VI. CONCLUDING REMARKS

Here, two severe wet-snow events in northern Iceland have been described and analyzed using systematic observations and reports of wet-snow loading, observations from a dense network of automatic weather stations as well as high resolution atmospheric simulations. The observed wet-snow accumulation varied greatly within the cases. It was more widespread in a certain elevation interval in the September event in North Iceland, while accretion was more localized and occurred mainly in the lee of mountains in the December event in Northwest Iceland. Both events were associated with very strong winds and high amounts of precipitation, in particular the September event where the snowfall amounts were exceptionally great so early in the season.

The observed wet-snow loading was close to 15 kg/m in the cases, with equivalent diameters greater than 20 cm and exceeding 40 cm in some places. Both the transmission and distribution systems were damaged during the events, with a total of more than 200 fallen or broken poles and H-frames for the two events. Blackout was widespread and lasted for few days at some of the locations, making these events some of the most severe documented in Iceland.

The first attempt was made to simulate observed wet snow accumulation, based on the wet-snow model presented in [10], which uses a physically based parameterization of the sticking efficiency. The model is forced, using input data from the atmospheric simulations, which includes parameters which are not routinely observed, such as the atmospheric water flux and liquid water fraction, which is critically dependent on the wet bulb temperature but has previously been based on in-situ observations of the temperature. A successful simulation of wet snow accumulation is critically dependent on: 1) a detailed and accurate icing model and 2) detailed and correct atmospheric input data. Here, the overall performance of the icing model is better for the September event, which occurred in less complex orography than the December event. This was somewhat as expected since atmospheric simulations are in general less accurate, and harder to perform, in complex orography than less complex orography. The strong dependence of the accretion process on a relatively narrow interval in both temperature and liquid water fraction of the falling snow, as well as the actual snow amounts, should be noted [16]. In fact, a large part of the error in simulated wet snow accumulation may be explained if the spatial variability in the simulated fields is accounted for. Often only a slight vertical or horizontal shift within the simulated dataset is needed to reach far more favorable conditions for efficient accretion of wet snow on conductors. A more thorough discussion of the comparison of observed and simulated wet snow accumulation for the current events, as well as for other events, is given in [15].

REFERENCES

[1] P. Admirat, "Wet snow accretion on overhead lines," *Atmospheric Icing of Power Networks*, pp. 119-169, 2008.

[2] C. Klinger, M. Mehdianpour, D. Klingbeil, D. Bettge, R. Häcker and W. Baer, "Failure analysis on collapsed towers of overhead electrical lines in the region Münsterland (Germany) 2005," *Engineering Failure Analysis*, no. 18, pp. 1873-1883, 2011.

[3] P. Bonelli, M. Lacavalla, P. Marcacci, G. Mariani and G. Stella, "Wet snow hazard for power lines: a forecast and alert system applied in Italy," *Nat. Hazards Earth Syst. Sci.*, no. 11, pp. 2419-2431, 2011.

[4] Y. Sakamoto, "Snow accretion on overhead wires," *Philos. Trans. Roy. Soc. A*, no. 358, pp. 2941-2970, 2000.

[5] Á. J. Elíasson, E. Thorsteins and H. Ólafsson, "Study of wet snow events on the south coast of Iceland," in *9th International Workshop on Atmospheric Icing of Structures (IWAIS)*, Chester, England, 2000.

[6] H. Ólafsson, Á. Elíasson and E. Thorsteins, "Orographic Influence on Wet Snow Icing – Part I: Upstream of Mountains," in *10th International Workshop on Atmospheric Icing of Structures (IWAIS)*, Brno, Czech Republic, 2002.

[7] H. Ólafsson, Á. Elíasson and E. Thorsteins, "Orographic Influence on Wet Snow Icing – Part II: Downstream of Mountains," in *10th International Workshop on Atmospheric Icing of Structures (IWAIS)*, Brno, Czech Republic, 2002.

[8] L. Makkonen, "Estimation of wet snow accretion on structures," *Cold regions science and technology*, no. 17, pp. 83-88, 1989.

[9] L. Makkonen and B. Wichura, "Simulating wet snow loads on power line cables by a simple model," *Cold Regions Science and Technology*, Vols. 2-3, no. 61, pp. 73-81, 2010.

[10] B. E. K. Nygaard, H. Ágústsson and K. Somfalvi-Tóth, "Modeling Wet Snow Accretion on Power Lines: Improvements to Previous Methods. Using 50 Years of Observations," *J. Appl. Meteor. Climatol., in press*, 2013.

[11] W. C. Skamarock, J. B. Klemp, J. Dudhia, D. O. Gill, D. M. Barker, M. D. Duda, W. Wang and G. Powers, "A description of the Advanced Research WRF Version 3," *NCAR technical note*, no. 475, p. 125, 2008.

[12] Z. I. Janjic, "Nonsingular Implementation of the Mellor–Yamada Level 2.5 Scheme in the NCEP Meso model," *NCEP Office Note*, no. 437, p. 61, 2002.

[13] G. Thompson, P. Field, R. Rasmussen and W. Hall, "Explicit forecasts of winter precipitation using an improved bulk microphysics scheme. Part II: Implementation of a new snow parameterization," *Mon. Wea. Rev.*, no. 136, pp. 5095-5115, 2008.

[14] B. E. K. Nygaard, J. E. Kristjánsson and L. Makkonen, "Prediction of In-Cloud Icing Conditions at Ground Level Using the WRF Model," *J. Appl. Meteor. Climatol.*, no. 50, pp. 2445-2459, 2011.

[15] Á. J. Elíasson, H. Ágústsson, G. M. Hannesson and E. Thorsteins, "Modeling wet snow accretion - Comparison of cylindrical model to field measurements," in *15th IWAIS*, St. John's, Newfoundland and Labrador, Canada, 2013.

[16] S. Fikke and et al., " COST Action 727 Atmospheric Icing on Structures, Measurements and data collection on icing: State of the Art," *Publication of MeteoSwiss*, no. 75, pp. 1422-1381, 2007.

[17] B. Dalle and P. Admirat, "Wet snow accretion on overhead lines," *French report of experience Cold Regions Science and Technology*, vol. 65, no. 1, pp. 43-51, 2011.

[18] E. A. Podolskiy, B. E. K. Nygaard, K. Nishimura, L. Makkonen and E. P. Lozowski, "Study of unusual atmospheric icing at Mount Zao, Japan, using the Weather Research and Forecasting model," *J. Geophys. Res.*, no. 117, p. D12106, 2012.

[19] Ó. Rögnvaldsson, J. W. Bao, H. Ágústsson and H. Ólafsson, "Downslope windstorm in Iceland – WRF/MM5 model comparison.," *Atmos. Chem. Phys.*, no. 11, pp. 103-120, 2011.

Modeling wet-snow accretion
Comparison of cylindrical model to field measurements

Árni Jón Elíasson
Landsnet
Reykjavik, Iceland
arnije@landsnet.is

Hálfdán Ágústsson
Reiknistofa í vedurfræði
Reykjavik, Iceland
halfdana@belgingur.is

Guðmundur M. Hannesson
EFLA Consulting Engineers
Reykjavik, Iceland
gudmundur.m.hannesson@efla.is

Egill Thorsteins
EFLA Consulting Engineers
Reykjavik, Iceland
egill.thorsteins@efla.is

Abstract **—** Field measurements of wet-snow accretion have been made for numerous events in Iceland. The measurements are made with load cells in special test spans and, in some cases, in operating transmission lines. They can accurately identify the rate and size of accumulation and normally include measurements of air temperature as well. The largest events include wet snow accumulation above 15 kg/m within 10 hours, and they are associated with very large amounts of precipitation and/or gale force winds. Six cases are selected and used to evaluate how well two existing cylindrical accretion models of wet snow can predict the accretion of wet-snow icing. The weather parameters that were not directly measured in-situ and are needed for the accretion models, i.e., wind speed, precipitation rate and snowflake liquid water fraction, are derived by using A-WRF simulations that were specially made for the cases at high resolution, and by studying observations of weather from a dense network of weather stations. The performance of the cylindrical accretion models is analyzed with special attention to the influence of sticking efficiency on the amount and timing of wet-snow accretion. The strong and weak points of the models are discussed.

I. Introduction

Wet-snow icing is often an important aspect of structural loading for overhead transmission lines (OHTL), especially at low altitude. Wet-snow events are relatively rare, and it is thus often difficult to collect sufficient field data for statistical evaluation of the loading. It is important to use all available data when evaluating the risk of wet-snow icing, and today it is becoming more feasible to use icing models to calculate the wet-snow icing risk. The icing models need reliable input data, e.g., different weather parameters, and these can be prepared with state-of-the-art numerical atmospheric models. Several different wet snow models have been developed, but there is a lack of field data to verify the models.

Wet-snow icing has posed a great threat to overhead lines in Iceland, as revealed by an extensive data collection program, which has been in operation for decades [1]. The associated database contains detailed information on all known icing events on overhead lines, including wet-snow events, which are especially frequent and serious in coastal areas. The amount of wet snow accumulation varies greatly depending on the direction of the OHTLs and topography; often the most affected sites are found in downslope winds on the lee side of mountains. The wet snow accumulation in Iceland is usually combined with relative high wind speed compared to events in many other countries, due to orographically enhanced flow as well as the relatively low surface roughness associated with sparse vegetation. At the time of accumulation, the 10-minute average wind speed often ranges from 10 to 25 m/s, concurrent with heavy precipitation, as revealed by observations from a dense network of weather stations [2]. This often leads to high ice load and relatively high density of the snow sleeve ([3] and [4]). Additionally, numerous events of wet-snow accretion have been documented in detail by a network of dedicated test spans in Iceland. The field measurements can accurately identify the rate and magnitude of accumulation and normally include measurements of air temperature at conductor height. The measurements include events with loading above 15 kg/m, and the largest events are associated with very large amounts of precipitation and/or gale force winds. In this study, measurements from six cases of wet-snow accretion are used to evaluate how well two existing cylindrical accretion models of wet snow can predict the accretion of wet-snow. The weather parameters that were not directly measured in-situ and are needed for the accretion models, i.e., wind speed, precipitation rate and snowflake liquid water fraction, are derived from high-resolution A-WRF simulations and observations of weather from a dense network of weather stations. The performance of the cylindrical accretion models is analyzed with special attention to the influence of sticking efficiency on the amount and timing of wet-snow accretion.

II. Icing measurements

Field measurements of icing are made in many places in Iceland [5]. Most of the measurements are made in special test spans, but measurements are also made on some operating transmission lines. The measurements are made with load cells measuring loading at a frequency of 0.5-1.0 Hz and store maximum, minimum and average values for each at 10-minute intervals. The test spans are 80 m long, and the conductors are strung on wooden poles 10 m above the ground. End tension measurements are made, and the unit load of icing is derived by assuming equally distributed ice load on the measuring span and the guy wires supporting the poles. In operating overhead lines the loading is measured in suspension attachments. The measured loading includes both ice and wind load. By using estimated wind speed and fluctuation in load measurements, it is possible to subtract the wind load from the measured data to evaluate the ice load.

III. Simulation of weather

The atmospheric parameters needed as input for the wet-snow accretion models, including those not directly measured in-situ, are prepared based on atmospheric simulations with the non-hydrostatic mesoscale Advanced Research WRF-model [6]. The atmospheric model is forced with input data from the ECMWF, and the simulations are done at a horizontal resolution of 9, 3 and 1 km. The high resolution is necessary to adequately reproduce the complex topography of Iceland and the wet snow sites. The most relevant parameterizations for studies of wet-snow accretion are those of atmospheric water and precipitation processes, which are done with the Thompson scheme [7], a scheme previously used for similar studies. It is a bulk scheme, and the relevant water phases for wet-snow accretion are those of snow, rain and graupel.

After detailed verification of each simulated event, data at relevant locations were carefully post-processed, based on a comparison of the simulated data with available observations from a dense network of weather stations. This was done in order to correct some of the inherent errors in the simulated dataset and make it more accurate and suitable for input into the wet-snow accretion models. Due to the high sensitivity of wet-snow accretion on small variations in, e.g., atmospheric water content, temperature and winds, imperfect input data, inaccurate model parameterizations and surface characteristics, as well as a simplified representation of the accretion process itself, are only a few of the important sources of errors. A more detailed description of the setup of the atmospheric model and the methodology is given in [8].

IV. CYLINDRICAL ACCRETION MODEL FOR WET-SNOW ICING

Different models have been proposed for wet-snow icing accretion, such as: Admirat [9], Sakamoto [10], Poots [11], Makkonen [12], Finstad&Ervik [13], Nygaard et al. 2013 [2]. The most used approach is based on the simple time-dependent cylindrical accretion model that is described in ISO 12494-2000 [14]. It describes how particles, which can be either liquid (usually super cooled), solid or a mixture of different water phases, accumulate on objects. The accumulation rate (kg/s) is described by

$$\frac{dM}{dt} = \alpha_1 \cdot \alpha_2 \cdot \alpha_3 \cdot w \cdot V \cdot A \qquad (1)$$

where V is particle impact speed perpendicular to object (m/s); A is the cross-sectional area (m^2) perpendicular to object; w is water content (kg/m^3); α_1 is the collision efficiency; α_2 is the sticking efficiency, and α_3 is the accretion efficiency.

In this study the atmospheric water content for wet-snow accretion is based on the results of the aforementioned atmospheric simulations and includes the rain (Qr), snow (Qs) and graupel (Qg) phases. The snowflake impact speed is the vector sum of the wind speed U and the terminal velocity of the snowflakes, assumed here as 1 m/s.

For wet-snow icing it can be assumed that the collision efficiency and the accretion efficiency is unity (α_1=1 and α_3=1). The main difference in the wet-snow icing models is related to the assumption of the sticking efficiency (α_2) and density of the accumulation. Presently, theory on the sticking efficiency of wet snow is limited, and the available approximate methods are empirical equations, based on laboratory simulations and some field observations. The main factors that may influence the sticking efficiency are believed to be the liquid on the surface of the snow particles and the impact speed. The best approximation for sticking efficiency has been considered to be the Admirat approach [9]. Recently a new and promising approach was presented by Nygaard et. al. [2]. Below these two methods are briefly described and compared for the selected icing cases.

A. Admirat model (ADM)

The Admirat parameterization of the wet snow cylindrical accretion is mainly based on calibration of data from wind tunnel tests and field observations from Japan and France. In this study the Admirat model is taken as:

- Accumulation is in the temperature range of 0 to 2°C
- Sticking efficiency is α_2 = MAX[1/V ; 0.1]
- Water content is taken as w = Qs + Qr + Qg
- Density of wet snow = 100 + 20 V

B. Model by Björn Egil Nygaard et al. (BEN)

A new approach to modeling wet-snow icing, based on atmospheric simulations and the liquid water fraction of snow, was presented in [2]. Wet snow is identified in the atmospheric model (WRF with the Thompson scheme) when the falling snow melts and is transferred from the snow category to the rain category. Thus, wet snow conditions are identified when snow and rain coexists in a grid box, in prescribed ratios. The sticking efficiency in the model is based on the ”fraction of frozen precipitation” denoted as SR. It is calculated from the WRF output by: SR = (Qs+Qg)/(Qs+Qg+Qr). In this study the BEN model is taken as:

- Accumulation is when SR = (Qs+Qg)/(Qs+Qg+Qr) is in range of 0.5 to 0.98
- Sticking efficiency $\alpha_2 = \frac{1-\cos(9 \cdot SR-4.5)}{2 \cdot V^{0.4}}$ when 0.5 < SR < 0.98, otherwise α_2 = 0
- Water content is taken as w = Qs + Qr + Qg
- Density of wet snow = 700 kg/m^3, which is based on field measurements in Iceland.

V. STUDY OF SIX WET-SNOW ICING CASES

In this study six events of wet-snow icing at five different locations are studied. The observed ice load in the events varies greatly. Table 1 lists the cases and gives a brief description on the type of measurements. Events in Case 1 and Case 6 are the most extreme wet-snow events that have been recorded and were associated with extensive damage to both the electric transmission and distribution systems, and blackout in large regions in Iceland [8]. Ice accumulation was measured on energized lines in two of the events, up to the point when adjacent towers failed.

Table 1. Wet-snow icing cases

Case	Measurements	Acc. Time (hours)	Ice load (kg/m)
1	Susp. point in operating 132 kV OHTL	11.0[1]	14.5[1]
2	End tension in 80m test span	6.0	2.5
3	Susp. point in a test line with two spans	14.5	7.0
4	Susp. point in a test line with two spans	54.0	4.0-8.0
5	End tension in 80m test span	11.0	2.5
6	Susp. point in operating 132 kV OHTL	8.5	16.0

[1] Ice accumulation was ongoing when failure occurred at the measuring site.

Icing models are often made using the vertical cylinder approach, i.e., assuming that particle impact speed is perpendicular to the object. The field measurements used in this study have horizontal spans with fixed direction, and the accretion is thus reduced when the wind direction is not perpendicular to the span. The icing models used here (ADM and BEN) are used with the actual horizontal cylinder direction approach instead of the vertical approach. Potential icing accumulation (POT) is also presented for all cases, POT is defined as accumulation of all the available water mass (Qs + Qr + Qg) when the temperature is in range of 0°C to 2°C; this is equivalent to assuming that α_2 = 1.0 in the ADM model. The icing models use measured temperatures at sites when available, otherwise it uses calculated values from WRF-analysis. The icing models are run without the option of ice shedding.

Case 1 –132 kV KS1, Sept. 2012

On 10 September 2012, a severe wet snow storm hit Northeast Iceland. This event caused extreme ice load on many overhead transmission and distribution lines in the area. The wet-snow accretion was combined with strong winds, resulting in broken distribution poles and 132 kV H-frame towers. Such extreme snowfall so early in the autumn is exceptional, especially when associated with average wind speeds in excess of 20 m/s. There was widespread accumulation of wet snow in a certain altitude interval in the region. This event is described in more detail in [8].

The measurements of the wet snow accumulation were obtained from a load cell that was in operation in a suspension attachment of the 132 kV KS1 transmission line in wooden H-frame tower (N65°57'32.0" W16°59'00.7" 280 m.a.s.l.), see Fig. 1. The collected load data describe in detail both the exact timing and the magnitude of the load. The wet snow accumulation is shown in Fig. 2. The loading increases continuously for 11 hours when it suddenly drops. This drop is due to failure in adjacent towers that broke down. It is known that the accumulation continued for some time after the failure, and it can be seen in the load curve, although measurements are unreliable after the failure.

Fig. 1. Suspension tower in 132 kV KS1 with measuring equipment in left phase at Reykjaheiði site.

The topography in the region of interest is relatively simple, which contributes to the accuracy of the WRF simulations that are verified by observations from a dense network of both automatic and synoptic weather stations. The main uncertainty relates to the quality of the forcing data for the atmospheric model (ECMWF-analysis) and the representation of the surface characteristics in the region. Overall, the observed wind and temperature are well reproduced, with the greatest difference associated with overestimated temperatures during the accumulation period. However, during this period observations of temperature are unreliable at many stations as the shelter around the thermometer is packed with melting snow, consequently the thermometer reading is nearly constant at 0°C for an extended period. Due to the extreme wind speeds during the event, significant undercatch of the snowfall is expected at all precipitation gauges; however, the precipitation and atmospheric water content is expected to be reasonably reproduced. Several weather stations are located in the region with the most extreme wet-snow loading. Data from these stations have been used to post-process simulated values at the locations where observations of wet snow loading are available. The data used in Case 1 is based on the atmospheric simulations and observations from the nearby automatic weather station at Þeistareykir, which is 5.3 km south of the measuring site, as well as several other surrounding but more distant stations. The main modifications done are a simple correction, based on the error in simulated temperature and wind at the wet snow site and at Þeistareykir, but taking into account the low reliability of some temperature observations during the intense wet-snow accretion. The atmospheric water content and the liquid water fraction were adjusted, based on investigation of the spatial structure of the precipitation field and the adjustment made to the simulated temperature at the site. These adjustments lead to accurate parameters for the site.

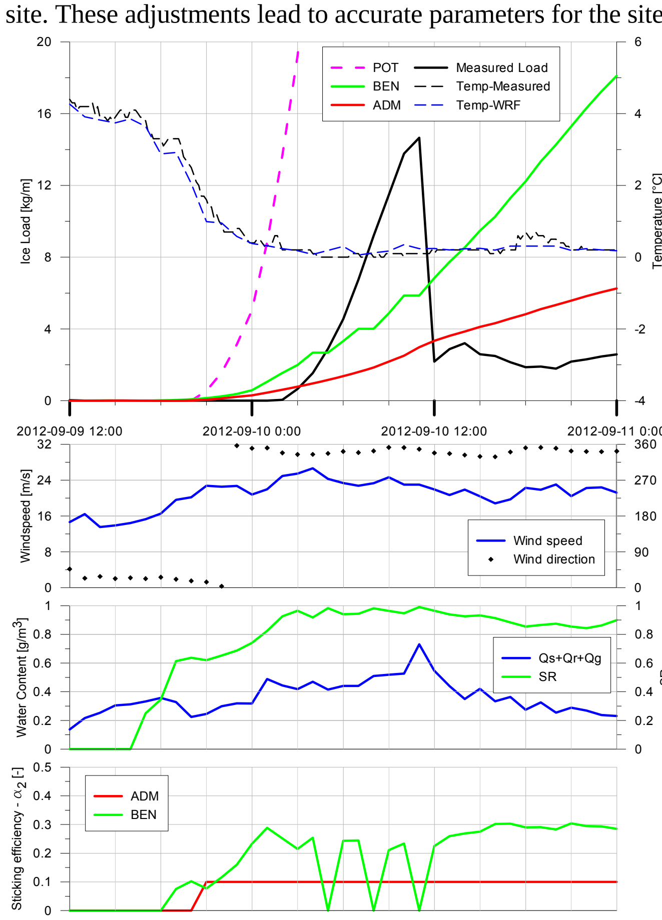

Fig. 2. 132 kV KS1. Comparison of icing measurements and icing model.

The comparison between the measured loading and the calculated icing reveals that there is a sufficient flux of water to explain the accumulation, see POT curve. The WRF analysis predicts that the water content is mainly rain (Qr) in the beginning but changes to snow (Qs) later, the SR is in range of 0.8 to 1.0 at the time of accumulation. Both icing models by BEN and ADM predict wet snow accumulation but less than observed. The BEN model predicts more icing than the ADM model and is closer to measurements, while the icing rate is too slow in both models. The accumulation in the icing models starts about 6 hours before it is identified in measurements, the WRF analysis predicts that SR is less than 0.8 in that period with significant amounts of rain. The icing models predict that accumulation continues about 12 hours after the loading drops due to failure of the adjacent towers. Accumulation did in fact continue for some time after the drop in loading, as can deduced from the load data.

CASE 2 – TEST SPAN, GÆSAFJÖLL, SEPT. 2012

This wet-snow event at Gæsafjöll occurred in same weather as is described in Case 1. The location of the measuring site is farther inland, 120 m higher in altitude and approx. 19 km south of the site in Case 1. Measurements were made in an 80-m-long test span. (N65°47'17.0" W17°00'12.8", 400 m.a.s.l.).

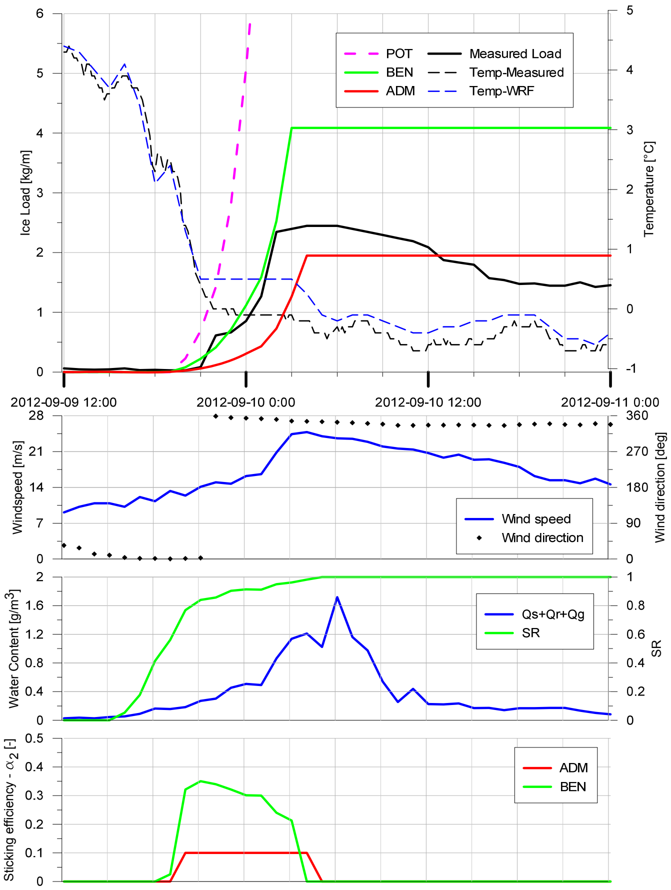

Fig. 3. 80 m test span at Gæsafjöll, 2012. Comparison of icing measurements and icing model.

At the Gæsafjöll site, there is, in addition to the test span, an automatic weather station giving accurate observations of wind and temperature at high temporal resolution. The overall quality of the simulations is the same as for Case 1, and at the test span in Gæsafjöll the observations were well reproduced by the atmospheric model. Only slight modifications were made in the post-process to the simulated data, and the input parameters at the site are classified to be accurate and reliable.

The comparison between the measured loading and the calculated icing in Fig. 3 reveals that there is a sufficient flux of water to explain the accumulation. The WRF analysis predicts that the water content is mainly snow (Qs), and SR is in range of 0.85 to 1.0 at the time of accumulation. The icing model by BEN predicts the wet snow accumulation rate very well but continues hour to long and ends with higher total accumulation. The ADM model also predicts accumulation, the accumulation rate is too low but it lasts for two hours to long. Total loading in ADM is slightly lower than the evaluated ice load.

CASE 3 – TEST SPAN, FLJÓTIN, MARCH 1999

This event occurred in an area where heavy wet snow accumulation has often been experienced on overhead lines, and today most of the distribution system has been put underground due to regular failures related to wet snow. The area's topography is complex, as it is located on a mountainous peninsula in North Iceland, reaching more than 1000 m above sea level. Typically, the heaviest ice load occurs in strong northeasterly flow when moist maritime air masses are lifted over the mountains and subsequently descend down the slopes on the lee side. This was also the case on 12 March 1999 when there was extreme accumulation of wet snow at the site. The accumulation started around 0100 UTC and continued for 15 hours. During the accretion, the temperature range was 0°C to 1.5°C, and the 10-minute average wind speed was estimated from a nearby weather station to be in the range of 10-25 m/s. This event has previously been described in [15] and [16].

Measurements are made in a test span consisting of three wooden towers; the towers are the remaining part of a 22 kV overhead line that has been replaced by underground cable due to frequent failure related to wet-snow icing. (N66°03'27.2" W19°01'01.8" 20 m.a.s.l.). The station is located leeward to the west of the mountains (Fig. 4).

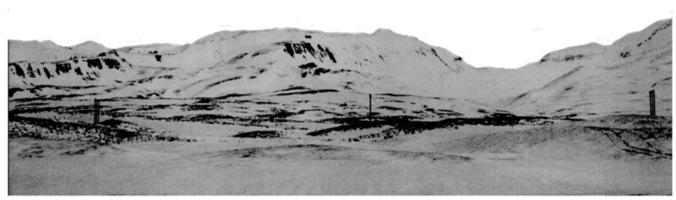

Fig. 4. Test site, two 110m spans facing the ice storms direction.

The very complex topography in the region complicates all atmospheric simulations. There is a relatively large number of weather stations in the region, and the atmospheric situation is well reproduced at many of the stations but far worse at others. The main errors and uncertainty relate to the quality of the forcing data for the atmospheric model (ECMWF-analysis), the quality of the representation of the surface characteristics in the region, and to what extent observations at individual sites can be considered representative of the weather on the horizontal scale of the model. Overall, the observed wind and temperature are well reproduced on the upstream (eastern and northern) side of the Tröllaskagi Peninsula, but as is often the case in complex terrain, the greatest errors are found in the lee of large mountains to the west. Precipitation was highly localized in the lee of the complex terrain, but due to the extreme wind speeds during the event, significant undercatch of the snowfall is expected at the available rain gauges. Precipitation and atmospheric water content is however expected to be reasonably reproduced, based on the available data and experience with the atmospheric model.

The location of the test span is characteristic for downslope windstorm locations, as is the location of an automatic weather station 10 km farther north. The conditions at the test span and the weather station are somewhat similar, especially in northeasterly and easterly winds. The flow was relatively poorly reproduced at the weather station, and hence it is not fully clear how well the input parameters at the test span site are simulated, where only temperature is measured. The very high spatial gradient in wind speed and atmospheric water content further complicates the matter but also shows that even if the extreme conditions at the site itself are not correctly reproduced, such conditions exist within a few grid cells (1-3 km) further upstream. The necessary adjustments to the data were significant, and the input parameters at the site are classified to be somewhat accurate.

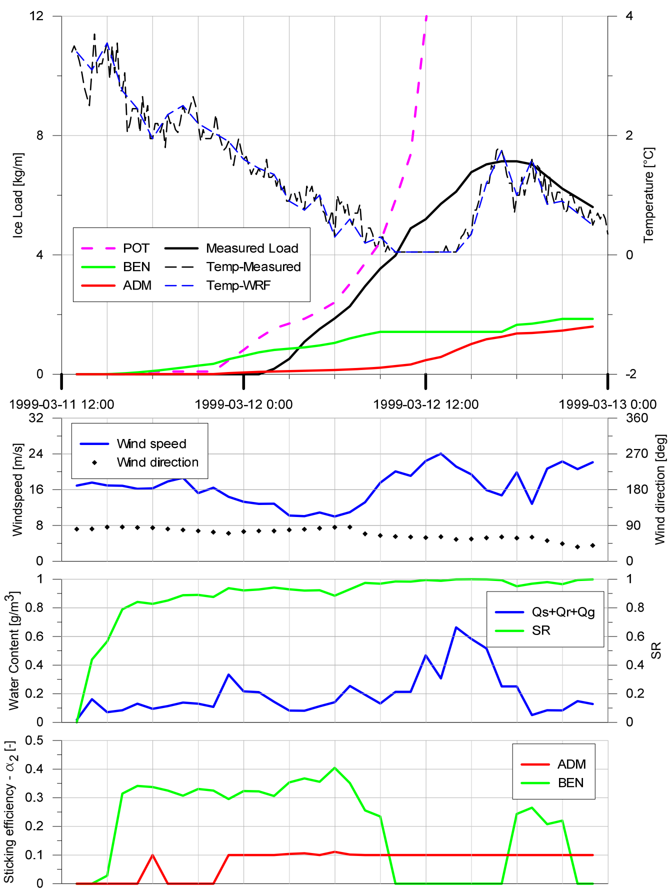

Fig. 5. Test span, Fljótin 1999. Comparison of icing measurements and icing model.

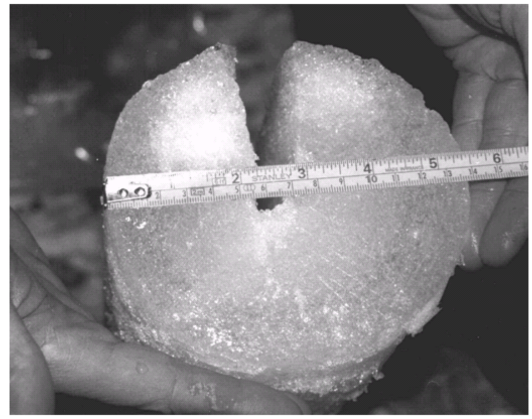

Fig. 6. Sample taken from ground in April 1999, four weeks after the accumulation.

The comparison between the measured loading and the calculated icing reveals that there is hardly sufficient flux of water in the WRF analysis to explain the accumulation in the first hours; almost all the water has to accrete on the wires to explain the loading. Both the BEN and the ADM model underestimate the accumulation. The BEN model predicts accretion more than 6 hours before it is measured, and at this time SR is above 0.5 and the temperature above 2°C. Presumably the bad fit of the icing models can be explained to a large extent by poor input parameters, based on the atmospheric simulations. Namely, the wind speed was presumably underestimated as was the liquid water content, which may be a result of underestimating the spatial extent of the downslope windstorm above the lee slopes of the mountain, as previously pointed out in [17]. In fact, more wet-snow accretion is simulated a few km further upstream (not shown).

CASE 4 – TEST SPAN, FLJÓTIN, JAN. 2013

This is the same measuring site as described in Case 3. The event of 28 January 2013 is in most respects very similar to Case 3 from 1999. The weather was characterized by very strong northeasterly winds of at least 20 m/s, associated with extreme amounts of precipitation. The temperature, which was only a few degrees above zero, slowly decreased during the event.

The measurements at this test site include three different conductor setups, with 2 m spacing between them. The setups counted from the icing direction are: (i) 12 mm conductor, (ii) 28 mm conductor and (iii) 18 mm conductor. In this event the different setups show all the same accumulation tendency, although there is a difference in the maximum loading, see Fig. 7. The greatest accumulation occurred on the 28 mm conductor that is positioned in the middle. The second greatest accumulation was on the 12 mm conductor positioned next to icing direction, and the lowest ice load occurred on the 18 mm conductor farthest away from the icing direction. It is not completely clear why loading for the 18 mm conductor gave the lowest accumulation, but it may at least partly be related to shielding effects.

Due to how recent this event is, the quality of the input data forcing the atmospheric model is somewhat better than for the event in 1999; furthermore, there is a greater number of weather stations with available data. The observed wind and temperature are overall well reproduced on the upstream (eastern and northern) side of the peninsula, but worse at many locations in the lee of large mountains. Precipitation was highly localized in the lee of the complex terrain, with significant undercatch at the available rain gauges, but the precipitation and atmospheric water content is nevertheless expected to be reasonably reproduced.

The flow is reasonably reproduced at the weather station nearest the site, and hence the quality of the simulated input parameters at the test span site is expected to be adequate but not necessarily good. As for the 1999 case, there is a high spatial gradient in wind speed and atmospheric water content further complicating the matter. After the necessary post-processing, the input parameters at the site are classified to be reasonably accurate.

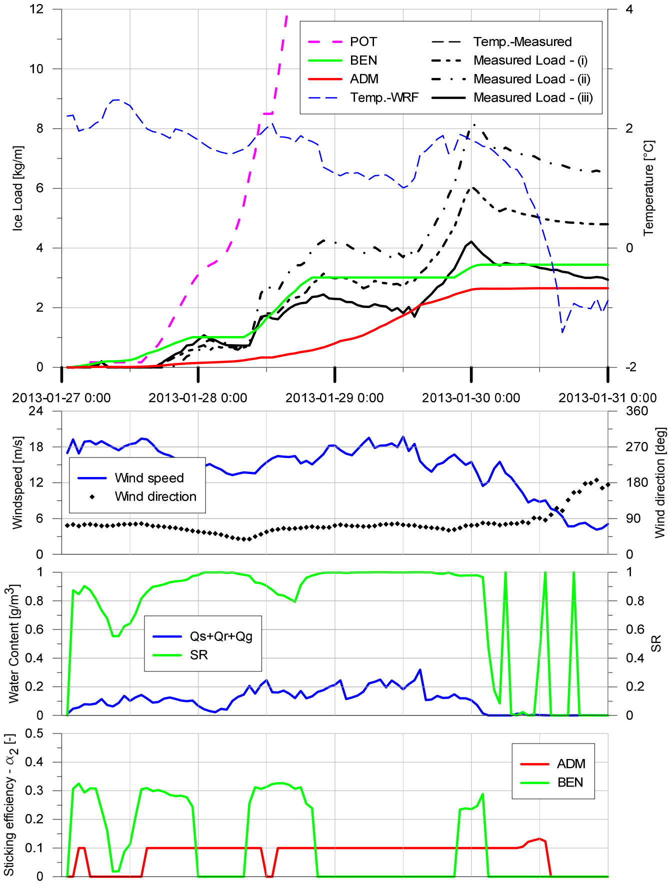

Fig. 7. Test span, Fljótin 2013. Comparison of icing measurements and icing model.

The comparison between the measured loading and the calculated icing for the 12 mm conductor reveals that there is a sufficient flux of water to explain the accumulation. The WRF analysis predicts that the water content is mainly snow (Qs), with SR in range of 0.8 to 1.0 at time of accumulation. The BEN model predicts the wet snow accumulation pretty well. The ADM model predicts too low accumulation in the beginning of the event. During the period 2013-01-28 20:00 to 2013-01-29 14:00 the ADM is predicting accumulation while no accumulation is observed. Due to this the peak loading in ADM is close to the peak of the evaluated ice load.

CASE 5 – TEST SPAN, ÓLAFSFJÖRÐUR, OCT. 2001

The weather during the Ólafsfjörður event of October 2001 was in many respects similar to the weather during the major events at Fljótin, described in cases 3 and 4, and occurs in the same region. Winds were very strong from the northeast and north, and were associated with large amounts of precipitation. Ólafsfjörður is a small fjord located on the upwind site of a mountainous peninsula (Tröllaskagi), and the weather there is strongly affected by proximity to the ocean on the upwind side and the surrounding complex topography (N66°03'50.6" W18°40'49.7" 10 m.a.s.l.).

Fig. 8. Test span in Ólafsfjörður, 80 m long on wooden poles and 10 m above ground.

Overall the weather at the Ólafsfjörður site and at many other weather stations in the region is very well reproduced by the atmospheric simulations. Wind speeds and wind direction are accurately captured, while the temperature is at some locations somewhat overestimated. Large amounts of precipitation were observed, but the expected undercatch of the rain gauges complicates direct comparison with the simulated precipitation field at many locations; however, atmospheric water content and precipitation amounts are expected to be reasonably accurate.

There is an automatic weather station near the test span, and here winds were excellently captured (approx. 10 m/s and directed along the main axis of the fjord), while there was an approximate 1°C temperature bias in the simulations. The modifications to the simulated data were limited to correcting the temperature bias and slightly adjusting the precipitation and atmospheric water amounts to reflect the temperature shift and observed amounts of precipitation. The post-processed simulated values are expected to be accurate and reliable.

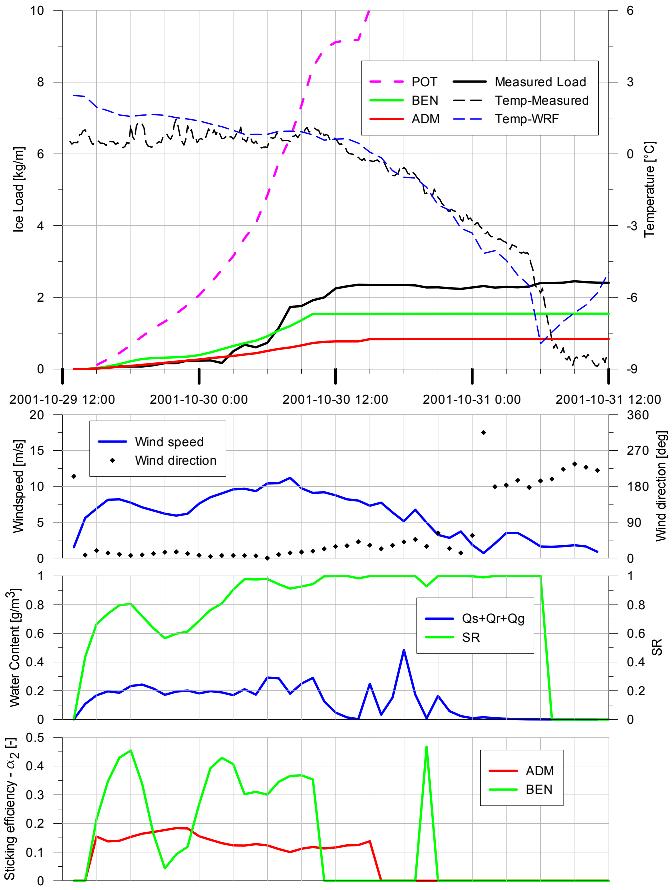

Fig. 9. Ólafsfjörður 2001, 80 m test span. Comparison of icing measurements and icing model.

The comparison between the measured loading and the calculated icing reveals that there is sufficient flux of water to explain the accumulation. The WRF analysis predicts that SR is in the range of 0.6 to 0.8 in the beginning of the accumulation, when the icing rate is slow. SR is in the range of 0.8 to 1.0 when the icing rate increases. The icing model by BEN predicts the wet snow accumulation quite well; the ADM model also predicts accumulation but somewhat too low. The time of accumulation is well predicted in both models, although accumulation in the BEN model stops too soon due at SR=1.0 (no sticking). The accumulation in measurements and models stops when temperature becomes negative and wind speed is reduced.

CASE 6 – 132 KV MJ1, DEC. 2012

On 30 December 2012 a severe wet snow storm hit Northwest Iceland, with heavy snowfall and very strong winds. Icing conditions and icing on overhead power lines were observed at many locations in the region, which is characterized by very complex orography, while mountains are generally not much higher than approximately 700 m. Wet snow accumulation on the conductors of transmission and distribution lines was mainly confined to locations on the immediate leeside of mountains and hills. There are indications that the heaviest accumulations were combined with drift snow from nearby hills, mountains and other landscape features where the flow was locally enhanced. The extreme wet-snow accretion and the very strong winds resulted in significant damage to both the transmission and the distribution system. This event is described in detail in [8]. Measurements are made in an operating 132 kV MJ1 overhead transmission line at the Kambur location; the load cell is located in a suspension attachment to one H-frame suspension tower (N65°29'40.5" W21°57'45.7" 40 m.a.s.l.).

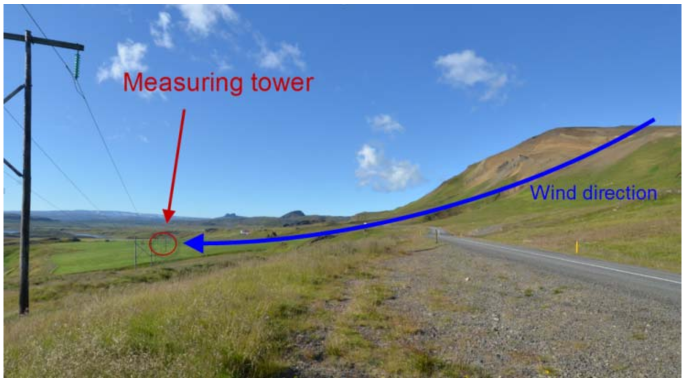

Fig. 10. Suspension tower at Kambur in 132 kV MJ1 with measuring equipment.

There is a relatively large number of automatic and synoptic weather stations in the region with useful data for verifying the simulations and analyzing the event. The observed atmospheric parameters are on average well captured by the simulations, but better captured on the upwind side of the mountains and on average very well in the mountains themselves. The performance is somewhat worse on the leeside of the mountains, including some of the sites where intense accumulation was observed. As for other wet-snow events, the strong winds during snowfall complicate the comparison of observed and simulated precipitation; however, the precipitation and atmospheric water content is expected to be reasonably captured. Winds are on average well captured but in some cases underestimated in the lee of mountains, while temperatures are in some cases slightly too high.

There are two weather stations some kilometers away from the icing measurement site at Kambur, which is located in the immediate lee of a mountain. At an upstream station in the mountains the observed weather is very well reproduced. At another leeside station slightly north of Kambur there are some errors in the simulated winds and temperatures, but the quality of the simulations is on average good. The necessary modifications at Kambur are based on a comparison with observed values at these two stations and the temperatures observed at the measuring site itself. The simulated data for Kambur is expected to be reasonably accurate and reliable. The model, however, is unable to correctly represent the effect of the highly complex and small-scale topographic features at the site itself, e.g., those seen in Fig. 10.

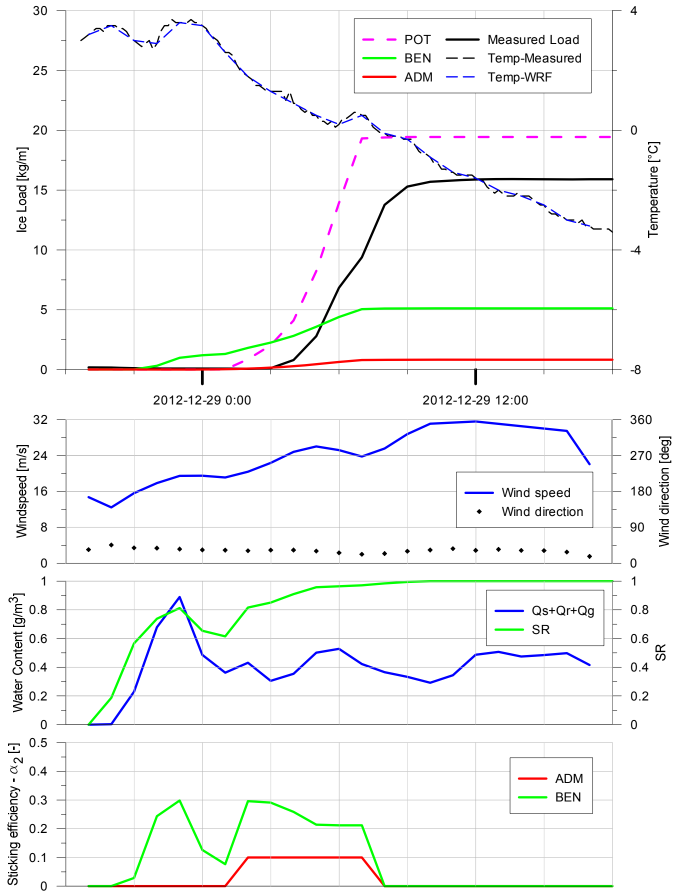

Fig. 11. Kambur 2012, 132 kV OHTL in operation. Comparison of icing measurements and icing model.

The comparison between the measured loading and the calculated icing reveals that the flux of water is hardly enough to explain the accumulation. It is believed that local small-scale landscape features may accelerate or lift the surface flow, causing significant amounts of drifting snow and enhanced water flux at the elevation of the conductors (Fig. 10). Furthermore, accumulation at the sites may also be affected by the advection of super-cooled cloud and rain water possibly formed due to orographic uplift in a dramatic gravity wave above the mountain. Such gravity waves and formation of super-cooled atmospheric water have been simulated at several locations in the region during the storm and in other cases where extreme wet-snow accretion has been observed on the lee-side of the mountains. This matter is subject to further investigation and is discussed in more detail in [8].

The BEN model predicts accumulation that starts too early and is too slow; it starts when SR passes 0.5, and it stops when SR becomes > 0.98, while, at the same time, the actual icing rate is high and continuous for 3 hours. The ADM model predicts small wet snow accumulation and much less than observed (Fig. 11).

VI. Conclusion

Six cases of moderate to severe wet-snow events have been described using field measurements of ice accumulation and temperature, observations from a dense network of weather stations as well as results from high-resolution atmospheric simulations. The accumulated wet-snow icing varies greatly between the cases, and the peak loading for each case is in the range of 2.5 kg/m to 16 kg/m. The wind speed is in general high during these events, and the largest events are associated with very large amounts of precipitation and/or gale force winds.

Time series of measured wet-snow loading were compared to calculated wet-snow accumulation using two cylindrical accretion models (ADM [9] and BEN [2]). The comparison reveals that the BEN model predicts more icing and gives better results than the ADM model. It predicts the smaller events (2-4 kg/m) well but underestimates icing in the larger events (> 10 kg/m).

The ADM model always underestimates the accumulation as well as the loading. Part of the explanation why the BEN model performs better here is the fact that it was calibrated using similar input data (NWP and WRF) and icing conditions as in the current events. That is, it was calibrated using observed and simulated climate data sets, characterized by relatively high winds and large amounts of precipitation, but including a large number of moderate to severe wet-snow events. The ADM model was calibrated using datasets characterized by far weaker winds in e.g., forest-covered regions in France and Japan [18], which traditionally give far less dense wet-snow sleeves than typically observed in Iceland (~700 kg/m3).

The largest difference between the two icing models is the approach to the sticking efficiency (α_2), and its dependence in the ADM model on a relatively wide temperature range (not wet bulb) used to indicate wet snow, while the BEN model uses a physically based parameterization of the melting of snow in a state-of-the-art atmospheric model. It can be concluded that the sticking efficiency is significantly underestimated in the ADM model, where it is often equal to 0.1 (wind speed > 10 m/s). The sticking efficiency in the BEN model is most often during accumulation in the range of 0.25 to 0.40, i.e., when SR is the range of 0.8 to 0.98. The model predicts small sticking efficiency when SR < 0.8. The BEN model is very sensitive at SR close to 0.98 since the sticking efficiency can be rather high at 0.98 but drops to zero when SR > 0.98. Small difference in the rain phase (Qr) can thus have large influence. There are indications that a better fit with observations may be achieved in some of the cases by allowing accretion of snow when SR is above 0.98. It is, however, difficult to assess if it is due to the evaluation and accuracy of SR, i.e., parameterization of atmospheric cloud and precipitation physics, or some physics allowing dry particles to stick to the accreted snow sleeve on the conductor.

Overall, using atmospheric data based on the results of high resolution numerical meteorological models (WRF), allows for a detailed analysis of wet-snow accretion in complex and data-sparse regions. More so as several of the relevant atmospheric parameters are not routinely observed, such as the snow flux and its liquid water fraction, which is critically dependent on the wet bulb temperature but has previously been based on in-situ observations of the temperature. Systematic comparison with weather observations indicates that the atmospheric simulations correctly reproduce the large scale and mesoscale flow. The flow is in general best captured away from very complex topography as well as on its upstream side. The worst performance, as well as the highest spatial variability in the relevant atmospheric fields is found in the lee of and near large mountains. Some of the highest wet-snow loading observed in the previously described cases may be related to phenomena that are poorly reproduced, or not reproduced at all, in the input data or in the accretion models. These phenomena can be separated into:

a. Relevant processes not presented in the accretion models themselves, which include complex dependence of accretion efficiency on the surface temperature and humidity of the snow sleeve/conductor, compared to the liquid water fraction of the precipitation. That is, accretion efficiency is different for a naked conductor compared to a snow sleeve, and very wet/dry precipitation may stick to a cold/warm and dry/wet-snow sleeve. The current models do not account for this.

b. Poor atmospheric input data, either due to biases in the actual parameters or phenomena not reproduced by the models. These include, but are not limited to: 1) Errors in the spatial extent or location of areas with the most favorable conditions for efficient wet-snow accretion, e.g., for leeside windstorms which are often associated with severe accretion in complex orography. 2) Small-scale topography (not represented in the atmospheric model) which may channel or lift the surface airflow and introduce snow drift or otherwise enhance the precipitation flux at the elevation of the conductors. Indications of this have in fact been previously found by careful inspection of accumulated snow sleeves. 3) Finally, simulations of events characterized by localized and severe wet snow accumulation in the lee of mountains indicate that gravity wave activity aloft may be of significance and enhance the surface water flux and accretion on the leeside.

References

[1] S. P. Ísaksson, Á. J. Elíasson and E. Thorsteins, "Icing Database - Acquisition and Registration of Data," in *8th IWAIS*, Reykjavík, Iceland, 1998.

[2] B. E. K. Nygaard, H. Ágústsson and K. Somfalvi-Tóth, "Modeling Wet Snow Accretion on Power Lines: Improvements to Previous Methods. Using 50 Years of Observations," *J. Appl. Meteor. Climatol., in press*, 2013.

[3] Á. J. Elíasson and E. Thorsteins, "Wet snow icing combined with strong wind - Field inspections and field measurments," in *7th IWAIS*, Saguenay, Canada, 1996.

[4] Á. J. Elíasson, E. Thorsteins and H. Ólafsson, "Study of Wet Snow Events on the South Coast of Iceland," in *9th IWAIS*, Chester, England, 2000.

[5] Á. J. Eliasson and E. Thorsteins, "Ice load measurements in test spans for 30 years," in *12th IWAIS*, Yokohama, Japan, October 2007.

[6] W. C. Skamarock, J. B. Klemp, J. Dudhia, D. O. Gill, D. M. Barker, M. D. Duda, W. Wang and G. Powers, "A description of the Advanced Research WRF version 2.," *Tech. Rep. NCAR/TN-468+STR, National center for atmospheric research*, p. 88, 2008.

[7] G. Thompson, P. Field, R. Rasmussen and W. Hall, "Explicit forecasts of winter precipitation using an improved bulk microphysics scheme. Part II: Implementation of a new snow parameterization," *Mon. Wea. Rev.*, no. 136, pp. 5095-5115, 2008.

[8] Á. J. Elíasson, H. Ágústsson and G. M. Hannesson, "Wet-Snow accumulation - A study of two severe events in complex terrain in Iceland," in *15th IWAIS*, St. John's, Newfoundland and Labrador, Canada, 2013.

[9] P. Admirat, "Wet snow accretion on overhead lines," *Atmospheric Icing of Power Networks*, pp. 119-169, 2008.

[10] Y. Sakamoto, "Snow accretion on overhead wires," *Philos. Trans. Roy. Soc. A*, no. 358, pp. 2941-2970, 2000.

[11] G. Poots, "Aspects of a Model of Wet-Snow Accretion on an Overhead Line Conductor," in *8th IWAIS*, Reykjavik, 1998.

[12] L. Makkonen, "Models for the growth of rime, glaze, icicles and wet snow on structures," *Phil. Trans. R. Soc.*, no. 358, pp. 2913-2939, 2000.

[13] K. J. Finstad, S. M. Fikke and M. Ervik, "A comprehensive deterministic model for transmission line icing applied to Laboratory and field observations," in *4th IWAIS*, Paris, 1988.

[14] ISO/TC98/SC3/WG6, Atmospheric icing of structures, International Standard, ISO 12494, 2000.

[15] Á. J. Elíasson and E. Thorsteins, "Field Measurments of Wet Snow Icing Accumulation," in *9th IWAIS*, Chester, England, 2000.

[16] H. Ólafsson, Á. Elíasson and E. Thorsteins, "Orographic Influence on Wet Snow Icing – Part II: Downstream of Mountains," in *10th International Workshop on Atmospheric Icing of Structures (IWAIS)*, Brno, Czech Republic, 2002.

[17] H. Ágústsson and H. Ólafsson, "Simulating a severe windstorm in complex terrain," *Meteorol. Z*, vol. 16, no. 1, pp. 111-112, 2007.

[18] P. Admirat, Y. Sakamoto and B. De Goncourt, "Calibration of Snow Accumulation Model Based on Actual Cases in Japan and France," in *4th IWAIS*, Paris, France, 1988.

[19] G. Thompson, B. E. Nygaard, L. Makkonen and S. Dierer, "Using the Weather Research and Forecasting (WRF) Model to Predict Ground/Structural Icing," in *13th IWAIS*, Andermatt, September 2009.

A study on the sticking efficiency of wet snow using 50 years of observations

Bjørn Egil K. Nygaard[1], Hálfdán Ágústsson2[2], Katalin Somfalvi-Tóth2[3]

[1]*Norwegian Meteorological Institute*
Oslo, Norway

[2]*The Icelandic Meteorological Institute*
Institute for Metorological ResearchUniversity of Iceland
Reykjavik, Iceland

[3] *Hungarian Meteorological Service*
Budapest, Hungary

[1]bek.nygaard@gmail.com
[2]Toth.k@met.hu
[3]halfdana@gmail.com

Abstract **—** Methods to model wet snow accretion on structures are developed and improved, based on unique records of wet snow icing events as well as large datasets of observed and simulated weather. Hundreds of observed wet snow icing events are logged in detail in a database, most of which include an estimate of the mean and maximum diameter of observed wet snow icing on overhead power conductors. Observations of weather are furthermore available from a dense network of weather stations. Common for wet snow accretion models is the vast uncertainty related to the bouncing of the snow flakes after collision (sticking efficiency), and its relation to the meteorological parameters. In the current study a standard cylindrical accretion model is updated with a snow flake liquid fraction based criterion to identify wet snow, together with an updated value for the terminal fall speed of wet snow flakes. By comparing extreme value distributions from modeled and measured wet snow loads, it is found that the widely used parameterization of the sticking efficiency strongly underestimate the accretion rate. A calibrated parameterization of the sticking efficiency is therefore suggested based on the long term statistics of observed and modeled wet snow loads. The results form a basis for mapping the climatology of wet snow icing as well as for preparing operational forecasts of wet snow icing and severe weather for overhead power transmission lines.

Keywords **—** *wet snow; wrf model; sticking efficiency; power lines; liquid water fraction*

I. Introduction

Wet snow accretion occurs when partly melted snowflakes collide with an object and adhere to its surface after collision. The accretion rate is dependent on the stickiness of wet snow which varies with the fractional mass of liquid water versus snow crystals (Liquid Water Fraction, LWF) in the snow flakes. At a certain LWF the adhesive forces of the wet snow has a maximum, and accordingly makes it ideal for accretion on structures like overhead power conductors.

Due to the importance of wet snow loading on the design of power lines, several attempts have been made to parameterize wet snow accretion based on standard meteorological measurements ([1]-[3]). However, as pointed out in [1], the results of studies on the meteorological conditions under which wet snow accretion occurs are controversial, because wet snow accretion is reported to occur under slightly different weather conditions, and no universal criteria have been obtained. The reason for this inconsistency may be that two of the main parameters controlling the wet snow accretion are not directly measured, i.e. the content of falling wet snow (mass concentration) in the air and the snowflake LWF. Hence these parameters have been parameterized based on the standard weather data such as precipitation rate, visibility, temperature and humidity. The uncertainty in these data may also be large, in particular the snowfall rate in strong winds, potentially introducing biases in calibration of the models.

In this study we make use of a unique dataset of observed wet snow accretion in the southern part of Iceland to evaluate and improve the wet snow accretion models. The dataset contains measurements of wet snow since the early twentieth century and is, to the authors' best knowledge, the largest collection of wet snow measurements ever reported but never before used to evaluate wet snow models. The observed wet snow loads are compared to modeled loads based on meteorological data from 50 years of downscaled weather at high spatial and temporal resolution using the Weather Research and Forecasting Model (WRF; [4]). By comparing extreme value statistics from both model and observational data, we are able to evaluate the model and its ability to reproduce the measured extreme ice load values. Uncertain aspects of the existing models are discussed, and improvements of the simple cylindrical accretion model are suggested. A modified version of the previous method is tested, and we suggest a new model using a LWF-dependent formulation of the accretion efficiency.

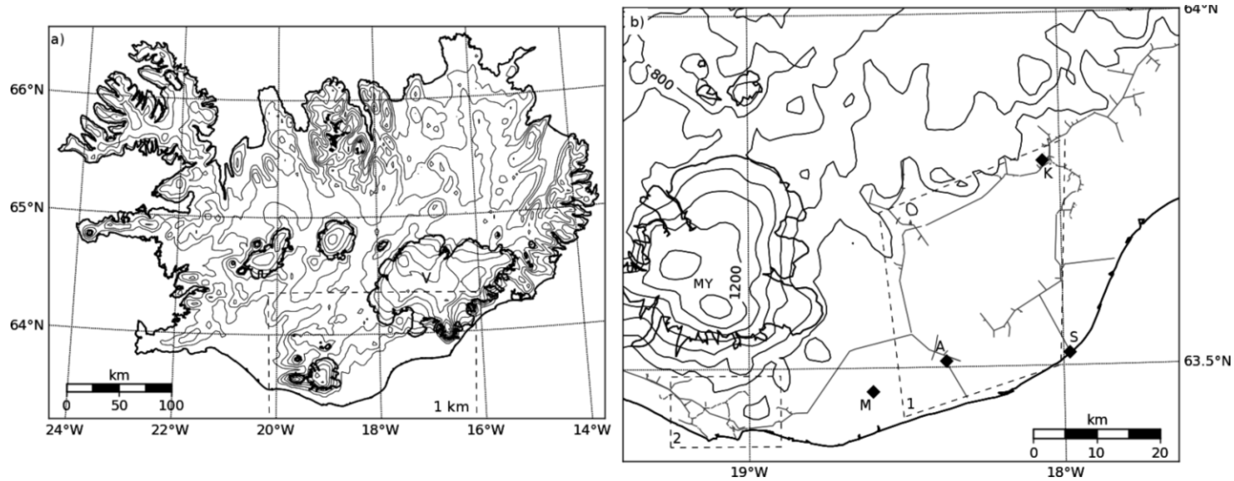

Figure 1. Topography at (a) a resolution of 9km in the RAV dataset and (b) a resolution of 1km in the case study of wet snow events. Also shown are the outlines of the 1-km domain and subregions 1 and 2 (dashed lines), coastlines and glacier outlines (thick lines), power lines (thin gray lines) and location of weather stations (diamonds). The contour interval for elevation is 200 m.

II. OBSERVATIONS AND MODEL DATA

A. *weather data*

The weather dataset used here is called The Reikningar a veðri (RÁV), and is based on dynamically downscaled weather in Iceland at high horizontal and temporal resolution. WRF (V3.0.1; [4]) is utilized to downscale the atmospheric analyses from the European Centre for Medium-Range Weather Forecasts (ECMWF). The model is run with 55 levels in the vertical at a 9-km horizontal grid spacing (95 X 90 points) for the years 1957–2011 (Figs. 1a,b). The 40-yr ECMWF Re-Analysis (ERA-40) reanalysis of the ECMWF covers 1957–2000 and thereafter its operational analysis is applied. The model is run continuously from 15 August until 1 September, discarding the first 15 days as spinup. All necessary variables for detailed atmospheric and icing analyses are stored at a temporal resolution of 3 h. For the subsequent statistical analysis, surface data and atmospheric variables from the lowest model level are extracted from the 9 X 9 km^2 grid box nearest to the location of interest, taking into account land-use characteristics and land height.

The main region of interest (subregion 1 in Fig. 1) is well represented at a resolution of 9 km, as it is composed of relatively flat land with the sea to the south and east. Verification against data from the nearest weather stations was performed in order to investigate the quality of the RÁV dataset. In general temperature and wind conditions are well captured by the model. The precipitation verification is more scattered, as expected taking into account the vast uncertainties related to measurements of solid precipitation in windy conditions, which is typical during wet snow events. In summary, the quality of the downscaled atmospheric was considered adequate for this study.

B. *Wet snow accretion measurements*

The database consists of recorded snow and ice load events on overhead lines (11–33 kV) in southeast Iceland since early in the twentieth century. The data are collected, organized, and owned by Landsnet, the national power transmission operator in Iceland. Observations of the typical and maximum icing diameters are used here, but the dataset also includes, for example, estimates of the start of the accretion period and its duration, main icing direction, and visual description of accreted mass. It is unique in the sense that the authors are not aware of another equally extensive and detailed database pertaining to systematic observations of atmospheric icing and wet snow accumulation in particular.

The observed wet snow accumulations used in this study have been collected in a sub-area in the south-east Iceland (Fig. 1b). 12 serious events with snow sleeve diameters up to 9 cm have been observed since 1981, and 2 catastrophic events in 1994 and 2000 with sleeves up to 16cm in diameter causing large-scale damage on the distribution system [5].

Figure 2 shows the maximum observed wet snow diameters from each event plotted as a function of the precipitation amount and wind speed measured during the events. In this dataset, the icing diameter is found to depend on the precipitation amount and as well as wind speed, as indicated by all the largest icing diameters tending to cluster in the upper-right part of Fig. 2, while only small icing diameters are found in the lower left area. Significant icing diameters also occur at relatively low precipitation amounts in combination with high wind speed, emphasizing the importance of wind speed in a the accretion process.

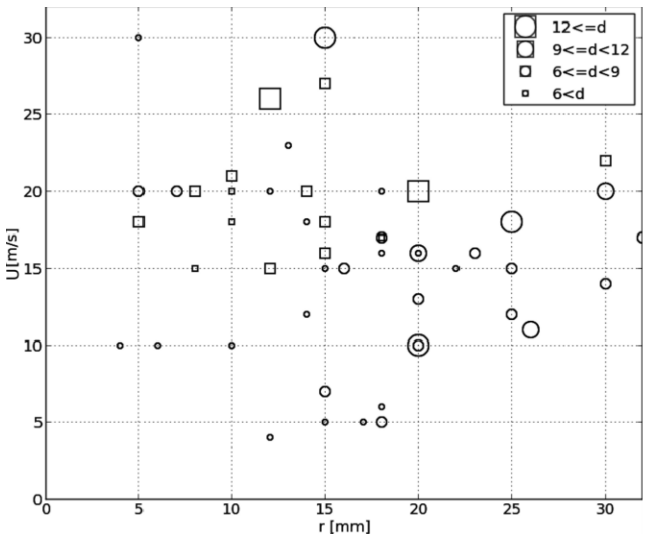

Figure 2 Observed wet snow icing diameter in southeast Iceland as a function of observed precipitation (r) and wind speed (U) during wet snow stormat a representative weather station. Circles are from subregion 1 close to Alftaver–Kirkjubæjarklaustur, while squares are from Myrdalur, subregion 2.

III. EXPERIMENTAL SETUP

A. The wet snow accretion model

In this study we are testing a simple cylindrical accretion model for wet snow. The model is based on a horizontally oriented cylinder with low torsional rigidity, such that the accumulated wet snow is distributed evenly around the cylinder and the geometric shape is maintained during the accumulation time. The details of the model are nicely described in [3]. The icing intensity per unit area is given by

$$I = \beta\sqrt{U^2 + v_s^2}w. \quad (1)$$

Where β is the sticking efficiency, U is the horizontal wind speed normal to the cylinder, v_s is the terminal velocity of wet snowflakes (set to 1.7 m/s in the current study [6] and w is the mass concentration of wet snow in the air. With meteorological data at 3 hors interval (Δt) from the RÁV database the accumulated wet snow mass M at time step i is given by:

$$M_i = M_{i-1} + I_{i-1}D_{i-1}\Delta t., (2)$$

where D_{i-1} is the snow sleeve diameter at the previous time step. Assuming a density ρs of the accumulated snow, the cylinder diameter can be updated for timestep i:

$$D_i = \left[\frac{4(M_i - M_{i-1})}{\pi\rho_s} + D_{i-1}^2\right]^{1/2}, (3)$$

By running this integration scheme through the entire period of 54 years, the modeled wet snow extreme value distribution can be compared with the measured extremes.

The first issue that a snow accretion model has to address is to identify the amount of wet snow during a given weather event. Reference [3] assumed that all precipitation reaching the ground at 2-m temperatures between 0ºC and 2ºC was in the state of wet snow. Reference [2] used a somewhat similar criterion but found an upper temperature limit that changed with altitude and weather condition prevailing during the storm. Similar results were found by [7] where air temperature limits of snow and rain were analyzed in Iceland. Reference [1] emphasized the role of atmospheric moisture for the presence of wet snow, and showed that one necessary condition was a positive wet-bulb temperature (T_w > 0ºC). While various criteria have been used to define wet snow, the theoretically correct and physically consistent measure is the LWF of the snowflakes. By definition wet snow is a mixture of frozen and liquid water molecules, hence 0>LWF>1. Reference [8] conducted specific laboratory tests to find that adhesive forces were strongest when the wet snow was in the ‘‘catenary area,’’ which means that the ice crystals are covered with a thin film of water, while air pockets fill the gaps between the crystals in the snowflake. The LWF of such wet snow was in the interval from a few percent up to maximum 25%, with a peak in adhesive strength at LWF between 10% and 15%. Reference [9] found similar results in wind tunnel tests. In the current study an estimate of the snow LWF is extracted directly from the modeled weather data, and wet snow is defined at LWF between 2% and 30%.

B. The sticking efficiency

The sticking efficiency introduced to account for the bouncing effect of snowflakes after collision with the cylinder. For dry snow, all snowflakes tend to bounce off the surface except for wind speeds below 2–3ms^{-1}. As soon as the snowflakes become wet, their stickiness increases rapidly and the chance of bouncing decreases [9]. The likelihood of bouncing has been shown to increase with snowflake impact speed [9], but a pure physically based model has not been feasible because of the complexity of the collision process itself with controlling factors such as the snowflake geometry and liquid water fraction, which are usually unknown.

Parameterization of the sticking efficiency β is particularly in focus because of its uncertainty. The most widely used formulation β = 1/U [3] implies that the accretion rate (I) is independent of wind speed (when inserted in (1)). Figure 2 shows that high loads may be obtained in periods of light or moderate precipitation (10–15mm) combined with high wind speed (25–30ms^{-1}). Hence, a new calibration of β is needed to reproduce the loads gained during high winds. In this study three different parameterizations of β are tested in the time-dependent accretion model, two that allow for substantially higher growth rate than the original Admirat model, particularly at high wind speeds:

1. ADM: The original parameterization used in Admirat (2008), β = 1/U.
2. BETA_U: A similar model but now inversely related to the square root of the wind speed,

$\beta=1/U^{0.5}$, which allows for higher accretion rate than ADM.

3. BETA_SRU: A slightly more sophisticated parameterization where β is a function of both the wind speed and the LWF, more comparable to the formulation suggested in Sakamoto (2000). A function is constructed using a cosine in the numerator to let β vary with SR[1] such that it has a maximum around SR = 0.85. The idea is to give β the highest values at a LWF that corresponded to the stickiest snow [highest adhesive forces in the tests of [8], and lowest chance of bouncing]. The effect of wind speed on the sticking efficiency is controlled by the factor b on the wind speed in the denominator, a factor that needs to be calibrated using observational data. The proposed function is given in (4) and is visualized in Fig. 3.

$$\beta = \frac{1-\cos(9SR-4.5)}{2U^b} \qquad [0.5 < SR < 0.98], \quad (4)$$

$$\beta = 0 \qquad \text{otherwise.}$$

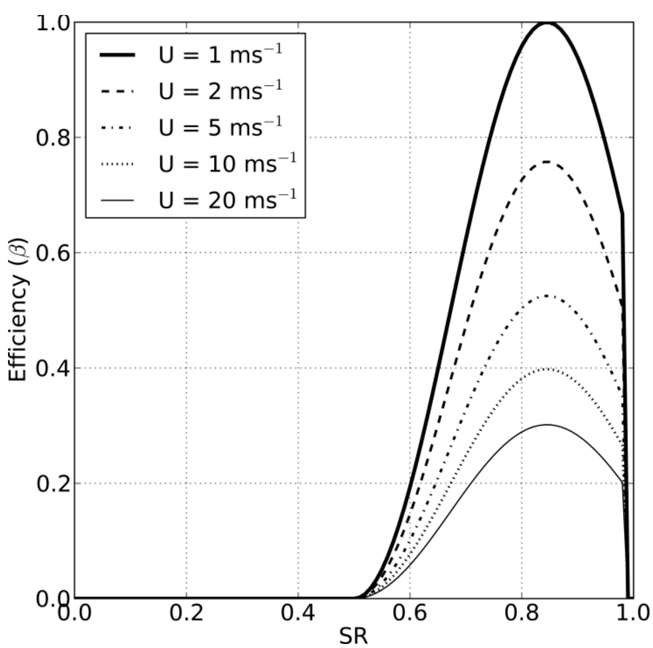

Figure 3. Parameterization of sticking efficiency as a function of fraction of frozen precipitation (SR) and wind speed (U) from WRF, plotted with b = 0.4 in Eq. (4).

C. Estimation of extreme values

Wet snow occurs in a very narrow temperature range and marginal differences between the actual weather and that used for modeling wet snow accretion may cause substantial errors in the modeled wet snow load. Validating and calibrating ice accretion models based on single case studies therefore has obvious limitations, unless precise in situ measurements of all necessary variables are available. To cope with this problem we use a slightly different approach of matching the measured climatological extremes with the modeled climatological extremes (comparing extreme value distributions). This implies that the model is not expected to reproduce every single wet snow storm, but it should reproduce correctly the climatology of such events and hence the statistically calculated extreme values with a given return period.

In total, the observed data consists of 39 values of observed maximum wet snow diameters where some years have multiple maxima and others are not represented. As all measurements are associated with reported problems with the power transmission system, it is assumed that the measurements represent fairly well the most severe wet snow loads (right tail of the distribution). Using this assumption an extreme value analysis (EVA) can be carried out applying the method of peaks over threshold (POT), with the aim of estimating extreme snow loads with certain return periods. Extreme value distributions are estimated both for the modeled and the measured loads using POT.

IV. RESULTS AND CONCLUSIONS

Results from the ADM experiment are plotted in Fig. 4b, and show a remarkable underestimation of the accumulated wet snow. The estimated 50-yr value is close to 4cm only and the distribution is far outside the 95% confidence interval based on the measurements. The average modeled precipitation amount during these events is 18.5mm (inside the wet snow interval), which is consistent with the typical values observed (Fig. 2), and therefore cannot explain the large underestimation. Figure 4c shows the results of the BETA_U experiment. The results agree better with the measured diameters, and the fitted distributions are much closer. The estimated extreme values are slightly below the observations, but well inside the 95% confidence interval. Based on these particular results it seems that the sticking efficiency is more closely related to the inverse square root of the wind speed (BETA_U) than to the inverse of the wind speed itself (ADM). Results from the BETA_SRU experiments are shown in Fig. 4d and give the best match with good agreement with the measurements, employing an optimum value of β = 0.4 (4).

The significant underestimation of the ADM experiment may be surprising as this formulation of sticking efficiency previously has provided reasonable results [3]. Compared with the work of [3] there are at least two other model assumptions in the ADM experiments that may have compensated for the low sticking efficiency.

[1] SR is the fraction of frozen precipitation directly ouputed from the WRF model. Note that LWF = 1-SR.

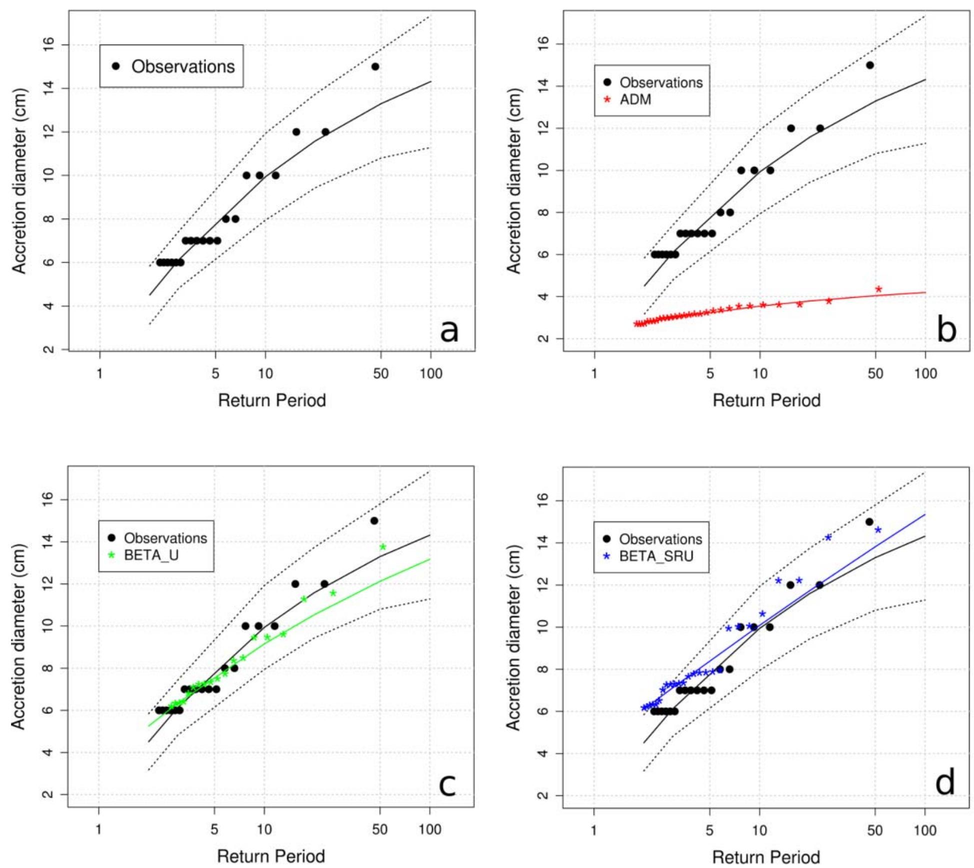

Figure 4. Estimated return period of wet snow icing diameter. (a) Black dots are the observed diameters, while the black line shows the fitted extreme value distribution (dotted lines to outline the 95% confidence interval). (b) As in (a), but with red dots showing modeled icing events from the ADM experiment. (c) As in (a), but with green dots from the BETA_U model. (d) As in (a), but with blue dots representing the BETA_SRU with β=0.4. Colored lines in (b)–(d) are extreme value distributions fitted to the model results.

1) The method to identify wet snow, for example, the width of the temperature interval, has often been assumed to be 0ºC–2ºC. To define all precipitation within this interval as wet snow will give too much wet snow compared to the more physically based LWF criterion used in the current study. Comparing LWF and wet-bulb temperature shows that more than 95% of the wet snow cases occur at wet-bulb temperatures between 0ºC and 1ºC (not shown).

2) Reference [3] uses measured precipitation rate at ground to estimate the wet snow content in the air, by assuming an average terminal velocity of snowflakes. This may be a reasonable approach if precise precipitation measurements are available; on the other hand, it is also sensitive to the assumed terminal velocity of the snowflakes. Reference [3] assumes 1ms^{-1} as an average value for wet snow. More recent measurements [6] suggest, however, that a fall speed closer to 2ms-1 is a better approximation.

The direct use of LWF from the WRF model to identify wet snow in a grid box has the important advantage that it is dependent on the flux of different precipitation species from the grid box above, and thus contains information about the thermal stratification in the atmosphere and the history of the precipitation particles reaching ground level (melting and possibly refreezing). Also the terminal fall speed of different precipitation species are now predicted precisely and can readily be extracted from the WRF model.

In order to fully explore the universality of the new calibrated model, further testing of the model in different climatic regions and with different numerical weather prediction models will be necessary.

ACKNOWLEDGMENT

The authors thank the Top-Level Research Initiative of the Nordic Council for funding through the IceWind project. The work was done within the frame of the European COST Action ES1002 WIRE (Weather Intelligence for Renewable Energies). The work was also supported by Statnett the Norwegian TSO. The authors are indebted to Árni Jón Eliasson at Landsnet for making the wet snow observations available. HaraldurOlafsson at the University of Iceland and Egill Þorsteins at Efla consulting engineers are thanked for valuable discussions. The RÁV project was supervised by Haraldur Olafsson and Olafur Raognvaldsson at the Institute for Meteorological Research with a grant from the Icelandic research fund (RANNIS), and additional funding from Landsnet, Landsvirkjun (the national power company), Orkuveita Reykjavíkur (Reykjavík public power utility company), and Vegagerðin (Public Roads Administration).

REFERENCES

[1] Makkonen, L., 1989: Estimation of wet snow accretion on structures. Cold Reg. Sci. Technol., 17, 83–88.

[2] Sakamoto, Y., 2000: Snow accretion on overhead wires. Philos. Trans. Roy. Soc. London, A358, 2941–2970.

[3] Admirat, P., 2008: Wet snow accretion on overhead lines. Atmospheric Icing of Power Networks, M. Farzaneh, Ed., Springer, 119–169.

[4] W. Skamarock et al., "A description of the advanced research WRF version 3," NCAR Tech. Note, Boulder, CO, US, 2008,113 p.

[5] Elíasson, Á. J. and H. Ólafsson, 2000: Study of wet snow events on the south coast of Iceland. Proc. Ninth Int. Workshop on Atmospheric Icing of Structures (IWAIS), Chester, United Kingdom

[6] Yuter, S. E., D. E. Kingsmill, L. B. Nance, and M. Löffler-Mang, 2006: Observations of precipitation size and fall speed characteristics within coexisting rain and wet snow. J. Appl. Meteor. Climatol., 45, 1450–1464.

[7] Olafsson, H., and S. H. Haraldsdottir, 2003: Diurnal, seasonal, and geographical variability of air temperature limits of snow and rain. Proc. Int. Conf. on Alpine Meteorology and MAPMeeting 2003, Vol. , Brig, Switzerland, MeteoSwiss, 473–476. Available online at http://www.map.meteoswiss.ch/mapdoc/icam2003/ProceedingsB.pdf

[8] Sakakibara, D., Y. Nakamura, K. Kawashima, and S. Miura, 2007: Experimental result for snow accretion characteristics of communications cable. Proc. Int. Wire and Cable Symp. (IWCS), Lake Buena Vista, FL,

[9] Wakahama, G., 1979: Experimental studies of snow accretion on electric lines developed in a strong wind. Nat. Disaster Sci., 1, 21–33.

Met mast configuration guidelines in Cold Climate

Cédric Arbez [#1], Antoine Amossé [#2], Matthew Wadham-Gagnon[#3]

[#] *TechnoCentre Éolien, 70 rue Bolduc, Gaspé (Québec) Canada, G4X 1G2*

[1] carbez@eolien.qc.ca

[2] aamosse@eolien.qc.ca

[3] mgagnon@eolien.qc.ca

Abstract — Many options are given for wind farm developers to assess appropriately cold climate sites: Lidar (wind profiler), Sodar, tilt up tower (temporary met mast) and permanent met masts. For all options, wind farm developers need to optimize the data availability of each technology to reduce uncertainties during measurement campaigns.

In this paper, we explain met mast problematic management based to maintenance statistics and field experience over three test sites. In the same way, this paper will introduce additional recommendations for met masts configuration consistent to IEA Task 19.

To increase the data availability, many considerations need to be taking into account: booms configuration, choice of sensors, heat sensors recommendations, power supplies, communications features, and tower design.

Keywords — cold climate, resource assessment, wind, sensors, met mast, icing, low temperatures, anemometer

I. Nomenclature

A.G.L = above the ground level
AWG= American Wire Gauge
BD= Base dimension
CC = Cold Climate
LTC = Low temperature climate
IC = Icing climate
IEC = International Electrical Commission
IR = Infrared
ITA= Ice throw area
FIA= Falling Ice Area
Level = sensors installed at the same height a.g.l.
LTIC = Low Temperature and Icing Climate
OF= Overhang factor
RH= Relative humidity
R&D= Research and development
SA = Swept area
SDT = Standard differential temperature
TCE = TechnoCentre Éolien
VAC = Alternative Voltage

II. Introduction

Before the installation of a wind farm, measurement campaign needs to be realized. Many technologies exist to determine the overall atmospheric boundary conditions over a terrain [1-3]. Over all of these systems, the permanent met mast represents a technology that can assess many meteorological parameters (wind, pressure, temperature, icing rate, vertical wind speed, etc.) over all the atmospheric boundary layer. This technology permits to test many types of sensors on an expandable platform.

This paper is based on the experiences, statistics and data on three met masts (Table 1):

Table 1: Met mast description table

Abbreviation	Locations	Height (m) A.G.L.	Tower type
TMV2	Murdochville, (Needle mount)-Québec province, Canada	15	Tripod permanent self-supported tower
TMV3	Murdochville (town), Québec province, Canada	20	Temporary monopole 4 directions wire
MMV2	Rivière-au-Renard, Québec province, Canada	126	Tripod permanent guyed wire

These two locations (Rivière-au-Renard and Murdochville) are complex terrain (over 300m of difference in level) with various vegetation cover. These three sites are conformed to the cold climate definition developed in the GL Technical Note 069 [4]. Since their commissioning, these met masts have been equipped with more than 140 critical sensors over 10 years divided as:

- 5 cameras
- 43 heat and unheated anemometers,
- 6 icing detectors,
- 3 precipitation gauges
- 24 thermometers (including RH sensors, and SDT probe),
- 13 ultrasonic anemometers,
- 2 vertical anemometers,
- 7 wind monitors (anemometer and wind vane in the same sensor),
- 23 heat and unheated wind vanes,
- 10 others sensors (visibility sensors; ceilometer, barometer, etc.).

A maintenance log book stores each failure for each sensor. Each failure is classified according to 5 types: falling ice or ice accumulation, communications failure, inappropriate heating, sensor choice, and other. This follow up is performed weekly or when a failure is detected. The statistics shown in this article are extracted from this log book.

The majority of sensors are calibrated and installed in accordance to IEC 61400-12-1 (or other standard when it's applied). A periodic preventive maintenance is done annually or less. All data are archived through Osisoft-PI - real time historian (archived system) [5] or stored on site (at 1 Hz frequency).

Within all of these sensors installed on met masts, we classified these problems according to six topics as shown in Figure 1 and established the structure of this article:

A. Booms configuration
B. Choice of sensors in CC
C. Heat sensors recommendations to deice during icing events and anti-icing sensor
D. Communications features
E. Power supplies
F. Tower design

For this paper, we propose the guidelines around the four first topics (see Figure 1– red circles). For these three sites, the cold climate is defined as a mix in between icing climate and low temperature [6]. Especially in this article, we highlight on the icing climate (IC).

III. Guidelines

A. *Boom configurations*

Before met mast installation, many issues need to be taken into account to reduce the maintenance cost and increase the sensor data availability. During the choice of the sensors, it is important to decide the direction of booms. In the same line of thinking, the issues are defined as follow: (1) met mast configuration to reduce falling ices on sensors; and (2) booms recommendations for cold climate. On our facilities, the falling ice is the source of more than 40% of all the failures listed.

i) Met mast configuration to reduce falling ice on sensors

According to IEC 61400-12-1, it's very difficult to add an ice-shield over anemometer and wind vane without influencing the air flow [7]. Most of the time, these sensors are directly exposed to ice falls. (as shown in Figure 2)

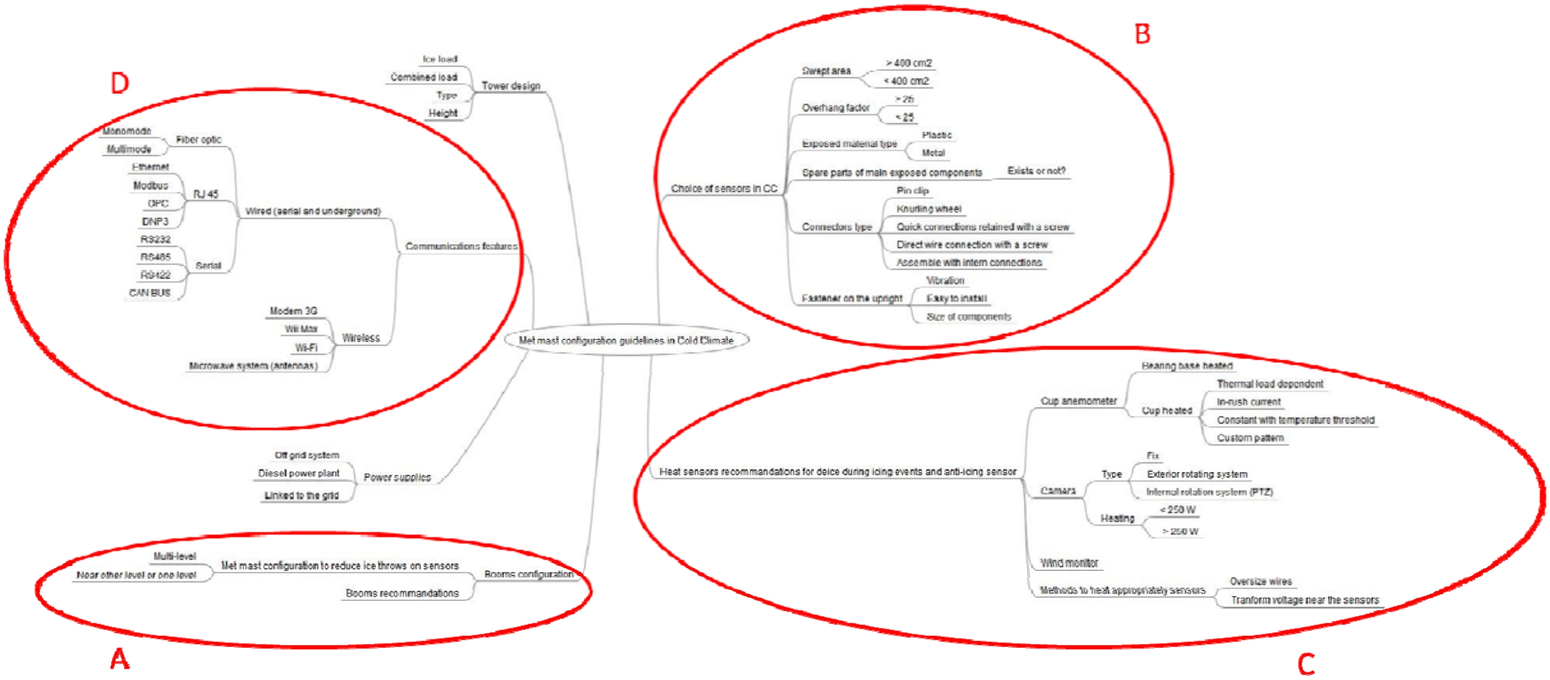

Figure 1: Topics for met mast installation in cold climate

Figure 2: Example of falling ice failure due to direct surface exposure

When the difference between each level is vertically higher than 5 m, it's recommended to keep a special attention for the directions of booms (and sensors in the same way) to reduce the risk of falling ice on sensors.

On a met mast, the icing accumulation (by instrumental icing detection) is more present compare to a wind turbine. [8] During de-icing period, this accumulated ice drops from the met mast and hits the sensors. This falling ice is distributed from opposite direction of wind. For example, at Rivière-au-Renard site (MMV2), the falling ices occur most of the time from south-east and north-east zone (opposite side from the prevailing winds that mean north-west and south-east).

For a triangular base tower, when the wind comes aligned to the legs of the tower, the falling ice describe a cone of 90 degrees starting from the legs of the tower divided equally on each side of the bissectrix. The figure 2 shows an example:

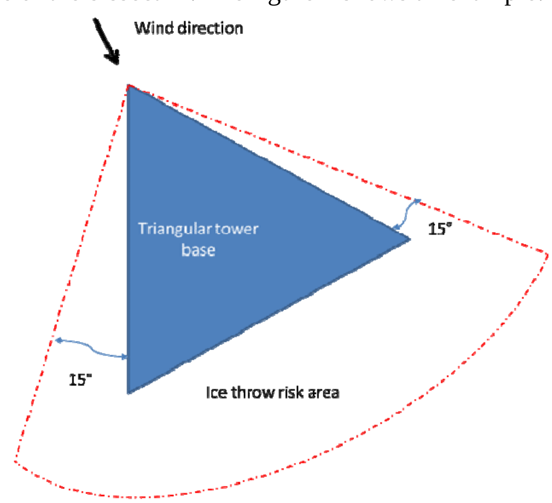

Figure 3: Falling ice zone risk around met mast

With a good knowledge of the prevailing wind rose (or ice rose if existing), the developer is able to determine an area where falling ice is more likely. This ice accumulation grows with the altitude above the ground level [8]. In the same way, the falling ice risk area is then higher when the sensor is located near the ground compare to the top of the tower (due to the weight, impact strength and frequency of the ice throw). With compiling these three conditions, it's recommended to design the boom directions into two main patterns. A pattern from the top of the met mast (that implies that the sensors are located within the falling ice area (FIA) and another pattern for the base of the met mast (that implies that the sensors are located out of the FIA)

For sensors located at the ground, a distance of half the tower height outside the FIA will protect sensors that do not need ice shields.

When the difference between each level is vertically lower than 5 m , the falling ice risk on the sensors can be reduced with using pyramidal configuration. While maintaining IEC 61400-12-1, a lower boom length needs to be place at near the top of the met mast. The booms installed below each other need to be longer than the other above. Since this configuration is already used on TMV2 (in 2011), no failure has been recorded coming from falling ice on the sensors installed at the top of the tower.

ii) Booms recommendations for CC

The CC, especially the IC, occurs when an ice accumulation arises on all the structure and the sensor itself. Even if a sensor is designed to de-ice, the boom and its upright do not de-ice by themselves. In this situation, the ice accumulation on the upright affects wind flow and induces a statistical bias on data (this bias is hard to detect without a rigorous quality control). The figure 3 shows the heat sensors de-ice adequately but the ice accumulation disturbed the wind flow.

Figure 4: Ice accumulation on an upright for a heat cup anemometer on TMV2 (Murdochville)

For this ice accumulation, it is recommended to heat the upright with external heating.

B. Choice of sensors in CC

The choice and quality of the sensors influences the maintenance cost, data quality and data availability. Many standards exist to help developers to qualify sensors (IEC 61400-12-1, ASTM D5096-02) [9]. But, no criteria exists to help developers to decide which sensor is the more appropriate to install in CC site in the goal to reduce their maintenance cost. Based on the field experience, we determine 6 factors that influence the failure of the sensors: swept area, overhang factor, exposed material type, spare parts of main exposed components, connector types and fastener means on the upright.

i) Swept area (SA)

As mentioned previously, due to meteorological or aerodynamic considerations, many sensors cannot be protected with an ice shield. In this situation, sensors that have a bigger SA are more exposed to falling ice. As shown in Figure 5, this SA is calculated with the exposed area parallel to the ground level.

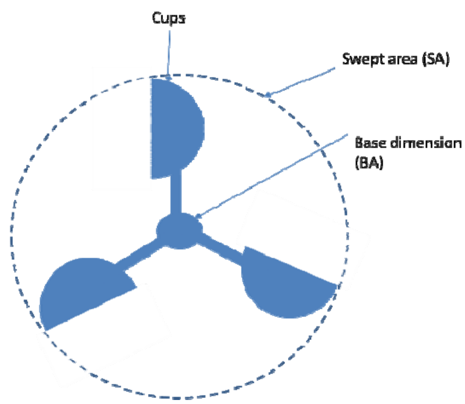

Figure 5: Swept area definition for cup anemometer

We perform statistical calculations on the SA of each sensor. We determine two bins of swept area to categorize sensors: smaller or greater than 400 cm^2 (Table 2).

Table 2: Source of failure compare to the swept area

Failure reason	Swept area	
	< 400 cm^2	> 400 cm^2
Falling ice or ice accumulation	9,3%	29,6%
Communications	0%	11,1%
Inappropriate heated	5,6%	1,9%
Sensor choice	14,8%	3,7%
Other	13,0%	11,1%
TOTAL:	42,6%	57,4%

On the 57% failures for sensors over 400 cm^2, the wind vane and the wind monitor represents 20% from these failures. This represents 35% of failures coming from falling ice for sensors over 400 cm^2. The wind vane and wind monitor are more sensitive of the failure on this characteristic due to their design (long thin rod turning around a pivot).

ii) Overhang factor (OF)

The overhang factor defines a sensor mechanical rigidity. This factor is calculated as follow:

$$OF = \frac{SA}{BD}$$

Conforming to the previous section, statistics are calculated on this criterion and shown in the Table 3. We determine two bins of overhang factors to categorize sensors: smaller or greater than an overhang factor of 25. We noticed that on the 52 sensor failures, 52% are coming from an overhang factor greater than 25, and more than 50% of them from falling ice.

Table 3: Source of failure compare to the overhang factor

Failure reason	Overhang factor	
	< 25	> 25
Falling ice or ice accumulation	13%	27%
Communications	2%	10%
Inappropriate heating	6%	0%
Sensor choice	8%	12%
Other	19%	4%
TOTAL:	48%	52%

Also, the table 4 shows the failure rate with this factor on 43 cup anemometers. We observed this criterion generates a high failure rate due to falling ice (14,0% on the 37,3% of general cup anemometer failure i.e. 1/3 of failure).

Table 4: Source of failure compare to the overhang factor on all cup anemometers

Failure reason	Overhang factor	
	< 25	> 25
Falling ice or ice accumulation	0,0%	14,0%
Communications	0,0%	0,0%
Inappropriate heating	0,0%	0,0%
Sensor choice	7,0%	9,3%
Other	7,0%	0,0%
TOTAL:	14,0%	23,3%

iii) Exposed material type

Another characteristic is to compare the failure source of the exposed material for each sensor. Two categories have been defined:

- Metal (aluminum, steel, brass)
- Plastic (including composite).

When we compile the overall sensors exposed material, a similar number of failures (46,9% with plastic and 53,1% with metal) is notified. Specifically for falling ice failure, the table 5 shows a comparison between the failure rate of cup anemometer and wind vane according to the exposed material type.

Table 5: Broken sensors cause by falling ice compare to the exposed material type (plastic or metal)

Sensor type	Falling ice failure	
	Plastic	Metal
Cup anemometer	11,6%	2,3%
Wind vane	4,3%	17,4%

With these statistics, no evident type of exposed material stands out compare to the other. In this type of failure, the shape and the manufacturing design have more influence than the exposed material type.

iv) Spare parts of main exposed components

Before deciding to choose which sensor, the recommended practice is to verify spare parts availability for each of them. That means if the sensors can be repaired directly on site (if no calibration is needed). Even if the sensor needs to be calibrated, spare parts existence removes the step of repairing the sensor before calibration.

When we change a component on a sensor and no calibration is required, it's recommended to practice another commissioning likeness a new sensor installation.

v) Connector types

The connector type is an undervalued characteristic on a sensor in CC. In fact, this connector needs to stay connected on the sensor during ice accumulation of more than 40 mm occurs [10]. On all tested sensors, five categories of connections are mainly used:

1) Pin clip
2) Knurling wheel
3) Quick connections retained with a screw
4) Direct wire connection on the sensor
5) Assemble with internal connections

In order to detect which type of connectors is more reliable in CC, we correlate the communication failure type with the kind of connection. The table 6 demonstrates the result of a total of 6 communications failures.

Table 6: Communication failures compare to the connector type for the sensor

Failure type	Connector type				
	Pin clip	Knurling wheel	Quick connections retained with a screw	Direct wire connection on the sensor	Assemble directly within the sensor
Communications	0	1	0	3	2

This table demonstrates that the sensor with direct connections is more prone to a communication failure. This statistic is logic with the level of complexity of the task and number of operations needed to connect wires. In fact, it is easier when you work at height to screw one connector compare to connect several small wires on sensor directly. Also, the knurling wheel gives some communications problems because the operation to tighten adequately is hard when you work at height. This type of connectors obliges the worker to remove gloves to screw the connector.

vi) Fastener means on the upright

Four characteristics about the manner to fasten the upright on the sensor need to be taken into account to be sure that the sensor stays on the upright appropriately:

- Screw do not unscrew with vibration
- Screw can be tighten easily by the climber
- Screw are enough big to be retained by a climber without removing glove.
- For sensors that record wind direction, , it is recommended to ensure a mechanical link in order to avoid these sensors the possibility to twist on themselves (and loss the north reference).

C. Heat sensor recommendations for deice during icing event and anti-icing sensor

In CC, the aim is to acquire an accurate sensor with an appropriate heating and reduce the ice accumulation on the sensor. The heating or anti-icing sensors need to be adapted to icing accumulation, icing type and temperature when the icing accretion occurs. We will discuss about these icing characteristics, over four sides of views: cup anemometer, cameras, wind monitor, methods to heat appropriately sensors.

i) Cup anemometer

Recent years, the development of heat cup anemometer fastly increases. Thirty years ago, a heat anemometer means an anemometer with infrared (IR) lamp [11]. Now, two main families of heat cup anemometer have been developed and are discussed:

- Bearing base heated
- Cup heated (directly or by conduction)

<u>Bearing base heated</u>

This type of cup anemometer is characterized by heater installed near the bearing. The goal to develop this type of heat anemometer is to ensure data availability of wind speed during temperatures below -20°C. With this type of sensor, the friction lost inside the bearing is controlled for every temperature. So, this cup anemometer can perform in any low temperature with adequate friction coefficient in accordance to IEC61400-12-1.

The cup anemometer with bearing base heated is defined by 3 characteristics:

- This type of sensor has a less than 25 W of heating.
- The heater is located only near the main base bearing
- No other parts (expect the bearing) is heated.

For this sensor, the de-icing capacity of the cups is weak because the heater is distant from cups.

<u>Heated cups</u>

This type of heat sensors is described by 2 characteristics:

- The sensor has a more than 50 W of heating.
- The heater is located near the cups of the anemometer

One of the keys when you choose an anemometer with heated cups (linked with the two criteria explained above) is to verify the control pattern of the heater. Four categories of heating control pattern exist:

- Thermal load dependant
- In-rush current
- Constant with temperature instruction
- Custom pattern

The thermal load dependant is a heating control pattern that is characterized by a linear control of heater in function of temperature. Generally, this anemometer reaches a maximum heating at -40°C. The major disadvantage of this anemometer is the inappropriate level of heating power during the icing events from -10 to 0°C. The Figure 6 shows a heated anemometer with a thermal load dependant control freezing during an icing event at -4.7°C.

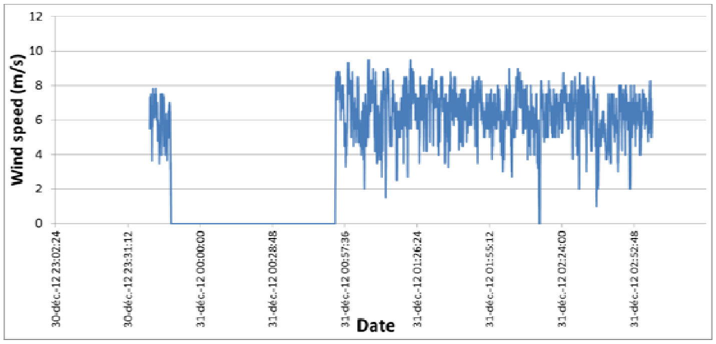

Figure 6: Frozen heated cup anemometer at 126 m a.g.l. from december 30 to 31, 2012

During 2012-2013 winter on MMV2, a total of 735 hours of instrumental icing has been detected between unheated and heated anemometer. During these events, the heated cup anemometer with heat cups and using a thermal load dependent has been affected for at least 118 hours (that means 16% during an icing event that represents 1,3% data of the year) at 126 m A.G.L at an average temperature of -1.5 °C. Briefly, this type of heated anemometer has the possibility to cause a statistical bias during icing conditions because the thermal load dependent control heating load do not deliver the maximal heating power during icing events (that occurs around -10 to 0 °C) [6].

TechnoCentre éolien (TCE) does not test the two other heating controls with heated cup anemometer.

A custom heating pattern appears to be the best approach. Because this control can mix an appropriate heating to de-ice during the icing conditions and heat appropriately during extreme low temperatures [12].

ii) Cameras

Because the icing is a complex phenomenon on sensors, one approach is to have a visual observation of them. To visualize the sensors, we tested more than 5 cameras following 3 types of different configurations: fixed, exterior rotating system and internal rotating system (PTZ). These cameras have been tested with coaxial and Ethernet communication link. We tested the camera under two heating configurations: standard heater and additional heating. The goal of these cameras is to follow the ice accretion without icing by itself. All cameras tested with heating below 250W freezes. The biggest problem with camera is to avoid the ice accumulation on and around the casing of the camera. In most of the case, the ice accumulation generates an obstruction of the view (see Figure 7)

Figure 7: Icing on recover over camera on TMV2 site in 2011

The figure above is a camera equipped with an exterior rotating system heated by the manufacturer heating system and communicates with coaxial cable.

iii) Wind monitor

This type of sensor is unheated and recovered with anti-icing coating. In Table 7, we compare an unheated cup anemometer, a wind monitor and heated ultrasonic anemometer. We detected icing events by heated vs unheated method from November 29th, to December 18th, 2012:

Table 7: Instrumental icing percentage compares wind monitor and unheated cup vs ultrasonic heat sensor

Comparison sensors	% of instrumental icing
Wind monitor vs heated ultrasonic sensor	8,4%
Unheat cup anemometer vs heated ultrasonic sensor	30,4 %

We concluded that the wind monitor model is less prone (22% free of ice less than unheated cup anemometer) to icing. But, the wind monitor can frost too during heavy icing condition.

Also, the wind monitor is reliable when it’s installed on the top of a met mast (as present in the analysis of the table 7). In multi-level configuration, the lifetime of this type of sensors is short. On MMV2 from March 2012 to May 2013, we has a low data availability (9,8%) due to falling ice failure.

iv) Methods to heat appropriately sensors

Many strategies can be used to supply an appropriate electrical power for a heated sensor. The developers need to be aware about Joule’s effect (voltage drop into wire) [13]. Many wires furnished by sensor manufacturer are undersized to ensure an appropriate heating source. This low electric efficiency affects the nominal power delivery at sensors. TCE experimented this problematic on MMV2 met mast.

To resolve this inappropriate heating, two solutions are possible: transforming the voltage near the sensor (within junction box including the voltage transformer) or oversizing the power cable. The Table 8 shows the advantage and inconvenient of each solution. For MMV2, TCE chose to install junction boxes with power transformer near the sensor because this solution permits the expandability for future project in order to test other sensors in CC. Furthermore, this expansibility (requested for R&D projects) is the reason that TCE chose this solution for MMV2

Before the modifications done (in winter 2012 and summer 2013), the power of sensors was supplied from the ground through a power converter in the acquisition box. In that case, the wires were oversized between the acquisition box (as recommended by sensor manufacturer) and the sensor. Now, the modified electrical configuration consists in installing a voltage converter to supply power at maximum distance of 20 m from the sensor. The goal is to reduce the Joule's effect loss. The Table 9 shows that the original configuration implies a 58% electric losses at maximum current and 16% at nominal current.

Table 8: Advantages, inconvenients and recommendations for two types of electrical configuration

Characteristics	Oversize wires	Transform voltage near 20 m from sensor
Advantages	Unique cable from the ground to each sensor	If the level is equipped with more than 2 heat sensors, the installation is lighter than oversize wire for each sensor. Expandable when needed.
Inconvenients	Wire weight increasing One wire needs to be install for each sensor	Installation of junction box in the met mast Connections and maintenance need to be achieve on the met mast by a qualified climber
Recommendations	Sensor with low current consumption	Sensor with high current consumption:

Table 9: Joule's effect loss with two electrical met mast configurations

Type of sensor					Before modification				After modification (transform at level of sensor)			Increasing nominal power delivery	
Heated sensor	Voltage for power	Material of wire	Maximum current (A)	Normal use amperage (A)	Gauge by manufacturer (AWG)	Distance (m)	Voltage drop / decrease power delivery (%)	Voltage at norm amperage (%)	Distance (m) cable from power supply	Voltage drop / decrease power delivery (%)	Voltage drop at normal amperage	Maximum current (A)	Normal current (A)
Cup anemometer (cup heated)	24 VAC	Aluminium	4	2	22 + 14	15 + 115	8,2 + 50	3,2 + 25,1	12	33,42	16,71	60	17
Wind vane	24 VAC	Alunimum	6	1.5	20 + 14	12 + 95	7,8 + 62	1,9 + 15,5	10	26,25	6,58	143	13

The Table 9 shows the difference between the original configuration and their results after modifications. The two sensors are heated and use a thermal load dependant control for heating. This table leads two major conclusions. First, the Joule's effect has a direct relation with the current, so a sensor with high current is more affected by this modification. In the example shown in table above, the modification for a heated cup anemometer and wind vane increase the maximum power delivery from 60% and 143%. In relation with section *C – i) Cup anemometer*, sensors using in-rush current (usually 9 A to 10 A) to de-ice are more affected by this effect compare to the thermal load dependant during icing event.

D. Communication links

The communication feature is chosen by the location of the met mast, the communication speed rate and the access possibility desired by the developer. On all infrastructures, we tested wired and wireless system. The section D from the Figure 1 is a non-exhaustive list of the communication links and protocol tested by TCE. The Table 10 gives a summary of each technology tested by TCE with the maximum communications distance and the recommendations in CC.

Table 10: Maximum distance, requirements and recommendations for different communications linked in cold climate

Communication link	Maximum distance or requirements	Recommendations in CC when installed on site
Micro-Wave (parabolic antenna)	Unlimited if the receptor and transmitter has direct link	Two antenna needs to be heated An ice-shied needs to be installed on two antennas
Wi-Fi	1 km	If possible, heated antennas
Modem 3G	Unlimited where 3G coverage exists	The antenna needs to be protect against ice throws
Ethernet cable	100 m	Use appropriate exterior cable
Wii Max	55 km	If possible, heated antennas
Fiber optic–underground	Unlimited	No problem
Fiber optic – Aerial	Unlimited	If near wind turbine [6], the wire is prone to ice throw

i) Micro wave system experience on TMV2

The micro wave system has been evaluated by TCE at TMV2 during winter 2009-2010 and 2010-2011. During the first winter, the micro-wave antenna has frozen [14]. We lost communication during 53 days on 250 days of winter (21,2% reduction in data availability). These three periods occur at the beginning of the winter as shown in Figure 8.

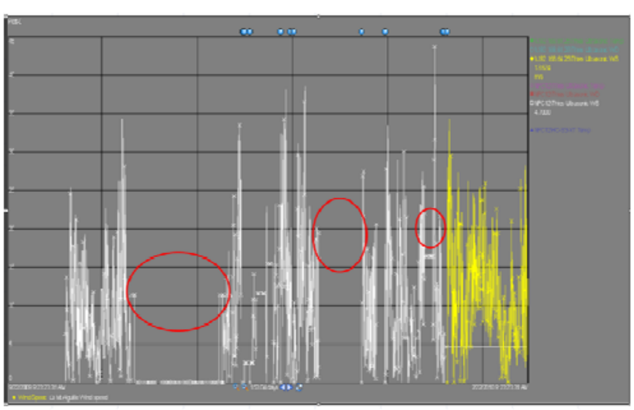

Figure 8: Communication loss period in winter 2009-2010 on TMV2

In winter 2010-2011, the micro-wave system has stopped to communicate due to misalignment between the transmitter and receptor. This misalignment is due to a heavy icing event (same event shown in Figure 7) on the antenna (because the antenna is protected by an ice-shield). Later in the winter, the receiver broke due to falling ice from the ice shield.

IV. Recommendations

Following the four topics present in the introduction, we formulate recommendations for each of them.

A. Booms configuration

In CC, the major goal to orientate with different configuration the booms along the height of the tower (excepted aerodynamic considerations) is to reduce the failure provided by falling ice. When the difference in level between each sensor is lower than 5m , a pyramidal approach is recommended. When a configuration with difference in level between the levels is more than 5m, a configuration with two (or more) types of orientation is recommended in taking into account the prevailing wind direction. On heavy icing site, a special attention needs to be given to determine if the upright needs to be heated or not.

B. Choice of sensor in CC

According to what has been shown, it's suggested having a sensor with these characteristics:

- A sensor with a swept area less than 400 cm^2
- Especially for anemometer, an overhang factor less than 25
- A sensor with spare parts availability of the exposed components to facilitate the maintenance,
- A sensor with connector type specified to pin clip and quick connections retained by a screw
- A sensor with fasteners enough big to be easy tighten on the upright by a climber
- Camera with internal rotating system with additional electric heating is the more appropriate

C. Heat sensors recommendations to deice during icing events

Prior to determine a heated sensor, the developer needs to determine in which meteorological conditions, the sensor will undergo. For LTC without icing events, the bearing base heated anemometer is sufficient. For low-temperature climate with few icing event, a heat anemometer with heated cup controlled by a thermal load dependent and a wind monitor with anti-icing coating are adequate. For the heavy icing event (see Table 7), a cup anemometer with heated cup controlled by in-rush with temperature instructions current or custom heating pattern is mandatory (but need to be tested).

After choosing the sensor type, the developer needs to calculate the wire losses following the Joule's effect depending on the heating electrical pattern. For thermal load dependant heating or low current consumption sensor, wire oversizing (as specified in electrical book or standard) is a correct solution for a permanent installation. For in-rush current consumption or expandable installation, the transformation of voltage near the sensor (20 m) gives the maximum power delivery.

D. Communications features

To communicate directly with the data logger, a communication linked is necessary. By experience, TCE has problem with all system with big antennas or system with big exposed components. In this context, modem 3G, underground fiber optic, Wi-Fi presents less risk to be installed in CC compare other technology.

V. Conclusion

So, many factors are important when we plan a meteorological assessment in CC. These factors are a mix between experience, statistics and knowledge. This article gives a brief overview on the experience with the managing of three met masts in cold climate. Also, we compile statistics from failure type linked with sensor type. In the future, these statistics have while the advantage to be compared to verify the trend of failure type for each sensor. Also, comparison with ice classes and the performance of each sensor gives us a practical issue to verify if the sensors are appropriately heated in CC [15].

Eventually, these series of experiences, statistics and knowledge could be included inside a matrix of decision. The development of this tool would permit to quantify the risk of met mast configuration compare to the needs of developers.

Acknowledgements

Towers , sensors use for this article provide from public subsidies: Développement Économique Canada, Ministère Finances et Économie, Foundation communautaire de la Gaspésie, and Natural Resource Canada.

All data used and archived from TCE's infrastructure are linked with a historian provide by private partner: Osisoft PI.

References

[1] M. Pelletier, D. Faghani, M. Boquet, R. Dexter, B. Boucher, E. Osler, C. Masson and L. Landberg ,"Lidar Validation in Complex Terrain,. presented at *EWEC*, Brussels, March 2011

[2] Integrated Environmental Data LCC (2011, July), "Recommended Practices for the Use of Sodar in Wind Energy Resource Assessment", [Online] 1-20, Available: http://www.iedat.com/documents/SODARRecommendedPractices_IEARevised13Jul2011.pdf

[3] C.Arbez, H.Ibrahim, "Highest meteorological station in Canada designed for cold climate and complex terrain recognition", presented at *Winterwind*, Skefelltea (Sweden), February 2012.

[4] *GL Wind-Technical Note 067 Certification of Wind Turbines for Extreme Temperatures (here: Cold Climate*), GL Standard, Revision 2, 2005

[5] PI product [Online] Available on www.osisoft.com

[6] Ian Baring-*Gould, et al., Expert Group Study on Recommended Practices for Wind Energy Projects in Cold Climates. IEA Wind Recommended practices no. 13. 2012.* [Online] Available at: http://arcticwind.vtt.fi/

[7] *IEC 61400-12-1- Wind turbines – Part 12-1: Power performance measurement of electricity producing wind turbines*, 1st edition, 2005-12.

[8] M.Wadham-Gagnon, "Ice profile classification – based on ISO12494", presented at *Winterwind*, Ostersund (Sweden), February 2013.

[9] R. Coquilla, "Review of anemometer calibration standards", presented at *CanWEA*, Toronto (Canada), Sept. 2009

[10] CSA - *S37-01 Antennas, Towers and Antenna-Supporting Structures*, Revision 2011, 2011.

[11] A. Judson, *An infrared de-icing unit for cup anemometers* Rocky Mountain Forest and Range Experiment Station, Forest Service, U.S. Dept. of Agriculture, 1971

[12] A.. Bégin-Drolet, *Développement d'un anémomètre anti-glace chauffant pour le domaine de l'énergie éolienne*, Ph.D Thesis, Université Laval, Canda, 2012

[13] T. Wildi and G. Sybille, *Électrotechnique*, 4th Edition, Les presses de l'Ùniversité Laval, 2005.

[14] .C. Arbez, D.Boulay, « *Tour multi mesures pour la caractérisation des événements givrants* » , Report – submit at Fondation communautaire iles de la Madeleine et Gaspésie, 2009

[15] *Atmospheric Icing of structures*, ISO 12494, 2001

Icing of a 326 m tall tower - a case study

Lasse Makkonen
VTT Technical Research Centre of Finland
Espoo, Finland
lasse.makkonen@vtt.fi

Gregory Thompson
National Center for Atmospheric Research
Boulder, Colorado, U.S.A.
gthompsn@ucar.edu

Bjørn Egil K. Nygaard
Norwegian Meteorological Institute
Oslo, Norway
bek.nygaard@gmail.com

Pertti Lehtonen
Espoo, Finland
pertti.ta.lehtonen@kolumbus.fi

Abstract — We present detailed field observations of an icing event on a 326 m tall guyed television tower. Ice samples were collected and photos taken from various heights on the tower which was equipped with anti-iced anemometers and thermometers at five levels. Modeling of the accumulation of ice on the tower was made by the Weather Research and Forecasting model combined with a numerical icing model. The simulated time series of temperature, wind velocity, cloud and drizzle liquid water contents and median volume droplet sizes were used to drive the icing model. The measured vertical distribution of the ice load was compared with that modeled by the WRF simulations. The cloud microphysics scheme and WRF provide remarkably accurate predictions of the meteorological conditions and result in very useful estimates of the ice loads at different levels on the tower. We also used a simple icing model, based on the observed weather data, to estimate the ice load. The results from both models support the approximate height distribution of ice mass proposed in the ISO 12494 code for atmospheric icing.

Keywords — *Ice load; Icing; Tower; Height dependence*

I. Introduction

Icing is a common cause of a failure of tall towers [1,2] and hence a critical input for their structural design. A poorly known but crucially important aspect of icing is its dependence on the height above the ground. In addition to the design of communication towers, this issue has become of interest in evaluating the production potential of wind energy in icing climates. The modern wind turbines are so big that their blade tips reach over the 200 m level.

Direct observations of ice on tall structures have been rarely done. This is because collecting natural icing data is difficult as such and because the towers used for that have not been very tall [3]. In the few cases where a tall structure has been available, it has either measured only the total load and not the vertical distribution (Ylläs [4]), or the tower has been located in a moderate icing climate (Ostankino [5]). Therefore, standards for engineering design for ice loads on tall towers, SNiP II-6-74 and ISO 12494 have been based on indirect calculations following the methods developed in e.g. [5-9]. For the same reason, the role in-cloud icing in ice loads on tall towers has sometimes been underestimated [10].

In January 1996 a significant icing event that lasted for a week took place in the Helsinki area in Finland. No icing occurred at the ground level and there was almost no precipitation measured. However, tall lattice towers in the area collected a lot of ice. After the icing event, ice samples were taken by the authors from various heights on the 326 m tall guyed television tower in Espoo. These data provide a unique case for a study on the height dependence of ice loads.

The Espoo TV-tower is equipped with anti-iced anemometers and thermometers at five levels. Thus, the data of the icing event can be used for verifying the indirect methods for estimating the vertical distribution of ice on a tower as well as the related standards. Here we also make comparisons against sophisticated icing simulations by the Weather Research and Forecasting model (WRF). This method includes detailed cloud microphysics modeling, and has recently been successfully used in simulating icing on the ground [11-13]. We also evaluate the appropriateness of ISO 12494 [14] in regard to the vertical distribution of ice based on our ice data and the model results.

II. Observations

A. Ice data

The Espoo TV-tower is a guyed lattice tower located on the southern coast of Finland a few kilometers inland. The base of the tower is at 44 m ASL.

At the end of the icing event, on 18th January 1996, the first and fourth authors of this paper, together with two technicians went up the tower to take ice samples and photos. It was possible, up to the level of 265 m, to use a small elevator located inside the lattice structure. The elevator crushed ice on its path, but its use did not cause

Fig. 1. Ice on the ladder at 55 m (left) and 265m (right).

Fig. 2. Ice on the ladder at 298 m showing also a diagonal from which an ice sample has been removed.

shedding of ice on the other parts of the tower. The elevator was stopped at five levels to make observations. For observations at the top level at 298 m the technicians climbed up by ladders fixed to the tower. Example photos of the ice accretions on the tower are show in Figs. 1 to 3.

At each level ice samples were taken from two cylindrical components, a vertical part of the 20 mm diameter ladder and a diagonally oriented 102 mm diameter component of the tower. At 298 m the diagonal had a diameter of 64 mm, however. The samples were knocked off by a hammer and it was this way possible to remove large blocks of ice without noticeable loss of ice pieces. The length of the ice samples was measured afterwards in a laboratory and varied from 15 to 40 cm. Each sample was put in a plastic bag for transportation to the ground level. The pieces removed during transportation were thus retained and included in the reported ice mass. The samples from the

Fig. 3. Ice on the upper part of the tower. Photo is taken upwards from the 265 m level.

top level, however, had to be transported down in a back-bag and we estimated that approximately 10% of the ice was lost in this process. This is taken into account in the reported ice mass for that level.

All samples were subsequently packed in an insulated box and transported to VTT cold laboratory. The length of the samples was measured but this included some subjectivity due to the uneven ends of them. We estimated that the accuracy of determining the length was ±5%. This is thus our estimate for the accuracy of the measured ice mass.

The density of the ice samples taken from the diagonals was estimated as follows. A shorter ice piece was cut from a sample and weighed. It was then put into a bag made of soft thin plastic material and fully submerged into cold water. The volume change in the water container was measured thus obtaining an estimate for the volume of the ice piece. We calibrated this method by pieces of solid ice, and estimate that the accuracy of our ice density measurements was ±15%. We note, however, that since the surface of rime ice samples is rough in many scales (see Figs. 1 to 3), its overall volume is not well defined. Thus, the measured density may not be directly comparable to that given our icing model.

TABLE 1. OBSERVATIONS OF ICE ON THE ESPOO TOWER ON 18 JANUARY 1996. THE HEIGHT IS THAT ABOVE THE BASE OF THE TOWER. "LADDER" IS A VERTICALLY ORIENTED CYLINDER WITH A DIAMETER OF 20 MM AND "DIAGONAL" IS A DIAGONALLY ORIENTED CYLINDER WITH A DIAMETER OF 102 MM, EXCEPT AT 298 M WHERE THE DIAGONAL HAS A DIAMETER OF 64 MM. THERE WAS NO ICE AT THE GROUND LEVEL.

Height (m)	Object	Ice mass (kg/m)	Ice density (kg/m^3)
298	ladder	6.8	
	diagonal	6.6	520
265	ladder	6.2	
	diagonal	4.6	520
210	ladder	3.3	
	diagonal	3.1	510
160	ladder	2.9	
	diagonal	2.1	540
110	ladder	1.6	
	diagonal	1.7	770
55	ladder	0.63	
	diagonal	0.65	810

The results of the measured ice mass per unit length of a cylinder and ice density are shown in Table 1. They, together with the photographic material, show glaze-type ice at the lowest level and hard rime at the other levels, and a very significant increase of the ice amount with height. The ice mass corresponds to ISO ice class R1 at the lowest level and ice class between R5 and R6 at the highest level.

B. *Meteorological data*

The Espoo tower is equipped with thermometers and hygrometers at levels of 2 m, 26 m, 91 m 186 m and 298 m and anemometers at levels of 26 m, 91 m, 186 m and 325 m. We did not attempt to use hygrometer data in identifying cloud levels due the fundamental problems involved in measuring humidity in icing conditions [15]. Icing did not affect the wind measurements, however, because the anemometers used were the heated Hydro-Tech devices which have been shown to remain ice-free even under much more serious icing conditions [16].

Cloud base height data from Helsinki-Vantaa airport and precipitation data from Helsinki-Kaisaniemi weather observatory were also available. These stations are located approximately 25 km northeast and east, respectively, of the Espoo tower.

The air temperature during the icing event varied between -6 and 0ºC so that at the top of the tower it was typically about 1ºC lower than at the base. However, towards the end of the event, there were also periods when the highest temperature was measured at the top. At the top level wind was blowing from the south throughout the event at a speed of 2 to 8 m/s, except of 14 and 15 January when it reached 20 m/s at times. At lower levels there was more variation in the wind direction and the speed was lower reaching 10 m/s at maximum at 186 m.

The weather during the icing event was cloudy and foggy. In spite of this, the precipitation amount during the event was only 3 mm. In fact, January 1996 with total precipitation amount of 4.6 mm, was the driest January ever observed at Helsinki-Kaisaniemi. According to the airport observations, the cloud base during the event was lower than the top of the tower for almost all of the time, below the 160 m about half of the time, and below 55 m for about 10% of the time.

Overall, the meteorological observations during the event show persistent non-precipitating stratus-clouds at the level of the tower at temperatures which are slightly below freezing. The wind direction was from the ice free area of the Baltic Sea, transporting moist are, and the wind speed reached at times 20 m/s at the top of the tower. These conditions produced significant ice accumulations on the Espoo TV-tower, while no traces of ice were observed at the ground level.

III. WRF MODELING

In an effort to make the most realistic simulation of this event, the WRF model Version 3.4.1 was configured with a triple nested grid with 1 km grid spacing in the region of the TV tower. The simulation began at 0000 UTC 09 Jan and ran through 0000 UTC 19 Jan, ending after the first Espoo tower observation. The model simulation was forced by gridded meteorological data at 6 hour temporal resolution, obtained from the ECMWF re-analysis project ERA-INTERIM.

Particularly important for the icing simulation was the use of an advanced cloud microphysics scheme, which was originally developed with the primary goal to improve explicit forecasts of supercooled liquid water for aviation forecasts. The scheme is extensively described in [17] and is available within the WRF model system.

Supercooled droplets may be present in two different forms in the WRF simulation. Either as small cloud droplets, or as larger drizzle droplets, with diameters almost an order of magnitude larger than the cloud droplets. Due to the large sensitivity of icing rate to the size of the supercooled droplets, the conversion from cloud droplet size to drizzle sized drops is essential.

The production of drizzle is calculated by a prognostic equation in microphysics scheme. The production term is a function of the cloud LWC and the assumed droplet concentration for cloud droplets (100 per cm^3). It represents a parameterization of the collision/collection process that converts cloud droplets to drizzle size droplets, also called autoconversion. For the icing calculations it is important to take into account the supercooled water mass in both categories, and compute their collision efficiency using their respective MVD.

Overall, the WRF simulation produced a very long-lived and low cloud sometimes contacting the ground. The cloud LWC is displayed as time series at six different levels in figure 4. Figure five show the corresponding drizzle LWC at the same levels. Note that high contents of drizzle is found just after periods of high cloud LWC values, indicating that the model autoconverts cloud water mass to the drizzle category when the cloud water reaches high contents. Precipitation values appear very small with only about 6 mm over 10 full days.

One major discrepancy with the model simulation is the slightly too high model temperature forecast during the maximum observed on 15-16 Jan (not shown). The model forecasted 0.5 to 1.0°C, whereas the maximum in the observations remained at or below 0°C. This relatively minor error obviously directly impacts any calculations of ice load since ice would not accumulate when temperature exceeds 0°C. For illustrative purposes, this error was compensated for in the calculations of ice load by assuming temperature did not rise above melting.

IV. ICING MODELING BY WRF INPUT

The icing calculations by utilizing the WRF model input follow the numerical icing modeling approach of [18,19] and its applications as described in [11]. Since WRF produces supercooled water in terms of both cloud droplets and drizzle droplets, the time dependent accretion model is constructed so that for each time step, the icing rate from cloud water and from drizzle is calculated individually.

Due to the large size of the drizzle drops the collision efficiency for drizzle remains close to 0.9 and is not very sensitive to the size (except for very large cylinder diameters). Ice deposit density is also calculated individually before a weighted average density is used to update the deposit diameter, which is passed to the next time step. The MVD for cloud water is calculated from the equations presented in [11] while the MVD for drizzle is set to a constant value of 100µm.

Figure 6 shows the predicted ice growth at the six vertical levels where samples were taken. The distinct increase of icing with height is mainly due to a higher cloud LWC and wind speed. The shorter total duration of icing affected the final ice mass at the lowest levels only. This is an interesting result considering that the duration of icing has conventionally been thought to be the most important factor in the height dependence of icing.

The icing contribution from drizzle does not increase with height in the same way (see in Fig. 5) as the total ice mass. Thus, the relative contribution from drizzle is largest for the lower heights. The large drizzle drops will also contribute to a higher ice density, which is confirmed by the density of ice samples shown in Table1.

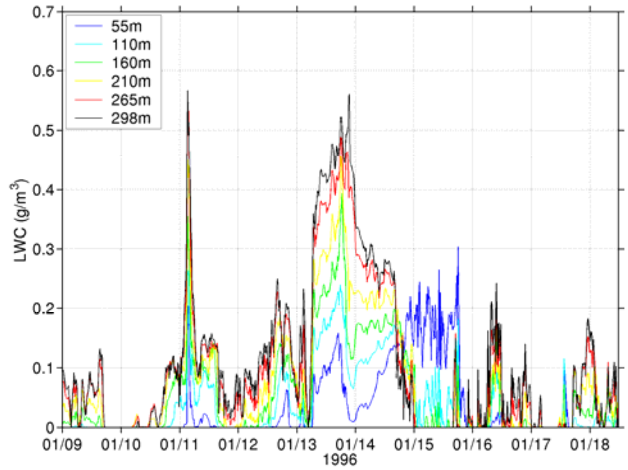

Fig. 4. WRF model results for the cloud liquid water content.

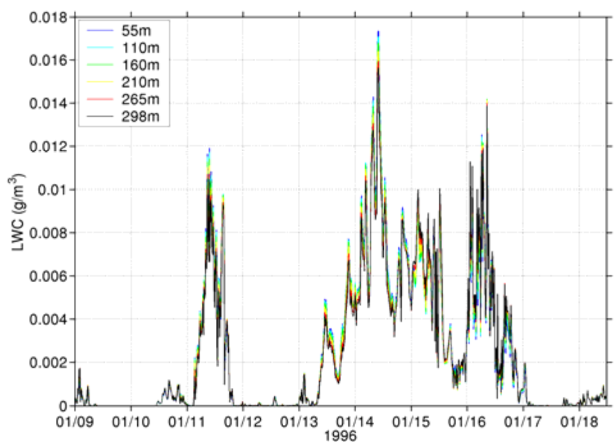

Fig. 5. WRF model results for the drizzle liquid water content.

V. SIMPLE ICING MODELING

WRF simulations provide all the meteorological variables for the icing modeling, including MVD and LWC. This sophisticated technique is, however, new. Previously, icing estimates have been made based on very simple models which ignore the variations in MVD and LWC and their effect [5-9] and utilize observed meteorological data. These models use the height of the cloud base as a discrete limit for LWC and ignore the vertical variation of the microphysical parameters within the cloud. Such an approach has a long history [20] and has been used in e.g. mapping of ice loads and icing frequency [8,21,22]. It is, therefore of interest to consider how well such a conventional method can predict the ice masses in this case for which detailed meteorological data exist.

We used the simple icing modeling method explained in detail in reference [9]. The basic equation for the ice mass *M* (kg/m) formed during an icing event in this method is

$$M = c\,V\,t \qquad (1)$$

where c is a constant, V is the mean wind speed (m/s) during the event and t is the event duration (h). The constant of $c = 5.5*10^{-3}$ was used, following [9].

Wind speed data was obtained directly from the observations at various levels on the tower at 10 min intervals. The duration of icing was based on the observed height of the cloud base at Helsinki-Vantaa airport (53 m ASL) in relation to the levels on the tower. The cloud base observations were made for aviation purposes at intervals of 30 min and with a resolution of 30 m. This allowed reasonably accurate estimation of the time at which a certain level of the tower was within a cloud. The implicit assumption here, that the cloud base height at the tower location was the same as measured 25 km away, is supported by the flat terrain in the area.

The results of the simple icing modeling are shown in Table 2. The ice mass calculated by this method is independent of the cylinder diameter.

TABLE 2. ICE MASS AT DIFFERENT LEVELS CALCULATED BY THE SIMPLE ICING MODEL. THE OBSERVED WIND SPEED AND CLOUD BASE HEIGHT WERE USED AS INPUT.

Height (m)	Ice mass (kg/m)
298	7.9
265	5.9
210	3.9
160	3.0
110	1.7
55	0.46

VI. DISCUSSION

We compared the meteorological conditions predicted by the WRF modeling with the observations. For the majority of the time the air temperature was remarkably well predicted by the WRF model. The wind speed was also in good agreement, except for a period of high winds at the top level. While the model produced drizzle, it predicted almost no precipitation depleting to the ground level, in accordance with observations.

The WRF-modeled ice mass at different heights was well predicted, as seen by comparing Table 1 and Fig. 6.

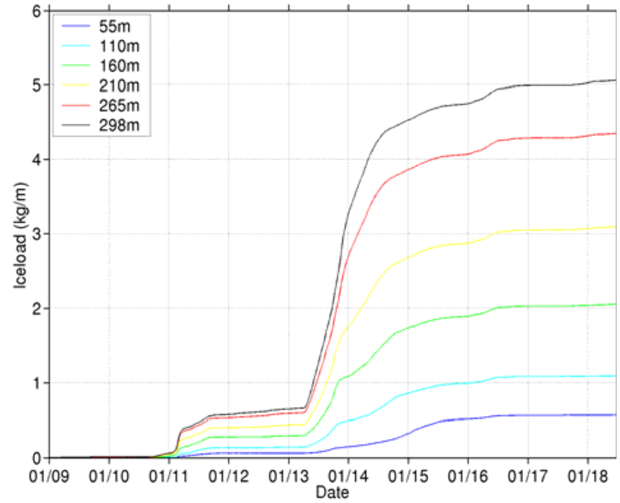

Fig. 6. Ice growth at various levels on the tower on a 20 mm diameter cylinder as predicted by the icing modeling based on the meteorological input from the WRF model.

The difference in the ice mass was almost within the measurement accuracy of the ice samples at the lower levels, but the model underestimated the ice mass by about 30% at the two highest levels. A simple explanation for this may the difference in the modeled and measured wind speeds at the top level. There is also a considerable difference in the geometry of the ice deposits. While the observations show feather-like icing on the upstream side of the cylindrical components, the simulation is based on flow around a cylinder.

The scaled vertical distribution of the ice mass on the tower at three times during the event is shown in Fig. 7. The modeled vertical distribution of the final ice mass agrees well with that observed (Table 1). Both the modeled and measured vertical distribution also agrees well with the height factor relationship proposed in the ISO 12494 code.

The results of the simple icing modeling (Table 2) are also in surprisingly good agreement with the observed ice mass at all levels. The quantitative values predicted by the simple method, of course, critically depend on the constant c used. Nevertheless, the results seem to support the simple icing model which appears to predict well the vertical distribution of the ice mass in this case. The assumption in the simple model, that there is no dependence of ice mass on the cylinder diameter, is also a reasonable approximation based on our data.

The cloud base data required by the simple model are not usually available and cannot be well extrapolated from weather stations in rough terrain. The WRF-based icing modeling, however, is entirely independent of locally observed data and is, therefore, a very promising method for further studies on the vertical distribution of ice loads on tall structures.

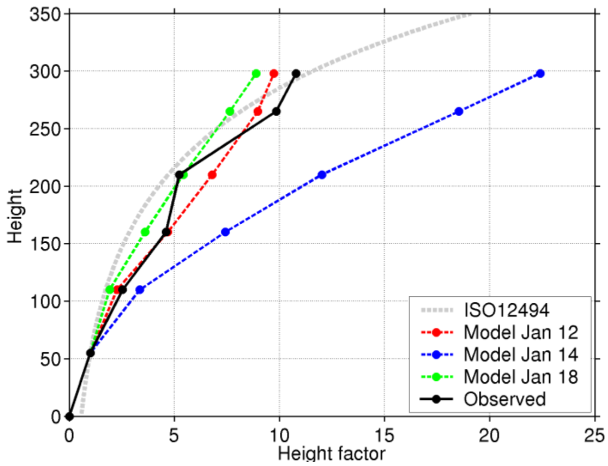

Fig. 7. Ice mass at various heights on the tower scaled by its value at 55 m, i.e. the height factor. The curves represent the height factor as given by the ISO 12494 code, as predicted by the icing model at different times of the event, and as shown by ice observations on the tower on January 18th.

ACKNOWLEDGMENT

This study was part of the Icewind project funded by the Top-Level Research Initiative of Norden.

REFERENCES

[1] E. Sundin and N. Mulherin, "Icing-relaed tower failures in the U.S.A. and Fenno-Scandinavia. 6th International Workshop on Atmospheric Icing of Structures (IWAIS), pp. 273-278, Budapest, Hungary, September 20-23, 1993.

[2] N.D. Mulherin, "Atmospheric Icing and Tower Collapse in the United States" 7th International Workshop on Atmospheric Icing of Structures (IWAIS), Chicoutimi, Canada, June 3–6, 1996.

[3] S.M. Fikke, G. Ronsten, A. Heimo, S Kunz, M. Ostrozlik, P-E. Persson, J. Sabata, B. Wareing, B. Wichura, J. Chum, T. Laakso, K. Säntti and L. Makkonen, "COST727: Atmospheric icing on structures - Measurements and data collection on icing: State-of-the-art," Veröffentlichung MeteoSchweiz Vol. 75, 110 pp. ISSN 1422-1381, 2007.

[4] P. Lehtonen, K. Ahti and L. Makkonen, "The growth and disappearance of ice loads on a tall mast," 3rd International Workshop on Atmospheric Icing of structures (IWAIS), Vancouver, Canada, Proceedings, pp. 363-368, 1991.

[5] M. N. Mytarev, "Considering ice loads in the design of tall structures," Trudy GGO, vol. 515, pp. 58-65, 1987 (in Russian).

[6] V.P. Bojkov, "On indirect estimation of ice loads on tall buildings" Trudy GGO, vol. 408, pp. 19-26, 1978 (in Russian).

[7] V.G. Glukhov, "Tall building icing on plain territory of the USSR", Leningrad Gidrometeoizdat, 144 p., ISBN 5-286-00006-1, 1989 (in Russian).

[8] L. Makkonen and K. Ahti, "Climatic mapping of ice loads based on airport weather observations," Atmos. Res., vol. 36, pp. 185 – 193, 1995.

[9] E. Sundin and L. Makkonen, "Ice loads on a lattice tower estimated by weather data," J. Appl. Meteor., vol. 37, 523-529, 1998.

[10] L. Makkonen, "Combined wind and ice loading on antenna towers: Discussion", Canadian J. Civil Eng. vol. 22, 205-206, 1995.

[11] G. Thompson, B-E. Nygaard and L. Makkonen, "Using the weather research and forecasting (WRF) model to simulate ground/structural icing events," 13th International Workshop on Atmospheric Icing of Structures (IWAIS), Andermatt, Switzerland, 8-11 September 2009.

[12] B.E.K. Nygaard, J.E. Kristjánsson, and L. Makkonen. "Prediction of in-cloud icing conditions at ground level using the WRF model." J. Appl. Meteorol. Climatol. 50, 2445-2459, 2011.

[13] E.A. Podolskiy, B.E.K. Nygaard, K. Nishimura, L. Makkonen and E.P. Lozowski, "Study of unusual atmospheric icing at Mount Zao, Japan, using the Weather Research and Forecasting model. J. Geophys. Res., vol. 117, D12106.

[14] International Standardization Organization ISO International Standard 12494 "Atmospheric Icing of Structures," 56 pp, 2001.

[15] L. Makkonen and T. Laakso, "Humidity measurements in cold and humid environments", Boundary-Layer Meteorol., vol. 116, 131-147, 2005.

[16] L. Makkonen, P. Lehtonen and L. Helle, "Anemometry in icing conditions", J. Atmos. Oceanic Technol., vol. 19, 1457-1469, 2001.

[17] G. Thompson, P.R. Field, R.M. Rasmussen and W.D. Hall, " Explicit forecasts of winter precipitation using an improved bulk microphysics scheme. Part II: Implementation of a new snow parameterization", Mon. Wea. Rev., 136, 5095–5115, 2008..

[18] L. Makkonen, "Modeling of ice accretion on wires," J. Climate Appl. Meteor, vol. 23, pp. 929-939, 1984.

[19] L. Makkonen, "Models for the growth of rime, glaze, icicles and wet snow on structures," Phil. Trans. Roy. Soc. London, vol. A358, pp. 2913–2939, 2000.

[20] J. Rink, "The melt water equivalents of rime deposits", Reich. Wetterdienst Wiss. Abh, vol. 5, 1938. (in German)

[21] V.M. Mihel, " Aeroclimatic characteristics of the influence of low cloudiness on icing of tall structures", Trudy GGO, 283, 123-131, 1971. (in Russian)

[22] B.C. Bernstein, L. Makkonen and E. Järvinen, "European icing frequency derived from surface observations", 12th International Workshop on Atmospheric Icing of Structures (IWAIS), 8-11 September 2009, Andermatt, Switzerland.

A New Severe Weather Test Site for OHL Conductors and Fittings

Dr J B Wareing#1, D P Horsman#2

[1] *CEO, Brian Wareing.Tech Ltd,*
Rosewood Cottage, Vounog Hill, Penyffordd, Chester, CH4 0EZ, UK,
[1] *Brian Wareing.Tech Ltd*
UK
jbwareing@btinternet.com

[2] *Principal Consultant, EA Technology Ltd, Capenhurst Technology Park, Capenhurst, Chester, CH1 6ES, UK*
[2] *EA Technology Ltd*
UK
David.horsman@eatechnology.com

Abstract — The UK suffers from severe wind, wet snow and differing icing conditions which can affect overhead electricity supplies and result in supply disruption. For the last 24 years, EA Technology has operated several severe weather test sites. These sites are aimed at providing the worst weather conditions for the testing of OHL conductors and fittings. The only remaining functional site is at Deadwater Fell which is located on an isolated hill top at an height of 590m near to the Scottish/English border has just been rebuilt and had a major refurbishment. The site is fully equipped with meteorological instruments to measure wind speed and direction, humidity, precipitation and temperature. It is used commercially by National Grid, Nexans, CTC, EGU, Nokia Cables, Alliance, etc to test their conductors and fittings and has been used to develop a new weather maps for the UK. All conductors have load cells and vibration monitors and a series of time lapse colour video cameras are used to monitor sag, galloping and accretion type. The newly rebuilt site has two steel supports that can take up to 10 conductors on a 190m span and a further steel support that can take further conductors on a 100m span. The site is currently testing Rubus AAAC and HD copper conductors along with porcelain/composite insulators and wedge clamps. In a normal winter the site suffers over 20 icing incidents with regular wind speeds to storm force. It is now the only severe weather test site for OHL conductors in Europe.

Keywords — Severe weather; test site; test spans; wet snow; rime ice; ice load tests

Nomenclature

AAAC	All Aluminium Alloy Conductor
IR	Infra Red
OHL	Overhead line
Rubus	A 500mm², 31.5mm diameter AAAC OHL conductor
UTS	Ultimate tensile strength
%RH	Percentage Relative Humidity

I INTRODUCTION

Overhead line (OHL) equipment has to suffer many types of climatic events. Although laboratories can provide specific equivalent testing for ice, vibration, salt fog etc, the testing of equipment in the field is the ultimate test. EA Technology Ltd in the UK has operated a range of test sites located in severe weather areas (high winds, salt corrosion, wet snow and rime ice etc) since 1987. This paper describes one particular site, Deadwater Fell, which has been in operation since 1991 [1], testing OHL conductors, fittings and insulators under severe winter weather conditions and which has recently been rebuilt and refurbished so that it can provide even more data on conductor and equipment performance in severe weather conditions.

II THE SITE

The EA Technology test site consists of a 100 and 190m span at Deadwater Fell, an isolated hill top on the English/Scottish border at a land height of 590m (Figure 1). Each span has steel support structures and can take several conductors at any one time. Although the original test site was set up in 1991 using wood pole support structures, it has recently been substantially rebuilt so that permanent 190 and 100m test spans were set up with steel structures as supports and with extended video camera monitoring, load cells, vibration monitors and full meteorological equipment, all data being logged at 10 minute intervals. The new site was finally completed in September, 2012. Figure 2 shows the termination of a Rubus conductor with a 132kV polymeric insulator whilst Figure 3 shows a general view along the southern terminal support for the 190m span.

Figure 1 The 100 and 190m spans with the main 15m platform on the left.

Figure 2 A Rubus conductor with the polymeric insulator on the 15m platform, showing a vibration monitor

Figure 3 The southern 15m termination structure with small copper conductors in the foreground and four Rubus conductors in the background. Several video cameras can also be seen monitoring each conductor. The turnbuckles are greased and wrapped between the insulators and the load cells.

The Deadwater Fell site is on a flat hill-top (Figure 4) which is equidistant between the East and West coasts of the UK and open to wind and weather from all directions. Each terminal steel support structure has an integral platform (Figures 3 and 5) to enable access for conductor erection and the fitting of load cells, turnbuckles, and vibration monitors etc. It is equipped with meteorological measuring instruments and eight time lapse colour video cameras connected to digital video recorders. All data is automatically sent back to EA Technology daily by mobile phone.

Figure 4 The Deadwater Fell test site viewed from the 'South' platform

Figure 6 shows a schematic of the site. The spans are orientated North-South and the site experiences severe wet snow and rime ice episodes many times each winter with conductor ice loads up to 7kg/m and wind speeds to 35m/s.

Figure 5 The 'South' 15m steel platform (left) with the 5m platform (100m span) and, behind it, the 10m platform ('North' terminal of the 190m span).

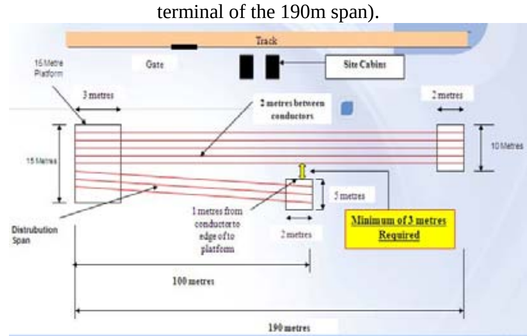

Figure 6 Schematic of the test site

III DATA

The test site generally has around 20 snow/ice incidents each winter with the most severe taking the conductors to over 60%UTS. Aero-Z, Gap, ACCC and the Lumpi-Berndorf HACIN all compared against equivalent ACSR and AAAC conductors. Figure 7 shows a comparison between new conductor types Gap and ACCC compared with a standard AAAC Sycamore on the 190m span with two rime ice and one wet snow incident in the period 4-11 January, 2008. Figure 8 shows data from January, 2010, showing how loads can differ on conductors of different ages (older ones have suffered more ice loads in the past). This also showed the effect of different pre-tensioning procedures on conductor tensions during ice load incidents.

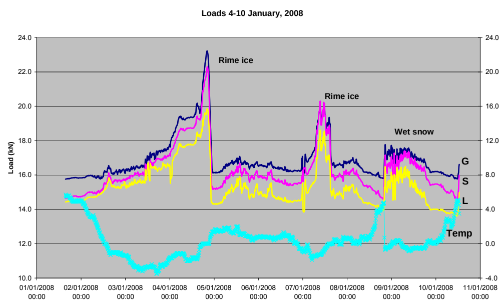

Figure 7 Load cell measured conductor tensions for Gap (G), ACCC Lisbon (L) and AAAC Sycamore in January, 2008.

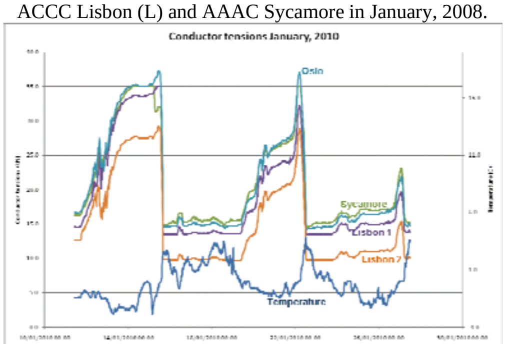

Figure 8 Load cell measured conductor tensions for ACCC Oslo, new and old ACCC Lisbon and AAAC Sycamore in January, 2010

Figure 9 shows a common wet snow incident on 14 December, 2012, with tensions going up to 35%UTS.

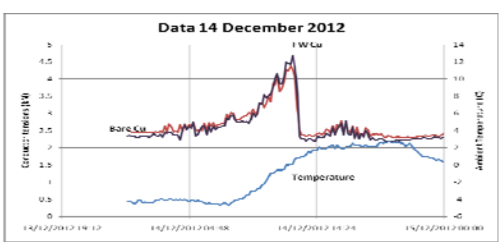

Figure 9 A wet snow incident in December, 2012, comparing bare and fibre-wrapped conductors.

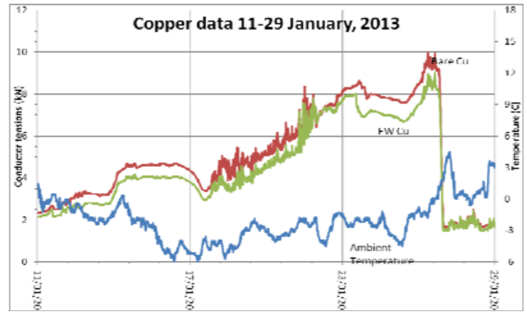

Figure 10 A combined rime ice and wet snow incident with galloping and an overall tension reaching 75%UTS.

Figure 10 shows a period of galloping under rime ice conditions on 18/19 January, 2013, with the overall icing incident finishing with a wet snow blizzard resulting in conductor tensions reaching 75%UTS. This data shows how the test site can be used to test various conductor behaviours under various weather conditions. Two different types of fittings were also compared as well as porcelain and polymeric insulators during the 2012/13 winter.

IV TEST EQUIPMENT

The site is currently (2012/13 winter) to test wedge and compression fittings as well as the effect of 132kV polymeric long rod and porcelain cap and pin insulators on Rubus conductor vibration. Other current tests are to determine the effect of wrapping fibre optic cables on distribution conductors. Figure 11 shows the Rubus conductors with load cells and turnbuckles and the video cameras and vibration monitors with one of the video cameras with IR diode lighting (before being sealed against the weather).

Figure 11 The 15m platform with the Rubus tests and the video cameras used to monitor the conductors

The meteorological equipment includes ultrasonic and cup anemometers and wind vanes, %RH, ambient temperature and precipitation measurement (tipping bucket type).

V RESULTS

A. Galloping

Conductor tensions are logged every 10 minutes and record not only wind and ice loads but also galloping episodes. Galloping causes rapid, impulsive tensions on the conductors which can result in clashing and conductor damage. As the site has complete meteorological equipment as well as conductor monitoring, the conditions in which galloping occurs can be determined. Often this is associated with light icing or ice shedding and an appropriate wind direction but sometimes only one conductor will gallop. The video data can confirm the galloping picked up by the load cells. Figure 12 shows two galloping episodes in December, 2012, and January, 2013. The first shows galloping with minor icing at sub-zero temperatures but the second (still in December) is associated with a rise in the ambient temperature leading to ice shedding. The other part of Figure 12 shows galloping as ice load increases over a few days in January but then ceases as the ice load increases further. Figure 13 shows two conductors with one galloping and one not – at the same time.

This type of data can indicate whether particular fittings, tensions or insulators can affect the performance of identical conductors.

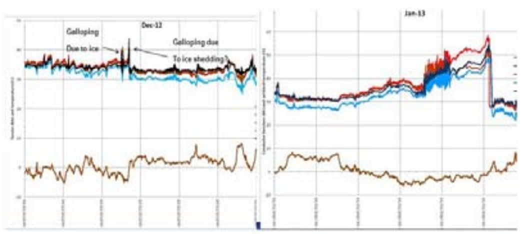

Figure 12 A double galloping episode in December (left) and some longer term galloping in January.

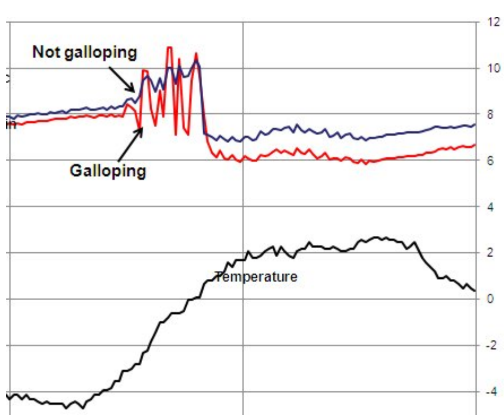

Figure 13 Two conductors in the 2012/13 winter with one galloping and one stable.

B. Vibration

Figure 14 shows identical conductors but with totally different vibration performances due to the different insulators and fibre wrap used. The Deadwater site has also been used to compare conventional and new conductor types and the effect of tension on vibration.

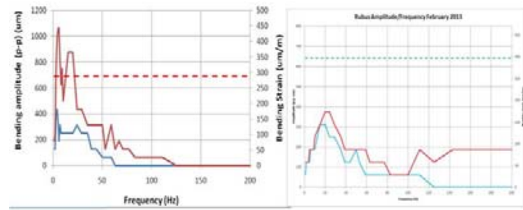

Figure 14 Vibration data on two sets of identical conductors under ice load but with different insulator types and also fibre-wrapping.

C. Ice loads and sags

Video cameras at mid-span can monitor how much different conductor types sag under ice load. This is a vital aid to line design. Figure 15 shows data from the 2010/11 winter from a mid-span camera with and without icing on the conductors. There is obviously a substantial difference between the conductor types. The individual conductors are distinguished by small markers. Since that winter, the cameras have all been upgraded to provide clearer pictures and IR lightning installed.

Figure 15 Mid-span video camera stills before and during an icing period at the site

VI WIND/ICE MAPPING

Current and historical data from Deadwater has been used in the development and calibration of wet snow and rime icing models as measured ice loads are compared with measured and modelled meteorological data. These models were used to create a wind/ice map of the UK for OHL conductors [2] and the application of this to line design (Figure 16) will be demonstrated at this workshop.

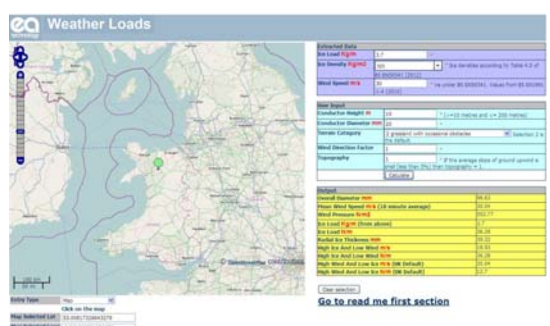

Figure 16 Wind/ice mapping software of the UK

VII CONCLUSIONS

The completely rebuilt and refurbished severe weather test site at Deadwater Fell in the UK provides a unique test bed for investigating the performance of conductors, fittings and insulators under field conditions. In its first winter of operation since the refurbishment, it has ice-loaded some conductors to over 70% of their UTS and produced some unexpected results on the effect of insulator type on conductor performance. The site is also used during the summer months to test conductor under wind only conditions (no icing) and to make comparisons between the un-iced and ice-loaded performance of conductors and fittings. All test data is provided together with meteorological and video data. The site has also been invaluable in the development and calibration of ice models leading to a wind/ice map of the UK [2].

REFERENCES

[1] J. B. Wareing, "Deadwater Fell Test Site" *9th IWAIS, Andermatt, Switzerland, 2009*. Poster PO. 067

[2] Fikke S M, Nygaard B E K, Seierstad I A, Horsman D P, Wareing J B; "The development of new design maps for ice and wind loads for Great Britain"' *11th IWAIS, St Johns, Newfoundland, September, 2013*.

Winter Measurements of Sea Spray at Mt. Desert Rock

Kathleen f. Jones #1 and Edgar L Andreas *2

#1 Cold Regions Research and Engineering Laboratory,
Hanover, New Hampshire, U.S.A.
1 kathleen.f.jones@usace.army.mil
*2 NorthWest Research Associates
Lebanon, New Hampshire, U.S.A.
2 eandreas@nwra.com

Abstract — As part of a project to investigate the severity of sea spray icing on fixed offshore structures, we spent a month in the winter of 2012-2013 on an island in the Gulf of Maine measuring sea spray. Mt. Desert Rock is about 500 m long and 200 m wide at low tide, loses about half that area at high tide, and is underwater in severe storms. College of the Atlantic's Edward McC. Blair Marine Research Station occupies the lighthouse and associated structures on the island and serves as a base for marine mammal research. We collected sea spray on microscope slides from the lighthouse catwalk at 20 m above sea level, to sample the spray generated over the ocean rather than the local splash drops from waves breaking on the rocky shore. We had hoped to also characterize the sea spray using a rotating multicylinder, long used to characterize super cooled clouds at the Mt. Washington Observatory, but it was not quite windy enough. In this paper we present and discuss our drop slide measurements and compare the resulting liquid water contents to simulated spray profiles. Finally, we discuss the advantages and challenges of using multicylinder observations to characterize sea spray.

NOMENCLATURE

D	cylinder diameter
dC/dr	spray drop concentration distribution function
dW/dr	liquid water content distribution function
E	collision efficiency of drops with cylinder
$H_{1/3}$	significant wave height
m	ice mass
r	sea spray drop radius
$r_{\max}$	maximum drop radius
r_{min}	minimum drop radius
t	time
$U(z)$	wind speed at height z
U_{10}	wind speed at 10 m above the ocean surface
$u*$	friction velocity
v_g	fall velocity of drop with radius r
z	height above sea level
κ	von Kármán constant
π	3.14
ρ_w	density of water

I. INTRODUCTION

Sea spray drops are carried by the wind and collide with objects in their path. When the air temperature is below freezing, spray drops may accumulate as ice on the components and equipment on offshore structures. Fixed offshore structures, including oil exploration and production platforms, are anchored and many designs have little area at the waterline. For these kinds of structures, sea spray freezing to the superstructure comes from the interaction of wind and waves. Film drops (radius ~ 1 µm) and jet drops (radius ~ 10 µm) are generated by the bursting of bubbles in whitecaps, while the larger spindrift drops (radius > 20 µm) are ripped off the crests of waves and carried aloft only in high winds.

Data on severe sea spray icing is provided in records kept by the meteorologist-observers on the semi-submersible exploratory drilling rig *Ocean Bounty* during the winter of 1979–1980 when it was deployed in Lower Cook Inlet, Alaska. A number of papers ([1] - [4]) present and analyze the weather and qualitative icing data from that winter. In that area of Cook Inlet, winds are funnelled through gaps in the mountains, and wind speeds vary significantly over short distances. Six storms between 24 September 1979 and 26 April 1980, each one lasting between one and seven days (21 days total) with wind speeds exceeding 25 m s^{-1}, caused sea spray icing on the superstructure of the *Ocean Bounty*. The data from handwritten weather, ocean, and icing observation sheets from the *Ocean Bounty* are provided electronically in [3].

In the next section, equations from [4] for sea spray concentration in high winds, along with relationships for computing liquid water content and icing rate, are reviewed. In the third and fourth sections, we present our field measurements of sea spray in the winter of 2012-2013 and discuss the use of multicylinder measurements for characterizing sea spray.

II. SIMULATION OF SEA SPRAY ICING

Based on data from the *Ocean Bounty* and *SEDCO 708* [5], spray icing on fixed structures at wind speeds less than about 20 m s^{-1} does not appear to be significant. At those speeds spray drops are generated primarily by the bursting of bubbles in whitecaps. To include spindrift at higher wind speeds, [4] proposed modifications to the sea spray concentration function in [6], with a stronger dependence on wind speed and a broader drop distribution:

$$\frac{dC(r)}{dr}\left[\mathrm{m}^{-3}\mu\mathrm{m}^{-1}\right]=\frac{30U_{10}^{\;4}}{r}\exp\left(-\frac{1}{2}\left[\frac{\ln(r/0.3)}{\ln 4}\right]^2\right). \quad (1)$$

Eq. (1) is the spray concentration at the level of the significant wave height $0.5H_{1/3}$. Above that height the concentration decreases as given in [7]

$$\frac{dC(r,z)}{dr}=\frac{dC(r)}{dr}\left(\frac{z}{0.5H_{1/3}}\right)^{-\frac{v_g}{\kappa u*}}, \quad (2)$$

where z is the height above sea level (asl), v_g is the fall speed of drops with radius r, $\kappa = 0.4$ is the von Kármán constant, and $u*$ is the friction velocity.

The liquid water content distribution of the spray at z is then:

$$\frac{dW(r,z)}{dr}\left[\mathrm{g\ m}^{-3}\mu\mathrm{m}^{-1}\right]=\rho_w\frac{4}{3}\pi r^3\frac{dC(r,z)}{dr}. \quad (3)$$

The integral of Eq. (3) over drop radius is the total liquid water content of the sea spray. We can use Eq. (3) to calculate the mass icing rate on a cylinder with diameter D and length L:

$$\frac{dm(z)}{dt}=U(z)DL\int_{r_{\min}}^{r_{\max}}E\left(U(z),r,D\right)\frac{dW(r,z)}{dr}dr, \quad (4)$$

where m is the mass of accreted saline ice, $U(z)$ is the wind speed at z, and $E(U(z),r,D)$ is the collision efficiency of drops of radius r with a cylinder of diameter D at wind speed $U(z)$. The integration limits are $r_{\min} = 5$ µm and $r_{\max} = 200$ µm for the high wind speeds that generate spindrift.

There are very few data sets with spray concentrations for wind speeds greater than 20 m s^{-1}, so the wind speed dependence and the shape of the distribution in Eq. (1) are not well defined. Therefore, we undertook a field experiment in the winter of 2012-2013, and have another planned for 2013-2014, to attempt to augment the available data and revise Eq. (1) as appropriate.

III. FIELD OBSERVATIONS 2012-2013

For a project funded by the Office of Naval Research, we spent a month from 29 December 2012 to 28 January 2013 on Mt. Desert Rock in the Gulf of Maine (Fig. 1) making sea spray measurement from the lighthouse. Mt. Desert Rock (Fig. 2) is less than two hundred meters across at low tide, and about half its area is under water at high tide (Fig. 3). The high point on the island is just 8 m above sea level and the entire island is under water in some storms.

The lighthouse, station MDRM1 in the National Data Buoy Center (NDBC) Coastal-Marine Automated Network (C-MAN), is the most exposed lighthouse on the east coast of the United States. Wind speed and direction, air temperature, dew

Fig 1. C-MAN stations Mount Desert Rock (MDRM1), Matinicus (MISM1), and NERACOOS buoy 44034 in the Gulf of Maine.

point, and pressure are measured at various levels on the lighthouse. The anemometer is 20 above ground level and 25 m asl. Water temperature, salinity, and significant wave height are measured at a number of buoys in the Gulf of Maine. The nearest is station 44034 (Buoy I01 in the Northeastern Regional Association of Coastal Ocean Observing Systems), 16 km north of Mt. Desert Rock. As weather data from MDRM1 are not transmitted reliably for QA and archiving, we augmented that data set with data from Matinicus Rock (MISM1), southwest of Mt. Desert Rock (Fig.1).

The lighthouse and associated structures on Mt. Desert Rock are now home to College of the Atlantic's Edward McC. Blair Marine Research Station. The island provides a land-based site for open ocean observations. COA uses the research station primarily in the summer for marine mammal research. Students and staff from COA handled logistics for our Winter Rock Experiment (WREx), including water, food, fuel (propane for heat, gas and diesel for generators to augment the solar panel that charged the battery array), boat transportation to the island, facilities and systems maintenance, and help with deploying instruments.

During WREx we used the lighthouse as a platform to measure sea spray. The rail of the lower catwalk is 20 m above the waves breaking on the rocks below, so locally generated splash drops are blown past the lighthouse before they are carried as high as the catwalk. Spray observations could not be made while it was raining or snowing. Sea smoke on some days deposited small amounts of rime on the rocks and lower portions of structures, but did not reach the catwalk level. As the granite lighthouse is not insulated or heated, has vents to the outside and doors at the 1st, 5th and 6th levels, and has a large thermal mass, the interior temperature and humidity are likely similar to outside conditions. Water in a pan to catch drips from the ceiling in the 2nd level was often

Fig. 2. Mt. Desert Rock from the northwest.It is the site of the most exposed lighthouse on the east coast of the United States.

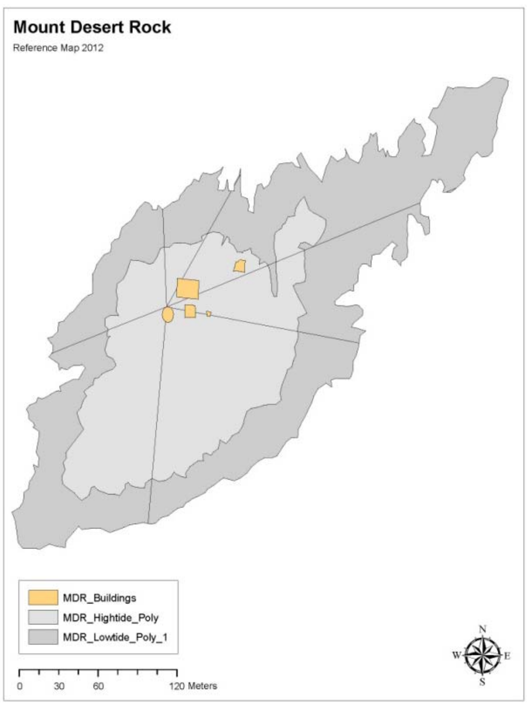

Fig. 3. College of the Atlantic map of Mt. Desert Rock, delineating the high and low tide lines and the locations of buildings. Hurricane Bill in 2009 washed out all except one wall of the boat house, the northernmost structure on the map. The oval shows the location of the lighthouse.

frozen.

We prepared microscope slides for collecting sea spray drops by coating them with Vaseline, and then heating to obtain a smooth, thin, hydrophobic surface. We exposed the half-width slides (12.5 mm wide) on a bracket mounted to the rail of the lower catwalk (Fig. 4), recording the start and end times of the exposure. The duration of the exposure varied from over an hour at low wind speeds to just two minutes at speeds around 20 m s^{-1}. We immediately carried the exposed slide down to the microscope set up in the 2nd level of the lighthouse. We captured typically 20 images of the drops on each slide at the lowest magnification, which distinguishes drops as small as 6 μm in diameter. An image from an observation on 20 January 2013 is shown in Fig. 5. Observations with excessive exposure times resulted in drops that are close together on the slide. As closely spaced drops tend to coalesce, exposure times were limited by the spray drop concentration.

We used Image-Pro software to count and size the drops in the images, then binned the drops in 2-micron diameter increments for drops up to 60 μm, and 20 μm-increments for larger drops, and corrected the binned counts for collision efficiency, using the average wind speed for the exposure. The collision efficiency for ribbons is provided in [8]. The sample volume for calculating the spray drop concentration from the corrected count is the product of the exposure time, the total image area on the slide, and the wind speed. The measured drop concentrations for nine exposures with U_{10} varying from 11.2 to 19.8 m s^{-1} (our highest wind speed at 10 m with drop slide observations) are shown in Fig. 6. Note that the drop concentration depends on significant wave height as well as on wind speed. For winds from the northwest, the fetch is

Fig. 4. Bracket for collecting spray drops on microscope slides, mounted to the catwalk rail. The half-width slide is clamped to a flat section at the top of the 12.5 mm diameter vertical rod.

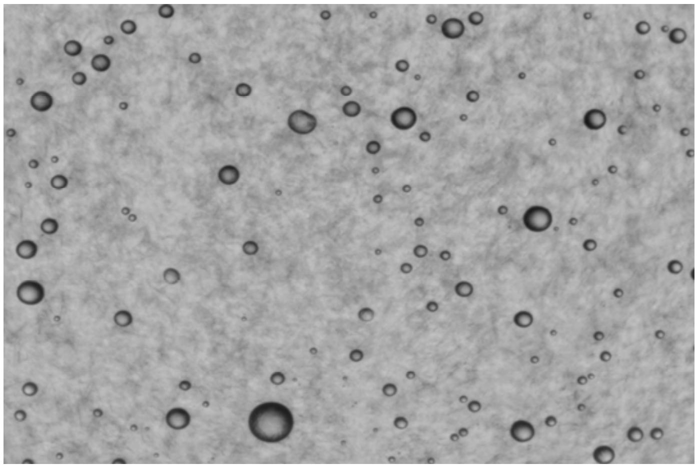

Fig. 5. Observation L Image 11 from a drop slide on 20 January 2013. The image is 1944 by 2592 pixels, with an area of 1.4 mm^2. The largest drop, in the lower center of the image, has a diameter of 89 µm.

limited and wave heights are significantly smaller than for winds from the southwest. For the observations in Fig. 6 the sample volume varies by a factor of ten, from 0.083 to 0.849 m^3.

We can compare the liquid water contents based on these drop compilations with simulated spray liquid water contents obtained by integrating Eq. (3) over the range of drop radii. The top panel of Fig. 7 shows liquid water content profiles for U_{10} from 21 to 40 m s^{-1}, calculating u^* and $H_{1/3}$ using [9] and [10], assuming a neutrally stable atmosphere. The bottom panel focuses on the lower wind speeds in which we expect to be able to measure sea spray from the lighthouse on Mt. Desert Rock. The spray liquid water contents at 20 m asl from the nine observations in Fig. 7 are all smaller than the

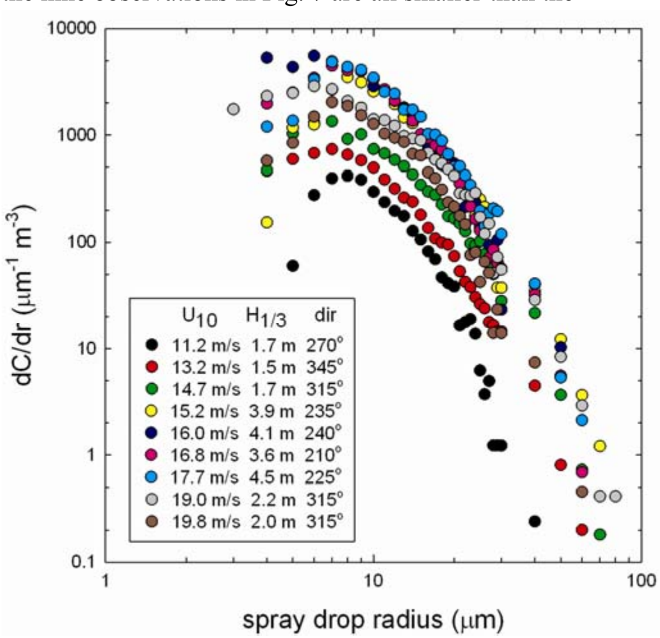

Fig.6. Sea spray concentrations for nine observations for U_{10} from 11.2 to 19.8 m s^{-1}. The concentration also depends on significant wave height, which in turn depends on wind direction.

simulated liquid content for U_{10} = 19 m s^{-1}. These relatively low values may be because our highest wind speeds were from the northwest, with limited fetch and relatively small significant wave heights. An additional concern is the limited sample volume in each observation. The dominant contribution to the spray liquid water content is from the relatively rare large drops and the calculated liquid water content may vary significantly depending on how many of these large drops happen to be in the images of the sample on the microscope slide. While the sample volume could be increased by taking more images of the drops from each slide, this would provide sample volumes up to only about five times the volume obtained by using the 20 images on each slide typical for WREx, at the cost of the additional time to collect and process the images. While the image processing software does a good job of differentiating the drops from the background and outlining them for sizing, time-consuming user input is required to correct outlines of drops that are not evenly illuminated and remove anomalies. In the next section we discuss an alternative approach for characterizing the spray drop distribution.

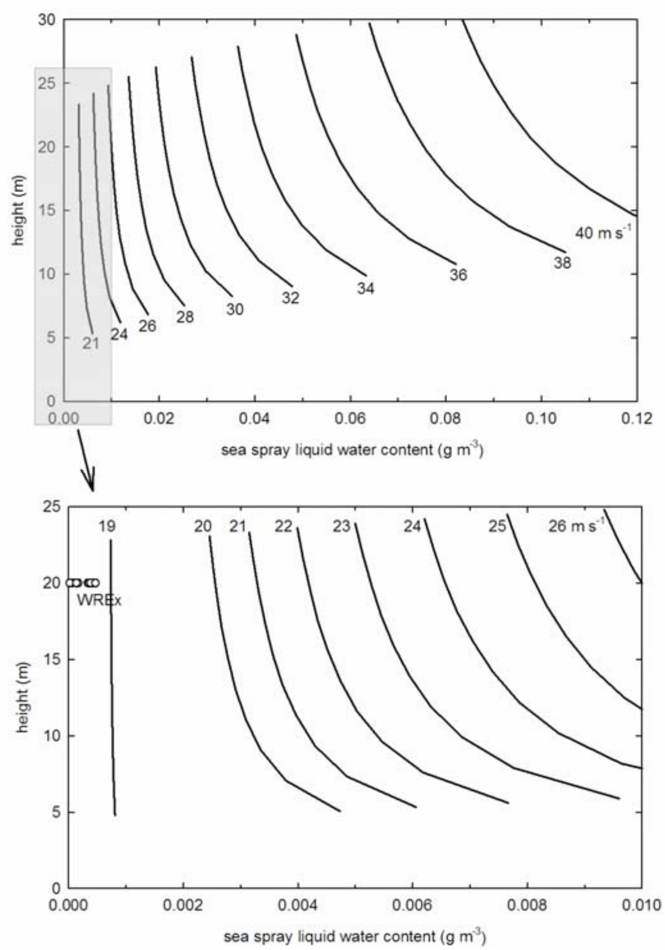

Fig. 7. Spray liquid water contents from integrating Eq. (3). In the top panel U_{10} varies from 21 to 40 m s^{-1}. The bottom panel focuses on wind speeds from 19 to 26 m s^{-1}, and includes liquid water contents calculated from the WREx measurements.

IV. Investigation of Multicylinder Measurements of Sea Spray

Multicylinder measurements have been made in supercooled clouds at Mount Washington Observatory in the White Mountains of New Hampshire since the early 1940s [11]. The multicylinder method relies on the variation in the collision efficiency of the drops in the cloud with cylinders of different diameters. From the measured mass of ice on each of the cylinders, the cloud liquid water content and median volume diameter of the drops are typically calculated. For the wind speeds and liquid water contents at the summit of Mt. Washington, the multicylinder exposure time varies from 7 to 22 minutes, giving a sample volume range from 80 to 290 m^3. The large sample volume makes this an attractive alternative to collecting drops on slides. Because of the intrinsic differences between drops in clouds and sea spray, we did an analysis to determine the usefulness of the multicylinder for characterizing sea spray. The issues are:

- even in winter, temperatures at sea level in the Gulf of Maine are not reliably below freezing,
- liquid water contents in sea spray are small compared to cloud liquid water contents,
- the sea spray drops that are significant for icing are large compared to the drops in the stratifrom clouds that surround Mt. Washington,
- the vertical gradient in sea spray liquid water content,
- evaporation of ice/water from the cylinders in the unsaturated air.
-

We address each of these issues in the following paragraphs.

The multicylinder can be adapted for above freezing conditions by covering the cylinders with absorbent paper. This has been done occasionally at Mt. Washington [11]. The aborbent covers must be well enough attached to the cylinders that they are not ripped off by the wind, and the exposure must be monitored to ensure that the covers do not become saturated, with excess water dripping from one cylinder to the next lower cylinder in the stack.

To determine appropriate exposure times for the multicylinder in the low liquid water content conditions in sea spray, we simulated the accretion of ice from sea spray using the spray liquid water contents underlying Fig. 7 with collision efficiencies from [12]. The accreted mass of ice on each cylinder was calculated in 10-minute intervals for exposure times up to two hours. From the results, we chose an exposure time at each wind speed that results in ice masses on the cylinders in the range of typical values for multicylinder observations at Mt. Washington. Fig 8 shows the results at 20 m asl for five wind speeds, along with the cylinder mass distribution for a supercooled cloud observation at Mt. Washington. The sample volumes for these wind speeds and exposure times range from 700 to 1800 m^3, so these observation times would well represent the spray conditions. Any variations in the mean wind speed during the long exposures would have to be taken into account in the analysis of the cylinder masses to determine the spray characteristics.

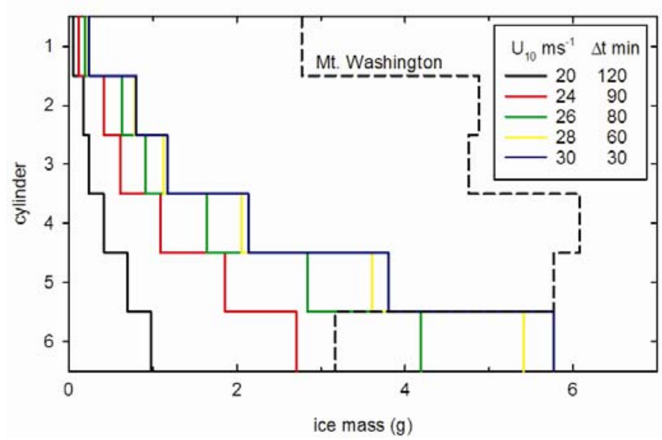

Fig. 8. Simulated ice masses on the six cylinders of a rotating multicylinder for five winds speeds. Exposure times are chosen to give ice masses similar to observations in supercooled clouds at Mt. Washington Observatory. An example of multicylinder masses from Mt. Washington is shown as a dashed line.

Fig. 8 shows that the distribution of ice mass on the cylinders is markedly different for sea spray drops than for cloud drops. The large spray drops that contain most of the water have relatively large collision efficiencies, even with the large diameter cylinders. For example, the volume-weighted collision efficiencies at 20 m asl for U_{10}=24 m s^{-1} range from 0.94 for the smallest cylinder with a diameter of 0.16 cm to 0.54 for the largest cylinder with a diameter of 7.6 cm. In contrast, the multicylinder observations at the summit of Mt. Washington often have little or no ice on the largest cylinder because of the near zero collision efficiencies for small stratiform cloud drops at moderate wind speeds.

The cylinders in the multicylinder are arranged in a vertical stack 0.65 m tall. At 20 m asl, the simulated spray liquid water content decreases by about 1% from the largest to the smallest cylinder for U_{10} between 20 and 30 m s^{-1}. Multicylinder observations at 10 m asl would see about a 3% difference in liquid water content at these wind speeds.

Saline drops evaporate to a size determined by the relative humidity, and reach this size over seconds to minutes [13]. At a relative humidity of 80% and with a typical ocean salinity of 24 psu, the equilibrium diameter is about half the drop diameter at formation. The drops reaching Mt. Desert Rock are entrained over the entire upwind fetch and can be assumed to be at their equilibrium diameters. Any further evaporation from the absorbent cylinder covers or sublimation from the frozen layer of saline ice would be inconsequential.

V. Summary

Ice accretion documented on the *Ocean Bounty* and *SEDCO 708* indicate that sea spray drops from spindrift at high wind speeds are the source of accreted ice. The equations describing the spray drop concentration distribution at wind speeds above 20 m s^{-1} are based on only a few measurements. We spent a month on Mt. Desert Rock in the winter of 2012-2013 hoping to make spray measurements in high winds. While the wind speeds during WREx were not quite as high as we would like, we learned a lot about working from the lighthouse and the limitations of determining the spray concentrations from drops collected on microscope slides.

We are planning another field campaign for Mt. Desert Rock in the coming winter, again looking for high winds. We will rely primarily on the multicylinder for characterizing the sea spray distribution, augmenting those measurements with drop slides. We plan to use full-width slides to limit the collection of smaller drops, and to test slide coatings and vary illumination of the slide in the microscope to get better drop discrimination by the image processing software.

ACKNOWLEDGMENT

This work was supported by the U.S. Office of Naval Research, contracts 12PR04090-00 (Jones) and N00014-12-C-0290 (Andreas). Equipment for the spray measurements was built by CRREL's Christopher Williams and Christopher Donnelly. Logistics for WREx were provided by College of the Atlantic. We thank Christopher Tremblay (Cornell University), Toby Stephenson (COA), Alex Borowicz (COA), Tanya Lubansky (Rutgers University), and Lindsey Nielsen (COA) for getting us and our equipment to the Rock, providing heat, power, and water, and helping deploy instruments.

REFERENCES

[1] J.A. Williams, "Charting heavy Alaskan weather," *Offshore*, PennWell Petroleum Group, Houston, TX, pp. 49–54, 5 June, 1981.

[2] J.W. Nauman, "Superstructure icing on the semi-submersible *Ocean Bounty* in Lower Cook Inlet, Alaska," *Proceedings of the 2nd International Workshop on Atmospheric Icing of Structures*, Trondheim, Norway, EFI Technical Report 3439, pp. 71–79, 19-21 June, 1984.

[3] K.F. Jones and E.L Andreas, "Sea spray icing of drilling and production platforms," ERDC/CRREL TR-09-3, Cold Regions Research and Engineering Laboratory, Hanover, NH, 2009.

[4] K.F. Jones and E.L Andreas, "Sea spray concentrations and the icing of fixed offshore structures," *Quarterly Journal of the Royal Meteorological Society*, vol. 138, pp. 131–144, 2012.

[5] L.D. Minsk, "Ice observation program on the semi-submersible drilling vessel *SEDCO 708*," CRREL Special Report 84-2, Cold Regions Research and Engineering Laboratory, Hanover, NH, 1984.

[6] E.R. Lewis, and S.E. Schwartz, *Sea Salt Aerosol Production: Mechanisms, Methods, Measurements, and Models—A Critical Review*, Geophysical Monograph 152, American Geophysical Union, Washington, DC, 2004.

[7] C.W. Fairall, M.L. Banner, W.L. Peirson, W. Asher, and R.P. Morison, "Investigation of the physical scaling of sea spray spume droplet production," *Journal of Geophysical Research*, vol. 114, C10001, DOI:10.1029/2008JC004918, 2009.

[8] I. Langmuir and K. Blodgett, "Mathematical investigation of water droplet trajectories", Report No. RL-22, in *Collected Works of Irving Langmuir*, Pergamon Press, Elmsford, New York, 1960, pp. 348-393, 1946.

[9] E.L Andreas, P.O.G. Persson, and J.E. Hare, "A bulk turbulent air–sea flux algorithm for high-wind, spray conditions," *Journal of Physical Oceanography*, vol. 38, pp. 1581–1596, 2008.

[10] E.L Andreas, S. Wang, "Predicting significant wave height off the northeast coast of the United States", *Ocean Eng.* vol. 34, pp. 1328–1335. DOI:10.1016/joceaneng.2006.08.004, 2007.

[11] J.B. Howe, "Rotating multicylinder method for the measurement of cloud liquid water content and droplet size", CRREL Report 91-2, Cold Regions Research and Engineering Laboratory, Hanover, New Hampshire, 1991.

[12] K.F. Finstad, E.P. Lozowski, and E.M. Gates, "A computational investigation of water droplet trajectories", *Journal of Atmospheric and Oceanic Technology*, vol. 5, pp. 160-170, 1988.

[13] E.L Andreas, "Time constants for the evolution of sea spray droplets," *Tellus*, vol. 42B, pp. 481–497, 1990.

Laboratory Experiments of Saline Water Spray Icing
– Features of Hydrophilic and Hydrophobic Pliable Sheets –

Toshihiro Ozeki[#1], Haruhito Shimoda[*2], Daisuke Wako[*3], Satoru Adachi[+4], Takatoshi Matsuzawa[*5]

[#] *Hokkaido University of Education*
Sapporo 002-8502, Hokkaido, Japan
[1] ozeki.toshihiro@s.hokkyodai.ac.jp

[*] *National Maritime Research Institute*
Mitaka 181-0004, Tokyo, Japan
[2] shimoda@nmri.go.jp
[3] wako@nmri.go.jp
[5] zawa@nmri.go.jp

[+] *Snow and Ice Research Center, NIED*
Nagaoka 940-0821, Niigata, Japan
[4] stradc@bosai.go.jp

Abstract **—** Ice accretion caused by seawater spray is a major problem faced not only by fishing vessels and trawlers, but also by offshore structures. Marine disasters caused by such accretion occur frequently in cold regions. Yet, even in this age of high technology, deicing continues to be a manual operation that usually involves the use of a hammer.

We conducted a cold experiment on an ice model basin to investigate the wet growth from spray icing. Experiments using the two textiles—a high hydrophobic sheet and a high hydrophilic sheet—were conducted to reveal the sea spray icing characteristics of hydrophobic and hydrophilic surfaces. A PVC coating sheet was selected to compare the ice accretion effect. The air temperature in the cold room was maintained at approximately –10 °C and –14 °C. Small water particles were supplied by nozzles and sprayed on the cylindrical test specimen. The wind speed was 3–5 m/s and 5–7 m/s. The salinity of the supplied water was 26–29 wt‰. The liquid water flow, initial growth, and growing pattern of ice were observed during the experiments.

Wet growth from spray icing occurred on the windward side of both test materials. The initial icing depended considerably on whether the surface of the sheet model was hydrophobic or hydrophilic. The initial growth on the hydrophobic surface was characterized by the formation of hemispheric water droplets and a vein of ice on the textile surface. Irregular projections were observed on the spray ice surface. Spray water formed fluid flowing film on the highly hydrophilic surface. Exfoliated pieces of the membranous ice were often observed during the initial growth. Deicing of both the pliable sheets was easy owing to the low adhesion strength of saline ice and the aforementioned exfoliation.

I. Introduction

Sea spray icing is a major problem faced by ships and offshore structures. Light beacons on breakwater, which face the Sea of Japan and the Sea of Okhotsk, are not initially equipped with countermeasures for spray icing. Heavy sea spray icing on lighthouses severely affects their maintenance in the northern harbors of these bodies of water.

Marine disasters caused by ice accretion occur frequently around Newfoundland and Nova Scotia [1] and around Kuril Islands [2]. Ice accretion represents a substantial challenge for fishing vessels, trawlers, patrol boats, and commercial vessels. When the icing is heavy, it increases the need for maintenance when navigating through cold regions. Yet, even in this age of high technology, deicing continues to be a manual operation that usually involves the use of a hammer. The effects of low adfreeze materials or anti-icing coatings are considered insufficient for long periods under severe conditions in the northern sea.

Several recent studies have investigated the feature of sea spray ice and deicing methods for lighthouses and ships. The typical accumulation of ice resulting from sea spray icing occurs as follows. First, seawater spray is generated from the bow of the ship. Next, the spray drifts and impinges upon the superstructure, after which there is a wet growth of ice from the brine water flow. Makkonen [3] developed a theoretical model of salt entrapment in sea spray ice. According to Makkonen, a thin liquid-water film on the icing surface runs off from the surface and consequently traps liquid in the spray ice matrix. He suggested that the salinity of sea spray ice depends mainly on the accretion fraction. Ryerson and Gow [4] studied the microstructural features of spray ice on ships and confirmed the presence of a channelized network of brine. Ozeki et al. [5] measured the three-dimensional microstructure of sea spray ice using the NMR imaging technique, and likewise confirmed the presence of such a channelized network of brine in natural sea spray ice samples. Lozowski et al. [6] reviewed computer simulations of marine ice accretion and discussed the US Coast Guard's cutter Midgett model and a three-dimensional time-dependent vessel-icing model.

Numerous laboratory experiments and field observations have been performed to test the adhesion strength of saline ice (e.g., [7]-[11]). Laforte and Lavigne [12] investigated the adhesion strength of spray icing on an aluminum cylinder in a cold room at –18 °C. The results of the adhesion tests showed that the addition of NaCl to spray icing greatly reduces adhesion strength. The Japan Aids to Navigation Association [13] tested canvas cloths for use in anti-icing in a laboratory experiment. The test samples were prepared by spraying fresh water on the canvas cloths in a cold room at –15 °C. The cloths were coated with polypropylene, vinylidene fluoride, vinyl chloride, and silicone. The results of the adhesion tests showed that the silicone coat exhibited reduced adhesion strength. A pendulum impact test on the polyvinylidene-difluoride coated cloth revealed that the deformation of the cloth was effective in deicing. However, coated canvas cloths are not practically used for the deicing of lighthouses. Ozeki and Yamamoto [14] designed covers to envelop light beacons. These covers consist of pliable polymer sheets. Ice is expected to exfoliate easily from the sheet owing to its low ice adhesion property and rapid distortion. Ozeki and Yamamoto obtained a preliminary result stating that deicing could be easily performed. Ozeki et al. [15] investigated the growth rate of sea spray icing using telephotographs recorded in intervals. The growth rate of the cross section of the spray icing monotonically increased with the product of air temperature and wind speed (i.e., the heat loss by convective heat flux). Ozeki et al. [16] performed laboratory experiments on the saline ice adhesion using several synthetic textiles and polymer films. The hydrophobic materials exhibited lower adhesion strength than the other test materials in the experiments using pure ice. On the other hand, the results of the saline ice adhesion tests at –20 °C indicate that the adhesion strength decreases very rapidly as the salinity increases for both hydrophilic and hydrophobic materials. The deicing conditions were verified through cold experiments conducted in the laboratory.

In this study, we investigated the wet growth of spray icing on synthetic textiles through a cold experiment conducted on an ice model basin. We tested high hydrophilic and high hydrophobic pliable sheets that were wrapped around the light beacon model.

Fig. 1. Specimen of light beacon model

II. Laboratory Equipment for Experiments

We were unable to observe the growth pattern of sea spray icing in the field because the ice accretion occurred under the impinging pressure of the heavy spray jets. To solve this problem, we investigated the wet growth patterns of water spray ice through laboratory experiments. The liquid-water flow, initial growth, and growth pattern of ice were observed. The experimental apparatus was set in an ice model basin, (length: 35 m; width: 6 m), at the National Marine Research Institute (Tokyo). The textiles were set on a cylinder (Figure 1, height: 2 m; diameter: 0.3 m), whose diameter was identical to dimensions of the typical small lighthouse in the test field [15].

TABLE 1
Mechanical properties of fabrics tested

	Tensile strength (N/cm)	Thickness ($\times 10^{-3}$ m)
FGT	1227	0.6
SCC125J	409	0.54
C-18	425	0.55

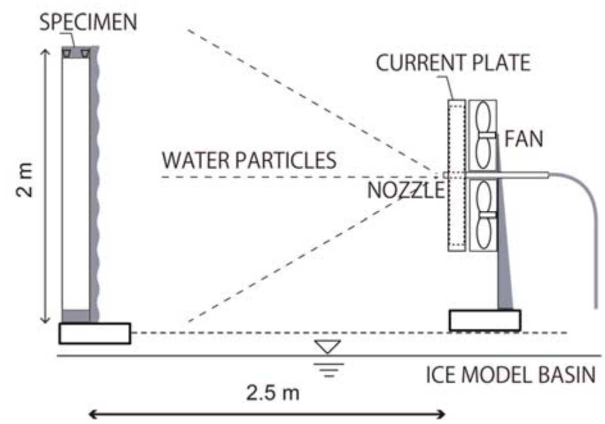

Fig. 2. Apparatus for experiment 1

III. Spray Icing Experiment 1

Experiments using the two textiles—Ever Fine Coat (FGT) and Sky Clear Coat (SCC)—were conducted to reveal the saline water spray icing characteristics of hydrophobic and hydrophilic surfaces. FGT (Taiyo Kogyo Corp., Tokyo, Japan) consists of a glass fiber cloth and polytetrafluoroethylene (PTFE) and has a combination of PTFE and TiO_2. The surface of FGT exhibits hydrophobic behavior with a water contact angle of 110°–120°. SCC (Taiyo Kogyo Corp., Tokyo, Japan) comprises polyester cloth and polyvinyl chloride coated with a TiO_2 film; it exhibits hydrophilic behavior with a water contact angle of less than 30° owing to the photoinduced effect on the TiO_2 surface [16]. The two synthetic textiles are suitable for fabricating covers to envelop light beacons. Table 1 lists the mechanical properties of fabrics used. The thickness of FGT and SCC (125-J) were 0.6 mm and 0.54 mm respectively. A schematic view of the apparatus is shown in Fig. 2. The air temperature in the cold room was maintained at approximately –10 °C. Small water droplets with a diameter of approximately 0.3–0.5 mm were supplied by a fan-shaped spray nozzle; they were sprayed on the cylindrical test specimen. The distance of the specimen from the spray nozzle was 2.5 m. During the experiments, the wind speed was 3–5 m/s. The salinity of the supplied water was approximately 29 wt‰, which is very close to the salinities of the Sea of Japan and the North Pacific Ocean. Therefore, the wind distribution and the liquid-water flow on the specimens in experiment 1 should be close to the field conditions, although wind speed was lower than that in the field conditions.

In both experiments, i.e., for the FGT and SCC surfaces, the water was sprayed for 60 min. Table 2 shows the spray supply in each experiment. Under the abovementioned conditions, wet growth of ice occurred on the windward side of both test materials. The initial growth on the FGT (high hydrophobic) surface appeared to be identical—hemispherical water droplets were formed on the textile, and part of the water froze into frazil ice as the materials were pulled down on the textile surface by gravity. This is probably due to the material's hydrophobic property. Frazil ice and slush moved down until the windward side of FGT was covered by spray ice. This icing procedure was characterized by remarkable irregularities on the spray ice surface (Fig. 3).

TABLE 2
Spray supply in the experiment 1

	Spray supply (l/h)		
	120	42	30
FGT (hydrophobic)	×	×	
SCC (hydrophilic)	×	×	×

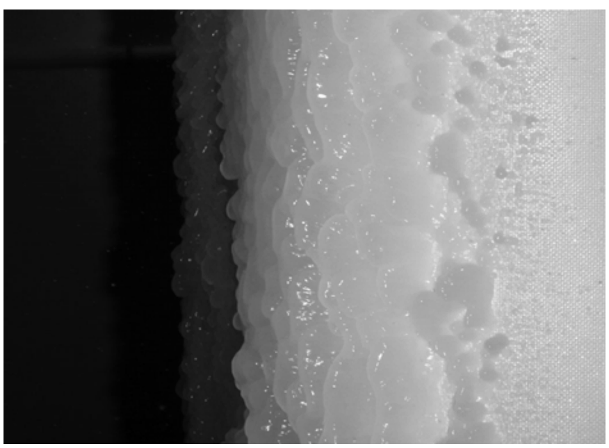

Fig. 3. Irregularities of the spray ice surface on FGT (high hydrophobic).

The liquid-water flow and initial growth of ice on SCC (high hydrophilic) were different from those on the hydrophobic materials. Spray water formed a thin fluid film flowing on SCC, which has a hydrophilic surface. Part of the water froze into spongy ice as it flowed down the textile surface. The surface gradually began to be covered by sheet-like ice. It is noteworthy that pieces of the sheet ice often exfoliated and slid down the surface as slush (Fig. 4) in the experiment where the spray supply was at 120 l/h. Slush moved down automatically owing to the weight of the ice 35 min after the spraying of water began. As shown in Fig. 5, ripples were produced on the ice surface; this may be a characteristic of the wet growth of ice on hydrophilic surfaces.

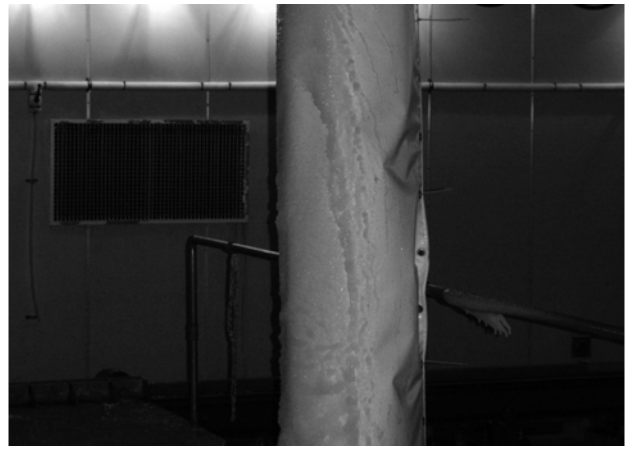

Fig. 4. Exfoliation of icing on SCC

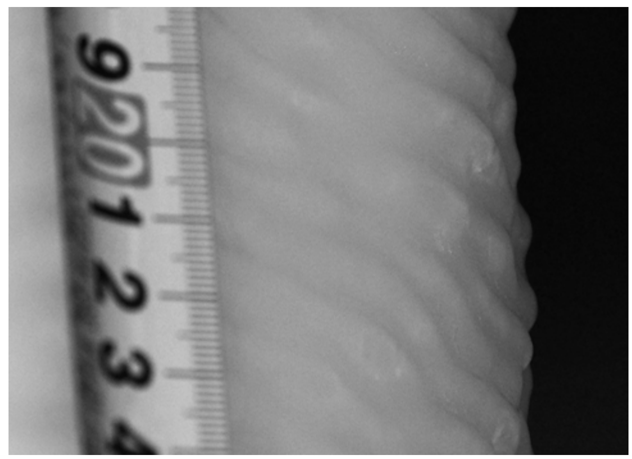

Fig. 5. Ripples on the ice surface of SCC (high hydrophilic)

The weights of the water spray ice formed in the experiments when the spray supply was 120 l/h and 42 l/h were measured. The results are as follows: the weights on the FGT and SCC surfaces in the experiments when the supply rate was 120 l/h were 12.9 kg and 11.5 kg respectively, and the weights on the FGT and SCC surfaces in the experiments when the supply rate was 42 l/h were 7.9 kg and 7.3 kg respectively. The weight on the SCC surface was slightly less than that on the FGT surface. This is because the weight of ice included slush.

IV. Spray Icing Experiment 2

The wet growth of spray icing was investigated under strong wind conditions in experiment 2. A schematic view of the apparatus is shown in Fig. 6. We made a simple wind tunnel by using a panel (height: 2 m; length: 5.1 m) in the passage of the ice model basin. A blowing unit was attached to the inlet of the wind tunnel, and the spray unit was installed at the middle of the wind tunnel. The specimen was set at the end of the wind tunnel. The distance between the specimen and the spray nozzle was 3.7 m. The wind speed was approximately 5–7 m/s in the vicinity of the specimen in experiment 2. Strong spots of 9 m/s were also observed along the sides of the center. Consequently, experiments could be performed under strong winds.

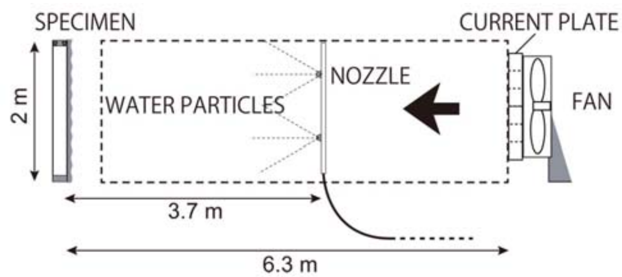

Fig. 6. Apparatus for experiment 2

TABLE 3
Spray supply in the experiment 2

	Room temperature (°C)	
	–10	–14
FGT	×	×
SCC	×	×
C-18	×	

Experiments using the two types of textiles—FGT and SCC—were also conducted in experiment 2 as a follow up to experiment 1. Ultra Max type C (C-18) was selected for comparison. C-18 (Hiraoka & Co. Ltd., Tokyo, Japan) comprises polyester cloth and polyvinyl chloride coated; it exhibits hydrophilic behavior. The thickness of C-18 was 0.55 mm (Table 1). The air temperature in the cold room was maintained at approximately –10 °C and –14 °C (Table 3). Small water particles with a diameter of approximately 0.3–0.5 mm were supplied by two conical-shaped spray nozzles; they were sprayed on the cylindrical test specimen. The salinity of the supplied water was approximately 27±1 wt‰.

In both experiments, for the FGT and SCC surfaces, the water was sprayed for 45 min (with the exception of 1 run for 60 min). The salinity and weights of the ice accretion in the 45 min experiments were measured. The spray ice samples were divided into four per quarter height. Comparing the amount of icing on the three sheets at the same room temperature (–10 °C) and same amount of sprayed water, we found that there was no significant difference in the total icing weight. This is because the amount of collision and the cooling flux for the liquid film was the same for all sheets.

Fig. 7 shows the percentage of icing weight at each height for each sheet model. The exfoliation phenomena of icing did not occur on C-18. Meanwhile, the exfoliation occurred near the center of the specimens in FGT and SCC. Therefore, the amount of icing at the 50–150 cm height range was reduced by 10% to 20 % compared to C-18. The amount of icing at the 0–50 cm height range on the FGT and SCC surfaces increased by 50% compared to C-18, because the exfoliated ice piled up on the lower end of the light beacon model, which was set up on the floor (Fig. 8). Thus, the total amount of icing on the FGT and SCC surfaces were almost same as that on C-18. The amount of the icing on the sheets might have been greatly reduced if the debris of the lower ends were removed sequentially.

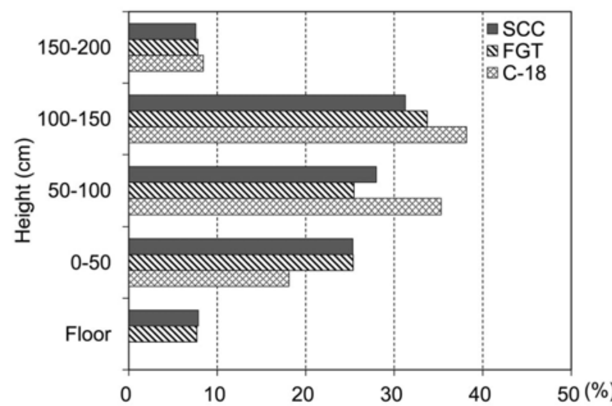

Fig. 7. percentage of icing weight of each height for each sheet model

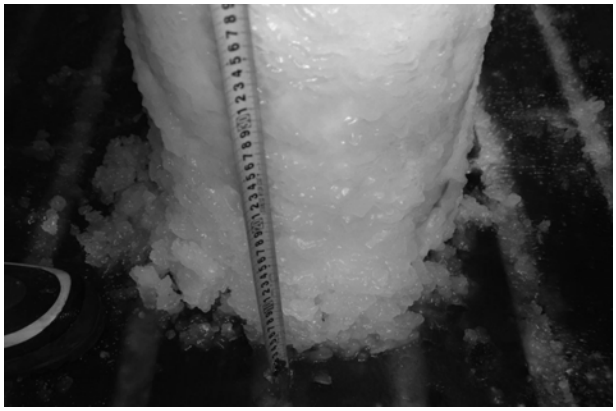

Fig. 8. the exfoliated ice on the lower end of the specimen

To increase the growth rate of icing, the room temperature was reduced to –14 °C, and the experiments were conducted on FGT and SCC fabrics. In these experiments, the exfoliation occurred more frequently than the experiment in the room kept at a temperature of –10 °C. In particular, the exfoliation of icing on the SCC material was observed continuously during the experiment. As a result, the exfoliated ice accumulated on the lower end of the SCC material (Fig. 9). Therefore, it was suggested that SCC would be effective in reducing the amount of icing.

The identity of the sheets appeared in the initial growth of icing and the exfoliation process. It appeared in the same manner as in the experiment 1 results. Hemispherical water droplets were formed on the FGT material, and were frozen into frazil granular ice. Finally, the textile was covered by an irregular spray ice surface. On the other hand, water drops colliding at C-18 and the SCC surface formed a fluid flowing film. A part of the water froze into sheet-like ice. Ripple patterns were produced on the ice surface. Deicing of the FGT and SCC materials was extremely easy owing to the low adhesion strength of the ice.

Deicing was not as effective on C-18 as compared to the former, though deicing was possible. It indicates that the selection of the pliable polymer sheet is important to the suitability of deicing.

V. Conclusions

To address the problems of sea spray icing, saline spray icing tests on high hydrophobic and high hydrophilic polymer sheets were conducted using an ice model basin. The air temperature in the cold room was maintained at approximately –10 °C and –14 °C. Small water particles, with a salinity of 26–29 wt‰, were sprayed on the cylindrical test specimen. The wind speed was 3–5 m/s and 5–7 m/s.

Wet growth of icing occurred on the windward side of all test materials. The initial icing depended considerably on whether the surface was hydrophobic or hydrophilic. On the high hydrophobic surface, the initial ice growth was characterized by the formation of hemispherical water droplets and streaks of ice on the textile surface. Irregular projections were observed on the spray ice surface. On the high hydrophilic surface, spray water formed a thin fluid flowing film.

Exfoliation of the pieces of the sheet ice was often observed during the initial growth, especially on the high hydrophilic surface. The experiments conducted at –14 °C and at wind speed of 5–7 m/s, the exfoliation occurred more frequently than the experiment conducted at –10 °C. It is possible that the frequent exfoliation was driven by an increase in the growth rate of icing. In particular, the exfoliation on SCC materials was observed continuously during the icing experiment.

Deicing was extremely easy in the case of both pliable polymer sheets. The SCC material was effective for the deicing of sea spray ice on a pliable sheet. This suggests that a combination of the property of low ice adhesion and rapid distortion or heating is effective for the deicing of sea spray ice.

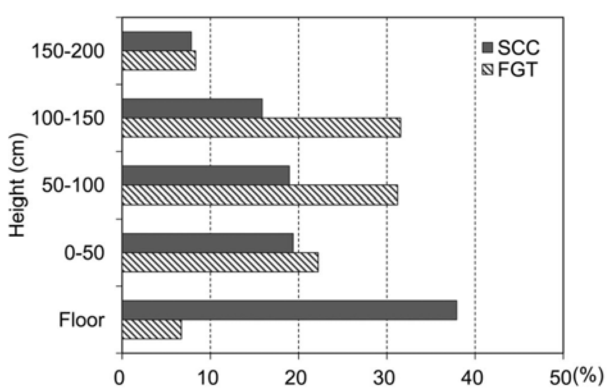

Fig. 9. percentage of icing weight of each height for SCC and FGT. the exfoliated ice accumulated on the lower end of SCC

Acknowledgment

We wish to express our gratitude to Dr. S. Uto of National Maritime Research Institute, Dr. K. Izumiyama of North Japan Port Consultants Co. Ltd., and M. Tsuda of Sapporo Daiichi High School for their support during the laboratory experiments. This research was supported by JSPS KAKENHI Grant Number 22310110.

References

[1] I. Kubat and G. Timco, “NRC marine icing database,” in *Proc. 11th Int. Workshop Atmos. Icing Structures*, 2005, 6 pp.

[2] N. Ono, “Studies on ice accumulation on ships. 4. Statistical Analysis of Ship-Icing Condition,” *Low Temp. Sci.*, A32, pp. 235–242 [in Japanese with English summary], 1974.

[3] L. Makkonen, “Salinity and growth rate of ice formed by sea spray,” *Cold Regions Sci. Technol.*, 14, pp. 163–171, 1987.

[4] C. C. Ryerson and A. J. Gow, “Crystalline structure and physical properties of ship superstructure spray ice,” *Phil. Trans. Roy. Soc. Lond.*, A358, pp. 2847–2871, 2000.

[5] T. Ozeki, K. Kose, T. Haishi, S. Nakatsubo and Y. Matsuda, “Network images of drainage channels in sea spray icing by MR microscopy,” *Mag. Res. Imag.*, 23, pp. 333–335, 2005.

[6] E. P. Lozowski, K. Szilder and L. Makkonen, “Computer simulation of marine ice accretion,” *Phil. Trans. Roy. Soc. Lond.*, A358, pp. 2811–2845, 2000.

[7] N. S. Stehle, “Adfreezing strength of ice,” in *Proc. Int. Symp. Ice*, 1970, 13 pp.

[8] W. M. Sackinger and P. A. Sackinger, “Shear strength of the adfreeze bond of sea ice to structures,” in *Proc. 4th Int. Conf. Port Ocean Eng. Arctic Conditions*, 1977, pp. 607–614.

[9] H. Saeki, T. Ono and A. Ozaki, ” Mechanical properties of adhesion strength of ice to pile structures,” in *Proc. Int. Symp. Ice*, 1982, pp. 641–649.

[10] H. Saeki, T. Ono, T. Takeuchi, S. Kanei and N. Nakazawa, “Ice forces due to changes in water level and adfreeze bond strength between sea ice and carious materials,” in *Proc. 5th Offshore Mech. Arctic Eng. Conf.*, 1986, pp. 534–540.

[11] L. Makkonen and E. Lehmus, “Studies on adhesion strength of saline ice,” in *Proc. 9th Int. Conf. Port Ocean Eng. Arctic Conditions*, 1987, pp. 45–55.

[12] J. L. Laforte and L. Lavigne, “Microstructure and mechanical properties of ice accretions grown from supercooled water droplets containing NaCl in solution,” in *Proc. 3rd Int. Workshop Atmos. Icing Structures*, 1986, 5 pp.

[13] Japan Aids to Navigation Association, “Kouro-hyoushiki-kinou ni eikyou wo oyobosu koori no jokyo-taisaku ni kansuru tyousa-kenkyu,” Japan Aids to Navigation Association, Tokyo, Japan, Research Rep., 53 pp. [in Japanese] , 1986.

[14] T. Ozeki and R. Yamamoto, “Ice adhesion tests of pliable polymer sheets for deicing of sea spray icing,” *Proc. 18th IAHR Int. Symp. Ice*, 2006, pp. 153–160.

[15] T. Ozeki, Y. Tamate, S. Adachi, K. Izumiyama and T. Tazawa, “Field observation of sea spray icing on lighthouses and ice adhesion test of superhydrophilic pliable sheet for deicing,” *Proc. 13th Int. Workshop Atmos. Icing Structures*, 2009, 4 pp.

[16] T. Ozeki, R. Yamamoto, K. Izumiyama and T. Sakamoto, “Ice adhesion tests on pliable polymer sheets for protection against sea spray icing,” *J. Adhesion Sci. Tech.*, pp. 651–663, 2012.

Ice Growth Prediction Model of Transmission Lines Based on Mamdani-type Fuzzy Neural Network

Xin-bo Huang, Shu-fan Lin, Jia-jie Li

***Abstract* —** As the global extreme climate phenomena occur frequently, ice disasters on power grid become more and more serious all over the world, they exert a more tremendous influence and cause greater harm than ever before. The transmission lines icing that affected by terrain and micro-meteorological condition often causes serious accidents, such as hardware and insulator damaged, break line, inter-phase short-circuiting and collapsed towers, which is easy to evoke a serious threat to power system security and cause huge economic loss. On the basis of the analysis of field measured data, the relation between micro-meteorological condition (environmental temperature, humidity, wind speed) , conductor temperature and transmission lines icing is researched, and a prediction model of ice growth of transmission lines based on Mamdani-type fuzzy neural network（FNN） theory is put forward in this paper, which overcomes the lack of adaptive ability under fuzzy system and the incompetence of fully express the human reasoning capabilities under neural network. The programing result shows that this model has an error less than 10% between the predicted value and the actual value on the ice thickness, and the method for establishing ice growth prediction model based on Mamdani-type FNN theory is feasible and practical. Therefore, this model has provided theoretical basis for the prediction of the ice thickness. Knowing well of the ice condition in transmission lines in real time plays a meaningful and significant role in ensuring the safety and stabilization of power systems.

***Keywords* —** Fuzzy neural network（FNN, icing, ice thickness, model validation, prediction model, transmission line

Ⅰ. Introduction

Ice disaster is one of the most serious threats among various kinds of natural disasters to power system. Once there is ice covering on transmission lines conductor, devastating ice disaster will be an inevitable consequence. As a special kind of meteorological disasters, icing caused serious influence—icing flashover, collapse of tower and even ravage of the power grid, on the safe operation of overhead transmission lines all over the world [1].

Recently, many articles about ice models on transmission lines have been published around the world, and many ice growth prediction models of transmission lines were put forward[2]-[12]. Different ice models explain ice growth mechanism from different angles of view and different forms of calculation formulas, to a certain extent, they predict different parameters of the ice, but they only take effect in the same terrain and micro-meteorological condition, when applied to the discrepant environment, they don't work. To advoid the more and more serious ice disasters on transmission lines, more in-depth analysis, research and experimental study of mechanism of ice on the basis of existing theory and practice, which will provide solid theoretical foundation and effective means for the prevention and treatment of ice disasters, are no time to delay.

We have established ice growth prediction model based on Mamdani-type fuzzy neural network(FNN). The details are as follow.

Artificial neural network has strong generalization ability and associative memory ability, and has a high level of learning ability and the ability to accurately fit arbitrary nonlinear function, and it can learn through the response data of the target system, constantly improve the fitting precision[13].

Fuzzy system, which is based on the fuzzy set theory founded by Zadeh, seize the fuzziness of human thought, use a priori knowledge of experts in the field for approximate reasoning, fuzzy recognition and fuzzy measurement for complicated things[14].

The combination of fuzzy system and artificial neural network can effectively play their respective advantages and make up for the deficiencies of each other, and improve the ability of expression and learning of the whole system[15].

Ⅱ. Basis of the Mamdani-type FNN

A. Structure of the Proposed Mamdani-type FNN System

The structure of the proposed Mamdani-type FNN system [16] is as shown in Fig.1.

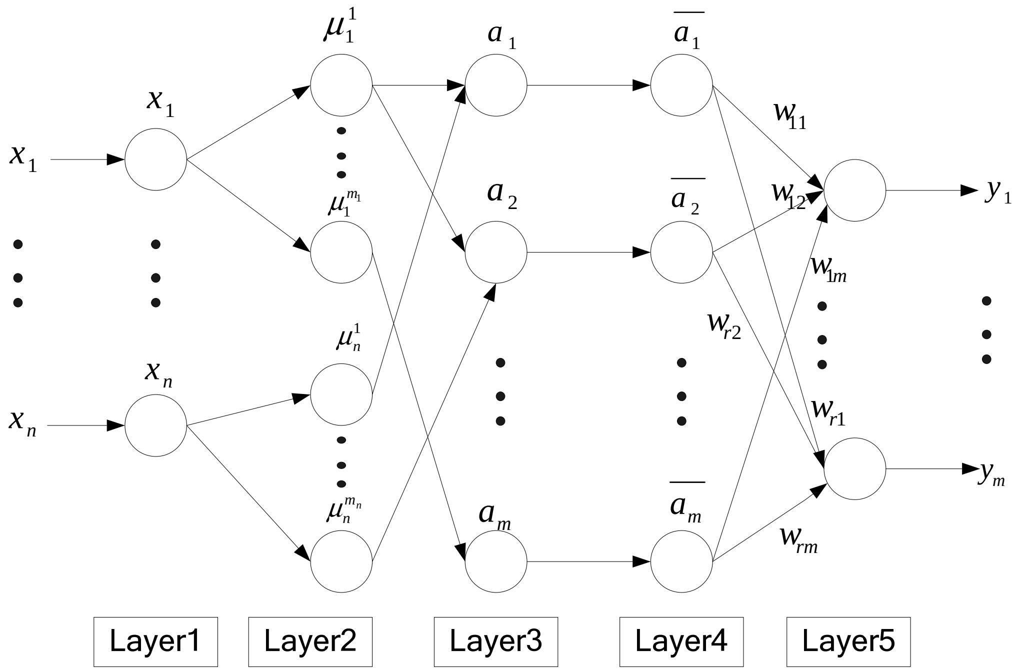

Fig.1 Proposed Mamdani-type FNN structure

(1) Input Layer: The node in this layer just transmit input value x_i to the next layer directly, the node number of this layer is $N_1 = n$.

(2) Membership Layer: Each node represents a linguistic variable. The output function of this node should be the fuzzy set membership function of each linguistic variable of each input variable.

$$\mu_i^j = \mu_{A_i^j}(x_i) \tag{1}$$

Where $i = 1, 2, ..., n$, $j = 1, 2, ..., m_i$, n and m_i are the dimensions of the input and the number of partitions of x_i, respectively. The node number of this layer is $N_2 = \sum_{i=1}^{n} m_i$.

(3) Rule Layer: Rule layer implements the fuzzy inference mechanism, each node represents a fuzzy rule and matches the premises of fuzzy rules and produces a matching factor as outputs for each rules. The output of this layer is given as

$$\alpha_j = \mu_1^{i_1} \mu_2^{i_2} ... \mu_n^{i_n}. \tag{2}$$

Where $i_1 \in \{1, 2, ..., m_1\}$, $i_2 \in \{1, 2, ..., m_2\}$,…, $i_n \in \{1, 2, ..., m_n\}$, $j = 1, 2, ..., m$, $m = \prod_{i=1}^{n} m_i$ 。 The node number of this layer is $N_3 = m$.

*(4) Normalization Layer:*This layer is implemented by normalized calculation. The node number of this layer is $N_4 = N_3 = m$.

$$\overline{\alpha_j} = \frac{\alpha_j}{\sum_{i=1}^{m} \alpha_i}, \quad j = 1, 2, \ldots, m \tag{3}$$

(5) Output Layer: Final layer is the output layer, this layer is for solving ambiguity.

$$y_i = \sum_{j=1}^{m} w_{ij} \overline{\alpha_j}, \quad i = 1, 2, \ldots, r \tag{4}$$

B. Learning Algorithm of Mamdani-type FNN

The center c_{ij} and width σ_{ij} of the membership functions and the connected weights w_{ij} of Mamdani-type FNN can be adjusted by parameter learning phase[16].

Firstly:

$$\delta_i^5 = t_i - y_i . \tag{5}$$

Where t_i and y_i are the desired output and actual output, respectively.

Secondly:

$$\frac{\partial E}{\partial w_{ij}} = -\delta_i^5 x_j^4 = -(t_i - y_i)\overline{\alpha_j} . \tag{6}$$

Thirly:

$$\delta_j^4 = \sum_{i=1}^{r} \delta_i^5 w_{ij} , \tag{7}$$

$$\delta_j^3 = \sum_{i=1}^{r} \delta_i^4 \frac{\sum_{\substack{i=1 \\ i \neq j}}^{m} \alpha_i}{(\sum_{i=1}^{m} \alpha_i)^2} , \tag{8}$$

$$\delta_{ij}^2 = \sum_{k=1}^{m} \delta_k^3 s_{ij} e^{-\frac{(x_i - c_{ij})^2}{\sigma_{ij}^2}} . \tag{9}$$

If multiplication operator is used in the layer 3, and when u_i^j is one of the inputs of the kth rule node:

$$s_{ij} = \prod_{\substack{j=1 \\ j \neq i}}^{n} u_j^{i_j} . \tag{10}$$

Thus, the first order gradient can be calculated by:

$$\frac{\partial E}{\partial c_{ij}} = -\delta_{ij}^2 \frac{2(x_i - c_{ij})}{\sigma_{ij}^2} , \tag{11}$$

$$\frac{\partial E}{\partial \sigma_{ij}} = -\delta_{ij}^2 \frac{2(x_i - c_{ij})^2}{\sigma_{ij}^3}. \quad (12)$$

Finally, the learning algorithm for adjusting parameters can be used:

$$w_{ij}(k+1) = w_{ij}(k) - \beta \frac{\partial E}{\partial w_{ij}}, \quad i = 1, 2, \ldots, r, \quad j = 1, 2, \ldots, m, \quad (13)$$

$$c_{ij}(k+1) = c_{ij}(k) - \beta \frac{\partial E}{\partial c_{ij}}, \quad i = 1, 2, \ldots, n, \quad j = 1, 2, \ldots, m_i, \quad (14)$$

$$\sigma_{ij}(k+1) = \sigma_{ij}(k) - \beta \frac{\partial E}{\partial \sigma_{ij}}, \quad i = 1, 2, \ldots, n, \quad j = 1, 2, \ldots, m_i. \quad (15)$$

where β is the learning rate, and $\beta > 0$.

Ⅲ. Building of Ice Growth Prediction Model of Transmission Lines Based on Mamdani-type FNN

A. Structure of Mamdani-type FNN Model

Data for building the ice growth prediction model are provided by transmission line on-line monitoring device of Guizhou Power Grid, partial data are shown in Table1. 65 groups of data are chosen for building model, and 20 groups of data are used to test the accuracy of the model.

Table1 partial data

environment temperature (℃)	*environment humidity* (%RH)	*environment wind speed* (m/s)	*conductor temperature* (℃)	*ice thickness* (mm)
-3	95	4	1	2.37
-1	92	0	-2	3.78
-2	95	2.2	1	3.81
-3	96	2.2	1	4.49
-2	96	0	-3	5.83
-2	99	1	1	5.89
1	96	5.5	1	5.97
2	95	3.8	1	6.14
2	85	3.7	2	6.19
2	92	1.5	1	6.22
1	98	2.9	0	6.24
3	95	1.9	3	6.26
1	95	0.8	0	6.4
-2	96	1.7	-3	6.62
-2	97	6	1	21.55
-2	97	4.9	1	21.6
-1	93	5	4	21.71
-1	94	2.1	3	21.96

-5	96	0	3	22.84

*(1) Layer 1:*Layer 1 is the input layer, the input variables are *environment temperature*, *environment humidity*, *environment wind speed* and *conductor temperature*, thus the node number of this layer is 4.

*(2) Layer 2:*Layer 2 is fuzzification layer, the fuzzy information is preprocessed here. Its main function is to normalize the input value and output value, which can make the information adapt to the following network processing. Input variables are divided into 5 language variable values: *NB（Negative Big）*、*NS（Negative Small）*、*O(Zero)*、*PS（Positive Small）*、*PB（Positive Big）*. Their membership functions are shown in Fig.2, and in（16）、（17）、（18）、（19）, respectively. The node number of this layer is $4\times5=20$.

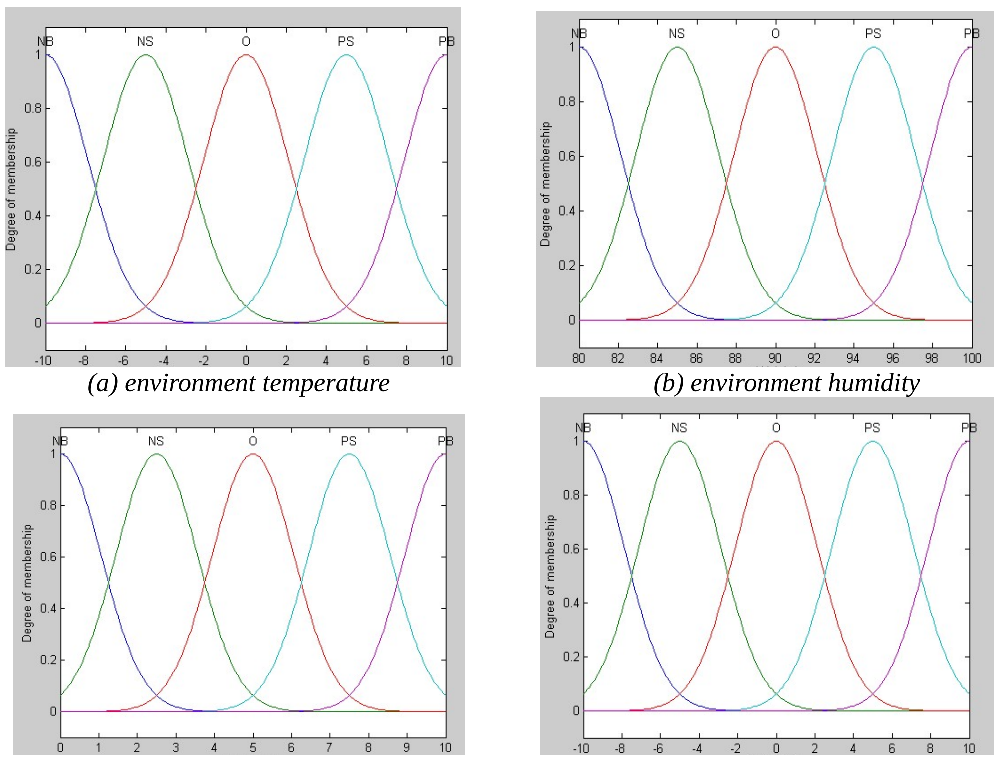

(a) environment temperature *(b) environment humidity*
(c) environment wind speed *(d) conductor temperature*
Fig.2 membership functions of input variables

$$\mu_A(x_1)=\begin{cases} e^{-(\frac{x_1+10}{2})^2}, & -10<x_1\le-7.5 \\ e^{-(\frac{x_1+5}{2})^2}, & -7.5<x_1\le-2.5 \\ e^{-(\frac{x_1}{2})^2}, & -2.5<x_1\le2.5 \\ e^{-(\frac{x_1-5}{2})^2}, & 2.5<x_1\le7.5 \\ e^{-(\frac{x_1-10}{2})^2}, & 7.5<x_1\le10 \end{cases}, \quad (16)$$

$$\mu_A(x_2)=\begin{cases} e^{-(\frac{x_2-80}{2})^2}, & 80<x_2\le 83 \\ e^{-(\frac{x_2-85}{2})^2}, & 83<x_2\le 87 \\ e^{-(\frac{x_2-90}{2})^2}, & 87<x_2\le 93 \\ e^{-(\frac{x_2-95}{2})^2}, & 93<x_2\le 97 \\ e^{-(\frac{x_2-100}{2})^2}, & 97<x_2\le 100 \end{cases}, \tag{17}$$

$$\mu_A(x_3)=\begin{cases} e^{-(\frac{x_3}{1})^2}, & 0<x_3\le 1.5 \\ e^{-(\frac{x_3-2.5}{1})^2}, & 1.5<x_3\le 3.5 \\ e^{-(\frac{x_3-5}{1})^2}, & 3.5<x_3\le 6.5 \\ e^{-(\frac{x_3-7.5}{1})^2}, & 6.5<x_3\le 8.5 \\ e^{-(\frac{x_3-10}{1})^2}, & 8.5<x_3\le 10 \end{cases}, \tag{18}$$

$$\mu_A(x_4)=\begin{cases} e^{-(\frac{x_4+10}{2})^2}, & -10<x_4\le -7.5 \\ e^{-(\frac{x_4+5}{2})^2}, & -7.5<x_4\le -2.5 \\ e^{-(\frac{x_4}{2})^2}, & -2.5<x_4\le 2.5 \\ e^{-(\frac{x_4-5}{2})^2}, & 2.5<x_4\le 7.5 \\ e^{-(\frac{x_4-10}{2})^2}, & 7.5<x_4\le 10 \end{cases}. \tag{19}$$

(3) *Layer 3:*Layer3 is fuzzy inference layer, there are 38 rules in fuzzy rule base [17], as is shown in Table2, thus the node number of this layer is 38.

Table2 fuzzy rule base

numerical order	*environment temperature*	*environment humidity*	*environment wind speed*	*conductor temperature*	*Ice thickness*
1	PB	PB	O	PB	NB
2	PS	PB	NS	O	NB
3	PS	PS	PB	PS	NB
4	O	PB	NS	O	NB
5	O	NB	O	O	NB

6	NS	NS	NS	O	NB
7	NS	O	PS	O	NB
8	NS	PB	O	NS	NB
9	PS	PS	NB	O	NS
10	PB	O	NS	PS	NS
11	PB	PS	NS	PB	NS
12	PB	PS	O	PS	NS
13	PS	PS	O	PS	NS
14	PS	PB	NB	O	NS
15	O	NB	NB	PS	NS
16	O	O	NB	NB	NS
17	O	PS	NS	NS	NS
18	O	PB	NS	PS	NS
19	NB	NB	O	O	NS
20	NB	PS	NB	NB	NS
21	NB	PS	NS	O	NS
22	NS	O	NS	O	NS
23	NS	O	O	NS	NS
24	NS	PS	NB	NB	NS
25	NS	PS	NS	NB	NS
26	NS	PS	O	O	NS
27	PS	PS	NS	PS	O
28	PS	PB	O	O	O
29	O	PS	NS	O	O
30	O	PS	O	O	O
31	O	PB	NB	PS	O
32	NS	PS	NB	O	O
33	NS	PS	NS	O	O
34	NS	PB	NS	O	O
35	NS	PB	O	O	PS
36	NS	PB	NS	NS	PS
37	NB	PB	NB	NB	PB
38	NS	PB	NB	NS	PB

(4) *Layer 4:* Layer 4 is Normalized layer, its output is a preparation for defuzzification.

$$\overline{\alpha_i} = \frac{\mu_1^{i_1}\mu_2^{i_2}\mu_3^{i_3}\mu_n^{i_n}}{\sum_{i=1}^{38}\mu_1^{i_1}\mu_2^{i_2}\mu_3^{i_3}\mu_n^{i_n}} \tag{20}$$

(5) *Layer 5:*Layer 5 is output layer, center average defuzzifier will output an accurate value of *ice thickness*, the node number of this layer is 1.

$$y=\sum_{i=1}^{38} w_i \overline{\alpha_i} \tag{21}$$

B. Training of Mamdani-type FNN Model

Programs for the training and prediction of Mamdani-type FNN are written according to the calculation process above. Therefore, basing on the historical data, the model runs the learning algorithm of neural network, then automatically corrects the parameters of fuzzy system, after 660 times of training, the revised membership functions of the 4 input variables meet requirements, they are shown as Fig. 3 to Fig.6.

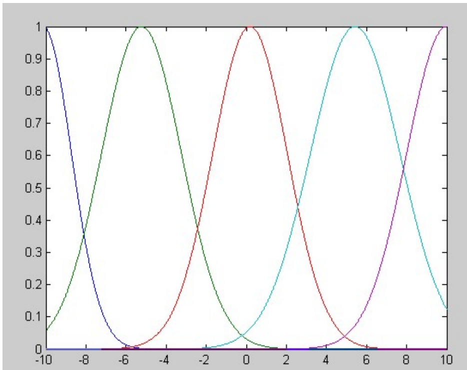

Fig.3 membership function of *environment temperature*

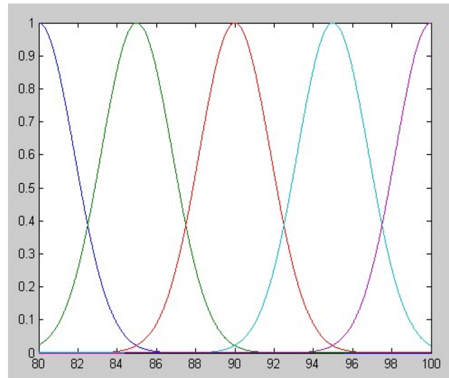

Fig.4 membership function of *environment humidity*

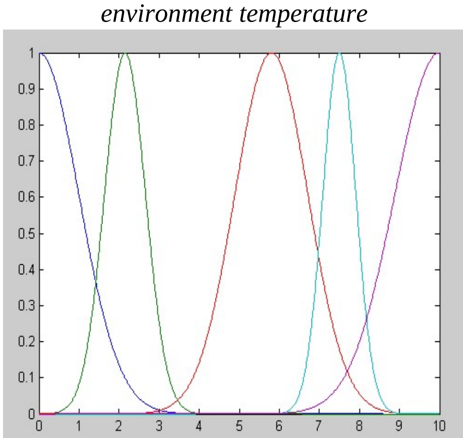

Fig.5 membership function of *environment wind speed*

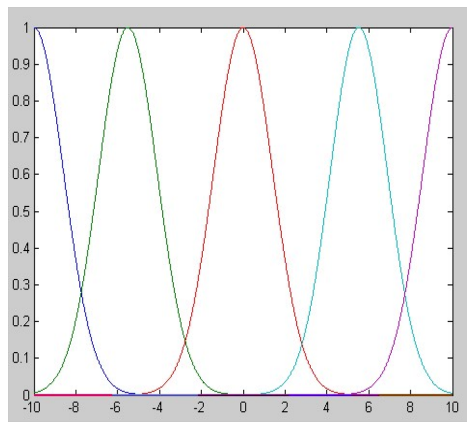

Fig.6 membership function of *conductor temperature*

The revised membership functions are shown in（22）、（23）、（24）、（25）, respectively.

$$\mu_A(x_1)=\begin{cases} e^{-(\frac{x_1+10.134}{1.4142})^2}, & -10<x_1\le -8 \\ e^{-(\frac{x_1+5.229}{1.998})^2}, & -8<x_1\le -2.15 \\ e^{-(\frac{x_1-0.186}{1.864})^2}, & -2.15<x_1\le 2.51 \\ e^{-(\frac{x_1-5.432}{2.234})^2}, & 2.51<x_1\le 8 \\ e^{-(\frac{x_1-10.001}{2})^2}, & 8<x_1\le 10 \end{cases}, \tag{22}$$

$$\mu_A(x_2)=\begin{cases} e^{-(\frac{x_2-80}{1.8142})^2}, & 80<x_2\le 83 \\ e^{-(\frac{x_2-85}{1.8142})^2}, & 83<x_2\le 87 \\ e^{-(\frac{x_2-90}{1.8142})^2}, & 87<x_2\le 93 \\ e^{-(\frac{x_2-95}{1.8142})^2}, & 93<x_2\le 97 \\ e^{-(\frac{x_2-100}{1.8142})^2}, & 97<x_2\le 100 \end{cases}, \tag{23}$$

$$\mu_A(x_3)=\begin{cases} e^{-(\frac{x_3}{1})^2}, & 0<x_3\le 1.43 \\ e^{-(\frac{x_3-2.1495}{0.5142})^2}, & 1.43<x_3\le 3.5 \\ e^{-(\frac{x_3-5.8046}{0.9142})^2}, & 3.5<x_3\le 7 \\ e^{-(\frac{x_3-7.5}{0.4142})^2}, & 7<x_3\le 8.2 \\ e^{-(\frac{x_3-10}{1.1142})^2}, & 8.2<x_3\le 10 \end{cases}, \tag{24}$$

$$\mu_A(x_4)=\begin{cases} e^{-(\frac{x_4+10}{1.4142})^2}, & -10<x_4\le -7.9 \\ e^{-(\frac{x_4+5.5096}{1.3973})^2}, & -7.9<x_4\le -2.9 \\ e^{-(\frac{x_4}{1.4142})^2}, & -2.9<x_4\le 2.9 \\ e^{-(\frac{x_4-5.5269}{1.3667})^2}, & 2.9<x_4\le 7.9 \\ e^{-(\frac{x_4-10}{1.4138})^2}, & 7.9<x_4\le 10 \end{cases}. \tag{25}$$

C. Prediction of Mamdani-type FNN Model

Table3 comparison between practical Data and prediction data

numerical order	*environment temperature* (℃)	*environment humidity* (%RH)	*environment wind speed* (m/s)	*conductor temperature* (℃)	*Practical ice thickness* (mm)	*prediction data by FNN* (mm)	absolute error (mm)	*prediction data by fuzzy system* (mm)	absolute error (mm)
1	4	90	0.8	0	1.02	1.063	0.043	1.526	0.506
2	2	95	5.7	1	1.81	1.843	0.033	2.177	0.367
3	-2	68	2.9	2	2.01	2.506	0.496	1.132	0.878
4	-5	98	1.5	-2	4.56	5.187	0.627	7.271	2.711
5	1	98	2.6	5	5.22	5.192	0.028	2.546	2.674
6	2	97	2	3	5.84	5.613	0.227	2.149	3.691
7	-2	98	0.1	1	6.01	5.879	0.131	5.128	0.882

8	-5	97	0.1	-1	7.3	6.298	1.002	7.511	0.211
9	-1	99	3.2	-2	8.77	10.236	1.466	8.478	0.292
10	-3	97	1.5	-4	9.89	10.754	0.864	11.314	1.424
11	-4	97	1.8	-4	10.64	11.407	0.767	15.445	4.805
12	-5	97	2.1	-5	11.79	10.622	1.168	12.359	0.569
13	-1	98	2.3	-2	12.69	13.154	0.464	14.771	2.081
14	-3	98	2.2	-4	13.75	12.181	1.569	15.122	1.372
15	-1	99	3.9	1	14.27	13.969	0.301	14.156	0.114
16	-2	99	3.4	-1	15.56	15.734	0.174	15.235	0.325
17	-4	99	4.2	-2	16.56	15.455	1.105	14.281	2.279
18	-5	98	5.2	-3	17.22	17.528	0.308	15.98	1.24
19	-2	97	3.5	1	21.65	19.447	2.203	17.78	3.87
20	-8	97	4.3	-6	23.39	23.485	0.095	25.454	2.064

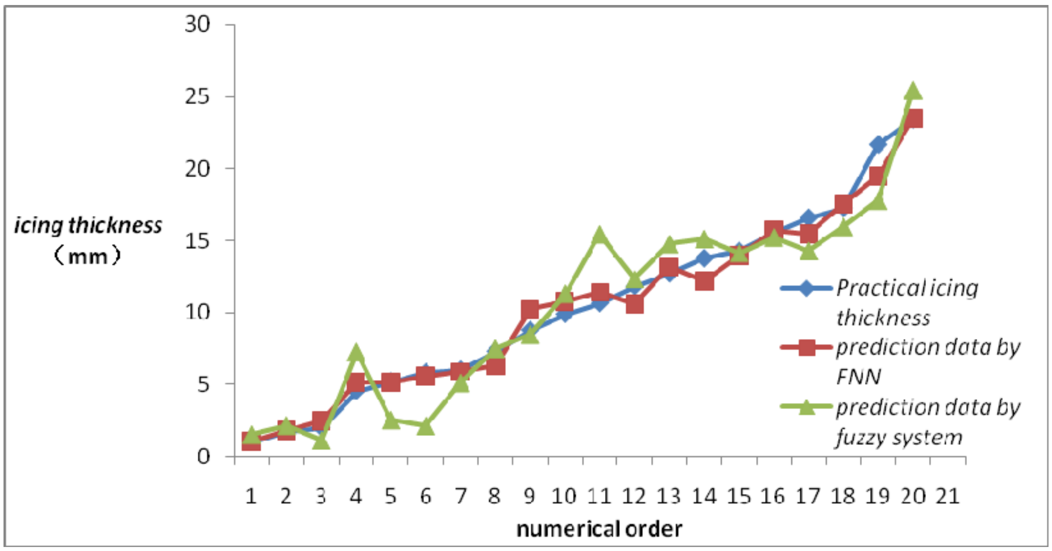

Fig.7 comparison chart between practical Data and prediction data

Table3 and Fig.7 show that the prediction data by Mamdani-type FNN is similar to the practical data, the maximum error is less than 2.5 mm, and the average relative error is less than 10%. Basing on the fuzzy system, the Mamdani-type FNN introduces the neural network into the model, which makes the model have a good ability of self-learning and makes the accuracy of prediction data of Mamdani-type FNN better than fuzzy system (The maximum error is less than 5 mm[17]).

Ⅳ conclusion

Using Mamdani-type FNN theory for prediction of *ice thickness* of overhead line can predict *ice thickness* with reasonable accuracy, the model has good fitting precision, generalization ability and adaptability, and its computational accuracy is better than either neural network or fuzzy system. On the whole, the model improves precision of prediction of *ice thickness* of overhead line, and provides necessary theoretical basis for the prediction of *ice thickness*. Knowing well of the ice condition in transmission lines in real time plays a meaningful and significant role in ensuring the safety and stabilization of power systems.

References

[1] China Southern Power Grid, "summary," in *Technology and Application of Power Grid Anti-icing and De-icing*, *1*st ed. Beijing, China: China Electric Power Press, 2010, ch. *1*, sec. 1, pp. *1–2*.

[2] L. Makkonen, "Modeling of ice accretion on wires," *Climate and Appl. Meteor*, vol. *23*, no. *7*, pp. *929-939*, Jun., 1984.

[3] E. J. Goodwin III, J. D. Mozer, J. AM. DiGioia, BA Power, "Predicting ice and snow loads for transmission lines," presented at the *1st international workshop on atmospheric icing of Structures*, Hanover, USA, 1983.

[4] I. Imai, "Studies on ice accretion," *Researches on Snow and Ice*, vol. *3*, no. *1*, pp. *35-44*, 1953.

[5] H. Y. Liu, D. Zhou, J. P. Fu. "A Simple Model for Predicting Glaze Loads on Wires," *Periodical Proceedings of the CSEE*, vol. *21*, no. *4*, pp. *44-47*, Apr., 2001.

[6] H. Y. Liu, J. P. Fu, D. Zhou. "Dimensional Analysis of the Collection Coefficient Wire Covered by Ice," *J.Huazhong Univ. of Sci. & Tech.*, vol. *29*, no. *10*, pp. *76-77*, Oct., 2001.

[7] C. X. Sun, X. L. Jiang, Q. X. Xiong, H, Yi. "Analysis of Critical Icing Conditions of Conductor and Wet-dry Growth," *Periodical Proceedings of the CSEE*, vol. *23*, no. *3*, pp. *141-145*, Mar., 2003.

[8] RA. Da. Silveira, C. R. Maliska, D. A. Estivam, et al, "Evaluation of collection efficiency methods for icing analysis," presented at the *17th international congress of mechanical engineering*, Sao Paulo, BR, 2003.

[9] E. K. László, F. Masoud , R. K. Anatolij. "Modeling droplet collision and coalescence in an icing wind tunnel and the influence of these processes on droplet size distribution," *International Journal of Multiphase Flow*, vol. *31*, no. *1*, pp. *69-92*, Jan., 2005.

[10] F. Ping, F. Masoud, B. Gilles. "Two-dimensional modelling of the ice accretion process on transmission line wires and conductors," *Cold Regions Science and Technology*, vol. *46*, no. *2*, pp. *132-146*, Nov., 2006.

[11] L. Makkonen, W. Bodo. "Simulating wet snow loads on power line cables by a simple model," *Cold Regions Science and Technology*, vol. *61*, no. *2-3*, pp. *73-81*, May., 2010.

[12] L. Makkonen. "A model of hoarfrost formation on a cable," *Cold Regions Science and Technology*, vol. *85*, pp. *256-260*, Jan., 2013.

[13] Z. Q. Yu and H, Yu, *Neural Network Control*. Xi'an, China: Xi 'an university of electronic science and technology press, 2009.

[14] L. X. Wang and Y. J. Wang, *A Course in Fuzzy Systems & Control*. Beijing, China: Tsinghua University Press, 2003.

[15] J. L. Zhang, *Fuzzy Neural Network Control Theory and Engineering Application*. Harbin, China: Harbin Institute of Technology Press, 2004.

[16] G.Y.Li, "Fuzzy neural and fuzzy clustering and their implementation in MATLAB," in *Intelligent control and its implementation in MATLAB*, *1*st ed. Beijing, China: Publishing House of Electronics Ind., 2005, ch. *6*, sec. *1*, pp. *261–267*.

[17] X. B. Huang, J. J. Li, L. S. Ouyang, L. C. Li, B. Luo. "Icing Thickness Prediction Model Using Fuzzy Logic Theory," *High Voltage Engineering*, vol. *37*, no. *5*, pp. *1245-1252*, May, 2011.

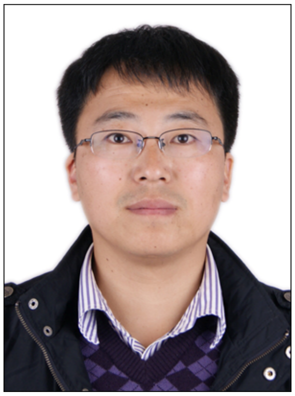

Xin-bo Huang was born in Shandong Province, China, in May 1975. He received the B.S. and M.S degrees in automation from Qingdao Technological University, Qingdao, China, in 1998 and 2001, respectively. He received the Ph.D. degree in automation from XiDian University, Xi'an, China, in 2005.

Since July 2005, he has been a teacher at Xi'an Polytechnic University, and since December 2008, he has been a full Professor with the College of Electronics Information at Xi'an Polytechnic University. From October 2005 to March 2008, he was a post-doctor in the State Key Laboratory of Electrical Insulation and Power Equipment and the School of Electrical Engineering at Xi'an Jiaotong University, engaged in the snow and ice warning system on transmission lines. Since May 2009, he was a post-doctor at South China University of Technology, engaged in the transmission conductor galloping monitoring and mechanism. His current research interests include the online monitoring technology and condition maintenance of power equipment, the wireless network sensor. He has published more than 50 journal articles and conference papers, and 4 monographs. He may be reached at hxb1998@163.com.

Dr. Huang received the 2011 new century excellent talent support plan of China Ministry of Education (MOE), 2010 teacher of the year award in China's "textile light" for teachers, 2009 Hong Kong SangMa research grants award, and several other awards and prizes from Chinese Government.

Shu-fan Lin is currently working toward the M.S. degree with the College of Electronics and Information, Xi'an Polytechnic University, Xi'an, China.

Her research interests include ice growth mechanism on transmission lines. She may be reached at afanfano@yeah.net.

Jia-jie Li received the M.S degree in control engineering from Xi' an Polytechnic University, Xi'an, China, in 2013.

She is currently working toward the Ph.D. degree with the Xidian University.

She has published 1 journal article and 1 conference paper. She may be reached at lijiajie1987@163.com.

Session 4: Conductors/Insulators/Flashover

Influence of Electric Field on Conductor Icing

F. Yin[1, 2], M. Farzaneh[1], X. Jiang[2], T. Li[2]
[1]NSERC / Hydro-Quebec / UQAC Industrial Chair on Atmospheric Icing of Power Network Equipment (CIGELE) and Canada Research Chair on Engineering of Power Network Atmospheric Icing (INGIVRE) www.cigele.ca
Université du Québec à Chicoutimi, Chicoutimi, QC, Canada
[2]State Key Laboratory of Power Transmission Equipment & System Security and New Technology, Chongqing
Chongqing University, Chongqing 400044, China
*Email:AndyYinee@gmail.com

Abstract — The influence of electric field on the appearance, amount and density of ice accretion and spacing between icicles on aluminum conductors were investigated in the laboratory. It was found that the mass and density first rise as the electric field increased and then decreased with higher electric field strength. When the electric field is lower and no corona phenomenon occurs, the freezing water conductivity has little influence on the mass and density of the ice accretion. It was also found that the spacing of icicles is independent of conductor diameter and liquid water content. As the water droplet will be elongated by the electric field, the spacing is decreased as the electric field increases.

Keywords — Composite insulator; Icing flashover; icing energized

I. INTRODUCTION

Atmospheric icing occurs when freezing raindrops, snow particles or super cooled droplets contact with construction surfaces. The icing on transmission lines is one of the most serious threatens to the safety of the power system. Researchers all over the world have carried out a large numbers of investigations on conductor icing performance through artificial icing tests [1-5]. The characteristics of the ice accretions grown on the transmission lines not only depend on the meteorological conditions, but also on the electric field strength. The spacing of icicles has important effect on the ice amount on the conductor. With decreasing icicle spacing, the number of icicles will increase, leading to a change in the total ice load. In this paper, the study of ice accretion on aluminum conductor with and without applied voltage was investigated and an explanation was given to the changes of ice amount, density and spacing of icicles occurring in the presence of electric field.

II. TEST FACILITIES AND PROCEDURES

A. *Test Facilities*

The experiments were carried out in the multi-function artificial climate chamber in Chongqing University. The chamber has a diameter of 7.8 m and a height of 11.6 m. The temperature of the chamber can be lowered down to -45℃±1 ℃ and the atmospheric pressure can be depressed to a minimum of 30 kPa, which can simulate the atmospheric environment of altitude as high as 9000 m. The wind velocity can be adjusted from 0 to 12 m/s. The power was supplied by a 500 kV/2000 kVA test transformer with a maximum short circuit current of 75 A. Two rows of fast oscillating water sprinklers with 14 sprayers, which are about 3.65 m away from the center axial of the insulator string is located 4 to 6 m above the floor of the chamber. The volume diameter of droplets from the sprayer ranges between 20 and 120 μm. The test circuit of the experiment is shown in Figure 1.

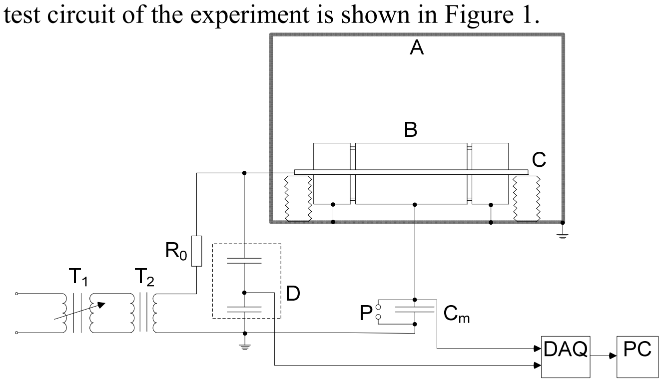

Fig. 1 T_1 is the voltage regulator, T_2 is the test transformer, R_0 is the protective resistor, D is the voltage divider, A is the climate chamber, B is the corona cage, C is the conductor, P is the protective circuit, C_m is the Capacitance, DAQ is the Data Acquisition Card and PC is the computer.

Two aluminum conductors were used in the experiments with the diameters of 18.9 mm and 21.5 mm respectively. The conductor was fixed and supported by the post insulators, placed along the axis of the corona cage, 1.6 m in diameter. Air temperature was kept constant at -15℃ and -5℃ for rime and glaze respectively during the experiments. The liquid water content W was measured by the rotating cylinder [6]. The intensity of accretion [7], was calculated by the following equation:

$$I = E_m * V * W \tag{1}$$

Where E_m, V, W are collection efficiency, air speed and liquid water content respectively. The air speed was kept constant at 1.5 m/s during the experiments. The weight and volume measurements were adopted to calculate the mean density of ice as described by [8]. In order to investigate the influence of water conductivity on ice accretion, 5 μS/cm, 200 μS/cm and 400 μS/cm were chosen in the experiment. As the maximum electric field in the actual Extra High Voltage and Ultra High Voltage transmission lines is between 15 kV/cm and 20 kV/cm [9], the electric field at the surface of the conductor was controlled in 20 kV/cm.

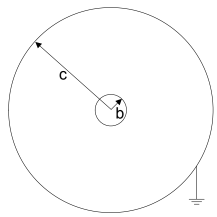

Fig. 2 Schematic diagram of conductor and corona cage

The electric field at the smooth surface of conductor is calculated by the following formula:

$$E_b = \frac{U_{app}}{b\ln(c/b)} \tag{2}$$

Where U_{app} is the applied voltage, b and c are the radiuses of the conductor and corona cage respectively. 5 kV/cm, 10 kV/cm, 15 kV/cm and 20 kV/cm were chosen in the experiments for the conductor with diameter of 18.9 mm. The applied voltages were 20.1 V, 41.9 V, 62.9 V and 83.9 V accordingly.

III. RESULTS AND ANALYSIS

A. Mass and Density of Ice Accretions

Fig. 3 to Fig. 6 shows the mass and density of accretions on the aluminum conductor at increasing values of electric field strengths. The duration of each ice accretion test lasted for 1.5 hours under the specific conditions. It can be seen from Fig. 3 and Fig. 5 that the weight of the accreted ice first increases with electric field strength up to 10 kV/cm and then decreases as the electric field strength increases further. The initial increase of mass can be explained that when the electric field strength is small, the super-cooled water droplet approaching the conductor will the polarized and then be attracted toward the conductor. However, as the electric field strength increases further, the corona activity becomes intensive and ion concentration rises leading to a repulsive force which make the water droplet decelerate or even move backward. Fig. 4 and Fig. 6 show the density of rime and glaze accretions on the aluminum conductor respectively. In the rime accretion, the density first increases up to 5 kV/cm and then decrease with higher electric field strength. In the glaze accretion, the density increases up to 15 kV/cm and then decrease when the electric field is 20 kV/cm. The density of ice is determined by the air gap between the super-cooled water droplets. When collided with the surface of the conductor, the water droplet will be deformed. One of the major factors affecting the deformation is the velocity. When the velocity is higher, the deformation will be greater which leads to a larger density. As the electric field strength increases, the velocity of water droplet approaching the conductor will increase which leading to a growth in the density. As the electric field strength increases further, the corona effect will decelerate the water droplet and decrease the density. From Fig. 3 to Fig. 6, it can be seen that the mass and density of ice accretion in different freezing water conductivity under the same icing condition have the similar tendency and are almost the same. From Fig. 4 and Fig. 6, it can be conclude that the influence of electric field is larger in rime accretion than in glaze accretion.

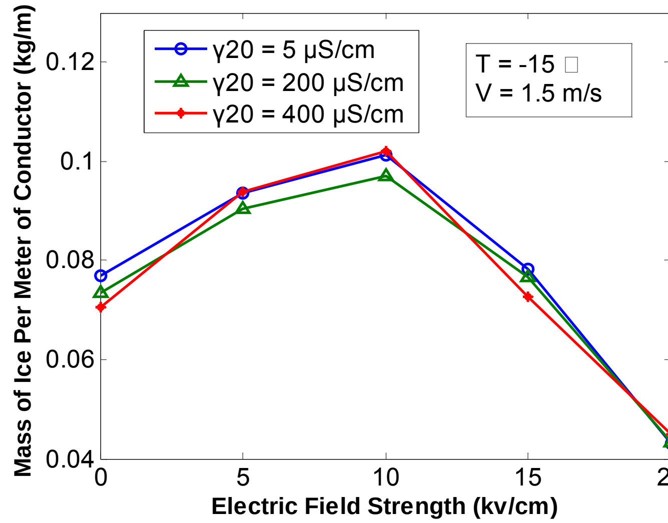

Fig. 3 Weight of rime accreted per meter of aluminum conductor

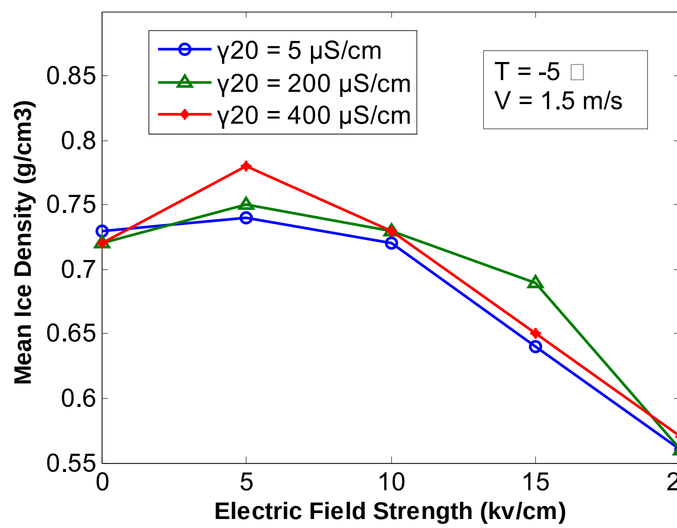

Fig. 4 Density of rime accreted on the aluminum conductor

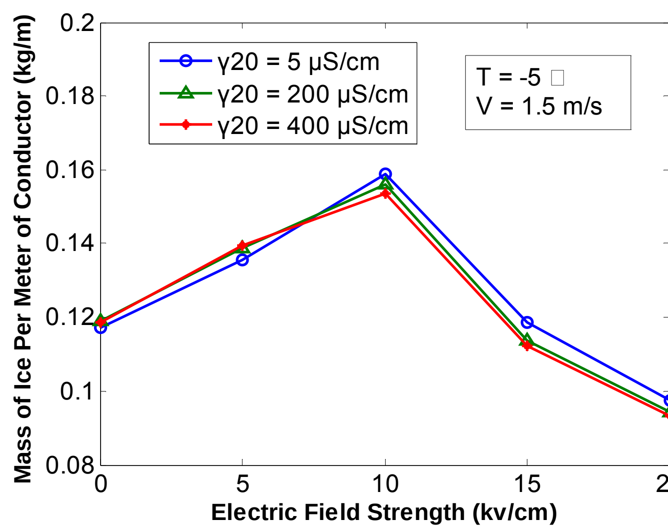

Fig. 5 Weight of glaze accreted per meter of aluminum conductor

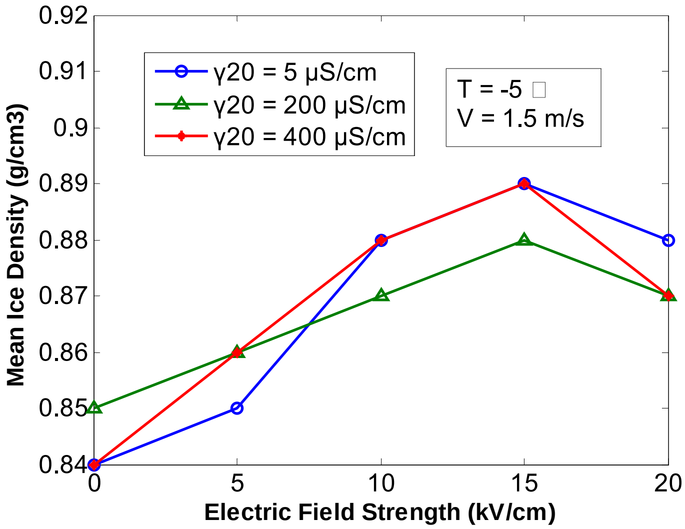

Fig. 6 Density of glaze accreted on the aluminum conductor

B. Spacing of icicles

When there is enough unfreeze water, pendant drops form on the surface of conductor. As water flows to the tip due to gravity and freezes, the icicles. Two conductors were used in the experiments and the results are given in Table 1. The results showed that the icicle spacing is between 17 and 23 mm on the two conductors. As the electric field is increased, the spacing of icicles decreases. This is evident because as the electric field increases, the initial pendant drop will be elongated leading to a smaller spacing. It can also be seen from the results that icicle spacing appears to be independent of air temperature, conductor diameter, and liquid water content when these parameters are varied by the same order of magnitude.

As the icicles grow, unfreezing water flows along the surface of the icicles to the tip thus keeping the spacing of icicles almost constant [3]. Thus, the spacing of icicles is decided by the spacing of the pendant drop during its initial stage of formation, namely the diameter of the drop.

To calculate the diameter of the pendant drop, a quasi-equilibrium state can be assumed due to the pendant drop's slow growth. The equilibrium shape of the pendant drop under an electric field can be determined by the surface tension, which tends to make the drop spherical, by gravity and by the electric field which tend to elongate the drop downward vertically.

The shape of the pendant drop is symmetrical about the z-axis as shown in Fig. 6.

Table 1 Results of the experiments

Experiment No.	Conductor Diameter (mm)	Air Temperature (℃)	Wind Speed (m/s)	Liquid Water Content (g/m^3)	Electric Field (kV/cm)	Icicle Spacing (mm)
1	18.9	-5	1.5	4.6	0	22
2	18.9	-5	1.5	8	0	21
3	21.5	-5	1.5	4.6	0	23
4	18.9	-5	1.5	4.6	5	21
5	18.9	-15	1.5	8	5	21
6	21.5	-5	1.5	4.6	5	22
7	21.5	-5	1.5	8	5	22
8	21.5	-15	1.5	4.6	5	20
9	18.9	-5	1.5	4.6	10	19
10	18.9	-15	1.5	8	10	20
11	18.9	-15	1.5	4.6	10	19
12	21.5	-5	1.5	4.6	10	20
13	21.5	-15	1.5	8	10	21
14	18.9	-5	1.5	4.6	15	18
15	18.9	-15	1.5	8	15	18
16	18.9	-15	1.5	4.6	15	19
17	21.5	-5	1.5	4.6	15	17
18	21.5	-15	1.5	8	15	18
19	21.5	-5	1.5	8	15	20

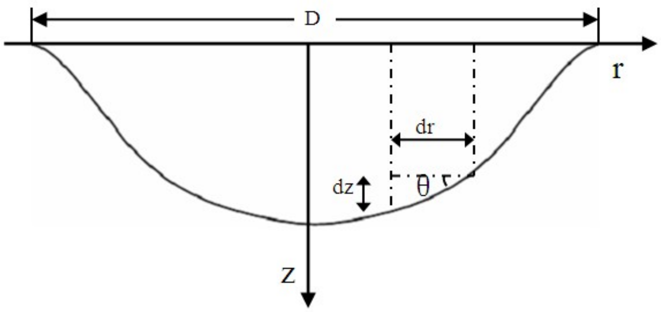

Fig. 6. Cross-section of a pendant drop

The electrical pressure at the drop surface can be calculated by the following equation

$$P_e = \frac{1}{2}[\varepsilon^{(a)} E_n^{(a)2} - \varepsilon^{(b)} E_n^{(b)2} + \varepsilon^{(b)} - \varepsilon^{(a)} E_t^2] \quad (3)$$

where En and Et are the tangential and normal components of the electric field E at the drop surface, ε is the permittivity of the fluid, and superscripts a and b refer to the air and the water drop liquid, respectively. When the water conductivity is 400μS/cm, it can be assumed that there is no electric field inside the drop and that the electric field is normal to the drop surface. Thus, the governing equation for conducting drops can be simplified as

$$P_e = \frac{1}{2}\varepsilon_r \varepsilon_0 E_n{}^2 \quad (4)$$

As the drop is relatively flat at its initial stage, En can be assumed constant and equal to E.

Let z be the ordinate, γ the surface tension, ρ the water density, g the acceleration of gravity. The equilibrium equation is as follows:

$$\frac{d(\gamma r \sin\theta)}{dr} + r\rho g z + P_e r = 0 \quad (5)$$

According to the geometry,

$$\tan\theta = \frac{dz}{dr} \quad (6)$$

$$\sin\theta = \frac{\tan\theta}{\sqrt{1+\tan^2\theta}} \quad (7)$$

Substituting Eqs. (4), (6) and (7) into Eq. (5) yields

$$\gamma \frac{d\left(\frac{r\frac{dz}{dr}}{\sqrt{1+(\frac{dz}{dr})^2}}\right)}{dr} + r\rho g z + \frac{1}{2}\varepsilon_r \varepsilon_0 E^2 r = 0 \quad (8)$$

The appropriate boundary conditions are

$$\frac{dz}{dr} = 0 \quad \text{at } r = 0 \text{ and } D/2. \quad (10)$$

Due to the difficulty of obtaining an analytical solution, a numerical method is used. The diameters calculated are tabulated in Table 2.

Table 2 Computational Results of Water Droplet Radius under Different Electric Field

Electric Field (kV/cm)	Diameter (mm)
0	21.5
5	20.3
10	19.4
15	18.6

IV. CONCLUSIONS

The mass, density of ice accretion and spacing of icicles on the aluminum conductor are influenced by the electric field on the surface of the conductor. When the electric field strength is above 5 kV/cm and the temperature is -15 ℃, ice treeing is formed on the surface of the conductor. For the rime and glaze accretion, the amount of ice accreted first increases with electric field strength up to 10 kV/cm and then decreases as the electric field strength increases further. As for the density, it increases first up to 5 kV/cm and 15 kV/cm and then decrease with higher electric field strength for the rime accretion and glaze accretion respectively. It was also found that the spacing of icicles is independent of conductor diameter and liquid water content. As the water droplet will be elongated by the electric field, the spacing is decreased as the electric field increases. The numerical calculations are consistent with the experiments.

ACKNOWLEDGMENT

This work was supported by The National Basic Research Program of China (973 Program) (2009CB724501) in collaboration with NSERC / Hydro-Quebec / UQAC Industrial Chair on Atmospheric Icing of Power Network Equipment (CIGELE) and Canada Research Chair on Engineering of Power Network Atmospheric Icing (INGIVRE)

REFERENCES

[1] W.C. Macklin, “The density and structure of ice formed by accretion”
[2] Lasse Makkonen, “Modeling power line icing in freezing precipitation,” Atmospheric Research, Vol. 46, 131-142, 1998
[3] Lasse Makkonen, “Spacing of icicles”, Cold Regions Science and Technology, Vol. 21, Issue 3, May 1993, Pages 317–322
[4] Kathleen F. Jones, “The density of natural ice accretions related to nondimensional icing” Q. J. R. Meteorol. Soc, 116, pp. 477-496, 1990
[5] M. Farzaneh, W. A. Chisholm, C. de Tourreil, J. F. Drapeau, “Insulator Icing Test Methods and Procedures a positive paper prepared by the ieee task force on insulator icing test methods,” IEEE Transactions on Power Delivery, Vol. 18, No. 4, pp. 1503-1515, Oct 2003
[6] Jun Ma, “Influence of Electrical Stress on Insulator’s Icing and the Discharge Characteristic of Iced Insulator”, Phd thesis, 2010.
[7] Farzaneh, M, J.L. Laforte, “Ice Accretion on Conductors Energized by AC or DC: A Laboratory Investigation of Ice Treeing,” International Journal of Offshore and Polar Engineering, Vol.4, No.1, 1994.
[8] Farzaneh, M, and Laforte JL, “Effect of Voltage Polarity on Icicles Grown on Line Insulators,” Int Offshore and Polar Eng (IJOPE), Vol 2, No 4, pp228-233, 1992.
[9] Anderson J G. “Transmission Line Reference Book: 345 kV and Above,” China WaterPower Press, 1979.

Study on the Influence of Mixed-phase Ice on Corona Inception Voltage of Smooth Conductor

ZHANG Zhi-jin, WANG Yao-xuan, JIANG Xing-liang, LIN Li
The State Key Laboratory of Power Transmission Equipment & System Security and New Technology
School of Electrical Engineering, Chongqing University
Chongqing 400030, P.R.China
E-mail: xljiang@cqu.edu.cn

Abstract — Mixed-phase ice disaster which has happened frequently in China's winter affects the safe operation of transmission line seriously. Iced surface on conductor become so rough that the growth of the dentritic crystal and icicle make the electrical field distorted seriously and then it will decrease the conductor corona onset voltage. Although the international and domestic academics has done much research on the corona problems of different conductors, there had been no in-depth analysis of the regularity of conductor corona onset voltage caused by mixed-phase ice. Therefore a series of test of AC corona of mixed-phase iced smooth conductors were implemented in the artificial climate chamber combined with the icing morphology to establish conductor's electrical field model to research its corona characteristics, and the UV imaging technology and I-U curve fitting measurement are employed to analyze the inception voltage. The results show that mixed-phase ice can cause the inception voltage value to fall significantly. As the icing time increase, corona onset voltage will decrease continually, but it will gradually become saturated. The conclusion of this paper may be a reference for the design and onset voltage calculation of the overhead transmission line in areas suffered mixed-phase ice.

Keywords — smooth conductor; mixed-phase ice; inception voltage; ultraviolet imagery

0 INTRODUCTION

The microclimate in China varies dramatically with the complex terrain. Some areas where the freezing rain and fog are frequent tend to suffer from the icing events of mixed-phase ice, thus severely threatening the security and reliability of power systems[1-3]; The mixed-phase ice is an alternating accretion of dry-wet icing growth, with the glaze accretion on the contact surface of conductor first and the rime afterwards, thus making it melded with the two forms of ice[4,5]. The mixed-phase ice which grows fast and dose great damage to the transmission line gets more and more attention recently.

The icicles of glaze which is longer and the dendritic crystal of rime which make the ice protuberance rough will jointly cause the change in the morphology of lines after icing. The ice tree as well as the tip of icicles would deform the voltage distribution on the surface, leading to Corona Discharge of conductor in lower voltage[6-8]. In company with the corona discharge, there will be high-frequency electromagnetic pulse that could cause radio interference, the increase in energy dissipation of transmission line, the electric wind leading to conductor galloping and the local temperature increase in conductor where the metal surface reacts with the ambient air. Given this, the corona phenomena has been attached more importance by power industry[9-11].

Many tests of smooth conductor in conditions of clean, contamination, rain or high-altitude have been established for the research on its startup property of corona[12-15], however, there is no study on the corona characteristics and the inception voltage of smooth conductor under the condition of mixed-phase ice.

As a conclusion of plenty of tests, reference [16] gives a empirical formula of corona inception field strength, however, the Peek formula doesn't account for the ice accretion and other external environment conditions, making the calculated value doesn't accord with the engineering practice[17,18] . Reference [19] describes the influences of AC field on the icing shape and considers that the forms of dendritic crystal of rime would affect the corona discharge quantity. This paper doesn't have research on the corona inception voltage under mix-phase ice condition. Although reference [19] gives an inception voltage forecasting model taking different atmospheric parameters as input, it takes no consideration of effects of ice accretion on the corona characteristics.

A series of test of AC corona of mixed-phase iced smooth conductors were implemented in the artificial climate chamber, and the UV imaging technology and I-U curve fitting measurement are employed to analyze the inception voltage, and the finite element model of electric field is established according to the morphology of mixed-phase ice. These results may provide reference for the design and model selection of power transmission.

1 TEST FACILITIES, SPECIMENS AND TEST PROCEDURE

1.1 TEST FACILITIES AND SPECIMENS

The experimental investigations were carried out in an artificial climate chamber, with an inner diameter of 2.0m and a length of 3.8m. The minimum temperature in the chamber can be adjusted to -36℃ and the air pressure in the chamber can be as low as 34.6kPa. The chamber is fitted with nozzles according to the IEC standards, which can simulate the morphology of glaze, rime or the mixed-phase ice combined with the blowing device that can control the air speed and also ensure the even distribution of the temperature and mist particles in it. The power supply is leaded in through a wall bushing from the other side of the chamber and all of these can meet the requirements of the test. The test circuit of the ice-covered experiment is shown in Figure 2.

Fig. 1 Multi-function artificial climate chamber

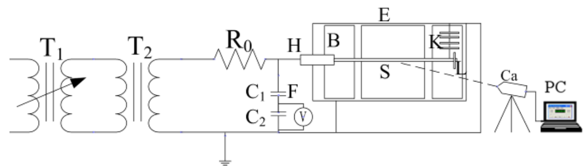

Fig. 2 Schematic diagram of test circuit

T1：voltage regulator，T2：test transformer，R0：protective resistor，H：wall bushing，F：capacity voltage divider (the divider ratio is 10000：1)，V：voltmeter，E：climate chamber，S：specimen，B：corona cage，K：isolating insulator，L：grading ring，Ca：UV imager

The smooth conductor is placed in a corona cage to ice. The cage with a diameter of 2m consists of 3 parts, the first and the last part with a length of 0.5m earthed and the middle one with a length of 1m used for measurement. The specimen is smooth conductor with a length of 2m and a diameter 18.9mm and the grading rings are mounted in the end of it. The mixed-phase ice covered on the specimen is an alternating ice accretion of the glaze accretion first and the rime afterwards with the same accretion time and the experimental conditions is shown in the Table 1. The environmental parameter is measured with PTU200, which is an integrated measuring set to meter temperature, humidity and air pressure, and the MVD as well as the liquid water content measured with the laser diffract instrument. As the most of optical spectrum generated by the corona discharge is invisible UV spectrum, the CoroCAM IV+ UVI is used for observation on the development of the corona, with which the photon number detected by the UVI corresponds well [21] . The water conductivity in 20℃ is measured with DD-810E, a precision conductivity meter. The specimen, equipment and the testing arrangement diagram are shown in the Figure 3 and Figure 4.

Table 1 Forming condition for Mixed-phase ice

Type of ice	*MVD* d_a/μm	Liquid water content *W*/g/cm^3	Temperature T_a/□	Total icing time *T*/min
Glaze	100	8.5	-5	15 30 45 60
rime	20	2.5	-15	15 30 45 60

(a) UV imager (b) PTU 2000 (c) conductivity meter

Fig. 3 Test equipments

Fig. 4 Arrangement for experiment

1.2 TEST PROCEDURES AND THE CRITERION OF INCEPTION VOLTAGE

The smooth conductor is to ice in the artificial climate chamber and the icing time is 15, 30, 45min and 60min respectively. The AC voltage shall be applied on the specimen to the 90% of the corona inception voltage, and then increased at a rate of 3kV/s; when the photon number or every time a rise of it is observed, video it with the UVI for 30s[22]. Figure 5 gives the pictures from UVI of corona discharge of smooth conductor in the AC voltage when the mixed-phase ice accretes for 30min on the specimen. As seen in the pictures, when the voltage is between 35.6kV and 45.6kV there is few photons around the specimen which indicates no corona occurred on the surface of ice-coated conductor and when the voltage outnumbers 51.2kV the photon number increase dramatically so it is considered that the inception corona voltage is about 51kV. The photon number videoed 3 times at certain voltage within 30s is averaged to obtain the characteristic curve of the photon number and voltage. As shown in the Figure 6a, the voltage corresponding to the inflection point of the curve is the inception corona voltage and the errors between the measurements are less than 5% which is in acceptable range. Figure 6b gives the inception voltage value calculated by curve-fitting method.

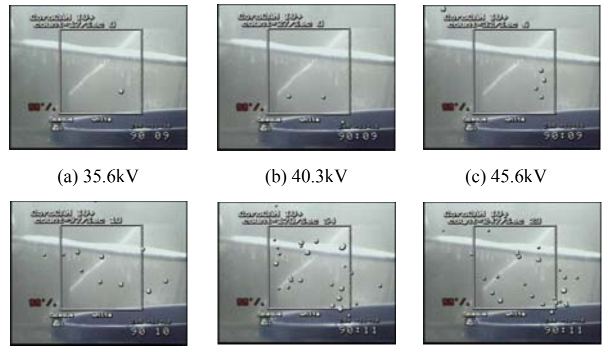

(a) 35.6kV (b) 40.3kV (c) 45.6kV

(d) 51.2kV (e) 55.6kV (f) 60.7kV

Fig. 5 Corona discharge images of smooth conductor

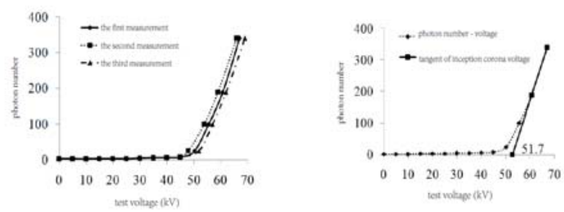

(a) measurements of 3 times (b) inception voltage by tangent method

Fig. 6 Calculation for corona onset voltage in 30min mixed-phase icing

2 EFFECT OF ICING ON THE INCEPTION VOLTAGE

The tests are established to investigate the influence of mixed-phase ice coating extent on the inception corona voltage of the specimen, with a fixed water conductivity of 400 μS/cm that has been corrected to the value under 20℃. The geometry features of the mixed-phase ice covering on the conductor in different icing time are shown in the Figure 7 and 8. When the artificial icing completed the UVI is applied to obtain the photon number, which as well as the corresponding voltage value are analyzed using the I-U curve-fitting method. The trend of the inception corona voltage is shown in Figure 9.

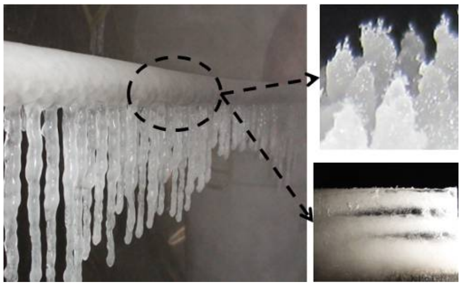

Fig. 7 Mixed-phase ice morphology close-up

(a) icing for 15min

(b) icing for 30min

(c) icing for 45min

(d) icing for 60min

Fig. 8 Mixed-phase ice morphology under different time

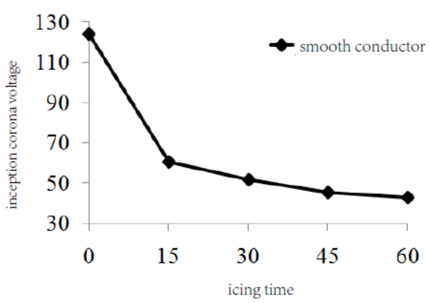

Fig. 9 Corona onset voltage before and after ice coating

The inception corona voltage of the smooth conductor in the Figure 9 varies considerably after ice-coated, the value of which is only 50% of those without ice even though the icing time is only 15min. This may be due to that the mixed-phase ice accretion will produce many wee dendritic crystals on the upper surface of the conductor and long icicles on the lower surface so that geometrical morphology of the conductor is altered, as is shown in the Figure 7. As a result, the corona characteristic depends on the condition of the ice accretion on the conductor. The dendritic crystals and the tips of icicles will distort the surface field of ice-coated conductor seriously, as lead to a local corona effect on the surface of the ice-coated conductor with a lower voltage and a inception voltage drop of the iced conductor.

With the rise of icing degree, the inception corona voltage of icing conductor will decrease with a rate that gradually reduces and finally becomes saturated. It is because that the icicles grow more slowly and the curvature radius of their tips tends to be constant while the morphology of the dendritic crystals of rime is nearly invariable. In the ice accretion period of glaze, as there is going to be icicles on the lower surface of the conductor and the collision efficiency of the water drop will decline along with ice depth on the specimen increasing, it takes a longer time for the water drops to move to the tips of the icicles so that the geometry of the glaze alters more and more slowly. On the other side, the droplets of fog which is going to generate the rime will turn into crystals on impacting on the conductor. Therefore the shape parameters of the dendritic crystals are not affected by the icing time. Besides, a larger equivalent diameter of the conductor leads to smaller collision efficiency in the ice accretion of rime. Given these factors of the glaze and rime, the mixed-phase ice accretion will take a longer time and as a result the decent rate of inception corona voltage.

3 FIELD SIMULATION AND THE APPLICATION

3.1 FEM OF SURFACE FIELD DISTRIBUTION OF SMOOTH CONDUCTOR COATED MIXED-PHASE ICE

The FEM is build by Maxwell with a 2D section view. The roughly model is shown in Figure 13 and its morphological parameters are shown in Table 2. The conductor in the model is placed in coaxial electrode with a diameter of 2m and applied with an rms voltage of 66kV. The material of conductor is set to Aluminum when that of icicles is set to Ice and its relative permittivity is 75. The background region of field is set to Vacuum and the boundary condition of the coaxial electrode is balloon boundary where the finite field is 0. The calculation is performed after mesh division automatically and the model which is not drawn in proportion is shown in Figure 13.

Table 2 Parameter of Mixed-phase ice morphology

Smooth conductor on mixed-phase ice				
Icing time	15min	30min	45min	60min
Ice thickness(mm)	2.34	3.82	5.1	5.94
Bottom diameter of crystal(mm)	1.56	1.55	1.53	1.55
Height of crystal(mm)	1.43	1.45	1.44	1.45
Length of icicle(mm)	11.8	23.4	30.1	35.2
Bottom diameter of icicle(mm)	5	5.8	6.7	8.4
Diameter of icicle tip(mm)	4.9	4.7	4.4	4.0

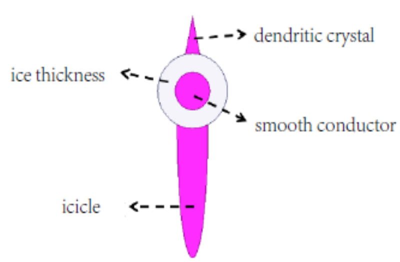

Fig. 13 Mixed-phase ice simulation model of smooth wire

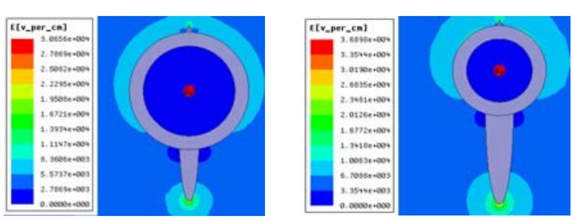

(a) icing for15min (b) icing for 30min

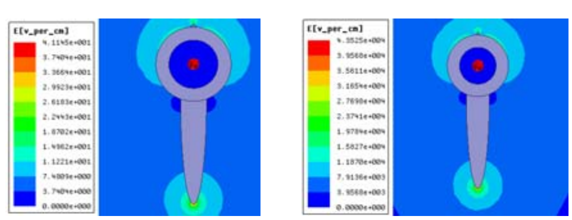

(c) icing for 45min (d) icing for 60min

Fig. 14 Field distribution on the iced surface

With a voltage of 66kV on the surface of non-icing conductor, its field is 15kV/cm which is the same as actual operated circuit and the field intensity map is shown in the figure 14. The maximum field for different icing time is 30.7, 36.9, 41.1 kV/cm and 43.5kV/cm respectively, which is usually distributing around the tips of dendritic crystals and the icicles and the trend of which is gradually increasing with a rate slowly down. The simulation examples are seen to verify the test results well.

3.2 MODIFIER FORMULA OF THE INCEPTION CORONA VOLTAGE

It is known from the simulation results that the inception corona voltage of conductor keeps falling down with the icing time going when the mixed-phase ice is coated. However, the distortion effect of field around the conductor is weaken with the rise of ice thickness and the slowing down increase of icicle length, which leads to a slower rate of decent of inception voltage. On these grounds, the coefficient of deformation is introduced to indicate the relationship between the inception voltage and the deformation of icing conductor. Supposing the diameter of conductor D is 18.9mm, ice thickness K is 2.34, 3.82, 5.1 and 5.94mm respectively and L , the ice length is 11.8, 23.4, 30.1 and 35.2mm, the formula is

$$W = \frac{K+L}{D} \tag{14}$$

The relationship between the coefficient of deformation and inception voltage is shown in Table 3,

Table 3 Deformation coefficient VS corona inception voltage

Smooth conductor on mixed-phase ice				
Icing time(min)	15	30	45	60
Coefficient of deformation W	0.75	1.44	1.86	2.18
Inception corona voltage U(kV)	60.52	51.7	45.1	41.7

The data fitting is carried on using Matlab with a fitting degree of 0.998 and the formula is

$$U_c = mU_0 \cdot e^{(-a \cdot W)} - B \qquad (15)$$

Where U_0(kV) is the inception voltage of smooth conductor under 20℃, U_c(kV) is the inception voltage after icing, m is roughness coefficient of 1 when smooth conductor is applied, and a is a constant of 0.164 when b is a constant of 30.31.

4 CONCLUSIONS

1) There is going to be a partial corona discharge around conductor coating mixed-phase ice on a lower voltage and its inception corona voltage is distinctly less than the non-icing conductor.

2) The inception corona voltage of conductor after icing will decline continually with the rise of icing degree, but the rate falling down is getting smaller and smaller and tends to be a constant finally.

3) The modifier formula of inception corona voltage can be used to calculate the inception voltage quickly, which would be a reference of the transmission line design.

References

[1] HU Yi. Analysis and Countermeasures Discussion for Large Area Icing Accident on Power Grid [J]. High Voltage Engineering, 2008, 34(2), 215-219(in Chinese).

[2] LI Cheng-rong, Lv Yu-zhen, CUI Xiang, DU Xiao-ze, CHENG Yang-chun, WANG Zhang-qi, AI Xin, XIAO Xiang-ning. Research Issues for Safe Operation of Power Grid in China under Ice-Snow Disasters [J]. Power System Technology, 2008, 32(4): 14-22(in Chinese).

[3] YANG Lin, HAO Yan-peng, LI Wei-guo, LI Zhao-ting, DAI Dong, LI Li-cheng, LUO Bing, ZHU Gong-hui. Relationships Among Transmission Line Icing, Conductor Temperature and Local Meteorology Using Grey Relational Analysis[J]. High Voltage Engineering. 2010, 36(3), 775-781(in Chinese).

[4] Chen Yong, Wang Qifa, Huo Feng. Corona characteristics of conductors for 1000 kV AC transmission lines[J]. High Voltage Engineering, 2007, 33(11): 43-45 (in Chinese).

[5] JIANG Xing-liang, YI Hui. Icing Transmission Lines and the Protection [M]. Beijing: China Electric Power Press, 2001.

[6] JIANG Xing-liang, DU Zhen, WANG Hao-yu, ZHANG Zhi-jin. Icing Features of Wire in Chongqing Region[J]. High Voltage Engineering, 2011, 37(12), 3065-3069(in Chinese).

[7] WANG Xiu-ling, YANG Jia-xiang, SUN Yong-xin, WANG Xin-xue. Numerical simulations for formation mechanism of mixed-phase ice on overhead lines[J]. East China Electric Power, 2008, 36(12), 26-29(in Chinese).

[8] Ndiaye, I；Fofana, I；Farzaneh, M. Contribution to the study of the appearance and development of corona discharges on a surface of ice[J]. Electrical and Computer Engineering, 2003. IEEE CCECE 2003. Canadian Conference on. 2003 , Page(s): 639 - 642 vol.1

[9] Zeng Qingyu. Study on electric characteristic and corona performance of UHV AC transmission line[J]. Power System Technology, 2007, 31(19): 1-8(in Chinese).

[10] Sarma M P，Janischewskyj W. Electrostatic field of a system of parallel cylindrical conductors[J]. IEEE Transactions on Power Apparatus and Systems，1969，88(7)：1069-1079.

[11] Hu Baixue. Research on Electromagnetic Environment of Power Frequency EHV and UHV Transmission Lines[D]. Zhejiang University, 2006:65-67.

[12] Liu Youwei，Li Jihong，Li Bin．Influence of air density and humidity on the corona performance of conductor[J]. Power System Technology, 1990, 14(4): 46-50(in Chinese)．

[13] Phillips D B，Olsen R G，Pedrow P D．Corona onset as a design optimization criterion for high voltage hardware[J]. IEEE Trans. on Dielectrics and Electrical Insulation, 2000, 7(6): 774-751．

[14] Yong Liu, Du, B.X. Recurrent plot analysis of leakage current on flashover performance of rime-iced composite insulator [J]. Dielectrics and Electrical Insulation, IEEE Transactions on, 2010, Page(s): 465 – 472.

[15] CHEN Yong, XIE Xiong-jie, BIAN Xing-ming, LIU Yun-peng, ZHOU Wen-jun, WANG Li-ming. Analysis on Altitude Correction Factor of Corona Inception Voltage/Electric Field of AC Transmission Lines Using the Mobile Corona Cage [J]. High Voltage Engineering, 2010, 36(6): 1385-1391.(in Chinese).

[16] Gildas H．Theoretical evaluation of Peek's law[J]．IEEE Trans. on Industry Applications, 1984, 20(6): 1647-1651．

[17] Tiebing Lu, Gaolin Xiong, Xiang Cui, Hong Rao, Qi Wang. Analysis of Corona Onset Electric Field Considering the Effect of Space Charges[J]．Magnetics, IEEE Transactions on. 2011, Page(s): 1390 – 1393.

[18] Li，Z.-X； Fan，J.-B； Yin，Y；Chen，G. Numerical calculation of the negative onset corona voltage of high-voltage direct current bare overhead transmission conductors. Generation, Transmission & Distribution，IET. 2010，Page(s)：1009 – 1015.

[19] SHU Lichun, LI Te, JIANG Xingliang, HU Qin, LUO Baosong, YANG Zhangang. Influences of AC Electric Field Strength on Conductor Rime Icing Performance[J]. Proceedings of the CSEE. 2012, 32(19): 140-147(in Chinese).

[20] HU Qin, SHU Li-chun, JIANG Xing-liang, YUAN Qian-fei, GONG Lin, LIN Rui. Conductor's AC Corona Onset Voltage Prediction Under Different Atmospheric Parameters and Conductor Surface Conditions[J]. High Voltage Engineering, 2010, 36(7): 1669-1674(in Chinese).

[21] Ma Bin，Zhou Wenjun，Wang Tao，et al．Corona discharge of the severe non-uniform electric field based on the UV-light imaging technology[J]．High Voltage Engineering，2006，32(7)：13-16(in Chinese)

[22] Ren Lei-Jian；Liu Yun-Peng；Lu Jie；Yu Tao. Research on Method to Get Corona Inception Electric-Field Intensity Based on Small Corona Cage. Power and Energy Engineering Conference，2009. APPEEC 2009. Asia-Pacific. 2009，Page(s)：1 – 4.

Xingliang Jiang was born in Hunan Province, China, on 31 July 1961. He received the M.Sc. and Ph.D. degrees from Chongqing University, Chongqing, China, in 1988 and 1997, respectively. His employment experiences include the Shaoyang Glass Plant, Shaoyang, Hunan Province; Wuhan High Voltage Research Institute, Wuhan, Hubei Province; and the College of Electrical Engineering, Chongqing University. His research interests include high-voltage external insulation and transmission line icing and protection. He is the member of working groups of CIGRE B2.29 and IWAIS.

Dr. Jiang has published two books and over 120 papers about his professional work. And He received the Second-Class Rewards for Science and Technology Advancement from the Ministry of Power in 1995 and 2009; Beijing Government in 1998; Ministry of Education in 1991 and 2001, respectively; the first-class Reward for Science and Technology Advancement from the Ministry of Power in 2004 and 2005; the Second-Class Reward for Science and Technology Advancement from the Ministry of Technology in 2005; the First-Class Reward for Science and Technology Advancement from the Ministry of Education in 2006; and the First-Class Reward for Science and Technology Advancement from Chongqing City in 2006 and 2008.

Yaoxuan Wang was born in Henan, China, in 1983. He received his B.Sc. degree from North China University of Water Resources and Electric Power in 2007. He is currently pursuing the Ph.D. degree in the college of electrical Engineering, Chongqing University. He is mainly engaged in the field of high-voltage external insulation and transmission line's icing.

The Braced Post Assembly and the I Insulator String Dynamics Comparison at the Snow Shedding

Borut Zemljarič [#1], Valentine Ažbe [*2]

[#] *Electrical Engineering Department, Elektro Gorenjska d.d.,*
Ulica Mirka Vadnova 3a, 4000 Kranj, Slovenia, Europa
[1] borut.zemljaric@elektro-gorenjska.si
[*] *Electrical Engineering Department, University of Ljubljana,*
Tržaška 25, 1000 Ljubljana, Slovenia, Europa
[2] valentin.azbe@fe.uni-lj.si

***Abstract* —** Narrowing the overhead line tower can be achieved by using post line insulators. A post line insulator with its base rigidly attached to the supporting structure must withstand unbalanced loads and the bending stress inside the insulator's fiberglass core. Because the insulator mechanical limits, at higher conductor cross section it is necessary to using rotating post line insulators base on tower. Two problems arise from the insulator rotating base at the compact line. First problem is distance between the conductors in mid span. Most of compact line solutions use the same insulators length, so the conductors lie in vertical disposition. In that case the distances should be big enough to prevent short circuit at snow shedding. The second problem is to satisfy the safety distance to the ground obstacles.

By rotating post line insulator base, the conductor behavior is different as in the case using classical vertical I suspension insulator string, especially in areas where additional loads caused by snow can be expected. So our goal is to get additional knowledge about sag behavior when we using the rotating braced post assembly.

The dynamical numerical model based on lumped conductor mass was developed to predict conductor and insulator movements during snow accretion or shading. The model is compared with model based on Adina program. At next step, comparison in conductor movement and forces between classical string and rotating post line insulator has been made. Based on comparison the basic recommendations using rotating post line in snowy area were developed.

***Keywords* —** overhead lines, cable, dynamics, shedding

I. Introduction

Narrowing the overhead high voltage line route of way is important issue in spatial planning and designing stage of project. One of possible technical solutions to reduce tower head dimensions and overall line route of way dimension is using post line insulators, so called compacted lines. Post line insulator can be attach to supporting structure with rigid or pivoted connection, depend on a loads applied on insulator. A post line insulator with its base rigidly attached to the support structure should withstand unbalanced loads and the bending stress inside the insulator's fiberglass core. Because the post insulator mechanical limits, at higher cross conductor section it is necessary to use rotating brace post insulators assembly on tower. Those solutions are already used in practice [6], but some questions are still to be answer in future, to make technical solution more acceptable in terrain region where snow accretion can occur. At the beginning from a point of view of overhead line designer, two problems arose. The first problem is determination the distance between the conductors on tower head taking into account rotating base braced post assembly. Most of the compact line solutions use the same insulators length, so the conductors lie in vertical plane disposition. In that case distance should be big enough to prevent short circuit at snow shedding. The second problem is to satisfy the required safety distances to the ground obstacles in the case of snow shedding.

By rotating the insulator assembly base, the conductor behavior is different as in case using classical vertical insulator I suspension string. That is especially important in areas where additional loads caused by snow shedding or high winds can be expected. So our goal is to get additional knowledge about the cable dynamic when we are using the rotating insulating brace post assembly. In figure 1 the problem is illustrated. With blue color initial state of the conductors and the insulators are marked and corresponding distance to ground D is marked. For sake of simplicity only one conductor is drawn. With red color the deflected conductor state is sketch if accretions in span occur.

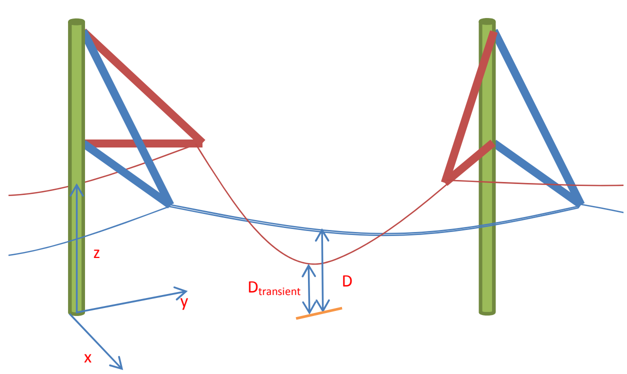

Fig. 1. Change in the cable distance to obstacles.

To calculate corresponding deflections, the dynamical numerical model based on the lumped conductor mass was developed. With model it is possible to predict the conductor and insulator movements during snow accretion or shading from it. The model is still in development and research phase. The results get from the numerical model are compared with results based on Adina program [1, 2]. At next step, time dependent comparison of the conductor movement and forces on tower between classical string and rotating braced post assembly was made. Based on comparison the first recommendations using rotating post line in snowy area were developed, but it still work to be done in future.

II. The Insulator string motion

To get more into problem background, the first step is comparing motion analyses of classical I insulator string and the brace post assembly string shown in figure 2. The conductor suspension point T at the end of string in both cases move in space. But from the figure 3 can be assumed that rotating have different influence on conductor motion. To estimate the value of influence is our first task. The conductor attaching to the end of insulator is moving general speaking in two different ways. Let we illustrate that by assuming that force act only in y axis. In the case of I string, insulator deflect from initial vertical position in the same plane as force act, that is yz. In the case of brace post assembly, they also deflect from initial state, but out of initial plane, to new x,y,z point if post insular is inclined toward z axis.

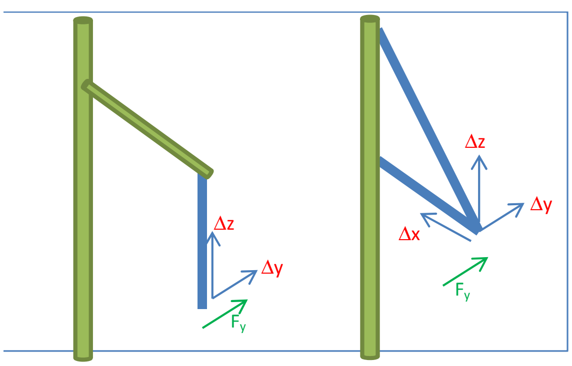

Fig. 2. Difference in insulators end movements for different insulators types.

The mathematical approach in analyses we use is the mathematical pendulum. Using the inertial coordinate system, the I string has three degrees of freedom. That are movements in x and y direction and the bending the insulator string around z axis. In brace post assembly we have also three degrees of freedom. Those are movement in y direction and the rest two acts to bending insulator string. By now, we are in our study focused only on movement and no internal forces inside insulators assembly were studied. The insulator bending is important in the stage determination mechanical internal forces and bending inside insulator string.

In figure 3 the movement of the conductor attachment point T from initial point is presented. In the presented case, the used length of I insulator was 1.35 m, and the post insulator length was the same 1.35m, mounted 12° up from horizontal plane. Brace insulator has length 1.55 m and has 55° angle regarding post insulator. As we mentioned before we will be focused only on snow accretion or shedding. Let we imagine longitudinal force act to point T in figure 2. The brace post assembly insulator always rotate in 3D space and through that also conductor movement, while classical I insulator string act in same direction as generated force. That means if there is no wind load perpendicular to conductor, insulator string move only in 2D plane. Comparing coordinates movements, the longitudinal coordinate y is identical for both suspension string types. When in the case of I insulator string rotating act on vertical z coordinate movement significantly in the case of the braced post assembly vertical deflection is very low. The values depend on braced post assembly dimensions and angles between insulators and attachment to tower.

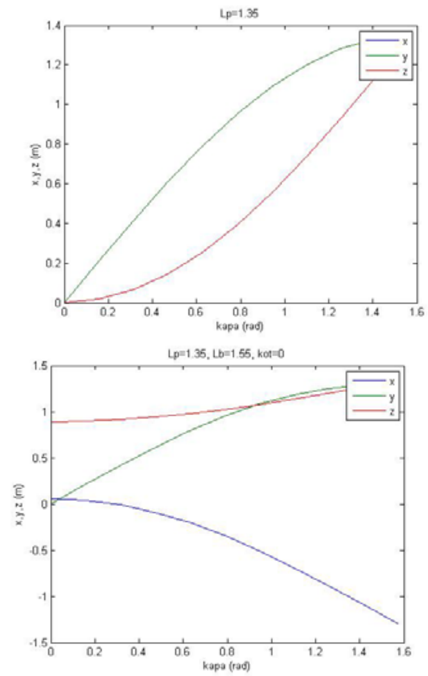

Fig. 3. Insulator end movements regarding initial position for I string (up) and brace post assembly (down).

Based on previous figure 3 analyses the question arose, how the different insulator string rotation and the conductor attachment point movement impact to cable dynamic in the conductor tension field.

III. Numerical model

In this section we outline and explain basic approach to our numerical model, used to predict the cable and the insulators dynamics in transient loads. We decide to develop our own numerical model and after that transfer this to the MATLAB environment, rather than using closed program solutions. By that we are capable to understanding and have insight in model and also approach model to overhead line designer thinking.

The numerical model based on the cable discretizing into the sequence of lumped mass elements, interconnected via springs and dampers as show figure 4. As stated the cable is assumed as perfectly flexible and an aerodynamic damping is at this stage ignored.

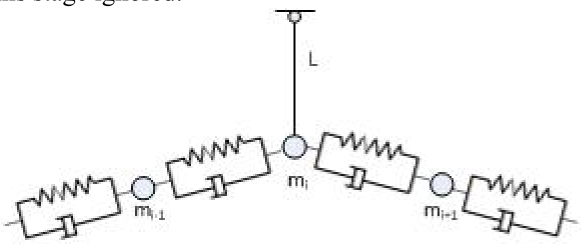

Fig. 4. Cable discretization by lumped masses.

To determine the lumped masses and their point locations, at first the initial conductor catenary state in tension field is determined regarding cable characteristics and conductor tension. The end points on tension towers in tension field are fixed. The dynamic equations for the cable are derived through second Newton law using inertial coordinates of the lumped masses as

$$m_{js}\ddot{\mathbf{x}} = \mathbf{F}^{v}_{js} + \mathbf{F}^{d}_{js} + \mathbf{F}^{g}_{js}\,. \qquad (1)$$

In equation F represent tension force, damping force, gravitational force act on lumped mass m. The force determinations base on work [3]. The conductor suspension point inside tension field which represent insulator is subject to its own dynamical kinematic motion as

$$I_{js}\ddot{\Theta} = \mathbf{l}\times(\mathbf{F}^{v}_{js} + \mathbf{F}^{d}_{js} + \mathbf{F}^{g}_{js})\,, \qquad (2)$$

where I is moment of inertia and Θ insulator rotating angle from initial position. Moments of inertia have been determined for both cases, I insulator string and braced post insulator.

IV. NUMERICAL RESULTS

A. Input data

Encouraged by work [1] we predicted and calculated at this stage of the research the two basic cases named Case 1 and Case 2. Case 1 consists of two equal spans 200 m long, and the case 2 consist of three equal span model of same length. The basic cable data for cable 240/40ACSR are: cable diameter 21.8 mm, mass 0.98 kg/m, modulus of elastic 77000 N/mm^2 and cable cross section area 282 mm^2. The initial horizontal conductor tension in the tension field is 9300 N. The case 2 have two sub cases. They differ in the length of snow accreted on conductors. The half and the third of length of tension field were studied.

In dynamic model snow accretion is modeled as time depending force act on lumped mass. The initial catenary state is taken at 0°C and then additional load caused by snow accretion rise linear from 0 N/m to 21 N/m in 15 s time. At 20 s time from beginning snow shading occur in determined length on the right spans. We predicted that span shed from conductors in 1 s time, as show figure 5. On left spans the force stay continuous to the end of observed time, which is 50 s. The figure 5 illustrates time variation of accreted and shaded snow.

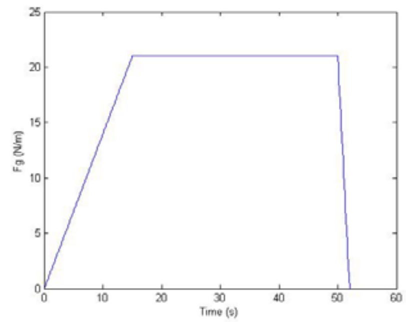

Fig. 5. Quantity of the snow accretion and shedding scenario.

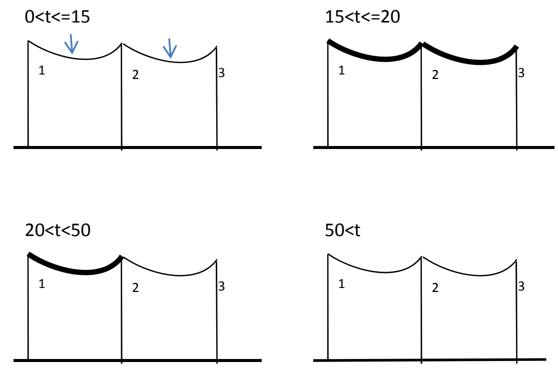

Fig. 6. Snow accretion and shedding scenario in the tension field.

With this approach we believe that in future can be studied different cases with arbitrarily time function the accreted snow on conductors.

B. Frequency prediction

To predict dynamical behavior of the conductor and insulators strings in the tension field, the mode shapes and frequencies were estimated with approximate equations given by [7]. Together with the geometric conductor data the parameter λ^2 was calculated and expected natural frequencies and periods were estimated. Based on the conductor loading scenario two cases were predicted: span loaded (OS-L) and the other span is bare, free of load (OS-B), as illustrated figure 6. For those cases, the horizontal conductor tensions and sags were calculated in final (static) position. In table 1 the results are given for first two symmetric and antisymetric in-plane modes. In table H is horizontal tension, f conductor sag and a span length.

TABLE I
ESTIMATED MODE FREQUENCY

Case		*OS-B*	*OS-L*	*OS-B*	*OS-L*
H	(N)	18399	19536		
F	(m)	2.67	7.86		
a	(m)	200.35	199.65		
λ^2		13.08	104.86		
symmetric		*Mode 1*	*Mode 1*	*Mode 2*	*Mode 2*
f	(Hz)	0.49	0.52	1.02	0.70
T	(s)	2.04	1.92	0.98	1.42

Antisymmetric		*Mode 1*	*Mode 1*	*Mode 2*	*Mode 2*
f	(Hz)	0.68	0.40	1.37	0.80
T	(s)	1.46	2.51	0.73	1.25

In bare cable we expected first symmetric mode and on load cable first antisymmetric mode.

C. Dynamical response

At this stage the results obtain by calculating input data for I insulator string and braced post insulators were compared. First result we analyzed is mid span point movement from initial position and second analyzed is regarding rotation the insulator string assembly. The results for case I are illustrated in figure 7. It is interesting for us, that dynamic response in the analyzed case, when two spans are taken and load act on 50% of the tension filed, is practically similar for classical I insulator string and the braced post assembly. The only small difference is movement the braced post assembly in x axis.

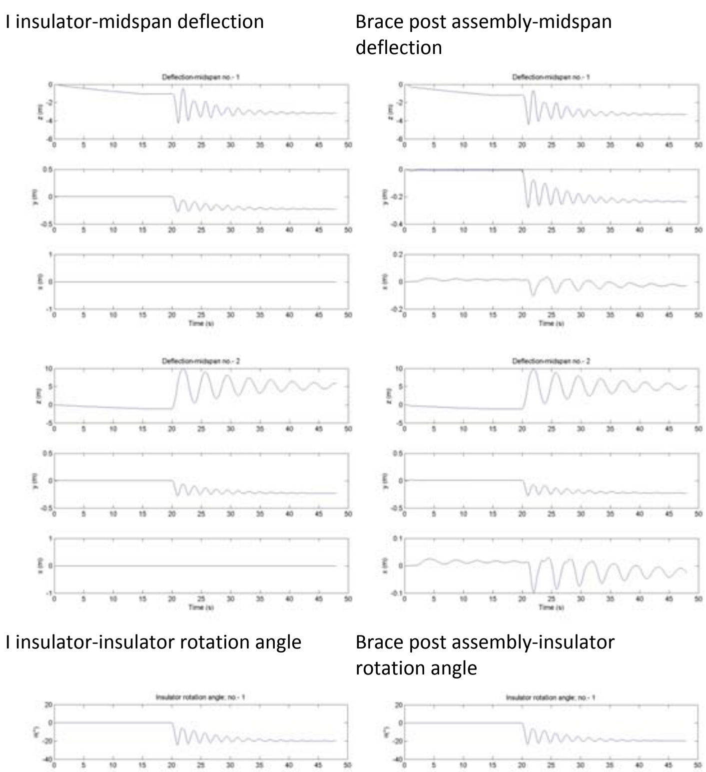

Fig. 7. Time histories of response in case 1 (from top: left and right midspan, insulator rotating angle) on left I insulator and on right brace post assembly.

From the practical point of designer, which must reach required safety distances to obstacles in the case two span tension field replacing I with braced post assembly insulator string can be done instantly. The same result we get in the case the insulator string length was increased by 1 m.

The second case 2 we want to present is three span tension field, when right two spans shed. In figure 8 the time histories response for midspan point and insulators are presented. Comparing results, we can observe that first and last span conductor movement is same in both solutions, but middle span in the case of braced post insulator assembly have smaller conductor jump. Also the difference in rotating insulator string on insulator where bare and load cable meet is high and on the other side the difference is small. The conductor discretization was in both cases taken to 40 elements in span. The taken damping ratio was 2% of critical cable damping.

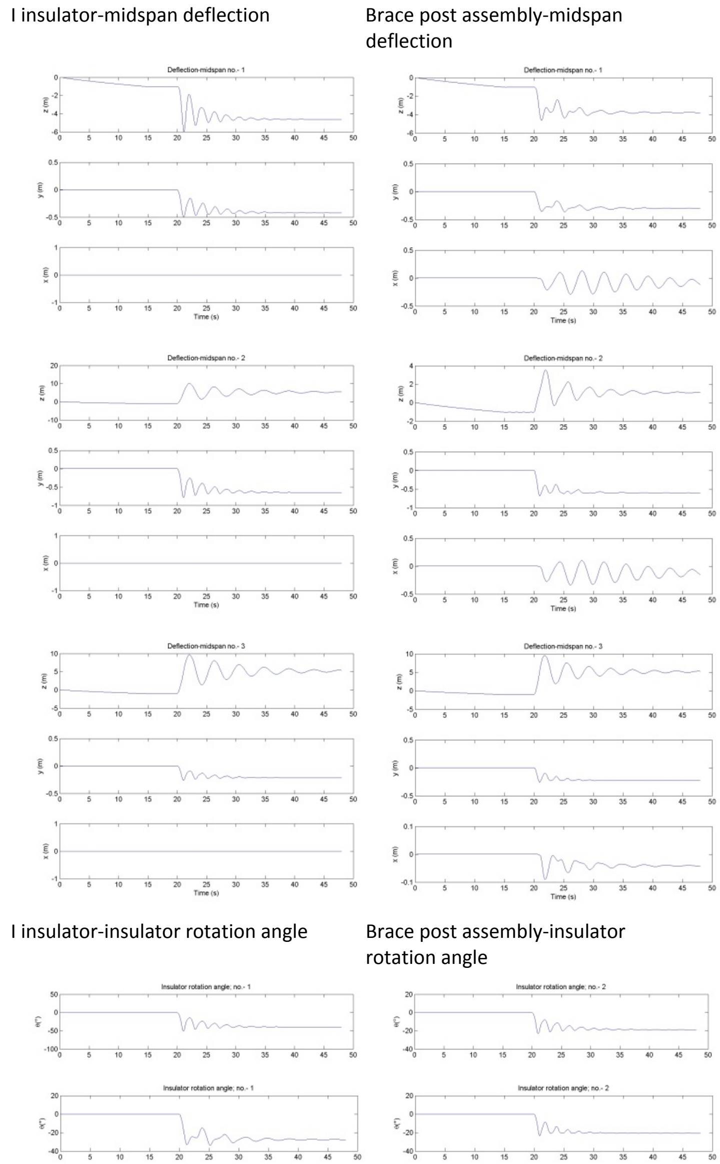

Fig. 8. Time histories of response in case 2 (from top: first, second and third midspan deflection, second and third insulator angle deflection).

The identical simulation was done where half of the tension field was covered by snow accretion. The results show that is no significant difference between I and braced post assembly in that case. The calculated natural frequencies are lover then estimated.

V. CONCLUSION

The numerical model to predict the conductor and insulator dynamic response to snow accretion and shedding was developed. The main goal was to estimate the main differences comparing overhead line with classical I insulator string with the compact rotating brace post insulators.

At this stage of research we can conclude that dynamical response from point satisfying the midspan clearance between conductors and clearance to obstacles is similar in both insulators types when small number of spans is taken.

The model will be in future developed and expanded in the way of accuracy, aero dynamical damping and including wind force act on conductor. Also more research has to be done in the sense of tension field with large number of spans.

REFERENCES

[1] M. R. Fekr,"Dynamic response of overhead lines to ice shedding", Master thesis, McGill University, Montreal, 1995
[2] M. Roshan Fekr, G. McClure, "Numerical modeling of the dynamic response of ice shedding on electrical transmission lines", Proceedings 7-th International workshop on atmospheric icing of structures, 1996, pp. 49-54
[3] P. Williams," Dynamics of a cable with attach sliding mass", ANZIAM J.47 (EMAC 2005) pp. C86-C100, 2006
[4] M.B. Thomas, A.H. Peyrot, " Dynamic response of raptured conductors in transmission lines", IEEE Transactions on power apparatus and systems, Vol. Pas-101, No. 9, 1982, pp 3022-3027.
[5] A.C.Baker et al,"IEEE guide for braced insulator assemblies for overhead transmission lines 0 kV and greater", IEEE Transaction on power delivery, Vol . 23, No 2, 2008, pp 785-791
[6] H.M.Irvine, "Cable structures", The MIT press, 1981

Evaluation of Flashover Voltage of Snow Accreted Insulators for 154 kV Transmission Lines

Hiroya Homma, Kohei Yaji, Teruo Aso, Masato Watanabe, Gaku Sakata
Central Research Institute of Electric Power Industry (CRIEPI)
2-6-1 Nagasaka, Yokosuka, Kanagawa 240-0196, Japan
homma@criepi.denken.or.jp

Andreas Dernfalk and Igor Gutman
STRI AB
Box 707, SE-77180 Ludvika, Sweden

***Abstract* —** In December 2005, Japan experienced a major outage in Niigata Kaetsu area due to a large amount of wet snow mixed with sea-salt accreted on several transmission insulators. To clarify the causes of the snow damage and increase reliability of the networks, a 154 kV class full-scale snow test procedure to be used for evaluation of different insulator designs was developed and artificial flashover voltage tests of snow accreted insulators were carried out. The test procedure consisted of four steps, 1) generation of artificial snow with defined conductivity, 2) accretion of packed snow on the insulator sample, 3) increase of liquid water content of the accreted snow, 4) voltage application. As illustrated by the test results, the target values for wet and packed snow with defined conductivity were reproduced and the effectiveness of the test procedure for the evaluation of flashover properties of 154 kV class insulators was verified. High voltage flashover tests showed that the flashover voltage of both long-rod and cap & pin insulators were decreased with the increase of snow conductivity. Also, cap & pin insulators showed significantly higher flashover voltage than long-rod insulators. Thus, substitution of cap & pin insulators for long-rod insulators seemed to be reasonable as a countermeasure against snow induced flashovers.

***Keywords* —** component; insulator, wet snow, packed snow, sea-salt, flashover

I. INTRODUCTION

In December 2005, Japan experienced a major outage in the Niigata Kaetsu area which lasted for up to 30 hours and was caused by snow accretion on insulators. During the event, porcelain long-rod insulators on several 154 kV and 66 kV lines were completely covered by wet and packed snow of relatively high conductivity. The observed conductivity was attributed to salt transported from the sea by the strong wind. The large amounts of wet snow mixed with the sea-salt reduced insulation strength of the insulator strings and caused flashovers [1].

While extensive research has been performed on the effect of ice accretion and snow covering of insulators on flashover characteristics [2-14], knowledge related to the effect of salt-containing wet snow is very limited, as these conditions are rare [15, 16]. In order to increase the reliability of Japanese networks, CRIEPI initiated a comprehensive project related to the effect of ice and snow on overhead line reliability [17]. Part of this project was to develop a 154 kV class full-scale snow test procedure to be used for evaluation of insulator designs.

As the first step, flashover voltage tests of snow-accreted insulators with controlled snow conductivity, liquid water content, density, etc. were carried out using 33 kV class insulators. The target values for wet and packed snow with defined conductivity were verified on 33 kV insulators. High voltage flashover tests showed that the flashover voltage was comparable to the service voltage for conditions present during the Niigata outage, and the results were also repeatable [18]. Based on these test results, the test procedure was considered feasible for testing of 33 kV insulators covered by wet and packed snow with defined conductivity. The test method was also verified on a preliminary basis for the full-scale 154 kV class insulators of various types and working positions.

This paper discusses the procedures for generation and accretion of wet and packed snow with well defined properties onto 154 kV class insulators in laboratory and the results of the flashover voltage tests.

II. FLASHIOVER VOLTAGE TEST PROCEDURE FOR SNOW-ACCRETED INSULATORS

The proposed test required generating snow with well defined conductivity, density, etc. The target values of the snow parameters were: snowflake size of 0.1-0.2 mm, snow density of 0.5 g/cm^3, liquid water content of 20-30%, and snow conductivity 2 and 7 mS/m, as shown in Table I. The target snow conductivity was the same as observed after the blackout at Niigata Kaetsu in 2005 and continuous field observation at the same geographic region from 2007 to 2011 [19].

The test procedure consisted of four steps, 1) generation of artificial snow with defined conductivity, 2) accretion of packed snow on the insulator, 3) increase of liquid water content of accreted snow, 4) voltage application. A 154 kV class porcelain long-rod insulator and cap & pin suspension insulator string were utilized for the tests. The number of insulator sheds, connection length, creepage distance and total length of both insulators is shown in Table II. All the tests were performed using the test facilities of STRI in Ludvika, Sweden.

TABLE I. TARGET VALUES OF SNOW PARAMETERS.

Parameter	Target value
Size of snowflakes	0.1-0.2 mm

Shape of snow	Cylindrical
Snow density	0.5 g/cm^3 and higher
Liquid water content	20-30%
Snow conductivity	2 and 7 mS/m

TABLE II. SPECIFICATION OF TEST INSULATORS.

Insulator type	Long-rod	Cap & pin
Shed number / profile	21	Anti-fog
Shed diameter [mm]	160	254
Connection length [mm]	1,025	146
Creepage distance [mm]	2,140	430
Number of units	2	13
Total length [mm]	2,050	1,898

A. Artificial Snow Generation

During n snow generation, water with conductivity of 2 or 7 mS/m was sprayed inside a large climatic chamber of 18 m diameter and 23 m height at -9 to -10°C, which generated fine ice particles in the form of artificial snow (Fig. 1). Snowflake size was about 0.1 to 0.2 mm, and the visual appearance was very similar to natural snow. The conductivity of the artificial snow was approximately 1.7 and 8.0 mS/m, as targeted, but the liquid water content was still zero. The collected artificial snow was kept in a storage freezer at -10°C.

B. Accretion of Packed Snow

For the snow accretion and voltage tests, the artificial snow was brought back to the large climate chamber where the temperature was adjusted to about +1°C. The snowflakes were blown onto the insulator by a small handheld vacuum cleaner operating in reversed mode until the snow accreted and filled the gaps between the sheds. The distance between the vacuum cleaner and the insulator was about 500 mm, and the wind velocity at the insulator was approximately 15 m/s.

Fig. 2 shows photographs of insulators with well packed, accreted snow at a density in the range of 0.5-0.6 g/cm^3. Cylindrical snow accretion, as observed in the Niigata case, was achieved by rotating the insulator on a turntable during accretion. Thickness of the accreted snow at the shed surface was about 20 mm for both the long-rod and cap & pin insulators.

For the long-rod insulator, all the shed-to-shed spaces were filled with high density packed snow, and cylindrical snow accretion was complete (Fig. 2a). The cap & pin insulator strings maintained their disk spacing after snow accretion (Fig. 2b).

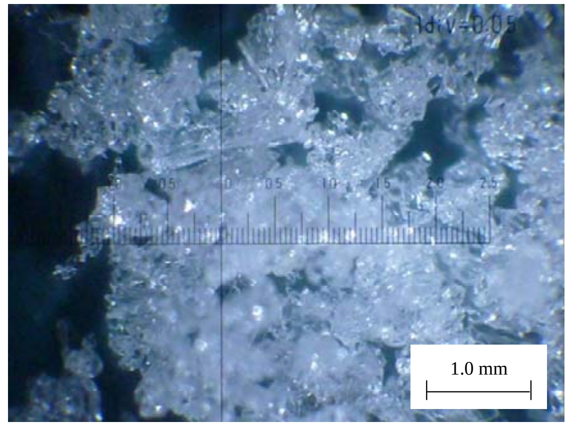

Fig. 1. Appearance of the artificial snow.

C. Increase of Liquid Water Content of Accreted Snow

A certain volume of water with defined conductivity (the same as use for snow creation) was sprayed onto the accreted snow to increase the liquid water content to the range of 20-30%, which resulted in a snow density of 0.7-0.8 g/cm^3. As the result, the target values for wet and packed snow with defined conductivity, density, etc. (Table I) were attained and verified for the 154 kV insulators.

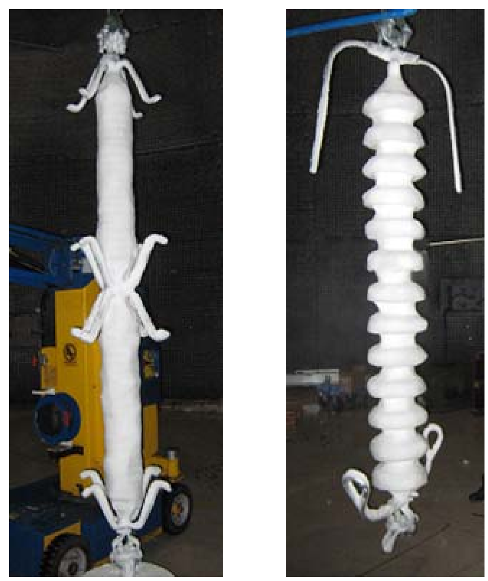

a. Long-rod insulator. b. Cap & pin insulator string.

Fig. 2. Snow accreted insulators.

D. *Flashover Voltage Test*

After spraying the conductivity-adjusted water onto the accreted snow surface, high voltage flashover tests were performed in the same test chamber used to create the samples, but at a temperature in the range of +1 to +2°C using a 250 kVac, 500 kVA test transformer. The applied voltage was increased rapidly up to the desired value at a rate of 3-7 kV/s and thereafter kept constant until the insulator either flashed over or withstood, i.e., when the risk of flashover was deemed negligible based on monitoring of leakage current levels. If flashover occurred at the applied test voltage, the test voltage was decreased about 7% for the next test.

III. Results of Flashover Voltage Tests of 154 kV Class Insulators

Fig. 3 shows the photographs of discharge activity at 134 kV during the voltage tests with the long-rod insulator. Fig. 4 shows the time variation of applied voltage and leakage current observed during the same test. Typically, three phases of flashover process were identified during the voltage test. During the initial period of voltage application, small visible discharges appeared inside the accreted snow, and the leakage current increased with increased applied voltage. A few tens of seconds after voltage application, intensive discharges developed and distributed along the insulator. A number of air gaps were created in the snow as a result of melting, and maximum currents in the range of 100-600 mA were observed. Thereafter, an arc grew along the surface and finally developed into a complete flashover after a few minutes.

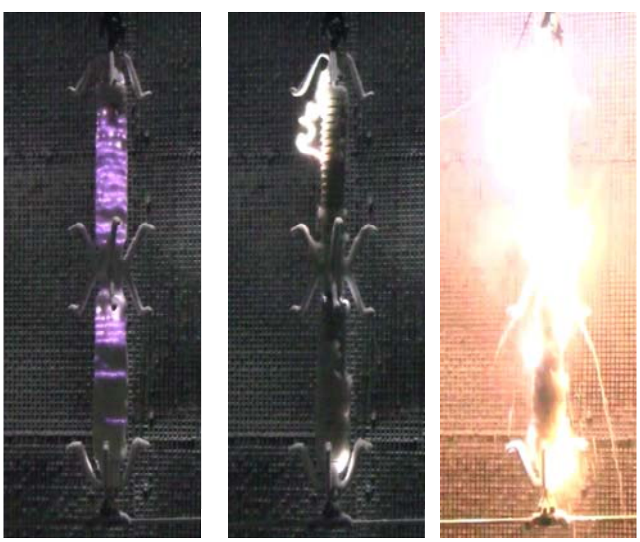

a. Initial period of voltage application. b. Before flashover. c. Flashover

Fig. 3. Photographs of discharge activity during a voltage test with the long-rod insulator.

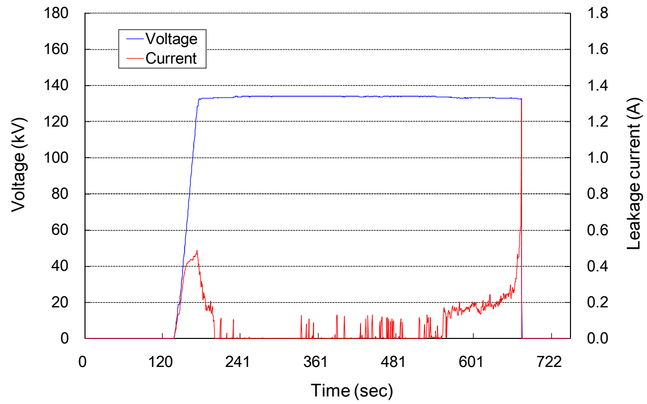

Fig. 4. Time variation of voltage and leakage current during the test.

Fig. 5 shows typical waveforms of the leakage current observed at the initial period and can be seen that the sinusoidal waveform observed during the initial period changed to distorted waveform reflecting the short circuit discharge.

Several flashover voltage tests of the snow accreted 154 kV class long-rod and cap & pin insulators were carried out with the snow conductivity of 1.7 and 8.0 mS/m. In this study, the minimum flashover voltage of an insulator was defined as one voltage step higher than the maximum withstand voltage which the insulator withstood twice.

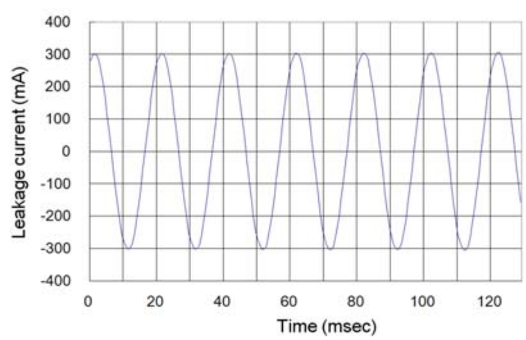

a. Initial period of voltage apply.

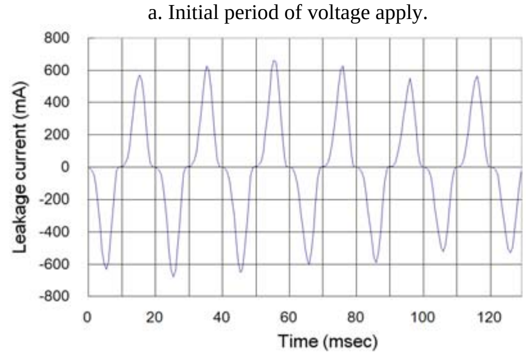

b. Intensive discharge developed.

Fig. 5. Waveforms of leakage current during the test.

Fig. 6 shows the minimum flashover voltage of the snow accreted long-rod and cap & pin insulators. The results showed that the flashover voltage of both long-rod and cap & pin insulators decreased with the increase of snow conductivity. Also, the cap & pin insulators showed significantly higher flashover voltage than the long-rod insulators. Thus, substitution of the cap & pin insulators for the long-rod insulators seem to be reasonable as a countermeasure against snow induced flashovers.

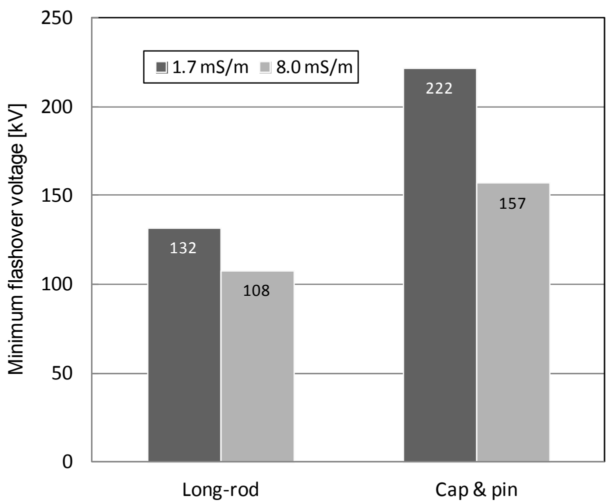

Fig. 6. Results of flashover voltage tests of snow accreted insulators.

IV. Conclusions

Flashover voltage tests of snow-accreted insulators with controlled snow conductivity, liquid water content, density, etc. were carried out using the full-size 154 kV class insulators to develop a test method for transmission class insulators of various designs. The test procedure consisted of four steps, 1) generation of artificial snow with defined properties, 2) accretion and packing of snow on the insulator, 3) increasing the liquid water content of accreted snow in a controlled manner, and 4) AC voltage withstand tests of the snow-accreted insulators. The target values for wet and packed snow with defined conductivity were reached and verified on 154 kV insulators.

The tests data indicate that the flashover voltage of both long-rod and cap & pin insulators decreased with increase snow conductivity. Also, the cap & pin insulators had significantly higher flashover voltage than the long-rod insulators. The flashover voltage of the long-rod insulators with accreted snow of 8.0 mS/m conductivity was comparable to service voltage during the Niigata outage. Thus, substitution of the cap & pin insulators for the long-rod insulators appears to be a reasonable countermeasure against snow induced flashovers.

References

[1] T. Onodera, H. Inukai and T. Odashima, “Overview of Power Outage in the Niigata Kaetsu Area Caused by a Snowstorm”, IWAIS XII, 2007.

[2] CIGRE TF33.04.09, “Influence of Ice and Snow on the Flashover Performance of Outdoor Insulators Part 1: Effects of Ice”, Electra No. 187, Dec. 1999.

[3] CIGRE TF33.04.09, “Influence of Ice and Snow on the Flashover Performance of Outdoor Insulators Part 2: Effects of Snow”, Electra No. 188, Feb. 2000.

[4] M. Farzaneh et al, IEEE Task Force on Insulator Icing Methods, “Selection of station insulators with respect to ice and snow – Part 1: Technical context and environmental exposure”, IEEE Transactions on Power Delivery, Vol. 20, No. 1, pp. 264-270, 2005.

[5] M. Farzaneh et al, IEEE Task Force on Insulator Icing Methods, “Selection of station insulators with respect to ice and snow – Part 2: Methods of selection and options for mitigation”, IEEE Transactions on Power Delivery, Vol. 20, No. 1, pp. 271-277, 2005.

[6] M. Farzaneh et al, IEEE Task Force on Icing Performance of Line Insulators, “Selection of line insulators with respect to ice and snow – Part 1: Context and stresses”, IEEE Transactions on Power Delivery, Vol. 22, No. 4, pp. 2289-2296, 2007.

[7] M. Farzaneh et al, IEEE Task Force on Icing Performance of Line Insulators, “Selection of line insulators with respect to ice and snow – Part 2: Selection methods and mitigation options”, IEEE Trans. on Power Delivery, Vol. 22, No. 4, pp. 2297-2304, 2007.

[8] R. Harting and S. M. Fikke, “The Performance of Vertically Installed Insulator Strings under Ice and Snow Condition”, IWAIS VIII, 1998.

[9] I. Gutman, K. Halsan and D. Hubinette, “Application of Ice Progressive Stress Method for Selection of Difference Insulation Options”, International Symposium on High Voltage (ISH), 2003.

[10] S. M. Berlijn, I. Gutman, K. Å. Halsan, M. Eilersten, I. Y. H. Gu, “Laboratory Tests and Web Based Surveillance to Determine the Ice - and Snow Performance of Insulators”, IEEE Transactions on Dielectrics and Electrical Insulation, Vol. 14, No. 6, pp. 1373-1380, 2007.

[11] Y. Watanabe, “Flashover Tests of Insulators Covered with Ice or Snow”, IEEE Transactions on Power Apparatus and Systems, Vol. 97, No. 5, pp. 1788-1794, 1978.

[12] T. Fujimura, K. Naito, Y. Hasegawa and T. Kawaguchi, “Performance of Insulators Covered with Snow or Ice”, IEEE Transactions on Power Apparatus and Systems, Vol. 98, No. 5, pp. 1621-1631, 1979.

[13] M. Yasui, K. Naito and Y. Hasegawa, “AC Withstand Voltage Characteristics of Insulator String Covered with Snow”, IEEE Transactions on Power Delivery, Vol. 3, No. 2, pp. 828-838, 1988.

[14] H. Wieck, I. Gutman, T. Ohnstad: “Investigation of Flashover Performance of Snow-covered Breakers, IEEE Trans. on Dielectrics and Electrical Insulation, Vol. 14, No. 6, Dec. 2007, p.p. 1339-1346

[15] S. M. Fikke, T.M. Ohnstad, H. Forster and L. Rolfseng, “Effect of Long Range Airborne Pollution on Outdoor Insulation”, Nordic Insulation Symposium, pp. 103-112, 1994.

[16] N. Sugawara and K. Hosono, “ Insulation properties of long rod and line post insulators for 33 kV transmission line in wet-snow storm on January 2004”, IWAIS XI, 2005.

[17] H. Homma, K. Yaji, T. Aso and G. Sakata, “Snow Accretion Properties of Various Insulators Exposed to an Artificial Wet Snow Accretion Test”, IWAIS XIII, 2009.

[18] H. Homma, K. Yaji, G. Sakata, T. Aso, A. Dernfalk and I. Gutman, “Development of Withstand Voltage Test Method for Snow Accreted Insulators – Preliminary Test with 33 kV Class Insulator Samples -”, IWAIS XIV, 2011.

[19] H. Homma, K. Yaji, T. Aso, M. Watanabe and G. Sakata, “Evaluation on Flashover Voltage Property of Snow Accreted Insulators for Transmission Lines, Part I – Full-scale Flashover Voltage Tests of Snow Accreted Insulators, Simulating Wet and Packed Snow Mixed with Sea-salt -”, CRIEPI Report, No. H11018, 2012. (in Japanese)

Summarizing knowledge from laboratory ice and snow tests on glass and composite insulators for overhead lines

Sonja Berlijn, Kjell Halsan, Igor Gutman*
Statnett, Oslo, Norway; *STRI, Ludvika, Sweden E-mail: Sonja.Berlijn@statnett.no

Abstract **—** This paper summarizes practical experience with ice testing performed at STRI on behalf of Statnett and SvK. for more than decade. Also the results obtained by snow test method developed by CRIEPI (Japan) in collaboration with STRI are discussed. Practical, representative and repeatable test methods were applied for different glass, porcelain, and RTV-coated and composite insulators. The intention was to provide flashover performance curves directly applicable for the Line Performance Estimator software program. This program is used by Statnett on a regular basis for the insulation coordination of the upgrading of 1500 km overhead lines from 300 kV to 420 kV. Examples of how the laboratory-obtained data was used in practice are given in the paper.

Keywords — insulator; ice test; snow test; statistical dimensioning

I. INTRODUCTION

The demand for new transmission capacity on a relatively short notice is very high in Norway. The main reasons are the change of power flow within the country and the increasing power consumption. Since there is public resistance against new overhead power lines and since it takes a long time to get permission to build new lines, Statnett has decided to upgrade a major portion of the 300 kV lines to 420 kV (approximately 1500 km) [1]. In general, uprating of 300 kV lines to 420 kV will enhance the power capacity of the lines significant, with a relatively low visual impact.

When voltage upgrading, the tower top clearances must be utilized in an optimum way since available air clearances are quite limited. Furthermore, the upgrading process is very complex since, due to complicated topography, basically every tower needs to be engineered individually. Because of this, the need for a more accurate and statistical method arose that would give maximum design flexibility in the upgrading proposal. Therefore, the final verification of the insulation performance is made by statistical insulation coordination using the specialized software program Line Performance Estimator (LPE) [1], [2] developed by STRI on behalf of Statnett and SvK. The LPE program allows import of tower top clearance data from the line design software (PLS CADD). The main requirement from Statnett is that the upgraded line should have similar fault rate as before uprating **Feil! Fant ikke referansekilden.**. The principle of the statistical coordination is shown Figure 1. The stress parameters, i.e. pollution stress in ESDD and ice stress in conductivity of ice/snow are obtained though pollution or ice monitoring respectively, in service. The strength parameters, i.e. flashover performance curves from the pollution and ice tests are obtained through laboratory tests. These stress/strength parameters are further used for calculating the risk for flashovers using statistical characterisation of pollution and icing conditions.

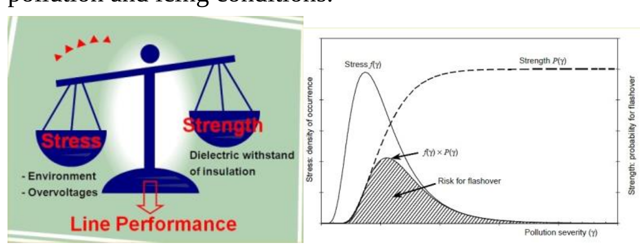

Figure 1 Principles of coordination according to IEC 60815-1 for pollution (similar approach for ice and snow).

Two typical Norwegian environmental issues, i.e. pollution and ice/snow are important for Statnett while dimensioning insulators.

This article summarizes the results of the development of ice/snow tests and the practical results obtained (about 20 tests during latest 10 years). Examples of the practical implementation of the flashover performance data into the LPE program are also provided.

II. DEVELOPMENT OF ICE TESTS

The ice testing has to be performed in representative environmental conditions to find the optimal insulator type, profile and length for the uprate of 300 kV lines. Typical environmental conditions in Norway that effect the insulation are areas with icing influenced by light pollution of sea origin which can be however transported rather far from the coast and make the ice/snow salty and conductive (see Figure 2).

Figure 2 Illustration of ice environment at Statnett.

Thus the Ice Progressive Stress (IPS) test method has been developed at STRI with support from Statnett and it was presented for the first time at IWAIS-2002 [3]. The IPS test consists, similar to other ice tests, of two typical phases: 1) ice deposition under service voltage, 2) flashover performance evaluation by increase of the test voltage up to flashover. Based on the results of this test the 50% flashover voltage can be estimated. Therefore the results from a progressive test will provide more information than a withstand test. In addition the progressive stress test gives similar results as the up-and-down method, but is much faster and cheaper than other tests as it accounts for the parallel testing of insulators [4], see Figure 3.

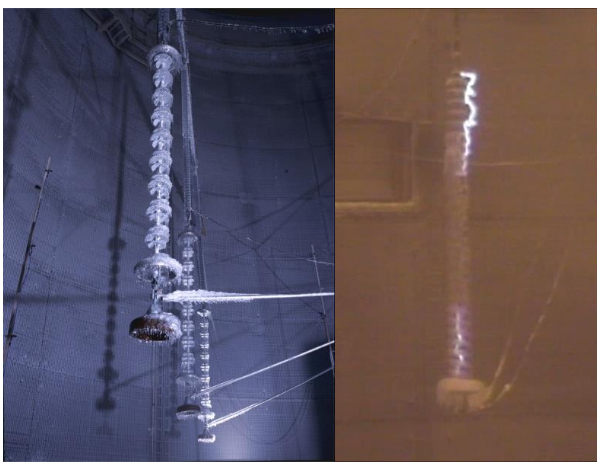

Figure 3 To the left: Set-up for the Ice Progressive Stress (IPS) test. To the right: Flashover during the flashover phase.

Since the comprehensive ice testing on full-scale insulators at operating voltage normally takes several weeks to perform, a reduction in use of laboratory time will give substantial economical savings.

The IPS test was used with success in a number of projects confirming its repeatability [4]-[6] and was finally included in the IEEE Guide for ice test methods and procedures [7], the only international guide existing at present (no CIGRE/IEC guides or standards are available). Since then, the IPS method was used not only for the investigations for Statnett in Norway, but also for specific ice tests for Japan [8], Island [9] and Russia [10].

III. DEVELOPMENT OF SNOW TESTS

This type of test was developed by CRIEPI in Japan [11]-[12] with the participation of STRI and the test method was applied for Statnett investigations. The driving force for the development of this method was the climatic event in December 2005, when Japan experienced a major outage in the Niigata Kaetsu area which lasted for up to 30 hours and was caused by snow accretion on insulators. During the event, porcelain long-rod insulators on several 154 kV and 66 kV lines were completely covered by wet and packed snow of relatively high conductivity. The observed snow parameters were explained by salt transported from the sea by the strong wind. The large amounts of wet snow mixed with the sea-salt reduced insulation strength of the insulator strings and caused flashovers [11]-[12]. Based on careful field investigations performed by CRIEPI the test method was developed and verified at STRI. The test simulates snow with defined density, conductivity and liquid water content. The test procedure comprises four steps: 1) generation of artificial snow with defined conductivity; 2) accretion of packed snow on the insulator; 3) increase of liquid water content of accreted snow; 4) voltage application [12]. The accretion of snow on Statnett insulators is shown in Figure 4 (left) and control of conductivity is illustrated in Figure 4 (right).

Figure 4 Illustration of different phases of the wet snow test method: left – snow accretion; right – control of conductivity.

IV. PRACTICAL RESULTS FROM ICE TESTS

Since the development of the IPS test method, Statnett performed at STRI about 20 tests, which includes the investigation of the following insulator types, which were tested full-scale for 420 kV voltage class (some of the test objects are shown in Figure 5):

- Glass cap-and-pin insulators of standard profile from two different manufacturers
- Porcelain cap-and-pin insulators standard profile
- Combinations of insulators of standard - and aerodynamic profile in the same string (two different combinations)
- Two different lengths of composite longrod insulators of a certain manufacturer
- Composite longrod insulator of another manufacturer with the same length, but three different profiles

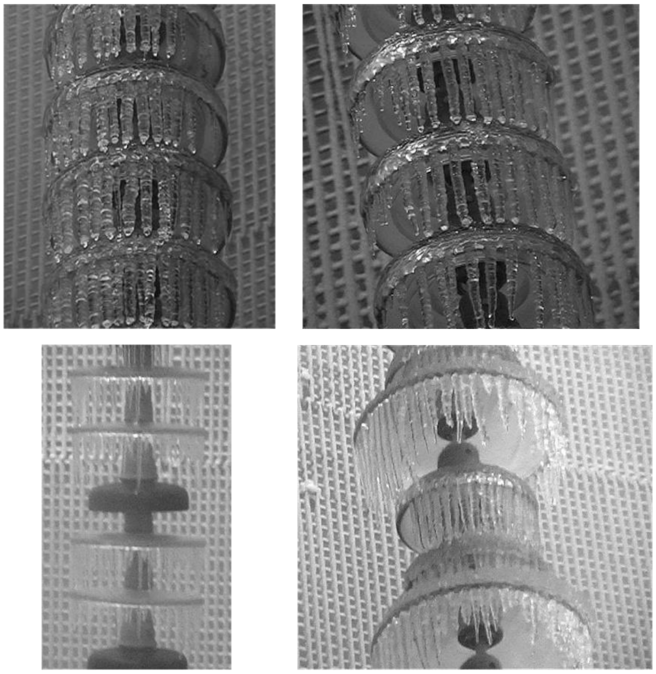

Figure 5 Examples of different strings of cap-and-pin insulators tested by the IPS method: top – excellent repeatability in testing of the same insulator with 1 month interval; bottom – examples of different combinations to increase anti-ice performance.

This comprehensive testing of full-scale 420 kV insulators by IPS ice tests has led to the following practical results:

- Generally the IPS test method is applicable for full scale testing of 420 kV insulators, is repeatable, fast and cost effective and therefore is considered as a preferable method.
- Composite insulators of standard profile perform inferior to glass and porcelain cap-and-pin insulators due to different spacing, the results are presented in Figure 6.
- Using the IPS test method the design curves for the three composite insulator profiles intended for the ice areas, see Figure 7, were created and are directly applicable for use in the LPE software program.
- Glass, porcelain as well as composite insulators with longer shed spacing will increase ice accretion time needed to reach condition of maximum bridging
- Combination of glass insulators with different diameters in one string is effective countermeasure against ice, see Figure 5.
- The time to total bridging over the insulator string seems to be a critical parameter for the flashover results
- For high conductivity there is no general and clear trend indicating which of the three tested composite insulator gives the highest flashover performance for both long (5 h) and short (3 h) ice accretion times. (Figure 8). No significant advantages in performance were found for the “ice-breaker design compared to insulators with alternating and standard profile. There is an indication indication that the alternating profile may perform better than the other profiles, as it performs better for low conductivity.
- The IPS test method is directly applicable to simulate freezing rain service conditions and is even applicable for the evaluation of sunrise service conditions

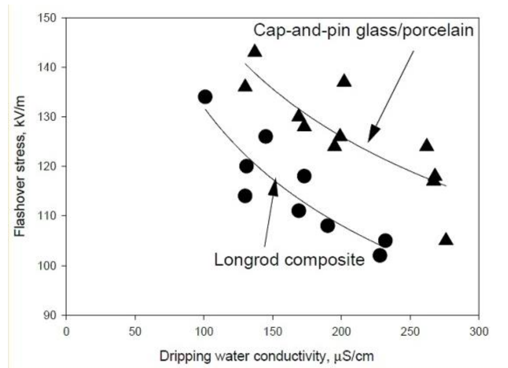

Figure 6 Comparative flashover results of 420 kV cap-and-pin glass/porcelain and longrod composite insulators over dripping water conductivity.

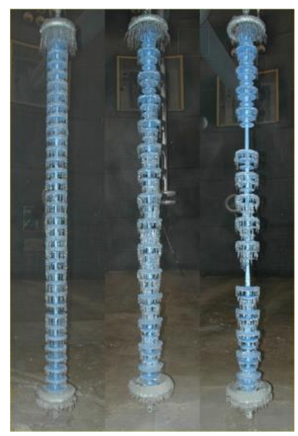

Figure 7 Composite insulators with 3 different profiles (standard, alternating, ice-breaker) tested by IPS method.

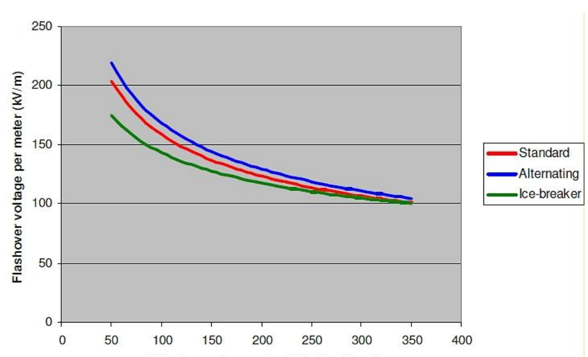

Figure 8 Comparative flashover results of 420 kV longrod composite insulators as a function of the dripping water conductivity.

V. PRACTICAL RESULTS FROM SNOW TESTS

The results of snow tests were obtained very recently. The test objects were glass cap-and-pin insulator and RTV-coated glass cap-and-pin insulators of standard profile. They were tested in the strings of the total length of approximately 1,4 m. The flashover performance of the insulators is presented in Figure 9 as flashover stress ($E_H=U_{FO}/H_{ins}$) along the insulation length (H_{ins}) as function of the conductivity. Trying to minimize the number of tests to obtain valuable data, a reduced multiple level test procedure was performed, thus the flashover voltage was estimated as the level half between the highest withstand voltage level and the first flashover level. The test results show that there is no significant difference between un-coated glass insulators and RTV-coated insulators in flashover performance. The data provided can be used as a direct input in the LPE program.

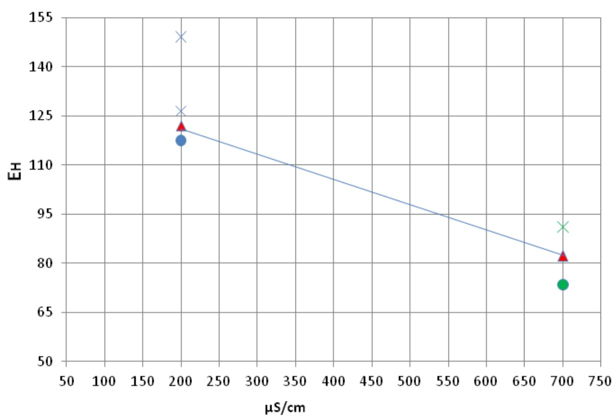

Figure 9 Voltage stress as a function of the snow conductivity of RTV coated cap-and-pin glass insulator.

VI. THE NEED FOR ICE TESTING AND LINE PERFORMANCE ESTIMATION

Ice and snow outages can cause outages of long durations. These should be prevented as much as possible. It is therefore important to investigate a) which type of insulator string and material is advantageous to use in areas with high ice loads b) what the flashover performance of the insulators are to be able to calculate the length needed and compare insulator types and to c) estimate the line performance of the line.

Therefore it was needed to develop a method for ice testing that made it possible to compare the performance of insulators for icing conditions. Further this method should allow to determine the 50% flashover voltages, so that the results could be used for insulation coordination (both deterministic and statistic) and for the line performance estimations. The developed methods and the results obtained are presented in the previous paragraphs.

Insulation coordination is an important part of the work when designing new lines and when working with voltage upgrading. When performing insulation co-ordination different aspects have to be taken into account as for example, the pollution performance, the lightning performance, the snow and ice performance and the switching performance. The difficulty is to choose an insulator (type and length) that gives good results when looking at the whole picture. Sometimes, for instance when regarding pollution, composite insulators will be beneficial to use, while when regarding ice performance glass insulators will be beneficial to use.

To be able to get a complete overview of which type of insulators and insulator lengths would be the best to use when regarding all aspects, LPE (the Line Performance Estimator program) was developed).

The ice test developed and used, together with the line performance estimator are useful tools for accurate insulation coordination and are used regularly in the voltage upgrading project in Statnett. Two examples of use are presented in the following two chapters.

VII. FIRST EXAMPLE OF LINE PERFORMANCE ESTIMATION USING ICE DATA

The first example of a practical application of ice pollution performance in overhead line performance estimation is a 63 km, 300 kV line comprising 153 suspension towers and 24 tension towers. The line is equipped with a double conductor bundles and two shield wires. The suspension insulator strings, with a striking distance of 2,1 m, are equipped with 14 glass cap-and-pin insulators having a 170 mm unit length and a creepage distance of 380 mm per unit. The actually measured tower footing resistances vary from 6 Ω to 280 Ω, the soil resistivity is assumed as 2000 Ωm, and the average altitude is 290 m. The pollution and ice flashover performance of the insulators were determined through laboratory tests at STRI as functions of salt deposit density and melting water conductivity, respectively. For the statistical insulation coordination, the various stresses on the line insulation are expressed in statistical terms as shown in Table I. The switching overvoltage profile was calculated using an EMTP/ATP model of the line. It should be noted that single-pole reclosing is applied upon single line to ground faults; the decisive switching overvoltage levels on the line are therefore determined by three-phase energization.

Table I. Input data for LPE.

Parameter	Value	Note
Average ground flash density	0,4/km^2/year	lightning statistics 2001-2009
Switching overvoltage profile (2% levels)	Max. 1,83 p.u.	1,40-1,83 p.u. (energization)
Pollution severity (2% level)	0,04 mg/cm^2	10 events/year
Ice severity (2% level)	120 µS/cm	10 events/year

Four different load cases need to be analysed and with the help of the accurate PLS-CADD model it is possible to extract the accurate minimum clearances for these four different load cases: maximum ice load, maximum temperature, 3 year wind and 50 year wind. PLS-CADD® gives accurate minimum clearances from all the phases to the tower. The results are then exported from PLS-CADD® into excel sheets.

The actual data is extracted from PLS CADD® to an Excel® file that is used as input for LPE. This file is then imported into PLS CADD®.

These four checks are done for three cases (A, B and C) and its results are presented in Table II:

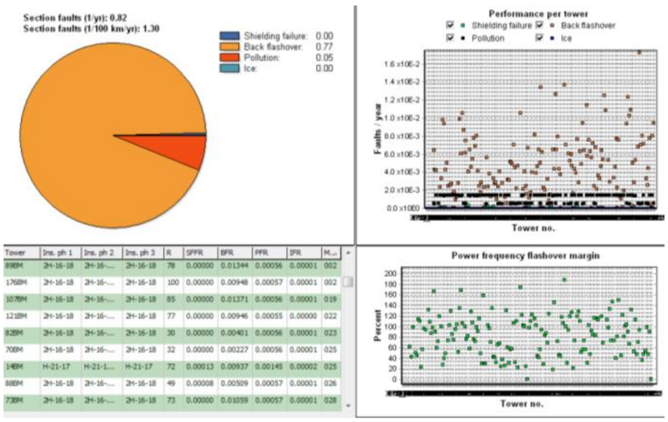

Figure 10 Screenshot from a LPE calculation.

A. Before voltage upgrading, for the line as it is today (operated at 300 kV)

The LPE calculations for the 300 kV line show that the expected lightning flashover rate is 1,5/100 km/yr. The calculated pollution flashover rate is 0,01/100 km/yr, while the icing flashover rate is practically zero. Switching flashovers do not occur for 3-year wind, and the power frequency flashover margin is 122% for 50-year wind. These results completely agree with service records for a 20-year period (1,1/100 km/yr; only lightning outages).

B. Upgraded line with increased number of insulators of the same type (operated at 420 kV)

LPE calculations for the upgraded line (service voltage 420 kV and number of insulators increased from 14 to 17 units) show that the expected lightning flashover rate is reduced to 1,2/100 km/yr, while the insulator icing flashover rate is still practically zero. The calculated pollution flashover rate increases to 0,08/100 km/yr. These results indicate that the increased service voltage is well compensated by the longer insulator strings as far as lightning or ice performance is concerned, but not with regard to pollution performance. The calculated switching flashover rate increases to 0,12 per switching event due to increased overvoltage levels and reduced clearances for 3-year wind, while the power frequency flashover margin for 50-year wind is reduced to about 2%. These results agree well with the violations of air clearances and show the need for modification of some of the insulator strings.

C. Upgraded line with increased number of insulators of the modified type (operated at 420 kV)

Since the general switching performance and the power frequency flashover margin presented above were considered as unacceptable, the tower-by-tower information provided by LPE regarding insulation performance was used to identify specific problematic towers. It was found that the inferior performance could be attributed to roughly only 5 out of 153 suspension towers (see screenshots from LPE in Figure 11).

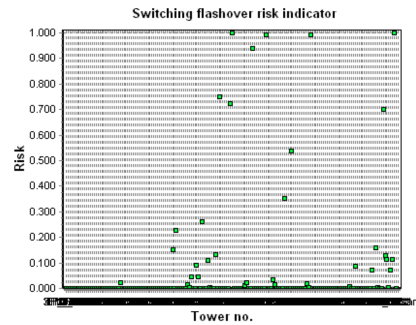

Figure 11 Tower by tower information provided by LPE

Through modification of the critical insulators, e.g., by using 16 instead of 17 units in the center phase, or by introducing supporting insulators for reduction of swing angle, it was possible to improve the switching flashover rate to 0,001 per switching event, and the power frequency flashover margin to 22%. At the same time, the lightning and pollution flashover rates were changed marginally to 1,1/100 km/yr and 0,09/100 km/yr, respectively.

Table II. Results from LPE calculations.

Results	A	B	C
Lightning flashover (1/100 km/yr)	1,5	1,2	1,1
Pollution flashover (1/100 km/yr)	0,01	0,08	0,09
Ice flashover (1/100 km/yr)	0,00	0,00	0,00
Switching (1/event)	0,000	0,12	0,001
Power frequency flashover margin (%)	122	2	22

VIII. SECOND EXAMPLE OF LINE PERFORMANCE ESTIMATION USING ICE DATA

For a short section (8,5 km) of an overhead line, a calculation was made to estimate the expected number of outages for just one load case. The overhead line had two ground wires and had a simplex conductor configuration. The phases were horizontally arranged. The flashover length of the I-strings was 1,82 m for the 14 disc configuration. Other relevant data is presented in Table III.

The reason for the investigation was to find the difference in performance for 14 and 15 insulator discs in the chain.

As can be seen in Figure 12 and Figure 13, the expected outage rate for 14 discs was 1,62, or better 2 outages per year and for 15 0,82, or better 1 outage per year on this particular section. For the 14 disc configuration around 55% of the outages are caused by pollution or ice and 45% by lightning. When extending the insulator string from 14 to 15 discs the number of outages caused by ice are reduced from around 10% to around 7%.

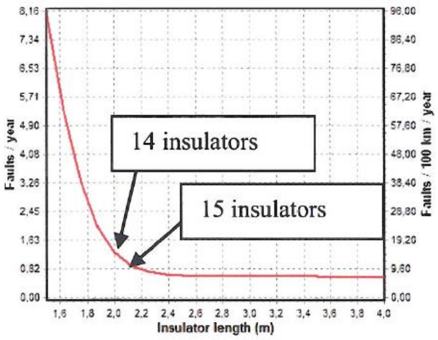

Figure 12 Number of fault as function of the insulator length

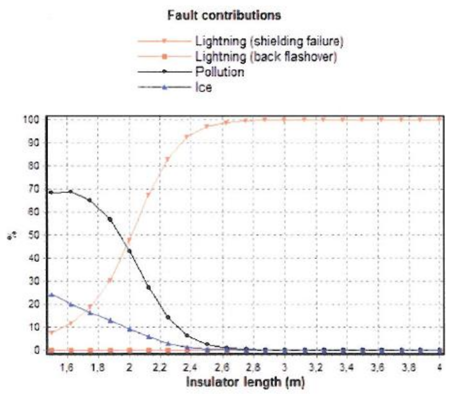

Figure 13 Contribution in % for the different fault causes as function of the insulator length

Table III. Input data for LPE.

Parameter	Value	Note
Average ground flash density	0,6/km^2/year	lightning statistics 2001-2009
Soil resistivity	1000 Ohm	
Footing resistance	27 Ohm	
Pollution severity (2% level)	0,1 mg/cm^2	10 events/year
Ice severity (2% level)	100 µS/cm	10 events/year

IX. SUMMARY

This paper summarizes practical experience with and the results from ice and snow testing performed for more than decade. The described Ice Progressive Stress test method has been included in IEEE Standard.

Tests have been performed on different glass, porcelain, RTV-coated and composite insulators, most of them were tested full-scale for 420 kV voltage class. Tests results provide flashover performance curves directly applicable for the Line Performance Estimator software, used regularly in the voltage upgrading project, and compare the performance of different insulators. Two examples of LPE calculations are given in this paper.

The test results showed that, for icing conditions, composite insulators of standard profile perform inferior to glass and porcelain cap and pin insulators. Combination of glass insulators with different diameters in one string is an effective counter measure against icing. However, no significant advantages in performance are found for the 'ice breaker' design compared to composite insulators with alternative and standard profile. RTV-coating is not an effective measure when trying to increase the snow performance.

X. REFERENCES

[1] S. Berlijn, K. Halsan, R. I. Jonsdottir, J. Lundquist, I. Gutman, K. Kupitz: "Voltage Uprating of Statnett's 300 kV Transmission Lines to 420 kV", CIGRE-2012, B2-102

[2] I. Gutman, J. Lundquist: "Optimization of AC and DC Insulation Using Software for Statistical Dimensioning", World Congress & Exhibition on Insulators, Arresters & Bushings, Seoul, Korea, 17-20 April 2011

[3] I. Gutman, S. Berlijn, S. Fikke, K. Halsan: "Development of the Ice Progressive Stress Method applicable for the full-scale testing of 420 kV class overhead line insulators", IWAIS 2002, The Tenth International Workshop on Atmospheric Icing of Structures, Brno, Czech Republic, 17-20 June, 2002, paper 6-3

[4] I. Gutman, K. Halsan, D. Hübinette: "Application of Ice Progressive Stress method for selection of different insulation options", ISH-2003, Netherlands 2003, Smit (ed.), 2003 Millpress, Rotterdam, ISBN 90-77017-79-8, p. 179

[5] I. Gutman, K. Halsan, D. Hübinette, T. Ohnstad: "Ice Progressive Stress Method: Repeatability During Full-Scale Testing of 400 kV Line and Apparatus Insulators and Application of the Test Results", Conference Record of the 2004 IEEE International Symposium on Electrical Insulation, Indianapolis, IN USA, 19-22 September 2004, p.p. 560-563

[6] S.M. Berlijn, I. Gutman, K.Å. Halsan, M. Eilersten, I.Y.H. Gu: "Laboratory Tests and Web Based Surveillance to Determine the Ice- and Snow Performance of Insulators", IEEE Transactions on Dielectrics and Electrical Insulation, Vol. 14, No. 6, December 2007, p.p. 1373-1380

[7] M. Farzaneh et al.: "IEEE Guide for Test Methods and Procedures to Evaluate the Electrical Performance of Insulators in Freezing Conditions", IEEE Std 1783TM-2009, 17 October 2009

[8] I. Gutman, A. Dernfalk, K. Halsan, S. Berlijn, L. Carlshem, M. Uehara, J. Seifert: "Optimization of profiles of line composite insulators intended for ice environment, IWAIS-2009, Andermatt, Switzerland, 8-11 September, 2009, paper PO.002

[9] I. Gutman, J. Lundengård, N. Gustavsson, A. Bosma: "Comparative Performance of Hollow Silicone Rubber and Porcelain Apparatus Insulators under Specific Ice and Salt Fog Conditions of Iceland", IWAIS-2009, Chongqing, China, 8-13 May, 2011, paper P1_01_ID8

[10] I. Gutman, G. Porporkin: "Comparative Performance of Conventional 220 kV Insulator Strings and Multi-Chamber Insulator-Arresters Strings Under Specific Ice Conditions of Russia", IWAIS-2009, Chongqing, China, 8-13 May, 2011, C1_1_ID9

[11] H. Homma, K. Yaji, G. Sakata, T. Aso, A. Dernfalk, I. Gutman: "Development of Flashover Voltage Test Method for Snow Accreted Insulators - Preliminary Test with 33 kV Class Insulator Samples", IWAIS-2009, Chongqing, China, 8-13 May, 2011, paper C2_1_ID26

[12] H. Homma, K. Yaji, T. Aso, M. Watanabe, G. Sakata, A. Dernfalk, I. Gutman: "Evaluation of Flashover Voltage of Snow Accreted Insulators for 154 kV Transmission Lines", IWAIS-2013, (submitted)

Session 5: Icing Climate and Icing Forecasting

Forecasting of Icing Events and Icing Accumulation on a Test Transmission Line at Hawke Hill, Newfoundland and Labrador

William Henson
Environment & Infrastructure
AMEC
Ottawa, ON, Canada

David Bryan
Environment & Infrastructure
AMEC
St. John's, NL, Canada

Asim Haldar
Research and Development
Nalcor Energy
St. John's, NL, Canada

Michael Abbott
Environment & Infrastructure
AMEC
St. John's, NF, Canada

Jerry English & Karl Tuff
C-CORE
St. John's, NL, Canada

***Abstract* —** The island of Newfoundland, given its relatively high latitude and marine location, is noted as a location that receives frequent freezing rain events [1]. The frequent icing conditions and the remote nature of much of Newfoundland present challenges for electrical transmission lines and other infrastructure. To mitigate the risk of damage due to ice loading, it is desirable to model the meteorological conditions under which icing may occur, predict the amount of ice accumulation and estimate the ice load on transmission line cables.

In order to address this issue, Newfoundland and Labrador Hydro (NLH) set up a test site at Hawke Hill, Newfoundland in the early 1990's. A suite of instruments were deployed with the aim of observing meteorological conditions with a focus on icing events. Hawke Hill also resides within radar coverage of the Environment Canada's Holyrood radar. AMEC used the observation data and a combination of Numerical Weather Prediction models, icing models and probabilistic models to provide a forecasting system for the Hawke Hill site. AMEC was then asked to perform a blind forecast for two periods in the winter of 2012-2013 during which icing was known to have occurred. An overview of these events and the results of the forecast, as well as some of the challenges that were faced, will be presented.

I. Introduction

The purpose of a long-term ice monitoring program is twofold. First, the program is to predict the design wind and ice loads on overhead lines with an adequate confidence level. Second, the program is to update the loading information on existing lines to ensure that the management of these lines is done in a manner such that the forced outages due to combined wind and ice overloading can be minimized. The remote monitoring will also provide long-term, trend-line data which can be used by NLH to make decisions on future upgrading and/or up-rating of lines in a more proactive manner. It may also help NLH to avoid a major system failure in the future. The real-time monitoring data can be brought directly to the NLH's Energy Control Center (ECC) via networking and can also provide an alarm to the system operator based on specific design threshold levels set into the system for various regions.

In the early 90's, NLH developed the Hawke Hill test site (Fig. 1) to monitor long term wind and ice loads on a non-energized single phase line built to 230 kV standard. The test site is 35 km west of the St. John's International Airport and is located 275 m above mean sea level. The main objective was to study the occurrence of the glaze icing phenomenon and to validate various ice accretion models under freezing precipitation conditions using long term field data. The site consists of one suspension steel lattice tower (guyed-V) to support the phase conductor and two single guyed wood pole dead end structures to terminate the conductor. The two spans are approximately 214 m in length and the central tower supports a single phase conductor with a 28 mm diameter [2].

The objective of this paper is to analyze two significant icing events that occurred in January and February/March of 2013 at the Hawke Hill test site near St. John's, Newfoundland.

This paper is organized as follows. The datasets and instrumentation is described in Section II. The AMEC model is described in Section III. In Section IV, the results are analyzed and discussed and finally summarized in Section V.

II. Datasets and Instrumentation

The Hawke Hill test site (Fig. 1 and Table 1) was specifically designed to serve as an instrumented monitoring station to continuously record: wind speed, wind direction, temperature, precipitation, ice accretion rate using ice detector, horizontal

and vertical loads at the insulator attachment point, swing angles in both directions and end tension in the cable. The site is also equipped with a Remote Ice Growth Detector (RIGD) which is situated 1.5 m above the ground level and is made of a 25.4 mm diameter aluminum hollow pipe, one meter long and uses three strain gauges to monitor the ice load (Fig. 2).

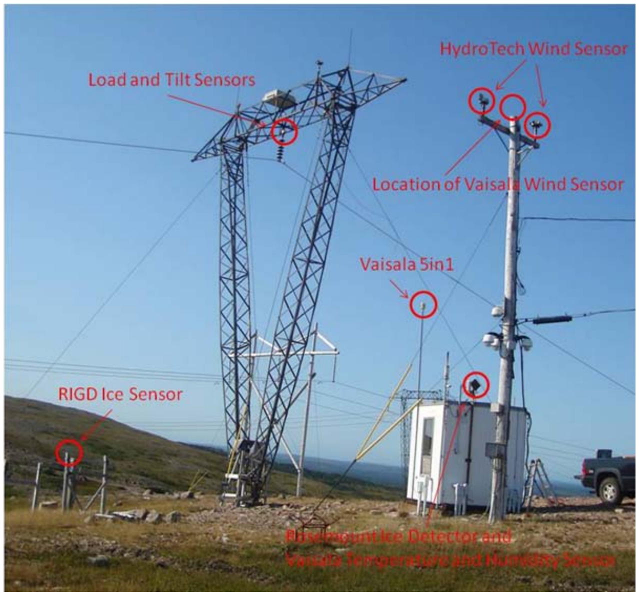

Fig. 1. Photograph of the Hawke Hill test site.

The test site also has an ice detector which provides the accumulated ice mass based on frequency shift. The initial rest frequency is set as 40 kHz and a 500 Hz shift in frequency is used to estimate a predetermined amount of ice accretion with known thickness. As soon as this frequency is reached, the heater is activated to de-ice the sensor. A new cycle begins, and the probe starts accumulating ice. A frequency time history during the March 31, 2007 storm event is shown in Fig. 3 and the accumulated ice on RIGD beam in Fig. 2. The frequency time history can be used to estimate the cumulative mass on the probe. This icing mass can also be used to calibrate against the conductor load based on a long term data.

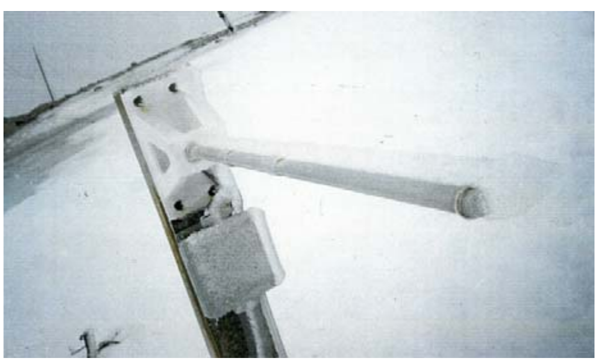

Fig. 2. RIGD Beam with Accreted Ice, March 31, 2007 (Haldar, 2007)

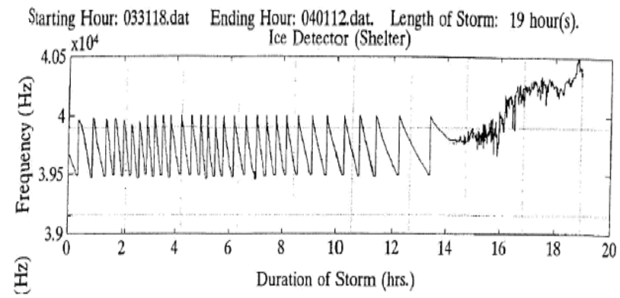

Figure 3 Frequency response time history during March 31, 1997 storm (Haldar, 2007)

III. MODELING

AMEC uses the Weather Research and Forecasting (WRF) Model on an operational basis as part of its forecasting products. The WRF model is a next-generation mesoscale numeric weather prediction system designed to serve both operational and atmospheric research needs. In this work, WRF version ARW 3.2 was used. The initial and boundary conditions were provided by National Centers for Environmental Prediction (NCEP) Global Forecast System (GFS) analyses at 0.5 degree resolution every 6 hours. The sea-surface temperatures were obtained from the daily NCEP SST analysis.

Table 1. List of Sensors Installed at Hawke Hill, NL.

Datalogger	Sensor	Parameter(s) Measured
Campbell Scientific	RIGD	Ice Thickness
	Rosemount Model 0872E3 Ice Detector	Ice Accumulation
	Vaisala Model RG13H	Precipitation
	Geneq Model P1500	Precipitation
	HydroTech Model WS-3	Wind Speed and Direction
	Vaisala Model WMT700	Wind Speed and Direction
	Vaisala Model HMP155	Temperature and Relative Humidity
	Vaisala Model WXT-510	Wind Speed and Direction Temperature and Relative Humidity Barometric Pressure Precipitation
Weir-Jones	10 KIP Load Cell	Conductor Weight
	30 KIP Load Cell	Conductor Tension
	Tilt Sensor	Longitudinal Conductor Motion
	Tilt Sensor	Transverse Conductor Motion

Three two-way nested domains with respective horizontal resolutions of 9, 3 and 1 km, and 51 vertical levels were used, 17 below $\sigma = 0.9$ and 25 below $\sigma = 0.7$. A time step of 54 seconds and a model spin-up of 6 hours were used.

Two turbulent kinetic energy (TKE) planetary boundary layer (PBL) parameterizations were chosen for this study: Quasi-Normal Scale Elimination (QNSE) and Mellor-Yamada-Nakanishi-Niino Level 2.5 (MYNN). These PBL parameterizations have been chosen among others because TKE closure schemes have been demonstrated to be better at simulating cases dominated by stable conditions [3], conditions that were expected during these icing events. Both PBL parameterizations operated in concert with the WRF Single-Moment 5-class microphysics scheme which provides ice and snow processes suitable for mesoscale grid sizes while allowing for mixed-phase processes and super-cooled water. More information regarding the WRF Model can be found in [4].

AMEC combines the two WRF models described above, to create an ensemble model which provides a more accurate overall prediction of the meteorological conditions. Each WRF model has different physics settings, including different planetary boundary layer (PBL) parameterizations. AMEC's experience has concluded that specific meteorological parameters are more accurately modeled with different physics settings. Combining models in an ensemble forecast provides a better prediction than any individual model.

There are several well-known characteristics with WRF model forecasts; two of primary interest involve timing and bias. Timing is addressed by performing a cross-correlation in the training period and applying the determined lead or lag time to the forecast period. Bias is addressed by performing a regression analysis, with either a particular model or a suite of models and producing the optimal forecast output based on the results. Furthermore, due to model spin-up issues, the first 6 h of any WRF model run is not used in a forecast. The optimal forecast is then determined by concatenating all subsequent model runs together into a single forecast.

Given that over the years several models of icing due to freezing rain have been developed, the Simple model [5] was used to forecast ice accretion. The Simple model determines the accretion of ice from freezing precipitation on horizontal cylinders orientated perpendicular to the wind given a wind speed and precipitation rate. The model also assumes that all of the precipitation freezes to the cylinder in a uniform layer. The Simple model is:

$$R_{eq}\ (\mathrm{mm}) = \sum_{j=1}^{N} \frac{1}{\rho_i \pi}\left[\left(P_j\rho_o\right)^2 + \left(3.6U_jW_j\right)^2\right]^{1/2} \qquad (1)$$

Where P_j is the precipitation rate (mm.h^{-1}), ρ_o is the density of water (g.m^{-3}), ρ_i is the density of ice (g.m^{-3}), U_j is the wind speed (m.s^{-1}), W_j is the liquid water content of the air (g.m^{-3}) and N is the duration of the icing event (h). The liquid water content of the air was determined using the following relation [6]:

$$W_j = 0.067P_j^{0.846} \qquad (2)$$

Even though the Simple model has been known to over-estimate the icing accumulation it has also, at times, performed well against other more detailed models under certain conditions [7]. Furthermore, given that the Simple model can be considered a worst-case scenario, it is conservative to use it for forecasting purposes.

IV. Results and Analysis

The optimal WRF forecasts and observations for the surface pressure, wind speed and temperature for the icing event of 11 January 2013 can be seen in Fig. 4 to 7. Also shown in Fig. 4 to Fig. 7 is the data for the week preceding the icing event in order to illustrate how the model and observations compare over a longer period. It should be noted that the surface pressure shown in Fig. 4 was not scaled.

It can be seen in Fig. 4 to 7 that the method employed by concatenating the WRF model runs captures the event quite well even though there was data missing on 9 and 10 January 2013 and that the wind speed sensor appears to have suffered from being iced on late 11 January and early 12 January 2013. The missing data issue is attributed to the fact that the data logging system was not operational due to a scheduled software upgrade.

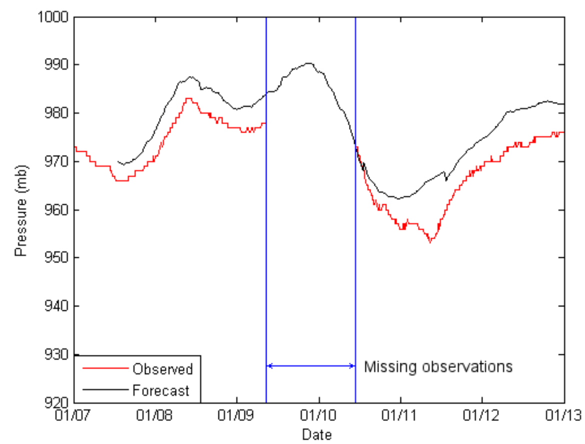

Fig. 4. Observed (red line) and modelled (black line) surface pressure as a function of time at Hawke Hill in January 2013. Also indicated is a period of missing observations (blue).

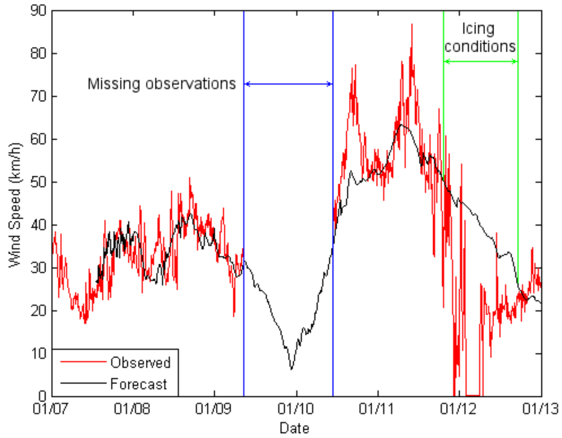

Fig. 5. Observed (red line) and modelled (black line) wind speed as a function of time at Hawke Hill in January 2013. Also indicated is a period of missing observations (blue) and approximately when icing conditions occurred (green).

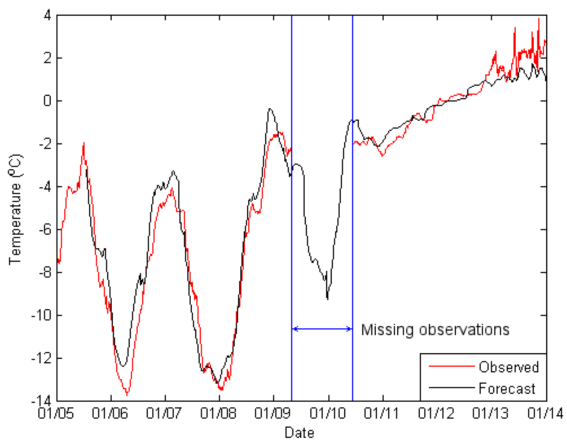

Fig. 6. Observed (red line) and modelled (black line) temperature as a function of time at Hawke Hill in January 2013. Also indicated is a period of missing observations (blue).

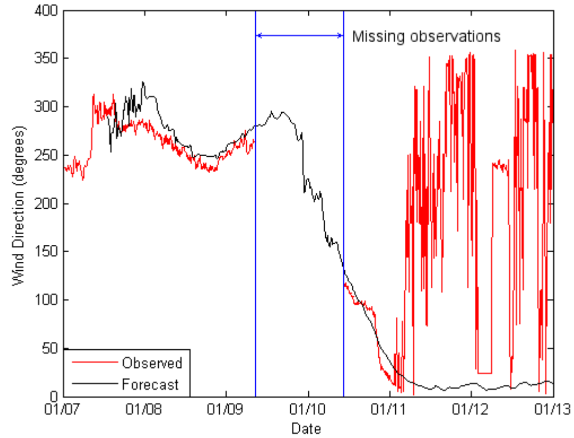

Fig. 7. Observed (red line) and modelled (black line) wind direction as a function of time at Hawke Hill in January 2013. Also indicated is a period of missing observations (blue).

While not shown, WRF model runs also performed similarly well for the other meteorological parameters and for both icing events. The correlation coefficient for temperature, pressure, wind speed and wind direction for both icing events can be seen in Table 2 below. It should be noted that the correlation coefficient for wind direction was performed on transformed data on WRF model due to issues regarding wind directions around 0^{o}. It can be seen that all parameters shown had a correlation coefficient of 66% or higher. Given that the wind speed data has suffered due to icing, the true correlation coefficient will likely be similar to or higher than those shown in Table 2 for these two parameters. This was the case as can be seen in Table 2 with the correlation increasing from 66 to 79% for the first icing event when the icing period is excluded. The correlation for the second icing event is, however, unchanged.

Table 2. Correlation coefficient for various meteorological parameters for the icing events of 11 January and 28 February 2013. The values inSide the brackets are when the known icing condition periods are excluded from the calculations.

Event	Temperature	Pressure	Wind Speed	Wind Direction
11 January 2013	90	94	66(79)	82
28 February 2013	79	97	66(64)	76

One parameter not shown above is the precipitation rate. This is due to the fact that WRF accumulates the precipitation over a 3 h period which makes comparison at a smaller time division difficult. However, given the results above, it is reasonable to assume that the WRF predicted accumulation will reasonably predict the conditions that occurred.

Using the optimal WRF model forecasts and employing equations (1) and (2) above, the results are summarized in

Table 3 below. It should be noted that the results presented in Table 3 assumed that the wind flow was perpendicular at all times to the possible cable and as such can only be considered the maximum radial thickness possible.

Table 3. The forecast maximum radial equivalent thickness (mm), added weight force (N/m) and the wind force factor increase (%) as well as the measure peak ice thickness for the icing events of 11 January and 28 February 2013. Note that a 1 inch transmission cable was assumed and the ice density was 800 kg/m3.

Event	Forecast Maximum Radial Equivalent Thickness (mm)	Forecast Added Weight Force (N/m)	Forecast Increase in Wind Force Factor (%)	Measured Peak Ice Thickness (mm)
11 January 2013	13.5	12.7	110	9.7
28 February 2013	6.4	4.9	52	19.4

It is clear that the results of the WRF model over-estimated the ice accumulation for the event of 11 January 2013 but underestimated the icing for the event of 28 February 2013. The over-estimation for the earlier event could be due to a combination of the Simple model, the assumption of perpendicular wind flow or errors due to the WRF model. However, it is not inconceivable that this would be within an acceptable limit given the various errors and as such was deemed acceptable.

The underestimation for the second icing event is off by almost a factor of three and as such cannot be considered acceptable. One possible reason for inaccuracy in forecasting the ice load for the event of 28 February 2013 is the conditions that Hawke Hill experiences. Hawke Hill has been observed in the past to experience significant accretion due to rime ice [8]. However, at this time the conditions that lead to rime ice are generally not adequately determined by meteorological models. This is an area of obvious improvement for future work.

The forecasted additional weight due to ice accumulation alone and due to increase in wind force was significant for the first icing event with almost an extra 13 N/m weight due to the ice and over a doubling of the force that the wind would exert. Given this information is available many hours in advance of an icing event, steps can be taken to mitigate possible structure failures.

V. Summary

It has been shown that using an ensemble of WRF model runs, each set-up to best determine certain meteorological parameters, can describe the important factors that predict an icing event. Using the best forecast, a prediction of icing accumulation was performed and performed adequately under certain conditions. The correlations were all above 66% for the parameters shown which suggests that the WRF model predicts the conditions even when measurements may be difficult to accurately obtained.

Several improvements to the forecast system employed by AMEC are possible and these include using a more sophisticated icing model such as that described in [9], employing more WRF models, using ensembles of models and further investigating the conditions of events that cause significant rime ice and the forecasting of those conditions.

Acknowledgment

The authors would like to thank Mr. Terry Gardiner, Manager of Engineering, T & D and Mr. Rick Leggo, Manager of Engineering, PC & C of Newfoundland and Labrador Hydro for providing the financial support in maintaining the Hawke Hill test site for the past three years.

References

[1] Cortinas, J.V., Jr., B.C. Bernstein, C.C. Robbins and J.W. Strapp, 2004: An Analysis of Freezing Rain, Freezing Drizzle, and Ice Pellets across the United States and Canada: 1976–90. *Wea. Forecasting*, **19**, 377–390.

[2] Haldar, A.K., M.A. Marshall, and R, Van Cauwenberghe 1993: Wind and Ice Load Monitoring on a Test Line. 6th IWAIS, Budapest, 1993.

[3] Shin, H. H., and S. Hong, 2011: Intercomparison of Planetary Boundary-Layer Parameterizations in the WRF Model for a Single Day from CASES-99. *Boundary-LayerMeteorology,* **139**, 261-281.

[4] Skamarock, W.C., J.B. Klemp, J. Dudhia, D.O. Gill, D.M. Barker, W. Wang, and J.G. Powers, 2005: A description of the Advanced Research WRF Version 2. NCAR Tech Notes-468+STR.

[5] Jones, K.F., 1998: A simple model for freezing rain ice loads. *Atmos. Res.*, **46**, 87–97.

[6] Best, A.C., 1950: The size distribution of raindrops. *Quart. J. Roy. Meteor. Soc.*, **76**, 16-36.

[7] Jones, K.F., A.C. Ramsay, J.N. Lott, 2004: Icing Severity in the December 2002 Freezing-Rain Storm from ASOS Data*. *Mon. Wea. Rev.*, **132**, 1630–1644.

[8] Haldar, A., 2007: Twenty Years of Ice Monitoring Experience On Overhead Lines In Newfoundland and Labrador. 12th IWAIS, Yokohama, 2007.

[9] Makkonen, L., 1984: Modelling of Ice Accretion on Wires. *J. Climate Appl. Meteor.*, **23**, 929-939.

Application of Numerical Weather Forecasting Models on Atmospheric Icing in LRM

Svein M. Fikke [*1], Bjørn E.K. Nygaard [*2] and Kyle Tucker [*3]

[*1] *Meteorological Consultant*
Lindeveien 1, 1470 Lørenskog, Norway
fikke@metconsult.no

[*2] *Norwegian Meteorological Institute, POB 43 Blindern, NO-0313 Oslo, Norway*
New affiliation: Kjeller Vindteknikk AS, POB 122, NO-2027 Kjeller, Norway
bjorn.nygaard@vindteknikk.no

[3*] *Nalcor Energy, St. John's, Newfoundland, Canada*
KTucker@nalcorenergy.com

***Abstract* —** The electric power to be produced at the Lower Churchill Project in Labrador will be transmitted over to Newfoundland by a HVDC link. This link has to pass over the Long Range Mountains (LRM) and through areas where extreme weather may cause unknown, but probably severe loadings on such electric overhead lines. These weather impacts must be taken into account both for safe design and for reliable operation of this electric connection which has an extremely high socio-economic importance and value for Nalcor Energy and its customers. The local weather and icing patterns are studied by using a modern numerical weather forecasting model where local topography and physical icing models are included. In combination with Google Earth it is possible to look at icing conditions in detail along the planned HVDC line route.

I. Introduction

Electric power from the Lower Churchill Project in Labrador has to be transmitted over to Newfoundland and elsewhere by a HVDC overhead power link. This link has to cross over the Long Range Mountains (LRM), running along the Northern Peninsula and ranging up to more than 600 m above sea level (m asl). The conditions for atmospheric icing in Newfoundland in general and especially over the LRM have been studied since the commissioning of transmission lines in Newfoundland in the 1960's. A summary of major failures and particular studies since then is given in [1].

Considering developments in icing studies and modern meteorology over the last decade or so, it was decided to review earlier ice load assumptions, especially in the light of using the university developed "Weather research and forecasting model" (WRF model). This meso-scale model describes the physical and dynamic processes in the atmosphere at greater details than conventional weather forecasting models normally do. By using a nesting technique such models can transform the global weather situation into detailed descriptions of important weather parameters like wind and icing conditions for local overhead lines, with a spatial resolution adequate for the span lengths of such lines, where also the topography and land surface characteristics are of similar scales. The model has been applied mostly for quantitative assessments of rime (in-cloud) ice loads [2], but it is also applicable for studying wet snow loads and freezing rain. Also for historic failure studies such models are very useful.

As input to this model is used 6-hourly gridded weather data for the whole atmosphere. This weather data base contains assimilated and interpolated sets of all relevant weather parameters from regular weather stations, automatic stations, ocean buoys, weather radars, satellites, etc., and gives therefore a complete 3-D description of the state of the lower atmosphere (troposphere) globally at 6 hours intervals. Fig. 1 shows an illustration of how the surface of the Earth as well as the atmosphere is divided into such a 3-D grid.

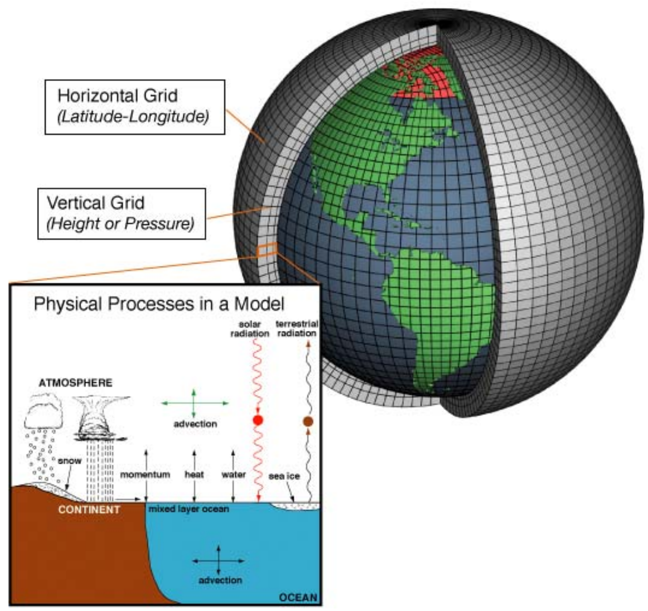

Fig. 1. The weather observations on the surface of the Earth are interpolated into grid points over land and sea. Weather data from the upper atmosphere is likewise interpolated into several grid layers in the vertical of the atmosphere. The box indicates the physical processes included in a weather forecasting model. Illustration: NOAA.

By using this model for special transmission line projects it is possible to identify locations where severe icing may occur, and also how the topography influences local icing conditions and hence give credibility to alternative line routes where such severe icing will not occur, or is much less likely. By selecting a variety of potential icing cases from regular meteorological data bases, it is possible to get detailed impressions of local icing conditions under different wind and humidity conditions, and hence assist significantly to select ice loadings for design of new lines in such areas where no relevant data are otherwise available. This approach is greatly enhanced when supplementary measurements can be done in parallel. This model has been applied now several times for such purposes, as is demonstrated in this paper.

Finally, the output of the WRF model can easily be presented in Google Earth and hence it gives an excellent visualisation of the icing conditions along various alternatives for the line routing through the area.

This approach has earlier been applied on electric transmission line projects in Norway, Greenland, Chile and the UK [3].

The final ice load assessments for the HVDC Labrador – Newfoundland Transmission Link were selected with supplementary input from local field measurements and the analyses of historic weather observation data with the WObs model [4].

II. THE WRF MODEL

The Weather Research and Forecast (WRF) model is a state-of-the-art meso-scale (10 – 10 000 km horizontal resolution) numerical weather prediction system, used both in operational forecasting and in atmospheric research (http://www.wrfmodel.org/ and http://www.wrfuserspage.com). WRF solves coupled equations for all important physical processes (such as winds, temperatures, stability, clouds, radiation etc.) in the atmosphere based on both initial fields and lateral boundary values derived from global analysis data. Historic model runs can be initiated with three dimensional analysis of the state of the atmosphere obtained from the ECMWF (European Centre for Medium-range Weather Forecasting) data archive which goes several decades back.

Because atmospheric icing often occurs as a very local phenomenon, and icing intensity is varying greatly in space, especially in complex terrain, it is necessary to run the model at high horizontal resolution to produce useful icing maps. In order to obtain a good representation of the local terrain in the model, data sets at about 90 m horizontal resolution can be implemented.

The model is set up with nested domains, which means that the model goes stepwise from the global scale to local scale with a grid resolution in the range of 0.4 – 0.8 km in the finest resolution domain. This resolution is considered as extremely high for meso-scale models.

A second important factor for simulation of atmospheric icing is how the model computes or parameterises the cloud microphysics. So far the so-called Thompson microphysics is considered to provide a correct representation of the physical transformations of all water phases in clouds and precipitation, also at ground level [5].

The icing simulations are carried out in a two step manner:

1. Meteorological data is produced at high spatial and temporal resolution using the WRF model. In addition to standard variables like wind speed, temperature and humidity, the WRF model also output data like mass concentration of supercooled cloud water, and also an estimate of the median volume droplet size.
2. The data from WRF is processed through an accretion model for rime icing or wet snow, calculated using the standard ISO specification [6], where the load is accumulated on a theoretical vertical and rotating cylinder with diameter 30 mm.

Accumulated ice load is calculated in all grid cells in the model domain, serving the basis for an icing map, which can also be used as an overlay in Google-Earth. The output files also contain information on predicted precipitation, wet snow and maximum wind speed. Meteograms showing the time evolution of icing together with weather parameters can be extracted from these files, as well as vertical profiles of the same parameters.

III. RESULTS

The WRF study was performed for a selection of four incidents where the weather was considered to be favorable for either wet snow accretion or rime icing. These events were identified from data from regular weather stations on the western side of the Northern Peninsula, mainly Daniel's Harbour (Climate ID: 8401400) at the North-Western corner of the model area in Figs 2-5, provided by Environment Canada.

Four examples of the output from the WRF model are shown in Figs. 2-5 from a 36 hour period starting at 2010-01-02 00:00 and ending 2010.01.04 12:00. The innermost domain of the WRF model over the central part of LRM is seen with colors within the figures. The four figures show the following results:

- Fig. 2: Accumulated precipitation (mm)
- Fig. 3: Accumulated wet snow load (kg/m)
- Fig. 4: Accumulated rime ice load (kg/m)
- Fig. 5: Maximum 10 minute average wind speed (m/s) during the 36 hours.

Color bars show the absolute values of the relevant parameter at the lowest model height, roughly 25 m above ground.

The prevailing wind direction at Daniel's Harbour was from NE during this event.

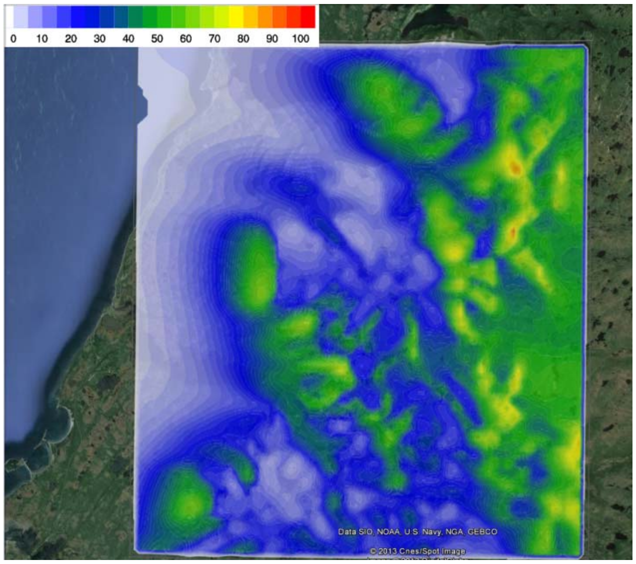

Fig. 2. Accumulated precipitation (mm). Period: 2010-01-02 00:00 – 2010.01.04 12:00.

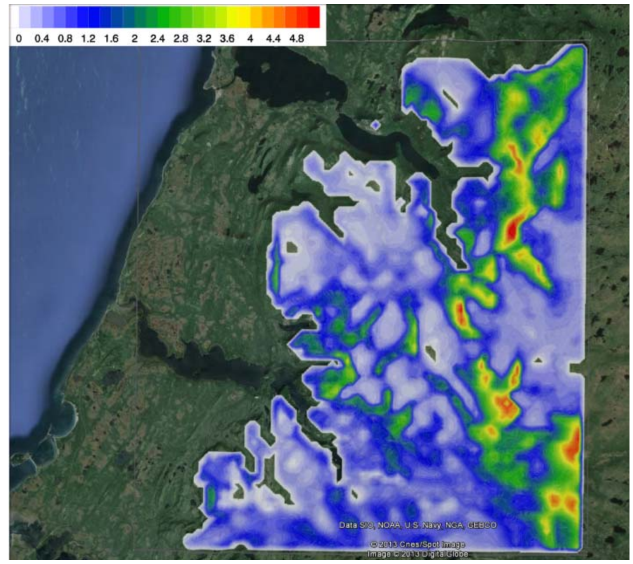

Fig. 3. Accumulated wet snow load (kg/m). Period: 2010-01-02 00:00 – 2010.01.04 12:00.

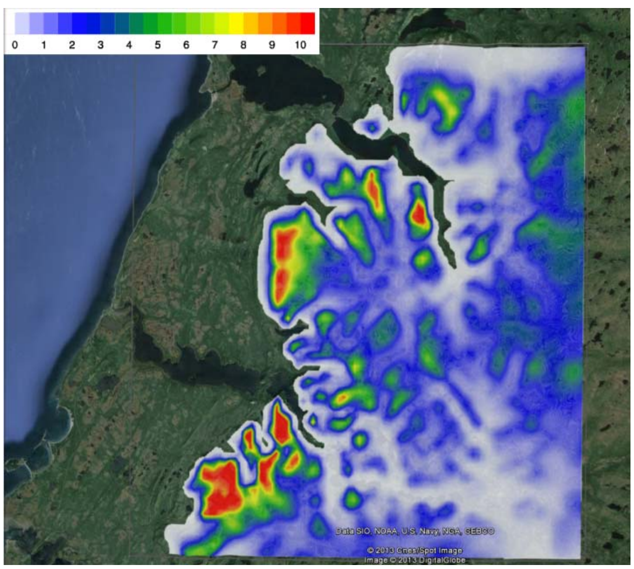

Fig. 4. Accumulated rime ice load kg/m). Period: 2010-01-02 00:00 – 2010.01.04 12:00.

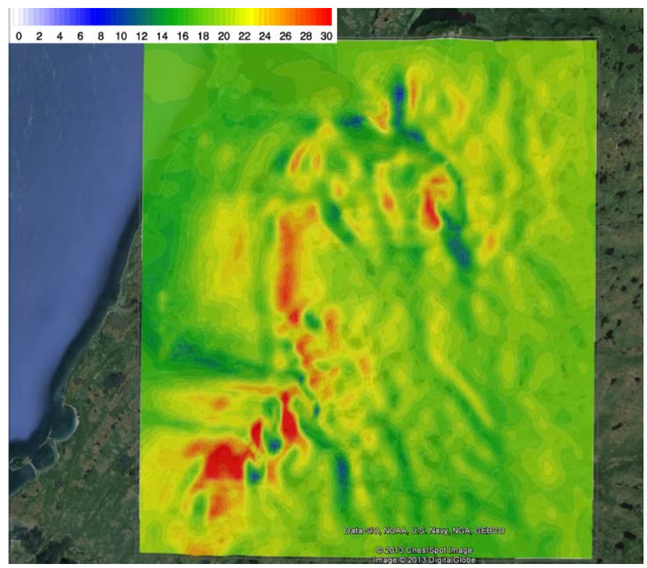

Fig. 5. Maximum 10 min mean wind speed (m/s). Period: 2010-01-02 00:00 – 2010.01.04 12:00.

It can be clearly seen from Figs. 2-5 how the small scale topography influences the local precipitation, wet snow formation, rime icing as well as the maximum wind speed. From Figs. 4 and 5 it is seen how the rime icing and wind speeds increase over the mountain tops, while the wet snow (Fig. 3) is strongly depending on the temperature. In cases with low temperature, the strongest wet snow accretion occurs in lower regions (example not shown here), while in higher temperatures the wet snow occurs mainly in the mountain areas. An example of the importance of the local terrain surrounding the area is shown in Fig. 6. This figure shows the vertical icing gradient for the three lowest levels of the WRF model (25, 90 and 175 m above model ground) for five locations along one alternative of the line route.

During Case 1 the prevailing wind was from NE. We see for locations 1, 2 and 3 that the ice accumulated loads in the 25 m level is almost insignificant at locations 1, 2 and 3, due to the protection of the surrounding terrain. Above this height the ice loads increase significantly at 90, and especially at 175 m levels. For the further planning of this line any displacement of the route into slightly higher altitude areas where there are some openings towards the eastern sector, should be carefully avoided.

Another point to make is that a double circuit line in vertical configuration, where the upper phase conductors and earth wires may reach more than 50 m above ground, may get significantly higher risk concerning ice loads and high winds compared with a double circuit line with horizontal configuration.

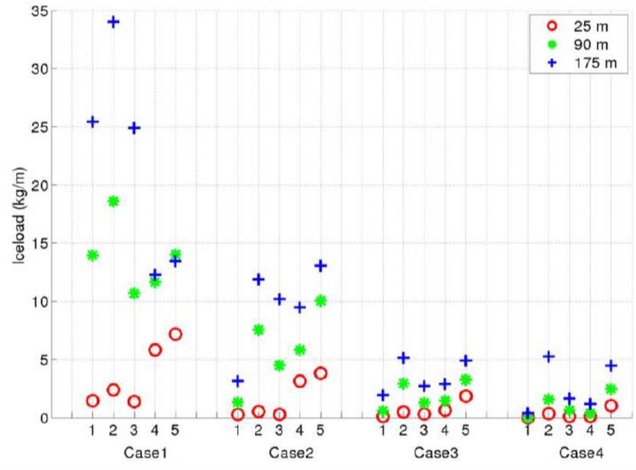

Fig. 6. Ice loads extracted from the three lowest levels of the WRF model (25, 90 and 175 m above model ground) for four different weather events, and for five different locations along one alternative line route.

Although less pronounced, similar effects can be seen in Case 2 when westerly winds prevailed during the accretion. In this case there is also an increment in ice loads from 90 to 175 m at locations 4 and 5, but very light icing above location 1. Cases 3 and 4 had the lowest ice loads of all cases, due to northerly to north-easterly winds.

IV. Comparisons With Measurements and WObs model

Nalcor Energy installed in 2009, for the purpose of these studies, test spans at two different locations, here called "Nalcor 1" and "Nalcor 2", respectively ([4] and [7]). Some measured parameters from the period 01-04 January are here shown in Fig. 7 (panels 1 and 2). The modelled parameters from the WRF model are shown as well (panels 1-3 and 5-6) and from the WObs model [7] (all panels). The WRF model is run only for the period when the model itself detected some significant ice accretion.

Panel 1 shows a significantly higher ice load from the WRF model, compared with the measurements, even with the maximum recordings. There are two main reasons for this: First, the WRF model accretes ice from all wind directions, while the test span has only one direction. Second, the lowest layer of the WRF model is roughly 20m above the height of the test conductors. From Icelandic experience, the actual ice load on the test conductors are close to the minimum values of the load cell.

The temperatures differ less than 2 °C most of the time (panel 2). Panel 3 shows the wind speeds (solid curve) and wind directions (dotted curve) from Daniels Harbour (blue), WRF model (green) and WObs model (red). Panel 4 shows the cloud base observed from Daniels Harbour. Panel 5 shows the liquid water content (LWC) at the Nalcor 1 site from WRF and WObs. The WObs model did not identify icing in this case, due to missing observations of the cloud base. Finally, the collision coefficient ("alfa 1") from WRF and WObs are shown in panel 6.

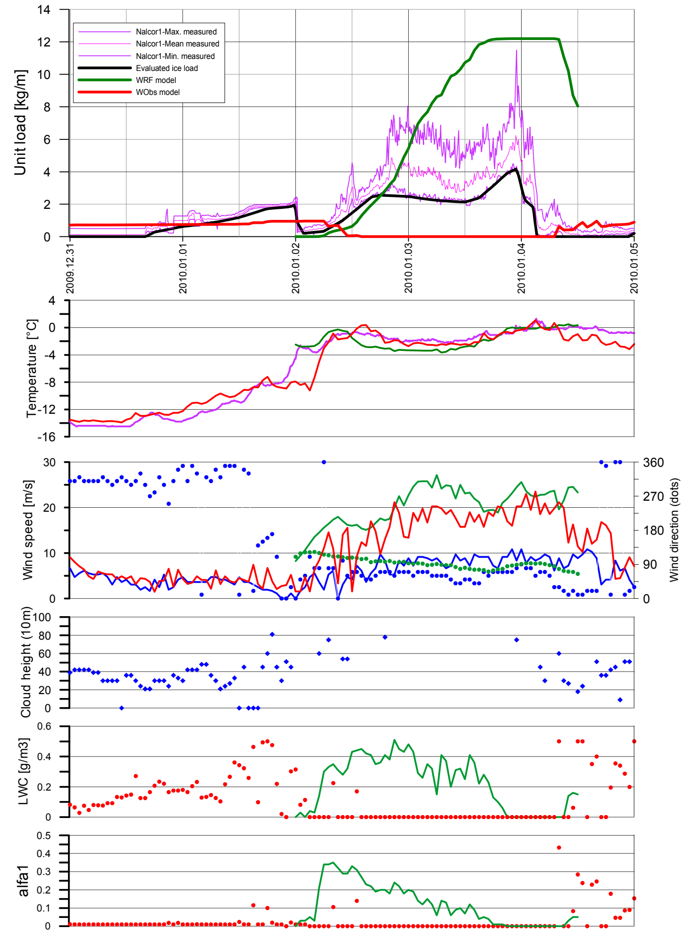

Fig. 7. Comparisons between a) measurements from two test spans ("Nalcor 1" and "Nalcor 2"), b) evaluated ice loads (from measurements), c) modelled icing parameters from the WRF model, and d) modelled results from the WObs model. Upper panel: Unit ice loads in kg/m. Second panel: Air temperature (°C). Third panel: Wind speed (solid curves) and wind direction (dotted curves). Fourth panel: Cloud height above mean sea level (x10 m). Fifth panel: Liquid water content in cloud. Sixth panel: Collision coefficient (alfa 1) Colors: See box in upper panel. Red graphs are from the WObs model, green graphs from WRF and blue graphs from Daniels Harbour. From [7].

V. Concluding Remarks

This paper has shown some examples of the application of a modern, high-resolution weather forecasting model where conventional ice accretion models were incorporated. The main purpose of this study was to learn more about how the local topography and climate dominate wet snow and rime icing processes over the Long Range Mountains. This method cannot yet be used to assess probability based ice loadings with certain return periods, unless it is combined with long term point measurements. Until such data may be available, the results from this study will be a supplement to the variety of information from other sources and models, and hence to enhance the confidence of the design loads which will finally be selected for this line.

In particular, freezing rain or drizzle may as well be important for the selection of design loads. It was hoped that the measuring sites would catch some events of this kind, and that the WRF model could be used also to test this icing phenomenon in the Long Range Mountain area. A study by Hosek et.al. [8] has already shown the potential of such methods also for freezing rain and drizzle in Newfoundland. However, that study focused on the Bonavista peninsula and did not cover the LRM area dealt with in the present paper.

REFERENCES

[1] A. Haldar, "Twenty years of ice monitoring experience on overhead lines in Newfoundland and Labrador" in Proc. 2007 IWAIS XII, Yokohama, Japan, October 2007.

[2] B. E. K. Nygaard, “Evaluation of icing simulations for the COST 727 icing test sites in Europe” IWAIS XIII, Andermatt, Switzerland, September 2009.

[3] S. M. Fikke, B. E. Nygaard, D. Horsman, J. B. Wareing and K. Tucker: “Extreme weather studies by using modern meteorology”, in Proc. 2012 Session, paper B2-202, Cigré 2012.

[4] A. Gudmundsson, S. M. Fikke, Á. J. Elíasson, Egill Thorsteins and B. E. K. Nygaard, “Lower Churchill Project, HVDC Labrador-Newfoundland Transmission Link. Evaluation of in-cloud icing in the Long Range Mountain Ridge, Report 3.” Nalcor 2012

[5] B. E. K. Nygaard, J.E. Kristjánsson, L. Makkonen (2011) Prediction of in-cloud icing conditions at ground level using the WRF model. Journal of Applied Meteorology and Climatology, **50**, 2445-2459.

[6] ISO 12494 Atmospheric icing of Structures. ISO/TC98/SC3, 2007-07-20.

[7] Evaluation of in-cloud icing on the Long Range Mountain Ridge. Report 2. Landsvirkjun Power in collaboration with EFLA Engineering and S.M. Fikke Meteorological Consultant – Overhead Lines. Reykjavik, December 2010.

[8] J. Hosek, P. Musilek, E. Lozowski and P. Pytlak (2011) Forecasting severe ice storms using numerical weather prediction: the March 2010 Newfoundland event. Nat. Hazards Earth Syst. Sci., **11**, 587-595.

A new set of climatic loads maps for Russia

Sergey CHERESHNYUK[1], Larisa TIMASHOVA[2], Vladimir LUGOVOI
«R&D Center @FGC», JSC
22, bld. 3, Kashirskoye shosse, Moscow, 115 201, Russia
[1] Chereshnyuk_SV@ntc-power.ru
[2] Timashova_LV@ntc-power.ru

***Abstract* —** In Russia regional maps are used to assess the climatic loads for the existing and newly designed transmission lines. For each of the 79 federal subjects of the Russian Federation it was developed a set of 4 climatic regional maps (wind load map, ice load map, combined ice-wind load map, lightning activity map). For the maps developing we have used observation data of nearly 2000 meteorological stations all over the country, most of them have a period of observations more than 50 years. For the climatic characteristics (wind load, ice load, combined ice-wind load) according to national standards we have used a return period of 25 years with possibility to recalculate loads to return periods up to one in 500 year. All maps were created in electronic format, using ArcGIS system, having scale 1 : 500 000. The work was done in years 2010-2013 and it is for the first time that a complete set of climatic loads maps was developed for all regions of the country as a requirement from the Federal Grid Company.

I. Introduction

It is historically established in Russia that climatic loads for transmission lines design purposes are calculated using regional climatic maps. This became customary because of several reasons: vast territory of the country, different climatic conditions (from subtropic to arctic) and availability of long term standard meteorological obserbation data (including icing) of good quality for all over the country. First maps were created in 1950s, though observations on icing were started in 1920s – early 1930s. Statndards for ice-loads assessment have changed in time and so have changed regional climatic maps. So if first maps were created for loads having return period of 5 years (probability 0.8) then nowadays regional climatic maps are created for loads having return period of 25 years (probability 0.96). Last time that regional climatic maps has been created was in 1980s. For many regions no regional climatic maps have been created. So in 2010 the Federal Grid Company (FGC) in order to increase the effeciency and reliability of overhead transmission lines decided to create a complete set of climatic loads maps for all regions of the country.

II. Work tasks and goals

The creation of ice-load maps has been imposed by the following reasons and with the subsequent tasks and goals:

- The need to update existing maps, partially due to climate change;
- The need to create maps for regions where no regional maps was previously created;
- The need to create a full set of climatic regional maps for the bussiness purposes of Federal Grid Company;
- The availability of a new, long-period observation data from meteorological stations network;
- The availability, fast development and vast usage of modern GIS technologies;
- The application of GIS technologies in FGC;
- The enhancement of efficiency of managing electroenergy infrastructure in FGC;
- The automation of works of climatic loads assessment for the purposes of design and maintainance of OHL.

III. Observation data and methodology of regional maps creation

The creation of ice-load maps is based on meteorological information that is collected from the meteorological stations network covering all the territory of the country.

Ice observations on meteorological stations are performed using a special designed device (icing device). This icing device consists of four non-rotating rods of 5 mm in diameter, fixed in pair towards meridional and latitudinal directions and suspended at the two different heights of 1,9 and 2,2 m above the ground for each pair. For every icing event are measured size of ice accretion, its weight and type (glaze ice, hard rime, etc.). During every icing event are also measured other meteorological parameters, such as air temperature, wind speed and direction.

The meteorological stations network in the territory of the Russian Federation has carried on mass observations of icing events since 1951. Today's observations of icing events are performed by 1254 meteorological stations (out of nearly 2000 existing meteostations) all over the territory of Russia. The period of instrumental observations reaches today 58 years, and for some stations even beyond.

Long-period observations data collected on every meteorological station is used to create statistical arrays on the base of yearly maximums.

In order to automate the work of climatic data processing, we have created a specialised information system for climate conditions.

The information system consists of a database of climate conditions (DB) and of a specific program.

The DB contains the following information about icing events: date of observation, icing type, its size and weight, speed and direction of the wind at the beginning of the icing event, maximum wind speed during the icing event. On figure 1 is shown the current database scheme.

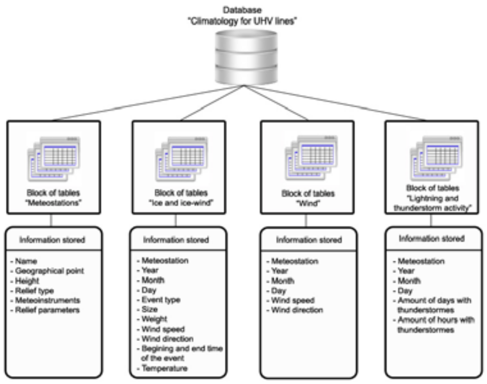

Figure 1: Database scheme

For every meteorological station the DB stores the following information: its name, administrative belonging, height above the sea level, meteostation's vicinity description and technical characteristics such as height of weather-vane and height of wind meter.

The program allows performing automatic data update in the DB in an electronic format, their handling, their processing in order to get uniform data, statistical arrays and statistical parameters. The program also allows describing the arrays with different statistical distributions, obtaining climatic characteristics having different return period.

For types and subtypes of large-scale relief we build a graph of functional dependence of climatic characteristic (wind speed, equivalent radial ice-thickness, ice-wind load, maximum wind speed for icing event) from the height above sea level. The dependence is x=f(H) (where x – value of climatic characteristic, H - height above sea level) and is built considering local small-scale relief. In Russia for climatic characteristics we use a return period of 25 years.

For the break down of the territory into icing regions we distinguish 8 regions with equivalent radial ice thickness from 10 to 40 mm and above. Gradation range of the region is 5 mm.

For the break down of the territory into ice-wind load regions we distinguish 9 regions with the value of ice-wind load from 3 to 28 N/m and above. For every ice-wind load region it is specified the wind speed having a return period of 25 years and a conventional equivalent radial ice-thickness.

In order to create regional maps of the territory of the Russian Federation we use a geo-information system. This Geographical Information System (GIS) is a system for the management of geographical information, their analysis and representation. Geographical information is given as a series of selected geographical data, which model the geographical environment with simple, summarised and structured data. GIS includes a set of modern and powerful instrumental means to work with geographical data.

The use of GIS allows the making of regional maps with an elevate degree of detailed elaboration of the icing regions that takes into account local relief. Furthermore, the use of GIS improves significantly the effectiveness and quality of executed work.

We selected the GIS system of the company ESRI - ArcGIS 9.2. This system possesses a powerful set of instruments that allows processing all the range of cartographic work, the analysis of the data, mapping and final preparation of ready regional maps for printing. Moreover this GIS is now been installed in Federal Grid Company as a main company GIS for storing and managing all geographical information, including OHL and substations plans, their technical and other characteristics.

IV. Work overview

The work has been carried on over the years 2010-2013 (last maps for 9 regions of Russian Far East are to be finished by October 2013). During this time were created more than 300 regional climatic maps; for each of 79 federal subjects of Russian Federation has been developed a set of 4 climatic regional maps (wind load map, ice load map, combined ice-wind load map, lightning activity map).

For the purposes of maps creation observation data from nearly 2000 meteorological stations were used (1254 meteostations for icing maps). During icing maps creation it was analyzed and stored in the created database more than 698.000 icing events observed on meteorological stations during the period 1950-2010.

All maps were created in electronic format, using ArcGIS system. Maps were created having a scale 1 : 500 000 which is in 1 cm – 5 km (for regions having extra big area and low population density – for example Yakutia, Krasnoyarsky krai – it was used a scale 1 : 1 000 000 which is in 1 cm – 10 km).

On the figure 2 for example is shown fragment of ice-load map for Sverdlovsk region (Ural mountains). It can be noted high loads on upwind, west-oriented slopes of the mountains and comparatively low ice loads on the other side of mountains ridges, on leeward sides of the mountains.

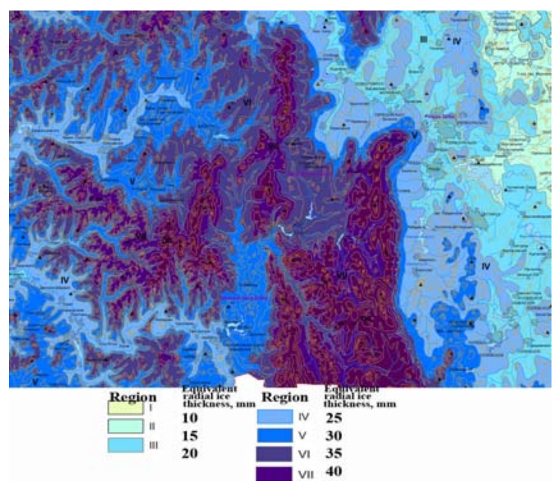

Figure 2: Fragmen of Ice loads map for Sverdlovsk region (Ural mountains)

IV. First results

Careful analysis of work results is matter for future work, but some intresting facts could be stated at this moment:

- Most severe ice and combined ice-wind loads are observed on the upwind slopes of mountains and highlands. For example, we could mention west-oriented slopes of Caucasus mountains and west-oriented slopes of Ural mountains;

- Highest ice and combined ice-wind loads are observed at the top and ridges of the mountains;
- Right after the highest peaks of mountains chains on leeward sides loads decrease very quickly, so if on windward side the value of radial ice thickness for example in Sverdlovsk region (Ural mountains) is 25-30 mm then on leeward side at the same height is only 10-15 mm (see fig. 2).

The Development of New Maps for Design Ice Loads for Great Britain

Bjørn Egil K. Nygaard [*1], Ivar A. Seierstad [*2], Svein M Fikke [*3], David Horsman [*4] and J. Brian Wareing [*5]

[*1] *Norwegian Meteorological Institute,Oslo, Norway*
New affiliation: Kjeller Vindteknikk, AS, Kjeller, Norway
bjorn.nygaard@vindteknikk.no

[*2] *Norwegian Meteorological Institute, Oslo, Norway*
ivaras@met.no

[*3] *Meteorological Consultant, Lørenskog,* Norway
fikke@metconsult.no

[*4] *EA Technology,* Chester, UK
David.horsman@eatechnology.com

[*5] *EA Technology,* Chester, UK
jbwareing@btinternet.com

Abstract **—** A new high resolution map of extreme snow and ice loads has been produced. Wet snow accumulations on overhead power lines are estimated using observations from a network of surface synoptic weather stations, while areas of severe in-cloud icing (rime icing) are identified from high resolution numerical weather prediction model simulations. Ice loads at 50 year return period were estimated using the "Peaks-Over-Threshold" (POT) method and interpolated to a high resolution map using regression kriging. The results indicate a significant variation both with altitude and latitude, with the highest loads expected in the wettest parts of the Scottish Highlands. In-cloud icing occurs mainly above 300-400 meters and is the dominant icing type above 500-700 meters depending on location. The final icing map demonstrates how state of the art atmospheric icing models can be successfully utilized to estimate the icing climate even when only very limited measurements of actual icing are available.

Keywords **—** *icing map; accretion model; wet snow; WRF model, extreme values; regression kriging*

I. INTRODUCTION

The current study was initiated by the Great Britain Distribution Network Operators (DNO), with the aim of producing an updated and physically consistent icing map that can be used for the design of new lines at all voltage levels, as well as for maintaining or reconstructing existing lines. Traditionally design ice loads in the British Isles have been provided by semi-probabilistic methods using UK Met Station data, whereas EN50341 required that wind and ice loads derived from various building design codes be used. Network owners and operators believe that lines are over-engineered in some regions and for some voltage levels. However, frequent icing related outages and collapses have been experienced in other regions, in particular for lower voltage lines with small conductors.

In the coastal, maritime climate of the British Isles there are two dominant types of atmospheric icing namely wet snow accretion and rime icing, and both should be considered when constructing an ice load map.

Wet snow accretion is caused by partly melted snowflakes adhering to a surface. This usually occurs in Britain every winter but the area that it affects and its severity varies greatly from year to year. Consequently, all overhead lines need to be designed to withstand a certain wet snow load.

Rime icing, also called in-cloud icing, is limited to elevated areas where the power lines more frequently come into contact with clouds. It is most common in hilly terrain directly exposed to the advection of moist air from the sea, and its severity increases rapidly with height [1]. Riming occurs when supercooled cloud droplets are present in the air flow, and these freeze immediately upon contact with an object.

Due to the distinct nature of the two icing types considered, it is appropriate to follow different model approaches to simulate each icing process and hence the required meteorological parameters will also differ. Common for both icing types, however, are that historic icing observations with sufficient details such as ice weight or icing diameters are almost non-existent in Great Britain (except icing measurements at the EA Technology Deadwater Fell test site [14]), and so modeling techniques need to be employed to estimate their frequency, magnitude, and the return period of extreme events.

II. METHODS AND DATA

For both icing types, so called ice accretion models [2] are used to estimate accumulated loads based on meteorological data at a given temporal resolution. In the case of power line icing it is appropriate to use a cylindrical model, which assumes that the ice or snow accumulates uniformly in a rotating cylinder (ISO-12494, 2001). Wet snow loads are estimated from weather station data all over GB, while rime icing is analyzed using a numerical weather prediction model.

a) Estimating wet snow loads

The wet snow accretion model used here is based on the theory described in [3]. It is a simple algorithm to estimate the rate of snow accumulation on a horizontal cylinder based on data from standard weather station observations. The accretion rate I per unit area is given by:

$$I = \beta\, Vw \quad (1)$$

where β is the sticking efficiency (reduced from 1 in windy conditions when snowflakes bounce or splash off the cylinder after collision), V is the snowflake impact speed normal to the cylinder and w is the wet snow content in the air (gm^{-3}).

The model relies on the measured precipitation rate at the ground (P) together with an assumed average terminal fall speed of wet snowflakes (v_s) to estimate the wet snow content in the air:

$$w = \frac{P}{v_s} \quad (2)$$

where v_s is set to 1.7 ms^{-1} in the current study, to represent an average value for wet snow [4]. [3] parameterized the sticking efficiency as 1/U. [4] showed that when validating against 50 years of wet snow observations in Iceland, the model significantly underestimated the wet snow loads. They suggested modifying the sticking efficiency by using:

$$\beta = U^{-0.5} \quad (3)$$

and this has been adopted in the current study.

One important issue to address is the criteria used to identify periods of wet snow, i.e. the range of atmospheric conditions conducive for wet snow to accumulate on power lines. [5] emphasized that in addition to temperature, humidity is also an important factor, and showed that a necessary criterion for the snowflakes to be 'wet' is that the wet-bulb temperature is positive (T_w > 0 °C). It was therefore decided to utilize the measured wet-bulb temperature, and define a T_w interval in which the precipitation is considered to be wet snow. Since measurements of wet snow are not available, a model approach is used to study the relation between T_w and the liquid water fraction (LWF) of wet snow. Laboratory studies ([6] and [7]) indicate that wet snow flakes have the strongest adhesive forces at LWFs within the range of 10-15%, and adhesive strength decreases rapidly when LWF increases above 20-30%. Additionally, [8] argued that snow has the ability to stick as soon as the LWF is around 3%. Based on these results, [4] defined wet snow as favorable for accretion when the modeled LWF was in the range 2% - 30% whilst calibrating a wet snow accretion model.

Figure 1 shows the modeled relative frequency of T_w values within different LWF intervals. Wet snow with LWF between 2 and 30% can be seen to correspond to T_w between 0 °C and slightly above 1 °C. A wet-bulb temperature interval of: 0.0 °C < T_w < 1.2 °C was therefore chosen as a criterion for wet snow.

With meteorological data at one hour temporal resolution, the numerical scheme described in [5] is used to calculate the wet snow loads. In total 131 UK Met Office weather stations, each with more than 10 years of continuous data, were used in the study.

The accuracy of measured precipitation during wet snow events may be questionable in particular for stations where unheated tipping bucket gauges are used. The main concern is that snow may accumulate on the instrument itself, leading to an undercatchment of the precipitation. As a consequence of this, a second model run (suite2) has been performed by shifting the temperature interval previously defined 2 degrees Celsius warmer. Wet snow is now defined as all precipitation in the wet-bulb temperature interval 2.0 °C < T_w < 3.2 °C. In reality, suite 2 reflects wet snow a few hundred meters above the ground level, whilst the actual surface precipitation is rain. The main advantage of suite2 is that the precipitation amount is accurately measured regardless of the precipitation gauge type used. On a case to case basis suite2 does not reflect real wet snow events, while for climatological purposes suite2 may provide a reasonable representation of the icing frequency since the width of the temperature interval remain the same in suite1 and suite2. This procedure may result in slightly conservative loads (due to possible increasing precipitation rate with temperature), but avoids placing any undue reliance on spurious precipitation data.

The wet snow model is applied for all the weather stations providing continuous time series, subject for further analysis using extreme value theory

a) Rime ice simulations

The high resolution simulations are carried out in a triple nested domain as shown in Figure 2 using the WRF-ARW model version 3.3.1. The innermost domain consists of a horizontal array of 581 x 709 grid boxes at a 1.5 km grid spacing with 32 vertical levels distributed on a sigma hydrostatic pressure coordinate system with model top at 50 hPa. The two lowest model levels are located approximately at 28 m and 96 m above the surface. The model is configured with the Thompson cloud microphysics scheme [9] which has shown to be well suited for icing application through direct validation with measured icing at ground level [10] and [11].

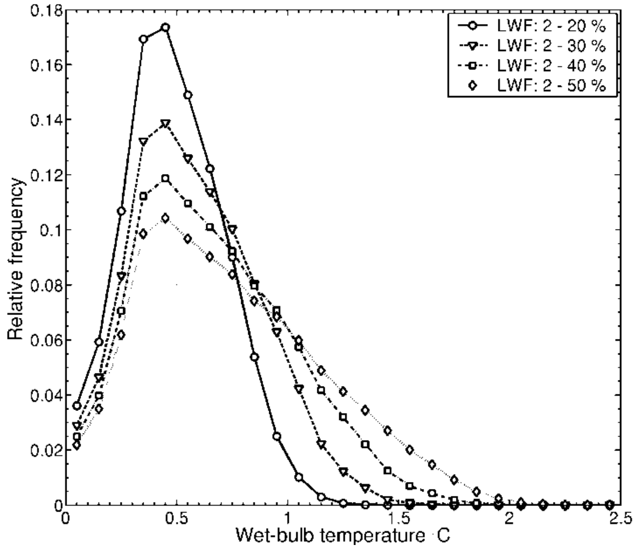

Figure 1. Frequency/probability of wet snow within different liquid water fraction intervals plotted against 2 m wet-bulb temperature, based on the WRF simulations described in section xx. All data points have total mass mixing ratio > 0.3 g/kg, with only land points considered.

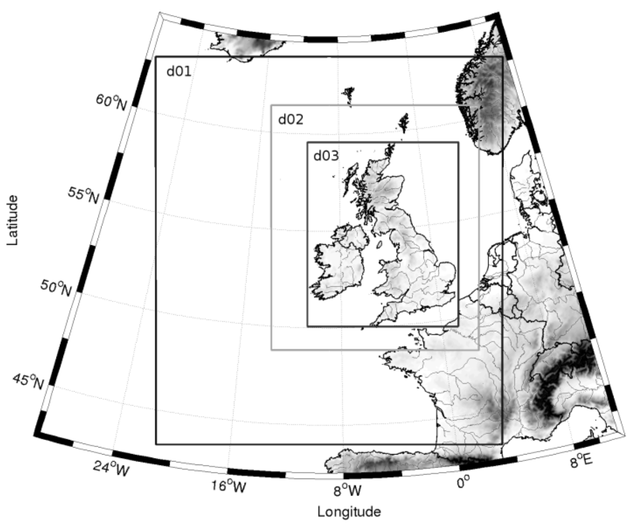

Figure 2. Setup of the nested WRF domains over the British Isles. The model grid spacing increase stepwise from 24 km via 6 km and 1.5 km from the outermost (d01) to the innermost (d03) domains respectively.

WRF simulations at a grid resolution of around 1 km are extremely computationally intensive particularly for a domain encompassing the British Isles. An examination of the icing measurements at the Deadwater Fell test site [12] have shown that the winter of 2009/2010 was a particularly icy winter with several significant rime icing events, occurring at different wind directions. It was therefore decided to simulate the entire 2009/2010 winter season at 1.5 km grid resolution. The atmospheric data generated by the WRF model was then fed into a cylindrical ice accretion model [13] and estimated rime ice loads are outputted. Deadwater Fell site data was used as a reference and validation point.

b) Extreme value analysis

The extreme value analysis of the modeled wet snow loads were performed using the "Peaks-Over-Threshold" (POT) method. This involves fitting the Generalized Pareto Distribution (GPD) to data points exceeding a chosen threshold. The estimated parameters of the GPD distribution can then used to estimate return levels. POT is the recommended approach for extreme value analysis particularly if more data than just the annual maximum are available. In the current study the POT approach is applied to all weather stations where wet snow loads are estimated. A high percentile approach was used to set the threshold in the analysis. Several tests were conducted, varying the percentile from 75 to 95. However, the estimated 50 year return values did not show a large sensitivity to the choice of threshold (not shown). The 85th percentile was used in the final POT analysis, and the fitted distributions were plotted for all the stations and manually inspected.

c) Extreme value analysis

A two stage process based on extreme values estimated at station locations was followed to generate wet snow load predictions. A multiple regression was performed with geographic factors as independent variables followed by interpolation of the residuals. In the regression model easting, northing, elevation and distance to coast were first tested as predictors in order to investigate the dependence of wet snow loads on geographic factors. Easting and distance to coast were then discarded as predictors as they had negligible impact on modeled wet snow loads in the regression model. Table 1 shows the regression variables, estimated parameter values and R^2 values for the chosen regression model for both suite1 and suite2 experiments.

Table 1. Regression models

Wet snow load (50 year)	Northing	Altitude	R^2
Suite 1	0.25 kg/100km	0.5 kg/100m	20%
Suite 2	0.24 kg/100km	0.6 kg/100m	35%

Secondly, a kriging technique was used to interpolate the regression residuals onto a regular grid. Despite there being only a weak spatial correlation between the stations for the estimated 50 year loads, kriging was chosen as it produces a smoother map compared to inverse-distance weighted interpolation. In the estimated variogram a nugget value of 1.4 was used as there is some uncertainty associated with the modeled wet snow loads also at the station locations. The final interpolated map thus differs from the station values also at the station locations. A "leave-one-out" cross validation was performed to evaluate the uncertainty introduced by the interpolation. For the suite2 experiment the mean absolute error is 1.0 kg/m (median absolute error is 0.66 kg/m).

In the case of rime icing there was no direct method to calculate the extreme values, since not enough computer resources were available in the project to calculate rime icing at this detail for a period of 20-30 years for such a big area. Therefore, the highest value modeled for the 2009/2010 winter was compared with the highest measured at Deadwater Fell. Hence, a factor of 2 was applied on the modeled rime ice, to provide a first estimate for the 50 year rime ice loadings over Great Britain.

III. RESULTS

Figure 3 shows wet snow loads on a 500 meter grid covering Great Britain together with the weather stations used in the analysis. The underlying dependence with latitude and land height can easily be recognized. However, with few weather stations above 300m the values above this height should be regarded as less reliable. They depend critically on the estimated elevation gradient in the regression model described in section 2.1.4. But from a physical point of view there are several factors that may explain why higher wet snow loads should be expected at higher elevations:

- Increased frequency of low temperatures during precipitation events
- Higher wind speeds
- Orographic enhancement of precipitation

While the map shown in Figure 3 is based on the suite 2 experiment, a similar map was also constructed from the suite1 results (not shown). As both experiments have their strengths and weaknesses, it is not obvious which provides the best representation of the actual conditions. Table 1 shows that the variation with land height is slightly less pronounced in suite1. Whether this is an artifact due to undercatchment of solid precipitation in windy conditions is uncertain. However, the undercatchment is expected to be most prone in windy conditions during solid precipitation (e.g. at higher elevations and exposed stations). Thus, it seems reasonable that the gradient with height should be slightly lower in suite1. The difference between suite1 and suite2 is also reflected in the coefficient of determination (R-squared) in Table 1.

Since wet snow accretion is a complex process in reality, the model is necessarily simplified in several ways. Effects such as joule heating, torsional rigidity, icing direction, etc. are not included, which are all effects that could possibly reduce the loads from the values estimated herein. However, there are already considerable uncertainties related to the observational data, and how the observations are used as input to the accretion model. The value of the model results would probably not be increased by raising the level of sophistication in the parameterizations.

The rime ice map is shown in Figure 4. Considering that the basis for this map is only one winter, this map should be used as an indicator of the relative severity of rime icing at different locations, thereby indicating where rime ice may be the dominant ice load for design purposes. It is strongly recommended that rime ice loads should be studied in more detail for the design of potential future installations in such areas.

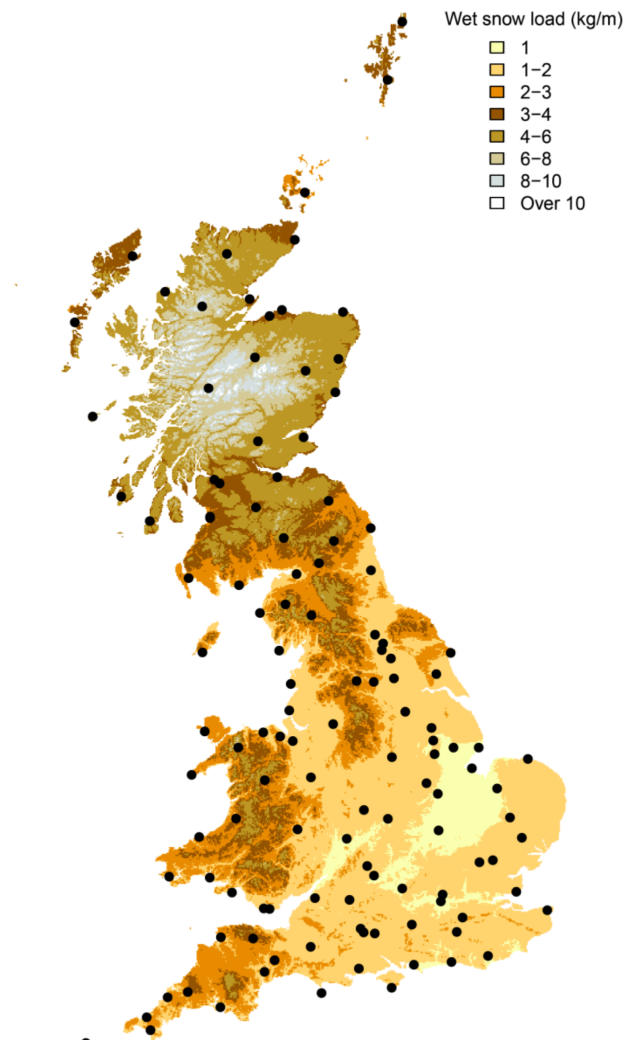

Figure 3. Estimated wet snow loads with 50 years return period, based on the suite2 experiment. Black dots: Locations of the weather stations used in the analysis.

IV. CONCLUSIONS

The results indicate that wet snow loads vary significantly both with latitude and altitude, with the highest values expected in the wettest parts of the Scottish Highlands. The vertical gradient is however uncertain due to a low number of weather stations located in elevated areas. The gradient identified was based mainly on stations below 300 m above sea level, while when constructing the map, loads were extrapolated above this level. The regression model estimates were particularly sensitive to a few stations located in Scotland that showed high 50 year values.

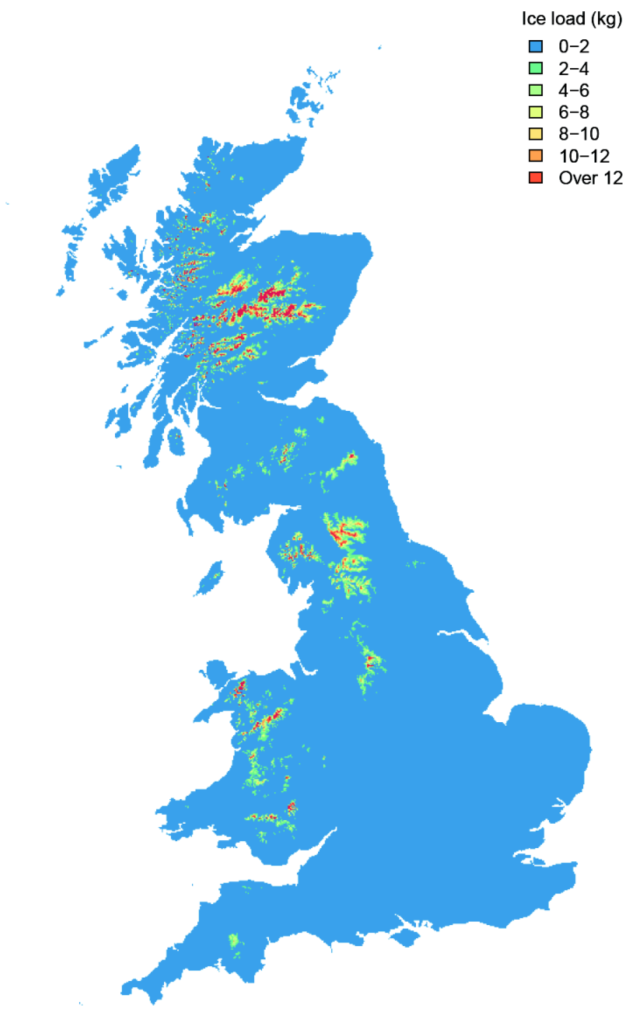

Figure 4. Estimated rime icing loads based on WRF simulations downscaled to the 500 x 500 m^2 grid.

In-cloud icing is shown to typically start at 300-400 meters, while being the dominant icing type above 400-600 meters depending on location and the model considered. On the highest peaks extreme rime ice events are expected (i.e. > 10 kg/m), however these areas are usually not considered for overhead line routes.

The data from Deadwater Fell have been used to evaluate both wet snow loads and rime ice loads, their relative contribution and vertical gradient. Deadwater Fell has thus been an important reference point for the map. Apart from Deadwater Fell, a quantitative validation of the map has not been possible due to the lack of direct wet snow measurements. However, the wet snow model used at all the weather stations, has previously been calibrated utilizing an extensive data set on wet snow measurements, covering 50 years of observations [4].

The data from these models has been incorporated into OHL conductor software using expressions from EN50341 (OH electrical lines exceeding 1 kV) to provide ice loads for OHL design [14].

ACKNOWLEDGMENT

The authors would like to thank Anthony T. Veal and Karl Kitchen (UK Met Office) for great support with the weather station data.

REFERENCES

[1] S. M. Fikke, J. E. Kristjánsson, and B. E. K. Nygaard. "Modern meteorology and atmospheric icing." *Atmospheric Icing of Power Networks* (2008): M. Farzaneh, Ed., Springer, 1-30.

[2] D. Kuroiwa, 1965. Icing and snow accretion on electric wires. U.S. Army. CRREL Rep., 123, 10 pp.

[3] P. Admirat, 2008: Wet snow accretion on overhead lines. Atmospheric Icing of Power Networks, M. Farzaneh, Ed., Springer, 119–169.

[4] B. E. K. Nygaard, H. Ágústsson and K. S. Tóth. "Modeling wet snow accretion on power lines: Improvements to previous methods using 50 years of observations." In press: Journal of Applied Meteorology and Climatology, (2013).

[5] L. Makkonen, 1989: Estimation of wet snow accretion on structures. Cold Reg. Sci. Technol., 17, 83–88.

[6] Wakahama, G., 1979: Experimental studies of snow accretion on electric lines developed in a strong wind. Nat. Disaster Sci., 1, 21–33

[7] Sakakibara, D., Y. Nakamura, K. Kawashima, and S. Miura, 2007: Experimental result for snow accretion characteristics of communications cable. Proc. Int. Wire and Cable Symp. (IWCS), Lake Buena Vista, FL.

[8] S.C. Colbeck and S.F. Ackley. “Mechanisms for Ice Bonding in Wet Snow Accretions on Power Lines”. Proceeding 1st International Workshop on Atmospheric Icing of Structures, Hanover, 1982

[9] G. Thompson, P.R. Field, R.M. Rasmussen and W.D. Hall, “ Explicit forecasts of winter precipitation using an improved bulk microphysics scheme. Part II: Implementation of a new snow parameterization”, Mon. Wea. Rev., 136, 5095–5115, 2008.

[10] E.A. Podolskiy, B.E.K. Nygaard, K. Nishimura, L. Makkonen and E.P. Lozowski, “Study of unusual atmospheric icing at Mount Zao, Japan, using the Weather Research and Forecasting model. J. Geophys. Res., vol. 117, D12106.

[11] B.E.K. Nygaard, J.E. Kristjánsson, and L. Makkonen. "Prediction of in-cloud icing conditions at ground level using the WRF model." J. Appl. Meteorol. Climatol. 50, 2445-2459, 2011.

[12] Fikke, S et al. "COST 727: Atmospheric Icing on structures." Measurements and data collection on icing: State of the Art, Publication of MeteoSwiss 75.110 (2006): 1422-1381.

[13] L. Makkonen, “Models for the growth of rime, glaze, icicles and wet snow on structures,” Phil. Trans. Roy. Soc. London, vol. A358, pp. 2913–2939, 2000

[14] J B Wareing, D P Horsman, “A new severe weather test site for OHL conductors and fittings”. Proceeding 15th International Workshop on Atmospheric Icing of Structures, St Johns, Newfoundland, 2013.

Icing conditions forecast using weather forecast model COSMO-RU

Gdaly RIVIN[#1], Inna ROZINKINA[#2], Sergey CHERESHNYUK[*3]
[#] *Hydrometeorological Research Centre of Russian Federation*
11-13, B.Predtechensky per., Moscow, 123 242, Russia
[1] gdaly.rivin@mail.ru
[2] inna.rozinkina@mail.ru
[*] *«R&D Center @FGC», JSC*
22, bld. 3, Kashirskoye shosse, Moscow, 115 201, Russia
[3] Chereshnyuk_SV@ntc-power.ru

Abstract — In 2009 the Russian Federation had joined the international consortium COSMO (the Consortium for Small-scale Modelling). The main goal of this consortium is to develop and maintain nonhydrostatic mesoscale weather forecast model COSMO used to produce high resolution forecasts for certain territory. From april 2011 weather forecast model COSMO-Ru (COSMO for Russia) is used as main in everyday work in Hydrometeorological Research Centre of Russian Federation and other forecast / prognostic institutions in Russia. At the moment forecasts for the European part of the territory of Russia are made on a grid with horizontal resolution 7 km. Forecasts are made for the period up to 3,25 days (78 hours). For some regions in Central and South part of Russia the forecasts are made on a grid with horizontal resolution 2.2 km for the same period. In this article it is performed an attempt to forecast icing conditions with high resolution to predict possible icing of OHL wires and towers.

I. INTRODUCTION

Since 2009 Russia (Roshydromet) is a member of the **Co**nsortium for **S**mall-scale **Mo**deling **(COSMO)**. The full list of countries participating in the Consortium is: Germany, Switzerland, Italy, Greece, Poland, Russia, Romania.

Each country supports its own technology, including data assimilation, based on the model codes provided by the Consortium, the initial and boundary conditions from the Deutscher Wetterdienst or from the European Centre for Medium-Range Weather Forecasts global models, and infrastructure elements (verification, post-processing). The model software allows using the initial and boundary conditions from a system of embedded grids.

High resolution forecasts from model COSMO-Ru could be used for prediction of icing events on wires of overhead transmission lines which is the main goal of ongoing joint work between Hydrometeorological Research Centre of Russian Federation and *R&D Center at Federal Grid Company.*

II. VERSIONS OF MODEL TECHNOLOGIES

Currently Hydrometeorological Research Centre of Russian Federation (WMC Moscow) is using several versions of COSMO model.

COSMO-Ru07 is a COSMO model version (7x7 km) adapted for the WMC Moscow infrastructure covering the area from France to the west of Western Siberia in the zonal direction and from the Barents and Kara Seas on the North to the Mediterranean Sea on the South. The number of grid points is 700×620×40.

COSMO-RuSib is a COSMO-Ru version with a 14x14 km grid covering the area from European Russia to the Far East and from the Arctic Ocean coast to the southern border of Russia and Mongolia (figure 1).

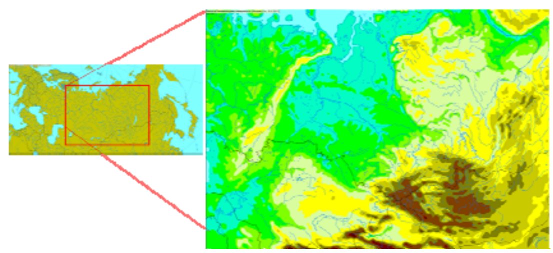

Figure 1: COSMO-RuSib domain

COSMO-Ru2cfo and COSMO-Ru2sfo are COSMO model versions (2.2x2.2 km) nested in the COSMO-Ru7 domain for the Central Federal District of Russia (Ru2cfo) and the Northern Caucasus region (Ru2sfo), respectively.

On figure 2 are shown COSMO-Ru07 and COSMO-Ru2 domains.

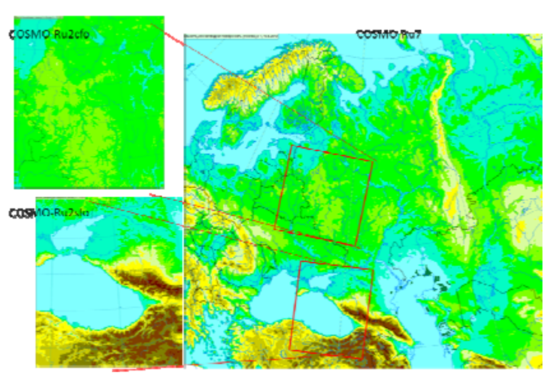

Figure 2: COSMO-Ru07 and COSMO-Ru2 domains

III. MODEL FORECASTS

A wide range of forecast products - GRIB messages is provided in the model grid in different vertical coordinates:

• Basic elements: temperature, wind speed, air humidity, geopotential heights at standard isobaric surfaces, radiation fluxes;

• One-level characteristics: clouds at different levels, near-surface air characteristics: air temperature at 2 meters, dew point at 2 meters, accumulated precipitation, wind speed components and gusts at 10 meters, surface pressure and sea-level pressure, heat and radiation balance components, snow depth and its water equivalent;

GRIB messages are provided to users according to choice lists via FTP to users' addresses.

About 2000 maps for 00:00 UTC are automatically generated in GRADS and are distributed to users via the Internet (FTP) and local networks:

• Sea-level pressure + mid-level clouds+ 3h accumulated precipitation;

• 500 hPa geopotential + near-surface air temperature+ sea-level pressure;

• Near-surface background wind and its gusts;

• Stream function, 10m wind and gusts over the Baltic, Black, and Caspian seas;

• Heights of convection boundaries and 500 hPa wind.

Forecasts are prepared every 3 hours with the maximum lead time 72h.

IV. Plans for Model Development and Improvement

The technology COSMO-Ru is in permanent development and improvement. Major changes in operational technology for the near future are the following:

• To organize operational runs of COSMO-Ru in new configuration for the whole territory of Russia with a 6.6-km step (after installing new hardware in 2013, the grid step was increased to 13.3 km for technical reasons).

• To implement algorithms of more precise analysis of lower-level air temperature and upper-level soil temperature using the information of the Deutscher Wetterdienst global modeling system and SYNOP observations (in 2013).

• To implement continuous cycles of nudging-based data assimilation coupled with the scheme for computing snow water equivalent and snow boundary mask (in 2013).

• To carry out works concerning the numerical weather prediction providing meteorological information for the Sochi 2014 Winter Olympics based on consolidated achievements of COSMO (CORSO project): mesoscale ensemble modeling, post-processing, forecast verification, data assimilation, modeling with a high (less than 2 km) resolution.

• To develop a COSMO technology with a 1-km step (by 2014-2015).

• To modify the COSMO model software by including a bog surface parameterization in the TERRA underlying surface model (2013).

V. Forecast of Icing Conditions

Icing conditions forecast is based on looking at several factors leading to icing event while acting simultaneously. This includes:

- Temperature near surface (T_s) which is near +0°C and has a tendency to grow cold;
- Positive temperature on 850 hPa surface (T_{850}>0°C);
- Precipitation of ~ 1mm/3h.

All these factors acting together could lead to freezing rain or freezing wet snow conditions.

We have made several experiments in late winter 2013 and some experiments based on historical data. These experiments have showed the adequacy of proposed technology. For example on figure 3 is shown meteogram for 25-28 December 2010. In those days Moscow region suffered strong icing rain that has damaged many overhead lines (6-110 kV) mainly because of iced trees falling on lines. It can be seen from the meteogram that all above mentioned icing conditions was present.

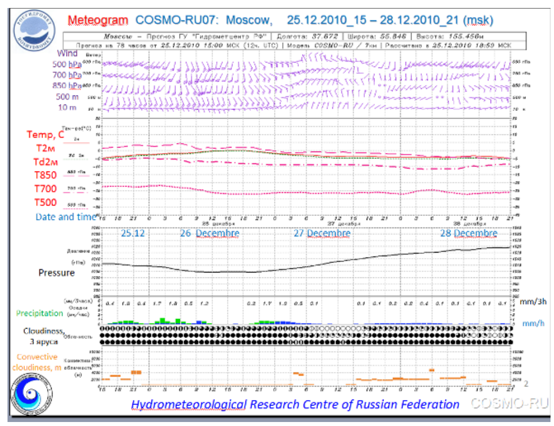

Figure 3: Meteogram for freesing rain 26 December 2010 in Moscow

In nearby future we plan to perform careful and lengthier study in coming winter 2013/14. To verify the forecasts quality we plan to use observations data from automatic meteorological stations installed on substations and overhead transmission lines' towers.

Short-term Winter Icing Climate Prediction Based on the Polar Vortex Area and the Subtropical High

Xunjian XU, Jiazheng LU, Hongxian ZHANG, Bo LI, Zheng FANG

Hunan Electric Power Research Institute, Power Transmission and Distribution Equipments Anti-icing and Reducing-disaster Technology key Laboratory of State Grid, Changsha, China 410007

Abstract — After adding up the historical meteorological data of 97 sites in Hunan province of China during the past 60 years, we count the average number of days that icing occurred each winter, so that we can then define the degree of icing in Hunan province base on it. After calculating correlation coefficient of 74 atmospheric circulation Indices in the past 60 years and the average number of days that icing occurred each winter, we found that the correlation between days of winter icing and some of 74 circulation Indices in spring, summer or autumn in the very same year is significant, such as the index of Asian polar vortex area in winter and the index of subtropical high strength over Western Pacific in winter. And by calculating, we found the index of Asian polar vortex area in winter has a significant correlation with the 74 circulation Indices of spring; summer, autumn in the very same year. Then, by regression analysis, we can predict the value of it. And by the same method, we can also predict the index of subtropical high strength over Western Pacific in winter. After all, we qualitatively predict the degree of icing through the index of Asian polar vortex area in winter and the index of subtropical high strength index over Western Pacific in winter. Then, we quantitatively predict the number of average icing days through all of 74 atmospheric circulation indices. By the very same method from 2008, we successfully predicted the degree of winter icing in every November to Feb of 2008-2009, 2009-2010、2010-2011, 2011-2012, 2012-2013, and the result exactly consistent with actual fact.

Keywords —Icing Climate Prediction; Polar Vortex Area; Subtropical High; 74 Circulation Indices

1. Introduction:

During January 2008, particularly serious icing disaster occurred on power lines in South China, especially in Hunan Province of China [1]. The icing disaster caused huge losses in South China. Accurate short-term winter icing climate prediction is required in advance to prepare icing disaster for reducing the huge losses. A model of power line icing already was proposed by Lasse Makkonen. However, this model just predicted the icing for several hours or days in advance as similar as weather forecast, and could not predict the icing level for several months. The icing climate prediction also was researched by many researchers, such as the CCM3model climate [3]. However, this model could not directly predict the icing degree.

For directly icing climate prediction, the icing degree rule based on the annual average icing days was proposed in this paper in this paper. Then, the short-term winter icing climate prediction based on atmospheric circulation indices, especially the index of Asian Polar Vortex Area and the index of the strength of the subtropical high over the western Pacific in winter is shown in this paper. Using 60 years of historical data of atmospheric circulation and annual average icing days, the two prediction methods of qualitative and quantitative analysis are proposed. The first method is qualitative prediction by conjointly analyzing based on the index of Asian Polar Vortex Area and the index of the strength of the subtropical high over the western Pacific in winter. The second method is quantitative prediction by regression analyzing based on 74 indices of Atmosphere Circulation. The prediction results are very similar to the real situation.

2. Annual Average Icing Days and Atmosphere Circulation Indices

2.1 Annual Average Icing Days and Degree of Icing

There are icing day records and no exact ice-covering thickness records of Hunan Province of China in the past 60 years' meteorological datum. Therefore, The average annual icing days (D) which equals to the total icing days of all observation stations to divide was proposed to describe the ice disaster level: Level 1 (D≤3 days, Light Level), Level 2 (3 days ＜ D ≤ 5 days, Medium Level), Level 3 (5 days ＜ D ＜ 11 days, Serious Level), Level 4 (D ≥ 11 days, Particularly Severe Level). We gathered and analyzed 60 years meteorological datum. There are four times Particularly Severe Level ice disaster during past 60 years in Hunan, 1955-1956 winter, 1968-1969 winter, 1975-1976 winter and 2007-2008 winter, as shown in Figure 1.

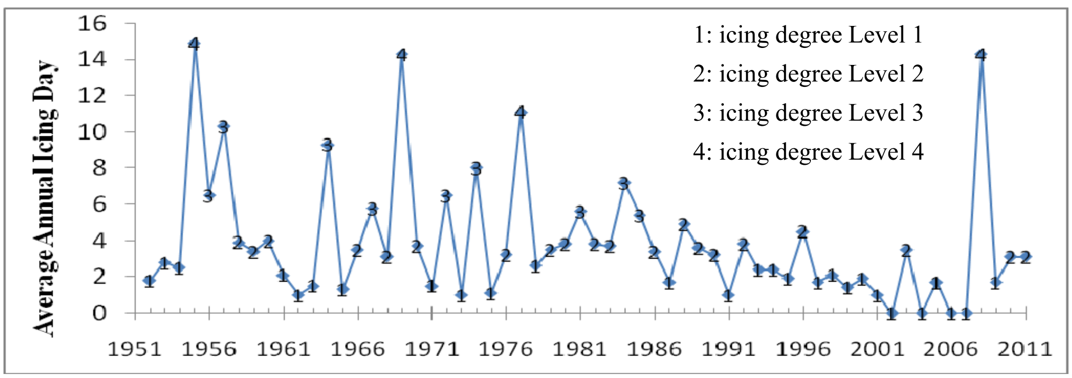

Figure 1 the annual average icing day in Hunan of China and ice disaster level in past 60 years

2.2 Correlation between the Average Annual Icing Days and the Atmosphere Circulation Indices

As we know, atmospheric icing was affected by multiplex climate factors, such as sunspot, ocean temperature (El Nino and La Nino phenomenon), subtropical highs, and so on. By analyzing the past 60 years meteorological datum, the correlation coefficients between the average annual icing days and the 74 atmospheric circulation indices have been calculated. And then, the area index of the Asian Polar Vortex in winter and the strength index of the subtropical high in the western Pacific in winter were found that their correlation coefficients were the largest and respectively reached 0.5 and -0.4, as shown in Figure 2 and Figure 3.

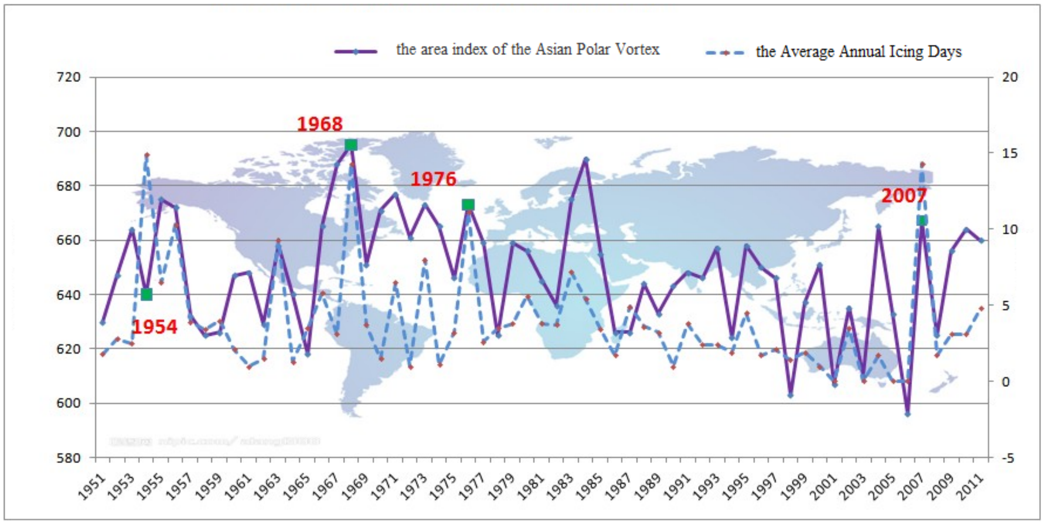

Figure 2 the area index of the Asian Polar Vortex in winter vs. the Average Annual Icing Days

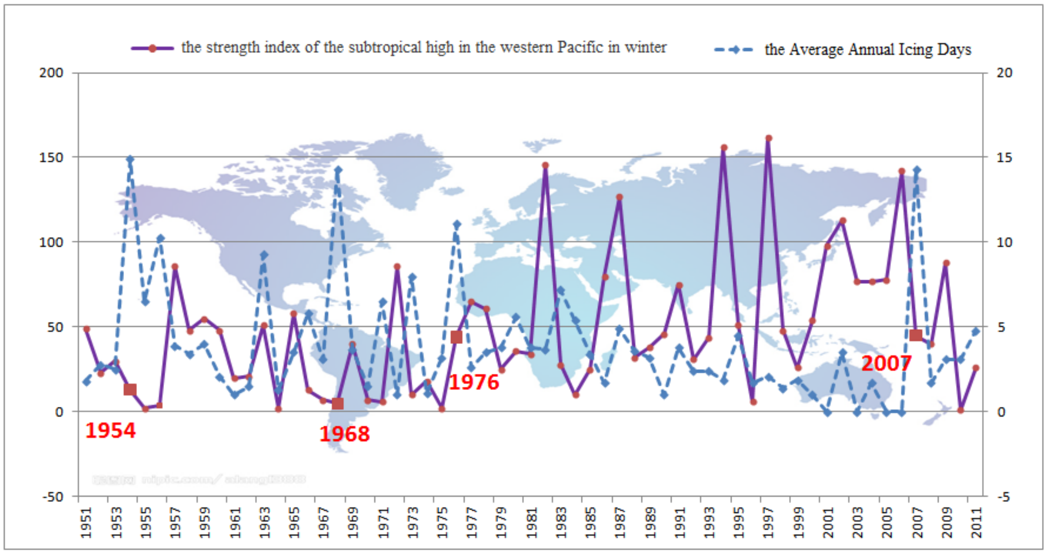

Figure 3 the strength index of the subtropical high in the western Pacific in winter

vs. the Average Annual Icing Days

2.3 Correlation between the Asian Polar Vortex Area and the Circulation Indices of Atmosphere

By the previous analysis, we already know that the average ice days in winter was positively correlated to the winter Asian Polar Vortex Area index. If we can accurately predict the winter Asian polar vortex area index, either indirectly predict the average winter icing days. Therefore, we analyzed the correlation coefficients between the 74 atmospheric circulation indexes and the winter Asian Polar Vortex Area index, the key influencing factors were found, as follows: the Tibetan Plateau (25N-35N,80E-100E) in October (X1), the Tibetan Plateau (25N-35N,80E-100E) in October (X2), the index of the area of the Northern Hemisphere subtropical high in October (X3), the Index of the area of the subtropical high over the South China Sea in October (X4), the Index of the area of the North America-Atlantic subtropical high in October (X5), the Index of the strength of the Northern Hemisphere subtropical high in October (X6), the Index of the strength of the subtropical high over the North African, Atlantic and North American in October (X7), the Index of the area of the subtropical high over the North African, Atlantic and North American in October (X8), the Index of the area of the subtropical high over the Atlantic in October (X9), the ridge line of the North African subtropical high in previous January (X10).

Then, using the least squares method, the linear regression equation for predicting the index of Asian Polar Vortex Area in winter (Y) was proposed as Equation 1.

$$Y = 1163 - 0.775\,X1 + 0.287\,X2 - 1.157\,X3 - 1.23\,X4 + 0.186\,X5 + 0.498\,X6 - 0.534\,X7 + 1.323\,X8 - 0.834\,X9 - 5.166\,X10 \qquad \text{Equation 1}$$

According to the Equation 1, the prediction value of index of Asian Polar Vortex Area in 2012-2013 winter was 665 (the real value is 663), and the real and prediction value from 1951 to 2012 was shown in Figure 4, and the correlation value reached to 0.7. That means the prediction result is very accurate.

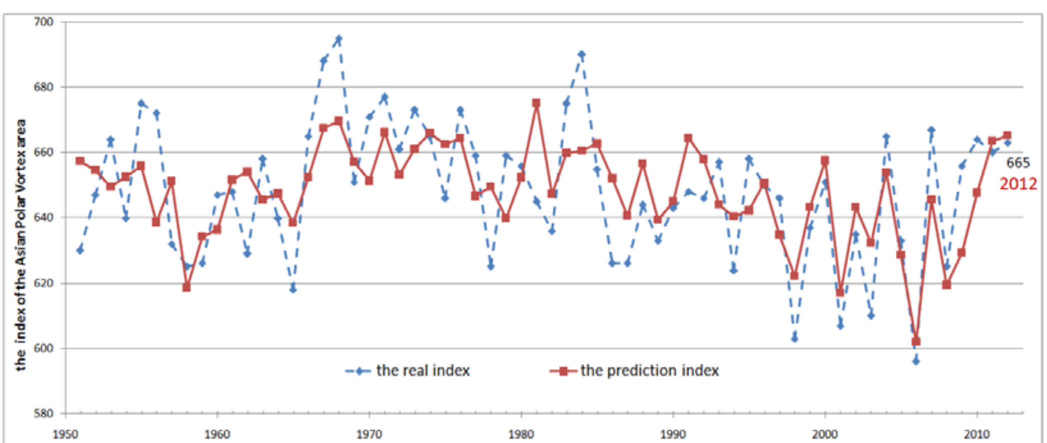

Figure 4 the real and prediction index of the Asian Polar Vortex in winter

2.4 Correlation between the Index of the strength of the subtropical high over the western Pacific and the Atmosphere Circulation Indices

Through 60 years of historical data analysis, the correlation between the Western Pacific Subtropical High in winter and the average winter ice days was negative. If we can predict winter Westpac strength index, it can indirectly predict average winter ice days. Therefore, we analyzed correlation coefficients between 74 atmospheric circulation indexes and the Index of the strength of the subtropical high over the western Pacific in winter, and then to identify the main influencing factors, as follows: SOI in May (X1), SOI in June (X2), SOI in July (X3), SOI in September (X4), SOI in October (X5).

Then, using the least squares method, the linear regression equation for predicting the Index of the strength of the subtropical high over the western Pacific in winter (Y) was proposed as Equation 2.

$$Y = 39.18 - 0.973\,X1 - 0.957\,X2 + 0.179\,X3 - 2.721\,X4 + 0.995\,X5 \qquad \text{Equation 2}$$

By the Equation 2 the prediction value of index of the strength of the subtropical high over the western Pacific in 2012-2013 winter was 65 (the real value is 39, the increase trend prediction is correct), and the real and prediction value from 1951 to 2012 was shown in Figure 5, and the correlation value reached to 0.81. That means the prediction result is also very accurate.

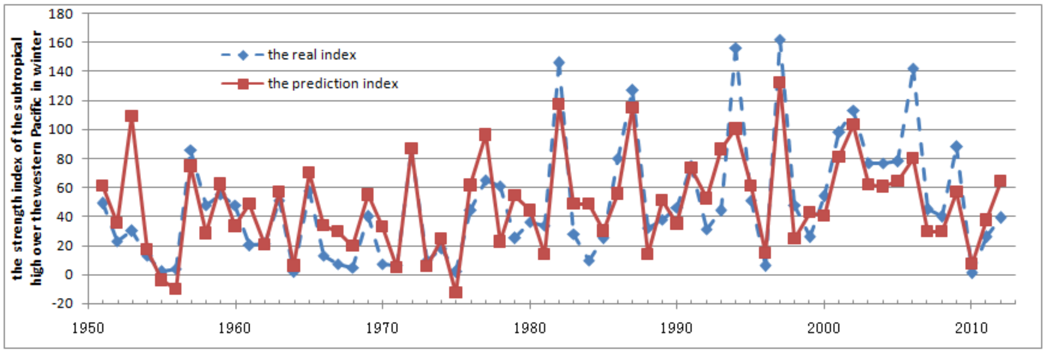

Figure 5 the real and prediction strength index

of the subtropical high over the western Pacific in winter

3. Short-term Winter Icing Climate Prediction in Hunan of China

3.1 Conjoint Analysis based on the index of Asian Polar Vortex Area and the index of the strength of the subtropical high over the western Pacific in winter

Through 60 years of historical data analysis, the departure values of the index of Asian Polar Vortex Area and the index of the strength of the subtropical high over the western Pacific in winter were shown with the annual degree of icing in Figure 6. In Figure 6, light level means Level 1, medium level means Level 2, serious and up level means Level 3 or 4. From this figure, we can found that the serious and up level icing concentrated in the fourth quadrant, light level icing concentrated in the second quadrant, and the medium level icing concentrated in the first and third quadrants. By using the prediction values of the index of Asian Polar Vortex Area and the index of the strength of the subtropical high over the western Pacific in winter from Equation 1 and Equation 2, the icing of 2012-2013 winter was shown in the first quadrants, and was predicted to be medium level. By using very same way, the icing degree of 2008-2009, 2009-2010, 2010-2011, 2011-2012 winters were predicted to light level, medium level, medium level, medium level respectively. And the real icing degree of 2008-2009, 2009-2010, 2010-2011, 2011-2012 and 2012-2013 winters are light level, medium level, medium level, medium level, medium level respectively. The prediction icing degree is same as the real situation. This method is belong to qualitative analysis.

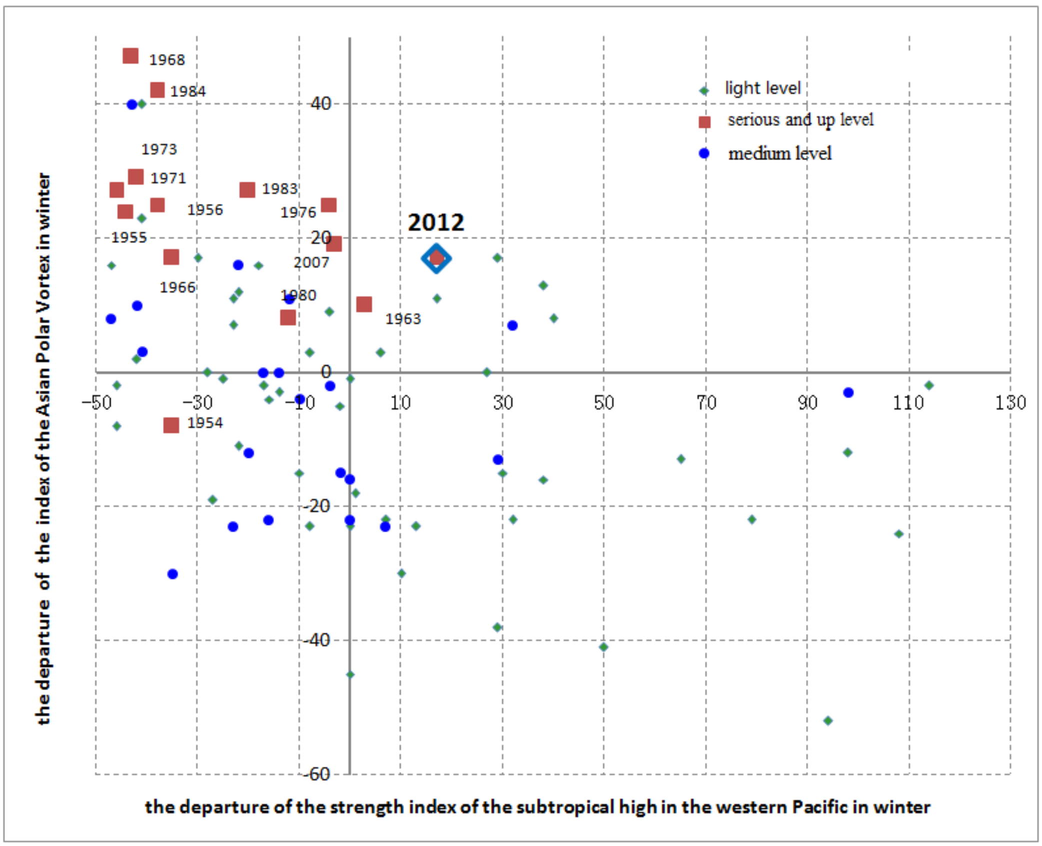

Figure 6 Conjoint Analysis based on the index of Asian Polar Vortex Area and the Index of the strength of the subtropical high over the western Pacific in winter

3.2 Regression Analysis based on 74 indices of Atmosphere Circulation

First, the correlation coefficients between the annual icing days and 74 atmospheric circulation indices were calculated, and then the best 15 indices were proposed. Second, using the linear regression method, the predication icing days since 2008-2009 winter were calculated as shown in Figure 7 and Table 1. From Figure 1, the correlation coefficient between the real and prediction values of annual average icing day is 0.7, that means the prediction of winter icing climate is accurate, and From Table I, since 2008-2009 winter, the short-term winter icing climate prediction accuracy is 80% during past 5 years.

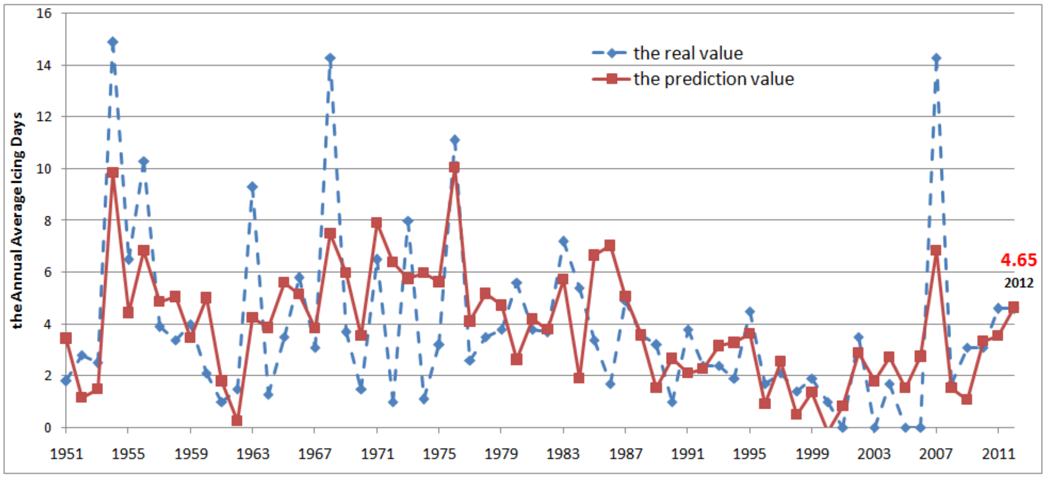

Figure 7 Regression Analysis based on 74 indices of Atmosphere Circulation

Table 1 the predication icing days since 2008-2009 winter

years	Predication average icing days	Real average icing days
2008-2009 winter	1.5 (level 1)	1.7 (level 1)
2009-2010 winter	1 (level 1)	3.1 (level 2)
2010-2011 winter	3.4 (level 2)	3.1 (level 2)
2011-2012 winter	3.6 (level 2)	4.6 (level 2)
2012-2013 winter	4.6 (level 2)	4.6 (level 2)

4. Conclusion

The short-term winter icing climate prediction based on atmospheric circulation indices, especially the index of Asian Polar Vortex Area and the index of the strength of the subtropical high over the western Pacific in winter is investigated. Using 60 years of historical data of atmospheric circulation and annual average icing days, the two prediction methods are proposed. The first method is qualitative prediction by conjointly analyzing based on the index of Asian Polar Vortex Area and the index of the strength of the subtropical high over the western Pacific in winter. The qualitative prediction shows that the prediction result is same as the real situation in past 5 years' winter. The second method is quantitative prediction by regression analyzing based on 74 indices of Atmosphere Circulation. The quantitative prediction shows the short-term winter icing climate prediction accuracy is 80% during past 5 years. Those short-term winter icing climate prediction results have been given to effective guidance for anti-icing work in Hunan of China.

Reference

[1] Jia-zheng LU, Zheng-long JIANG, Hong-cai LEI, et al. Analysis of Hunan Power Grid Ice Disaster Accident in 2008 [J]. Automation of Electric Power Systems, 2008, 32(11): 16-19. (in Chinese)

[2] Lasse Makkonen. Modeling Power Line Icing in Freezing Precipitation [J]. Atmospheric Research, 1998, 46: 131-142.

[3] P. J. Rasch, J. E. Kristjansson. A Comparison of the CCM3 Model Climate Using Diagnosed and Predicted Condensate Parameterizations [J]. Journal of Climate, 1998, 11: 1587-1614.

Session 6: Various Icing Topics

Guide for the Preparation of an Emergency Restoration Plan

Alex Mogilevsky
Transmission & Distribution Program Manager
CEATI International Inc.
Montreal, Quebec, Canada
Alex.mogilevsky@ceati.com

Asim Haldar
Manager of Engineering, Research & Development
Nalcor Energy
St. John's , NL, Canada
ahaldar@nalcorenergy.com

***Abstract* —** The “Guide for the Preparation of an Emergency Restoration Plan” provides a recommended procedure or road map for safe, efficient and orderly restoration of transmission lines after a major failure. It is designed to help the CEATI Wind & Ice Storm Mitigation Interest Group (WISMIG) members prepare their own Emergency Restoration Plans (ERPs) in relation to existing ERPs of their companies and government agencies.

***Keywords* —** *Emergency Restoration, Overhead Lines, Towers, Line Failures, Icing*

I. Introduction

This paper is based on a project by CEATI International (Centre for Energy Advancement through Technological Innovation) [1]. CEATI’s efforts are driven by over 120 participating organizations. Continuously expanding its international reach, CEATI members represent 17 countries on 6 continents, a diversity that contributes to many CEATI programs.

This Emergency Restoration Plan aims to:

- Ensure adequate utility response to restore equipment after a major failure
- Ensure the safety of employees, responders and the public
- Reduce the magnitude of environmental and other impacts
- Reduce the potential for property destruction and revenue losses
- Assist response personnel in determining and performing proper remedial actions quickly
- Implement a failure investigation in order to establish the cause of the failure
- Reduce recovery times and costs
- Inspire confidence in response personnel
- Ensure communications internally and externally
- Consider eventual needs for cooperation and assistance from neighbouring utilities.

The Plan provides guidance on training to be given to all employees involved in restoration activities. The training program includes participation in drills and exercises. In case of a significant emergency, the plan provides guidance to ensure that employee families receive the necessary assistance.

II. History

Over 5 million people in Canada and North-Eastern United States were affected by the 1998 Ice Storm. The area that was hit by the storm amounted to 400,000 square kilometers. It was a unique moment in the history of the region. The average annual freezing rainfall in the area is 25 to 50 hours. In January of 1998, the region received more than 70 hours of freezing rainfall in only 5 days. The ice on conductors was estimated to have a radius of 20 to 75mm. Environment Canada said this was “The most significant climatic event of the 20th Century.”

This incident resulted in damages to conductors and ground wires, thousands of towers, insulator strings, dampers, H frame wood poles, cross-arms, and foundations.

In 1999, the Ice Storm Mitigation Interest Group was initiated at the request of Hydro-Québec. Along with 13 other utilities, they started a group to discuss utility experiences, co-fund projects, and fill knowledge-gaps in the industry. Today, the group is made up of more than 30 utilities from around the globe, and has a portfolio of numerous topic-related projects.

III. Structure

This paper is based on a study report entitled “Guide For the Preparation of an Emergency Restoration Plan.”[1]. It was sponsored by a consortium of seventeen organizations from across the globe. Best practices, utility experiences, and training techniques were discussed and gathered from the participating utilities to create this report.

The definition of emergency, “A present or imminent event that requires prompt coordination of actions or special

The Participants of the Wind & Ice Storm Mitigation Interest Group regulation of persons or property to protect the health, safety, or welfare of people, or to limit damage to property and the environment," [1]. was rewritten to "a present or imminent event that threatens business continuity due to failure of critical transmission or distribution equipment, labour disruptions or failure of critical computer or communication systems and that requires prompt coordination of actions or special regulations of persons, assets and resources, to protect the health, safety or welfare of people, to limit damage to property and environment and to restore business continuity," in order to relate to the issue at hand.

The guide concentrates on emergencies triggered by a variety of causes: natural causes, human impact, and others, which include equipment failure.

The objectives of the Emergency Restoration Plan are to ensure the safety of employees, contractors, emergency response personnel, and the general public. It is put in place to protect business and public assets, and reduce the adverse impact on the environment and business continuity.

IV. EXTENT AND LEVELS OF EMERGENCY

Emergency classification is dependent on the size of the area covered by the utility, the resources required, and the expected time to restore service. It can change after the assessment of the emergency situation. The guide recommends a three-tier classification, with 1 being the lowest, and 3 being the highest level of emergency.

The components of the Emergency Restoration Plan (ERP) include an Emergency Response Policy, Communication and Restoration Teams.

An Emergency Restoration Plan needs to be simple, parallel and people friendly. Procedures need to be easy to find, understand and execute. The organization structure, roles and responsibilities should be similar to those of day to day operations, and the plan should fit the people and not try to fit people to the plan.

V. RISK IDENTIFICATION AND EXPECTED MAGNITUDES

Risk factors that need to be considered are severe weather, unstable ground conditions and public interference. Risk factors should normally be reflected in the design of the Emergency Restoration Plan, as it is not economically practical or technically feasible to reduce the risk to zero. When calculating risk acceptance, probability of the occurrence and the magnitude and extent of consequences must be taken into consideration.

TABLE I. TABLE TYPE STYLES

Risk Due to:	Spatial Distribution	Possible Damage Magnitudes	Emergency Response Level
Freezing Rain	High intensity 3 km x 40 km	Tower collapses and cascading of a several to more than 100 towers. Many lines could be affected	1 to 3
	Low intensity 25 km x 150 km	Ground wires ruptures and line grounding or premature failure of one component	1
Galloping	Moderate amplitudes	From a few spans to a complete line. Induce flashovers and leads to shutting the line	1
	Heavy ice and large amplitudes	From a few spans to a complete line. Line out of service and towers, conductors and hardware damage	2
In-cloud Icing	A few km. Very localized	10 to 20 towers	1 or 2
Wet Snow	A few kms to about 50 kms.	Tower collapses from a few to more than 100. Many lines can be affected.	1 to 3
	Many lines can be affected	Grounding of the lines by loss of insulation or Ground wires ruptures	1
Wind	A few spans	A few towers	1
Tornadoes	1 km x 5 km	Two or three towers	1
	1 km x 150 km	Two or three towers on many lines	3
Flood	A few square km.	A few towers by erosion or landslide	1
Right-of-way Fires	A few square km.	Grounding of the lines by insulation loss	1
Earthquakes	Localized	No damages but substations or major river crossings can be severely damaged	1 to 3
Volcanic Eruptions	Localized	A few towers by erosion or landslide or grounding of the lines	1
Avalanches	Localized	A few towers	1
Landslides	Localized	A few towers	3
Erosion	Localized	A few towers	1
Sabotage and Vandalism	Localized	A few towers or major river crossings	1 to 3
Equipment Failures	Localized	One tower but possibility of cascading of a few towers	1

VI Derivative Work

After the completion of the "Guide for the Preparation of an Emergency Restoration Plan," derivative work was initiated. Several of the titles include:

- De-icing Techniques Before, During and Following Ice Storms
- Inspection Techniques for Detecting Latent Damage to Existing Overhead Transmission Lines from Previous Ice and Wind Storms
- Review Various Options to Prevent Cascading Failures and Assess Their Cost Effectiveness
- Guide to Define Design Criteria for Outdoor Station Insulators Taking into Account Pollution and Icing
- Development of Common Structures for Emergency Restoration
- Safety Measures During Emergency Restoration
- Emergency Restoration Methods under Extreme Events: A Report on Best Practices
- Transmission Line Monitoring Package for Extreme Events

Acknowledgment

The report was sponsored by a consortium of seventeen organizations from across the globe. Best practices, utility experiences, and training techniques were discussed and gathered from the participating utilities to create this initiative.

Reference

[1] Wind & Ice Storm Mitigation Group, CEATI International, "Guide for the Preparation of an Emergency Restoration Plan," CEA Technologies, April 2002.

- Participants of the Wind & Ice Storm Mitigation Interest Group, CEATI International.

Research and engineering application of power grid large-scale ice-disaster prevention and cure technology

LU Jia-zheng, ZHANG Hong-xian, FANG Zhen, LI Bo, JIANG Zheng-long,
ZHOU Wei-hua, XU Xun-jian, TAN Yan-jun, LUO Jing, ZHAO Chun
Hunan Electric Power Research Institute, Power Transmission and Distribution Equipments
Anti-icing and Reducing-disaster Technology key Laboratory of State Grid， Changsha 410007
China

Abstract — Ice disaster of power grid has happened in more than 100 countries all around the world. Ice disaster is one of the biggest natural disaster to make threat on the safe operation of power grid, which may cause the tripping of transmission lines, towers broken down, even lead to severe paralysis of large area power grid. The research team has carried out a series of research works on the icing of power grid ever since 1998, including icing forecast, ice monitoring, insulator flashover and DC ice-melting technology. Through revealing the "Sun-Surface-Atmosphere Coupled" icing formation rules for power grid, we developed the first grid icing forecast system in the word, which has high prediction accuracy in short-term, medium-term and long-term power grid icing forecast. Besides, it invents the anti-fogging image monitoring method for conductor icing, proposes the icing thickness intelligent identification technology for the wire, and developed power grid icing monitoring and decision system. The regularity of iced insulators flashover is also revealed, and the the anti-icing composite insulator has been invented, which makes the line icing flashover rate decrease by 90%. Through overcoming the core technology of "impedance flow" rectifier transformer, series of DC de-icing technology and equipments have been developed, which have less harmonic, and can well satisfied the requirements of the standard with the reliability as high as 100%. Those proposed technology has been widely used in the 132 corporation in 8 provinces in southern China on 1023 transmission lines, and has fight against several frozen rain and snow disasters in 2009-2013 by accurate prediction, reliable monitoring, and ice melting with high efficiency. It has constructed the scientific and complete supporting system for ice disaster prevention of the power grid, which can provide the economic and efficiency solution for ice disaster control management.

Keywords — Icing Disaster; Icing Prevention; Icing Forecast; Icing Monitoring; Anti-Icing; DC Ice-melting; Supporting System

1 Introduction

Grid ice storms happen in dozens of countries throughout the world, the ice storm caused tripping down of towers, a large area of the grid resulting in severe paralysis, makes itself the greatest disaster in safe operation of power grid. During January 5th to 10th 1998, a serious snow and ice storms happened in the US and Canada. Eastern Ontario, southern Quebec in Canada, upstate New York and parts of Vermont, New Hampshire and Maine, the regional power grid was seriously damaged, the grid Quebec ice storm caused more than 1000 transmission tower collapsed, more than four hundred million power outages. In early 2005, China Hunan power grid suffered severe icing disaster, which caused sever damages [1]. By the time of 2008, several provinces in southern China suffered a particularly severe icing disaster [2-7], more than 70 millions of transmission lines and towers collapsed, which lead to direct property loss of more than 250 billion Chinese Yuan, due to snow and ice storms, resulting in nearly million users a power interruption, the Beijing-Guangzhou railway electrification outage seven days, seriously affected people's life and social stability.

After the catastrophic ice disaster happened in Canada in 1998,people in international power industry start to focus on the study of large-scale power grid icing disaster, A huge investment and wide range of transmission line devote to improve anti-icing design standards, but at the same time, the power company will bear the resulting upward pressure on costs. It is urgent to develop new ice disaster prevention and control technology approach. International counterparts in the power grid ice disaster prevention have carried out some of the positive exploration. Author of the research team carried out in this field for more than 10 years of research work, and made a breakthrough in power grid icing forecasts, ice monitoring, insulator flash and anti-icing DC thawing technology.

2 Icing and prediction of grid technology

In 2008, an icing disaster came in a sudden, because it is unpredictable, response measures cannot be prepared in advance, power companies suffered heavy losses. Carry out grid icing forecast, enabling early deployment various prevention measures. Grid ice forecasting techniques and electromagnetics, meteorology, geography, and many other factors related and influence each other, is extremely complex.

By establishing massive database of glaze days in the past sixty years, system analysis discovered sunspots affect ice grid, grid terrain, the polar vortex and other 17 key factors which is especially affective, such as "particularly severe icing occurred in extreme years in sunspots close (Figure 1) ", etc. For the first time revealed the "day to air coupling" Grid ice formation law (Figure 2), namely: Solar Cycle affect atmospheric circulation changes in the northern winter, cold air and warm air continued southwest intersection, east-west mountain ranges in the role of terrain , the cold air sinks, warm air climbs, to form a stable inversion layer (altitude greater than ˚C, the ground below 0 ˚C) and freezing rain, which causes the breaking down towers to form a large-scale grid ice disaster. Since we observed eight southern provinces grid icing process in 2008, we verify that the "Sun-Earth atmosphere coupled" ice formation law is correct. We applied the law and find the icing disaster-prone areas and conditions of icing disaster. While in northern China, temperature in winters are below ground and high altitude 0 ˚C, which lead to snow, but less prone to icing grid.

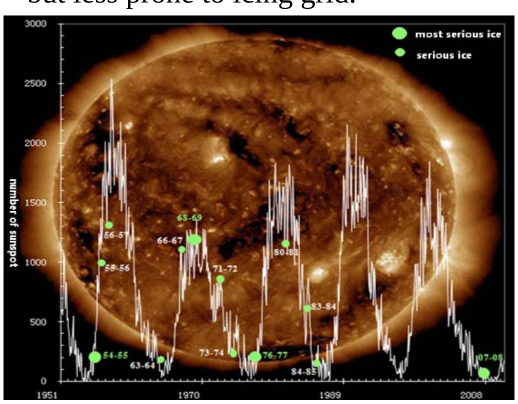

Figure 1 Sunspots vs. Icing Level

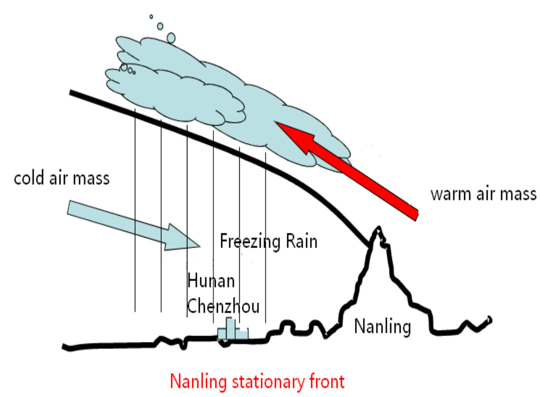

Figure 2 Icing Forming Theory

Due to different emphases, international weather forecasts do not predict grid ice thickness. We established a integrate model which covers the electromagnetic, weather, heat and other factors of ice growth, based on heat balance and wind-induced drop collision mechanism proposed ice thickness calculation formula, breaking the grid icing numerical prediction of complex problems, we found that to achieve the power grid ice thickness, the short-term forecasts for the first time down to the line, is workable. Developed the world's first automatic grid ice forecasting system (Figure 3), and filled domestic blank. November 2008 in China, Hunan, Jiangxi and other eight provinces, the system have been widely used, forecasting the results published in State Grid Corporation of China, accurately predicted the previous five years, varying degrees of freezing rain and snow disaster grid. After verification of the China State Grid Corporation, prediction accuracy rate (Figure 4) of Long, medium and short-term ice forecasting accuracy rate as high as 100%, 83.5% and 98%, for the fight against the ice storm to win a valuable one month, 7 days, 3 days, freezing rain and snow disaster improve effectiveness and efficiency of disposal.

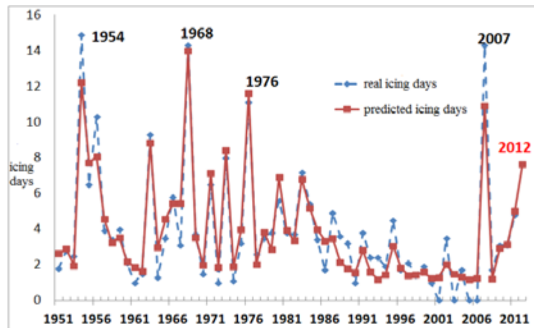

Figure 3 Power grid ice automatic forecasting system Figure 4 the real and prediction result of short time icing climate forecast

3 grid ice monitoring and early warning technology

Due to the poor environment of transmission line, existing international monitoring device find it difficult to monitor ice under low visibility conditions. Image features on the ice after the excavation, compare a variety of image processing technology, invented icing image fogging method, eliminating the water, fog and other interference on image acquisition, image color saturation to ensure fidelity (Figure 5).

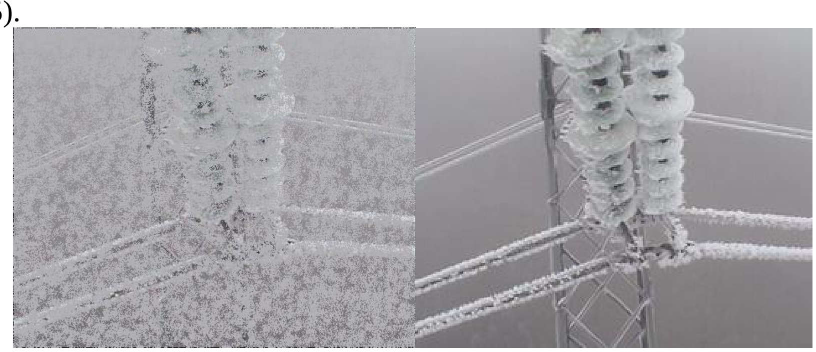

Figure 5 (a) fog before capturing an image map algorithm 5 (b) take pictures after fogging algorithm

Existing monitoring device can not get the image conductors ice thickness, ice project creatively put forward the image characteristic index thresholding methods (Figure 6), to achieve a thick icing automatic identification error is less than 10%, accuracy of 1mm.

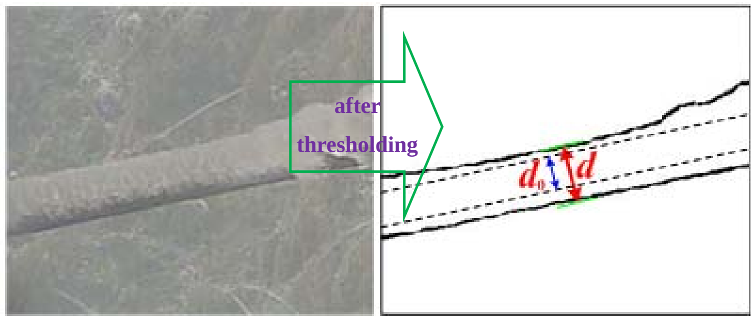

Figure 6 (a) before treatment thresholding Figure 6 (b) after thresholding

Based on methods described above, the use of low-power supply design and anti-jamming technology, developed a highly reliable power transmission line icing automatic monitoring system, on-site ice images, weather, stress and other online monitoring and automatic icing thickness identification. System in Hunan, Guangdong and other areas distribution 340 sets, ice-monitoring network established grid. The reliability rate of this system is 92%, after the verification of the China State Grid Corporation, our operational reliability ranked in the first place.

Anti-icing manual emergency decision grid has high security risk, while low efficiency. Based on characteristics of the icing disaster, in-depth analysis of the various early warning model and decision algorithm established ice disaster emergency decision-making models and methods (Figure 7), At the same time, we developed the grid ice disaster emergency automatic decision system, and as a result, decision-making speed up 95%, with significantly improved accuracy.

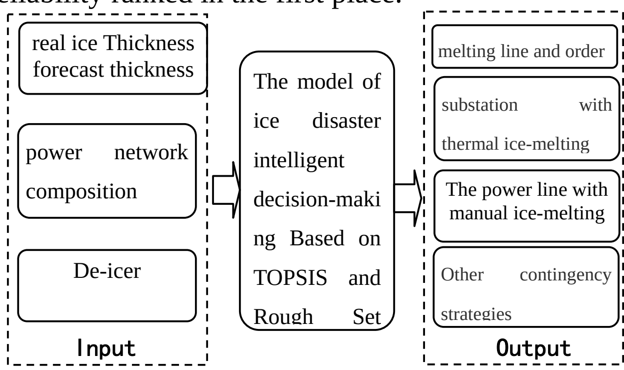

Figure 7 ice disaster intelligent decision-making methods

4 Insulator anti icing flash technology

Insulator ice bridge, causing serious accidents such as flash ice line tripping, severe grid large area blackout, so the tower had to use artificial icing on the insulator, in 2008 icing disaster, six electricity workers who died because of it. Through a large number of simulation experiments and natural scene, we confirmed that the flash mainly due to ice contamination and icing the joint action. Accordingly, creatively put forward the tape path, the rational allocation of long-distance method:

A) delay the ice bridge;

B) cover the small cap by bigger ones, then filthy production during ice crystals melting significantly reduced.

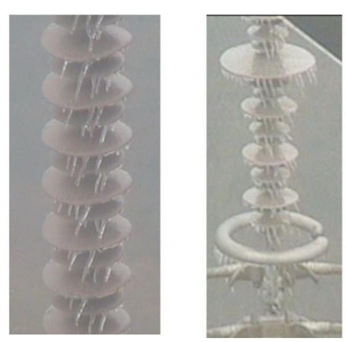

Normal Insulator **Bridging** Anti-ice Insulator **Un-bridging**

Figure 8 Application of anti icing flash

After the electric field calculation and optimization design, we invented the anti-icing flash composite insulators, tests showed flashes of composite insulators to extend anti-ice ice bridging time 11.3 times and improve ice lightning pressure 16% to 22% November 2008, the 500kV and 220kV composite insulators used in the line, four years of ice flash tripping accidents did not occur (Figure 8), which reduce tripping icing flashover rate of 90%, to avoid the artificial icing on the tower to ensure the personal safety.

5 DC Ice-Melting technology and equipment

Existing methods and communication technologies such robot, has a low efficiency of ice melting, can not meet the power requirements of a wide range of ice disaster prevention, DC thawing technology because of its high efficiency, an international research focus. The existing international DC thawing technology uses three-phase thyristor rectifier, harmonic serious, easy to cause damage to expensive equipment such as transformers, becoming DC thawing technology applications, "chronic", need to install large-capacity filter device, covering area, the project is difficult to promote the application.

We analyzed the structure and magnetic properties of proposed harmonic magnetic potential internal offset of the transformer winding new ideas, invention of multi-conductor pairs continuous coil winding method, developed a special structure 12-pulse rectifier transformer (Figure 10). Proposed diode rectifier, heat, reduced by 30%, power factor up to 0.95, can be air cooled, easy to maintain. Harmonic is minimum in international when compare to similar devices, which meet GB/T14549 standards, eliminating its safe operation of power hazards. Cancel bulky filter, cost reduction, covering significantly reduced, to solve the problems of DC thawing device applications were the biggest challenges.

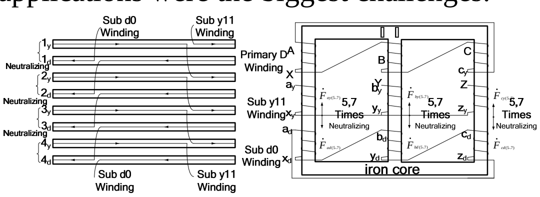

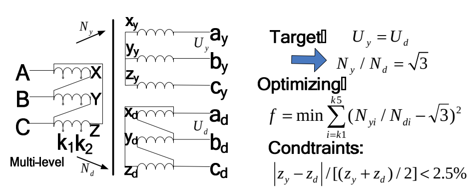

Figure 10 potential rectifier transformer schematic; Figure 11 "impedance of flow" optimization techniques

In order to obtain a large current melting ice, also to prevent damage to the rectifier bridge between the current imbalances in the general, large-capacity saturation equilibrium flow reactors have been widely used, though noisy and expensive. After magnetic circuit optimization and simulation, project development based on discrete optimization of the "impedance of flow" technique (Figure 11), to achieve the internal impedance transformer turns ratio and balance, the current between the rectifier bridge is less than 5%, the output current up to 12000A, while further reducing harmonics, canceled the balance reactor, size, cost and noise further reduced.

According the principles and technology above, through heat analysis, reliability design and extensive testing, we invented fixed, mobile, portable and other 3 Series 9 models DC thawing equipment (Figure 12), capacity from tens of kilowatts to tens of million kilowatts, which is able to meet the voltage level of 10kV ~ 500kV, wires and ground, the main network and agricultural distribution network, a variety of line and length of ice-melting needs.

In 2007,we developed China's first DC ice-melting device, large ice storm in

2008 during the Cold successful mine line in Loudi(Hunan province, China) 110kV line implemented a first line DC ice melting ice. After 2008, the ice-melting device is now been widely used in China Jiangxi, Anhui, Hunan and other provinces, 132 units of 1,023 lines, line anti-ice transformation of savings over investment 6.35 billion yuan. Implemented DC thawing 526 times, with the success rate of 100%.

(a) 500kV stationary (b) 220kV Mobile formula (c) portable agricultural distribution network
Figure 12 Series DC thawing device

Our ice-melting device project can melt ice in a line of hundreds of kilometers within 90 minutes. The device of ice-melting in Yun Tian substation 500kV transmission line cost only 20 million Yuan, covers an area of less than 1,200 square meters, the device economical, efficient, reliable and competitive international market. We also developed a "transmission line current icing Technical Guidelines" and other technical standards for DC thawing provided technical specifications. By using our devices, we save investment and steel, reducing the area, protect the environment, and effectively protect the safe operation of large power grids.

6 field application

Chenzhou City, locate in Hunan Nanling Mountains, experience different degrees of power grid ice disaster every year. In 2008, the area experienced the most sever icing disaster. January 3th to 12^{th} 2013, as same degree of seriousness of ice disaster happened, with the thickness of 40mm (Figure 13).By using the project, mobile, fixed, rural power portable equipment of 10 sets of melting ice, on the ice outside serious blessing I line and other lines carried 28 times intensive melting ice (Figure 14), there was no break down the tower, to ensure the safety of the grid Chenzhou, verification technology has been equipped to deal with a series of large-scale severe ice storm grid capacity, did not break down the tower accident occurred, without application of project technical lines, occurred many times in recent years, still ice down the tower accidents.

Figure 13 Chenzhou line icing conditions. Figure 14 processes and melting ice melting ice cubes falling

7 Conclusion

Icing disaster affect safe operation of power grid as the greatest natural disaster, affecting a wide range with great harm. In order to improve the grid's ability to withstand snow and icing disasters, the researchers developed a series of grid ice disaster prevention technology, including:

1) proposed the "Sun-Earth atmosphere coupled" Grid icing rule,make the power grid ice long, medium and short-term prediction accurately, won precious time for anti-icing work.

2) developed icing monitoring system to meet the harsh requirement in operation, to achieve a thick icing automatic identification, which can clearly monitor the scene of icing conditions.

3) developed a series of DC thawing equipment, fixtures, small size, low cost, high reliability, easy operation and maintenance, which have been widely applied in China, saving a lot of investment in upgrading the line anti-icing.

4) invented the tape path, long-distance anti-icing flash composite insulators, to effectively reduce line icing flashover trip rate and improve the reliability of power supply provided important technical support, to avoid the artificial icing on the tower.

Series of anti-ice disaster grid technologies ice disaster prevention provides a scientific and complete technical support system for power grid, as a result the grid's ability to withstand snow and ice storms has been significantly enhanced.

As global warming continues to develop, the outbreak of the frequency of extreme weather disasters is rising, a wide range of snow and icing disasters are likely to happen again, we must raise awareness of the importance to withstand icing disaster and continue to strengthen anti-ice disaster mitigation technology research efforts, increase grid anti-ice disaster and technological achievements to promote the application work when the recurrence of large-scale power grid ice disaster, to ensure normal production and life of people.

References

[1] LU Jiazheng，LIU Chun，CHEN Hongdong，et a1．Finite element calculation of 500kV iced power transmission system[J]．High Voltage Engineering，2007, 33(10)：167~169．

[2] LU Jia-zheng, JIANG Zheng-long, LEI Hong-cai, et al. Analysis of Hunan Power Grid Ice Disaster Accident in 2008[J]. Automation of Electric Power Systems, 2008, 32(11): 16～19.

[3] TANG Jie. Damage Analysis of Icing Disaster in Shaoguan Power Grid in 2008 and Corresponding Countermeasures. Guangdong Electric Power, 2009, 22(7),58-61.

[4] LING Ping, QIAN Zhi-yin, ZHAO Wen-bin. Research on icing disaster prevention and treatment systems for transmission lines in East China[J]. East China Electric Power, 2008, 36(11),1-5.

[5] Zhu Youliang,Liang Wen,Yang Jihai et al. Ice hazard on the grid analysis of disaster and emergency power grid construction of the platform[J]. Engineering Science, 2010, 15(4), 28-31.

[6] LIU Ping-yuan, HE Hong-ming, PAN Chun-ping. Investigation of Ice Disaster in 2008 and Research on Deicing in Guangdong Power Grid[J]. Guangdong Electric Power. 2010, 23(3), 34-37,44.

[7] PENG Xiang-yang, ZHOU Hua-min, PAN Chun-ping. Damage Condition of Overhead Transmission Lines in Guangdong Power Grid Caused by Icing Disaster in 2008 and Analysis on Key Impacting Factors[J]. Power System Technology. 2009, 33(9),108-112

Influence of Icing on Bridge Cable Aerodynamics

Holger Hundborg Koss [#*1], Jesper Frej Henningsen[#], Idar Olsen[#]

[#] *Department of Civil Engineering, Technical University of Denmark*
Brovej, Building 118, DK-2800 Kgs. Lyngby, Denmark
[1] hko@byg.dtu.dk
[*] *FORCE Technology*
Hjortekærsvej 99, DK-2800 Kgs. Lyngby, Denmark

Abstract — In recent years the relevance of ice accretion for wind-induced vibration of structural bridge cables has been recognised and became a subject of research in bridge engineering. Full-scale monitoring and observation indicate that light precipitation at moderate low temperatures between zero and -5°C may lead to large amplitude vibrations of bridge cables under wind action. For the prediction of aerodynamic instability quasi-steady models have been developed estimating the cable response magnitude based on structural properties and aerodynamic force coefficients for drag, lift and torsion. The determination of these force coefficients require a proper simulation of the ice layer occurring under the specific climatic conditions, favouring real ice accretion over simplified artificial reproduction. The work presented in this paper was performed to study the influence of ice accretion on the aerodynamic forces of different bridge cables types. The experiments were conducted in a wind tunnel facility capable amongst others to simulate in-cloud icing conditions.

I. Abbreviations and Nomenclature

α	- angular position of the ice layer relative to the position during accretion process [deg]
C_D	- aerodynamic drag force coefficient [-]
C_L	- aerodynamic lift force coefficient [-]
CWT	- collaborative Climatic Wind Tunnel facility
F_D	- aerodynamic drag force [kN]
F_L	- aerodynamic lift force [kN]
HDPE	- high-density polyethylene
I_u	- turbulence intensity of along wind component [%]
LWC	- liquid water content [g/m^3]
MVD	- median volume diameter [µm]
u	- wind tunnel airspeed [m/s]
θ	- angle for lift force antisymmetry axis [deg]
R_a	- average surface roughness [µm]
Re	- Reynolds number based dry tube diameter [-]
Re_{cr}	- critical Reynolds number [-]

II. Introduction

A. Background and Aim of the Study

Bridge cables are subjected to static and dynamic loading. The static loading mainly originates from by the weight of the bridge deck, the traffic load, time averaged wind action and from the dead weight of the cable itself. For inclined cables, the additional effect from pre-stressing to counteract the cable sag has to be considered as well. Dynamic loading on the other hand derives either from motion of the bridge structure due to traffic and wind action on the bridge deck and pylon or, more significantly, due to direct aerodynamic excitation of the cable.

Ambitious bridge projects with ever longer span widths push the capacity of structure and material to the limit. Presently the world's largest suspension bridges in terms of main span are the Akashi Kaikyo Bridge (Japan, 1998) with 1,991m, Xihoumen Bridge (China, 2009) with 1,650m and the Great Belt Bridge (Denmark, 1998) main span is 1,624m long. The largest cable-stayed bridges are the Sutong Bridge (China, 2008) with 1,088m, the Stonecutters Bridge (Hong Kong, 2009) with 1,018 and the Tatara Bridge (Japan, 1999) has a main span of 890m. The 2006 proposal for the Messina Bridge considered a single-span suspension bridge with a central span of 3,300m.

The large stay planes of long-span bridges can now produce more than 50% of the overall horizontal load on a bridge [1]. For this reason cover tubes of the structural cables are equipped with different types of surface patterns which beside mitigation of vortex shedding and rain-wind induced vibrations also reduce the aerodynamic drag forces at design wind velocities. Kleissl and Georgakis [2] performed a comparative study on three different cover tube types for bridge cables focusing on drag and lift forces and on the related aerodynamic effects at the tube surface in configurations perpendicular and inclined to the wind. The uniqueness of this study is the fact that the tests on all tube specimens were conducted in the same facility hence eliminating systematic errors due to different flow conditions or experimental setup for the comparison.

Knowing how the aforementioned cable types perform in dry and rain conditions this paper focuses on how much ice accretion alters the aerodynamic behaviour of these cable types.

B. Bridge Cable Tubes

The study of ice accretion effects on the cable aerodynamics was performed on the same tube types as used and described in [2]: (a) a plain HDPE tube, (b) a HDPE tube fitted with helical fillets and (c) a HDPE tube with a pattern-indented surface (Fig. 1).

The sectional models are original full-scale samples, supplied by bridge cable manufacturers. The plain HDPE tube has 160mm outer diameter and a measured average surface roughness of $R_a \approx 1.8$µm. The HDPE tube with two helically wrapped fillets has an outer diameter of 160 mm as well. The fillets are rounded with a height of approximately 3mm and a base width of approximately 4 mm. Furthermore, they have a 3.14 tube diameter pitch length (502mm and 45°). The average material surface roughness is in the order of $R_a \approx 3.0\mu m$. The pattern-indented tube has a diameter of 140mm, and is an actual sample of the most common diameter of cable used on the Sutong Bridge. The relative surface roughness is defined by the depth of the indentations, measured to be approximately 1% of cable diameter.

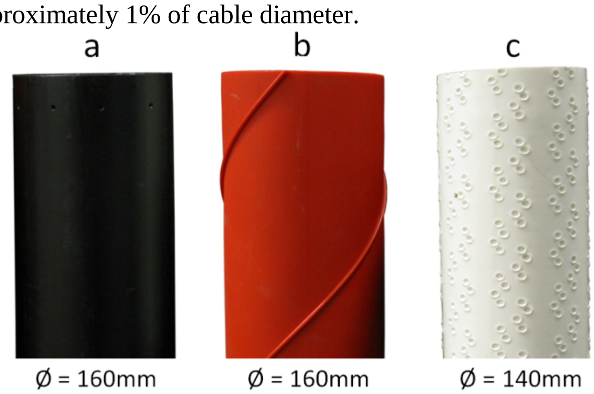

Fig. 1. Bridge cable cover tubes tested in the ice accretion study: (a) a plain HDPE tube, (b) tube wrapped with two helical fillets, (c) a tube with a pattern-indented surface texture.

The relevance of using original cover tubes instead of recreations is documented in studies focusing on the influence of surface roughness and non-circularity on aerodynamic force coefficients [3]. Especially the lift coefficient is sensible to surface roughness irregularities and cross-sectional distortion.

C. Reference Aerodynamic Performance

The aerodynamic performance of the three cable tubes shown in Fig. 1 have been studied and reported in [2]. Fig. 2 shows the development of the drag force coefficient, C_D, over Reynolds number.

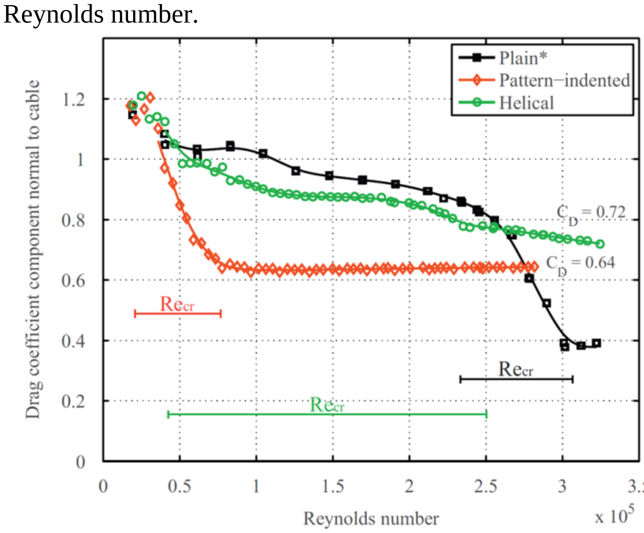

Fig. 2. Drag force coefficient, C_D, as function of Reynolds number for the three cable types in dry condition and flow normal to cable axis. For each cable type the corresponding critical range of significant drag force reduction is indicated [2]. Maximum turbulence intensity $I_{u,max} = 0.6\%$.

For the same flow conditions the lift coefficients, C_L, for the three cable types are shown in Fig. 3 as a function of Reynolds number. As shown in [3] the lift force on the plain cable tube is very susceptible to surface roughness and the measured result varies significantly on the angle of attack, α, even for wind normal to cable axis (cross-flow condition).

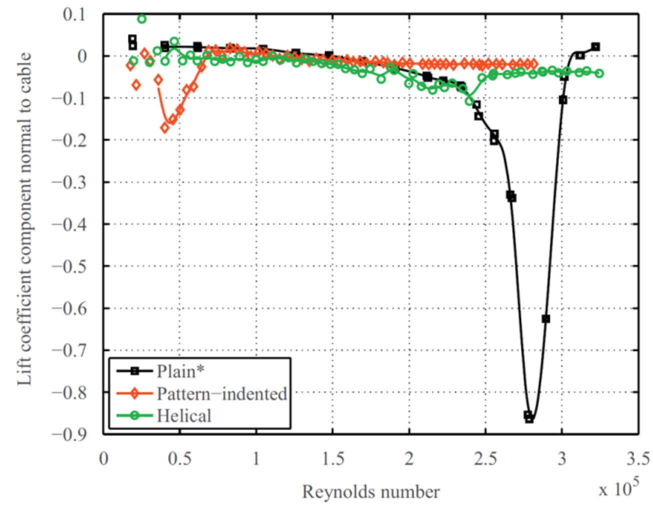

Fig. 3. Lift coefficient, C_L, as function of Reynolds number for the three cable types in dry condition and flow normal to cable axis [2]. Maximum turbulence intensity $I_{u,max} = 0.6\%$.

III. Experimental Setup & Test Conditions

The tests were performed in the collaborative Climatic Wind Tunnel (CWT) at FORCE Technology in Lyngby, Denmark. The wind tunnel was developed and built between 2008 and 2010 as a joint project between the Technical University of Denmark (DTU), FORCE Technology funded by the Danish bridge owners/operators Femmern Bælt A/S and Storebælt A/S.

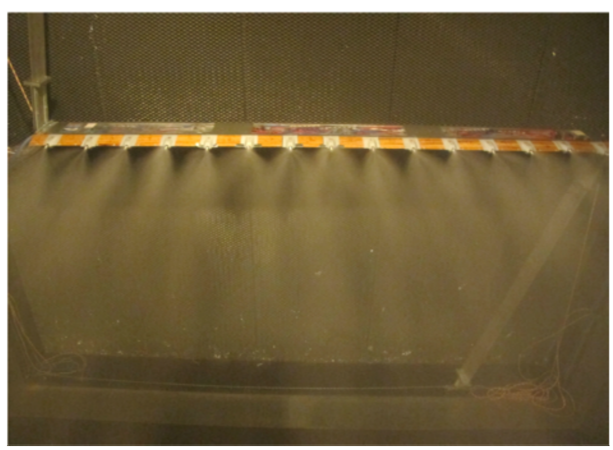

Fig. 4. Horizontally mounted 15 nozzle spray bar operating in the settling chamber of the wind tunnel to simulate in-cloud icing conditions [5].

The main technical specifications are: 5m long test chamber with a cross-section of 2 x 2m, maximum airspeed $u_{max} = 32m/s$, lowest turbulence intensity is $I_{u,min} = 0.6\%$. The lowest long-term average temperature at full speed is -4.5°C. The blockage ratio for a 160mm diameter cable segment is about 8%. Further information is available in [4].

Heart of the CWT is the cooling system capable of operating the facility at sub-zero air temperatures and the recently developed spray system allows for creation of in-cloud icing conditions. Fig. 4 shows the spray bar with 15 nozzles producing droplets in the size range between 10 and 80µm (median volume diameter, *MVD*) depending on the air/water pressure ratio and magnitude. The spray bar can be rotated steplessly to assume any position for testing inclined cables ([5], [6], [7]).

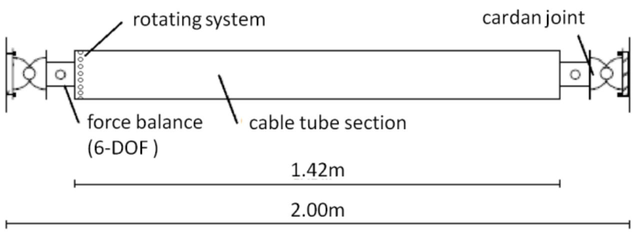

Fig. 5. Arrangement of force balances, cable tube tests specimen and connectors horizontally mounted in the middle of the test section to capture the aerodynamic loads for varying airspeed and rotation angle α.

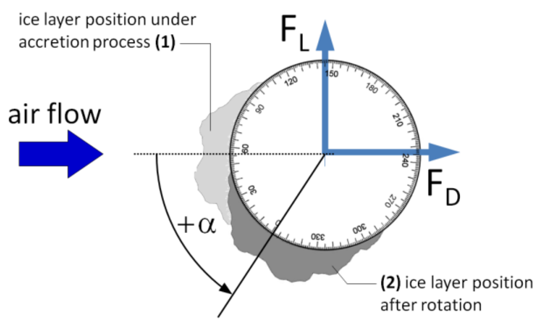

Fig. 6. Orientation of drag and lift forces. The angle of rotation α (counter-clockwise) corresponds to the clockwise relative angle of attack.

Fig. 5 illustrates the arrangement of the cable test specimen, the two 6-component AMTI MC3A-500 force balances on each side of the cable and the joint connections to the wind tunnel walls to avoid end-moment effects. The cable tube can be rotated in steps of $\Delta\alpha$ = 10° around its length axis. The corresponding lift and drag force coordinate system is shown in Fig. 6. The position of the ice layer is measured in degrees as the angular distance between its location during accretion (1) and the location during wind load testing (2) counting positive for counter-clockwise rotation.

In 2009 a fundamental study on ice accretion on circular cylinders at moderate low temperatures was performed at the National Research Counsil (NRC) in Ottawa, Canada [8]. 'Moderate low temperatures' refer to air temperatures between 0 and -5°C at which ice accretion and subsequent large amplitude wind-induced vibrations have been observed on bridges in the past. This temperature range can be divided into three sub-ranges: high moderate temperatures (0 to -2°C) characterised by wet ice accretion (glaze), low moderate (-3 to -5°C) with dry ice (rime) and a transition range around -3°C with a mixed ice type. In this study ice accretion in the high and low temperature range has been simulated with target temperatures of -2 and -5°C for wet and dry ice, respectively.

TABLE I summarises the boundary conditions of the simulations including the measured ice mass after 60 minutes of accretion. The airspeed during icing was u = 10.5m/s with a maximum along-wind turbulence intensity of I_u = 0.6%.

TABLE I
SIMULATION CONDITIONS: SETTINGS AND ACHIEVED VALUES

cable tube type	icing condition	ID [-]	mean air temp. [°C]	accretion time [min]	MVD[1)] [µm]	LWC[2)] [g/m³]	ice mass [kg/m]
a) standard plain	wet	SW	-2.0	60	10-15	0.4	0.60
	dry	SD	-5.1	60	10-15	0.4	0.56
b) helical fillet	wet	HW	-2.2	60	10-15	0.4	0.46
	dry	HD	-5.1	60	10-15	0.4	0.49
c) pattern-indented	wet	PW	-1.8	60	10-15	0.4	0.53
	dry	PD	-5.3	60	10-15	0.4	0.60

1) The MVD is estimated based on nozzle specification provided by the manufacturer using the air/water pressure ratio and magnitude.
2) The LWC of 0.4g/m³ is a target value. Comparison tests indicate that the true value might be higher by 30%.

Even though horizontal orientation is untypical for bridge cables the tube specimens were mounted horizontally for comparison with the observation data base from the NRC tests regarding the ice accretion characteristics [8]. Furthermore, the orientation allowed for dynamic testing of galloping instability in a simple free vibration setup for vertical cross-flow vibrations [5].

IV. Evaluation Considerations

The influence of the ice layer on the aerodynamic performance of the bridge cable tubes is in this study evaluated based on the drag and lift coefficients as a function of the rotation angle α and the applied airspeed u or Reynolds number Re, respectively. With a counter clockwise rotation α as shown in Fig. 6 the resulting angle of attack is measured positive in clockwise direction starting from the stagnation line of dry tube at the beginning of the accretion process (identical to α). The evaluation will focus on:

- development of C_D and C_L over rotation angle α
- dependency of C_D and C_L on Reynolds number
- influence of ice layer on symmetry of C_D
- influence of ice layer on antisymmetry of C_L
- influence of gravity on icing.

An ice layer perfectly symmetric around the stagnation point during the accretion process will be reflected by a symmetric drag force curve $C_D(\alpha)$ and an antisymmetric lift force curve $C_L(\alpha)$. Each deviation from this rule is due to irregularity of the ice layer in practice. A larger influence on the symmetry can be expected from gravity during the accretion process – in particular for wet ice accretion.

Fig. 7 shows a simplified example on an ice layer that due to gravity exhibits an asymmetry around the flow direction during the accretion process (1): the ice mass is shifted towards the underside of the cable. In this simplified case it appears that there is an axis around which the ice layer is still (almost) symmetric. The location of this axis is defined by the angle θ and for airflow along this axis the lift force should be zero: $C_L(\alpha = -\theta) \approx 0$. In this sense θ can also be interpreted as the *dominating angle for neutral lift* serving as a measure for gravity influence on ice accretion.

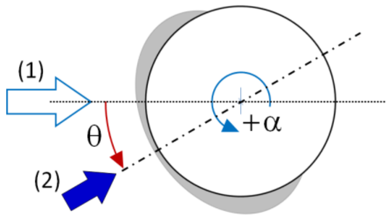

Fig. 7. Ice accretion under influence of gravity: the ice mass is shifted towards the underside of the cable tube. A symmetry axis can be found at an angle of θ around which the ice layer is (nearly) symmetric and the lift force (nearly) antisymmetric, depending on the irregularity of the ice layer.

The influence of icing affected by gravity on the aerodynamic performance is evaluated using the principle of lift force antisymmetry in a graphical approach illustrated in Fig. 8. An antisymmetric image of the measured lift curve, $C_L(\alpha)$, is projected on the measured data and shifted along the abscissa axis to find (graphically) the best match. The resulting shift angle equals 2θ.

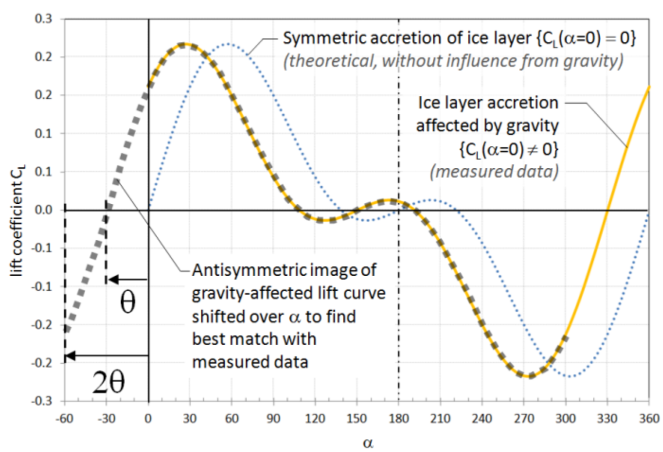

Fig. 8. Graphical method to estimate the influence of gravity on the ice accretion and on the resulting lift force. An antisymmetric image of the lift force coefficient curve is superimposed with itself to find the best match.

In practise, ice accretion affected by gravity exhibits large irregularity and asymmetry. For this reason ‘the best match’ may only be applicable to some features of the lift curve. The poorer the congruence between the measured lift curve and its antisymmetric image the less dominant is the identified angle for neutral lift. In extreme case θ marks only one out of many possible neutral directions.

V. STANDARD PLAIN CABLE

A. *Wet Ice Accretion (SW)*

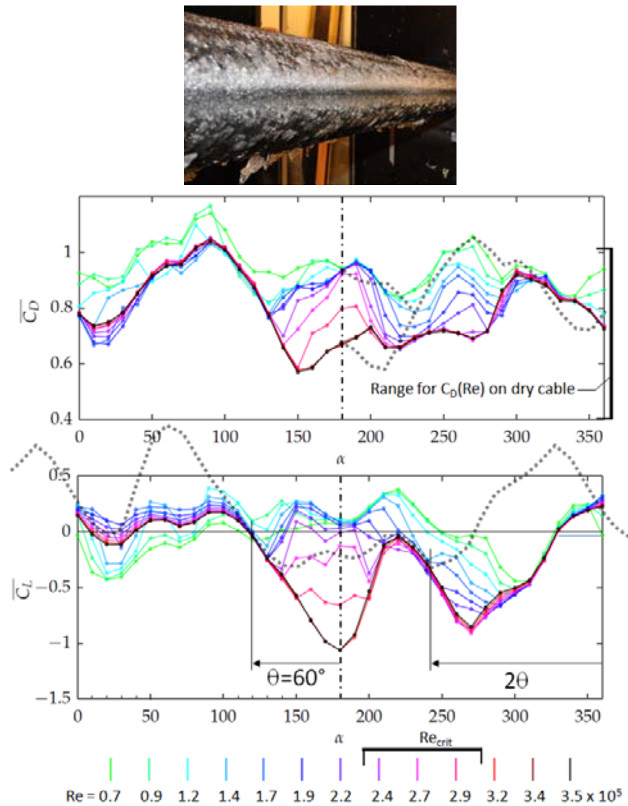

Fig. 9. Drag and lift coefficients of standard plain cable tube for wet ice accretion (Accretion time: 60min; mean air temperature: -2°C; ice mass: 0.6kg/m).

The ice layer exhibits a high irregularity hence the antisymmetric image of the lift curve matches the measured data only in few features. The resulting dominant angle for neutral lift at α = 120°, i.e. from rear below. The poor match in the lift curves indicates that gravity influences the wet ice accretion on the plain standard cable significantly.

The high irregularity affects the drag force as well. Expecting a curve mirrored around α = 180° (grey dotted line) only a vague resemblance between both sides can be observed. For some angles of attack the drag force of the iced plain cable still exhibits a Reynolds dependency as measured on the dry cable (Fig. 2). For other angles the dependency of C_D almost disappears. With the ice layer near the flow separation points the cable assumes a sharp-edged body characteristic.

It seems that the ranges of flow angles with a high Reynolds dependency of C_D are similar to those where C_L varies with Reynolds number as well.

In Fig. 9 the range for the drag coefficient measured on the dry cable (left graph border) and the corresponding critical Reynolds range are indicated for comparison purpose. Around α = 180° the critical Reynolds range of the iced cable is similar to the dry cable. As one could expect, the drag coefficient is generally higher on the iced cable but stays largely within the drag range of the dry cable.

B. *Dry Ice Accretion (SD)*

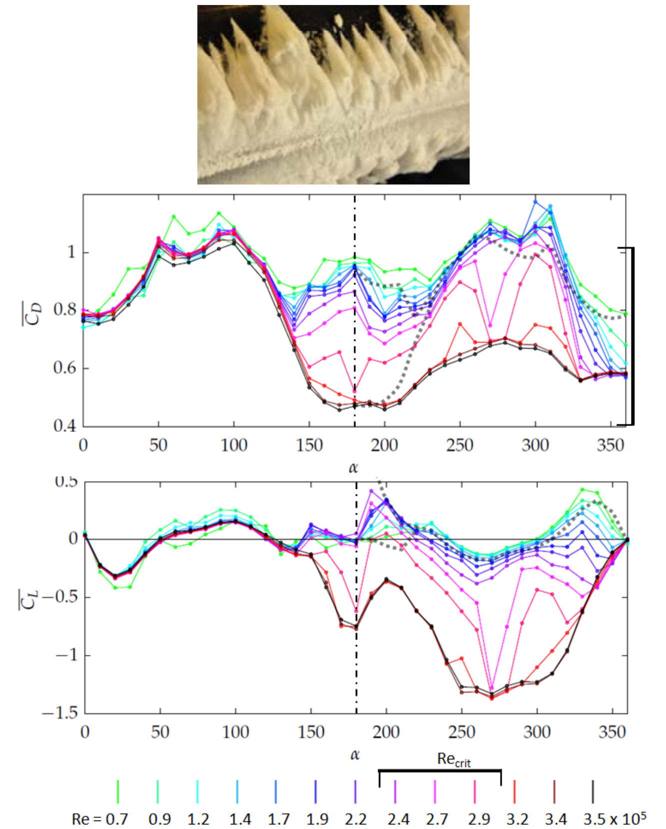

Fig. 10. Drag and lift coefficients of standard plain cable tube for dry ice accretion (Accretion time: 60min; mean air temperature: -5.1°C; ice mass: 0.56kg/m).

For dry ice accretion the ice layer is more concentrated around the stagnation line on the upstream side of the cable tube. For up to α = 120° the drag force is little affected by the Reynolds number indicating a rather sharp-edged body behaviour than of a circular cylinder. Between 120° and 180° the drag force is strongly dependent on Re. Here, the ice layer is fully immersed in the separated wake flow on the rear side of the cable and the tube appears aerodynamically similar to a dry cylinder with the characteristic critical Reynolds regime.

Around 180° the drag coefficient C_D is quite symmetric. This symmetry however does not extend to flow direction beyond 210°, where, according to observations below 120°, the drag force should become again independent of Reynolds number. A reason for this asymmetry of $C_D(\alpha)$ is a change in the surface roughness during the course of testing. Under dry ice accretion simulation fine spray dust creates small ice flake accumulation on the rear side of the cable surface. These flakes get blown off at higher airspeeds when directly exposed to the approaching wind. As a consequence the surface roughness is changed in the second half of the tests clearly affecting the Reynolds dependency for both drag and lift force.

VI. Helical Fillet Cable

A. *Wet Ice Accretion (HW)*

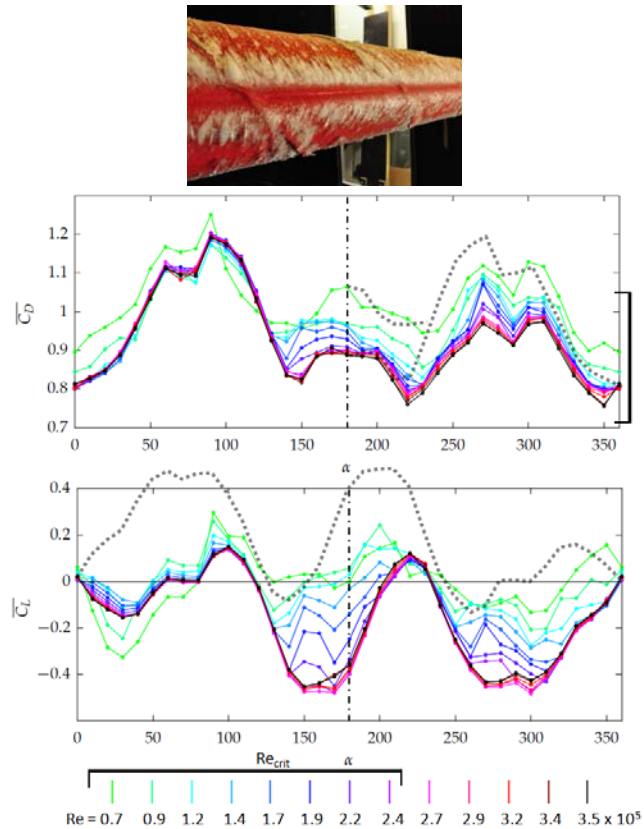

Fig. 11. Drag and lift coefficients of helical fillet cable tube for wet ice accretion (Accretion time: 60min; mean air temperature: -2.2°C; ice mass: 0.46kg/m).

The drag force coefficient is reasonably symmetric around α = 180°. Similar to the observation on the plain cable C_D is fairly Reynolds number independent up until 130°. Hereafter the ice layer enters the wake flow and the cable assumes an aerodynamic behaviour closer to dry cable conditions. The symmetry of the drag force is influenced by the irregularity of the ice layer. This is in particular reflected by the increased level of Reynolds dependency for relative flow direction above 180°.

The wet ice layer covers a larger part of the cable tube surface hence influencing the airflow along the tube surface even if the main part of the ice is in the wake flow zone. For this reason the drag coefficient reaches only for some specific angles the low drag level of the dry cable. When the ice layer is near the separation point, i.e. around 90° or 270°, the drag coefficient peaks and exceeds the level of the dry cable up to 15%.

Comparing the lift force coefficient curve with its antisymmetric image indicates a very low level of ice layer symmetry. Both curves show a certain resemblance to each other but differ significantly in magnitude.

B. *Dry Ice Accretion (HD)*

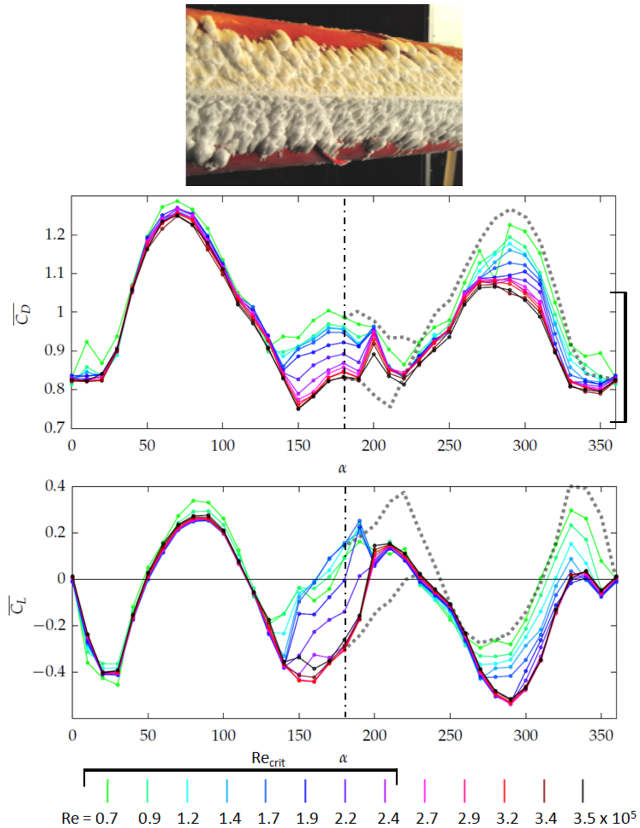

Fig. 12. Drag and lift coefficients of helical fillet cable tube for dry ice accretion (Accretion time: 60min; mean air temperature: -5.1°C; ice mass: 0.49kg/m).

As observed on the standard plain cable tube the ice accretion is more concentrated around the stagnation line compared to wet ice. Both drag and lift coefficient curves indicate a reasonable symmetry allowing for some irregularity.

The influence of the ice layer on the drag coefficient magnitude is higher than observed from wet ice accretion. For ice layer positions near flow separation (around 90° or 270°) C_D peaks 1.28, approximately 20% above the maximum drag of the dry cable tube.

According to Fig. 2 the dry cable exhibits a wide critical range. On the iced cable this dependency appears for relative flow direction placing the ice layer in the wake flow zone of the cable tube (130° < α < 230°). The symmetry of the drag curve is influenced by the natural irregularity of the ice layer and by the change of surface roughness throughout the test as discussed for the standard plain cable. The influence of the surface roughness change seems to be smaller on the helical fillet tube than on the plain cable. The fillets define at discrete positions the location of flow separation hence 'damping' the Reynolds number dependency.

As discussed above the lift coefficient curve shows a reasonable antisymmetry. The variation of C_L with Reynolds number seems to follow the pattern observed for C_D.

VII. Pattern-Indented Cable

A. *Wet Ice Accretion (PW)*

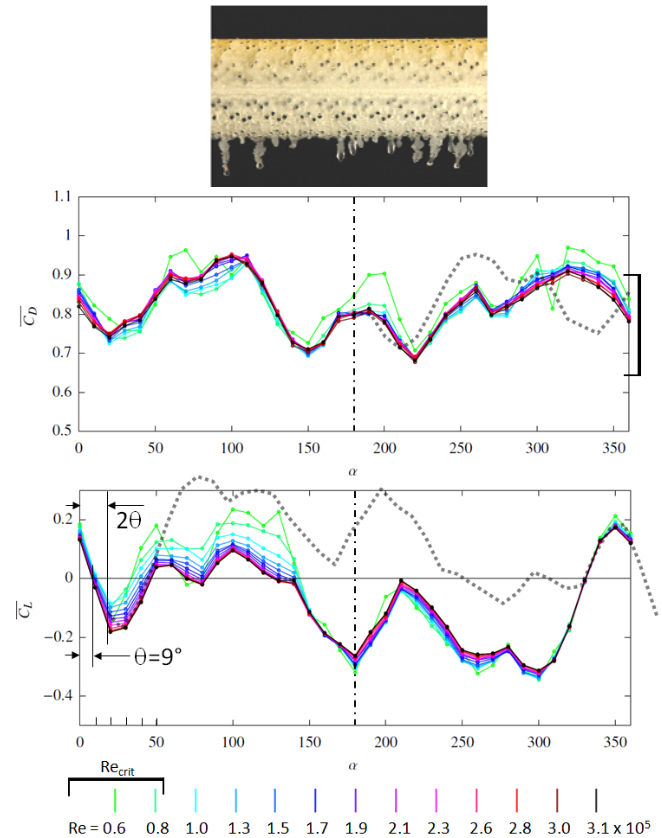

Fig. 13. Drag and lift coefficients of pattern-indented cable tube for wet ice accretion (Accretion time: 60min; mean air temperature: -1.8°C; ice mass: 0.53kg/m).

A main feature in the aerodynamic performance of the pattern-indented cable is the low drag coefficient almost constant in the supercritical range starting at a relatively low Reynolds number (Fig. 2). The C_D range of the dry cable over the Reynolds range applied in this study is indicated to the right in upper graph of Fig. 13. As it appears, the drag coefficients of the iced cable stay inside the dry cable drag range but reach only for few relative flow directions the characteristic low drag level.

However, the pattern-indented cable tube exhibits even with wet ice a very low Reynolds dependency of the drag force for all tested relative flow directions. This behaviour distinguishes the pattern-indented cable clearly from the standard plain and helical fillet cable.

The increased ice mass on the underside of the cable tube (e.g. icicles, shown in the photograph of Fig. 13) creates some irregularity and asymmetry in the ice layer leading to a limited symmetry of the drag curve.

The lift force curve shows for some flow directions a certain variation at low Reynolds numbers. Antisymmetric resemblance is limited and characterised by a difference of lift force coefficients as seen in case HW.

B. Dry Ice Accretion (PD)

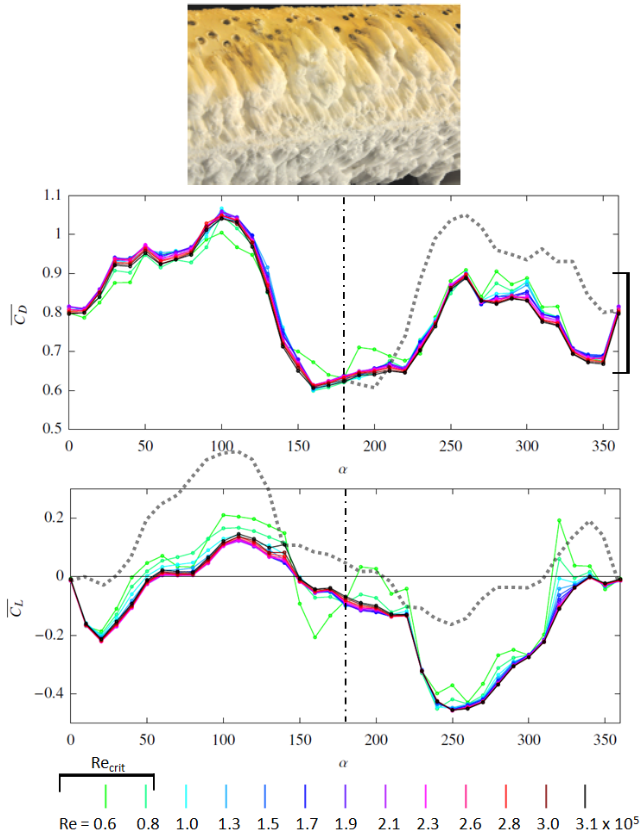

Fig. 14. Drag and lift coefficients of pattern-indented cable tube for dry ice accretion (Accretion time: 60min; mean air temperature: -5.3°C; ice mass: 0.6kg/m).

The dry ice layer changes the drag force of the pattern-indented cable stronger than observed for wet ice. The drag coefficients exceed the dry cable values by about 15% for flow directions where the ice layer is near the flow separation point.

The effect of ice layer and wake flow and the change of surface roughness on the drag force are similar to the dry ice accretion on the other cable types. Still, main characteristic is the very low dependency on the Reynolds number for all investigated angles α.

The lift force coefficient curve indicates a high irregularity but is, apart from lower airspeeds, Reynolds number independent.

VIII. Conclusion

The influence of icing on bridge cable aerodynamics was investigated on three different original full-scale samples of bridge cable cover tubes (standard plain, helical fillet and pattern-indented) for two different types of ice accretion (wet and dry). The tests were performed in specially built wind tunnel facility allowing for simulating in-cloud icing conditions.

The observation from the ice accumulation after 60min accretion time can be summarized to:

- *Wet ice*: the ice layer consists mainly of glaze ice exhibiting a noticeable asymmetry with increased ice mass on the underside of the cable due to gravity.
- *Dry ice*: consisting of rime ice apparently symmetric around stagnation line during accretion phase. Spray dust creates small ice flakes on the rear side of the cable tube surface.

With respect to the influence of the ice layer on aerodynamic performance of the three cable types following main conclusion can be drawn:

- The standard plain cable is most affected by ice accretion with respect to sensibility of drag to Reynolds number, to the magnitude of lift coefficient and to the sensibility of both force coefficients to surface roughness.
- Both helical fillet and pattern-indented cable are less susceptible to changes of the cable surface and ice accretion where the pattern-indented is least affected.
- The pattern-indented cable seems to cope best with the effect of ice accretion. For comparable icing conditions the pattern-indented cable has lower overall drag and lift coefficients compared to standard plain and helical fillet cable.

As an extension of the here presented work the susceptibility to aerodynamic instability was investigated using the Den Hartog criterion for galloping. Preliminary results indicate that under the given conditions only the plain standard cable exhibited tendencies for instability.

References

[1] N.J. Gimsing and C.T. Georgakis, *Cable Supported Bridges: Concept and Design*, 3rd ed. John Wiley & Sons Ltd., 2011.

[2] K. Kleissl and C.T. Georgakis, *Comparison of the aerodynamics of bridge cables with helical fillets and a pattern-indented surface*, Journal of Wind Engineering and Industrial Aerodynamics, vol.104-106, 2012, pp.166-175

[3] G. Matteoni and C.T. Georgakis, *Effects of bridge cable surface roughness and cross-sectional distortion on aerodynamic force coefficients*, Journal of Wind Engineering and Industrial Aerodynamics, Vol.104-106, 2012, pp.176-187

[4] C.T. Georgakis, H.H. Koss and F. Ricciardelli, *Design Specifications for a Novel Climatic Wind Tunnel for the Testing of Structural Cables*. Proceedings 8th International Symposium on Cable Dynamics, 2009, Paris, France

[5] H.H. Koss and M.S.M. Lund, *Experimental Investigation of Aerodynamic Instability of Iced Bridge Sections*, In: 6th European and African Conference on Wind Engineering, Robinson College, Cambridge, UK, 2013.

[6] C. Demartino, H.H Koss and F. Ricciardelli, *Experimental study of the effect of icing on the aerodynamics of circular cylinders – Part I: Cross flow*. In: 6th European and African Conference on Wind Engineering, Robinson College, Cambridge, UK, 2013.

[7] C. Demartino, C.T. Georgakis and F. Ricciardelli, *Experimental study of the effect of icing on the aerodynamics of circular cylinders – Part II: Inclined flow*. In: 6th European and African Conference on Wind Engineering, Robinson College, Cambridge, UK, 2013.

[8] H.H. Koss, H. Gjelstrup, C.T. Georgakis, *Experimental study of ice accretion on circular cylinders at moderate low temperature*., Journal of Wind Engineering and Industrial Aerodynamics, Vol.104-106, 2012, pp.540-546.

A Portable DC De-icer for Rural Power Network Transmission Line

Chun Zhao, Zhen Fang, Jiazheng Lu, Bo Li, Hongxian Zhang
Power Transmission and Distribution Equipment Anti-icing & Reducing-disaster Technology Key Laboratory of State Grid
Hunan Electric Power Corporation Research Institute
Changsha, China
zhaochunmail@tom.com

***Abstract* —** The rural power network transmission lines built in the mountain areas are very easy to suffer the accidents of tower collapse and line breakage under the atrocious icing weather. The widely used manual de-icing methods are hardworking and low efficient. The successfully used DC de-icing methods in the main frame grids cannot be applied to the rural power network directly. A portable DC de-icer is proposed in this paper to solve the problems of the rural power network transmission lines de-icing. A petrolic generator with adjustable output voltage provides the 200 Hz three-phase power supply. An uncontrollable three-phase bridge rectifier converts AC to DC. Fast clamps are developed to make the de-icing manipulation more convenient and more efficient. Onsite application of the portable DC de-icer for the rural power network transmission line was performed on the 10kV Yangta Line in Hunan Province of China. Under the environmental temperature of -7 °C, it took less than one hour to successfully remove the thickest covered ice of 16 mm from two sections of the line with the current of 300 A and 360 A from the portable DC de-icer. The application shows that the portable DC de-icer can operate reliably and can nicely meet the demand of rural power network de-icing.

***Keywords* —** rural power network；portable；DC de-icer；medium frequency technology

I. INTRODUCTION

The rural power network transmission lines are often built in the areas with complicated topography and cold climate. When confronted with the atrocious icing weather, the transmission lines are very easy to suffer the accidents of tower collapse and line breakage [1-4]. Manual de-icing methods are widely used in the rural power network, however these methods are hardworking, low efficient, and sometimes dangerous [5]. DC de-icing methods have been successfully used in the main frame grids in recent years, whereas the methods cannot be applied to the rural power network directly because of lacking power supply, especially in some mountain areas [6, 7]. New typed DC de-icer for the rural power network transmission lines is urgent to be developed to solve the above problems.

II. PRINCIPLE OF THE PORTABLE DC DE-ICER

A portable DC de-icer for the rural power network transmission lines is proposed in this paper. The de-icer mainly consists of a petrolic generator, a rectifier, DC output cables, three-phase fast connecting clamps, and three-phase fast shorting clamps.

The topology of the rectification is shown in Fig. 1. The petrolic generator provides three-phase AC power supply with adjustable output voltage. An uncontrollable three-phase bridge rectifier converts AC to DC. Diodes are adopted to improve the stability and decrease the volume of the rectifier.

The three-phase fast shorting clamps are used to form a closed circuit of the rural power network lines. With the DC

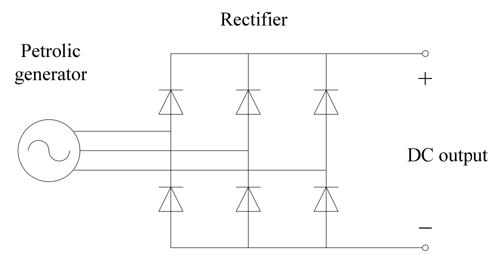

Figure 1. Topology of the rectification.

output cables and the three-phase fast connecting clamps, the DC current is injected into the rural power network lines, thus heat will be created in the lines and the covered ice can be melted.

III. DESIGN AND FABRICATION OF THE PORTABLE DC DE-ICER

A. Petrolic generator

The petrolic generator with adjustable output voltage is composed of an air-cooled petrolic motor, a three-phase brushless synchronous generator, a petrol box, a control panel, all mounted on a frame with four wheels.

The petrolic motor uses double cylinder, overhead valve, aluminum alloy structure. It is with the features of light weight and small volume. The engine oil safety device can prevent the motor damage lacking of engine oil. The parameters of the petrolic motor are shown in Table I.

The three-phase generator uses the brushless exciting method, with high reliability, free maintenance, and strong ability of load. The frequency of the generator is 200 Hz. Medium frequency technology is used to improve the efficiency and decrease the volume of the generator. By adjusting the exciting current, the generator can output a varied voltage. The parameters of the generator are shown in Table II.

TABLE I. PARAMETERS OF THE PETROLIC MOTOR

Parameter	Value
Rated power (kW)	20.1
Rated rotating speed (rpm)	3000
Number of cylinder	2
Diameter of cylinder (mm)	83
Length of stroke (mm)	57

TABLE II. PARAMETERS OF THE GENERATOR

Parameter	Value
Rated power (kW)	12
Number of phases	3
Rated voltage (V)	12~24
Rated current (A)	330
Rated rotating speed (rpm)	3000
Rated frequency (Hz)	200

The control panel is mounted with an amperemeter, a voltmeter, a voltage adjusting knob, fast connecting sockets, an alarming indicator, a starting button, a power supply switch, and a starting key. The function of the control panel is to adjust the ouput voltage and transfer the electric energy to the load.

The petrol box can store 12.5 L of petrol and can keep the petrolic generator running for three hours under rated conditions.

B. Rectifier

The rectifier uses an uncontrollable three-phase bridge. It can convert the three-phase AC to DC. As the generator outputs a varied voltage, diodes are used instead of thyristors, not influencing the function of voltage adjusting. The adoption of diodes can improve the stability and decrease the volume of the rectifier.

The rectifier is also installed on the frame. The main body of the de-icer is shown in Fig. 2. The parameters of the de-icer are shown in Table III.

C. Accessories

The accessories include DC output cables, three-phase fast connecting clamps, and three-phase fast shorting clamps.

The three-phase fast shorting clamps are developed to make the de-icing manipulation more convenient and more efficient, as shown in Fig. 3. Clamps are mounted on the long insulated rods, connected with shorting wires. By put up the fast shorting clamps on the rural power network lines to be de-iced, a closed circuit of the rural power network lines are very easy to form.

TABLE III. PARAMETERS OF THE DE-ICER

Figure 2. The main body of the de-icer.

Parameter		Value
Rated power (kW)		12
Rated output DC voltage (V)		15~30
Rated output DC current (A)		25~400
Net weight (kg)		120
Dimension	Length (mm)	870
	Width (mm)	596
	Height (mm)	635

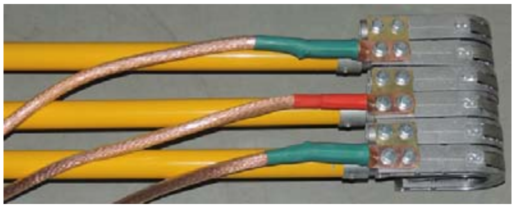

Figure 3. The three-phase fast shorting clamps.

The three-phase fast connecting clamps are similar to the three-phase fast shorting clamps, just connected with the DC output cables. By put up the fast connecting clamps on the rural power network lines to be de-iced, the DC current can be easily injected into the rural power network lines.

IV. ONSITE APPLICATION OF THE PORTABLE DC DE-ICER

Onsite application of the portable DC de-icer for the rural power network transmission line was performed on the 10kV Yangta Line in Hunan Province of China on January 5 of 2013.

The 10kV Yangta Line is located in Changning District, Hunan Province. The line type was LGJ-70. On January 5 of 2013, serious icing occurred on the line. The icing of Tashan was the most serious, with the altitude of 1250 meters. The environmental temperature was -7 °C and the thickest covered ice at support 228 of the line had reached 16 mm by then.

The portable DC de-icer was utilized to solve the covered ice. With the portable DC de-icer, it took less than one hour to remove the ice from two sections of the line with the most serious icing. For the section from support 233 to support 234 with the length of 120 meters, 40 minutes were taken to complete the de-icing under the current of 300 A. For the section from support 228 to support 229 with the length of 30 meters, only 15 minutes were taken to complete the de-icing under the current of 360 A. The portable DC de-icer at the application site is shown in Fig. 4. Fig. 5 shows the putting up of the three-phase fast connecting clamps. Fig. 6 snaps the instant of falling of the melted ice. Fig. 7 shows the fallen ice.

Figure 6. The putting up of the three-phase fast connecting clamps.

Figure 7. The portable DC de-icer at the application site.

The successful onsite application shows that the portable DC de-icer can operate reliably and safely. It can relieve the people of hard labor and can remarkably improve the efficiency of rural power network de-icing.

V. Conclusion

1) A portable DC de-icer for the rural power network transmission lines is developed in this paper.

2) Medium frequency technology is used to improve the efficiency and decrease the volume of the petrolic generator. Diodes are adopted to improve the stability and decrease the

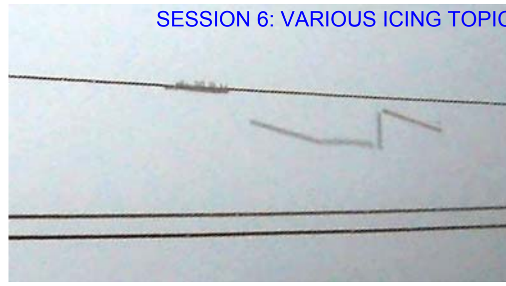

Figure 5. The instant of falling of the melted ice.

Figure 4. The fallen ice.

volume of the rectifier. Fast clamps are developed to improve the efficiency of the de-icing manipulation.

3) Onsite application of the portable DC de-icer for the rural power network transmission line was performed. The results show that the portable DC de-icer is successful and can nicely meet the demand of rural power network de-icing.

References

[1] Dong-xiao Niu, Zhuang-zhi Liu, Yan Gao, and Hong-lei Yang, “Analysis on ice-coating withstanding ability of typical conductors and towers in rural power networks,” Power System Technology, vol. 33, no. 18, pp. 176–181, 2009 (in Chinese).

[2] Xue-jun Liu, “Cause analysis and countermeasure of the transimission line ice covering in rural network,” Ningxia Electric Power, no. 2, pp. 8–10, 2010 (in Chinese).

[3] Yan-yang Wang, Xian-zhi Zhu, and Da-qi Guo, “Influence of icing disaster on Yichang rural power network and defence countermeasure,” Rural Electrification, no. 6, pp. 24–25, 2008 (in Chinese).

[4] Zhi-xin Xie, Lei Li, Jun Wang, Hui-dong Zhang, and Wen-zheng Liang, “The cause analysis and countermeasures of 10 kV and below transmission lines ice coating accident in rural power network of Ningxia Guyuan area,” Ningxia Electric Power, no. 1, pp. 21–25, 2008 (in Chinese).

[5] Xiang Wang, and Fang-fan Liu, “Discussion of manual de-icing in rural power network,” Guizhou Electric Power Technology, no. 12, pp. 78–79, 2009 (in Chinese).

[6] Yan-jun Tan, Jia-zheng Lu, Bo Li, et al, “Research and application of new AC/DC de-icing devices in Hunan Power Grid,” The 14th International Workshop on Atmospheric Icing of Structrures, China: Chongqing, 2011.

[7] Xun Zhang, Xiao-hong Ma, Guo-bang Ban, “Application and study of DC ice-melting technology on the ground line,” Guizhou Electric Power Technology, vol. 14, no. 7, pp. 14-16, 2011 (in Chinese).

Atmospheric Icing on Structures: COLDTECH-RT3 Perspective

Muhammad S. Virk
Atmospheric Icing Research Team, Department of Technology
Narvik University College, 8505 Narvik, Norway
Email: msv@hin.no

Abstract — When planning technological activities in polar and sub-polar regions, atmospheric icing on structures is very likely to occur and need to be considered. The *COLDECH-RT3* project vision is to establish a competence platform for development of new and improved infrastructure, safe and environmentally friendly industrial operation in the arctic regions under icing conditions. This paper gives an overview about the ongoing research activities related to *COLDTECH-RT3*, at Narvik University College by its atmospheric icing research team. The work was initiated later in 2010. The activities described in this paper are mainly focused on three areas, field measurements of atmospheric icing, design and development of icing sensor & numerical modeling of atmospheric icing. The overall objective of *COLDTECH-RT3* project is to facilitate the development of sustainable infrastructure and operations in the high north under icing conditions.

Keywords — Atmospheric icing, COLDTECH, Field measurements, Sensor design, CFD

I. Introduction:

The capacity and ability to execute technology based research and development activities is of vital importance for the industrial operations in the cold regions. Due to large undiscovered natural resources in cold regions, human activities are increasingly extending, where atmospheric icing on structures is becoming a key factor, when planning infrastructures due to its huge economic consequences. The vision of *ColdTech-RT3 project* (Atmospheric icing & Sensor) is to establish a competence platform for better understanding of atmospheric icing physics and the development of improved, safe and environmental friendly infrastructures for both onshore and offshore activities in icing conditions. This research task (RT3) is a part of major research project '*COLDTECH*'(http://www.arctictechnology.com/home), funded by Norwegian research council and consortium of various industrial companies. The ColdTech project has five research tasks, where COLDTECH consortium partners (*Narvik University College, Norut, DNV and Luleå University*) are working with 04 academic partners (*Canadian hydraulics, RusHydro Institute and Norwegian coast guard*) and 12 industry partners such as (*SHELL Technology, TOTAL Norge, Statkraft, Nordkraft, North energy etc.*). *ColdTech- RT3* is one research task among five research task of *COLDTECH* project and is being coordinated/conducted by atmospheric icing research team of Narvik University College (NUC), where the research activities has primarily been focused on the field measurements of atmospheric icing, design and development of icing sensor & numerical modeling of atmospheric icing on structures.

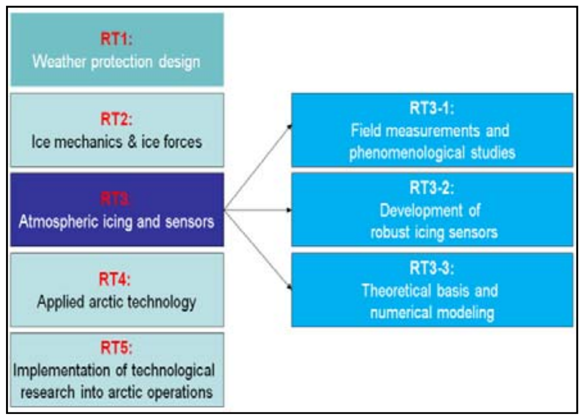

Figure 1: An overview of COLDTECH Project

II. Field Measurements of Atmospheric Icing

Better knowledge about frequency and duration of icing events as well as critical ice loads are crucial parameters for the improved and safe structural design in cold regions. The unpredictability elements in such situations could easily cause extensive ice loading on equipment and structures within no time. The diversity in the nature of intensive cold environment makes it all important to evaluate the icing events and loads in perspective of the other atmospheric parameters. This requires efficient and reliable data collection & evaluation through appropriate sensors able to withstand the harsh nature of the cold environment. A meteorological atmospheric ice monitoring station was designed within the ColdTech-RT3 project at Narvik University College, and was installed at the mountain, 'Fagernesfjellet (*1007 m.a.s.l., 68˚25'20" N, 17˚27'26'' E*)'located east from the Ofotfjorden and towards the north east from Beisfjorden on the western coast of Norway. The mountain faces open sea from the south across the SW and to the west. This region is affected by gulf streams flowing across the North Atlantic Ocean. Air masses related to these streams are usually humid and have air temperatures favorable for atmospheric icing during the winter season (-25<T ºC <0). The main goal of the mentioned ice monitoring station was to utilize experimental and mathematical tools jointly to better predict the expected upcoming icing loads and events, which would help in better planning for cold climate regions and would reduce the losses due to severe icing loads on equipment and structures.

Figure 2: Ice load from NUC icing station, installed at Fagernsfjellet Narvik [1].

The ice monitoring station consists of an ice load monitor (Combitech), HoloOptic (T44) ice sensor, advance multifunctional weather station (Lambrecht /EOLOS-IND) and advanced data acquisition system (CR-1000). So far metrological and icing data from winter 2012/2013 have been analyzed to understand the icing trends and their relation with other metrological parameters. [2, 3]. This field measurement was focused on the statistical analysis performed on the data acquired from the ice monitoring stations and conventional weather station parameters. The objective was approached in two phases; the first phase involved the data extraction, validation and filtering along with the observing the visible trends on the graphs by comparison. The second phase involved regression analysis of the data curves obtained from icing load parameter depending on the relative humidity, atmospheric temperature and wind speed. The data recorded each second was averaged on the daily basis and then monthly regression plots were formulated to distinguish the icing load impact with the weather transitions. The mathematical formulation can be used to predict the icing loads for the coming key seasons, which could be the significant input to the infrastructure designers to plan and design accordingly. The Ice loads were calculated for period from Dec-12 till Apr-13. The values were plotted against 24 hours' time period for over the range of one month. The ice load is calculate in grams and averaged over the 24 hour period. The results can be shown as:

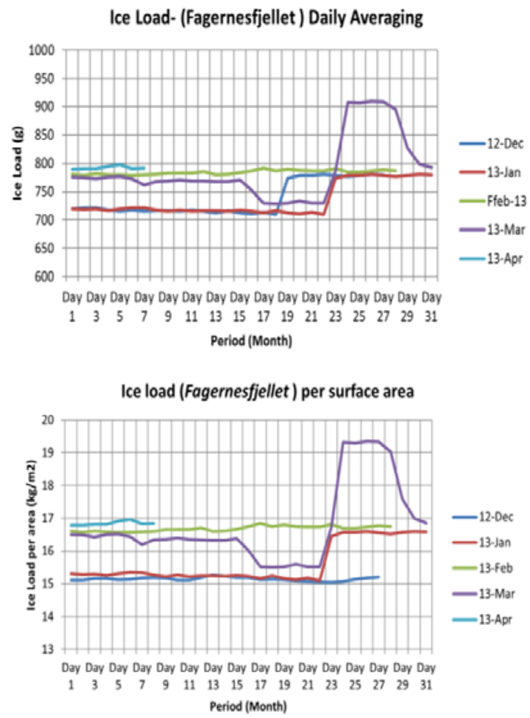

Figure 3: Average daily icing load on Fagernesfjellet-Narvik during winter 2012/2013

The problems encountered in installation, maintenance and operations of equipment in the cold climate regions are far more complicated than others. The contributing factors and problems that can affect the system operation and performance should also be identified, assessed and focused within well-defined parameters before its installation in cold climate regions. The performance of the same equipment in two different climatic conditions might be similar during initial phase, but as the time progresses the performance might vary to a considerable extent, hence mean time between failures (MTBF) of the system becomes questionable. The installed system in the cold environment is subjected to various types of metrological conditions[4], such as storms, rain, variable wind conditions and ice/snow are among the major environmental factors, whereas the geographic position of the installed equipment also accounts for the localization factors, challenging the equipment life and related performance parameters.

Based on the RT3 team's experience of installation, operations and maintenance of ice monitoring station at Fagernesfjellet, it was found that factors leading to the equipment failure in cold climate region are generally overlooked and ignored. The indirect contributing factors such as logistics, transportation and access to the site become vital, which demands remote monitoring of the system in effective manner. In addition to that anticipated and preventive maintenance culture should be invoked as a regular practice, which could encounter the unpredictable impact of harsh environment upon the on-site system. The problem areas discussed can be utilized as a guideline in equipment integration, installation and maintenance viewpoint.

III. Design of Atmospheric Icing Sensor

Design and development of robust sensor to detect and measure atmospheric ice accretion on structures is critical and challenging task. So far, there is no ice sensor commercially available that can detect and measure all important icing parameters such as: icing rate, load and type under any icing conditions simultaneously. Most ice detectors available are capable of measuring either one or two phenomena such as detecting ice and indicating the rate of icing only. In terms of atmospheric icing sensor, so far RT3 team has focused on two main techniques: ice detection using dielectric properties of ice, and ice detection using thermal infrared image processing. [5, 6] .

Based on the dielectric concept, a simple experimental setup comprised of two rectangular aluminum bars in parallel connected with an LCR meter, a CCTV camera, low speed frequency controlled ice generator, high pressure air regulated water spray gun, thermocouples, weather station, data acquisition system and computer was designed at the cold room chamber facility of Narvik University College to study the transient response of dielectric constant of ice at different operating atmospheric conditions for both rime and glaze ice conditions [5].

Figure 4: Experimental Setup, designed at Cold room chamber

To study the dielectric properties of wet glaze ice, simple analysis were carried out at atmospheric temperature of -3 ^{o}C and wind speed of 3 m/sec for large water droplets. The generated glaze ice width averaged at five different locations along the rectangular bar was 5.7cm and the thickness measured was 0.6cm. By using the measured capacitance values at test frequency of 100Hz, the real dielectric constant *k was calculated*. The dielectric constant k' response at the test frequency of 100 Hz was transient and varied in the range from 90.2 – 40 during ice accretion process, while the droplets were being sprayed. After the spraying has stopped, the dielectric constant started to decrease from 40 to 4.72 and became stable after 35 minutes. This decrease in the dielectric constant was exponential and was mainly due to the dielectric dispersion [5].

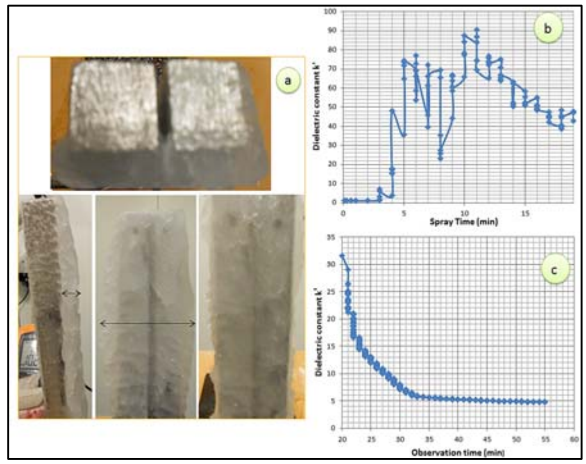

Figure 5: (a) Ice accretion at -3 ºC, at wind velocity of 3 m/sec; (b) Real dielectric constant *k'* at the time of spraying liquid water at -3 ºC; (c) Observation of decreasing dielectric constant after spraying stopped.

To study the dielectric properties of rime ice, analysis were carried out at atmospheric temperature of -10.3 ^{o}C and wind velocity of 3 m/sec for small water droplets. In this case study, average ice thickness was 9.3cm, where a maximum value of real dielectric constant of 50 was obtained during spraying. After stopping the droplet spraying, the dielectric variation goes on a linear decrease and became stable at 8 at 46 minutes of observation.

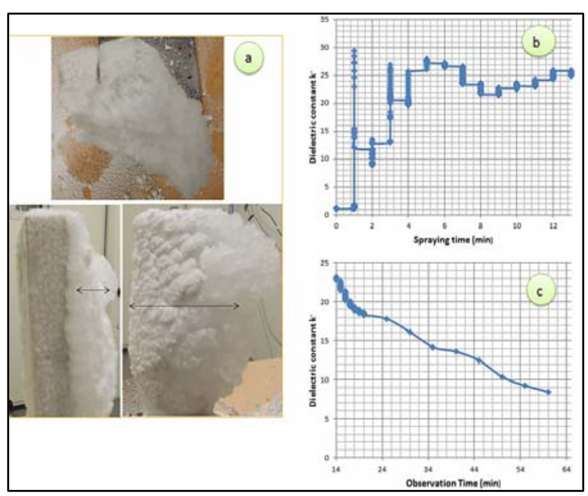

Figure 6: (a) Ice captures at -10.3 ºC, at wind velocity of 3 m/sec; (b) Real dielectric constant *k'* at the time of spraying liquid water at -3 ºC; (c) Observation of decreasing dielectric constant after spraying stopped

The capacitive ice sensor was tested at different temperatures and depending on the ice type it is found that, the capacitance decreased with a decrease in temperature. This phenomenon can help in differentiating the ice types as, glaze ice will have the higher dielectric constant and rime ice will have the lower dielectric constant than the glaze. As the dielectric constant keeps on decreasing after the icing event, therefore we couldn't get the relaxation time to trace out. But we cannot conclude that the processing of ice, we have generated had created this unstable relaxation time. No one explained this before about the long dielectric dispersion or relaxation time. It can be concluded that, ice deposition was detected promisingly by capacitive based technique and also it does have the potential to know about type of ice by considering the peak value of the dielectric constant.

One of the difficulties in ice detection is how to precisely represent the amount of ice accreting on a large surface. Most ice detectors are point devices. That is, they measure the icing rate, the presence of ice or its thickness at only one location. Despite of wide variety of techniques used to detect the atmospheric ice accretion, yet the interest of operators has been often in ice accretion over large surfaces of a structure, instead of at a particular point, which can measures the icing intensity at particular point only. Ice detection technology interference with the accretion process may also affect the accuracy at the same time, as it could be affected by icing itself. A comprehensive survey conducted by researchers at Narvik University College revealed that reliable measurements of ice accretion on large surface such as wind turbines are scarce due to the fact that measurement techniques, available so far still suffer problems in their accuracy and persistence under icing conditions [7]. This fact makes it important to explore new methodologies in ice detection over large surface areas.

A thermal infrared image processing based technique can be a good alternative to monitor ice accretions over large surface area, while covering most important areas of interest. In this technique, a thermal image is constructed using a focal plan array (FPA) sensor that captures the radiated infrared energy from the object. The amount of radiation energy emitted from surface at given wavelength and a specific temperature depends on the surface material and the condition of its surroundings. Every object in the world emits thermal radiations, which are mainly the function of object temperature and surface emissivity. When temperature increases, the radiation also increases. Thermal infrared imaging devices capture these thermal radiations and allow one; to study such variations in temperature. During winter 2012/ 2013, field measurements were performed by RT3 team to detect the atmospheric icing using thermal infrared image processing based technique on various structures (road, buildings, wind turbines, ships etc.) in the surroundings of Narvik [8-10]. A long wavelength (17 µm), FLIR A615 thermal infrared camera was used for this study.

Ease of remote sensing capability of thermal infrared technology has edge over the physical sensing devices especially when it comes to sensing in extreme climates. This field measurement study by RT3 team validated the concept of using the thermal infrared based ice detection technique for large surfaces in harsh cold environment. Analysis showed promising results. Following figures show results from different cases performed in this fields study.

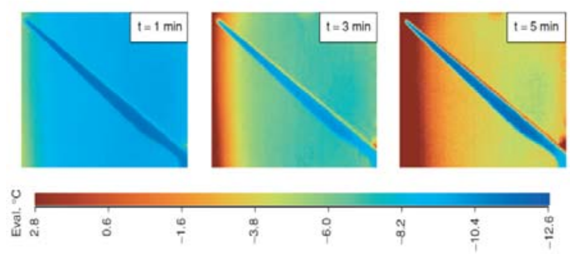

Figure 7: Ice detection on wind turbine blade.

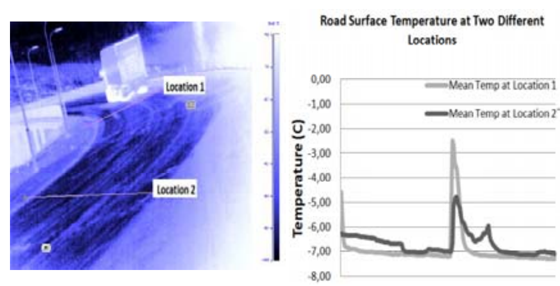

Figure 8: Ice detection on road surface.

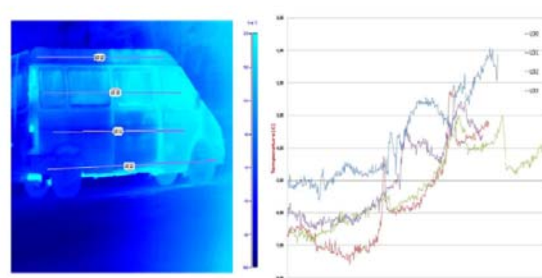

Figure 9: Ice detection on automobiles.

Results show that with the use of thermal infrared ice detection technique the surface areas covered with ice can be detected. Moreover with the help of advance image processing techniques, we can also determine the type and thickness of accreted ice. As an overall this concept is seen as an effective solution towards the detection of ice, where computation on larger surface area is required.

Moreover a new senor's design has been proposed by atmospheric icing research team of Narvik University College (applied for patent rights), where researchers are now working on development of its first prototype.

IV. Numerical Modeling of Atmospheric Icing

Numerical modeling of atmospheric ice accretion on structures is a complex coupled process, which mainly involves the air flow simulation, water droplet behavior, boundary layer characteristics and iced surface thermodynamics involving the phase change. During *COLDTECH-RT3* project, researchers at Narvik University College have used both finite element and finite volume based computational fluid dynamics approaches, to numerically simulate the rate and shape of ice accretion on various structures such as wind turbines, circular power conductors, building's air intake louvers etc. [11-13]. The work was initiated in year 2010 to simulate the ice accretion on large wind turbine blade profiles; later this work was extended to further simulate the ice on a full scale 5MW NREL wind turbine blade. During this study effects of both operating (*temperature, LWC, droplet size, droplet distribution spectrum*) and geometric parameters (*blade size and orientation*) were analyzed to understand the resultant ice growth. The work was published and presented on different scientific platforms by researchers of NUC [13, 14].

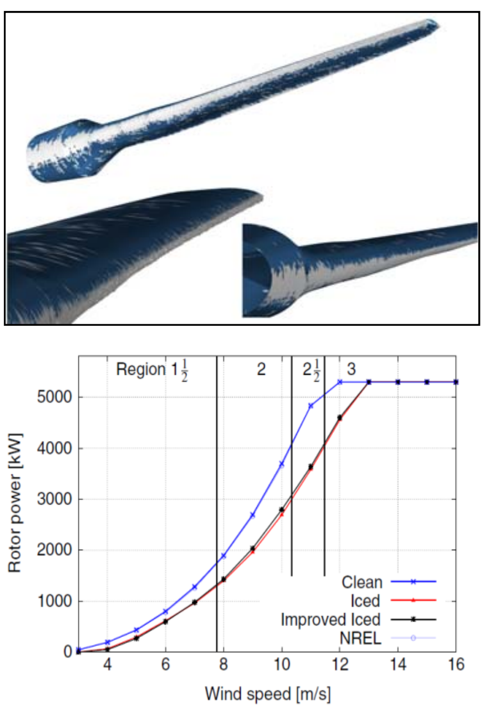

Figure 10: Atmospheric icing on large wind turbine blade and its effect on rotor power

Analyses have also been carried out to simulate the rate and shape of ice accretion on non-rotating circular overhead conductors, both in single and tandem arrangement at different operating conditions. To validate the numerical model, initially the results of ice accretion on single circular cylinder were compared with the experimental data obtained from CIGELE atmospheric icing research wind tunnel [15]. A good agreement was found between experimental and numerical results [16].

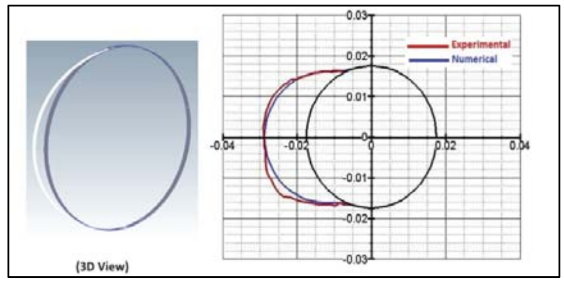

Figure 11: Comparison of accreted ice shape, obtained from numerical simulations with experiments.

After validation of the numerical model for single conductor, analysis were extended to ice accretion on two cylinders in tandem arrangement, where effect of droplet size, atmospheric temperature and distance between two cylinders was numerically analyzed [11]. Analysis showed that distance between the circular conductors in tandem arrangement effects the ice growth on each cylinder. Moreover smooth ice shape on front cylinder; whereas an abrupt ice shape is found on rear cylinder due to change in flow and droplet behavior. As an overall results showed a decrease in accreted ice load and thickness with the increase of the distance between the two circular cylinders in tandem arrangement.

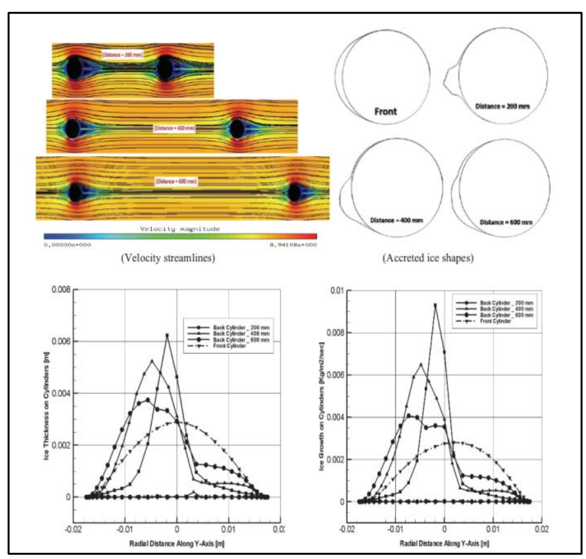

Figure 12: Effect of distance variation between cylinders on rate and shape of accreted ice.

In cold regions, air intake louvers are installed on buildings, so as to deflect foreign matter like ice and snow particles and prevent them from entering the buildings , while allowing air to pass. CFD based parametric numerical study has been carried out to simulate the rate and shape of atmospheric ice accretion on air intake louvers and to analyse the effects of various geometric parameters of louvers such as: placement angle, shape and size on the resultant ice accretion. It was concluded that ice mainly accretes at the front and top sides of the louver surface. It was found that the ice accretion increase with the increase of louver placement angle and decrease in the spacing between the louver slats. Moreover more streamlined flow behaviour is observed in the case of circular shape slat corners as comapred to rectangule shape, which leads to a smoother accreted ice shape in the case of circular slat corner.

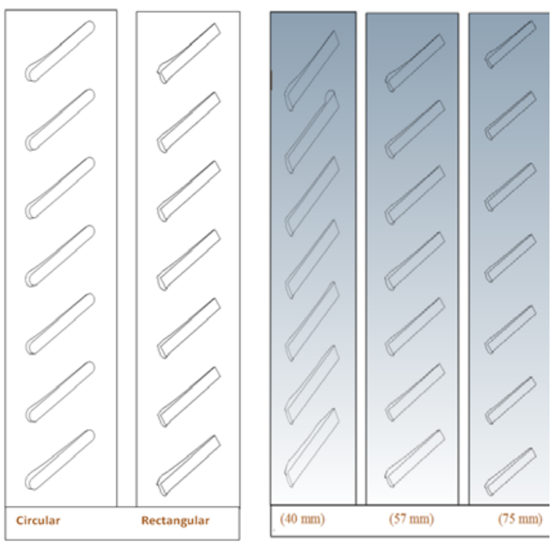

Figure 13: Ice accretion on air intake louvers, effect of louver placement angle and louver shape

V. Acknowledgment:

The work reported in this paper was partially funded by the Research Council of Norway, project no. 195153/160 and partially by the consortium of the project ColdTech- Sustainable Cold Climate Technology.

References:

1. Muhammad S Virk, Mohamed Y Mustafa, and U.N. Mughal. *Field Measurements of Atmospheric icing from an ice monitoring station installed at Fagernesfjellet in northern Norway*. in *COMADEM*. 2013. Helsinki, Finland.
2. Muhammad S Virk, Mohamed Y Mustafa, and U.N. Mughal. *Experimental Investigation of Appropriate Conditions for Atmospheric Ice Accretion on Onshore Structures in the Arctic Region.* in *2nd LATIN AMERICAN & CARIBBEAN CONFERENCE ON THEORETICAL AND APPLIED MECHANICS (LACCOTAM 2012)* 2012. Caracas, Venezuela.
3. Muhammad S Virk, Mohamed Y Mustafa, and U.N. Mughal. *Mathematical Prediction of In-Cloud Icing Conditions Using Data from a Ground Meteorological Station.* . in *38th Conference on Applications of Mathematics in Engineering and Economics*. 2012. Sozopol, Bulgaria.
4. Foder., M.H., *ISO 12494 – Atmospheric icing on structures and how to use it*, in *11th International Offshore and Polar Engineering Conference*2001: Norway.
5. Sharavan K B, Umair N Mughal, and M.S. Virk., *Experimental study of relative permittivity of atmospheric ice.* International journal of Energy and Environment, 2013. **4**(3): p. 369-376.
6. Umair N Mughal, Mohamed Y Mustafa, and M.S. Virk., *Review of Capacitive Icing Sensor.* Sensor & Transducers Journal, 2013. **18**: p. 24-32.
7. Matthew C Homola, Per J Nicklasson, and P.A. sundsbø., *Ice sensors for wind turbine.* cold regions science and technology, 2006. **46**: p. 125-131.
8. Muhammad S Virk, Taimu Rasheed, and U.N. Mughal. *Ice Detection on Road Surface Using Passive Thermal Infrared Technique*. in *COMADEM*. 2013. Helsinki, Finland.
9. Virk., M.S., *Application of Passive Thermal Infrared Imaging to Study Ice and Snow Accretion on Automobiles in Cold Regions.* Advanced Materials Research, 2013. **739**: p. 481-485.
10. Muhammad S Virk and R. Ghani., *Experimental study of atmospheric ice detection on wind turbine blades using thermal infrared techniques.* Wind Engineering, 2013. **37**(1): p. 71-78.
11. Virk, M.S., *Atmospheric Ice Accretion on Circular overhead powerline conductors installed in tandem arrangement.* journal of computational multiphase flow, 2013. **5**(1): p. 73-81.
12. Virk, M.S., *Atmospheric Ice Accretion on Building's Air Intake Louvers in Cold Regions.* International Journal of MultiPhysics, 2012. **6**(4).
13. Muhammad S Virk, et al., *Performance losses due to ice accretion for a 5 MW wind turbine.* Wind Energy, 2012. **DOI: 10.1002/we.477**.
14. Muhammad S Virk, Matthew C Homola, and P.J. Nicklasson., *Atmospheric Icing on Large Wind Turbine Blades.* International Journal of Energy & Environment, 2012. **3**(1): p. 1-8.
15. Ping Fu and M. Farzaneh., *Two dimensional modelling of the ice accretion process on transmission line wires and conductors.* cold regions science and technology, 2006. **46**: p. 132-146.
16. Virk., M.S., *Atmospheric Ice accretion on non rotating circular cylinders.* The journal of computational multiphase flows, 2011. **3**(4): p. 197-205.

Wind tunnel glaze ice simulation on a vertical angle member for different aerodynamic angles

H. Banitalebi Dehkordi[1], M. Farzaneh[1] and P. Van Dyke[2]
[1]NSERC / Hydro-Quebec / UQAC Industrial Chair on Atmospheric Icing of Power Network Equipment (CIGELE) and Canada Research Chair on Atmospheric Icing Engineering of Power Networks (INGIVRE), www.cigele.ca, Université du Québec à Chicoutimi, Chicoutimi, QC, Canada
[2]Hydro-Quebec Research Institute (IREQ), Varennes, QC, Canada
* Email: hamid.banitalebi-dehkordi@uqac.ca

Abstract — Atmospheric icing is one of the major problems in cold climate regions, which can impose serious damage to the structures, notably power network transmission lines. This paper investigates the glaze ice accretion on power transmission network pylons. In order to simulate the natural winter condition, an icing wind tunnel is utilized. Initially an aluminum angle member was mounted vertically in the test section of the wind tunnel. The angle member was then rotated in three dimensions to evaluate the effect of different angles (angle of attack, yaw angle, and rolling angle) on ice morphology and ice accretion mass per unit length. The tests were performed with liquid water content (LWC) of 0.9gr/kg^3 and the duration of each test was 30 min.
Ice profiles and morphologies were affected by gravity effects, which where produced by various aerodynamic angles, and the drag effects. The formation of glaze ice initiates with the formation of ice dendrites on the surface. Due to the effect of gravity forces and relatively warm temperatures, these ice dendrites will then grow into a glaze ice structure. A new parameter was defined as ice mass per unit length, which quantifies the effects of gravity and drag mechanisms on ice accretion. It was shown that ice mass per unit length was a function of different aerodynamic angles.

Keywords — Atmospheric icing, Aerodynamic angles, Angle member, Angle of attack

1. Introduction

In areas where ice accretion on power network equipments is possible, besides different types of ice, the load resulting from added weight or increased aerodynamic forces in combination with wind force become important. This phenomenon, leading to failure on towers and some damages on transmission lines, has been observed and studied for many years. Most of the atmospheric icing models consider an icing objects placed in an air flow carrying a super cooled droplet. Such a geometrical arrangement involves the possibility to simplify the model to a two dimensional (2D) representation. This simplification is advantageous for immediate freezing under extremely cold conditions. However, when the axis of the icing object is placed in an angle with the air velocity, then 3D models are essential for reliable simulation.

It is significant to consider the type of ice because under specific conditions, different ice shapes appear: this latter is found intrinsically depending on geometry parameters and aero-thermal conditions. Vargas and Tsao presented a photography investigation on the growth of ice on swept wings in the icing research tunnel (Vargas, M. and Tsao, J.-C., 2007). They observed roughness elements, icing feathers, initial scallop and complete scallop in the glaze icing conditions while Presteau et al. showed that the results from 3D numerical model for scallop ice shape were in a good agreement with experimental tests for a plain cylinder (Presteau, X. et al., 2009). Vargas and Tsao conducted an experiment in natural icing conditions using icing research aircraft for different sweep angles to compare the mechanism of scallop formation with the results which were collected from tunnel investigation (Vargas, M. et al., 2002).

Another effect of aerodynamic parameters is on the quantity of the accreted ice. Virk et al. conducted a numerical in order to study the angle of attack variation on atmospheric ice accretion near the blade tip. The results showed that atmospheric icing is less severe at lower angles of attack, both in terms of local ice mass and relative ice thickness (Muhammad S. Virk et al., 2010). Rejado et al. investigated an experimental study on airfoil with simulated rime and glaze ice. They studied the effect of angle of attack on drag coefficient for different ice profiles. However for the structure immersed in the wind or ice storm, the bluff bodies have an important role in icing phenomena (C Cuerno-Rejado et al., 2001). Kollar and Farzaneh studied the effects of various angle of wind velocities and axis of a cylindrical icing object experimentally. They calculated the mass, shape and profile of ice accretion as a function of cylinder inclination (L.E. Kollar and M. Farzaneh, 2010).

In order to study the effects of aerodynamic angles on the bluff bodies the present investigation was mainly focused on reduced model of tower leg icing which is well known as an angle member for different aerodynamic angles. The angle member was mounted vertically in the test section of closed loop icing tunnel for three different aerodynamic angles as sketched in Figure 1.

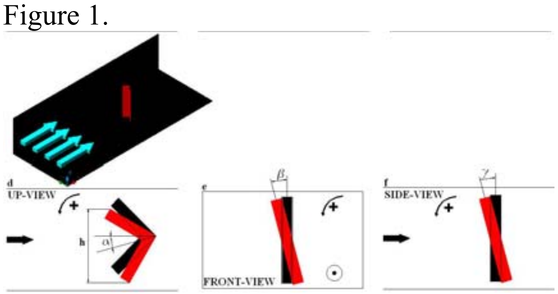

Figure 1: Sign convention and definition of aerodynamic angles for vertical angle member (a) angle of attack (b) side slip angle and (c) rolling angle

2. Experimental Apparatus

2. 1. Test Facility

All experiments were performed at a closed-loop low-speed wind tunnel, available at CIGELE, Quebec, Canada. The tunnel is 30m in total length with maximum cross section of $1\text{m}\times 1\text{m}$. The test section is rectangular $0.92\text{m}\times 0.46\text{m}$ and 3m in length. The maximum velocity in the test section is $28\text{m/s}\pm 0.01$; at 25 m/s the turbulence level, both longitudinal and transverse is less than 0.2. The minimum temperature in the test section is -30 ˚C.

A horizontal spray bar with three air assisted nozzles was used to model in-cloud icing for different icing conditions. It is located at the midpoint of the tunnel cross section. The nozzles are manufactured by spraying systems Co., and consist of a 2050 stainless steel water cap and 67147 stainless steel air caps. LWC (Liquid Water Content) produced by these nozzles can be in the range of 0.3 to 12 gr/m^3. The spray bar with the nozzles was located at 4.4m up-stream from the angle member, which distance is sufficient for the droplets to become super cooled. This distance is also long enough for water droplets to be mixed in the air flow and to obtain a uniform aerosol cloud in the middle of the test section where the icing object is placed (Banitalebi D. et al., 2011).

2. 2. Test Model

The angle member fabricated from Al 6061-T6 with length of $a=0.46m$ and the extrusion profile of $b=0.051m\times b=0.051m\times c=0.006m$ was used as the icing object in this study. To alter angle of attack, α, for the model in the vertical direction, the angle member was fixed directly from two sides at the top and bottom of the test section while for the yaw angle, β, and rolling angle, γ, a special support with a spherical joint was used where it was mounted from the top of the test section. In all cases, special care was taken in order to keep the midpoint of the angle member at the tunnel center line. For more detailed discussion on the zone of uniformity see (Banitalebi D. et al., 2011).

2. 3. Selecting experimental conditions

Considering the effects of air temperature, LWC and ice thickness in detail was out of the scope of this study; consequently they were kept in all the experiments at values corresponding to what occurred in nature. The air temperature was set at -5˚C±0.8 ˚C in the tunnel section preceding the spray bar. The LWC of the aerosol cloud was set by combination of nozzle air and water pressure on p_a = 160 kPa and p_w = 120 kPa which was related to value of 0.9 gr/m^3 for LWC. The ice thickness during the experiment was calculated based on the time duration of each experiment. For each experiment this time was set on 30 min which represented the maximum thickness of ice. The air velocity was set at 10 m/s. The values of mass per unit length shown in this paper are the average of 2 values and the standard deviation on these average values is smaller than 0.87.

2. 4. Collecting data procedure

Mass of ice accretion per unit length of angle member, ice shape, and profile of ice accretion were collected for each test based on the process recommended in (L.E. Kollar and M. Farzaneh, 2010). Ice shapes were recorded by taking photos of their front and top views. In order to measure ice mass, the angle member was transferred carefully from its supports and set into the designed support for further examination outside the tunnel. A thin preheated aluminum cutter was used to cut the ice specimens for measuring their mass and length. Samples with length of about 25 to 30 cm were taken from the middle of the angle member. The maximum error for cutting ice process was evaluated to be around 1.7%. After cutting the ice accretion, additional photos from cross sectional view were taken to record ice profiles.

3. Results and Discussion

3. 1. Angle of attack (α)

Figure 2 shows the ice mass per unit length for the angle member mounted vertically. The maximum exposed area of the angle member is in α=0° and α=180°. This means that more droplets can freeze on angle member surfaces but for α=0°, the corner effects changes the stream lines direction and less ice accumulates on the surfaces of the angle member (see Figure 2). Another significant effect on the ice accretion for a vertical angle member is gravity. Figure 3 shows the accreted ice for different angles of attack. The ice morphology changes on angle member surfaces. It may be explained by two mechanisms: droplet drag force and droplet gravity force. More droplets tend towards the bottom of the angle member because gravity effects are more dominant than drag effects.

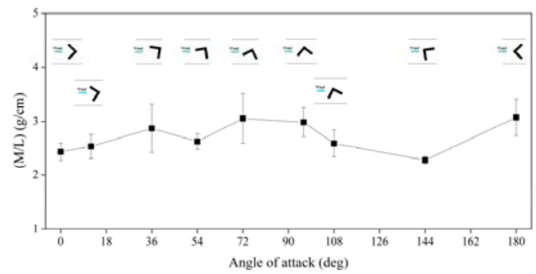

Figure 2: Ice mass per unit length for different angles of attack

Figure 3 shows that very small curved ice structure named roughness elements started to grow on the surface. They increased rapidly towards the bottom of the angle member because more droplets were caught between the roughness elements and froze.

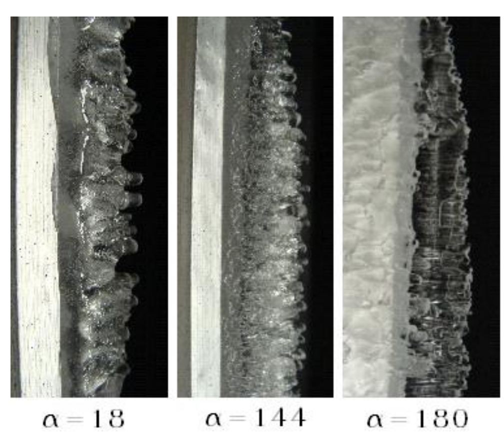

Figure 3: Ice accretion for three different angles of attack

3. 2. Yaw angle

Figure 4 shows accreted ice on a vertical angle member for β=6°. As shown, the roughness elements were formed at the beginning of the ice accretion process. The gravity effects on the droplet trajectory caused more droplets to move towards the bottom of the angle member. As a result, more droplets were trapped between roughness elements while towards the top of the angle member, the roughness elements developed into glaze ice feathers when they reached a preferred height in the direction of perpendicular to the flow streamlines. Figure 4b shows tightly packed feathers. For all other sideslip angles, the same results were obtained.

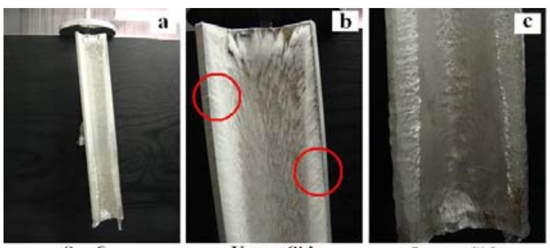

Figure 4: Ice accretion for a) α=6°, b) upper side, c) lower side

3. 3. Rolling angle

The ice mass per unit length of the angle member which was mounted vertically in the tunnel has a maximum at γ=6°. It seems that when the angle member rotates in two directions around a lateral axis, the ice mass decreases slightly (Figure 5). It may be explained by the effect of the exposed area. When the angle member rotates around a lateral axis, its exposed area decreases and fewer droplets can reach angle member surfaces.

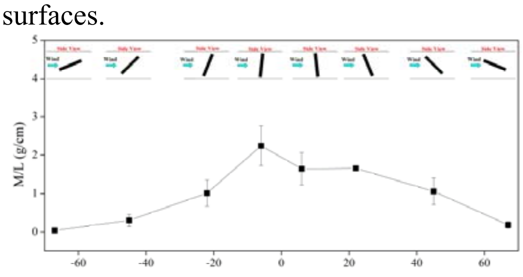

Figure 5: Ice mass per unit length for different rolling angles

Figure 6 shows the ice morphologies for positive rolling angles. At γ=67°, the ice accreted on the edge of the angle member. A side view of ice accretion showing tightly packed feathers on the edges. By decreasing γ to 45°, the ice is covered with glaze ice feathers with a preferred direction of growth that is perpendicular to the streamlines. Then the feathers reach a specific height and join each other, creating a scallop shape (Vargas, M. et al., 2002). For other angles, tightly packed feathers were simply observed after ice accretion.

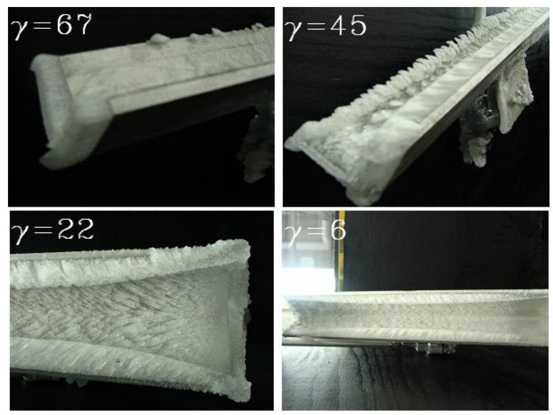

Figure 6: Ice accretion profiles for different rolling angles

4. Conclusion

- For some angles of attack the corner effects changed the stream lines direction and caused less ice accumulates on the surfaces of the angle member.
- It was observed that very small curved ice structure named roughness elements started to grow on the surface of the angle member. They increased rapidly towards the bottom of the angle member because more droplets were caught on angle surface.
- It was observed that for different yaw angles the roughness elements developed into glaze ice feathers when they reached a preferred height in the direction of perpendicular to the flow streamlines.
- It was shown that for higher rolling angles, tightly packed ice feathers created on the edges of the angle member while by decreasing the rolling angle the ice was converted to glaze ice feathers with a preferred direction of growth that is perpendicular to the streamlines.

5. Acknowledgement

This work was carried out within the framework of the NSERC/Hydro-Quebec/UQAC Industrial Chair on Atmospheric Icing of Power Network Equipment (CIGELE) and the Canada Research Chair on Engineering of Power Network Atmospheric Icing (INGIVRE) at Université du Québec à Chicoutimi. The authors would like to thank the CIGELE partners (Hydro-Québec, Hydro One, Réseau Transport d'Électricité (RTE) and Électricité de France (EDF), Alcan Cable, K-Line Insulators, Tyco Electronics, Dual-ADE, and FUQAC) whose financial support made this research possible. The authors are grateful to Caroline Potvin for FT-IR analysis.

Reference

Banitalebi D. et al. (2011), Experimental study of Spray Characteristics and its Uniformity under Different Icing Conditions. IWAIS

C Cuerno-Rejado et al. (2001), Experimental Aerodynamic characteristics of NACA 0012 Airfoils with Simulated Glaze and Rime Ice. Proc Instn Mech Engrs. IMechE.

L.E. Kollar and M. Farzaneh. (2010), Wind Tunnel Investigation of Icing of an Inclined Cylinder. Heat and Mass Transfer , 849-861.

Muhammad S. Virk et al. (2010), Effect of Rime Ice Accretion on Aerodynamic characteristics of Wind Turbine Blade Profiles. Wind Engineering , 34 (2), 207-218.

Presteau, X. et al. (2009), Experimental and numerical study of scallop ice on swept cylinder. 1 st AIAA Atmospheric and Space Environments Conference.

Vargas, M. et al. (2002), Ice Accretion Formations on a NACA 0012 Swept Wing Tip in Natural Icing Conditions. 40th AIAA Aerospace Sciences Institute of Aeronautics and Astronautics.

Vargas, M. T.-C. (2007), Observation on the growth of roughness elements into icing feathers. 45th AIAA Aerospace Sciences Meeting, (pp. 10889-10910).

A Remote Ice Detection System Suitable for Marine and Aerospace Applications

R.E. Gagnon, J. Groves, and W. Pearson

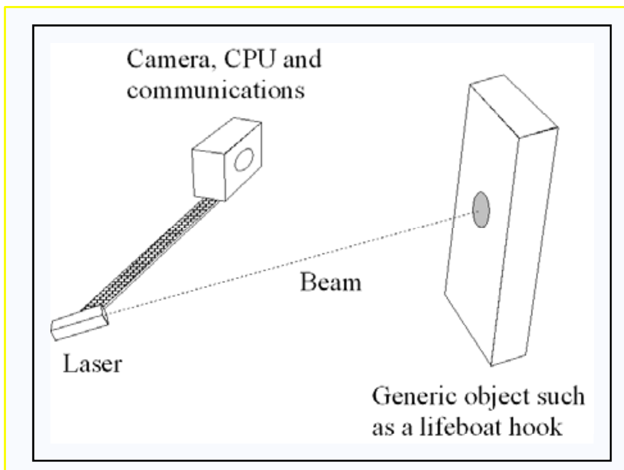

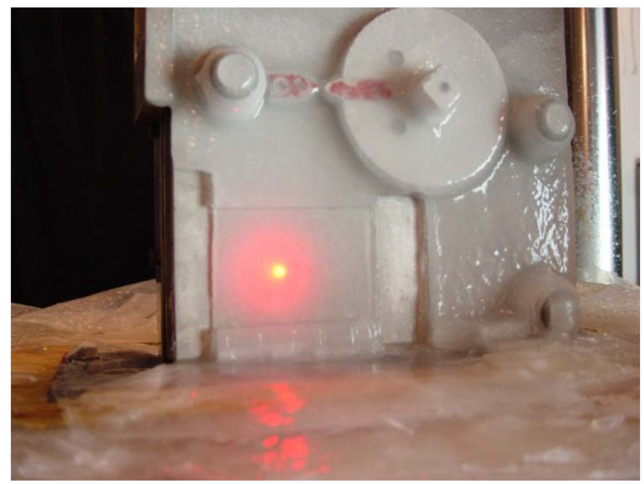

Ocean, Coastal and River Engineering

Applications

Aerospace and Energy

Marine

Technical Description

Optical Method 1

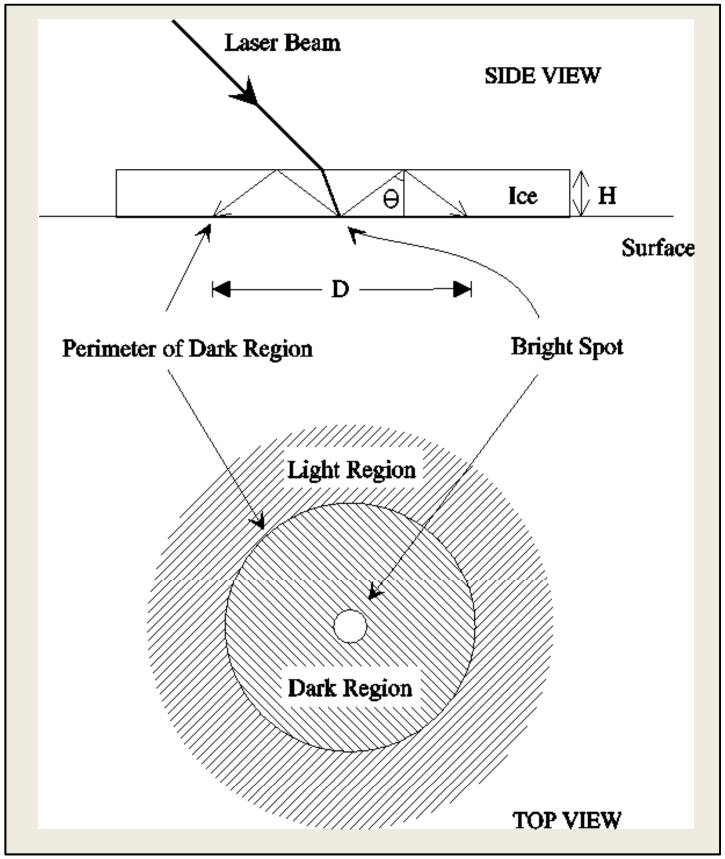

Illustration of the remote thickness measurement technique, optical method 1, used for clear solid or liquid layers. (From Gagnon et al., 2012)

$$H = \frac{D}{4*Tan(\Theta)}$$

$$\Theta = \sin^{-1}\left(\frac{1}{n}\right)$$

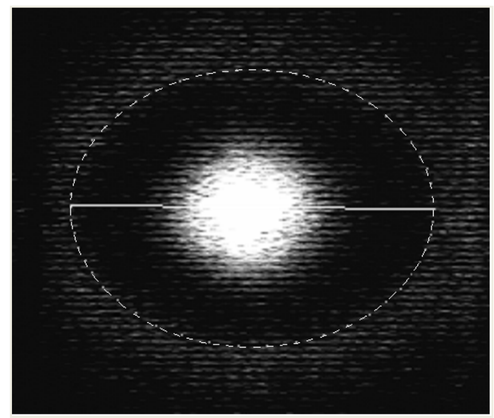

Image from an ice layer measurement showing the elliptical fit at the light/dark boundary and the major axis of the ellipse. The iced surface was tilted relative to the view direction, hence the pattern of illumination is elliptical rather than circular. (From Gagnon et al., 2012)

Technical Description

Optical Method 2

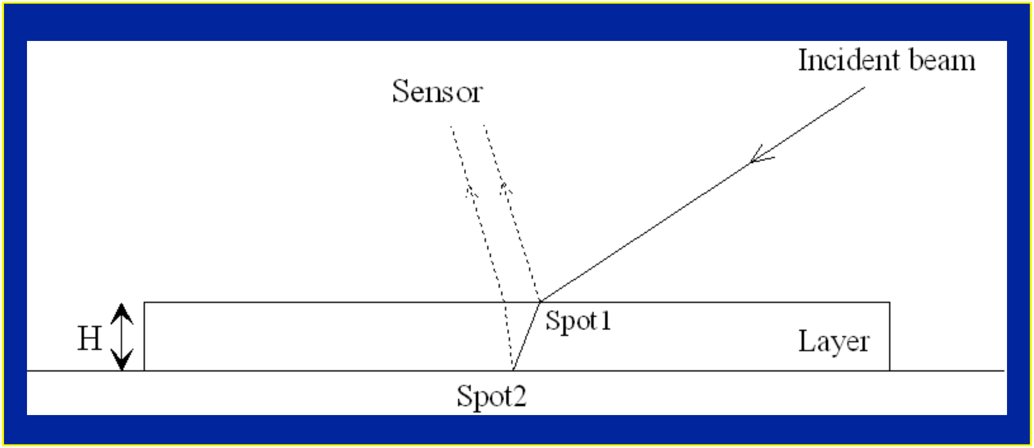

The basic operation of the second technique, optical method 2. The method can be used for clear or foggy layers of solids or liquids. (From Gagnon et al., 2012)

$$H = S / [(\tan(\sin^{-1}(\sin(V)/n)) + \tan(\sin^{-1}(\sin(L)/n)))\ \cos(V)]$$

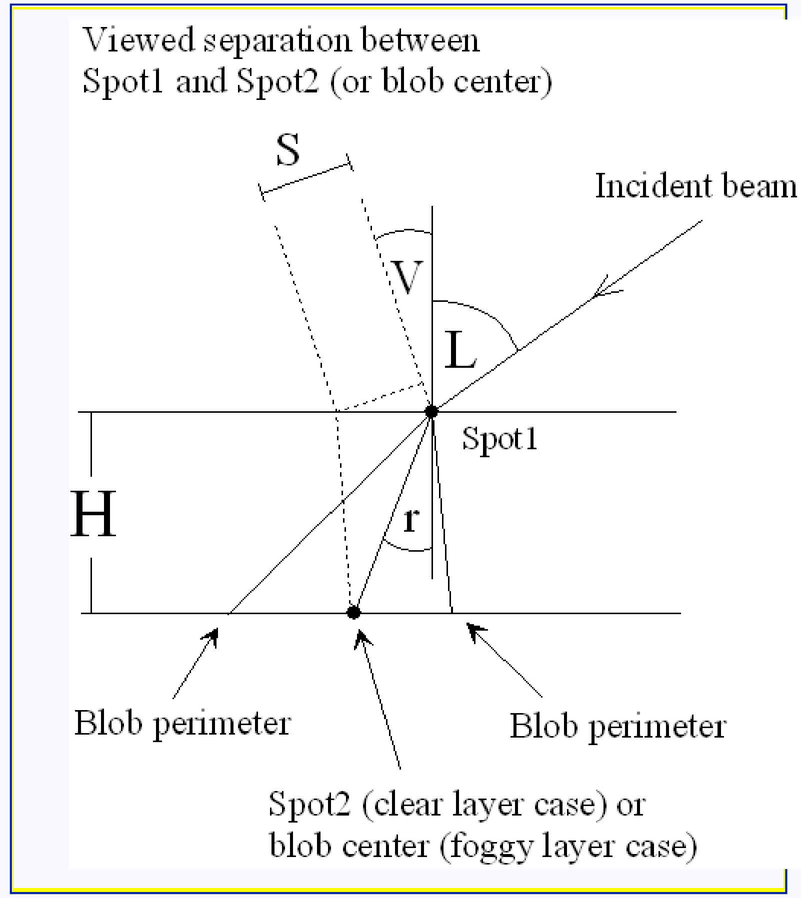

Detailed schematic for optical method 2. Note that the blob ‘perimeter’ is not a well-defined line but rather, for descriptive purposes in discussing the figure, it refers to an ellipse defined by a line of arbitrary equal brightness. (From Gagnon et al., 2012)

Technical Description

Optical Method 2

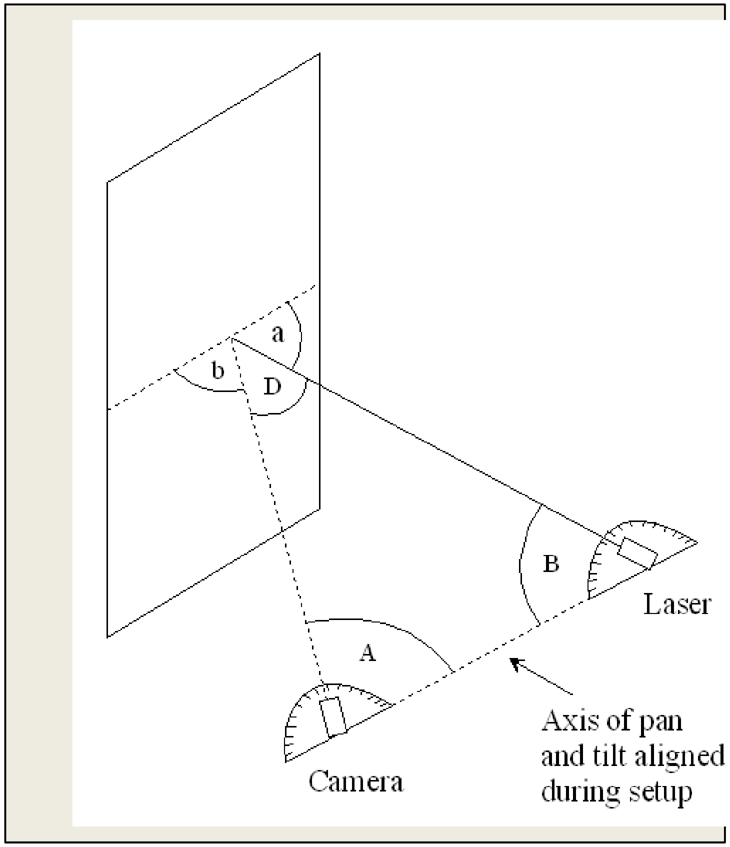

Schematic of the system setup where a measurement is made on a surface that is tilted relative to the plane defined by the camera, the laser and the measurement point location. Relevant angles used in the calculations are shown. (From Gagnon et al., 2012)

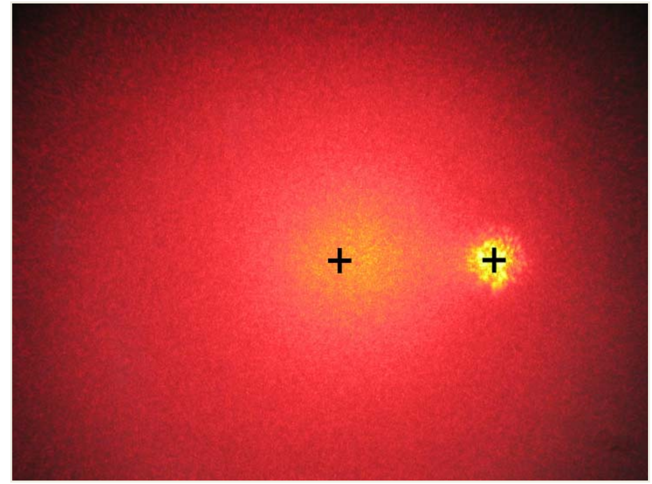

An image captured by the RIDE system during a test program where the thickness of a foggy ice layer on a metallic surface was determined. The bright spot at the right corresponds to the location where the low-power laser beam impinges on the top surface of the ice. The large and more diffuse illuminated region taking up the majority of the image corresponds to the light blob on the underlying surface caused by scattering of the laser beam by the tiny air bubbles in the ice as it propagates through the layer. (From Gagnon et al., 2012)

Technical Description

Optical Method 2

$$H = \frac{S}{\sin(b)\cos(RV)\tan(AV)\left[1 + \frac{\cos(RL)\tan(AL)}{\cos(RV)\tan(AV)}\right]}$$

where: $RL = \tan^{-1}(\tan(a)\sin(T))$; $RV = \tan^{-1}(\tan(b)\sin(T))$; $AL = \sin^{-1}(\sin(L)/n)$; and $AV = \sin^{-1}(\sin(V)/n)$.

where:

$$L = 90 - \tan^{-1}\left[\frac{\tan(a)\cos(T)}{\sqrt{1+\left(\tan(a)\sin(T)\right)^2}}\right] - (a - \tan^{-1}(\tan(a)))$$

$$V = 90 - \tan^{-1}\left[\frac{\tan(b)\cos(T)}{\sqrt{1+\left(\tan(b)\sin(T)\right)^2}}\right] - (b - \tan^{-1}(\tan(b)))$$

System Hardware Components

The two main system components situated on their respective tripods. The laser tripod is on the right. Also visible in the photo are the Lexan™ weather housings resting at the bases of the tripods. (From Gagnon et al., 2012)

System Hardware Components

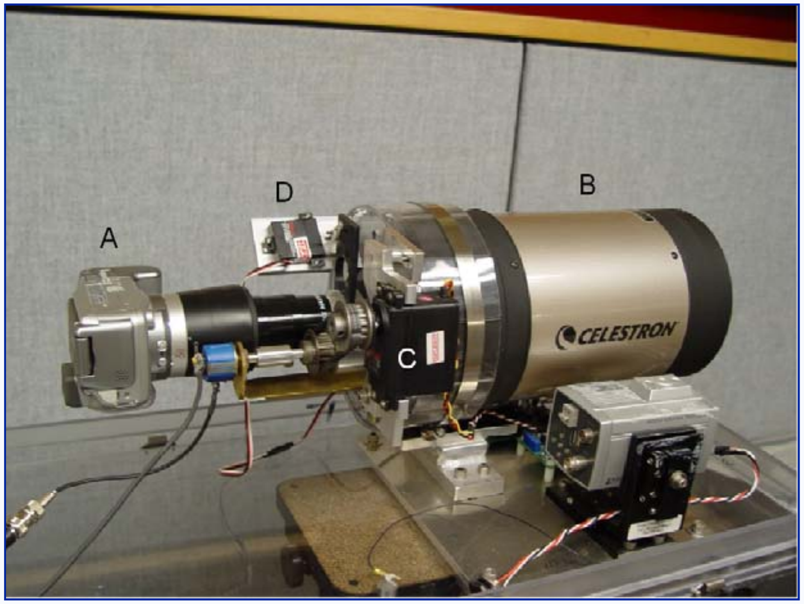

Digital camera (A) and telescope (B). The telescope's focusing knob is controlled by a servomotor (C). A filter, for use in bright sunlight conditions, can be deployed by a second servomotor (D). (From Gagnon et al., 2012)

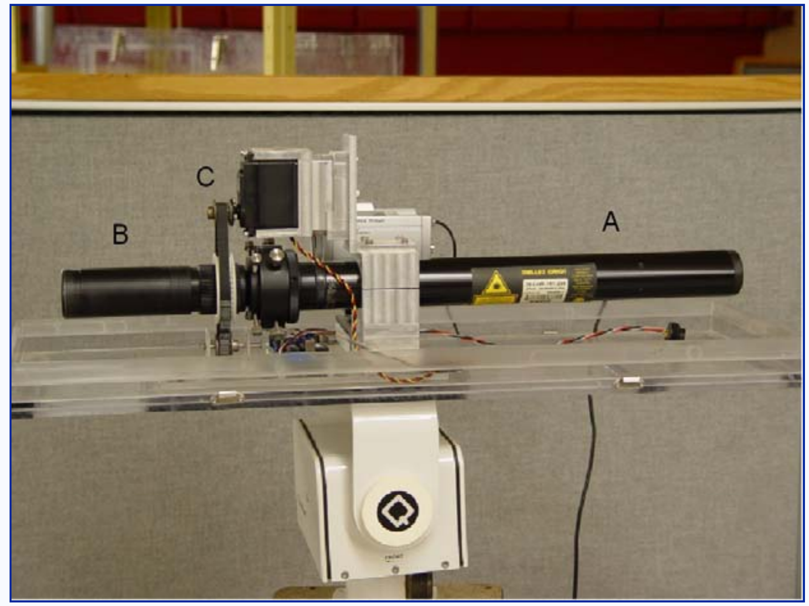

HeNe laser (A) and optic (B) for beam expansion and focusing. The optic is controlled by a servomotor (C). (From Gagnon et al., 2012)

Test Programs

Earlier Version of Remote Ice Detection Equipment (RIDE)

(Suitable for thickness measurements of clear ice layer accumulations)

Clear Ice Layer on Space Shuttle foam

Thickness Measurements at a Distance of ~15 m

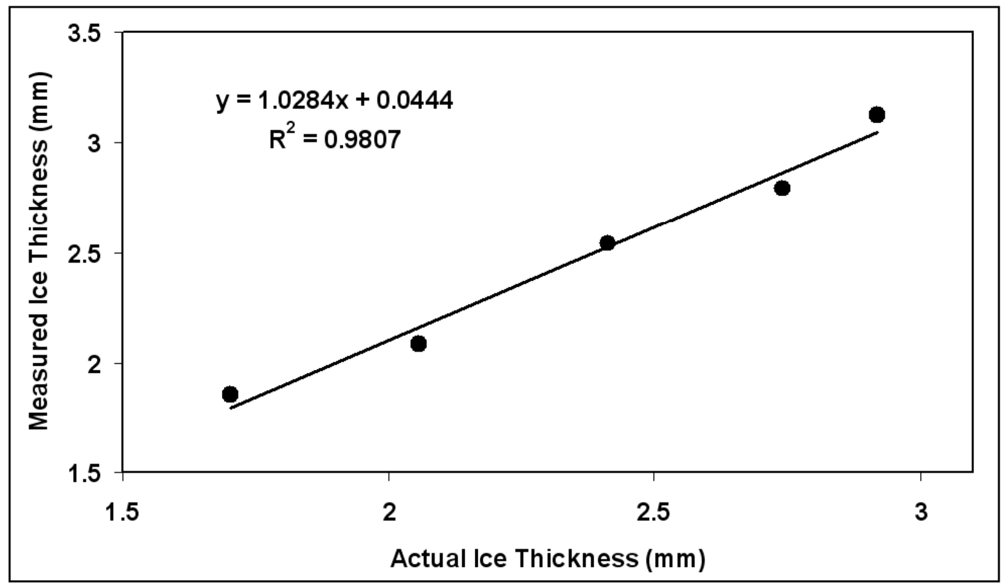

Test Programs

Other Earlier Test Programs

Icing on an Airfoil and Model Rotor (IAR/NRC Facility)

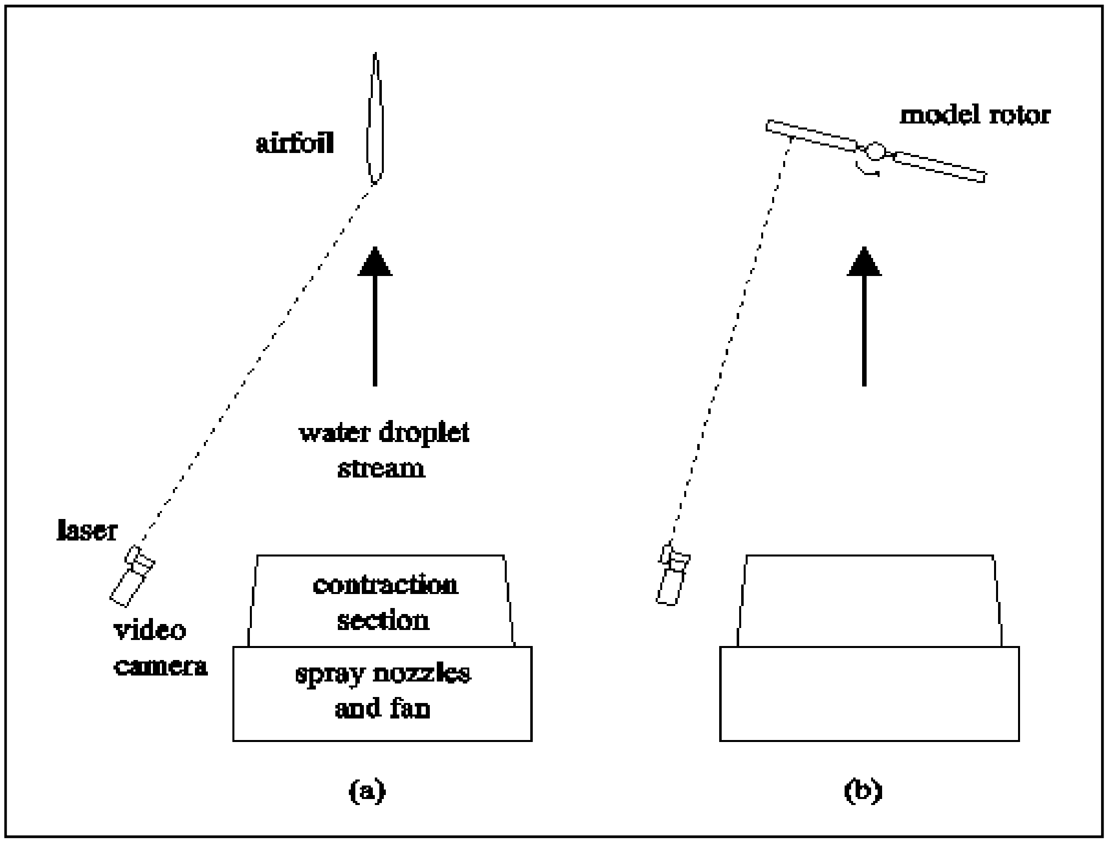

Gagnon, R.E., Marcotte. D.L., 1995. Icing Thickness Measurements from an Airfoil and Model Helicopter Rotor Using a New Remote Technique. Proceedings of the American Helicopter Society International Icing Symposium `95, Montreal, Canada, September, 1995, 417-428.

Test Programs

Earlier Test Program

Wing Performance in the Presence of Contaminated Fluid (IAR/NRC Facility)

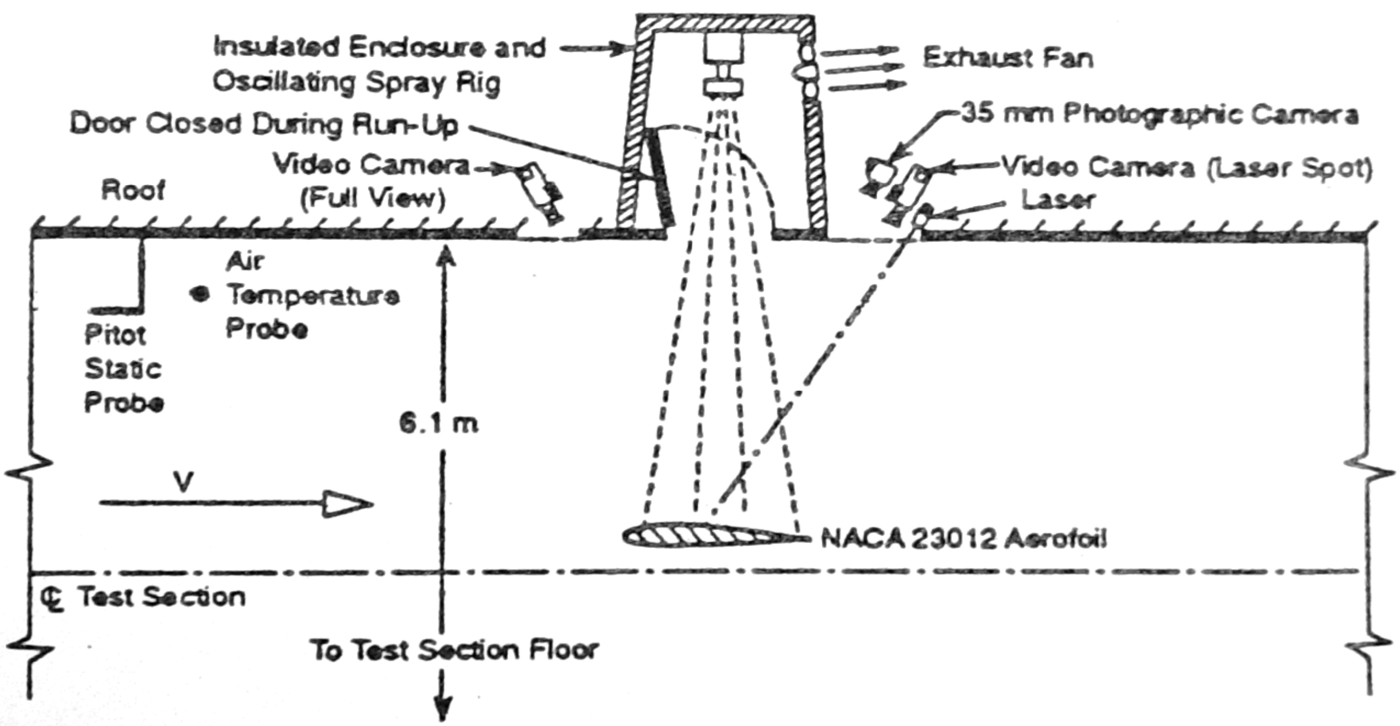

Oleskiw, M.M., Penna, P.J., Crabbe, R.S., Beyers, M.E., 1995. Full-Scale Wind-Tunnel Simulation of Takeoff Performance Degradation with Contaminated Fluid Runback. Proceedings of the American Helicopter Society International Icing Symposium `95, Montreal, Canada, September, 1995, 179-190.

Test Programs

Remote Ice Detection Tests on a Lifeboat Hook

OCRE/NRC Cold Room with Windows

Lifeboat Hook with Icing Accumulation

Test Programs

Remote Ice Detection Tests on a Lifeboat Hook

Ice Detector Prototype Setup

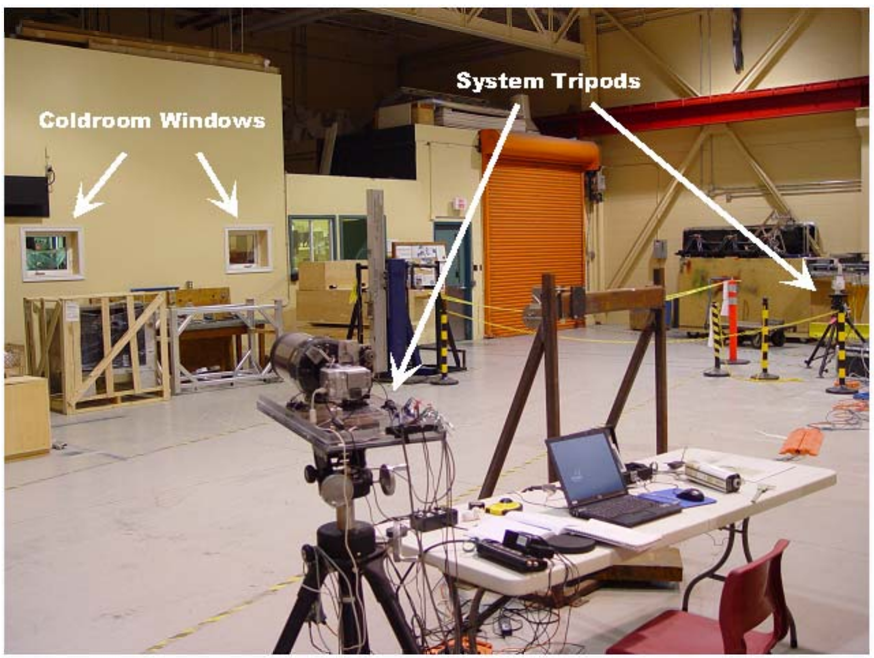

Lifeboat Hook with Icing Accumulation and Laser Beam Impinging on the Surface

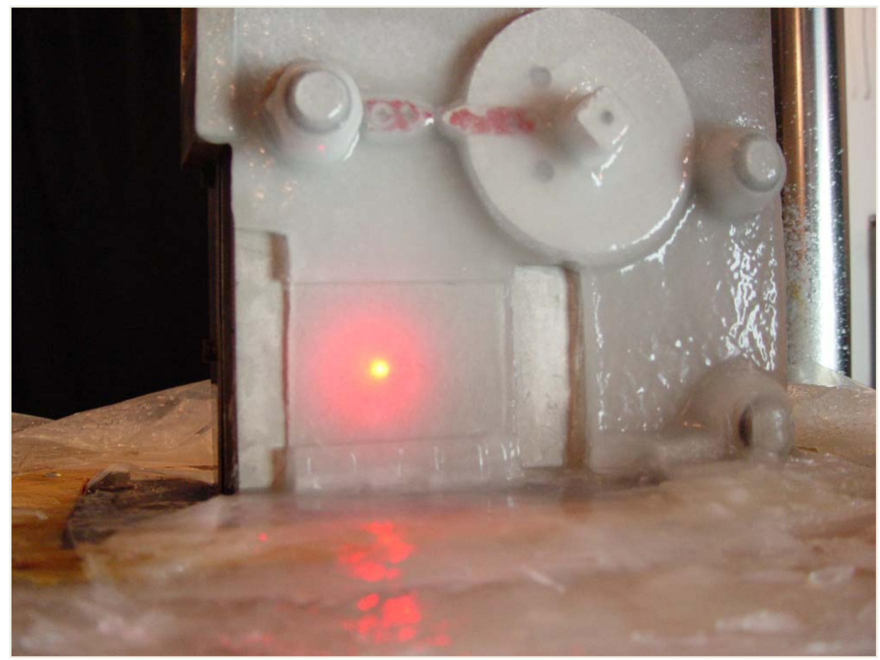

Test Programs

Remote Ice Detection Tests on a Lifeboat Hook

Automated data analysis from the Lifeboat Hook Experiments

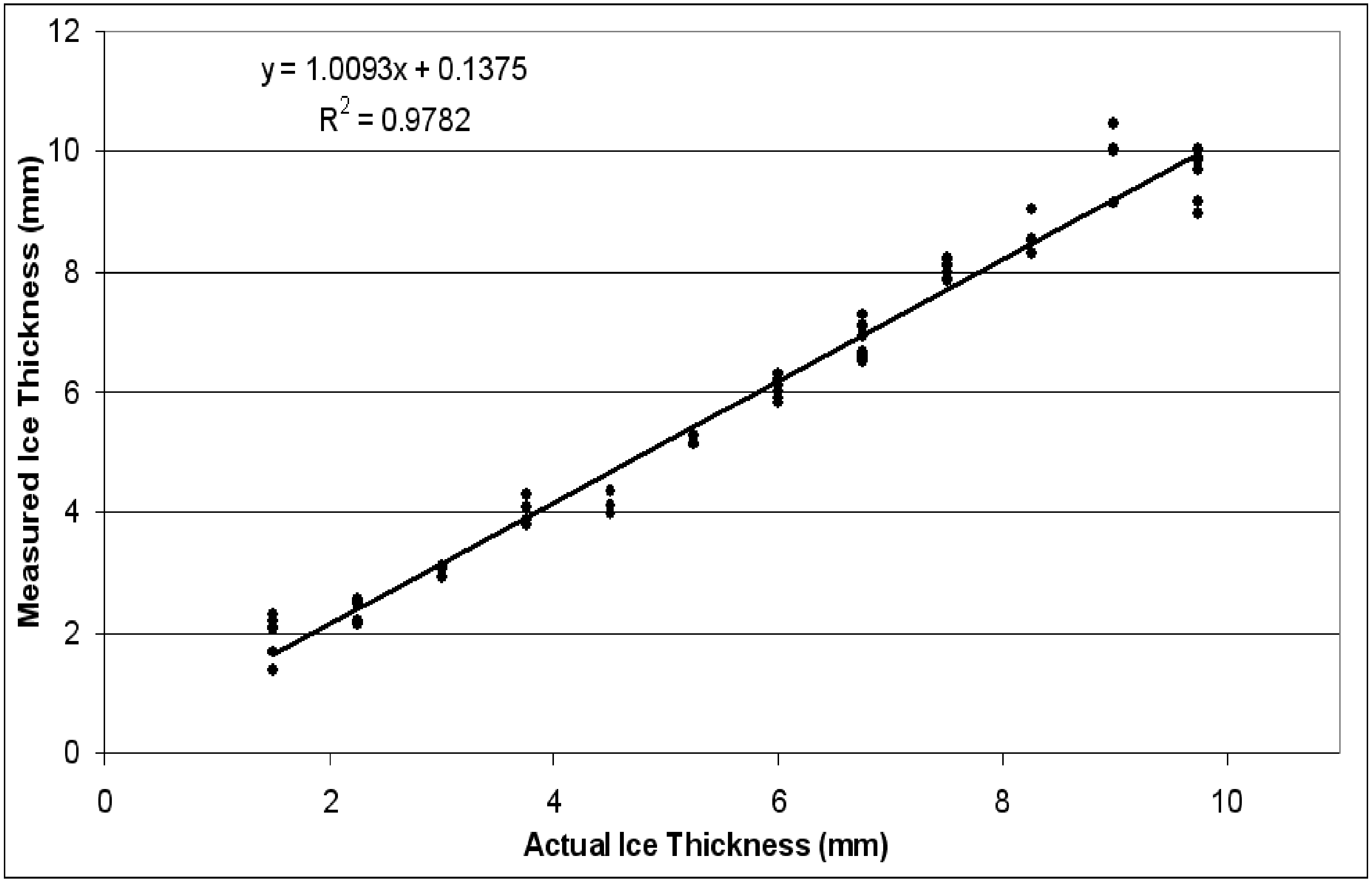

Conclusions

- **A** remote ice detection prototype device has been described that is capable of accurate thickness measurements of foggy or clear layers of ice or liquid on surfaces at distances in the range 6.5 - 30 m. The essential components of the prototype are a low-power laser with a long-distance focusing optic, a compact telescope and a digital camera.
- The system has many potential applications such as measuring the thickness of ice layers on aerospace vehicles, wind turbines, road surfaces, power lines, and safety and communications equipment on marine structures and ships.
- The prototype can be easily miniaturized for short-distance measurement applications. For example, a compact system could serve as a warning device to signal encumbrance of safety and communications equipment (e.g. lifeboat hooks) on vessels and structures.
- The device could also be used as a smart on-off switch for electrical heaters to remove icing accumulations from areas on vessels and structures that crew and passengers routinely access.

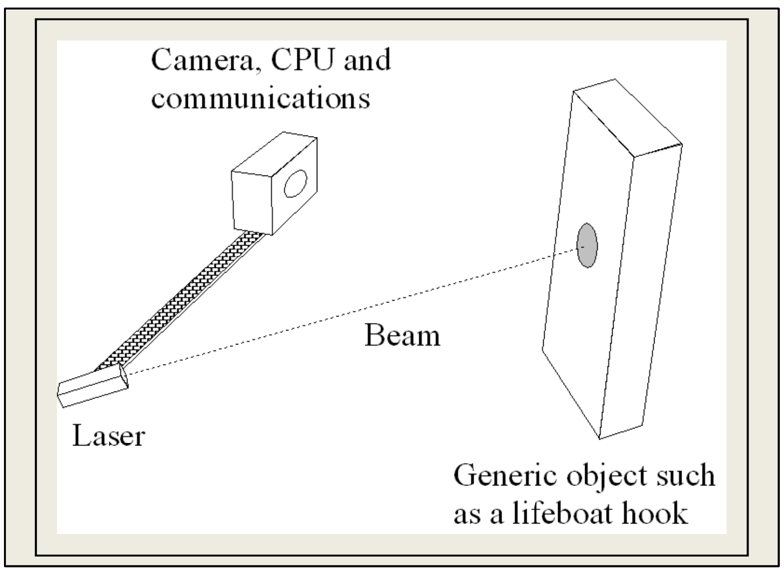

A configuration for a miniaturized RIDE device.

Poster Session

P-1

Research on Transmission Line Ice Automatic Identification System Based on Video Monitoring

Xinbo Huang(黄新波)、Ye Zhang(张烨)、Ling Feng(冯玲)

(College of Electrics and Information, Xi'an Polytechnic University, Xi'an 710048, China)

IWAIS

Abstract

Along with the implementation of the power transmission from west to east in China and the rapid development of UHV transmission project, the scale of power grid is continuously expanding, more and more transmission lines cross canyons, rivers and other regions where are so easy to cause icing. The icing disasters of transmission line such as conductor overload, conductor galloping, break line, pole collapse, insulator flashover and communication interruption have posed a serious threat to the security and stability of power system. Therefore, how to grasp transmission line ice situation with real-time visualize technology has become an urgent problem to be solved. In order to overcome this main hurdle, a system has been designed and developed in this paper, which has a camera installed at the tower to capture the conductor and insulator images of the transmission lines at intervals during daytime and nighttime. The captured images are transmitted to the background monitoring center, then the embedded icing identification algorithm can be used to analyze whether it is iced or not, if there is ice covered on it, the equivalent ice thickness of the conductor or the insulator can be calculated out, the alarm module would work while the ice thickness was over a given value. The ice automatic identification algorithms are mainly studied in this paper, including image preprocessing, image segmentation, edge detection, the camera calibration and other algorithms, meanwhile, test results shows that on-site acquired image of transmission lines verifies the algorithm can automatically identifies the icing status, and the conductor icing thickness error between the algorithm results and field manual measurements is less than 2 mm, and for the insulator, the error is less than 3mm.The system developed in this paper has been successfully put into use in multiple transmission lines, it is in good running condition and can realize the real-time monitoring on ice thickness and timely alarm of transmission line exceptional icing state.

1. The overall structure of transmission lines Ice automatic identification system

The overall structure of transmission lines ice automatic identification system is shown in Fig.1; it is mainly composed of monitoring terminal and monitoring center these two parts. Monitoring terminal is installed at every tower, it is mainly composed of camera, the video image compression module, main control board, communication part and power supply unit, which is responsible for collecting the transmission line images and transmitting data to the monitoring center by wireless 3G/OPGW; the collected images will be stored in a central database for image analysis by using image processing algorithm. Ice automatic recognition algorithm will be embedded in transmission lines automatic ice image recognition software, through the image analysis of the collected transmission line images, the ice thickness can be identified and calculated, the analysis results will be uploaded to the client-side or be sent to the lines maintenance staff in the form of MMS, simultaneously the corresponding alarm information will be sent out, which can realize the on-line condition analysis and condition assessment for the safety operation of the transmission lines.

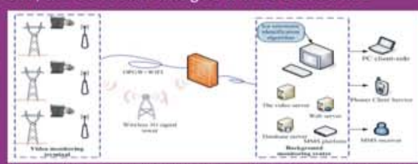

Fig.1 The overall structure of transmission lines Ice automatic identification system

2. Ice automatic identification algorithm

The calculation of ice thickness

We can calculate the ice thickness by comparing the edge distance of conductor and insulator before and after icing. The ice thickness calculation principle of conductor is shown in Fig. 3.

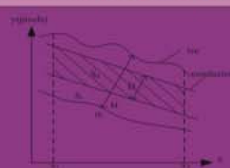

Fig. 3 The principle diagram of the conductor

Assume that the pixel area of ice area on the transmission line conductor at t time is , its original pixels area without ice is , we adopts this method to calculate the average ice thickness, the formula can be represented as:

$$\bar{y}=\frac{1}{2}(\frac{S-S_0}{S_0})\cdot d$$

Assuming that the outside diameter of the conductor after icing is H, the original diameter of conductor before icing is D, the actual diameter of the conductor is d, all of them are in pixels values, thus the average ice thickness calculation formula can be expressed as follows:

$$y=\frac{1}{2}(\frac{H-D}{D})\cdot d$$

We respectively calculate the distances, between conductor and insulator contours before and after icing, and the average ice thickness h of transmission line in metric units is:

$$h=\frac{D'-D}{2}$$

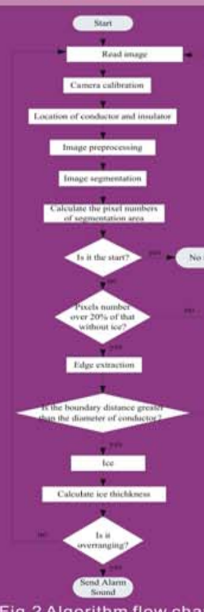

Fig.2 Algorithm flow chart

3. Field installation and running instance analysis

A. The field video monitoring device

The ice identification system has been running successfully at the transmission lines ice monitoring sites in several Grid Company. The field installation picture of the video monitoring device is as shown in Fig. 4.

Fig.4 The field installation picture of the video monitoring device

B. Verification of insulator ice thickness identification

(1) Firstly the collected field image is converted to a grayscale image, secondly the region-of-interest (ROI) of the conductor and insulator must be fixed by orientation detection method in gray-level image, the result image is as shown in Fig. 5.

Fig.5 processing area of conductor and insulator

(2) Image preprocessing: In order to eliminate the interference and noise caused in the process of image acquisition, quantization and transmission, the image preprocessing is used to eliminate noise in image, to enhance the features of conductor and insulator in the image and to improve the image quality, which paves a way for subsequent image segmentation, the preprocessing results are as shown in Fig. 6.

(3) image segmentation: Image segmentation plays a very important role in the whole process of transmission line ice automatic identification, the segmentation effect is directly related to the following ice recognition and ice thickness calculation of the conductor and insulator. The segmentation results after using the image segmentation algorithm is as shown in Fig. 7.

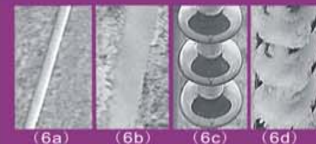

(6a) preprocessing result of conduc before icing
(6b) preprocessing result of conduc after icing
(6c) preprocessing result of insulat before icing
(6d) preprocessing result of insulat after icing

Fig.6 Preprocessing result of conductor and insulator

(7a)segmentation result of conduct before icing
(7b) segmentation result of conduct after icing
(7c)segmentation result of insulato before icing
(7d) segmentation result of insulato after icing

Fig.7 segmentation results

(4) Image edge extraction and ice thickness calculation: on the basis above icing judgment, the insulator image can be further extracted a calculated by the image edge extraction algorithm to determine whet there is ice, finally the ice thickness can be calculated out by approximate distance between the edge extract from the insulator ima before and after icing. Fig. 8 shows the mean value of the distance betw the insulator boundaries after multiple measuring under image coordinat the unit is the pixel.

(8a) Original conductor diamete (pixels)
(8b) The conductor diameter afte icing (pixels)
(8c) Original insulator diameter (pixels)
(8d) The insulator diameter after ic (pixels)

Fig.8 The insulator diameter before and after icing under image coordina

Table 1 The insulator ice thickness calculated by algorithm

object	Mean value of diameter before icing (pixels)	Mean value of diameter after icing (pixels)	Actual diameter (mm)	Average ice thickness (mm)
conductor	22.406	45.812	15	7.83
Insulator	161.279	186.297	100	7.76

In order to verify the effect of the ice thickness algorithm, the avera ice insulator thickness calculated by algorithm is compared with the man measurement ice thickness values, as shown in table 1.

Table 2 Insulator ice thickness

object	Average ice thickness calculated by algorithm (mm)	Average ice thickness measured by manual measurement (mm)	Error (mm)
conductor	7.83	9.1	1.27
insulator	7.76	10.5	2.74

Table 2 shows that the algorithm presented in this paper can accurat identify transmission lines ice cover, and the calculated values close actual ice thickness, which can reflect the actual icing condition transmission lines.

4. Conclusion

Aiming at the drawback of traditional transmission lines ic identification, A new transmission line icing identification system is propo in this paper, which is based on the image processing and recogni techniques for intelligent video monitoring system. This system can rea real-time monitoring on icing condition, with consideration of the comp background factors of the transmission line images, a new method is forward in this paper, which firstly fixes the region-of-interest(ROI) of insulator by location algorithm before icing identification, it not only grea reduce the computational complexities of this algorithm, but also reduce subsequent difficulties of icing identification and ice thickness calculation

1. Huang Xin-bo was born in Shandong Province, Chi in May 1975. He received the B.S. and M.S degree automation from Qingdao Technological Univers Qingdao, China, in 1998 and 2001, respectively. received the Ph.D. degree in automation from XiD University, Xi'an, China, in 2005.
Since July 2005, he has been a teacher at Xi Polytechnic University, and since December 2008, he h been a full Professor with the School of Electronics Information at Xi Polytechnic University. From October 2005 to March 2008, he was a po doctor in the State Key Laboratory of Electrical Insulation and Po Equipment and the School of Electrical Engineering at Xi'an Jiaot University, engaged in the snow and ice warning system on transmiss lines. Since May 2009, he was a post-doctor at South China University Technology, engaged in the transmission conductor galloping monitor and mechanism. His current research interests include the online monitor technology and condition maintenance of power equipment, the wirel network sensor. He has published more than 50 journal articles a conference papers, and 4 monographs. He may be reached hxb1998@163.com.
Dr. Huang received the 2011 new century excellent talent support plan China Ministry of Education (MOE), 2010 teacher of the year award China's "textile light" for teachers, 2009 Hong Kong SangMa research gra award, and several other awards and prizes from Chinese Government.
2. Ye Zhang(1988-) was born in Shaanxi Province, China, in Aug 1988. is currently working toward the M.S. degree with the Control Engineeri Xi'an Polytechnic University. Her research interests include on-l monitoring theory and key technology research on smart grid and ima processing technology. He may be reached at zhang.ye.cn@163.com

The Spatial Distribution of Icing in Germany Estimated by the Analysis of Weather Station Data and of Direct Measurements of Icing

Bodo Wichura

Regional Climate Office Potsdam, German Meteorological Service
Michendorfer Chaussee 23, 14473 Potsdam, Germany
bodo.wichura@dwd.de

Abstract— **The spatial distribution of atmospheric icing in Germany was analyzed using weather station data of 74 meteorological stations evenly distributed over the territory of Germany for the period 1980-1999 as well as direct measurements of icing at up to 35 stations in the east part of Germany for the period 1980-1989.**

The study was elaborated using the hourly ground SYNOP messages from weather stations as primary data in order to accomplish an accurate description of all icing phenomena from a homogeneous data set. All hourly ground SYNOP messages which report icing were analyzed. The frequencies of occurrence of icing were computed as the ratio of the number of SYNOP messages reporting icing phenomena to the total number of SYNOP messages.

Results of icing frequencies from weather station data were compared to the frequencies of occurrence of icing that were measured directly. The comparison shows, that low frequencies of icing are generally overestimated by the analysis of weather station data, whereas high frequencies of icing are mostly underestimated.

The spatial analysis of icing in Germany showed that freezing rain and in-cloud icing events occur more often in mountainous regions in altitudes between about 500 m and 1500 m above sea level than in lowland regions. The frequency of freezing rain decreases remarkable in high altitude areas, mainly at exposed locations, whereas the frequency of rime icing increases in those regions. Wet snow events are in general more frequent in lowland regions in (North-) West of Germany than in mountainous areas. The highest numbers of wet snow events were observed at stations that are situated in sheltered positions (e.g. valleys) in altitudes greater than 700 m a.s.l.

The frequency of occurrence of icing was examined for its dependence on the height above sea level. The results show that the frequency of icing occurrence increases with altitude in general. Furthermore, the (local) exposure of a location plays an important role in the icing process. Therefore, exposed (sheltered) locations may show much higher (lower) icing frequencies.

Finally, an icing map of Germany has been developed applying the knowledge on the dependence of icing on the height above sea level.

I. Introduction

“Atmospheric icing is a complex phenomenon involving multiple physical processes affected by large variations over time and space, and significantly influenced by topography.” [1] Atmospheric icing is classified according to two different formation processes, precipitation icing (including freezing rain and wet snow) and in-cloud icing (also called rime/glaze, including fog; cf. [2], [3]).

Atmospheric icing can represent a risk to human life and activities. Icing events may have several economic implications. They can affect the safety and the fluidity of the road and air transportation. They may damage power lines, affecting both the economic activities and the human comfort. Furthermore, icing events can damage renewable energy systems (wind turbines or solar panels) or decrease their efficiency. Finally, they may have an impact on the operational reliability of scientific equipment (e.g. for meteorological instruments, cf. [4]).

The goal of the study is to analyze the spatial distribution of atmospheric icing in Germany from the point of view of classical climatology. That means, the frequencies of occurrence of atmospheric icing are analyzed in order to get a general picture of their spatial distribution, without analyzing single events and their results (for instance ice loads). The paper continues the studies that have been carried out for freezing rain [4] and for wet snow [7] by the analysis of in-cloud icing events. It subsumes the results of analysis of frequency of atmospheric icing for the different formation processes, precipitation icing (freezing rain and wet snow) and in-cloud icing (rime and glaze, fog).

II. Data and Methodology

In this paper the spatial distribution of atmospheric icing in Germany is analyzed using weather station data of 74 meteorological stations evenly distributed over the territory of Germany as well as using results from direct measurements of atmospheric icing.

The study was elaborated using the hourly ground SYNOP messages as primary data in order to accomplish an accurate description of the phenomenon of atmospheric icing from homogeneous data sets. In addition, direct measurements of icing were used in order to compare icing frequencies from SYNOP messages (weather station data) to the frequencies of occurrence of icing that were measured directly.

All hourly ground SYNOP messages (ww-codes from WMO-table 4677) which report icing, that means all messages regarding the occurrence of precipitation icing (freezing rain and wet snow) and of in-cloud icing (rime and glaze, fog), were analyzed. The frequencies of occurrence of icing were computed as the ratio of the number of SYNOP messages that reported atmospheric icing to the total number of SYNOP messages.

For a detailed analysis using hourly SYNOP messages it was necessary to select those meteorological stations that fulfill the following criteria (see [4]):

- during the period of 20 years from 1980 to 1999 the stations provided continuously SYNOP messages with information about the state of the weather (ww-codes from table 4677),
- the stations are representative from the point of view of the geographic position and
- the final number of stations and their spatial distribution allow a correct evaluation of the atmospheric icing characteristics for Germany.

Fulfilling these criteria, 74 stations were selected for the evaluation of atmospheric icing. Five of these stations are situated at altitudes higher than 1000 m and 54 of them are situated at altitudes lower than 500 m. The locations of the selected 74 stations in Germany are plotted in Fig. 1.

The data set included hourly values of air temperature, of dew point temperature, of wind direction and wind velocity, of horizontal visibility and of SYNOP messages (ww-codes from table 4677).

Direct measurements of atmospheric icing were carried out at up to 35 stations in the east part of Germany during 1965-1990 [5]. At these stations the accumulated mass of ice accretion was determined and additional information (e.g. icing diameter and direction, ice vane dimension, icing type) were compiled. Since 1991 the number of locations with direct icing measurements in Germany has been reduced to a total of six (see [5], [6]). Ice load sensors are implemented at these six stations. They measure the weight of the ice accumulated on a vertical pole by the use of an electro-mechanical scale system.

In order to compare icing frequencies derived from weather station records with icing frequencies that were measured directly, data for 13 stations in the east part of Germany for the time period 1980-1989 were analysed. The use of this subset of data was necessary due to limited spatial and temporal availability of direct icing measurements as described above.

A. *Freezing Rain*

The following ww-codes from table 4677 codes in hourly ground SYNOP messages were used:

- freezing rain or drizzle during the preceding hour before observation (ww = 24),
- freezing drizzle phenomena (ww = 56, 57),
- freezing rain (ww = 66, 67),
- rain of various intensity with snow during the observation interval (ww = 68, 69),
- ice spheres (ww = 79).

In addition to those SYNOP messages which report freezing rain events directly, the following codes were used, if the wet bulb temperature was lower or equal 0°C (see [8], [9]):

- drizzle of various intensity, with or without breaks during the observation interval (ww = 50 - 55),
- drizzle of various intensity, mixed with rain (ww = 58, 59)
- rain of various intensity, with or without breaks during the observation interval (ww = 60 - 65).

Wet bulb temperature was not available directly from the meteorological data set. It was recalculated from dew point temperature using formulas published in [10], assuming a standard atmospheric pressure of 1013.25 hPa.

B. *Wet Snow*

The following ww-codes from table 4677 codes in hourly ground SYNOP messages were used:

- snow and sleet during the preceding hour before observation (ww = 22, 23),
- snow and sleet showers during the preceding hour before observation (ww = 26)
- snow of various intensity, with or without breaks during the observation interval (ww = 70 - 75),
- snow and sleet showers of various intensity during the observation interval (ww = 83 - 86).

When analyzing meteorological observations of snowfall, a criterion needs to be applied to select the wet snow events from all observations of snowfall.

This was done based on theory [11], [12], [13] so that wet snow is considered to occur when there is snow fall and the wet bulb temperature is greater than 0°C.

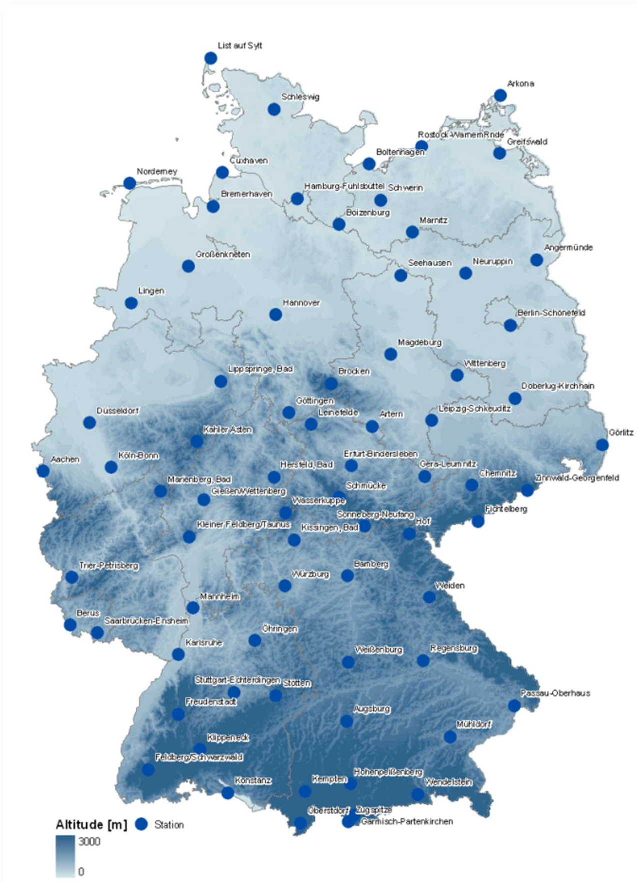

Fig. 1. Locations of weather stations in Germany whose SYNOP messages were analyzed in terms of atmospheric icing

C. *In-Cloud Icing*

The following ww-codes from table 4677 codes in hourly ground SYNOP messages were used:

- observation of soft or hard rime (ww = 48, 49) during the preceding hour before observation.

In addition to those SYNOP messages which report rime icing events directly, the following codes were used, if the air temperature was lower or equal 0°C:

- fog or freezing fog during the preceding hour before observation (ww = 28)
- fog or freezing fog during the observation interval (ww = 40 - 47).

III. Results and Discussion

A. *Freezing Rain*

The spatial distribution of freezing rain events is presented in Fig. 2. Frequencies of occurrence of freezing rain events vary between 3 ‰ in lowlands and 16 ‰ in mountainous regions of Germany (see [4]).

Fig. 2 shows that freezing rain events most often occur in mountainous regions of Germany with altitudes between about 300 m and 1500 m above sea level, having frequencies between 5 ‰ and 16 ‰. In lowland regions, mainly in the northern part of Germany, freezing rain and freezing drizzle events occur more seldom, with frequencies between 3 ‰ and 5 ‰.

In high altitude areas as in the Alps, mainly at exposed locations, the frequency of freezing rain decreases remarkable, as analysed for stations Hohenpeißenberg, Wendelstein and Zugspitze, for instance.

B. *Wet Snow*

The spatial distribution of wet snow events is presented in Fig. 3. Frequencies of occurrence of wet snow events vary between 2 ‰ and 18 ‰.

Fig. 3 shows that wet snow events most often occur in altitudes between about 0 m and 800 m above sea level, having frequencies between 4 ‰ and 18 ‰.

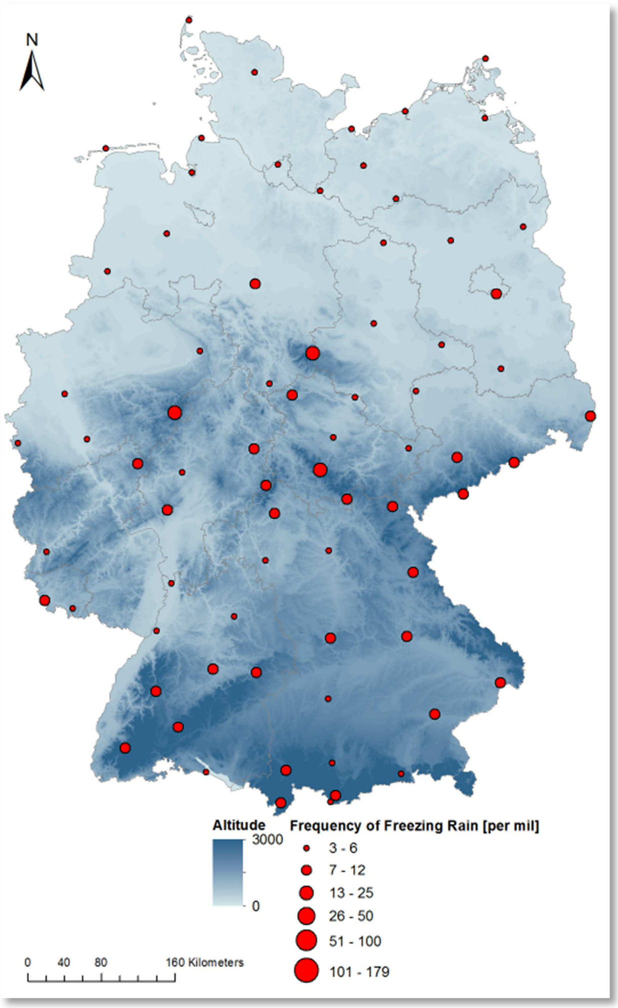

Fig. 2: Spatial distribution of frequency of freezing rain events for 74 stations in Germany during the observation period 1980-1999. Background colour varies with altitude.

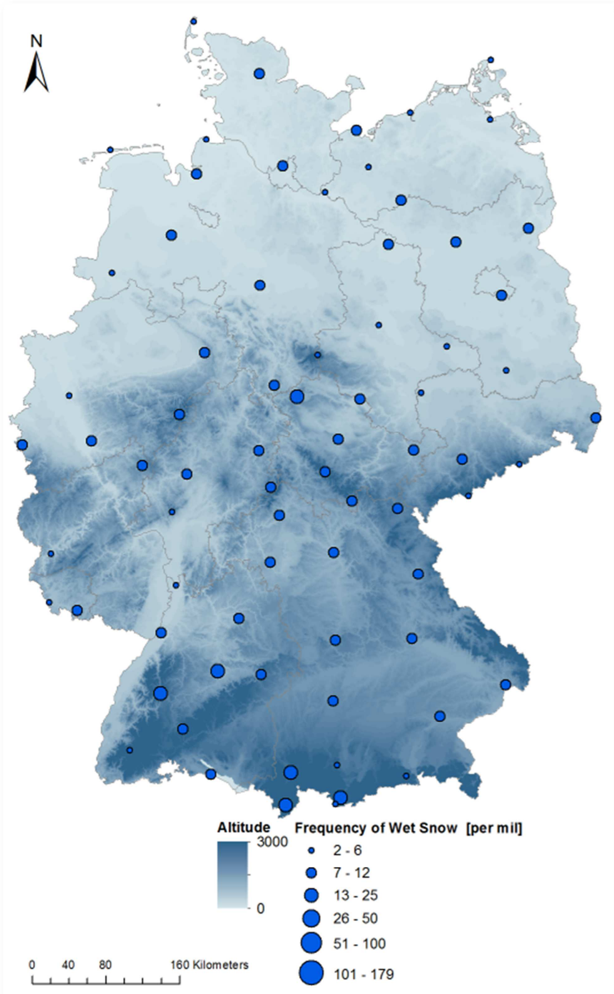

Fig. 3: Spatial distribution of frequency of wet snow events for 74 stations in Germany during the observation period 1980-1999. Background colour varies with altitude.

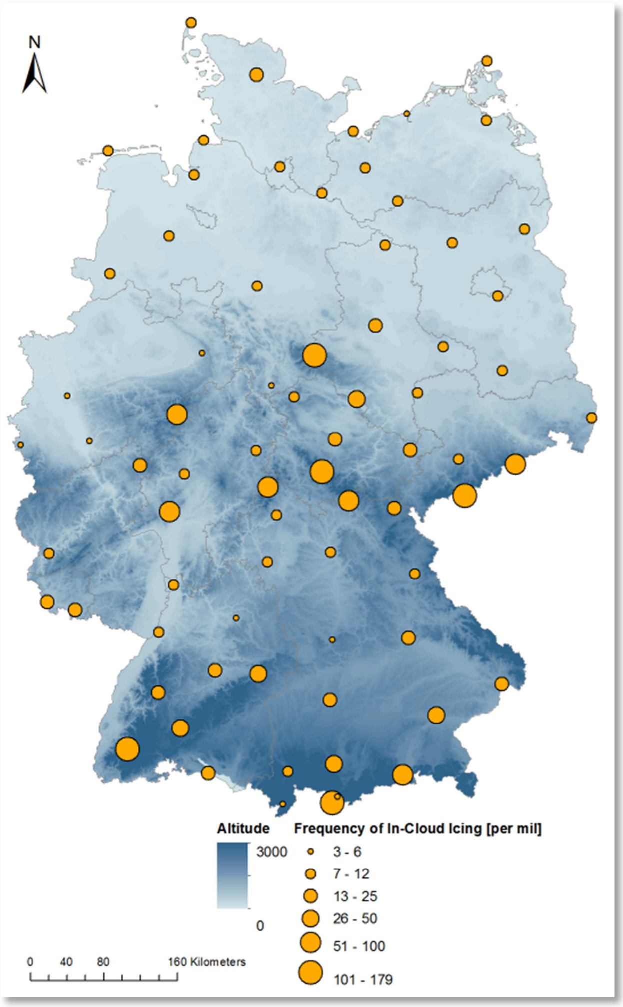

Fig. 4: Spatial distribution of frequency of in-cloud icing events for 74 stations in Germany during the observation period 1980-1999. Background colour varies with altitude.

The highest numbers of wet snow events were observed at stations that are situated in sheltered positions (e.g. valleys) in altitudes greater than 700 m a.s.l., as for instance in Kempten (17 ‰), Garmisch-Partenkirchen (17 ‰), Oberstdorf (18 ‰) or Freudenstadt (16 ‰).

The frequency of wet snow events is small at exposed locations in high altitude areas, as analysed for stations Fichtelberg (3 ‰), Wendelstein (2 ‰) and Zugspitze (3 ‰), for instance.

Please note, that the wet snow ratio (WSR), i.e. the ratio of wet snow observations to all observations reporting snowfall, shows a different picture (cf. [7]): Using WSR, the west part of Germany is more affected (WSR between 0,34 and 0,38) by wet snow events with the highest WSR of 0,44 in the north-west coastal region (Bremerhaven). In general, the wet snow ratio decreases with altitude.

C. *In-Cloud Icing*

The spatial distribution of in-cloud icing events is presented in Fig. 4. Frequencies of occurrence of in-cloud icing events vary between 3 ‰ and 180 ‰. In general, the in-cloud icing frequency increases with altitude.

Fig. 4 shows that in-cloud icing events more often occur in mountainous regions of Germany with altitudes higher than 500 m above sea level, with frequencies greater 25 ‰. In lower altitudes in-cloud icing events occur more seldom, mostly having frequencies between 3 ‰ and 25 ‰.

The highest numbers of in-cloud icing events occur at exposed locations in high altitude areas, as analysed for stations Brocken (179 ‰), Fichtelberg (169 ‰), Feldberg (124 ‰) and Zugspitze (151 ‰), for instance.

D. *Icing Total*

The spatial distribution of cumulative frequency of in-cloud icing, freezing rain and wet snow events (“icing total”) is presented in Fig. 5. Frequencies of occurrence of all icing events vary between 13 ‰ and 199 ‰. In general, the total icing frequency increases with altitude.

Fig. 5 shows that the total frequency of icing conditions is lower than 45 ‰ in altitudes below 600 m a.s.l. (cf. Fig. 7, Fig. 8). It increases to (much) greater values in higher altitudes.

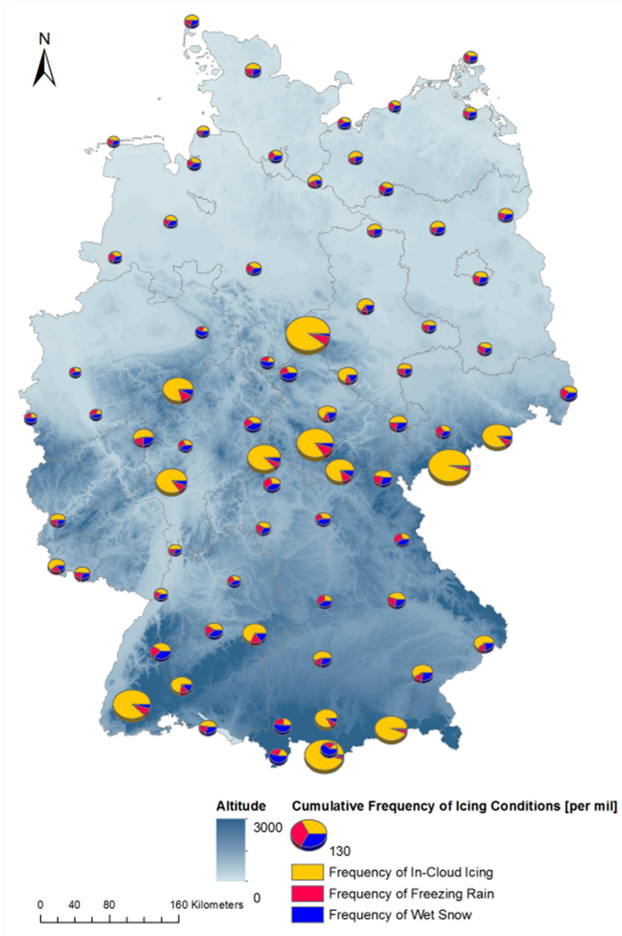

Fig. 5: Spatial distribution of cumulative frequency of in-cloud icing, freezing rain and wet snow events for 74 stations in Germany during the observation period 1980-1999. Background colour varies with altitude.

Maximum values occur at exposed locations in high altitude areas, for instance at stations Brocken (199 ‰), Fichtelberg (179 ‰), Feldberg (141 ‰) and Zugspitze (158 ‰).

Fig. 5 illustrates that these maximum values mainly result from in-cloud icing events. In-cloud icing is the dominant icing process in mountainous regions, whereas freezing rain and wet-snow conditions occur more often in lower altitudes.

E. Comparison to Results from Direct Icing Measurements

In order to compare icing frequencies derived from weather station records (see II.A – II.C) with icing frequencies that were measured directly, data for 13 stations in the east part of Germany for the time period 1980-1989 were analysed (see II).

Fig. 6 shows the results of correlation analysis for cumulative frequencies of icing (“icing total”), derived from weather station records and from direct icing measurements, respectively. The results of the analyses for mean, minimum and maximum cumulative frequencies of icing show a good agreement with linear relationships and statistically significant correlations (at the p = 0.01 level). This means that icing frequency analyses on the basis of weather station records can be used as a proxy for direct icing measurements in order to estimate cumulative frequencies of icing events.

Fig. 6 indicates that small cumulative frequencies of icing are generally overestimated by the analysis of weather station data, whereas high cumulative frequencies of icing are mostly underestimated.

The result for small cumulative frequencies of icing may be explained by the fact that they typically occur in the lowlands and in the lower mountainous areas. Ice accretions result most often from short icing events at such locations. These short icing events are not covered by the observation interval of direct icing measurements (24 hours, see [5]), but they are captured by the SYNOP observation intervals at weather stations.

The result for large cumulative frequencies of icing may be explained by the fact that they typically occur in higher mountainous areas (e.g. at mountain ridge lines) and at exposed locations.

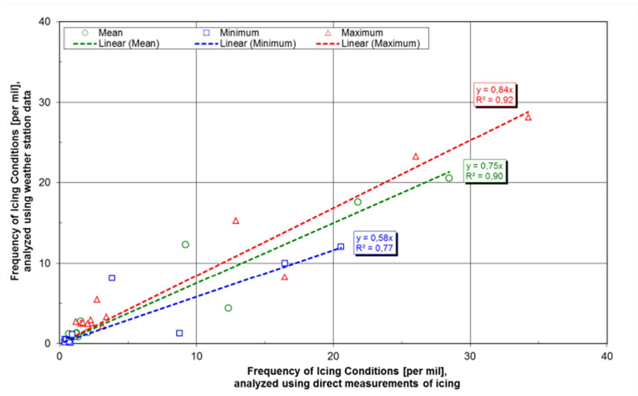

Fig. 6: Analysis of correlation for cumulative frequencies of icing (“icing total”), derived from weather station records and from direct icing measurements, respectively. Data for 13 stations in the east part of Germany for the time period 1980-1989 were analysed (see II).

Long-term icing events may be missed by SYNOP observations at these locations (observers do not realize cumulative icing events with small icing intensities, for instance), whereas extended icing events are covered well by the observation interval of direct icing measurements.

F. Icing Map of Germany

Fig. 7 shows the changes in cumulative frequencies of icing with altitude for all 74 stations (cf. Fig. 1).

The correlation analyses show acceptable results for linear as well as for exponential regression lines. The correlations are statistically significant (at the p = 0.01 level). Nevertheless, Fig. 7 leads to the hypotheses that results for exposed as well as for sheltered locations in high altitude areas (labelled in Fig. 7) deteriorate the correlations. Therefore, another correlation analyses has been carried out.

Fig. 8 shows the changes in cumulative frequencies of icing with altitude for 67 stations only, i.e. the results for exposed as well as for sheltered locations in high altitude areas (labelled in Fig. 7) were omitted for this analysis.

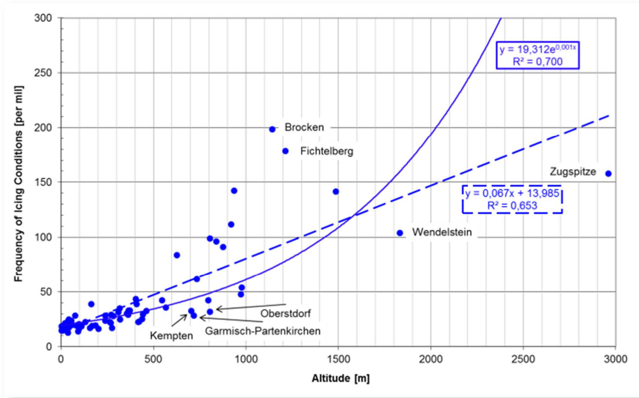

Fig. 7: Changes in cumulative frequencies of in-cloud icing, freezing rain and wet snow events (“icing total”) with the height above sea level for 74 stations in Germany during the observation period 1980-1999. Exposed as well as sheltered locations in high altitude areas are labelled.

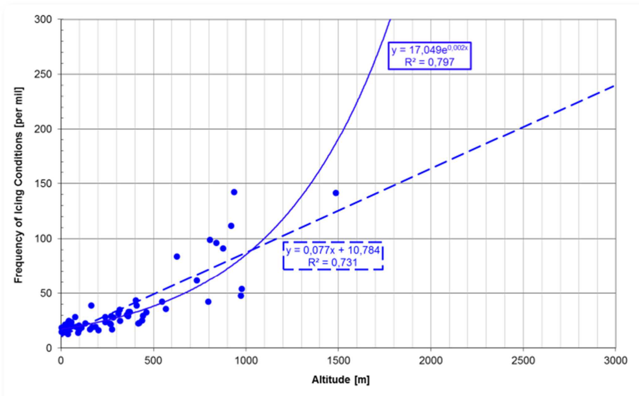

Fig. 8: Changes in cumulative frequencies of in-cloud icing, freezing rain and wet snow events (“icing total”) with the height above sea level for 67 stations in Germany during the observation period 1980-1999. Results for exposed as well as for sheltered locations in high altitude areas were omitted (cf. Fig. 7).

The correlation analyses show better results for linear as well as for exponential regression lines. The correlations are statistically significant (at the p = 0.01 level), too. On the other hand, one has to keep in mind that the results from Fig. 8 do not well represent exposed as well as sheltered locations in high altitude areas.

The icing map of Germany is presented in Fig. 9. It shows the (continuous) spatial distribution of cumulative frequency of in-cloud icing, freezing rain and wet snow events. It was generated on the basis of the linear regression line of Fig. 8.

Fig. 9 subsumes the findings of III.A – III.D. It shows that the total frequency of icing conditions is small in altitudes below 600 m a.s.l.. It increases (linearly) to (much) greater values in higher altitudes.

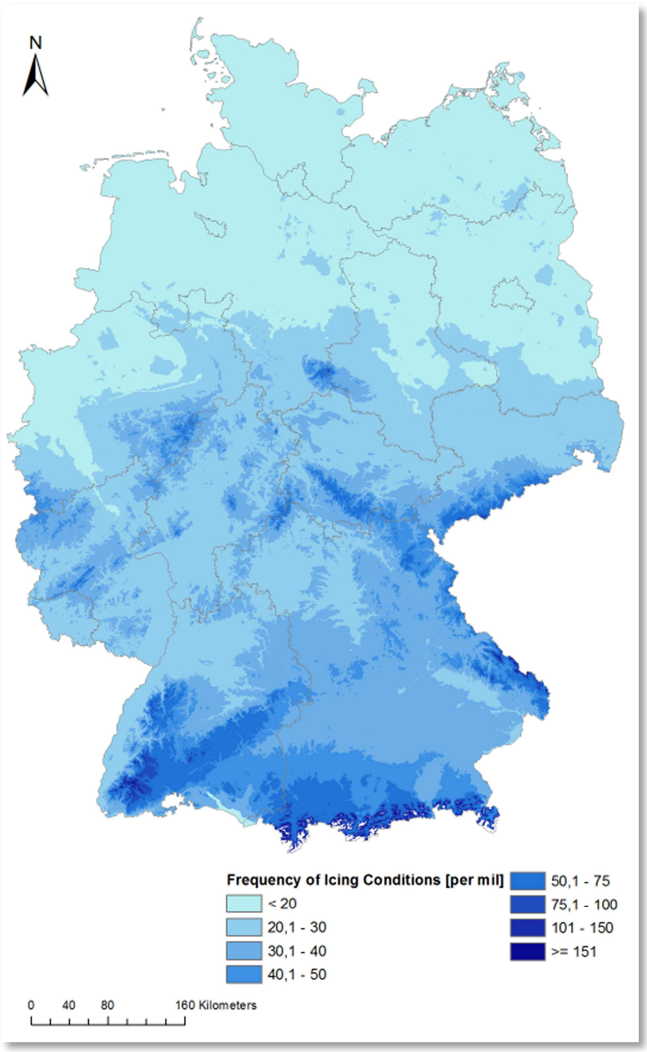

Fig. 9: Icing map of Germany. Spatial distribution of cumulative frequency of in-cloud icing, freezing rain and wet snow events, generated on the basis of the linear regression line of Fig. 8.

Fig. 9 gives a general picture of the frequency of occurrence of icing conditions all over Germany. Due to the fact that it was generated by the use of a linear relationship to altitude it should be used for general information only. It will certainly underestimate (overestimate) the cumulative frequency of icing for exposed (sheltered) locations in high altitude areas. Special investigations are still necessary for those locations.

IV. References

[1] A. Heimo et al., “Measuring and forecasting atmospheric icing on structures”, Final report of COST 727 – Action, 2011, in preparation

[2] ISO 12494, “Atmospheric icing of structures”, ISO/TC 98/SC 3, 2000-07-20.

[3] S. Fikke et al., “COST Action 727: Atmospheric Icing on Struc-tures; Measurements and data collection on Icing : State of the Art”, Publication of MeteoSwiss, 75, Zürich, pp. 110.

[4] A. Manea, I. Ralita, A. Dumitrescu, A. Sommerfeld and B. Wichura, “Analysis of spatial and tem-poral distribution of freezing rain events in Romania and Germany”, 13th International Workshop on Atmos-pheric Icing of Structures (IWAIS 2009), 2009, Andermatt, pp. 8.

[5] B. Wichura, “A Survey of Icing Measurements in Germany”, 12th International Workshop on Atmospheric Icing of Structures (IWAIS 2007), Yokohama, Japan, October 2007, 6 pp.

[6] B. Wichura, “Zinnwald test site for intercomparison of icing measurements”, 13th International Workshop on Atmospheric Icing of Structures (IWAIS 2009). Meteotest, Andermatt, 3 pp.

[7] D. Nikolov and B. Wichura, “Analysis of spatial and temporal distribution of wet snow events in Germany”, 13th International Workshop on Atmospheric Icing of Structures (IWAIS 2009), Andermatt, 2009, 6 pp.

[8] L. Makkonen and K. Athi, “Climatic mapping of ice loads based on airport weather observations”, Atmospheric Research 36, pp. 185-193, 1995.

[9] E. Sundin and L. Makkonen, “Ice Loads on a Lattice Tower Estimate by Weather Station Data”, Journal of Applied Meteorology 37(5), pp. 523-529, 1997.

[10] D. Sonntag, “Important new Values of the Physical Constants of 1986, Vapour Pressure Formulations based on the ITS-90, and Psychrometer Formulae”, Zeitschrift für Meteorologie 40, pp. 340-344, 1990.

[11] L. Makkonen, “The heat balance of wet snow”, Meteorological Magazine 110, pp. 82, 1981.

[12] L. Makkonen, “Estimation of wet snow accretion on structures”, Cold Regions Science and Technology, 17, pp. 93-88, 1989.

[13] L. Makkonen and B. Wichura, “Simulating wet snow loads on power line cables by a simple model”, Cold Regions Science and Technology, 61, pp. 73-81, 2010.

IWAIS 2013 - 15th INTERNATIONAL WORKSHOP
ON ATMOSPHERIC ICING OF STRUCTURES
St. John's, Newfoundland and Labrador
September 8-11, 2013

Deutscher Wetterdienst
Wetter und Klima aus einer Hand

The Spatial Distribution of Icing in Germany

Estimated by the Analysis of Weather Station Data and of Direct Measurements of Icing

Bodo Wichura

The spatial distribution of atmospheric icing in Germany was analyzed using weather station data of 74 meteorological stations evenly distributed over the territory of Germany for the period 1980-1999 as well as using direct measurements of icing at up to 35 stations in the east part of Germany for the period 1980-1989. The spatial analysis of icing showed that freezing rain and in-cloud icing events occur more often in mountainous regions in altitudes between about 500 m and 1500 m above sea level than in lowland regions. The frequency of freezing rain decreases remarkable in high altitude areas, mainly at exposed locations, whereas the frequency of rime icing increases in those regions. Wet snow events are in general more frequent in lowland regions in the North of Germany than in mountainous areas. The highest numbers of wet snow events were observed at stations that are situated in sheltered positions (e.g. valleys) in altitudes greater than 700 m a.s.l.. Results of icing frequencies from weather station data were compared to the frequencies of occurrence of icing that were measured directly. The comparison shows, that low frequencies of icing are generally overestimated by the analysis of weather station data, whereas high frequencies of icing are mostly underestimated. The frequency of occurrence of icing was examined for its dependence on the height above sea level. The results show that the frequency of icing occurrence increases with altitude. Furthermore, the (local) exposure of a location plays an important role in the icing process. Therefore, exposed (sheltered) locations may show much higher (lower) icing frequencies. Finally, an icing map of Germany has been developed applying the knowledge on the dependence of icing on the height above sea level.

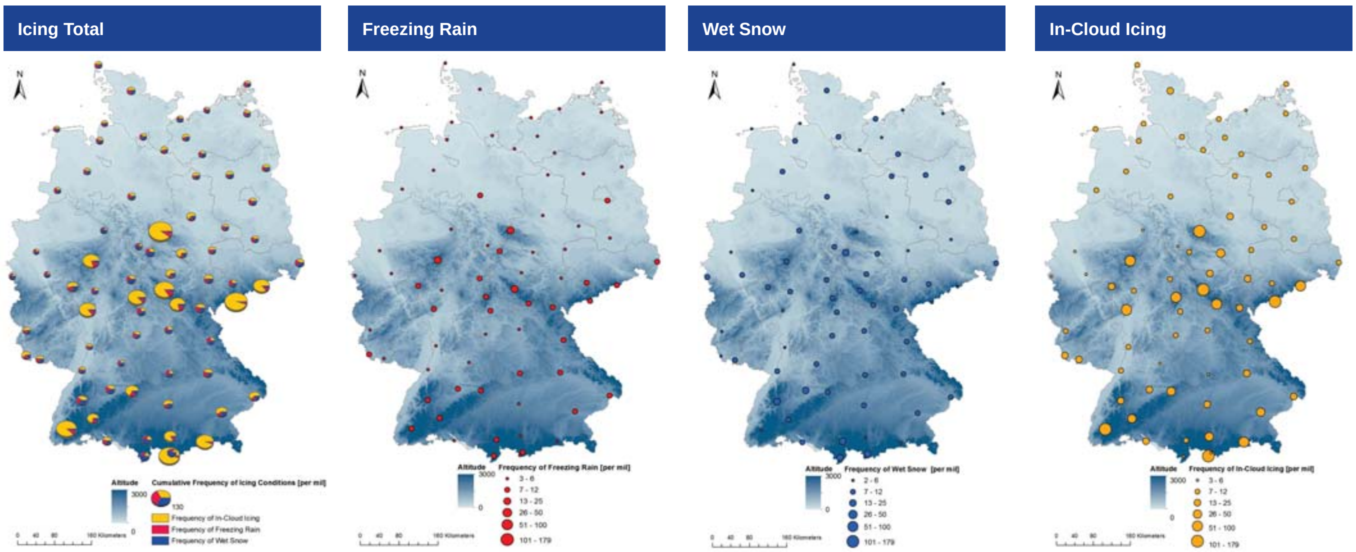

Fig. 1 – 4: Spatial distribution of (cumulative, "Icing Total") frequency of Freezing Rain, Wet Snow and In-Cloud Icing events for 74 stations in Germany during the observation period 1980-1999. Background colour varies with altitude.

Data and Methodology

- Use of hourly ground SYNOP messages (ww-codes of WMO-table 4677) of 74 stations for the time period 1980 – 1999.
- The stations are representative from the point of view of the geographic position in order to allow a correct evaluation of the atmospheric icing characteristics for Germany.
- All messages regarding the occurrence of precipitation icing (freezing rain and wet snow) and of in-cloud icing (rime, fog) were analyzed (see extended abstract or detailed information).
- Frequencies of occurrence of icing were computed as the ratio of the number of SYNOP messages that reported atmospheric icing to the total number of SYNOP messages.
- Use of data from direct measurements of atmospheric icing for 13 stations in the East of Germany for the time period 1980 - 1989 for comparison purposes. (The use of the subset of data was necessary due to limited spatial and temporal availability of direct icing measurements.)

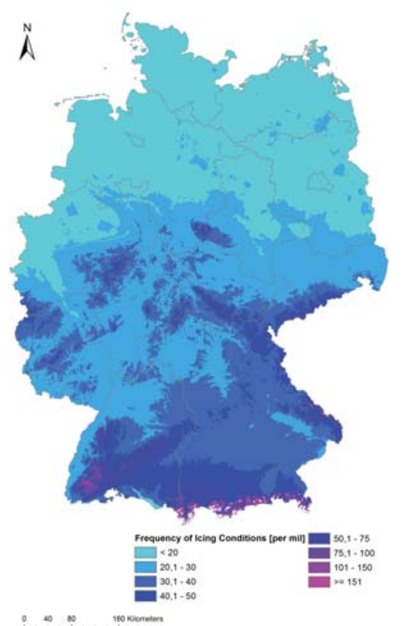

Fig. 7: Icing map of Germany. Spatial distribution of cumulative frequency of in-cloud icing, freezing rain and wet snow events, generated on the basis of the linear regression line of Fig. 6.

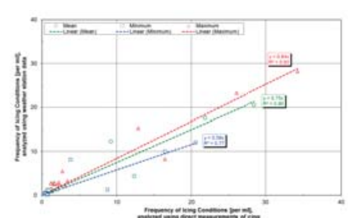

Fig. 5: Analysis of correlation for cumulative frequencies of icing derived from weather station records and from direct icing measurements, respectively.

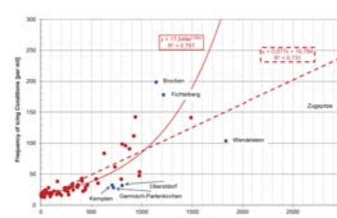

Fig. 6: Changes in cumulative frequencies of in-cloud icing, freezing rain and wet snow events with the height above sea level for 74 stations in Germany during the observation period 1980-1999. Exposed as well as sheltered locations in high altitude areas are labelled (blue). Results for exposed as well as for sheltered locations in high altitude areas were omitted for regression analysis (red lines).

German Meteorological Service, Regional Climate Office Potsdam
Michendorfer Chaussee 23, 14473 Potsdam, Germany
bodo.wichura@dwd.de

P-3

Wet-snow accretion on Overhead Lines

The RSE response to harmful winter blackouts in Italy

IWAIS 2013

M. Lacavalla*, P. Marcacci – *Sustainable Development and Energy Sources Dept. -*

RSE S.p.A. – Milan - Italy

***email: lacavalla@rse-web.it; website: www.rse-web.it**

What We Learned

- **The wet-snow are the principal cause of <u>major winter electrical blackouts</u> in Italy and the phenomenon is increasing related to the "*Global Climate Change*"**
- **NWP models properly validated by experimental data may contribute to develop forecast and alert system for TSO and DSO and to define the return periods of the wet-snow load useful for the design of future overhead lines**

Background

- The cost of damages due to wet-snowstorm is greater than 200 ML€, as reported by Italian DSO
- Some defence strategies e.g. anti-icing and de-icing techniques can be adopt to reduce the risk of ice on overhead lines.
- Dispatching solutions based on icing forecast system may become a new challenge

Purpose & Aims

This study describes the RSE response to harmful winter blackouts by establishing a weather forecast system for the wet-snow and through the design of an innovative ice station

Aims

- ❑ Deepen the knowledge of the icing atmospheric phenomenon
- ❑ Verify the NWP and accretion models by innovative measures
- ❑ Map the frequency of occurrence of wet-snow on the Italian territory

WOLF system

WOLF (**W**et-snow **O**verload a**L**ert and **F**orecasting) is developed to supply an on-line alert system for the electric grid management and provide an off-line work instrument for meteorologists, grid planning engineers and "Regulation Authorities". The system provides:

- Weather forecast of the principal meteorological variables
- Ice load and ice thickness estimation
- Load resulting from the combined action of wind and ice on conductors
- Anti-icing current

Models

- Driver model: **ECMWF** (1/8°) run:12UTC
- Non-hydrostatic LAM: **RAMS** (~1/12°)
- Accretion model: **Makkonen wet-snow model** [ISO 12494]
- **Cigrè' thermal model** (steady state)

Results

A) WOLF evaluation on the major blackouts

Map of failures winter: 2010-2011 source: Italian TSO

Helicoidally ice formation

Table of weather forecast for the major overhead power lines failures

Overhead Line Name	Ice Load (kg/m)	Air Temperature (°C)	wind speed (m/s)	Altitude (m. aslm)
San Fiorano - Robbia	**6.3**	**0 /+0.5**	**<1**	**1500**
Sasso Corvaro- S. Angelo in V.	2.9	-1.5 / +2	9	400
Montorio - Villanova	0.7	-1.8 / +2	8	450
Scafa Guardiagrele	1.2	-2.5 / +2	6	470
S. Massimo - S. Polo	0.5	-2.0 / +1.8	4	500
Teramo - Isola Gran Sasso	1.5	-1.5 / +1.5	6	380
Varazze - Cogoleto	0.3	+1 /+2	7	300
S. Angelo in V. - Città di Castello	0.3	-1/ +1	4	950
Orichella - Rogliano - Savuto	0.6	-2 / +2	6	1400
Valina - Chievolis	5.4	0 /+2	3	1100
Venamartello - Fonte del Campo	1.9	-2.5 /+1.8	5	1000
Sasso Corvaro- S. Angelo in V.	2.2	-1.5 / +1.8	7	500
Altedo - Ferrara sud	0.3	+1 /+2	10	20
S. Michele - Farneta	0.6	-0.2 / +2	2	360
S. Angelo in V. - Città di Castello	0.2	-0.5 / +2	4	700
Morigallo - Busalla	1.1	0 /+2	1.5	450
Gandellino – Ludrigno - Dossi	5.5	-0.5 /+0.5	<1	1500
Taio - Temù	2.7	-1 / -0.5	3	1600

B) WOLF evaluation at the ice station site

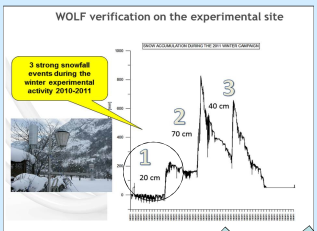

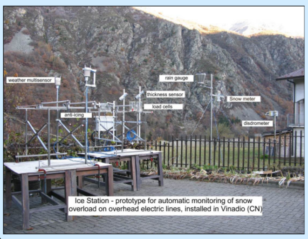

Ice Station - prototype for automatic monitoring of snow overload on overhead electric lines, installed in Vinadio (CN)

Weather forecast

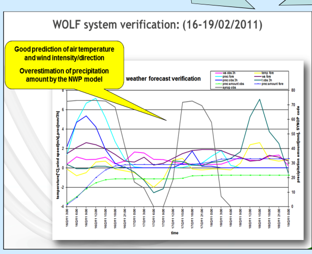

Ice load forecast

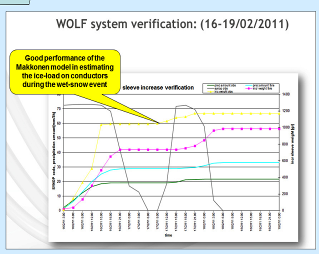

Discussion

- ✓ Proper identification of the areas where there have been electrical failures
- ✓ Good prediction of the ice load by the accretion model on the test site
- ✓ Overestimation of total SWE by the NWP model at the ice station
- ✓ Unpredictable "ice shedding" on sample conductors
- ✓ Good representation of "*Joule effect*" on anti-icing sample conductor

Next Steps

- ❖ Installation of an automatic fixed station **WILD** (**W**et-snow **I**ce **L**aboratory **D**etection) in the West Alps next winter season 2013-2014
- ❖ Maps of frequency of wet-snow occurrence over period of at least 10 years
- ❖ Calculation of the return periods of wet-snow critical loads on the whole Italian territory

Improvements

- Tuning of the accretion coefficients in the Makkonen model
- Reduction system of Ice shedding by slow rotating conductor
- Representation of the phenomenon of ice accretion on conductor to an appropriate scale

Acknowledgments

This work has been financed by the Research Fund for the Italian Electrical System under the Contract Agreement between RSE and the Ministry of Economic Development – General Directorate for Nuclear Energy, Renewable Energy and Energy Efficiency stipulated on July 29, 2009 in compliance with the Decree of March 19, 2009

The authors give thanks to their colleague Giovanni Pirovano for providing them suggestions and some data.

The authors would like to thank the Mayor of Vinadio, Angelo Giverso for his invaluable assistance

A novel approach to fabricate anti-corrosive coatings with hydrophobic properties on an aluminium alloy surface

S. Farhadi[1], M. Farzaneh[1], and S. Simard[2]
[1]NSERC / Hydro-Quebec / UQAC Industrial Chair on Atmospheric Icing of Power Network Equipment (CIGELE) and Canada Research Chair on Atmospheric Icing Engineering of Power Networks (INGIVRE) www.cigele.ca, Université du Québec à Chicoutimi, Chicoutimi, QC, Canada
[2] Aluminium Technology Centre, Industrial Materials Institute, National Research Council Canada (CNRC) (www.cta-atc.cnrc-nrc.gc.ca) 501, boul. de l'Université Est, Chicoutimi, QC, Canada, G7H 8C3
Email: shahram.farhadi@uqac.ca

Abstract- In cold climate regions, many structures such as transmission lines, telecommunication networks, bridges, etc. are exposed to ice and snow accretions. These accumulations are at the source of several types of damage and malfunctions. A way to reduce or prevent ice accumulation on exposed surfaces is to develop and apply icephobic coatings. At the same time, corrosion protection of metallic substrates such as Al and its alloys is another critical issue when these surfaces are exposed to moisture, water or other types of aggressive molecules. The main purpose of this paper is to systematically study certain organic coatings terminated with surface alkyl groups, which are expected to reduce the adhesion of ice to Al surfaces. More specifically, thin films of 1,2-bis-trioxymethyl-silyl-ethane [$C_{14}H_{34}O_6Si_2$] and octadecyltrimethoxysilane $C_{18}H_{37}Si(OCH_3)_3$ were prepared using wet-chemistry techniques on polished aluminium alloy (AA2024-T3). The first layer was used as an under-layer expecting to improve the anti-corrosive performance for the top-layer providing surface water and ice repellency. The stability of the prepared coatings was evaluated following exposition to water, basic and acidic media, showing gradual loss of hydrophobic properties over time and in different media. The ice accumulated on sample surfaces was prepared in a wind tunnel at subzero temperature by spraying supercooled water droplets simulating the deposit of reproducible glaze-type ice. While uncoated mirror-polished and as-received Al samples showed average ice detachment shear stress values of ~270±20 kPa and ~370±30 kPa, respectively, the coated samples showed reduced values of ~182±15 kPa. This reduction is attributed to the presence of a low surface-energy top layer. The ice-releasing performance of the sample gradually decreased after repeated icing/de-icing cycles. SEM observations revealed traces of corrosion products after wetting durability and icing/de-icing tests suggesting an interaction of water with the coatings during tests, gradually altering them. Potentiodynamic polarizations and salt spray exposure studies revealed that the corrosion resistance of modified aluminium alloys improved remarkably compared to unmodified samples. While extensive corrosion appeared on unmodified Al samples after only 8 cycles of salt spray exposure, only tiny traces of corrosion wer observed on the modified samples even after 81 cycles of exposure.

Keywords: Anti-corrosive performance; Low surface energy coating; Self-assembling process; Hydrophobicity; Ice adhesion strength; Durability; Potentiodynamic polarization; Salt-spray test.

I. INTRODUCTION

It is well known that ice and wet-snow accumulation and their extreme adhesion on outdoor structures and equipment can sometimes cause serious socioeconomical problems in cold climate regions [1]. Atmospheric icing occurs when the surfaces of exposed structures come into contact with supercooled water droplets or snow particles. Indeed, ice accumulation is the source of several types of damage and malfunctions hindering the operation and impairing the efficiency of affected infrastructural components, mechanisms and machines. In the specific case of power transmission and distribution lines, ice or wet snow may cause serious damage due to their high adherence to both metallic and insulator surfaces [1]. Each year, numerous failures due to ice accumulation are reported in Canada, the USA, Russia, Iceland, Japan, Norway, China, and so forth. Prevention of icing requires reducing its adhesive strength. Therefore, a variety of de-icing and anti-icing techniques were introduced and developed over the last decades [2]. Meanwhile, most of the effort in recent years has been devoted to acquiring a deeper understanding of the physicochemical phenomena which governs the icing processes in order to develop more efficient systems to prevent icing. While most of the techniques currently in use are active de-icing methods including thermal, electrical, chemical or mechanical techniques, all of them are employed where accumulations are substantial and thus consume a great deal of energy. In the meantime, the current-in-use techniques generally necessitate complex infrastructures and maintenance [2]. Passive approaches to the problem are gaining in popularity; amongst them is the development of anti-icing or icephobic coatings that inhibit ice accumulation [2, 3, 4]. Even though there is, as yet, no material which is completely capable of preventing ice/snow build-up on its surface [2], certain coatings bring about reduced adhesion. Thus far, such coatings have not been proposed as "*ready to use*", although a number of candidate coatings have been tested by several groups. The ideal solution to these problems would be the application of a solid, durable, easy to apply, and inexpensive material which reduces adhesion to such an extent that ice falls off under the pull of gravity [2, 3]. Alkyl-terminated coatings, e.g. alkylsilane and fluoroalkylsilane-based layers were previously proposed as potentially ice-releasing coatings [4, 5, 6 capable of reducing in ice adhesion by a factor of ~2 [4] compared to bare Al as reported. However, such coatings were not studied extensively, and no systematic work has been carried out on them. Indeed, in the methods used to evaluate ice-solid adhesion [4, 7, 8], in most of the cases water was artificially frozen on top of samples tested under unrealistic icing conditions. Therefore, testing adhesion of glaze ice prepared by spraying supercooled water droplets is expected to give more reliable results [3, 9, 10]. Reasonable correlation between hydrophobicity of a coated surface and their ice-repellecy has been reported earlier [3, 6, 10, 11]. In the meantime, metal corrosion should also be taken into account since metal or metallic alloys are subject to corrosion problems when placed in humid or aggressive environments. Hence, development of any ice-releasing coatings on Al structures is closely related to anti-corrosive protection of that specific metal. Providing and evaluating the anticorrosive performance of new coatings, more specifically environmentally friendly ones would be interesting for industrial applications and future demand.

In this study, organic coatings terminated with alkyl groups were prepared as potential ice and wet snow-repellent layers on the surface of aluminum alloy 2024 (AA2024) via one-layer and multilayer approaches. These surfaces were characterized and tested with appropriate procedures and their coating stability (in water, basic and acidic media) and ice-repellent performance over time was carefully studied. More precisely, thin films of octadecyltrimethoxysilane [$CH_3(CH_2)_{17}Si(OCH_3)_3$, TMSOD] as top-layer, providing surface water repellency, on 1,2-bis-trioxymethyl-silyl-ethane [$C_{14}H_{34}O_6Si_2$, BTSE], used as under-layer presumably providing a high density of -OH groups on the surface for the top-layer of TMSOD, were applied on polished AA2024 substrates. To study anti-corrosive performance of the prepared coatings, potentiodynamic polarization tests as well as salt spray exposure was carried out.

II. Experimental procedure

A. Sample Preparation

As-received AA2024-T3 (Al 90.7-94.7wt.%, Si 0.5wt.%, Fe 0.5wt.%, Cu 3.8–4.9wt.%, Mn 0.3-0.9wt.%, Zn 0.25wt.%, Mg 1.2–1.8wt.%, other impurity 0.15wt.% [12]) panels from industrial rolled sheets were cut into smaller 2×2 cm and 5.1 × 3.2 cm and 2-mm-thick plates used as substrates. This alloy is used extensively in many sectors of economy and industries. Prior to coating, they were mechanically polished to obtain mirror-polished surfaces. The polished Al substrates were then cleaned and degreased ultrasonically in deionized water as well as in organic solvents of methanol and acetone, each for 3 min, followed by cleaning in a Turco Redoline 53D alkaline solution (2-3 min), to produce a fresh and reproducible Al_xO_y layer. The cleaned Al plates were blow-dried in a N_2 gas flow and were kept in oven at 70 °C atmospheric temperature for 3 h. The pre-treated samples then placed in baths with different chemicals at room temperature. The deposition bath for the top layer used in this study was TMSOD 1% (V/V%) in isopropanol (ACS grade with water content of ≤0.2%)-deionized water as solvent. Different concentrations of TMSOD silane solution were tested, but no significant difference was found within a few mM range. Prior to use, the bath were vigorously stirred for 3 h to allow for dissolution and hydrolysis. A BTSE solution (4.7 ml in isopropanol-water) for silane deposition was prepared to deposit under layer. These conditions could offer the best compromise between silane hydrolysis and condensation [13]. Flat AA2024 samples were dipped into the BTSE solution for 1 min followed by blow-drying in N_2 and then immersed into the TMSOD-isopropanol bath solution for 15 min. Upon coating and prior to testing, the modified samples were removed from their corresponding solutions, rinsed with copious amounts of isopropanol and blown-dried with N_2. Afterwards, they annealed in ambient atmosphere at 80 °C for about 5 h to remove any volatile components or residual solvents and characterizations were done immediately following sample preparation. While the smaller samples were used to test the stability of the coatings in various media, the larger ones were further used to evaluate their ice-repellent and anti-corrosive performance.

B. Sample Analyses

Sample durability and stability over time in water, basic and acidic media was characterized by means of CA measurements on samples immersed in nano-pure water, tap water, basic (pH: 10.1) and acid (pH:4) buffer solutions over a range of time. The CA values reported in this work were obtained following the standard sessile drop method via a fully-automated DSA100 CA goniometer from Krüss with controllable volume of water droplets of 4 µl. For each sample, at least five different spots were randomly selected and measured and the reported CA values for each sample is an average value of about 12 measurements. Surface topographies were studied via scanning electron microscopy (SEM, Hitachi FEGSEM-SU 70) in high-vacuum mode. The ice adhesion test was conducted by creating glaze-type-ice of up to ~1 cm thick and ~4-5 gr weight over the ~3.2×3.0 cm^2 surface area prepared by spraying super-cooled micro-droplets of water (~65 µm) in a wind tunnel at subzero temperature (-10^{o}C) and wind speed of 11 m/s to simulate natural atmospheric icing conditions. Prior to icing, all samples were kept in a cold room for about 5-7 min to cool down. Iced samples were then spun in the centrifuge at constantly increasing speed. At the moment of detachment, the adhesion strength of ice is assumed to be equal to the centrifugal force, $F = mr\omega^2$, where m is the ice mass, r is the beam radius and ω is the rotational speed in rad/s. The shear stress, correspondingly, was calculated as $\tau = F/A$, where A is the de-iced area. Further experimental details regarding to this technique and its procedure can be found elsewhere [3, 9]. Potentiodynamic polarization was used to evaluate the overall corrosion behaviour of the bare and coated Al samples. The working cell was a standard three-electrode cell with a working electrode area of 1 cm^2. A platinized platinum net and saturated calomel electrode (SCE) was used as counter and reference electrode, respectively. Measurements were done at constant room temperature of ~20 ^{o}C. The setup used to control the experiments was a potentiostat/galvanostat system composed of a Solartron analytical 1252A frequency response analyzer (FRA) coupled to a Solartron SI 1287A electrochemical interface and were controlled by the software Corrware®. Measurements were performed in 3.5 wt.% NaCl solutions at room temperature. Potentiodynamic polarization curves were established and the corrosion potential (E_{corr}) and corrosion current density (i_{corr}) were determined using the Tafel extrapolation method. The polarization scan was started from 250 mV below the open circuit potential (OCP) in the cathodic region, through the corrosion potential, and 250 mV above the open circuit potential in the anodic region with a constant scan rate of 1 mV/s. The Al panels (two panels for each) were placed into the salt-spray chamber (Ascott) with the unmodified surface protected by a scotch tape and the modified surfaces exposed alternatively to salt mist, dry and wet conditions in accordance with ISO14993-Corrosion of metals and alloys [14]. Test specimens were placed in an enclosed chamber and exposed to a changing climate. Stereomicroscope images were obtained from a Leica Model MZ16 microscope equipped with a camera (Leica Microsystems, Banuockburn, IL, USA) and XYZ motorized stage (Clemex Technologies Inc., Longueil, Canada).

III. RESULTS AND DISCUSSION

A. Coating stability

It is well-known that metallic Al is extremely reactive with atmospheric oxygen and that a thin layer of aluminium oxide (~4 nm thickness) forms on exposed Al surface. Therefore, bare Al is a hydrophilic substance with water CA and surface energy of ~41.5±3^o and 58.56±1.64 (mN/m), respectively. The freshly formed Al_xO_y layer on Al surface, created after exposure to air, was then reacted with BTSE molecules to form a covalently bound coating on Al surface. The value of CA at this step, measured after BTSE deposition, was ~62^o. However, after TMSOD coating deposition, all samples (TMSOD alone and BTSE/TMSOD coatings) demonstrated initial values of CA ≥109^o (Figures 1 and 2a) which indicates well-coated flat hydrophobic Al surfaces. Figure 1 shows CA values as a function of immersion time in nano-pure and tap water as well as base and acid solutions for coated Al alloy with BTSE/ODTMS layers. While this sample demonstrated hydrophobic property (CA≥109^o), it can be observed that the CA values decrease over time. In other words, the coated surfaces are found to gradually lose their hydrophobic properties after immersion in different media and fully so after ~1100 h, which is associated with a considerable decrease of their water CA values (Fig.2b). This tendency to lose surface hydrophobic properties is probably due to the rupture of the Si-O-Si bond between the TMSOD molecules and the BTSE layer caused by hydrolysis of these bonds.

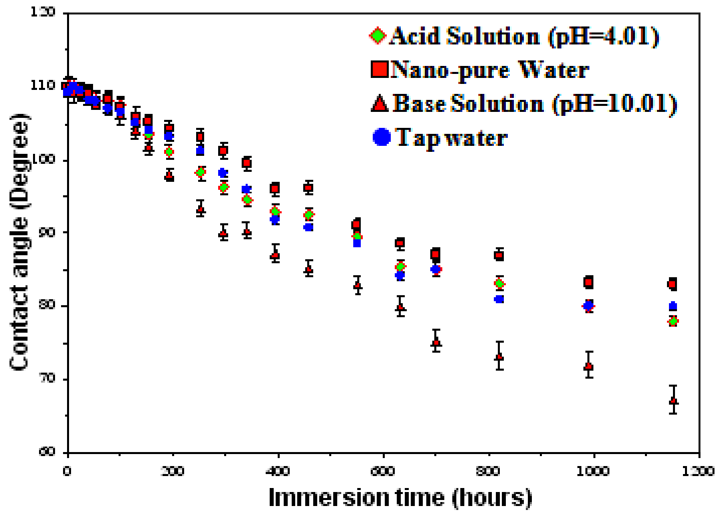

Fig. 1. Contact angle *vs.* immersion time of coated Al sample with BTSE/ODTMS in different environment.

Figure 2 shows water droplets images on coated Al surfaces before (a) and after ~850-h immersion in nano-pre water (b). By immersing Al surfaces to wet or more aggressive environment, indeed, the ~2-nm TMSOD layer undergoes some degree of degradation initially compared to the BTSE layer which are thicker, i.e., being ~100 nm [15]. As a result, alkylsilane molecules were removed from the surface, resulting in decrease of surface hydrophobicity.

Fig. 2. Water droplet images on coated Al surface with BTSE/TMSOD before (a) and after ~850-h immersion in pure water (b).

Surface morphology (SEM images) of Al alloy coated with TMSOD before (a) and after 700-h immersion in water for (b) TMSOD and (c) BTSE/TMSOD is presented in Fig.3.Signs of corrosion and corrosion products around second-phase inter-metallic particles which are nobler, compared to the surrounding AA matrix, can be clearly observed intensively in the sample coated with TMSOD alone. This explains well the results of the CA measurements presented in Fig.1. The TMSOD layer was not be dense enough to prevent water molecules from penetrating through the coating and reaching to the coating-substrate interface. This caused both the corrosion process, whose products are seen in Fig.3b, and the hydrolysis of the Si-O-Si bond, through which the TMSOD molecules were attached to the surface. As a result, some alkylsilane molecules were removed from the surface resulting in decreasing surface hydrophobicity. The corrosion products are also believed to have contributed to the CA decrease observed in Fig.1. However, in the case of Al surfaces coated with BTSE/TMSOD, corrosion and corrosion products around second-phase inter-metallic particles are significantly less compared to the TMSOD coating. In fact, the BTSE under-layer provided a denser coating on the Al surface preventing penetration of water molecules through the coating and reaching to the underneath metallic substrate.

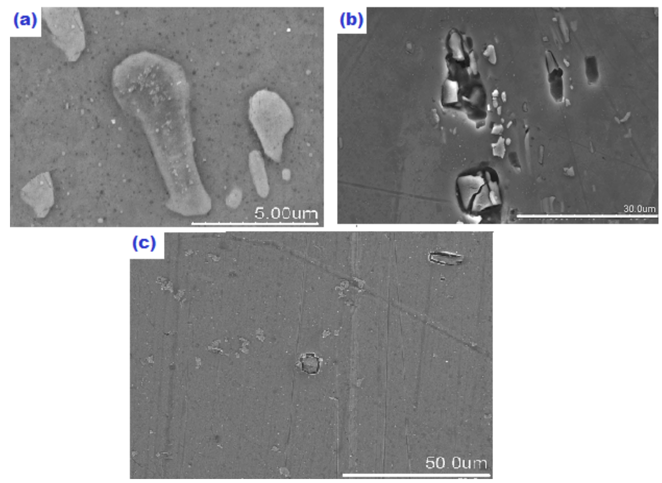

Fig. 3. SEM images of AA2024 samples coated by TMSOD before (a) and after immersion in water for 700-h for (b) TMSOD and (c) BTSE/TMSOD coating.

B. *Ice-repellent performance*

The glaze ice used to study sample ice repellecy was prepared in a wind tunnel at subzero temperature (-10^{o}C) by spraying water micro-droplets with an average size of ~65 µm under conditions similar to outdoor ice accretion [3, 9, 10, 13]. The procedure to evaluate ice adhesion strength was previously reported in detail elsewhere [9, 10, 16]. Figure 4 shows the shear stress of ice detachment as a function of icing/de-icing cycles on the sample surfaces tested. For each coating studied, one sample was subjected to 9 successive de-icing tests. As-received and mirror-polished bare Al was used as standard reference showing initial values of shear stress of ice detachment of ~370±30 kPa and ~270±20 kPa, respectively. Both TMSOD and BTSE/TMSOD samples showed close values for shear stress, implying very similar ice adhesion strength (*IAS*) on alkyl-grafted samples. While uncoated flat sample showed average shear stress of ice detachment of ~370±30 kPa, its TMSOD or BTSE/TMSOD coated counterparts coatings showed lower values of ~182 kPa. This reduction can be attributed to the presence of the low surface energy coatings on the samples. All flat coated surfaces demonstrated shear stress of ice detachment values of at least ~2 times lower than as-received Al surfaces and about ~1.5 times lower than those observed on mirror-polished Al surfaces. However, the adhesion stress of ice detachment values increased for both samples after as many as 9 icing/de-icing cycles, as shown in Fig.4. This increase in ice adhesion strength is believed to be associated with partial decay of the coatings caused by their contact with water. Meanwhile, water-repellency of the coated samples gradually deteriorated over repeated icing/de-icing cycles with a decrease of CA. In other words, CA values decreased after each icing/de-icing event possibly due to partial loss of the hydrophobic coating. The TMSOD layer degraded on BTSE underlayer in a manner similar to what happened on the Al surface. Water molecules can attack the R-Si-O- bond to hydrolyze it, resulting in hydrophilic –OH groups on surfaces.

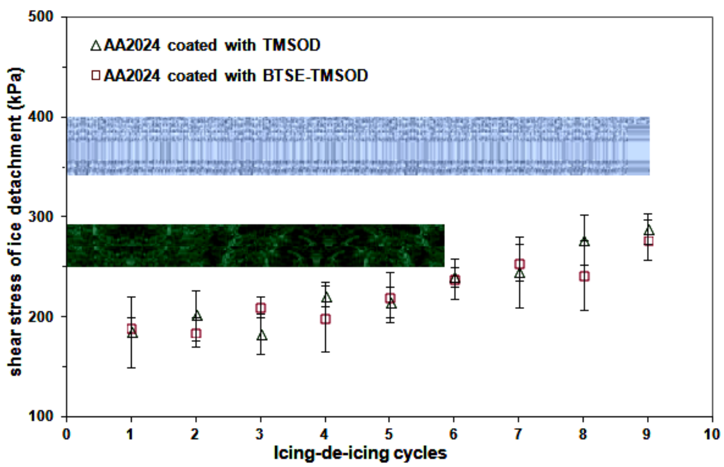

Fig.4 Shear stress of ice detachment vs. icing/de-icing cycle for Al surface coated with TMSOD and BTSE/TMSOD. The blue and green bares stand for bare as-received and mirror-polished Al sample, respectively.

C. Anti-corrosive performance of coating

It is well-known that all modern Al alloys use metallic additives to improve their strength. However, this also leads to increased electrochemical corrosion. Aluminum alloy 2024 is an alloy with Cu as a major alloying element and thus with poor corrosion resistance. Therefore, developing anti-icing coatings on Al substrates highlights the necessity of improving their anticorrosive resistance. This means that the anti-corrosive performance of coated AA2024 should be studied. The potentiodynamic polarization curves of (a) bare AA2024 and hydrophobic coatings of (b) TMSOD and (c) BTSE/TMSOD on the Al alloy in 3.5 wt.% NaCl solution are presented in Fig.5. In parallel, the E_{corr} and i_{corr} values derived from corresponding polarization curves using Tafel extrapolation are summarized in Table 1.

Table 1. Potentiodynamic results of AA2024 with and without coating in 3.5 wt.% NaCl solution.

Sample	E_{corr} (V)	i_{corr} (Amps/cm^2)
Bare AA2024	-0.68 ± 0.05	2.4890 E-5
TMSOD coating	-0.60 ± 0.04	1.2144 E-6
BTSE/TMSOD coating	-0.54 ± 0.04	8.0419 E-9

It is evident in Fig.5 and Table.1 that the value of E_{corr} positively increases from -0.68±0.05 V for bare Al to -0.60±0.04 V and -0.54±0.04 V in the case of the hydrophobic coatings of TMSOD and BTSE/ODTMS, respectively.

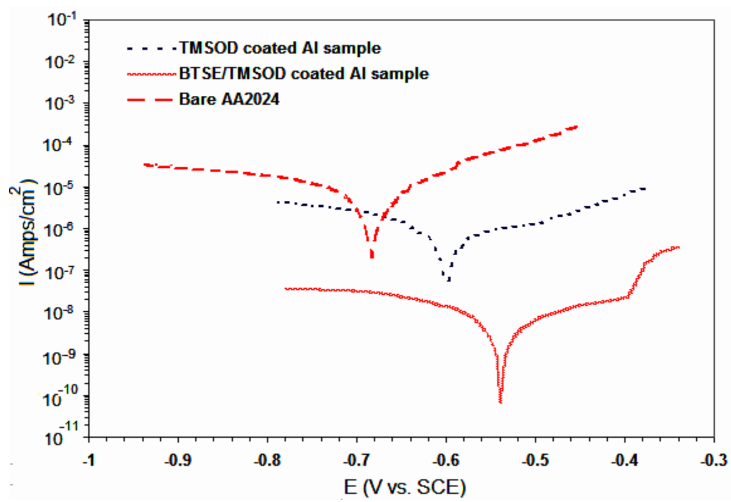

Fig. 5. Polarization curves of AA2024 with and without coating.

The positive shift observed in E_{corr} is obviously due to the improvement of the protective performance of the hydrophobic coating formed on the Al substrate. The corrosion current density, i_{corr}, for the hydrophobic coating of BTSE/TMSOD (8.0419E−9 Amps/cm^2) decreased by about 4 orders of magnitude as compared to that of bare Al (2.4890E−5 Amps/cm^2) and by 3 orders of magnitude as compared to TMSOD (1.2144E−6 Amps/cm^2). These results indicate that the hydrophobic coating of BTSE/TMSOD improved the corrosion resistance of Al surfaces. The aluminum oxide layer is permeable to electrolytes and moisture and is prone to undergo dissolution in humid environments, leading to accelerated corrosion rate. In contrast, the film formed from

BTSE/TMSOD is impermeable to corrosion accelerants. Indeed, comparing the obtained results suggests that the barrier property of the BTSE/TMSOD-modified Al sample improved significantly compared to the unmodified sample as well as to the coated Al surface with TMSOD with respect to E_{corr} and i_{corr} values.

D. Salt spray exposure

The anti-corrosive properties of modified and unmodified samples were further studied by Salt Spray Exposure Testing. More precisely, the Al panels (two panels for each) were placed into a salt-spray chamber (*Ascott*) with their unmodified side protected by scotch tape and their modified surfaces exposed alternatively to salt mist, dry and wet conditions in accordance with ISO14993-Corrosion of metals and alloys [14]. The test specimens were placed in an enclosed chamber and exposed to a changing climate repeating the following 3 steps: 1) 2-h exposure to a continuous indirect spray of neutral (pH: 6.5-7.2) salt water solution, which falls out on to the specimens at a rate of 1 to 2 ml/80cm²/hour, in a chamber at 35 ^{o}C; 2) 4 h of air drying in a climate of >30 %RH at 60 ^{o}C; and 3) 2-h exposure to a condensing water climate (wetting) of 95 to 100 %RH at 50 ^{o}C. As presented in Fig. 6, the unmodified flat Al samples exhibited extensive corrosion after only 8 cycles of salt spray exposure with the appearance of numerous black dots (pits) at micrometer scale. Meanwhile, the size and density of the black dots increased as the salt spray cycle number increased which is due to increasingly expanding localized.

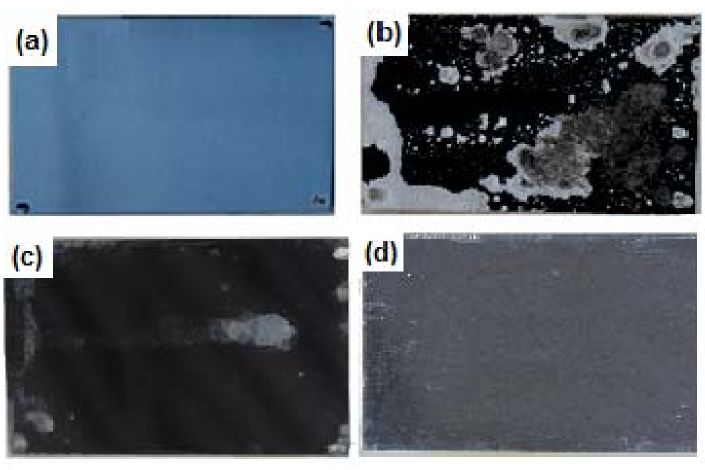

Fig. 6. Optical images of unmodified AA2024 before (a) and after (b) 18 cycles of salt spray test and modified AA2024 with TMSOD (c) and BTSE/TMSOD (d) after salt spray cycles.

However, the earlier stage of corrosion in the case of hydrophobic samples modified by TMSOD was observed after 18 cycles of exposure (Fig.6) and only a bit trace of corrosion was observed in the case of BTSE/TMSOD-modified samples even after 81 cycles of exposure (Fig.6). These observations revealed by salt-spray test confirmed the results presented earlier in Fig. 5 by potentiodynamic polarization curves which show the improvement in corrosion resistance of the modified samples compared to the unmodified ones. Because of the improved barrier properties of the Al surface modified by BTSE/TMSOD, the corrosion resistance of these samples improved compared to that of the bare samples. In other words, these results validate the fact that the BTSE layer formed on the Al surface has less defective areas and is dense enough as compared to the TMSOD layer. Therefore, it acts as a barrier to prevent easy penetration of corrosion accelerants beneath the Al surface. As a result, decreasing corrosion rate or further expansion of corrosion to the surrounding areas was observed.

IV. Conclusions

Alkyl-terminated surfaces were prepared by depositing layers of TMSOD on BTSE-grafted AA2024 and mirror-polished AA2024 surfaces. The stability of such surfaces in different media was tested by means of contact angle measurements, demonstrating gradual loss of hydrophobicity after ~1100-h-long immersion in water, this being associated with a significant decrease in water contact angle. The ice releasing properties of the coated surfaces were investigated by accumulating glaze ice under similar conditions as those in nature by spraying supercooled micrometer-sized water droplets in a wind tunnel at subzero temperature. Both ice-covered surfaces initially demonstrated shear stress of ice detachment values about 2 times lower than as-received Al surfaces and ~1.5 times lower than those observed on mirror-polished Al surfaces as references. These values gradually increased after as many as 9 successive icing/de-icing cycles. The increase in ice adhesion strength observed can be explained by the degradation of the coatings following their contact with water. The electrochemical measurement results pointed out that the corrosion potential of the BTSE-TMSOD hydrophobic coatings increased significantly, and their corrosion current density decreased by 4 orders of magnitude as compared to those on the uncoated sample. These results showed that the BTSE underlayer on the AA2024 substrate provides particularly enhanced corrosion resistance. This would be an excellent approach to improve the anticorrosive performance of metallic surfaces for outdoor applications instead of current-in-use toxic chromate-based coatings.

V. Acknowledgements

This research work has been conducted within the framework of the NSERC/Hydro-Quebec/UQAC Industrial Chair on Atmospheric Icing of Power Network Equipment (CIGELE) and the Canada Research Chair on Atmospheric Icing Engineering of Power Networks (INGIVRE) at Université du Québec à Chicoutimi. The authors would like to thank the CIGELE partners (Hydro-Québec, Hydro One, Réseau Transport d'Électricité (RTE), Rio Tinto Alcan, General Cable, K-Line Insulators, Dual-ADE, and FUQAC) whose financial support made this research possible.

VI. References

[1] M. Farzaneh, 'Atmospheric Icing of Power Networks', Ed., Springer, Berlin, pp. 320, August 2008.

[2] M. Farzaneh, ' Systems for prediction and monitoring of ice shedding, anti-icing and de-icing for overhead lines' CIGRÉ WG B2.29, CIGRE Publications, Technical Brochure #438, pp. 100, 2010.

[3] S. Farhadi, M. Farzaneh, S. A. Kulinich, 'Anti-Icing Performance of Superhydrophobic Surfaces', Applied Surface Science, vol. 257, pp. 6264–6269, 2011.

[4] B. Somlo and V. Gupta, ''A hydrophobic self-assembled monolayer with improved adhesion to aluminium for de-icing application'', Mech. Mater., vol. 33, pp. 471-480, 2001.

[5] S. A. Kulinich, M. Farzaneh, ' Hydrophobic properties of surfaces coated with fluoroalkylsiloxane and alkylsiloxane monolayers', Surface Science vol. 573, pp. 379–390, 2004.

[6] V. F. Petrenko and S. Peng, "Reduction of ice adhesion to metal by using self-assembling monolayers (SAMs)", Can. J. Phys, vol. 8, pp. 387-393, 2003.

[7] E. H. Andrews, H. A. Majid, N. A. Lockington, 'Adhesion of ice to a flexible substrate', Journal Materials Science, vol. 19, pp. 73-81, 19984.

[8] V. K. Croutch and R. A. Hartley, "Adhesion of ice to coatings and the performance of ice release coatings", *J. Coat. Technol*.**,** vol. 64, pp. 41-52, 1992.

[9] S. A. Kulinich, M. Farzaneh, 'How wetting hysteresis influences ice adhesion strength on superhydrophobic surfaces', Langmuir, vol. 25, pp. 8854–8856, 2009.

[10] F. Arianpour, M. Farzaneh, S. Kulinich, 'Hydrophobic and ice-retarding properties of doped silicone rubber coatings', Applied Surface Science, vol. 265, pp. 546-552, 2013.

[11] H. Saito, K. Takai, G. Yamauchi, 'Water- and ice-repellent coatings'. Surface Coatings International, vol. 80, pp. 168–171, 1997.

[12] http://www.matweb.com/search/DataSheet.aspx?MatGUID=57483b4d782940faaf12964a1821fb61.

[13] A. Franquet, C. Le Pen, H. Terryn, et al., "Effect of bath concentration and curing time on the structure of nonfunctional thin organosilane layers on aluminium", Electrochim. Acta, vol. 48, pp. 1245, 2003.

[14] http://www.iso.org/iso/home/store/catalogue_tc/catalogue_detail.htm?csnumber=24372.

[15] A. Frignani, F. Zucchi, G. Trabanelli, V. Grassi, 'Protective Action towards Aluminium Corrosion by Silanes with a Long Aliphatic Chain', Corrosion Science, vol. 48, pp. 2258–2273, 2006.

[16] S. Farhadi, M. Farzaneh, S. Simard, 'Nanostructured ultra superhydrophobic Al surfaces: stability and icephobic properties', International Journal of Theoretical and Applied Nanotechnology, vol. 1, pp. 38-44, 2013.

DC Icing Flashover Characteristics on Composite Insulators with Parallel Air Gap for Ground Wire

GUO Yu-jun, JIANG Xing-liang, DONG Bing-bing, WANG Yao-xuan, JIN Xi
The State Key Laboratory of Power Transmission Equipment & System Security and New Technology
School of Electrical Engineering, Chongqing University,
Chongqing 400030, P.R.China
E-mail: xljiang@cqu.edu.cn

ABSTRACT

Icing disaster of transmission line and its prevention has become an important and hot problem. Insulators with a parallel air gap are generally installed for overhead-ground-wire insulation, and the de-icing voltage is related with the insulator's flashover voltage and the air gap's DC flashover voltage, and thus the parallel air gap distance affects the de-icing length of the overhead ground wire. Quantitative contrast experiments to study the relationship between icing flashover performance of composite insulators used for overhead-ground-wire and its parallel air gap as well as ice thickness were carried out. The test results show that, flashover path is related with the length of insulator's parallel air gap, and the flashover voltage increases with parallel air gap distance increasing. When the parallel air gap is short and all the flashovers occur between the air gap, we can use the ice thickness and flashover performance of non-iced insulator used for overhead-ground-wire to estimate the icing flashover voltage effectively.

Index Terms — **DC, composite insulator used for overhead-ground-wire insulation, parallel air gap, icing, flashover performance.**

1 INTRODUCTION

Overhead ground wire, which is also called lighting wire, is used to protect transmission line from lighting. Under the same icing condition, the thickness of ice and the accretion rate on the overhead ground wire are both larger than those on the transmission wire. It is a result of the heat produced by load current that transfers through the transmission line can somewhat withstand icing. When ground wire is icing，the sag increases and it may be lower than the transmission line then causing discharge to it. While the power communication network is composited in the overhead ground wire, without effective method of melting ice, breakdown of overhead ground wire may cause communication channel interruption and endanger the normal operation of power grid's the control system. According to incomplete statistics, since 1954 China's first record to the transmission line icing accidents, the transmission line icing tripping accidents occur thousands of times [1-4]. The probability of icing accidents on overhead ground wires is much greater than that on transmission lines, and the method to melting ice is even more difficult.

DC ice-melting is always chosen as a effective method for overhead ground wire. It requires to install insulators with a parallel air gap used for overhead-ground-wire insulation in heavy icing areas, so that overhead ground wire keeps insulation from the ground when it is in normal operation or melting ice, while leads lightning current into the ground when the overvoltage caused by lightning punctures the air gap [5-8]. There are few researches on the problem of overhead-ground-wire insulation and how to determine the parallel air gap distance under icing condition, especially under heavy icing condition [9-17].

In order to provide technical reference for the selection of insulators with a parallel air gap used for overhead-ground-wire insulation, in this paper, the authors researched the DC icing flashover performance of two typical types of insulator in heavy icing and contamination conditions, analyzed the influence of the parallel air gap distance, icing condition, insulator types on the icing flashover performance.

2 TEST EQUIPMENT, SPECIMENS AND PROCEDURE

2.1 TEST EQUIPMENT

The experimental investigations were carried out in the multi-functional artificial climate chamber (with a diameter of 7.8 meters and a height of 11.6 meters) of State Key Laboratory of Power Transmission Equipment & System Security and New Technology in Chongqing University [5-7]. The power supply is a ±600 kV/0.5 A thyristor-controlled voltage-current feedback DC pollution test source with ripple factor less than 3.0%, and its voltage drop less than 5.0% when the load current is 0.5 A [7]. The negative DC voltage was applied in the tests.

2.2 TEST SPECIMENS

The samples were two typical DC composite insulators with a parallel air-gap used for overhead-ground-wire insulation (FXBZW-±25/120B for strain type and FXBZW-±25/120C for suspension type), and the profiles and parameters of the insulators are shown in Figure I and Table I.

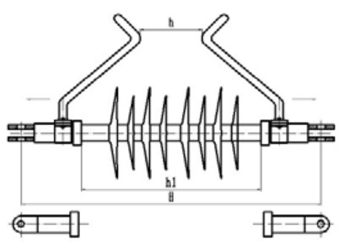

FXBZW-±25/120B

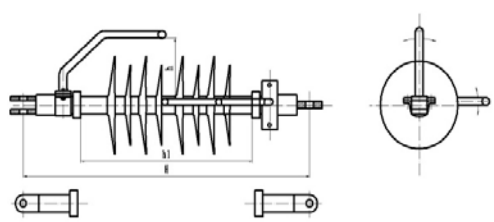

FXBZW-±25/120C

Fig. 1. Configuration of specimens

Tab. 1. Parameters of specimens

Type	H(mm)	h_1(mm)	h(mm)	L(mm)
Strain	600	339	120	1100
Suspension	590	33	120	1100

2.3 TEST PORCEDURE

2.3.1 PRE-POLLUTING OF SPECIMENS

Accident surveys show that most icing flashover of insulators of the transmission line results from the pollution on insulators before icing. Therefore, the solid layer method was used to simulate the pollution before icing [14-18]. The detailed procedure is described as follows:

Before the tests, all the specimens were carefully cleaned to ensure the removal of all traces of dirt and grease and then dried naturally. Then, the surfaces of the composite insulators used for overhead-ground-wire were coated with a very thin layer of dry kieselguhr to destroy the hydrophobicity to the degree of HC4 or HC5. Since the layer of kieselguhr was very thin, the effect of the kieselguhr on a nonsoluble deposit density (*NSDD*) could be neglected. In one hour after aforementioned preparation, the surfaces of specimens were polluted with the suspension of sodium chloride and kieselguhr which simulate the electric and inert materials respectively. In this investigation, the salt deposit densities (SDDs) were 0.08, where the salt is NaCl, and the ratio of SDD to NSDD is 1/6.

2.3.2 ARTIFICIAL ICE-COATING PROCEDURE

After 24h of naturally drying, the polluted specimens were arranged on the electric hoist at the center of the chamber, and the hoist rotated at one revolution per minute (rpm). At the beginning of icing, the surface of the specimens was wetted by the sprayer manually and covered with a 1-2 mm layer of ice to make sure the pollution layer not to be washed away.

For the reasons of security and limitation of facilities, the automatic spraying system was used to form wet-grown ice on specimens without service voltage in this paper [21-22]. Although the formation of air gaps during ice accretion which have influence on flashover voltage and ice deposit uniformity, the difference of the flashover voltage of energized and non-energized icing insulators is only 1 standard deviation according to the investigation of Chongqing University over the years [1].

The icing degree was monitored by a cylinder with a diameter of 28 mm and rotating at one rpm. The minimum clearances between any part of the specimens and the spraying system were larger than 3.8 m, the droplets size was 80-100 μm, the spray flux was about 60±20 $l/(h \cdot m^2)$, the freezing water conductivity was 100 μS/cm, the wind speed was 3.0-5.0 m/s, the temperature in the climate chamber was -10.0 °C to -7.0 °C [24]. The densities of glaze (Figure 2) on the samples were about 0.80- 0.90 g/cm^3.

Figure 2. Icing instance of some specimens in the artificial climate chamber.

In order to make the freezing-water in climate chamber as similar as the supercooling water in natural conditions, the freezing-water was pre-cooled to 4-5 °C before spray [24].

2.3.3 FLASHOVER TEST EVALUATION METHOD

The up-and-down method summarized by the authors from long-term experimental investigations was used to obtain the 50% dc flashover voltage of the iced specimens in this paper.

And the test method can be summarized as follows:

(1) The spraying was stopped when the ice amount reached the target value, the ice was frozen about 15 minute or longer to guarantee complete hardening of the ice and equalization of specimen and ice temperature. Then the airtight door of the chamber was opened to rise the temperature in chamber to -2 to 0 °C at a speed of 2-3 °C/h [18,23- 24].

(2) When the ice started to melt and the air pressure reached the target value, a series of flashover tests were carried out on each iced specimen with up-and-down method. Increasing the applied voltage at a speed of 3kV/s until the estimated value U_f is reached. After this every applied voltage is based on the test result of the prior one, if the result of the prior test is flashover, then increase the applied voltage by ΔU, if not, decrease the applied voltage by ΔU, which is 5% of the estimated value. Every specimen can be tested for only once, the withstand duration must be more than 30 minutes if flashover does not occur. The number of effective tests should be no less than 10 and the effective test is counted from the test whose result is different from the prior one.

According to the above test procedure, more than ten effective U_i should be obtained at one parallel air gas distance for each type of specimen. And the 50% DC flashover voltage $U_{50\%}$ (in kilovolts) and its standard deviation can be expressed as:

$$\begin{cases} U_{50\%} = \dfrac{\sum (n_i U_i)}{N} \\ \sigma = \sqrt{\dfrac{\sum_{i=1}^{N} (U_i - U_{50\%})^2}{N}} \end{cases} \tag{1}$$

where U_i is the applied voltage obtained from the test in the i time, kV; N is the total times of the effective test, $N \geq 10$; σ(%) is the standard deviation of the test result.

3 TEST RESUTLS AND ANALYSES

3.1 Relationship between flashover voltage and the parallel air gap

Experiment study on the relation between the parallel air gas distance d and flashover voltage U_f have been carried out. And the tested strain and suspension insulators are clean (non-iced) on their surface, the parallel air gas distance are 20, 40, 60, 80, 100, 120 mm , respectively. Under each condition we use the uniform boosting method to conduct DC flashover test for 5 times. The test results are shown in Figure 3.

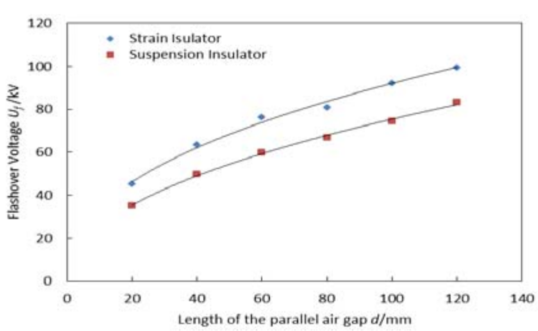

Figure 3. Relationships between U_f and d.

For clean insulators, the flashover voltage U_f can be expressed as:

$$U_f = A \times d^n \tag{2}$$

where U_f is the flashover voltage, A is a coefficient related to the type and contamination level and thickness of ice on the insulator used for overhead-ground-wire insulation; n is an exponent characterizing the influence of d on the flashover voltage. The value of n depends on the type of insulator, air pressure and voltage polarity. Fitting the data in Figure 3 according to equation (2), allows the coefficients A and the characteristic exponents n to be obtained, as shown in Table 2. In this table, R^2 is the correlation coefficient of data fitting when d is taken as the variable.

Table 2. Fitting values of A, n and R^2 according to thetest results in fig. 2 with equation (2).

Type	A	n	R^2
Strain	600	339	120
Suspension	590	33	120

When ice accretion on the reference cylinder is 20 mm, ESDD : NSDD = 0.08 : 0.48 mg/cm^2, and the parallel air gap distance was respectively 60, 80, 100, 120 mm , the relationship between 50% dc flashover voltage $U_{50\%}$ and the parallel air gap distance d is shown in Figure 4. The standard deviation of all the test results is between 2.7%~7.3%.

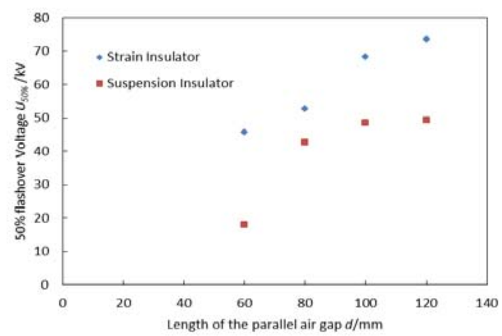

Figure 4. Relationships between $U_{50\%}$ and d.

According to Figure 3, Figure 4 and Table 2, it may be concluded as follows.

(1) For clean strain and suspension insulators used for overhead-ground-wire insulation, the relationship between U_f and d can be described as a power-law function, U_f increases with the increase of d, but the growth rate decreases. While for icing insulators on which the ice accretion t = 20 mm, $U_{50\%}$ and d are not satisfied with a power law.

(2) The coefficient A and characteristic exponent n are related to the type of insulators. The coefficient A of the strain insulator is greater than that of the suspension insulator, while the characteristic exponent n is quite the contrary.

(3) With the same d, the DC flashover voltage of clean strain insulator is 21%-29% higher than that of suspension insulator. The reason is that partial arc produced on strain insulators levitates due to thermal effect and the arc distance increases. When ice accretion on the reference cylinder was 20 mm, the 50% dc flashover voltage $U_{50\%}$ of strain insulators is higher than that of suspension insulators, too. It is a result

of DC arc levitation and two types of insulators arranged in different ways that causes the difference in ice accretion. The icicles on suspension insulators bridging the sheds that makes the flashover voltage lower.

3.2 DC FLASHOVER PERFORMANCE OF THE STRAIN INSULATOR USED FOR OVERHEAD-GROUN-WIRE INSULATION

The relationship between the 50% DC flashover voltage $U_{50\%}$ and the the parallel air gas distance d for the strain insulator used for overhead-ground-wire insulation is shown in Figure 5.

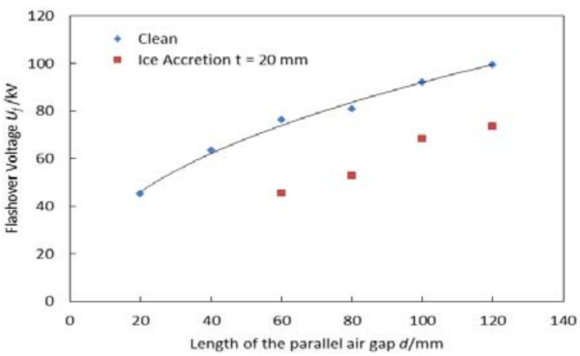

Figure 5. Relationships between $U_{50\%}$ and d.

For the clean strain insulator with a parallel air gap used for overhead-ground-wire insulation, all the flashover occurs in the air gap. When ice accretion t = 20 mm, the flashover path changes with increase of the parallel air gap distance, as shown in Figure 6.

d = 60mm(air gap)

d = 80mm(air gap)

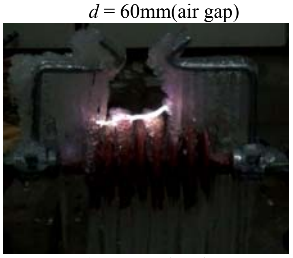

d = 80mm(insulator)

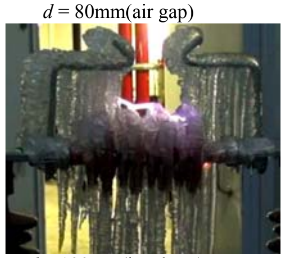

d = 100mm(insulator)

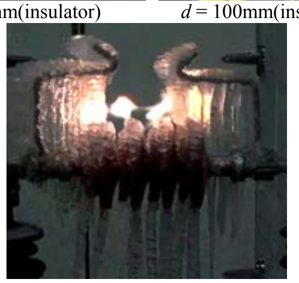

d = 120mm(insulator)

Fig. 6. Relationships between flashover path and d.

According to Figure 5 and Figure 6, it may be concluded as follows.

(1) When the thickness of ice accretion on the reference cylinder is 20 mm and the parallel air gap distance of strain insulators used for overhead-ground-wire insulation is 60 mm, U50% is 45.6 kV which is close to 45.3 kV of the clean strain insulators with a 20 mm air gap. Flashover occurs between the air gap, so when the parallel air gap is small (all flashover occurs in the air gap) we can use the flashover voltage of clean insulators to make approximate estimates on $U_{50\%}$ of iced insulators.

(2) When the ice accretion is 20 mm and the air gap distance is 80 mm, the flashover voltage is lower than that of clean insulators with a 40 mm air gap. Flashover occurs in both air gap and insulator. When the air gap distances are 100 and 120 mm, the flashover voltages are lower than those of clean insulators with 60 and 80 mm air gaps, respectively. All flashover occurs on the insulator.

(3) For the strain insulator, the icicles on parallel fittings bridge to the insulator. When the air gap is relatively larger and the flashover voltage on creep distance is lower than that of the air gap, flashover occurs on the insulator. With the increasing of the parallel air gap, the dry arc distance of the insulator increases. So the flashover voltage increases.

3.3 DC FLASHOVER PERFORMANCE OF THE SUSTENSION INSULATOR USED FOR OVERHEAD-GROUN-WIRE INSULATION

The relationship between the 50% DC flashover voltage $U_{50\%}$ and the length of the parallel air gas d for the suspension insulator used for overhead-ground-wire insulation is shown in Figure 7.

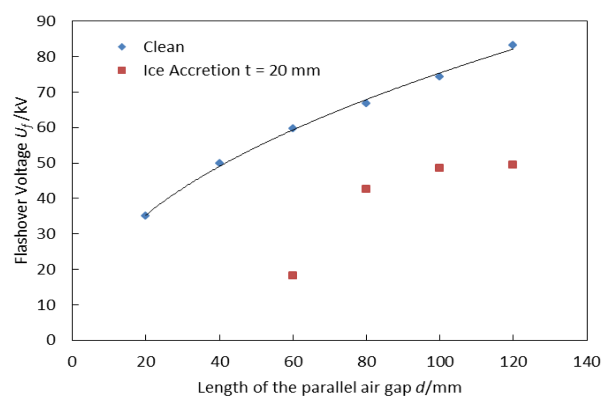

Figure 7. Relationships between $U_{50\%}$ and d.

For the clean suspension insulator with a parallel air gas used for overhead-ground-wire insulation, all the flashover occurs in the air gap. When ice accretion t = 20 mm, the flashover path changes with increase of the parallel air gap distance, as shown in Figure 8.

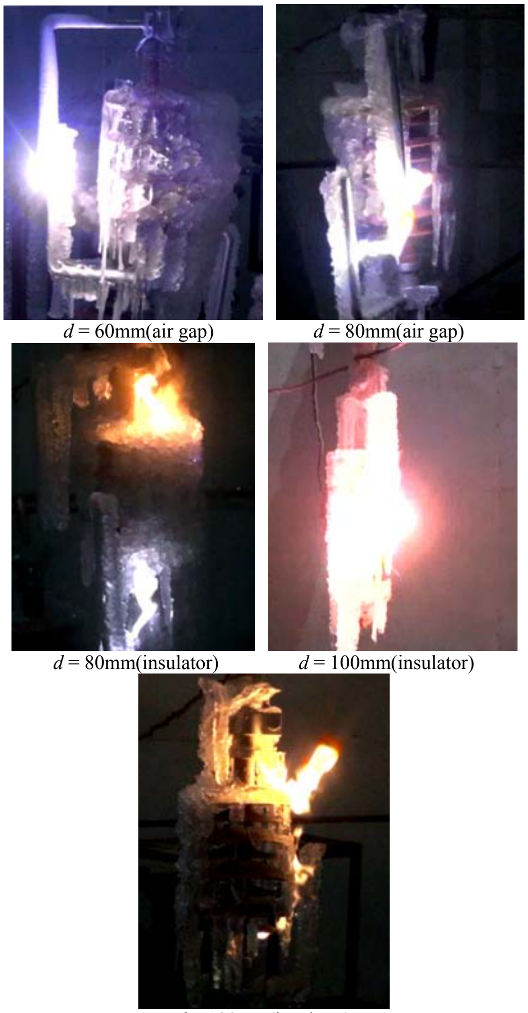
d = 60mm(air gap) d = 80mm(air gap)
d = 80mm(insulator) d = 100mm(insulator)
d = 120mm(insulator)

Fig. 8. Relationships between flashover path and d.

According to Figure 7 and Figure 8, it may be concluded as follows.

(1) When the thickness of ice accretion on the reference cylinder is 20 mm and the parallel air gap distance of the suspension insulator used for overhead-ground-wire insulation is 60 mm, $U_{50\%}$ is 18.2 kV which is far smaller than 45.3 kV of the clean suspension insulators with a 20 mm air gap. Flashover occurs between the air gap.

(2) When ice accretion is 20 mm and the air gap distance is 80 mm, the flashover voltage is lower than that of clean insulators with a 40 mm air gap. Flashover occurs in both air gap and insulator. When the air gap distances are 100 and 120 mm, the flashover voltages are 48.6 and 49.5 kV, which are very close. The reason is that the flashover under both conditions occurs on the insulator and the dry arc distance is nearly the same.

4 CONCLUSIONS

(1) For both the FXBZW-±25/120B and the FXBZW-±25/120C clean (non-iced) insulator used for the overhead-ground-wire insulation, the relationship between U_f and d can be described as a power-law function, U_f increases with the increase of d, but the growth rate decreases.

(2) The 50% DC flashover voltage $U_{50\%}$ of the FXBZW-±25/120B strain insulator is higher than that of the FXBZW-±25/120C suspension insulator with the same parallel air gap d and under the same icing condition.

(3) The coefficient A and characteristic exponent n are related to the type of insulators. The coefficient A of the strain insulator is greater than that of the suspension insulator, while the characteristic exponent n is quite the contrary.

(4) For the FXBZW-±25/120B strain insulator, when the parallel air gap is small and all flashover occurs in the air gap, we can use the flashover voltage of clean insulators to make approximate estimates on $U_{50\%}$ of iced insulators.

(5) For the FXBZW-±25/120B strain insulator, when the parallel air gap is relatively big and all the flashover occurs on the insulator. With the increasing of the parallel air gap, the flashover voltage increases. While for the FXBZW-±25/120C suspension insulator, when the parallel air gap is relatively big and all the flashover occurs on the insulator, the flashover voltage stays nearly the same.

REFERENCES

[1] X. Jiang, L. Shu and C. Sun, Insulation of Electric Power system under Pollution and Icing conditions, Beijing, China Electric Power Press, 2009 (in Chinese).

[2] Sun Caixin, Sima Wenxia, Shu Lichun. Atmospheric environment and external insulation of power system [M]. Beijing: China Electric Power Press，2002：103-130 (in Chinese).

[3] Jiang Xingliang, Yi Hui. Iceing of transmission line and countermeasures [M]. Beijing: China Electric Power Press, 2001: 1-9 (in Chinese).

[4] Lu Jiazheng, Jiang Zhenglong, Lei Hongcai, et al. Analysis of hunan power grid ice disaster accident in 2008 [J]. Automation of Electric Power Systems, 2008, 32(11): 16-19 (in Chinese).

[5] Li Qingfeng, Fan Zheng, Wu Qiong, et al. Investigation of ice-covered transmission lines and analysis on transmission line failures caused by ice-coating in China [J]. Power System Technology, 2008, 32(9): 33-36 (in Chinese).

[6] Tan Yanjun, Lu Jiazheng, Li Bo, et al, Research and application of new AC/DC de-icing devices in Hunan Power Grid, The 14th International Workshop on Atmospheric Icing of Structrures, China: Chongqing, 2011.

[7] Yun Zhang, Jiazheng Lu, Yanjun Tan , et al, Research of de-icing method and device based on 12-pulse rectification for 500kV transmission lines, The 14th International Workshop on Atmospheric Icing of Structrures, China: Chongqing, 2011.

[8] Du Yuan. Study on AC flashover performance of iced insulators connected with alternately large and small diameter sheds [D]. Chongqing: Chongqing University, 2007 (in Chinese).

[9] G. N. Ramos, M. T. R. Campillo, and K. Naito, “A study on the characteristics of various conductive contaminants accumulated on high voltage insulators”, IEEE Trans. Power Del., Vol. 8, pp. 1842–1850, Oct. 1993.

[10] Sun Peng, Chen Shaohui, Zhang Shaoquan．The study of DC melting ice for overhead ground wire [J]. International Conference on Electronics, Communications and Control (ICECC), 2011.

[11] X. Jiang, J. Hu and Y. Liang, “Pollution Flashover Performance of Short Sample for 750kV Composite Insulators”, IEEE Int’l. Sympos. Electr. Insul. (ISEI), Indianapolis, USA, pp. 19-22, 2004.

[12] Laforte J L, Allaire M A, Laflamme J. State-of-the-art on power line de-icing. Atmospheric Research 1998, 46: 143-158.

[13] Wu Lihui, Jiang Xingliang, Xiong Qixin, et al. DC flashover performance and voltage correction of iced XZP-160 insulator at low atmospheric pressure [J]. High Voltage Engineering, 2002, 28(10): 5-7 (in Chinese).

[14] Masoud Farzaneh M, Baker A C, Allen Bernstorf B R, et al. Selection of line insulators with respect to ice and snow, part i: context and stresses [J]. IEEE Trans. on Power Delivery, 2007, 22(4): 2298-2296.

[15] Masoud Farzaneh M. Atmospheric icing of power networks [M]. Berlin: Springer, 2008: 267-322.

[16]Zhang Zhijin, Jiang Xingliang, Ma Jun, et al. Study on icing performance of 110kv insulator strings at ac service voltage [J]. Proceedings of the CSEE, 2006, 26(25): 140-143 (in Chinese).
[17] IEEE Standard Techniques for High-Voltage Testing, IEEE Std. 4, IEEE Publ., 1995.
[18] Hu Jianlin, Sun Caixin, Jiang Xingliang, et al. Flashover performance of pre-contaminated and ice-covered composite insulators to be used in 1000 kV UHV AC transmission lines [J]. IEEE Transactions on Dielectrics and Electrical Insulation, 2007 , 14(6): 1347-1356.
[19] "Artificial pollution tests on composite insulators used on high-voltage ac system", 2004, DL/T859-2004, (in Chinese).
[20] IEEE Dielectrics and Electrical Insulation Society. IEEE Std 1783-2009 IEEE guide for test methods and procedures to evaluate the electrical performance of insulators in freezing conditions [S]. New York: The Institute of Electrical and Electronics Engineers, Inc., 2009.
[21] Jiang Xingliang, Chao Yafeng, Zhang Zhijin, et al. DC flashover performance and effect of sheds configuration on polluted and ice–covered composite insulators at low atmospheric pressure [J]. IEEE Transactions on Dielectrics and Electrical Insulation, 2011, 18(1): 97-105.
[22] D. Huang, Y. Liu, Y. Hu, W. Cai, Y. Chen and J. Ruan, "Icing Flashover Characteris tics of EHV AC Transmission Line Insulator Strings", High Voltage Engineering. Vol. 35, No. 3, pp. 568-573, 2009 (in Chinese).
[23] X. Jiang, S. Xie, Q. Wang, Z. Liu and M. Chen, "DC flashover performance and voltage correction of HV insulators at high altitude districts with icing", IEEE Intern. Conf. Properties and Application of Dielectric Materials, Nagoya, Japan, pp. 146-149, 2003.
[24] Guide for Test Methods and Procedures to Evaluate the Electrical Performance of Insulators in Freezing Conditions, IEEE Std 1783-2009, 2009.

Yujun Guo was born in Hubei province, China, on March 1989. He graduated from Huazhong University of Science and Technology and obtained the B.E. degree in 2011. He is presently working on his PhD in the College of Electrical Engineering, Chongqing University. His main research interests include high voltage technology and external insulation.

Comparison on AC Icing Flashover Performance of Porcelain, Glass, and Composite Insulators

XIANG Ze, JIANG Xing-liang, ZHANG Zhijin, DONG Bingbing, WANG Yaoxuan, JIN Xi

The State Key Laboratory of Power Transmission Equipment and System Security and New Technology
School of Electrical Engineering, Chongqing University
Chongqing 400030, P.R.China
E-mail: xljiang@cqu.edu.cn

ABSTRACT

The electrical performance of insulators under the comprehensive conditions of low air pressure, pollution and icing, is an important basis for the selection of external insulation of transmission lines and substations in icing regions. However, little research has been dedicated to the comparison on ac icing flashover performance of composite, porcelain and glass insulators in this environment. Based on the investigations carried out in the artificial climate chamber on three types of iced insulators, the ac flashover performances of insulators were researched in this paper. In addition, the paper analyzed and compared the effects of various factors, including ice thickness, pollution and air pressure on the flashover performance of three types of iced insulators. The experimental results show that the flashover voltage of three types of insulators decreased with the increase of ice thickness, pollution, and the altitude. The characteristic exponent characterizing the influence of the ice thickness, pollution and atmospheric pressure on the flashover voltage were related with the insulator types. The effect of ice thickness and atmospheric pressure on icing flashover voltage was more apparent for composite insulator than porcelain and glass insulator, and the characteristic exponent characterizing the influence of ice thickness and atmospheric pressure on the flashover voltage was obviously big for composite insulators. The characteristic exponent characterizing the influence of pollution on the flashover voltage was small for composite insulators. Under the same condition, the flashover voltage gradients of ice-covered composite insulators are slightly greater than porcelain and glass insulators.

Index Terms —**Insulators, icing flashover performance, ice thickness, low air pressure, pollution**

1 INTRODUCTION

China is one of the countries that have severe icing problems of transmission lines in the world. Current research and operational experience show that singly or in combinations, pollution, icing, low air pressure on insulators may cause a drastic decrease in the electrical insulation strength that can lead to flashover and power outages at normal service voltage. Most parts of Southern China encountered the most serious ice and snow disaster in the meteorological record history in January and February 2008. The power grid suffered severe damage in East China, Central China, South China, and Southwest China. In addition to a lot of mechanical damage, icing flashover was also an important reason for the large-scale power outage. The disaster brought greater concerns about icing problems of the power grid to Chinese power departments.

The electrical performance of insulators in freezing conditions is an important basis for the selection of external insulation of transmission lines and substations in icing regions, and it has been extensively investigated by researchers in recent decades in the world [1-20]. It is proved that the flashover voltage decreases with the increase of the conductivity of icing water, this change law has tended to become gentle, finally slowly decrease [1-3]. References [4-6] indicate that the flashover voltage of iced insulators is much lower in ice-melting period than that in ice accretion period. It is considered that m, characteristic index of the influence of air pressure on ice-covered insulators' flashover voltage, is related to insulator' material quality, structure type, pollution level and ice thickness [7-12]. Usually, some researchers adopted the ice thickness of rolling conductor monitoring to describe the icing degree of insulators [13, 14]. And the relationship between flashover voltage and ice thickness can be described as a negative exponent function [2, 15-19].

To date, little research has been dedicated to the comparison on ac icing flashover performance of composite, porcelain and glass insulators covered with ice, especially under the comprehensive conditions of low air pressure, pollution and icing. Based on the investigations carried out in the multi-function artificial climate chamber in the High Voltage and Insulation Technological Laboratory of Chongqing University, China, this paper investigates the ac flashover performance of three types of iced insulators. Then, the paper analyzed and compared the effects of various factors, including ice thickness, pollution and air pressure on the flashover performance of three types of iced insulators.

2 TEST EQUIPMENT, SPECIMENS AND METHODS

2.1 TEST EQUIPMENT

The experimental investigations were carried out in the multi-function artificial climate chamber [2], with a diameter of 7.8 m and a height of 11.6 m. The minimum temperature in the chamber can be adjusted to -45 °C; the air pressure in the chamber can be as low as 30 kPa, which can simulate the atmospheric conditions at an altitude of 9000 m.

The power was supplied by a 500 kV/2000 kVA test transformer. The major technical parameters are as follows: rated capacity 2000 kVA, rated current 4 A, input voltage 0-10.5 kV, output voltage 0-500 kV, and short-circuit impedance less than 6 percent under a rated voltage of 500 kV. The test power supply satisfies the requirements recommended by IEEE publication [20]. The test circuit of the ice-covered flashover experiment is shown in reference [21].

2.2 TEST SPECIMENS

This study, taking seven-unit porcelain, glass insulator strings and 110 kV composite insulators as objects, adopts the same test procedures and strictly controls environment parameters. Objects of the study are porcelain, glass and composite insulators, whose structure and parameters are described in Fig.1 and Table1. In Table 1, *D* is the diameter, *H* is the height, *h* is the minimum dry arcing distance, and *L* is the leakage distance.

Table 1. Parameters of test insulators

Type	*D*(mm)	*H*(mm)	*h*(mm)	*L*(mm)
XP-160	255	155	-	305
LXY_4-160	280	155	-	380
$FXBW_4$-110/100	150/115	1270	1050	3350

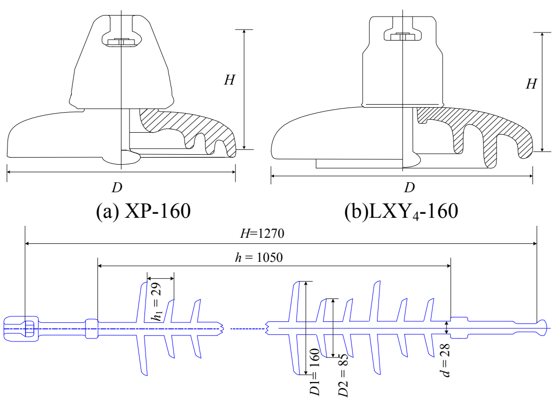

(a) XP-160 (b)LXY_4-160

(c) $FXBW_4$-110/100

Figure 1. Profiles of test insulators

2.3 TEST PROCEDURES AND METHODS

1) Preparation: Before tests, all samples were carefully cleaned to ensure the removal of all traces of dirt and grease and then dried naturally.

2) Artificial polluting: The solid-layer method (SLM) and the icing-water-conductivity method (IWCM) are widely used in the insulator icing tests. In [22], the equivalent relation of influence of the two methods on ice flashover stress was analyzed and studied. In this paper, the IWCM was used to form the pollution layer on the samples. The conductivities of freezing water (corrected to the values at 20 □, and the conductivities that will be mentioned are corrected to the values at 20 □) in this investigation were 300, 450, 630, and 1000 µS/cm, respectively.

3) Ice deposit: The specimens were suspended vertically from the hoist at the center of the chamber, rotating at one r.p.m.. Then the spraying system was used to form wet-grown ice on insulators without service voltage in this paper. The minimum clearances between any part of the specimens and the spraying system were larger than 3.8 m, the droplets size was 80-100 µm, the spray flux was about 60-80 $L \cdot h^{-1} \cdot m^{-2}$, the wind speed was 3.0-5.0 m/s, the temperature in the climate chamber was -10.0 °C to -7.0 °C. The densities of glaze on the samples were about 0.80-0.90 g/cm^3.

4) Characteristics defining the icing degree: As the amount of ice accretion on the insulators is one of the major parameters in evaluating flashover performance, the average thickness of ice on the insulators was checked by measuring the thickness d of the ice accumulated on a monitoring cylinder with a diameter of 28 mm and rotating at one r.p.m. [13].

5) Simulation of high altitude: The low atmospheric pressure in the chamber was used to simulate the high altitude conditions. References [23, 24] indicate that the relationship between the atmospheric pressure and the altitude *H* (in km) can be expressed as follows:

$$H = 45.1 \times \left(1 - \left(P / P_0\right)^{0.1866}\right) \tag{1}$$

Where P_0 is the standard atmospheric pressure (101.3 kPa). In this paper, the altitudes of 232 m, 1000 m, 2500 m, and 4000 m were simulated in the chamber, with atmospheric pressures of 98.6 kPa, 89.8 kPa, 74.6 kPa and 61.6 kPa, respectively.

6) Average flashover voltage method

Water spray stopped when the ice accretion on the reference cylinder reached its target value, and ice was hardened for 15 min at the icing temperature. Then, the ice-covered insulators were photographed and measured in a period that lasted less than 10 min. When the preparation phase was finished, the sealed door of the climate chamber was opened to raise the temperature at a rate of 1~2 □/h. When the temperature in the climate room rose to -2~0 □, the average flashover voltage method was used to determine the flashover voltage of the insulators.

Average flashover voltage method is one of the methods recommended by [25, 26] and can be summarized as follows: (a) First, increase the voltage at a non-specified rate to the value of about 75% of predicted flashover voltage U_p, and then change the rate to the value of 2%U_p /s till the flashover taken place. Finally, record the flashover voltage U_f ; (b) The temperature was lowered with the time interval about 3 minutes in order to re-freeze the ice layer, repeat (a). Stop the flashover test until the flashover test on each specimen was performed 3～4 times.

For an ice-covered specimen, a series of flashover voltage can be obtained by above procedures. Due to the melting and loss of ice during the flashover process, the subsequent flashover voltage may be different from the previous flashover voltages recorded of the same specimen. According to the margin of acceptable of 7.5% error in engineering, delete those data which are beyond the standard. The average value U_{ave} of the series of flashover voltages expressed by U_{f1}, U_{f2}, $\cdots$, U_{fN} (N is the valid times of flashovers, $N \geq 10$) and its standard deviation can be expressed as,

$$\begin{cases} U_{ave} = \dfrac{\sum_{i=1}^{N} U_{fi}}{N} \\ \sigma(\%) = \sqrt{\dfrac{\sum_{i=1}^{N}\left(U_{fi} - U_{ave}\right)^2}{N-1}} \times \dfrac{100\%}{U_{ave}} \end{cases} \tag{2}$$

where U_{ave}(kV) is the average flashover voltage of iced insulator; U_{fi}(kV) is the applied voltage; N is the total number of tests.

3 COMPARISON ON AC ICING FLASHOVER PERFORMANCE

The ac icing flashover performance of samples has been investigated based on the aforementioned artificial icing test methods in this paper. The test results in Figure 2 are gained under the conditions: air pressure P=98.6 kPa and freezing water conductivity γ_{20}=300 μS/cm (measured at 20 °C). The standard deviation of all results range from 2.4% to 6.5%. The results in Figure 3 are gained under the conditions: d=10 mm, respectively. The standard deviation of all results range from 1.2% to 7.6%.

3.1 COMPARISON ON THE INFLUENCE OF *d* ON U_{ave}

When air pressure is 98.7 kPa and γ_{20} is 300 μS/cm, the relationship between U_{ave} and ice thickness is shown in Figure 2.

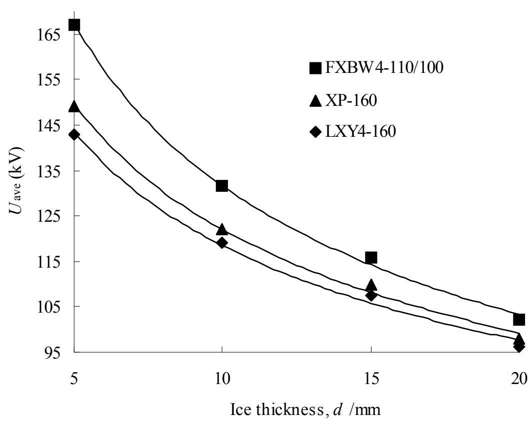

Figure 2. The influence of d on U_{ave}

The relationship between U_{ave} and d can be expressed by a power function as follows [15-17]:

$$U_{ave} = Ad^{-a} \tag{3}$$

Where A is constant related to the pollution degree, the profile and materials of the insulators, and air pressure etc.; d is the thickness of ice on the monitoring cylinder, in mm; a is the characteristic exponent characterizing the influence of ice thickness on ac icing flashover voltage.

Fitting value of A and a according to the test results of Figure 2 according to equation (3), the fitting results are shown in Table 2.

Table 2. The values of A, a, and R^2 for different types of insulators

Type	A	a	R^2
XP-160	241.4	0.296	0.995
LXY4-160	224.7	0.278	0.994
FXBW-110/100	293.6	0.349	0.997

According to Figure 2 and Table 2, it can be known that,

(1) For three types of insulators, the ac icing flashover voltage decreases with increase of ice thickness, and this decreasing tends to be gentle with the increase of d. And the relationship between U_{ave} and d can be described as a negative exponent function.

(2) U_{ave} of composite insulator is slightly higher than of porcelain and glass insulators. Differences in the icing flashover voltage between composite, porcelain and glass insulators narrow with an increase of d. For example, when d is 5mm, 10mm, 15mm or 20mm, U_{ave} of composite insulator is 12.0%、7.7%、5.5%、4.3% and 17.0%、10.5%、7.8%、6.2% higher than that of porcelain and glass insulators, respectively.

(3) For three types of insulators, the characteristic exponent a characterizing the influence of d on U_{ave} is related with the profile and materials of the insulators. When air pressure is 98.7 kPa and γ_{20} is 300 μS/cm, a is 0.349, 0.296 and 0.278 for composite, porcelain and glass insulators respectively. The effect of ice thickness on icing flashover voltage is more apparent for composite insulator than porcelain and glass insulators.

3.2 COMPARISON ON THE INFLUENCE OF *P* ON U_{ave}

When ice thickness is 10 mm, the relationship between U_{ave} and the air pressure is shown in Figure 3. The study focuses on the ice thickness of 10 mm, for the tested insulators are mainly used in the area where the ice thickness is about and below 10 mm.

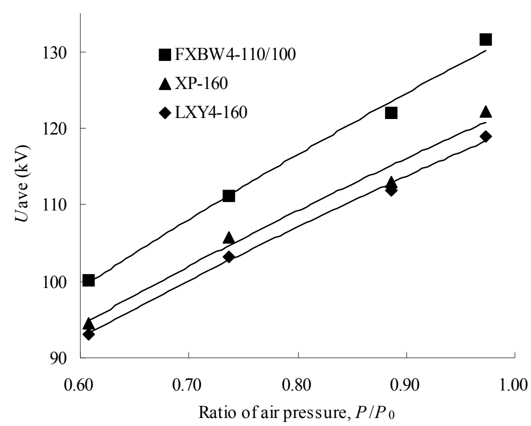

(a) γ_{20}=300 μS/cm

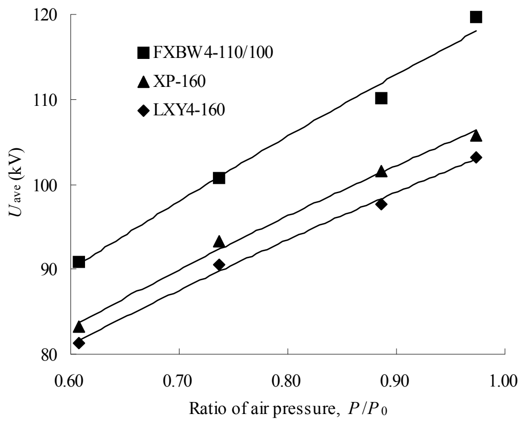

(b) γ_{20}=450 μS/cm

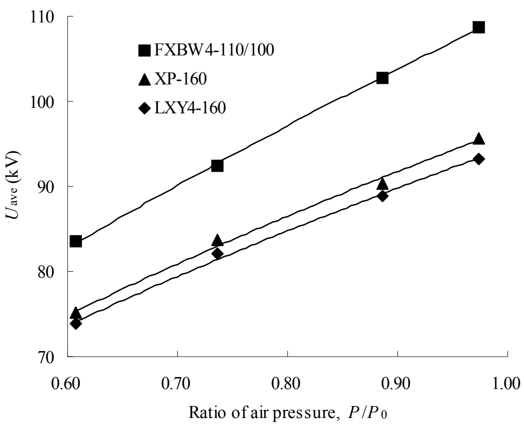

(c) γ_{20}=630 μS/cm

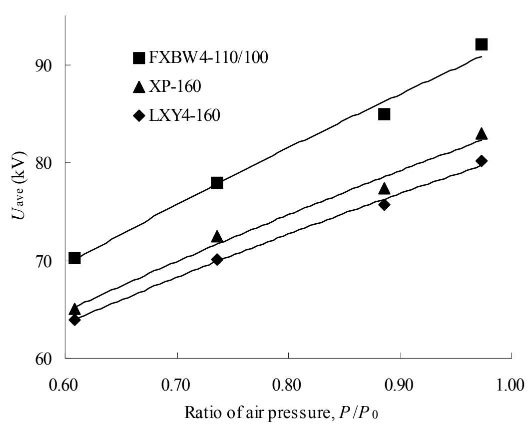

(d) γ_{20}=1000 μS/cm

Figure 3. Relation between U_{ave} and P/P_0 under various γ_{20}

The relationship between the flashover voltage of polluted or iced insulators and the air pressure is normally expressed as [7, 10, 21],

$$U_{ave} = U_0 \times \left(P / P_0 \right)^m \quad (4)$$

Where U_{ave} and U_0 are the average flashover voltages of insulators at air pressure P (high altitude) and pressure at sea level P_0 (101.3 kPa) respectively; the exponent m is a constant whose value characterizes the influence of air pressure on the average flashover voltage of insulators.

As mentioned above, the exponent m in Equation (4) characterizes the effect of atmospheric pressure on the flashover voltage of insulators, and constitutes an important parameter for the insulation design of transmission lines located at high altitudes. Through regression analysis on the test results, the values of exponent m were determined at pollution levels for different insulators, which are shown in Table 3.

Table 3. U_0, m and R^2 under various γ_{20}

Type	U_0、m and R^2	γ_{20} (μS/cm) 300	450	630	1000
XP-160	U_0	122.5	107.8	96.8	83.4
	n	0.514	0.508	0.502	0.495
	R^2	0.983	0.995	0.995	0.986
LXY_4-160	U_0	120.0	104.4	94.6	80.7
	n	0.508	0.493	0.489	0.470
	R^2	0.996	0.9995	0.997	0.997
$FXBW_4$-110/100	U_0	132.2	119.8	110.1	99.2
	n	0.564	0.562	0.561	0.554
	R^2	0.994	0.989	0.999	0.990

According to Figure 3 and Table 3, the following conclusions can be drawn,

(1) For three types of insulator samples, the average flashover voltage under ice conditions decreases with a decrease in atmospheric pressure. The average flashover voltage was power function law in the ratio of atmospheric pressure between at high altitude and at sea level with plus exponent.

(2) The value of exponent m for three types of insulators tested, decreases as γ_{20} increases. This variation tendency for exponent m runs counter to that in [27]. In [27], the results showed that the exponent m for porcelain insulator increases as freezing water conductivity increases. Generally, the higher the γ_{20}, the shorter the critical flashover arc. Thus, the influence of air density on the arc propagation decreases. This results in a lower decrease rate in flashover voltage and, accordingly, a lower m value.

(3) Under the same condition, the value of exponent m is 0.560 for composite insulator, whereas it was 0.505, 0.490 for porcelain and glass insulators respectively. Specifically, for composite insulator, the influence of atmospheric pressure on the average flashover voltage is bigger. This demonstrates that the material and profile of insulator can affect the exponent m.

3.3 COMPARISON ON THE INFLUENCE OF γ_{20} ON U_{ave}

The ac icing flashover voltage of three types of specimens decreases rapidly with the increase of freezing water conductivity. The decrease of U_{ave} can be expressed by a power curve which follows the relation [5, 18, 19, 28],

$$U_{ave} = B \times \gamma_{20}^{-b} \quad (5)$$

Where B is the coefficient whose value is related to the material and profile of insulators, air pressure and ice thickness; γ_{20} is freezing water conductivity, in μS/cm; b is the characteristic exponent characterizing the influence of γ_{20} on U_{ave}, whose value is related to atmospheric pressure, the material and profile of the insulators and ice thickness.

Fitting values of B and b of three types of specimens under different air pressure according to the test results of Figure 3 with equation (5). The relation curves between U_{ave} and γ_{20} under different air pressures are shown in Figure 4. And the fitting results are shown in Table 4.

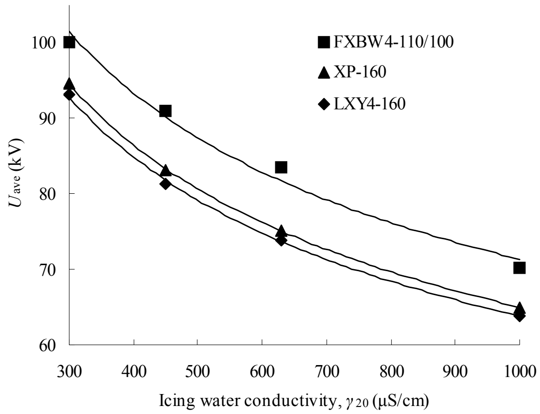

(a) P= 61.6 kPa

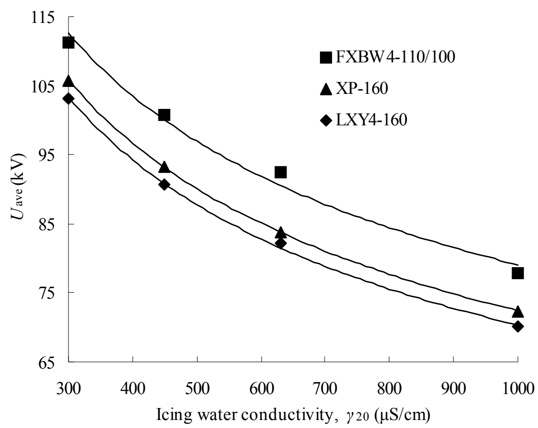

(b) P= 74.6 kPa

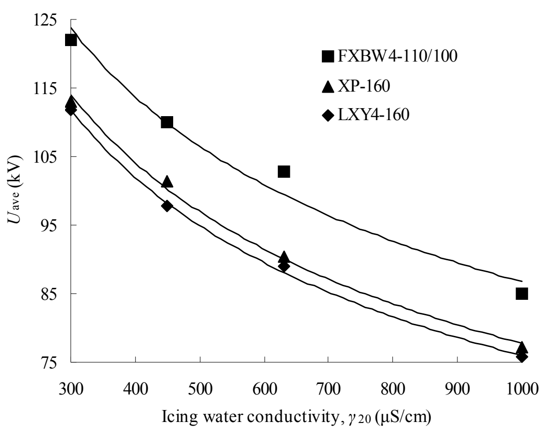

(c) P= 89.8 kPa

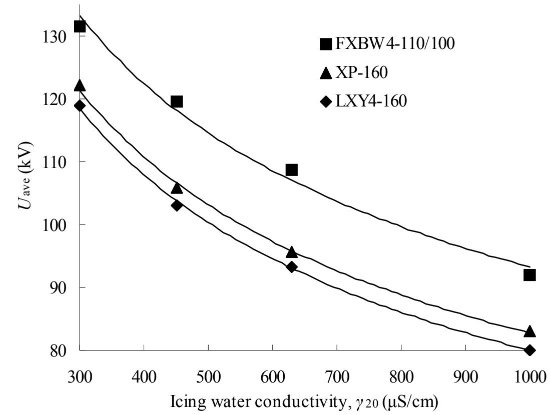

(d) P= 98.6 kPa

Figure 4. Relation between U_{ave} and γ_{20} under various P

Table 4. B, b and R^2 under various P

Type	B、b and R^2	P(kPa) 98.6	89.8	74.6	61.6
XP-160	B	747.2	699.8	640.8	557.6
	b	0.319	0.318	0.316	0.311
	R^2	0.999	0.996	0.997	0.995
LXY_4-160	B	763.2	697.2	638.7	545.6
	b	0.327	0.321	0.319	0.311
	R^2	0.999	0.999	0.999	0.999
$FXBW_4$-110/100	B	724.6	667.4	602.4	539.1
	b	0.297	0.295	0.294	0.293
	R^2	0.989	0.974	0.988	0.985

According to Figure 4 and Table 4, it can be known that,

1) The characteristic exponent b is related to the material and profile of insulator. When ice thickness is 10 mm, for composite insulator, the value of exponent b is 0.295, whereas it is 0.316, 0.320 for porcelain and glass insulators respectively. Furthermore, porcelain and glass insulator's b is little bigger than composite's under all the selected atmospheric pressures. That is, pollution severity has a more obvious effect on icing flashover voltage of porcelain and glass insulators than on that of composite insulator.

2) At the lower atmospheric pressure, the value of b is smaller, which means that the lower the atmospheric pressure, the lesser the influence of the pollution on the electrical performance of ice-covered insulators.

3.4 COMPARISION ON ICING FLASHOVER VOLTAGE GRADIENTS

In this paper, E_h (in kV/cm) is the flashover voltage gradient along the dry arcing distance h of the insulators, namely,

$$E_h = U_{ave} / h \tag{6}$$

Based on the tested results, E_h of the three types of insulator samples were calculated by the equation (6). And the relative deviations between the three types of insulator samples are defined as follows,

$$\begin{cases} \Delta_1\% = 100\% \times \left(E_{h(C)} - E_{h(P)}\right) / E_{h(C)} \\ \Delta_2\% = 100\% \times \left(E_{h(C)} - E_{h(G)}\right) / E_{h(C)} \end{cases} \tag{7}$$

Where $E_{h(C)}$, $E_{h\,(P)}$ and $E_{h(G)}$ is the icing flashover voltage gradient of composite, porcelain and glass insulator respectively. The relative deviations between the three types of insulator samples are shown in Table 5 and Table 6.

Table 5. The relative deviations of different insulators (P=98.6 kPa, γ_{20}=300 μS/cm)

Differences	d=5mm	d=10mm	d=15mm	d=20mm
Δ_1%	15.7	11.3	9.0	7.8
Δ_2%	20.9	14.2	11.4	9.8

Table 6. The relative deviations of different insulators (d =10 mm)

γ_{20}(μS/cm)	Differences	P/ kPa			
		61.6	74.6	89.8	98.6
300	Δ_1%	8.5	7.9	10.4	10.1
	Δ_2%	10.0	10.2	11.3	12.4
450	Δ_1%	11.4	10.4	10.8	14.4
	Δ_2%	13.4	13.0	14.1	16.6
630	Δ_1%	13.0	12.3	14.9	14.8
	Δ_2%	14.5	14.0	16.3	17.0
1000	Δ_1%	10.4	10.1	11.9	12.7
	Δ_2%	11.9	12.9	13.7	15.7

From Table 5 and Table 6, it can be summarized as follows,

1) When air pressure is 98.7 kPa, γ_{20} is 300 μS/cm, E_h of composite insulator is slightly higher than of porcelain and glass insulators under the similar condition. Differences in the icing flashover voltage gradient between composite, porcelain and glass insulators narrow with an increase of ice thickness.

2) The material and profile of insulators influenced the icing flashover voltage gradient, and under the similar ice condition, composite insulator has better icing electrical performance. When the thickness of ice on the monitoring cylinder is 10 mm, the value of E_h of composite insulator is little higher than that of porcelain and glass insulators.

4 CONCLUSIONS

(1) For three types of insulators, the average ac icing flashover voltage decreases with increase of ice thickness, and this decreasing became gentle with the increase of d. U_{ave} of composite insulator is slightly higher than of porcelain and glass insulators. Differences in the icing flashover voltage between composite, porcelain and glass insulators narrow with an increase of d. And the effect of ice thickness on icing flashover voltage was more apparent for composite insulator than porcelain and glass insulators.

(2) For three types of insulator samples, the average flashover voltage under ice conditions decreases with a decrease in atmospheric pressure. The characteristic exponent m was related with the insulator material and profile. For composite insulator, the value of exponent m is 0.560, whereas it was 0.505, 0.490 for porcelain and glass insulators respectively. Specifically, for composite insulator, the influence of atmospheric pressure on the average flashover voltage is bigger. And the value of exponent m for three types of insulators tested, decreases as γ_{20} increases.

(3) The characteristic exponent b is related to the material and profile of insulator. When ice thickness is 10 mm, for composite insulator, the value of exponent b is 0.295, whereas it was 0.316, 0.320 for porcelain and glass insulators respectively. Furthermore, porcelain and glass insulator's b is little bigger than composite's under all the selected atmospheric pressures. And at the lower atmospheric pressure, the value of b is smaller, which means that the lower the atmospheric pressure, the lesser the influence of the pollution on the electrical performance of ice-covered insulators.

(4) The material and profile of insulators influenced the icing flashover voltage gradient, and under the similar ice condition, the icing electrical performance of composite insulator was slightly better than that of porcelain and glass insulators.

REFERENCES

[1] Meghnefi F, Farzaneh M, Volat C. Measurement of the evolution of dripping water conductivity of an ice-covered insulator during a melting period[C] // Conference on Electrical Insulation and Dielectric Phenomena. Quebec, Canada: [s. n.], 2008.

[2] Hu J, Sun C, Jiang X, et al. Flashover performance of pre-contaminated and ice-covered composite insulators to be used in 1000kV UHV AC transmission lines [J]. IEEE Transactions on Dielectric and Electrical Insulation, Vol. 14, No. 6, pp. 1347-1356, 2007.

[3] Yunpeng Liu, Song Gao, Daochun Huang, et al. Icing flashover characteristics and discharge process of 500 kV AC transmission line suspension insulator strings [J]. IEEE Transactions on Dielectrics and Electrical Insulation, Vol. 17, No. 2, pp. 434-442, 2010.

[4] Farzaneh M, Fofana I, Tavakoli C, et al. Dynamic modeling of DC arc discharge on ice surfaces [J]. IEEE Transactions on Dielectrics and Electrical Insulation, Vol. 10, No. 3, pp. 463-474, 2003.

[5] Zhang J, Farzaneh M. Propagation of AC and DC arcs on ice surfaces [J]. IEEE Transactions on Dielectrics and Electrical Insulation, Vol. 7, No. 2, pp. 269-276, 2000.

[6] Hemmatjou H, Farzaneh M, Fofana I. AC arc characteristics on a snow-covered cylinder[C] // Electrical Insulation and Dielectric Phenomena. Nashville, USA: [s.n.], 2005.

[7] Tian Yuchun, Jiang Xingliang, Shu Lichun, et al. AC flashover performance and voltage correction of iced 10 kV composite insulator in high altitude area[J]. High Voltage Engineering，Vol. 28, No. 6, pp. 12-15, 2002 (in Chinese).

[8] Sima Wenxia, Jiang Xingliang, Wu Lihui, et al. DC electric performance of icing and polluted 10kV composite insulator at low atmospheric pressures [J]. Proceedings of the CSEE, Vol. 24, No. 7, pp, 123-126.2004 (in Chinese).

[9] Jiang Xingliang，Shu Lichun, Zhang Zhijin, et al. Study on AC flashover performance and process of long iced insulator strings [J]. Proceedings of the CSEE, Vol. 25, No. 14, pp. 158-163, 2005 (in Chinese).

[10] Zhang Jianhui, Sun Caixin, Gu Leguan, et al. Flashover performance and voltage correction of polluted and iced insulator at low air pressure [J]. Electric Power, Vol. 21, No. 11, pp. 8-12, 1993 (in Chinese).

[11] Sun Caixin, Shu Lichun, Jiang Xingliang, et al. AC/DC flashover performance and its voltage correction of UHV insulators in high altitude and icing and pollution environments [J]. Proceedings of the CSEE, Vol. 22, No. 11, pp. 115-120, 2002 (in Chinese).

[12] Farzaneh M, Zhang J, Sakakibara T, et al. Effects of high altitude and atmospheric icing on the performance of outdoor insulators[C]// Transmission & Distribution Conference and Exposition. Latin America

IEEE/PES 2006 1-6.
[13] CHENG Deng-feng, JIANG Xing-liang, GUO Shou-xian, et al. DC flashover performances of different types of ice-coated insulators [J]. High Voltage Engineering, Vol. 35, No. 4, pp. 965-970, 2009.
[14] Farzaneh M, Kiernicki J. Flashover performance of IEEE standard insulators under ice conditions [J]. IEEE Transactions on Power Delivery, Vol. 12, No. 4, pp. 1602-1613, 1997.
[15] ZHANG Zhi-jin, JIANG Xing-liang, SUN Cai-xin, et al. Icing flashover performance of UHV DC composite insulators at low atmospheric pressure [J]. Proceedings of the CSEE, Vol. 28, No. 6, pp. 7-12, 2008.
[16] JIANG Xing-liang, WANG Bo, ZHANG Zhi-jin, et al. Influence of length and arrangement of iced insulator strings on DC flashover voltage at high altitude districts [J]. Proceedings of the CSEE, Vol. 28, No. 3, pp. 1-5, 2008.
[17] JIANG Xing-liang, LU Jie, DU Yuan, et al. AC flashover performance of iced insulators string structured with alternately large and small diameter sheds [J]. Proceedings of the CSEE, Vol. 29, No. 10, pp. 12-16 2009.
[18] Jiang, X.L., Yi, H.: '*Ice accretion on transmission lines and protection*' (China Power, Beijing, China, 2002).
[19] Shu, L.C., Farzaneh, M., Li, Y., Sun, C.X.: 'AC flashover performance of polluted insulators covered with artificial ice at low atmospheric pressure'. Electrical Insulation and Dielectric Phenomena Conf., pp. 609–612. 2001.
[20] Farzaneh M, Baker T, Bernstorf A, et al. Insulator icing test methods and procedures: a position paper prepared by the IEEE task force on insulator icing test methods [J]. IEEE Trans. on Power Delivery, Vol. 18, No. 4, pp. 1503-1515, 2003.
[21] Jiang Xingliang, Sun Caixin, Sima Wenxia, et al. Study on AC flashover performance and process of iced 10kV composite insulator [J]. Proceedings of the CSEE, Vol. 22, No. 8, pp. 58-61, 2002 (in Chinese).
[22] Xingliang Jiang, Ling Chen, Zhijin Zhang, Caixin Sun, Jinalin Hu.: 'Equivalence of influence of pollution simulating methods on DC flashover stress of ice-covered insulators', IEEE Trans. Power Deliv., Vol. 25, No. 4, pp. 2113–2120. 2010.
[23] X. Jiang, J. Hu, Y. Liang, L. Shu and S. Xie, "Pollution flashover performance of short sample for 750 kV composite insulators", IEEE Intern. Symposium on Electr. Insul., Indiana, USA, pp. 312-315, 2004.
[24] X. Jiang, L. Yu, J. Hu, Z. Zhang and C. Sun, "Lightning impulse discharge performance and voltage correction of long air gaps at lower atmospheric pressure", Proceedings of the Chinese Society for Electrical Engineering, Vol. 25, No. 11, pp. 152-156, 2005 (in Chinese).
[25] X. Jiang, L. Shu and C. Sun, *Insulation of Electric Power system under Pollution and Icing conditions*, Beijing, China Electric Power Press, 2009 (in Chinese).
[26] International Electrotechnical Commission (IEC). Artifical pollution test on high voltage insulators to be used on a.c. systems[S]. International Standard 60507, 1991.
[27] M. Farzaneh, Y. Li, J. Zhang, L. Shu, X. Jiang, W. Sima, and C. Sun, "Electrical performance of ice-covered insulators at high altitudes," IEEE Trans. Dielect. EIectr. Insul., Vol. 11, pp. 870–880, 2004.
[28] Zhang Zhijin, Jiang Xingliang, Ma Jun, et al. Study on icing performance of 110kV insulator strings at ac service voltage [J]. Proceedings of the CSEE, Vol. 26, No. 2, pp. 140-143, 2006 (in Chinese).

Xingliang Jiang was born in Hunan Province, China, on 31 July 1961. He received the M.Sc. and Ph.D. degrees from Chongqing University, Chongqing, China, in 1988 and 1997, respectively. His employment experiences include the Shaoyang Glass Plant, Shaoyang, Hunan Province; Wuhan High Voltage Research Institute, Wuhan, Hubei Province; and the College of Electrical Engineering, Chongqing University. His research interests include high-voltage external insulation and transmission line icing and protection. He is the member of working groups of CIGRE B2.29 and IWAIS.

Dr. Jiang has published two books and over 120 papers about his professional work. And He received the Second-Class Rewards for Science and Technology Advancement from the Ministry of Power in 1995 and 2009; Beijing Government in 1998; Ministry of Education in 1991 and 2001, respectively; the first-class Reward for Science and Technology Advancement from the Ministry of Power in 2004 and 2005; the Second-Class Reward for Science and Technology Advancement from the Ministry of Technology in 2005; the First-Class Reward for Science and Technology Advancement from the Ministry of Education in 2006; and the First-Class Reward for Science and Technology Advancement from Chongqing City in 2006 and 2008.

Ze Xiang was born in Sichuan, China, in 1987. He received his B.Sc. degree from Harbin University of science and technology in 2009. He is currently pursuing the Ph.D. degree in the college of electrical Engineering, Chongqing University. He is mainly engaged in the field of high-voltage external insulation and transmission line's icing.

Study on the Critical Anti-icing Current of Conductors and Its Impacting Factors

ZHANG Zhi-jin, BI Mao-qiang, JIANG Xing-liang, HU Jian-lin
The State Key Laboratory of Power Transmission Equipment & System Security and New Technology
School of Electrical Engineering, Chongqing University
Chongqing 400030, P.R.China
E-mail: xljiang@cqu.edu.cn

***Abstract*—Conductor icing is one of the major factors which affects the safe operation of the transmission line, and the anti-icing method based on the Joule heating effect is feasible and effective. This paper tries to analyze the heat transfer process of conductor's surface in critical icing condition and the effect of geometric shapes and water film covering conductors on heat transfer process. Based on Joule heating effect and the improvement of heat calculation, the formula to solve the critical anti-icing current considering the skin effect of conductors is proposed and also tested in an artificial climate chamber. The results showed that the relative error is within 10%. In addition, this paper also analyzes the effect of factors on critical anti-icing current and the results indicated that critical anti-icing current of the conductor has a relationship with the diameter and geometric profile of the conductor, ambient temperature and wind velocity. The critical anti-icing current (I_c) will increase sharply with the increasing of wind velocity and decreasing of ambient temperature.**

I. INTRODUCTION

Transmission line is the key equipment for electrical power delivery. Icing on the transmission line will bring galloping, flashover of, and collapsing of towers, so it poses great threats on the normal operation and security of the power system [1]. Anti-icing is taken as the most effective way to deal with the ice storm i.e. preventing the formation of ice [2]. Anti-icing technology has become the world's research focus in most countries [3]. At present, a simple and effective anti-icing method is to use the load current of the transmission line by adjusting the load current reasonability [4]. If there is enough Joule heat generated by the load current, the conductor will be heated and the temperature of its surface will be higher than the temperature of ice formation, so as to achieve an anti-icing purpose of transmission line.

Under the icing condition, the minimum current flowed through the conductor which can prevent the formation of ice on the conductor is defined as the critical anti-icing condition. Many studies on the increasing model of ice have been carried out. However, there is only little literature on the critical anti-icing model. The first calculating model of critical anti-icing model was proposed by J.E. Clem in 1930[5]. And then, Mccomber, Personne, Makkonen, Peter, Heyun Liu, and Jishi Chen described their improved calculating model as well. However, existing models have some disadvantages as follows: (1) ignoring the influence of skin effect and geometric profile on the impact of heat transfer. (2) Heat loss calculation method is not uniform. (3) Being short of adequate experiments to verify and the analysis on the factors to affect the critical anti-icing current is not sufficient. Therefore, based on the influence of skin effect, geometric profile and surface water film on the impact of the heat transfer process, this paper improved the heat transfer calculation method of temperature, analysis the influence of wind velocity and ambient temperature on the critical anti-icing current. And then, the critical anti-icing testes were carried out in the artificial chamber. The test results showed that the calculating accuracy is improved by using this model.

II. CALCULATING MODEL OF CRITICAL ANTI-ICING CURRENT

A. Analysis of heat balance under icing condition

According to the literature [1], the heat balance equation under icing condition can be obtained as following:

$$q_f + q_v + q_k + q_a + q_n + q_R = q_{cq} + q_e + q_l + q_s + q_i + q_r \quad (1)$$

Where: q_f is the latent heat of the frozen water, q_v is the air friction heat of water droplets, q_k is kinetic energy heat, q_a is the released heat of water, q_n is the short-wave radiation heat of sunlight, q_R is the Joule heat generated by the load current, q_{cq} is the convective heat loss, q_e is latent heat of water evaporation, q_l is the heat losses when the water was heated from T_a to T_f, q_s is the long-wave radiation heat loss, q_i is the Heat conduction losses, q_r is the heat losses taken away by the removed water. They can be obtained as follow:

(1) Joule heat (q_R)

Joule heat generated by the current heats the conductor and it will exchange heat with the environment through the conductor's surface. In unit time, Joule heat generated by the load current (I) flowing through the conductor can be obtained as follows:

$$q_R = I^2 R_{dc} \quad (2)$$

Where: $R_{dc,}$ is the d.c. resistance of the conductor. Since the skin effect and the effect of temperature, the a.c. resistance of the conductor should be amended as follows:

$$\begin{cases} R_{ac} = (1+y_s)R_{dc} \\ R_{dc} = R_{dc,20}[1+\alpha_{20}(T_S-20)] \\ y_s = \dfrac{(8\pi\times10^{-7}/R_{dc})^2}{192+0.8(8\pi f\times10^{-7}/R_{dc})^2} \end{cases} \quad (3)$$

Where: y_s is the skin effect coefficient, $R_{dc,\ 20}$ is the d.c. resistance of the conductor (20 ˚C), a_{20} is the resistance temperature coefficient, f is the frequency of power.

(2) Convective heat loss (q_{cq}):

The convective heat loss can be described as:

$$q_{cq} = A_{cq}h(T_s - T_a) \quad (4)$$

Where: h is the convective heat transfer coefficient, T_s is the temperature of conductor's surface; T_a is the temperature of environment, A_{cq} is the convective heat transfer area of conductor's surface.

When laminar flow is flowing through the cylinder, the characterized size is equal to the diameter of the object (2*R*) [11]. Therefore, the convective heat transfer coefficient of conductor's surface is:

$$\begin{cases} h = \dfrac{(N_{uf}+N_{up})k}{2R} \\ N_{uf} = A(G_r P_r)^B \\ N_{up} = A_p R_e^n P_r^m \\ G_r = \dfrac{g(T_s-T_a)(2R)^3}{v_0^2(273.15+(T_s+T_a)/2)} \\ P_r = \dfrac{\mu C_a}{k} \\ R_e = \dfrac{2R\rho_a v}{\mu} \end{cases} \quad (5)$$

Where: N_{uf} and N_{up} are the Nusselt number for forced-convection heat transfer and natural-convection heat transfer respectively, G_r is the Grashof number, P_r is the Prandlt number，v_0 is the kinematic viscosity of air, R is the outer diameter of conductor, g is the acceleration of gravity, k is the thermal conductivity of air, ρ_a is the density of air, R_e is Reynolds number, μ is aerodynamic coefficient of viscosity, v is wind velocity. According to literature [12], under the icing condition, A=0.48, B=0.25. A_p, n, and m are the constant determined by the Reynolds number, the values of A_p and n are shown as table 1.

Table 1 Relation between values of A_p, n and R_e

R_e	A_p	n
$40\le R_e\le 4000$	0.683	0.466
$4000\le R_e\le 40000$	0.193	0.618
$40000\le R_e\le 400000$	0.0266	0.805

(3) Latent heat of water evaporation (q_e)

Because of the present of water film on the conductor's surface, in theory, the temperature of the boundary between water film and air(T_{as}) is less than the temperature of conductor's surface. However, it is difficult to estimate the thickness of the water film, the T_{as} can be obtained as (T_a + T_s)/2 approximately. Thus, the latent heat of water evaporation q_e is [13, 14]:

$$q_e = \frac{0.622A_e L_v h(e(T_{as})-e(T_a))}{c_a p_a} \quad (8)$$

Where: A_e is the evaporation area, L_v is the latent heat of vaporization, P_a is the Pressure, the constant 0.622 is the ratio between the molecular mass of water vapor to dry air, c_a is air specific heat, $e(T)$ is the saturated vapor pressure (T ˚C).

Saturated vapor pressure is calculated using Goff formula recommended by the World Meteorological Organization (WMO), which is calculated as follows:

$$\begin{cases} \log_{10}(e(T)) = e_1+e_2+e_3+e_4+e_5 \\ e_1 = -7.90298(373.16T^{-1}-1) \\ e_2 = 5.02808\log_{10}(373.16T^{-1}) \\ e_3 = -1.3816\times10^{-7}(10^{11.344(1-T/373.16)}-1) \\ e_4 = \log_{10}(1013.246) \\ e_5 = 8.1328\times10^{-3}(10^{-3.49149(373.16T^{-1}-1)}-1) \end{cases} \quad (9)$$

where：T is the temperature (K)，$e(T)$ is the saturated vapor pressure (T ˚C, 10^2Pa).

(4) Friction heat (q_v)

Air flow through the conductor's surface will generate friction heat, which can be calculated as follows:

$$\begin{cases} q_v = \dfrac{A_v h_p r_c v^2}{2c_a} \\ h_p = \dfrac{N_{up}k}{2R} \end{cases} \quad (10)$$

Where: r_c is the coefficient of restitution of conductor's surface, c_a is the specific heat of air, h_p is the air forced convection heat transfer coefficient, A_v is the contacted area between air and conductor's surface.

(5) Kinetic energy heat (q_k)

In the unit time per unit length of conductor, mass of the collisions water droplets is $2Ra_1vw$. Setting capture coefficient as a_2, the heat generated by collisions between water droplets and conductor's surface can be obtained as follows:

$$q_k = \alpha_1\alpha_2 Rwv^3 \quad (11)$$

Where: w is the liquid water content (LWC) in air, v is wind velocity, R is the outer diameter of the conductor.

(6) Short-wave radiation heating (q_n) and long-wave radiation (q_s)

During the icing process in the nature, the weather condition is normally foggy, rainy or cloudy. Therefore, there is no direct sunlight being able to reach to the conductor's surface. And the short-wave radiation heating q_n is usually ignored [1]. According to stefan-Boltzman law of thermal radiation, long-wave radiation (q_s) can be expressed as:

$$q_s = A_s\varepsilon\sigma(T_s^4 - T_a^4) \quad (12)$$

Where: ε is the total radiation coefficient of water film relative to blackbody (approximately 0.95) [11], σ is the Stefan-Boltzman constant (5.5670 × 10^{-8} W / (m^2 • K^4)), A_s is surface area of water film.

(7) Removed water heat loss (q_r):

Assuming no droplets rebound, i.e. a_2 = 1, and assuming that the temperature of water droplets which leaved the conductor's surface is heated to the temperature of conductor, thus the heat loss taken away by the removed water can be described as follow:

$$q_r = 2\alpha_1\alpha_2 Rwvc_w(1-\alpha_3)(T_s - T_a) \tag{13}$$

(8) Other heat (q_f, q_a, q_l, q_i)

The released and loss heat (q_f, q_a, q_l,) and thermal conduction losses (q_i) were described in literature [1] in detail. The critical icing condition was studied in this paper, which means that there is no ice layer formatted on the conductor's surface. So the q_f, q_a, and q_l, can be ignored. Because of the uniform heating and good thermal conductivity of the conductor, the q_i can be also ignored.

B. Numerical calculation of the collision coefficient

According to the literature [15-17], a_1 has a relationship with the conductor's diameter, wind velocity, droplet diameter, air viscosity coefficient, density of the water droplet and air, and other factors. The calculation formula of a_1 is:

$$\alpha_1 = \begin{cases} A - 0.028 - C(B - 0.0454) & (\varphi > 100) \\ 0.457(\log_{10}(8K_0))^{1.634} & (\varphi < 100 \text{ and } K < 3) \\ \dfrac{K}{K + H_e} & (\varphi < 100 \text{ and } K > 3) \end{cases} \tag{14}$$

The parameters in the equation (14) are as follows:

$$\begin{cases} R_e = \rho_a dv / \mu \\ K = \rho_w d^2 v / (9\mu D) \\ \varphi = R_e^2 / K \\ A = 1.066K^{-0.00616} e^{-1.103/K^{0.688}} \\ B = 3.641K^{-0.498} e^{-1.487/K0.694} \\ C = 0.00637(\varphi - 100)^{0.381} \\ K_0 = 0.125 + (K - 0.125)/(1 + 0.1206R_e^{0.59}) \\ H_e = 1 + 0.5708 \times F - 0.73 \times 10^{-4} R_e^{1.38} \\ F = 1 + 0.212R_e^{0.6} + 2.6 \times 10^{-4} R_e^{1.38} \end{cases} \tag{15}$$

Where: R_e is the Reynolds number of water droplets, μ is the dynamic viscosity of air, D is the characteristic dimension of conductor i.e the conductor's diameter (2R), d is the median volume diameter (MVD) of droplets, ρ_w and ρ_a are the density of water droplets and air respectively.

C. Calculation of A_{cq}, A_e, A_s, A_v

Because of the contacted area between air and conductor is large than that between air and the smooth cylinder with the same diameter, the influence of conductor's geometry on the heat transfer process cannot be ignored.

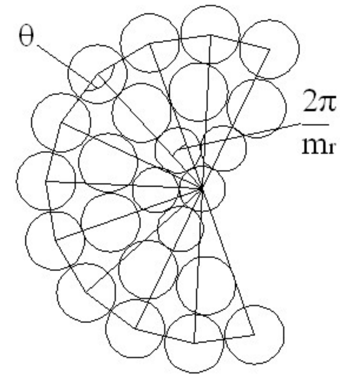

Fig.1 Cross-section map of conductor

Sectional view of conductor was shown in Figure 1. The m_r is the amount of the outermost aluminum wire. Surface area (S) of unit length of the conductor can be calculated by involving the equivalent radius R_{eq}, which can be described as follows:

$$\begin{cases} 2\pi R_{eq} = \dfrac{2\pi - \theta}{2\pi} \times 2\pi r_s m_r \\ \theta = \pi - 2\pi / m_r \end{cases} \tag{16}$$

And then

$$\begin{cases} R_{eq} = r_s(1 + m_r / 2) \\ S = 2\pi R_{eq} \end{cases} \tag{17}$$

Where: r_s is the radius of Aluminum wire, m_r is the amount of outermost aluminum wire.

Due to the impact of the water film, the conductor's superficial area contacted with air (S_a), called the surface of water film, should be less than the conductor's superficial area (S), as shown in Figure 2.

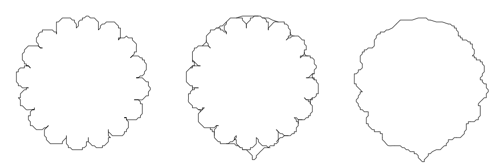

Fig. 2 Contact area of conductor with air in the state of critical icing

Then the surface coefficient (k_s) ban be defined as：

$$k_s = S_a / S \tag{18}$$

Obviously, the A_{cq}, A_s, A_v are equal to S_a. Literature [7,11] indicates that evaporation area (A_e) is half of the surface area of the conductor. However, during the test, the leeward of conductor can be covered by the water droplets because of its inertia or blowing by the wind. So in this paper, the evaporation area (A_e) is seen as equal to the superficial area of water film (Sa).

And then:

$$A_{cq} = A_s = A_v = A_e = S_a = 2\pi R_{eq} \times k_s \tag{19}$$

D. Calculation of critical anti-icing current

According to the literature [18], the critical icing condition is：

$$\begin{cases} \alpha_3 = 0 \\ T_s = 0 \end{cases} \tag{20}$$

Setting the equation (2-20) into equation (1), the critical anti-icing current can be obtained as:

$$I_c = \left\{ \frac{2\pi R_{eq} k_s}{R_{ac,c}} \left[h(T_s - T_a) + \frac{0.622h(e(T_s) - e(T_a))}{2c_a p_a} + \varepsilon\sigma(T_s^4 - T_a^4) - \frac{h_p r_c v^2}{2c_a} + \frac{R\alpha_1 wv}{2\pi R_{eq} k_s}\left(2c_w(T_s - T_a) - v^2\right) \right] \right\}^{0.5} \tag{21}$$

III. TEST OF CRITICAL ANTI-ICING CURRENT

A. Test equipment and samples

(1) Samples

Three types of aluminum cable steel reinforced, i.e. LGJ-95/15, LGJ-240/30, and LGJ-300/50 were tested in this paper, and their parameters were shown in table 2.

Table 2 Parameters of the conductors

Type	Amount (Al/Fe)	Diameter (Al/Fe)	Outer diameter (mm)	Resistance(d.c.) (Ω/km)	m_r
LGJ-95/15	26/7	2.15/1.67	13.61	0.3058	16
LGJ-240/30	24/7	3.60/2.40	21.60	0.1181	15
LGJ-300/50	26/7	3.83/2.98	24.26	0.09636	16

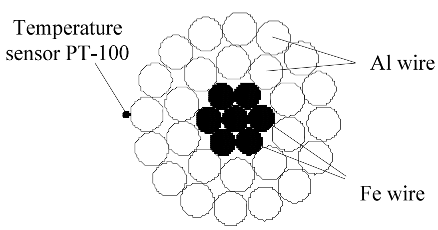

Fig. 3 Sections of three kinds of conductors

In order to reduce the influence of heat generated by the contact resistance on the heat balance of conductor under the critical icing condition, the clamps were installed at the two ends of the conductor, and the length of the conductor is more than 3 meters. To measure the temperature of conductor's surface, the temperature monitor (PT-100) was installed on outer surface of the windward side of the conductor, its installation position was shown in Figure 3.

(2) Equipment

The critical anti-icing current tests were carried out in the multifocal artificial chamber of Chongqing University. The detailed introduction of this chamber can be seen in literature [12, 15]. The arrangement of tested conductor is linear and horizontal, and the anti-icing a.c. current is generated by a current generator which can provide a maximum current of 5000 A.

The laser particle size analyzer was used to measure the median volume diameter (MVD) and liquid water content (LWC). Test water is tap water. In order to make the temperature of water droplets closer to the ambient temperature, the water was pre-cooling in the cooled environment, at the same time maintaining sufficient distance from the conductor and spraying system.

(3) Test method

(a) The samples were placed in the chamber for about 15 minutes, which made the conductor's temperature and the ambient temperature are the same.

(b) Starting the current generator, and let the a.c. current through the conductor. Meanwhile, the monitoring system for the temperature of the conductor's surface was also started; so as to monitor the conductor's surface temperature in real-time.

(c)Starting and adjusting spray system and speed control devices, and then the conductor was placed in the chamber for at less 30 minutes to make sure the temperature of the conductor reach stable.

(d) Monitoring the temperature of conductor's surface, if the temperature is under 0 ˚C, ice will form on the conductor' s surface, so ice layer should be removed and then the current (*I*) should be increased. If the temperature is higher than 0 ˚C, the current should be reduced. If the temperature is equal to 0˚C, the current (*I*) can be seen as the critical anti-icing current (I_c) under icing condition. It should be noted that after each change of current, the temperature must monitor for at least 30 minutes.

(4) Test results

Test environment condition is as follows: p_a = 98.51 kPa, Rh = 83.8%, MVD = 94.46 μm, LWC = 8.54 g/m^3.The test results were summarized in table 3. From table 3, it is easy to know that for all of the three types of samples, the critical anti-icing current increases sharply with the decreasing of ambient temperature. The critical anti-icing current is also impacted by the wind velocity , and it will increase with the increasing of wind velocity.

Table 3 Test results of critical anti-icing current

Type	Temperature (˚C)	wind velocity (m/s)	Test value (A)
LGJ-95/15	-1	1	98
	-3	1	174.2
	-5	1	212
	-5	3	274
	-5	5	331.2
	-7	1	252.8
	-9	1	300
LGJ-240/30	-1	1	166.5
	-3	1	300
	-6	1	430
	-5	3	549.7
	-5	5	605
	-9	1	518.1
LGJ-300/50	-1	1	210.5
	-3	1	365.4
	-5	1	451
	-5	3	577
	-5	5	678
	-9	1	593

B. Determination of surface coefficient ks

In fact, when the conductor reaches the critical icing condition, the surface of the water film thickness of the conductor is constantly changing, and its S_a is incalculable. In this paper, by comparing the experimental data with the calculated values, a surface coefficient k_s is selected to minimize the average relative error.

Though making the environmental parameters and conductor's parameters consistent with the experimental parameters, the calculating values of critical anti-icing current were obtained through the equation (21).The other calculating parameter can be set as follows: v_0=1.328×10^{-5} m^2/s, ρ_a=1.293 kg/m^3, μ=1.72×10^{-5} kg/(m·s), A=0.48, B=0.25, L_v=2492.78 kJ/kg, m=1/3, f=50 Hz, a_{20}=0.004℃, c_w=4.216 kJ/(kg·K), g=9.8 m/s^2, r_c=0.79, ρ_w=1000 kg/m^3, c_a=1.005×10^3 J/(kg·K), k=0.0244 W/(m·K), P_a=101.3 kPa.

Relative error (η) and the average relative error ($\overline{\eta}$) are calculated as follows:

$$\eta = \frac{|\text{Test value - Calculating value}|}{\text{Test value}} \times 100\% \qquad (22)$$

$$\overline{\eta} = (\sum^{n} \eta)/n$$

The calculated values were shown as figure 4.

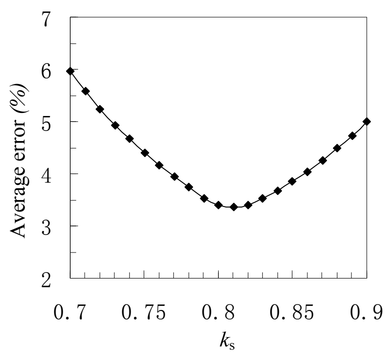

Fig. 4 Average relative error with different k_s

From the Figure 4, it is easy to know that, when k_s=0.81, the average relative error of critical anti-icing current is least i.e. 4.24%. Thus, in critical anti-icing current model of this paper, the surface coefficient k_s was chosen as 0.81.

C. Comparison with other calculating models

In order to verify this model, the calculated value using equation (21), test results and calculated values using other calculating model which described in literature [7,9,10] were summarized in figure 5. Figure 5 show that the calculated values are much closer to the real test value, which indicated that this calculating model is effective. And the calculating error is less than 10%. Compared with other model, the calculating accuracy of this model is improved.

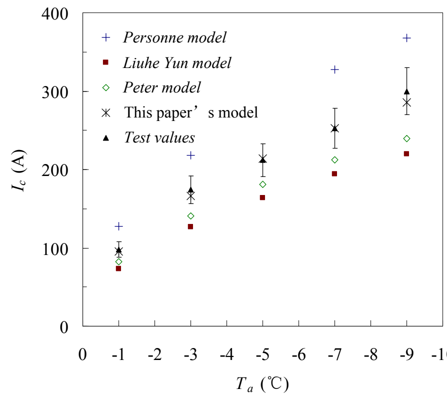

Conductor:LGJ-95/15，v=1 m/s，p_a=98.51 kPa，Rh=83.8%，d=94.46 μm，w=8.54 g/m^3，error bar：±10%

Fig. 5 Comparison of calculated values with the test results and other models

IV. CONCLUSIONS

(1) Under the icing condition, there is a critical anti-icing current(I_c) of conductor. If the load current of the conductor is greater than I_c, the Joule heat generated by the critical anti-icing current can prevent the formation of ice effectively.

(2) The calculating values through the model described in this paper keep in line with the test values. The calculating error is less than 10%. Compared with other model, the calculating accuracy is improved by using this model.

(3) The critical anti-icing current of the conductor has a relationship with diameter and geometric profile of the conductor, ambient temperature and, wind velocity. The critical anti-icing current (I_c) will increase sharply with the increasing of wind velocity and decreasing of ambient temperature.

REFERENCES

[1] Jiang Xingliang, Zhang Lihua. De-icing and Anti-icing of Transmission Lines[J]. High Voltage Engineering, 1997, 23(1): 73-76.

[2] Shan Xia, Shu Naiqiu. Discussion on Methods of De-icing for Overhead Transmission Lines [J]. High Voltage Engineering, 2006, 32(4): 25-27.

[3] M. Farzaneh. Atmospheric Icing of Power Networks[M]. New York: Springer, 2008.

[4] J. L. Laforte, M. A. Allaire, J. Laflamme. State-of-the-art on power line de-icing[J]. Atmospheric Research, 1998, 46(1-2): 143-158.

[5] V. Alexiades,A. D. Solomon. Mathematical Modeling of Melting and Freezing Processes[M]. New York: Hemisphere Publ. Corp., 1993.

[6] Jiang Xing,Yi Hui, Ice Accretion on Transmission Lines and Protection [M].Beijing: China Power Press, 2001

[7] Hu Yi. Analysis and Countermeasures Discussion for Large Area Icing Accident on Power Grid[J]. High Voltage Engineering, 2008, 34(02): 215-219.

[8] M. Farzaneh,K. Savadjiev. Statistical analysis of field data for precipitation icing accretion on overhead power lines[J]. IEEE Transactions on Power Delivery, 2005, 20(21): 1080-1087.

[9] S. Y. Sadov, P. N. Shivakumar, D. Firsov, S. H. Lui, R. Thulasiram. Mathematical Model of Ice Melting on Transmission Lines[J]. J Math Model Algor, 2007, 6(1): 273-286.

[10] K. Szilder,E. P. Lozowski. Simulation of icicle growth using a three-dimensional random walk model[J]. Atmospheric Research, 1995, 36(3-4): 243-249.

[11] M. Huneault, C. Langheit, J. Caron. Combined models for glaze ice accretion and de-icing of current-carrying electrical conductors[J]. IEEE Transactions on Power Delivery, 2005, 20(2): 1611-1616.

[12] P. Personne,J. F. Gayet. Ice accretion on wires and anti-icing induced by the Joule effect [J]. Journal of Applied Meteorology, 1988, 27(2): 101-114.

[13] Gu Ming, Ma Wenyong, Quan Yong, Huang Peng. Aerodynamic Force Characteristics and Stabilities of Two Typical Iced Conductors [J]. Journal of Tongji University(Natural Science), 2009, 37(10): 1328-1332.

[14] Guo Haifeng, Liu Tiantian, Li Xiquan, Ma Jinghao. The Review and Reconsider of Icing Disaster & Countermeasure in Hunan Electric Grid [J]. Central China Electric Power, 2008, 10(02): 25-28.

[15] Lu Jiazheng, Jiang Zhenglong, Zhang Hongxian, Lei Hongcai, Peng Jiwen. Technical Analysis of Hunan Power Grid Ice Disaster in 2008. [J]. Hunan Electric Power, 2008, 3(03): 1-9.

[16] G. Poots,P. L. I. Skelton. The effect of aerodynamic torque on the rotation of an overhead line conductor during snow accretion[J]. Atmospheric Research, 1995, 36(3-4): 251-260.

[17] Liang Wenzheng. Design and Countermeasure of fighting with ice and snow for overhead power transmission line[J]. Electric Power Equipment, 2008, 9(12): 19-22.

[18] Xu Shukai, Zhao Jie. Summarize the ice disaster accidents and its anti-icing technology in power system[J]. Southward Power System Technology, 2008, 2(2): 1-2.

[19] J. V. C. Vargas, A. Bejan, A. Dobrovicescu. The melting of an ice shell on a heated horizontal cylinder[J]. Journal of Heat Transfer, 1994, 116(3): 702-708.

[20] J. D. McCurdy, C. R. Sullivan, V. F. Petrenko. Using dielectric losses to de-ice power transmission lines with 100 kHz high-voltage excitation[J]. Conference Record of the 2001 IEEE Industry Applications Conference, Vols 1-4, 2001, 2515-2519.

[21] Jiang Xingliang , Fan Songhai , Zhang Zhijin , Simulation and Experimental Investigation of DC Ice-Melting Process on an Iced Conductor，IEEE Transactions on Power Delivery，2010，25(02) : 919−929

[22] Fan Songhai , Jiang Xingliang , Sun Caixin , Temperature Characteristic of DC Ice-Melting Conductor，Cold Regions Science and Technology，2011，65(1) : 29−38

[23] Jiang Xingliang, Fan Songhai, Hu Jianlin, Zhang Zhijin, Sun Caixin, Analysis of critical ice-melting current for short circuit DC transmission line, Proceeding of the CSEE，2010，30(1) : 111−116

[24] Jiang Xingliang, Wang Daxing, Fan Songhai, Zhang Zhijin, Hu Jianlin. Experimental research on maximum temperature of ice-covered conductors during DC ice-melting[J]. High Voltage Engineering, 2009, 35(11): 2796-2799

Comparison of AC Ice-melting Characteristics of Conductors with or without the Freezing Rain Falling

SHU Li-chun, YUAN Wei, LUO Bao-song, JIANG Xing-liang, HU Qin, HE Yan-zhun

The State Key Laboratory of Power Transmission Equipment & System Security and New Technology
School of Electrical Engineering, Chongqing University
Chongqing 400030, P.R.China
E-mail: xljiang@cqu.edu.cn

***Abstract*- The icing disaster of transmission line is becoming one of the most serious harm to power systems. So far, few researches have considered how the icing state of the conductor surface will influence ice-melting. In this paper, the glaze ice accretion on conductors was imitated in the artificial climate chamber, and tests about the ice-melting process with freezing rain falling were conducted. By means of thermodynamic theories and dynamic simulation of ice-melting process, the heat balance equation of the conductor ice-melting process has been established. . It shows that test results and simulation results are basically the same, the conclusions are listed as follows: （1）The joule heat generated by conductor conduct radiation heat through the leeward side of ice surface when freezing rain falling in environment. （2）The maximum temperature on conductor surface appears in the lower surface every moment during the ice-melting. （3）The highest temperature appears at the time when ice is shedding in the process of ice-melting.**

I. INTRODUCTION

The icing disaster on transmission line is one of the most serious damage to electrical power system. Glaze and rime ice accretion increasing the load of transmission lines, which have occurred in many countries including China, America, Canada, Russia, Switzerland, result in line break, pole collapse, insulator flashover, line trip, conductor gallop, communication interruption and damage of equipment such as insulator and fittings etc[1-4]. Thus far, what really work in transmission line anti-icing projects are the methods of AC and DC thawing[5]. But these methods of anti-icing and ice-melting which have been presented are remedies only applied after the icing disaster. At the moment ice-melting theory and tests have both considered without freezing rain falling[7-11]. However, prevention should be the basic principle of solving the problem about conductor icing, while remedies and emergency measures are taken after conductor icing seriously[12,13]. With increased awareness for security and reliability of power grid and the development of smart grid, there were some method like constant electricity, real-time anti-icing and de-icing of conductor found.

Therefore, it is practical significance to research characteristics of conductor ice-melting in the process of freezing rain falling.

II. TEST FACILITY, SPECIMEN AND METHODS

A. *Test facility*

There is the multi-function artificial climate chamber with a diameter of 7.8m, 11.6 m high for test, consisting of refrigerating system, vacuum system, regulatory system of wind speed, spray system etc. In this paper, we used LGJ-240/30 and LGJ-400/35 wires (the length of testing specimen is 4m) to conduct tests. The structure of testing wire is shown in Figure 1.1.

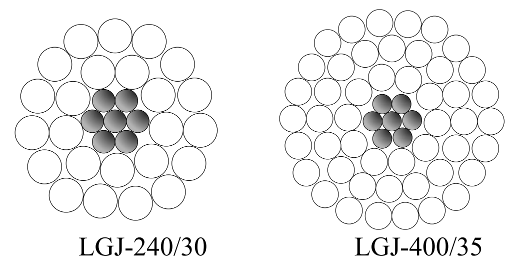

Fig.1.1 Schematic cross-section of ACSR(● is steel core, ○ is aluminum lamination)

Figure1.2 and 1.3 show the principle of experimental wiring and temperature sensor layout. The maximum current DC ice-melting device can provide is 5000A. In the test, acquisition system was used for data-collection, while thermocouple sensor sticking to surface was applied to the measure of surface temperature of wires and ice surface temperature. Wind speed was measured by handheld anemograph and ambient temperature was measured by the PTU2000 numerical temperature measuring instrument.

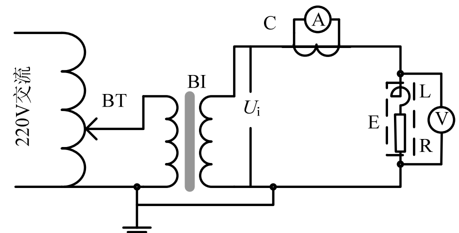

(BT:voltage regulator; BI:Current generator; C:Ammeter; E:Wire; L:Inductance; R:Resistance)

Fig. 1.2 Experiment circuit

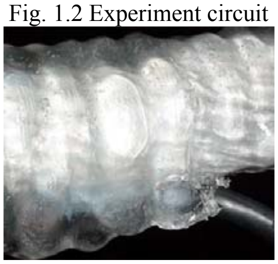

Fig.1.3 Sensor for measuring temperature

III. TEST RESULTS AND ANALYSIS

A. Physical and mathematical model of de-icing

The joule heat, which is produced by melting current, heats wires. Then heat transfers to the ice layer, and dissipates on the ice surface. The joule heat produced by current is used in five parts: □heat absorbed in the temperature rise of wires; □heat absorbed in the temperature rise of ice layer; □heat required for de-icing layer; □heat dissipation through radiation on the surface of ice layer; □heat dissipation through convection on the surface of ice layer. Unit length of the wires in the process of de-icing at any time of the thermal equilibrium equation can be expressed as[7] :

$$I^2 r_{\mathrm{T}} = \rho_{\mathrm{i}} L_{\mathrm{F}} \frac{dV_{\mathrm{m}}}{dt} + \sum_{j=1}^{3} \rho_{\mathrm{j}} V_{\mathrm{j}} C_{\mathrm{j}} \frac{dT_{\mathrm{j}}}{dt} + P_{\mathrm{C}} + P_{\mathrm{R}} \tag{2.1}$$

Where, I is the melting current, A; r_T is the conductor resistance, Ω; dV_{m} is the melting section increment, m^2 ; V_{j} (j=1, 2, 3), respectively, is the cross-sectional area of the ice layer, wire steel core and aluminum core, m^2; The V_{j} is a function of de-icing time; T_{j} (j=1, 2, 3), respectively, is the temperature of the ice layer, wire steel core and aluminum core in the process of de-icing at any time, and T_{j} is a function of time and space; ρ_{j} (j=1, 2, 3), respectively, is the density of the ice layer, wire steel core and aluminum core, kg/m^3 ; C_{j} (j=1, 2, 3) is the specific heat of the ice layer, wire steel core and aluminum core, J/(kg·K); L_{F} is the latent heat of fusion of ice, J/kg; P_{R} is the heat dissipation through radiation of unit long ice surface, W/m; P_{C} is the heat dissipation through convection of unit long ice surface, W/m.

According to plenty of experiments of wire de-icing in the artificial climate chamber, Jiang Xingliang, scholar of Chongqing university, comes to the conclusion [8] : when the wire surface temperature is 0 □, the ice inside surface in contact with the wire surface begins to melt. In the process of melting, ice temperature maintains at 0 □. The water melted from ice loses through a small hole in the ice, forming an air gap at the bottom of the wire. Under the action of gravity, the ice at the top of the wire gradually melts, and the air gap at the bottom of the wire gradually grows. The air gap surrounding the wire in the melting process is akin to the oval wire. The cross section of wires and the ice in the process of de-icing is shown in figure 2.1.

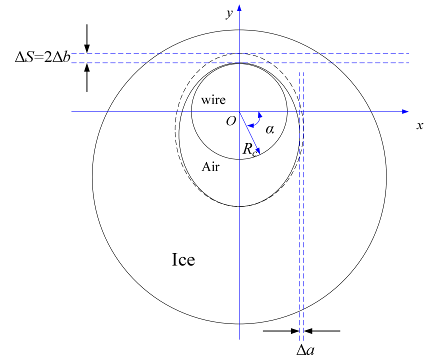

Fig.2.1 De-icing section diagram

When there is freezing rain, on the windward side of the ice, heat transfer process occurs between supercooled water droplets and the surface of wires. In order to analysis the de-icing process in freezing rain, that assume a uniform cylindrical glaze to simplify wire icing, and ignore the new ice.

When the wire surface temperature is 0 □, the ice in contact with the wire surface begin to melt. In the process of de-icing, the ice on the inner surface is de-icing state, its temperature remains at 0 □. In windward side of the ice new supercooled water droplets arrive, and latent heat released from icing, loses in the form of convection and radiation. The windward side of the ice surface will keep state of ice, its temperature remains at 0 □. The windward side of the ice is 0 □ isothermal body. In the leeward side of the ice, supercooled water droplets haven't arrived, and joule heat produced by wires makes convection and radiation loss with the environment through ice leeward side.

Through the above analysis, the boundary conditions are:

1) Ice windward surface meets the first kind of boundary conditions.

Outside the ice surface windward $\Gamma_{1\mathrm{Y}}$, supercooled water droplets always arrive and kept the ice state. Its temperature remain at 0□. So it satisfies the first kind of boundary condition:

$$T_{\Gamma 1Y} = 0 \tag{2.2}$$

Where, $T_{\Gamma 1\mathrm{Y}}$ represents the temperature of boundary of the ice on the windward side,□;

2) Ice boundary on the leeward side $\Gamma_{1\mathrm{B}}$ meets the third kind boundary condition

On the leeward side of ice boundary $\Gamma_{1\mathrm{B}}$, by convection and radiation heat exchange with the air, which meets[16]:

$$-\lambda \frac{\partial T_{\Gamma 1B}}{\partial n}\Big|_{\Gamma 1B} = h(T_{\Gamma 1B} - T_a) \tag{2.3}$$

Where, $-\lambda \dfrac{\partial T_{\Gamma 1B}}{\partial n}\Big|_{\Gamma 01B}$ is the heat flow density in the boundary $\Gamma_{01\mathrm{B}}$ normal direction, W/m^2; $T_{\Gamma 01B}$ is the temperature of the boundary $\Gamma_{1\mathrm{B}}$, □;

3) The junction Γ_2 of ice and the air gap meets the first kind of boundary conditions

When the ice begins to melt and the air gap has formed, the interface Γ_2 is always melt state and the temperature maintains at 0 □. So the interface Γ_2 meets the first kind of boundary conditions:

$$T_{\Gamma 2} = 0 \tag{2.4}$$

Where, $T_{\Gamma 2}$ represents the temperature of boundary Γ_2, □.

The temperature distribution of wires and ice at the initial moment is the foundation of accurately calculating de-icing time and wire's temperature. Whether there is freezing rain or not, the temperature distribution of wires and ice at the initial moment is different.

Therefore, firstly, accurately calculate the temperature distribution of wires and ice at the initial moment of current de-icing, when there is freezing rain. On the windward side of the ice keep it ice, and its temperature remains at 0 □. In the leeward side no supercooled water droplets arrive, so the heat there will lose in the form of convection and radiation. Heat transfer concludes ice windward side to wires, wires to the ice leeward surface and heat exchange with air. Ice wires meet heat conduction differential equation:

$$0 = \frac{\partial}{\partial x}(\lambda_j \frac{\partial T_j}{\partial x}) + \frac{\partial}{\partial y}(\lambda_j \frac{\partial T_j}{\partial y}) \tag{2.5}$$

Where, j(j=1, 2, 3) represents the division of ice conductor area, including ice, wire steel core and aluminum core. T_j represents the temperature of area j ; λ_j represents thermal conductivity of area j. Formula (2.5) meets the above boundary conditions 1) and 2). Solve formula (2.5) in the method of finite element static, we can get the temperature distribution of wires and ice at the initial moment.

B. Comparative analysis of simulation results and test results

Using the growth law of oval air gap and FEM(Finite Element Method) simulation algorithm described in the literature[8], after setting the input parameters, we can make dynamic simulation of current ice-melting under icing conditions. In Fig 2.2, the melting process of iced conductor (LGJ-400) is simulated under ice-melting condition as follows: LGJ-240/30, T_a=-3□, v_a=5m/s, d=9.7mm, I=600A.

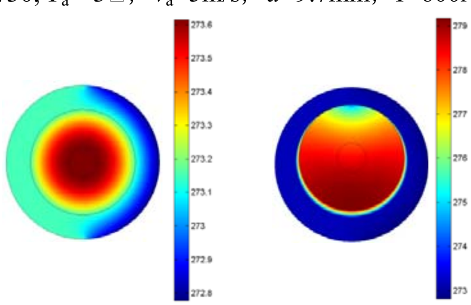

t=1min t=9min

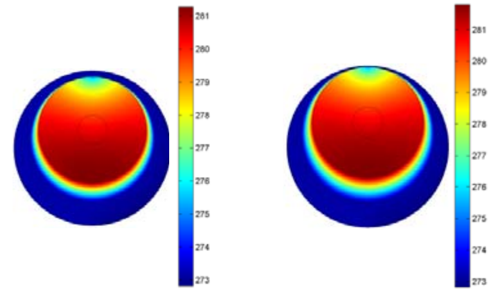

t=25min t=33min

No rain Rain

Fig 2.2 Temperature distribution simulation of ice-melting of ice covered conductor under icing condition

Comparative analysis to Fig 2.2 shows that:

□During the ice-melting progress, the windward side of ice temperature is kept at 0□, the leeward side of ice temperature is below 0□, these show that the joule heat generated by conductors passes through the ice layer of leeward side and conduct convection and radiation heat on the ice layer surface of leeward side.

□The upper surface of conductor, next to the ice, maintained the temperature of 0□;

while the conductor lower surface is at higher temperature because air gap hinders temperature conduction. It shows that the highest temperature of conductor surface appears in the lower surface of conductor during ice-melting.

③With time increases, the temperature distribution changes. With the growth of ice-melting time, the conductor temperature increases gradually. In the process of ice-melting, the maximum temperature of conductor is the position below conductor when ice is shedding , as shown in Fig 2.3.

Fig 2.3 shows the temperature characteristic curves of the conductor (LGJ-240/30) lower surface from experiments in the following conditions: T_a=-3□, v_a=5m/s, d=9.7mm, I=600A.

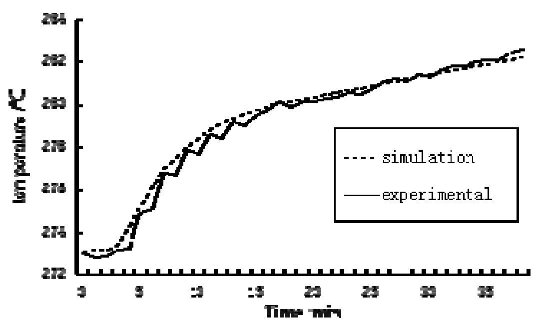

Fig 2.3 the temperature characteristic curves of the conductor lower surface

From Fig 2.3 we can see that with the growth of time the conductor surface temperature variation between simulation values and experimental values are basically consistent. The conductor temperature increases gradually with ice-melting time increases, and the highest temperature of conductor appears at the time when ice is shedding in the process of ice-melting.

Tab.2.1 Experimental verification of ice melting time

Wire models		LGJ-240/30		
d/mm		5	10	10
T_a /□		-3	-5	-5
v_a /(m/s)		5	3	5
I/(A)		600	800	800
t_{MR}/	Measure	30	40	35
(min)	Calculate	34	36	38

Wire models		LGJ-400/35		
d/mm		5	6	5
T_a /□		-5	-3	-1
v_a /(m/s)		5	3	1
I/(A)		800	800	1000
t_{MR}/	Measure	45	45	24
(min)	Calculate	46	44	23

Table 2.1 shows that simulation and experimental results are basically consistent, the absolute error ranges from 0.1% to 7%.

IV. CONCLUSION

In this paper, ice-melting experiment was carried out in the artificial climate chamber as well as ice-melting thermodynamic process was analyzed, meanwhile simulation analysis of ice-melting process simulation under the experimental condition was carried out. It shows that test results and simulation results are basically the same, the conclusions are listed as follows:

□ The joule heat generated by conductor conduct radiation heat through the leeward side of ice surface when freezing rain falling in environment.

□ The maximum temperature on conductor surface appears in the lower surface every moment during the ice-melting.

□The highest temperature appears at the time when ice is shedding in the process of ice-melting.

ACKNOWLEDGMENT

This work was supported by the National Key Program（973 program） on Basic Research (No.2009CB724502) from the Ministry of Science and Technology, China.

REFERENCES

[1] Xingliang Jiang, Lichun Shu, Caixin Sun, Insulation of Electric Power System under Pollution and Icing Conditions , China Electric Power Press, Beijing, China, 2009,160-179.

[2] Xingliang Jiang，YI Hui． Transmission line's icing and protection [M]. China Electric Power Press, Beijing, China, 2002.

[3] Phan L C，Matsuo H． Minimum flashover voltage of iced insulators[J]． IEEE Trans on Electrical Insulation，1983，EI-18(6)：605-618.

[4] Xingliang Jiang, Lihua Zhang. De-icing and Ant i-icing of T ransmission Lines[J]. High voltage Engineering, 1997(01).

[5] JIANG Xing-liang,MA Jun,WANG Shao-hua,et al. Analysis Icing Accident of Transmission Line [J]. Electric Power, 2005(11).

[6] Yamada M, Fukusako S, Morizane H, et al. Melting characteristics along a bundle of horizontal heated cylinders immersed in a liquid ice layer[J]. Experimental Thermal and Fluid Science, 1996,12(3):305-312.

[7] M. Farzaneh, C. Volat, “Electric field modelling around an ice-covered insulator using boundary element method”, Conference Record of the 2000 IEEE International Symposium on Electric Insulation, pp. 349-355, 2000.

[8] Jiang X, Fan S, Zhang Z, et al. Simulation and experimental investigation of DC ice-melting process on an iced conductor[J]. Power Delivery, IEEE Transactions on, 2010, 25(2): 919-929.

[9] Laforte J L, Allaire M A, Laflamme J. State-of-the-art on power line de-icing[J]. Atmospheric Research, 1998,46(1–2):143-158.

[10] PÉTER Z. Modeling and Simulation of the Ice Melting Process on a Current- Carrying Conductor[D]. UNIVERSITÉ DU QUÉBEC, 2006.

[11] M. Huneault C L J C. Combined models for glaze ice accretion and de-icing of current-carrying electrical conductors[J]. IEEE Transactions on Power Delivery, 2005, 20(2): 1611- 1616.

[12] M. C. Kim C K C D. Analysis of the onset of buoyancy-driven convection in a water layer formed by ice melting from below[J]. International Journal of Heat and Mass Transfer, 2008, 51 (21 -22):5097-5101.

[13] Asaithambi. N S. Numerical modeling of Stefan problems[J]. Mathematical and Computer Modelling, 1990, 14 (1): 139-144.

Research on Stranded Conductor Corona Onset Characteristic after Energizing Rime Icing

HU Qin, CHEN Ji, JIANG Xing-liang, HU Jian-lin

The State Key Laboratory of Power Transmission Equipment & System security and New Technology
School of Electrical Engineering, Chongqing University
Chongqing, 400030, China,

ABSTRACT

Rime makes conductor surface extremely rough and it will distort the electric field seriously. Numerous studies about icing conductors had been done but the fact that conductors operating under voltage was always ignored and Aluminum pipes were applied to study the actual conductors. Moreover, no lights had been thrown into decrease regularities of corona onset voltage(COV) after energized icing. Therefore, a series of AC corona tests of charged rime icing had been done in the Multi-functional Climate Chamber. UV imaging technology and I-U curve fitting were applied to measure the COV and the finite element model was established to research field strength after icing. Results show that rime can bring COV down significantly. Ice-tree of rime in various shapes lead to different COV values. Increasing in icing time will raise COV values while the rising speed slowed down gradually. Conductivity has no impact on rime form or COV. The sharper ice-trees are, the more seriously electric field distorted and the lower COV values. This paper can provide information about design of transmission lines in regard to corona losses after icing.

Index Terms —**stranded conductor, energized icing, rime, corona onset voltage, conductivity, UV imaging.**

1 INTRODUCTION

China has complicated topography and climates which will cause rime appears frequently in winter. After iced by Rime, the safety of transmission lines could be impacted and corona problems become more and more prominent due to the tips of rime ice-tree [1]. Surface of wires become so rough after coated by rime that the electric field will be distorted which can lead to partial corona discharge even wires operated under low voltage, after that COV will be cut down and leads to corona loss or electromagnetic pollutions, corona problem is getting more attention than before [2,3].

Nowadays, researches on conductor COV in depth is mainly under dirty, rainy and high altitude conditions in worldwide [4]. Although large numbers of tests carried out on icing wires, it may lead to the differences between practice and theory because most of them ignored that operating conductors energized icing, and there is no tests analyze how charged rime icing influents the regularities of conductor COV [5-7]. Peek formula were gained from massive tests on wires for COV [8], but different environmental factors were overlooked in Peek formula, so there exist many differences between calculation and engineering application [9]. In paper [10], studies show that icicle tips will appear during the icing process can distort electric field, and the corona points may appear partially even applied low voltage, but this paper ignored the changing law of COV after icing. Study on corona discharge characteristics of glaze icicle under DC positive voltage [11] shows that discharge quantity is larger when tips growing longer and sharper under the same voltage and higher conductivity will enhance discharge amount of glaze icicle. How the AC field affects shapes of rime ice-tree was discussed in paper [12] and quantity of corona discharge was measured under different rime shapes, results show that the longer and sharper ice-tree are, the easier corona discharge phenomenon will occur in rather low voltage. In paper [13], icing will influent corona discharge of wires in natural condition and results show that COV will drop after icing, but papers without taking notice of fall reasons.

To find out the change rule of COV after energized rime icing, a series of tests under various AC field to form different shape of rime are implemented, four stranded wires LGJ-(70/40, 185/25, 240/30, 400/35) are applied in this test. The UV imaging technology and I-U curve fitting method are adopted to measure and analyze COV. Meanwhile, influence of conductivity on COV is explored too. Meanwhile the finite element model is established to study the change regulation of electric field on wire's surface based on Maxwell software.

2 TESTS EQUIPMENT, SPECIMENS AND PROCEDURE

2.1 EXPERIMENTAL EQUIPMENT

This experiment is implemented in the Multifunctional Artificial Climate Chamber with diameter of 2.0m and length of 3.8m, as shown in Fig.1.

Figure 1. Multifunction artificial climate chamber

Temperature can drop to as low as -36℃ in chamber and some standard spray nozzles are installed into the chamber which was recommended by International Electro technical Commission (IEC) [14]. Accordingly, different icing forms can be simulated by spray nozzles such as glaze, rime and mixed-phase icing, etc. The fan in chamber can not only imitate wind with certain speed but also make the indoor temperature and particle size evenly distributed. Testing voltage is introduced from one side of the chamber by porcelain casing through the wall, AC icing test principle wire diagram as shown in Fig.2.

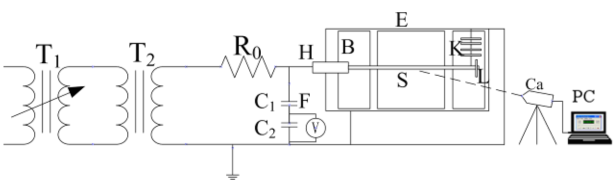

T_1: 10kV voltage regulator, **T_2:** AC testing transformer, **R_0:** protective resistance, **H:** high voltage wall bushing, **F:** AC capacitor divider (ratio 10000:1), **V:** voltmeter, **E:** artificial climate chamber, **S:** conductor, **B:** corona cage, **K:** insulator, **L:** grading ring, **Ca:** UV imaging instrument, **PC:** computer
Figure 2. Schematic diagram of AC test circuit

2.2 EXPEIMENTAL SPECIMENS

Conductors are energized icing in the center of a three-section corona cage whose diameter is 2m and length is 2.5m, and the middle section is applied to measure COV while other parts grounded. Four stranded conductors whose length are 2m and structure parameters are shown in Tab.1, where 2a and 2b represent for diameter of single Aluminum and steel core respectively, 2c is for wire diameter and n is outermost layer of wires, and wires' ends are fitted with grading rings to eliminate the end effect. As field density on transmission line surface is 15kV/cm in common [15], so five grades of field are set in this test namely 0, 5, 10, 15 and 20kV/cm in order to find out the general rules of how different rime ice-tree shapes affect COV respectively.

Rime belongs to dry growth characteristics, and droplets will be frozen quickly when it reaches wire surface due to the low temperature [16]. Forming condition of rime is shown in Tab.2, where d_a is droplet diameter, D is density of soft rime, T_a is environmental temperature, W is absolute humidity and γ_{20} is conductivity in 20℃. To gauge environmental parameters, PTU200 is adopted which is a digital temperature, humidity and pressure multifunctional measuring apparatus, droplet diameter and absolute humidity are measured by laser particle analyzer. Water conductivity is surveyed by DD-810E conductivity meter. As the major extent of spectra which is produced by corona discharge is in invisible ultraviolet region, CoroCam IV+ ultraviolet imager [17] is applied to observe development of corona discharge, because there exists an obvious relationship between photon numbers and corona onset voltage [18, 19], measuring devices are shown in Fig.3.

Table 1. Parameters of four stranded conductors

specimens	2a/mm	2b/mm	2c/mm	n
LGJ-70/40	2.72	2.72	13.60	12
LGJ-185/25	3.15	2.10	18.90	15
LGJ-240/40	3.42	2.66	21.66	16
LGJ-400/35	3.22	2.50	26.82	22

Table 2. Forming condition of rime in the chamber

Soft Rime				
d_α (μm)	D (g/cm^3)	T_α (□)	W(g/m^3)	γ_{20} ($\mu s/cm$)
20	0.52	-15	2.5	30 400 800 1200

(a) CoroCam IV+ (b) PTU 200 (c) DD-810E
Figure 3. Measuring devices

2.3 CRITERION FOR CORONA ONSET VOLTAGE

In Fig.4, the UV camera was adopted to record pictures of corona photons of LGJ-185/25 which was energized icing for 30min under 20kV/cm. From Fig.4a to 4b, we can find out that only a few photons appear when applied voltage was less than 65.4kV, that means there is no corona phenomenon occurs on conductor surface. When voltage was set to higher than 69.1kV, from Fig.4c to 4d, camera captured a sudden increase in number of photons. Hence, we can deduce that COV should be around 69kV.

Average photon number was calculated from 30sec video under certain voltage and measured for three times, afterwards the characteristic curves of photon-voltage are shown in Fig.5a, where N is photon numbers and U_a is testing voltage. Voltage values which corresponding to the knee point of curves are the COV. The values of COV are calculated by I-U curve fitting as shown in Fig.5b.

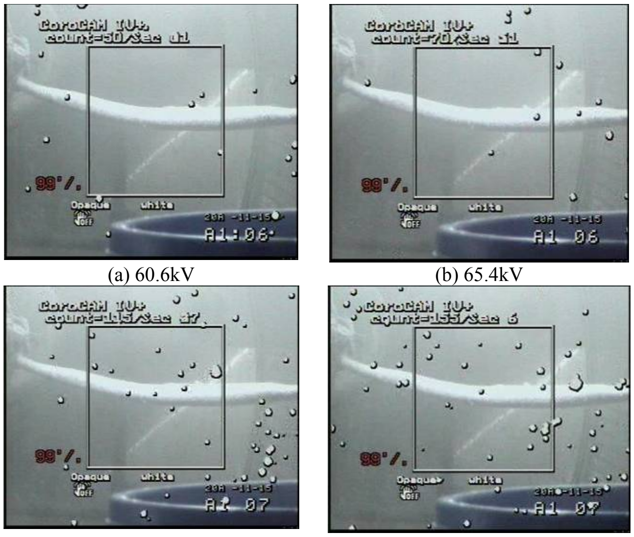

(a) 60.6kV (b) 65.4kV

(c) 69.1kV (d) 75.6kV

Figure 4. Corona discharge images of LGJ-185/25 after rime icing

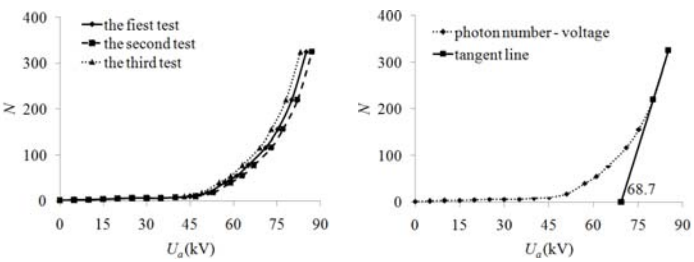

(a) measurements curve (b) corona onset voltage

Figure 5. Calculation for conductor corona onset voltage

2.5 ELECTRIC FIELD AROUND STRANDED WIRES

In order to simplify the comparison of calculation and test results, an infinitely long stranded conductor was placed in the center of cylinder which constitutes coaxial electrode structure, as shown in Fig.7. External diameter of stranded conductor is defined to be 2*b*, the number of strands which forming the outer layer is *n*, the radius of each strand is *a*, and radius of the grounded cylinder is *c*, where c≫b is assumed [20].

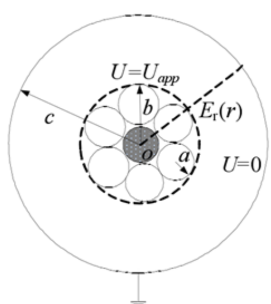

Figure 7. Calculation model of coaxial electrode

Once the external diameter 2*b* and number of strands *n* were given, radius of strand *a* can be determined by relationship:

$$a = \frac{b\sin(\pi/n)}{1+\sin(\pi/n)} \tag{3}$$

Numerical method has been applied to calculate electric field around energized conductor, and a semi-analytic expression developed by Andrews was adopted. The sag of wire was ignored when COV was calculated, and the equations can be written as:

$$E_0 = \frac{U}{b\ln(c/b)} \tag{4}$$

Equation (4) shows the field strength on stranded conductor, where *U* is applied voltage.

To apply four kinds of field strength which are 5, 10, 15 and 20kV/cm on stranded conductors, corresponding voltage values are shown in Tab.3.

Table 3. Voltage corresponding to selected field strength

Field strength (kV/cm)	5	10	15	20
LGJ-70/40 (kV)	17	34	51	68
LGJ-185/25 (kV)	22	44	66	88
LGJ-240/40 (kV)	24.5	49	73.5	98
LGJ-400/35 (kV)	29	58	87	116

3 TEST RESULTS AND ANALYSES

3.1 INFLUENCED BY ENERGIZED RIME ICING

Shapes of rime will change with icing field which produced by various voltages to conductors, thus it may lead to different COV values. To find out the law, water conductivity was set to 400$\mu s/cm$(corrected to 20℃), and conductors were iced under several voltages for 30min. Then UV camera was adopted to analyze COV. Different ice-tree forms of LGJ-185/25 under various field strength are shown in Fig.8 and COV values are shown in Fig.9, where U_{app} is COV and E_a is icing field.

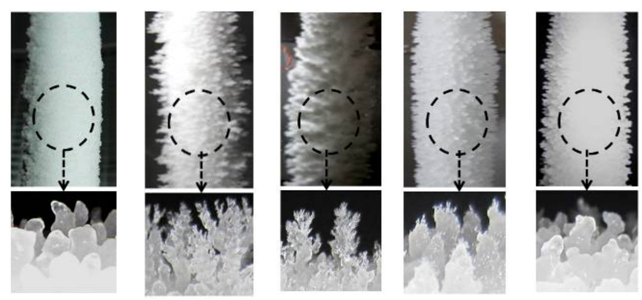

0kV/cm (a) 5kV/cm (b) 10kV/cm (c) 15kV/cm (d) 20kV/cm (e)

Figure 8. Rime icing morphology under different field strength

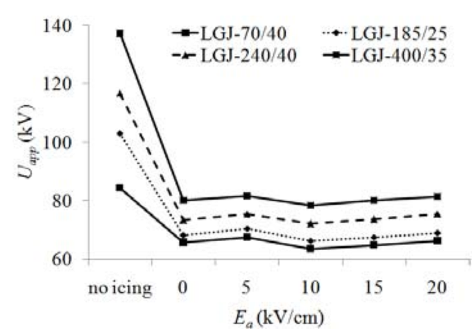

Figure 9. Corona onset voltage under different icing field

As shown in Fig.8 and Fig.9, various rime ice-tree forms will lead to distinct values of COV. Rime has a great influence on COV even conductor was iced under 20kV/cm where ice-trees are the shortest and tips are blunt, COV was only about 50 percent of naked wires. The main reason is that tips of rime ice-tree will make conductor surface roughness, so electric field around conductor can be distorted seriously by ice-tree, and then field strength could be enlarged significantly. Therefore, even wires operating under low voltage, corona discharge prone to appear on the iced surface and result in significant decrease in COV values.

Wires with larger diameter will get higher COV values when they are iced under the same condition which means rime causes little impacts on thicker wires than thinners. However, the reason why declination of COV on thicker wires is more serious than thinners at the beginning of icing is that thinners are easier to form a thicker ice coating at the beginning which can weaken field distortion by rime.

In Fig.9, COV shows a fluctuation trend with the increasing in icing field. This is because droplets will be attracted by electric field force under 0~5kV/cm which makes the lift velocity of thickness greater than ice-tree, so COV will go up slightly during this stage. When icing under 10kV/cm, ice-tree become longer and sharper as shown in Fig.8(c) while thickness increase is limited, so distortion effect by ice-tree plays a leading role and COV decline to the lowest point. However, ice thickness will decrease when in 15~20kV/cm and increased field intensity will heighten corona activity on tips of ice-tree, then ion bombardment and leakage current will cause the tips of ice-tree degradation, so the influence of filed distortion by rime will reduce and COV will go up again.

3.2 AFFECTED BY ICING EXTENT

To explore the law of how icing extent impacts conductor COV, icing time was set from 15min to 60min and then COV was measured by the UV camera, results are shown in Fig.10, where T is icing time and U_{app} is COV.

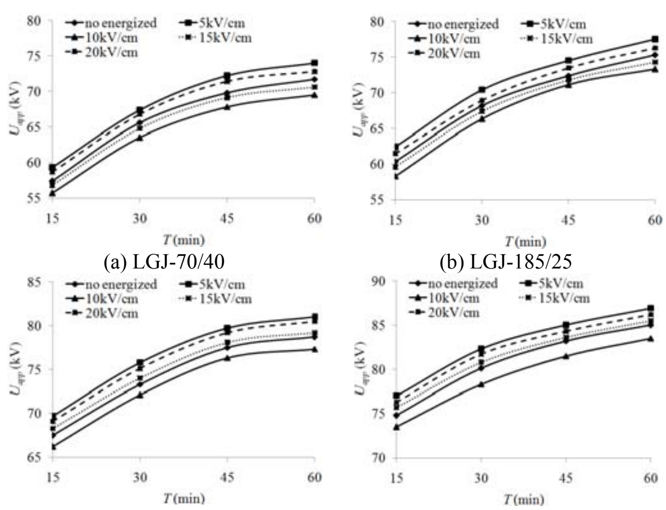

Figure 10. Corona onset voltage under different icing time

In Fig.10, with increase of icing time, COV will go up gradually with the speed slow down. This is because rime belongs to dry growth characteristics, the shape of ice-tree will not change with the different icing extent, however, ice thickness will weaken distortion effect of ice-tree and rise the COV. Meanwhile, collision efficiency of droplets will be reduced by the increasing in equivalent diameter of wires, so longer the icing time is, slower the COV goes up.

3.3 IMPACTED BY WATER CONDUCTIVITY

Conductivity on the iced surface of transmission line will be very high because the super-cooled water may be polluted by charged particles before it's condensation [21]. High conductivity can raise the number of conductive ionic so electrical performance of conductor will be reduced, for this reason it's necessary to study effect law of different conductivity on COV. So four kinds of conductivity namely 30, 400, 800, 1200$\mu s/cm$ were applied for icing wires 30min under 15kV/cm. Rime morphology on LGJ-185/25 and COV of four wires under different conductivity are shown in Fig.11 and Fig.12 respectively, where γ_{20} is conductivity in 20℃。

(a) 30$\mu s/cm$ (b) 400$\mu s/cm$ (c) 800$\mu s/cm$ (d) 1200$\mu s/cm$

Figure 11. Rime shapes under different conductivity

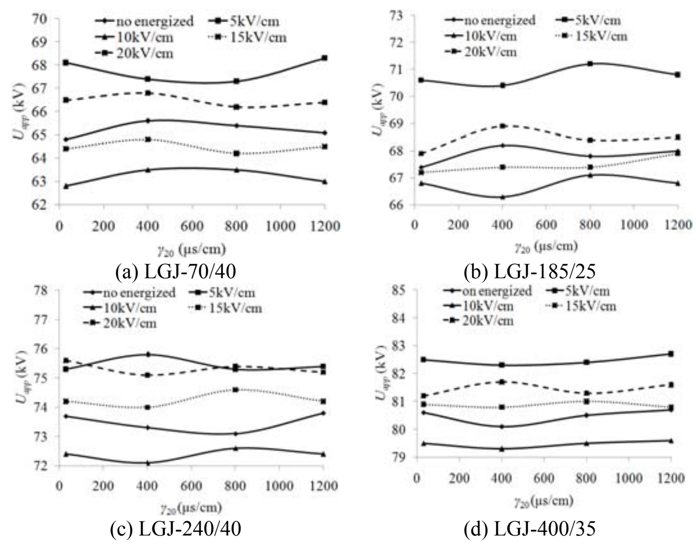

Figure 12. Corona onset voltage under different conductivity

As shown in Fig.11 and Fig.12, different conductivity has very little effect on rime morphology and COV values when wire was iced under 15kV/cm. This is because there is no direct relationship between field force and conductivity. Rime belongs to dry growth characteristic, that means droplets will be frozen quickly when it reaches wire surface due to the low temperature [22], so conductivity has little impact on corona discharge. Moreover, owing to the complex morphology of rime and ice-tree tips, COV would not be changed much by different conductivity.

4 SIMULATION SETTING AND ANALYSIS

4.2 FINITE ELEMENT MODEL OF ICE-TREE

Taking advantage of Maxwell software, the finite element model was established according to 4.1 section, then rime parameters of LGJ-185/25 conductor under different icing field and icing time are shown in Tab.4 and Tab.5 respectively, parameters of four wires under 15kV/cm in 30min are shown in Tab.6, where E_a is icing field, K is ice thickness, bottom diameter and height of ice-tree are M and N respectively.

Table 4. Rime Parameters of LGJ-185/25 in 30min under various fields

E_a (kV/cm)	K (mm)	M (mm)	N (mm)
0	4.1	1.55	1.45
5	5.3	1.56	2.54
10	5.9	1.54	5.15
15	4.6	1.57	1.83
20	3.8	1.54	1.01

Table 5. Rime Parameters of LGJ-185/25 in 30min under 0kV/cm

	15min	30min	45min	60min
K (mm)	2.6	4.1	5.3	5.9
M (mm)	1.56	1.55	1.53	1.55
N (mm)	1.43	1.45	1.44	1.45

Table 6. Rime Parameters of four wires in 30min under 15kV/cm

	LGJ-70/40	LGJ-185/25	LGJ-240/40	LGJ-400/35
K (mm)	5.2	4.6	4.1	3.8
M (mm)	1.53	1.57	1.54	1.56
N (mm)	1.84	1.83	1.88	1.87

Taking the iced conductor into coaxial electrode whose diameter is 2m, conductor's material is set to Aluminum and relative permittivity of rime is 75, background region is set to Vacuum while boundary of corona cage is set to balloon border condition namely infinity potential is zero, then generating automatic mesh and finally calculation.

Moreover, this paper is mainly concerned with whether ice-tree shapes can impact on conductor's COV, so the finite element method and 2D simulation models are established in section 4.1 and 4.2 respectively. The simulation model is shown in Fig.14 (not in proportion).

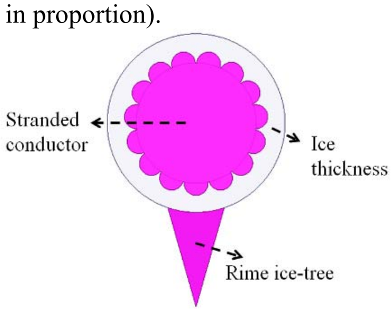

Figure 14. Simulation model of rime

4.3 FIELD STRENGHT OF ICED CONDUCTOR

Maxwell software is applied to calculate field strength of LGJ-185/25 after icing and results are shown in Fig.15. Along with increasing in icing time under 0kV/cm, field density is shown in Fig.16.

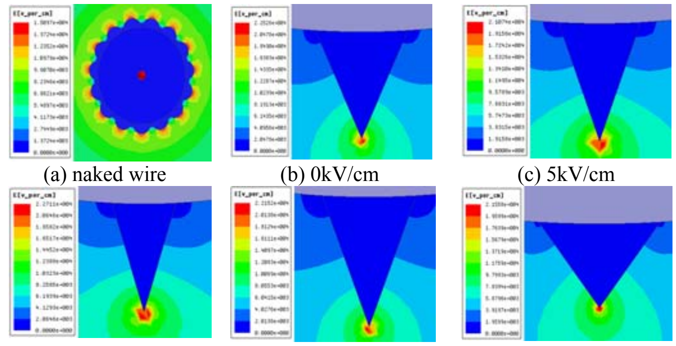

(a) naked wire (b) 0kV/cm (c) 5kV/cm

(d) 10kV/cm (e) 15kV/cm (f) 20kV/cm

Figure 15. Field strength of LGJ-185/25 after icing under various fields

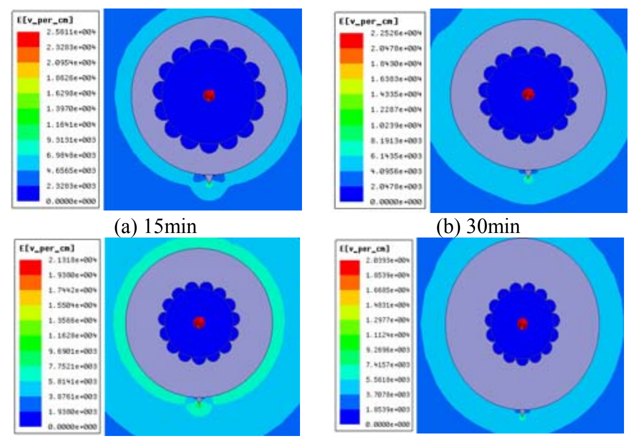

(a) 15min (b) 30min

(c) 45min (d) 60min

Figure 16. Field strength of LGJ-185/25 after icing in different time

As shown in Fig.15, field strength of naked conductor was 15kV/cm when it was applied 66kV voltage to its surface. If iced wire continued to be operated under 66kV, the maximum field intensity on conductor surface is 22.5, 21.1, 22.7, 22.2 and 21.5kV/cm respectively which are larger than naked wires.

In Fig.16, if LGJ-185/25 keeps on operating in 66kV with different icing extent, field strength were 25.6, 22.5, 21.3 and 20.4kV/cm respectively, it was a gradually downward trend with the speed slowing down. Calculation results agree with experimental results.

Four wires were iced for 30min under 15kV/cm and then they were operated under 40kV in corona cage, different field strength is shown in Fig.17.

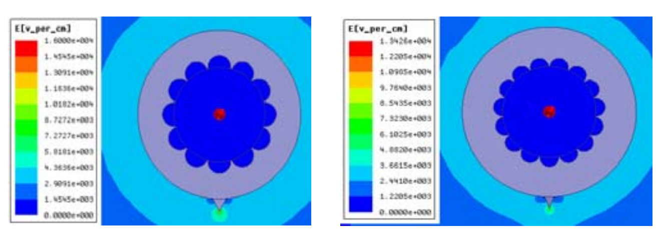

LGJ-70/40 LGJ-185/25

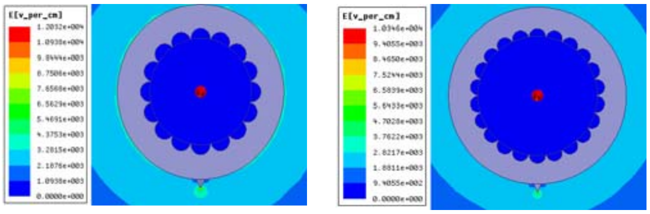

LGJ-240/40 LGJ-400/35

Figure 17. Field strength of four iced wires operating in same voltage

In Fig.17, maximum field strength of four iced wires are 16, 13.4, 12kV/cm and 10.3kV/cm respectively, which showed a decrease trend. This is because wires with larger diameter will get lower field density than thinners in coaxial electrode when applied the same voltage, so corona phenomenon on thinners will be easier to appear because of higher surface field strength than thicker ones.

5 CONCLUSION

Rime will reduce COV at least 50% and various icing field leads to different conductor COV because of the distinct ice-tree shapes. Field distortion on iced wires is so serious which could result in corona discharge even operating under low voltage, and the COV could be reduced too. Maximum field strength will be lessened by increased ice thickness, and COV will go up with the rate slowing down gradually. Different conductivity has very little impact on rime morphology or COV values. When ice-trees are longer and shaper, field strength of iced conductor would be greater, vice versa. Iced wires with larger equivalent diameter will be more difficult to appear corona discharge than thinners when they are operating under same voltage.

ACKNOWLEDGMENT

This work was supported by National Basic Research Program of China (973 Program: 2009CB724501/502/503) and State Key Laboratory Project (2007DA10512708101, 2007DA10512708102).

REFERENCE

[1] L. Shu, B. Luo, Q. Hu, X. Jiang, T. Li, Y. Zhang “Comparison and Analysis of Icing Performance Between T-type Wire and Ordinary Stranded Wire,” High Voltage Engineering, vol. 38, no. 6, pp. 1466-1472, 2012 (in Chinese).

[2] X. Jiang and H. Yi, *Icing and Protection for transmission lines*, Beijing, China Electric Power Press, 2001 (in Chinese).

[3] I. Ndiaye, I. Fofana and M. Farzaneh, “Contribution to the study of the appearance and development of corona discharges on a surface of ice,” Canadian Conference. Electrical and Computer Engineering, vol.1, Page(s): 639 – 642, 2003.

[4] Q. Hu, L. Shu, X. Huang, Q. Yuan, L. Gong and R. Lin, “Conductor’s AC Corona Onset Voltage Prediction Under Different Atmospheric Parameters and Conductor Surface Conditions,” High Voltage Engineering, vol. 36, no. 7, pp. 1669-1673, 2010 (in Chinese).

[5] M. Farzaneh and J. L. Laforte, “Ice accretion on energized conductors by AC or DC : a laboratory investigation of ice treeing,” International Journal of Offshore and Polar Engineering, vol. 4, no. 1, pp. 40-47, 1994.

[6] X. Jiang, L. Shu and C. Sun, “*Insulation of Electric Power system under Pollution and Icing conditions*,” Beijing, China Electric Power Press, 2009 (in Chinese).

[7] C. L. Phan and J. L. Laforte, “The influence of electro-freezing on ice formation on high-voltage DC transmission lines,” Cold Regions Science and Technology, vol. 4, no. 1, pp. 15-25, 1981.

[8] H. Gildas, “Theoretical evaluation of Peek’s law,” IEEE Trans. Industry Applications, vol. 20, no. 6, pp. 1647-1651, 1984.

[9] D. B. Phillips, R. G. Olsen and P. D. Pedrow, “Corona onset as a design optimization criterion for high voltage hardware,” IEEE Trans. Dielectrics and Electrical Insulation, vol. 7, no. 6, pp. 774-751, 2000.

[10] L. Boulet, L. Cahill and B. J. Jakubczyk, “Alternating Current Corona in Foul Weather II - Below Freezing Point,” IEEE Trans. Power Apparatus and Systems, vol. 85, no. 6, pp. 649-656, 1966.

[11] X. Lai, L. Shu, X. Jiang, D. Yu and J. Zhang and M. Farzaneh, “Research on Initial Corona Characteristics of Icicle to Ice-Covered Plane Model under Positive Polarity,” Power System Technology, vol. 30, no. 7, pp. 32-36, 2006 (in Chinese).

[12] L. Shu, T. Li, X. Jiang, Q. Hu, B. Luo and Z. Yang, “Influences of AC Electric Field Strength on Conductor Rime Icing Performance,” Proceedings of the CSEE, vol. 32, no. 19, pp. 140-147, 2012 (in Chinese).

[13] R. Gunn, “The Electrification of Precipitation and Thunderstorms,” Proceedings of the IRE, pp. 1331-1358, 1957.

[14] X. Jiang, Q. Shen, “Experimental Research on Influence of Environmental Parameters on the Conductor Icing Thickness”, High Voltage Engineering, vol. 36, no. 5, pp. 1096-1100, 2010 (in Chinese).

[15] F. Lu, S. Hua, Y. Liu, Q. Wan, Z. Zhao, “AC Conductors' Corona-Loss Calculation and Analysis in Corona Cage”, IEEE Trans. Power Delivery, vol. 27, no. 2, pp. 877-885, 2012.

[16] Y. Liu, Du, B.X, “Recurrent plot analysis of leakage current on flashover performance of rime-iced composite insulator,” IEEE Trans. Dielectrics and Electrical Insulation, vol. 17, no. 2, pp. 465-472, 2010.

[17] E.G Da Costa, T.V Ferreira, et al. “Characterization of polymeric insulator using thermal and UV imaging under laboratory condition”, IEEE Trans. Dielectrics and Electrical Insulation, 2009, 16(4): 985-992.

[18] B. Ma, W. Zhou, T. Wang, et al, “Corona discharge of the severe non-uniform electric field based on the UV-light imaging technology,” High Voltage Engineering, vol. 32, no. 7, pp. 13-16, 2006 (in Chinese).

[19] A. Zangeneh, A. Gholami, V. Zamani, “A New Method for Calculation of Corona Inception Voltage in Stranded Conductors of Overhead Transmission Lines”, IEEE International Power and Energy Conference, PECon '06. pp. 571-575, 2006.

[20] M. Farzaneh, T. O. Melo, “Properties and effect of freezing rain and winter fog on outline insulators”, Cold Regions Science and Technology, Vol. 19, pp. 33-36, 1990.

[21] M. Chiesa, A. J. Melheim, A. Pedersen, et al, “Forces Acting on Water Droplets Falling in Oil Under The Influence of An Electric Field: Numerical Predictions Versus Experimental Observations”, European Journal of Mechanics B-Fluids, 24(6): 717-732, 2005.

[22] Z. Feng, J. Yang, C. Wan and S. Xie, “Corona discharge analysis on high voltage transmission line with burrs,” Heilongjiang Electric Power, vol. 31, no. 6, pp. 441-445, 2009 (in Chinese).

PROCEEDINGS

IWAIS

IWAIS 2013 - 15TH INTERNATIONAL WORKSHOP ON ATMOSPHERIC ICING OF STRUCTURES

COMPUSULT